

**BN-DOPED π -CONJUGATED MATERIALS: FROM
MONOMERIC TO POLYMERIC BORAZINE
ARRAYS**

Jacopo Dosso

PhD Thesis

June 2020



Thesis submitted in accordance with the requirements for
the degree of Doctor of Philosophy

Supervisor:

Prof. Dr. Davide Bonifazi

School of Chemistry
Cardiff University

ACKNOWLEDGMENTS

First, I would like to thank Prof. Dr. Davide Bonifazi for giving me the opportunity to work in his group. His constant support and enthusiasm have been very inspirational and important during my PhD.

Second, I would like to thank Dr. Grazia Bezzu for the precious help with this manuscript and for all the nice chats at lunchtime. Your kindness and patience are admirable.

Many thanks to Tommaso, Cataldo, Rodolfo and Andrey. You contributed to make this PhD a great experience.

I am grateful to the borazine team members: Francesco, Davide, Maria, and Diem. Your help has been fundamental during my time inside and outside the lab.

Thanks to all the components of the Bonifazi research group for your help and patience, each one of you taught me something important during this experience.

I am particularly grateful to Dr. Tanja Miletic for her help at the beginning of my experience in Cardiff. You have been inspirational during my master thesis and I will never forget your help when I first got here.

I want to thank my parents for the constant support and for always believing in me. Without you this would have never been possible.

Special thanks to Ilaria, you made this time in Cardiff amazing and your presence helped me through the hard times. You are a special and talented person, always believe in yourself!

Finally, I want to thank all my friends. You always managed to make me feel close despite the distance. Your friendship is a real honour.

Fuarce Friû!

TABLE OF CONTENTS

ABSTRACT	VI
LIST OF ABBREVIATIONS	IX
CHAPTER 1	1
INTRODUCTION	
1.1 Graphene: an overview	1
1.2 Towards semiconducting graphene.....	4
1.3 Physically constrained graphene: nanoribbons	5
1.4 Graphene heteroatom doping	7
1.4.1 Boron doped graphene.....	8
1.4.2 Nitrogen doped graphene.....	8
1.4.3 Oxygen doped graphene.....	10
1.4.4 Phosphorus and Sulphur doped graphene	10
1.4.5 Boron-Nitrogen doped graphene	10
1.5 Top-down synthesis limits	14
1.6 Bottom-up approach: Synthesis of BN-doped PAHs.....	17
1.7 BN clusters: borazines	26
1.7.1 Borazine synthesis	26
1.7.2 Mechanism of formation	28
1.7.3 Stability of borazine derivatives	30
1.8 Borazines as precursors in the synthesis of nanographenes.....	33
1.9 Outlines of the dissertation.....	35
1.10 References	36
CHAPTER 2	43
BORAZINE-DOPED NANOGRAPHENES: SYNTHESIS OF HEXA-PERI-HEXABENZOBORAZINOCORONENE	
2.1 Aim of the project	45
2.2 Previous work towards the synthesis of 2-1	46
2.3 <i>Ortho</i> -functionalized borazines as precursors in the BN-doped nanographenes synthesis.....	47
2.4 Synthetic strategies for planarization of <i>ortho</i> -halo borazines.....	49
2.5 Retrosynthetic approach towards 2-1	51
2.6 Bromo Hexaaryl-borazine.....	51
2.7 Chloro Hexaaryl-borazine.....	53
2.8 Fluoro Hexaaryl-borazine	56
2.9 Optimization of the reaction conditions.....	62
2.10 Synthesis of unsubstituted HBBNC 1-1	66
2.11 Effects of different WCAs on the reaction outcome	70
2.12 Synthesis of functionalized HBBNC derivatives.....	72
2.13 Conclusions and perspectives.....	77
2.14 References	78
CHAPTER 3	81
BN vs CC: EFFECTS OF BORAZINE DOPING ON PROPERTIES OF PAHs	
3.1 Aim of the Project.....	83
3.2 Synthesis of soluble hexa- <i>peri</i> -hexabenzocoronene	85
3.3 Synthesis of all-carbon gulf derivative	86
3.4 Synthesis of pyrilium gulf derivative	89
3.5 Crystal structure comparison.....	93

Table of contents

3.6 ESP Plots	94
3.7 HBBNC solvates	95
3.8 Aromaticity of heteroatom doped nanographenes	98
3.9 UV-Vis Comparison	102
3.10 Electrochemistry	105
3.11 HOMO-LUMO calculations.....	108
3.12 Conclusions and perspectives	109
3.13 References	110
CHAPTER 4.....	111
SYNTHESIS OF MULTI-BORAZINE SYSTEMS: TOWARDS EXTENDED BORAZINE-DOPED NANOGRAPHENES	
4.1 Aim of the project.....	112
4.2 Synthesis of test Multi-borazine derivatives	113
4.3 UV-Vis properties of multi-borazine derivatives.....	123
4.4 Synthesis of fluorine-functionalized Multi-borazine derivatives.....	126
4.5 Conclusions	131
4.6 References	131
CHAPTER 5.....	133
BORAZINE-DOPED POLYPHENYLENIC POLYMERS: SYNTHESIS AND APPLICATIONS	
5.2 Aim of the project.....	138
5.3 Synthesis of Monomer 5-4	139
5.4 Synthesis of Polymer 5-1	142
5.5 Solid state NMR studies.....	144
5.6 PXRD on 5-4 Sample.....	147
5.7 Gel formation and rheological studies	148
5.8 BN-Polymer as support in solid state electrolytes (SSE).....	151
5.9 Conclusion.....	158
5.10 References	158
CHAPTER 6.....	162
EXPERIMENTAL PART	
6.1 Instrumentation	162
6.2 Materials and general methods.....	166
6.3 X-Ray Measurements	166
6.4 PXRD Parameters	174
6.5 Synthetic Procedures.....	176
APPENDIX A: ¹H, ¹³C, ¹¹B-NMR AND HRMS SPECTRA OF SELECTED MOLECULES.....	220

ABSTRACT

Since the first isolation of graphene by Geim and Novoselov in 2004, a new field involving the preparation of tailored derivatives of this material has been exponentially growing. One of the major targets of this scientific endeavour is the conversion of graphene from conductor to semiconductor, leading to a new generation of miniaturized high-performance transistors and spintronics. To prepare semiconductors based on graphene, many different strategies have been pursued, mostly based on physical methods, or doping of graphene. In the latter approach, the most interesting results have been achieved using surface assisted chemistry, resulting in the formation of graphene presenting various heteroatoms as dopants (B, N, O, S) and semiconducting properties. However, this approach has been often limited by a difficult control over structure and inclusion of the dopants. A possible solution to these limitations comes from the preparation of BN-doped graphene. This highly polar couple is isoelectronic and isosteric with CC double bonds, thus allowing for an inclusion of the dopant without important changes in graphene structure. This results in a material with very similar morphology but different opto-electronic properties, featuring a wider bandgap compared to pristine graphene. From this point of view, evidence of a dependence of the bandgap size of graphene from doping percentage and position was obtained from theoretical investigations, highlighting the importance of a precise synthesis of the materials, which is not achievable with top-down methods. Consequently, a bottom-up approach in which BN-doped PAHs are synthesised using organic synthesis and then used as building blocks to form extended systems, represents the most reliable strategy towards precisely doped materials.

A vast library of BN-doped PAHs has been synthesised by many different groups using different precursors, doping patterns, and strategies. Among these, the use of functionalized borazines as precursors has been often neglected and limited to the synthesis of the archetypal borazine-doped nanographene, namely “Hexa-*peri*-hexabenzoborazinocoronene” (HBBNC). The high interest towards this molecule, which can be considered as the smallest unit of a borazine-doped graphene (Figure 1A), is related to theoretical studies predicting an efficient HOMO-LUMO gap widening in this derivative compared to the full carbon congener. Synthetic attempts resulted in HBBNC formation in low yield as very insoluble product, thus resulting in incomplete characterizations, which failed to produce comprehensive experimental evidence for the effect of the borazine doping on nanographene systems.

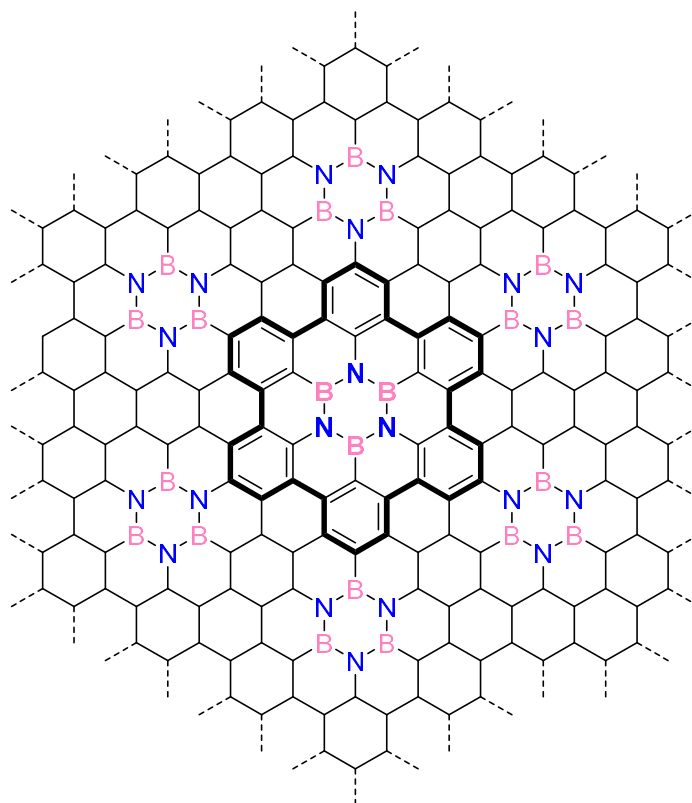


Figure 1A: Example of a borazine-doped graphene and HBBNC as its smallest unit.

In this dissertation we present a synthetic strategy towards soluble HBBNC derivatives, leading to an extensive characterization of the borazine doping effects, thus providing a solid experimental confirmation of the ability of this doping strategy to widen the HOMO-LUMO gap of PAHs.

This work is presented in 5 chapters, starting with an introduction regarding the state-of-the-art results in the field in *Chapter I*. In this part the most important achievements in the preparation of doped graphene and PAHs are reported, thus giving an overview on the open questions in the area, which will be addressed in the following chapters.

Chapter II reports the synthesis of *ortho* halogen functionalised borazines and their use in the preparation of soluble HBBNC derivatives (Figure 2A). Various approaches are investigated to obtain the full planarization of the borazine precursors, leading to the successful use of fluoro hexaaryl-borazines in presence of silylium ion reagents resulting in a six-fold Friedel-Crafts like reaction producing the desired soluble HBBNC. Along with the target molecule, different by-products were formed depending on the precursors used. These PAHs, presenting $B_2N_3H_2$ and B_3N_2O doping patterns, were isolated and characterized as well. Moreover, the suitability of the reaction towards a variety of functional groups has been tested, leading to a clear understanding of the viable precursors for this reaction.

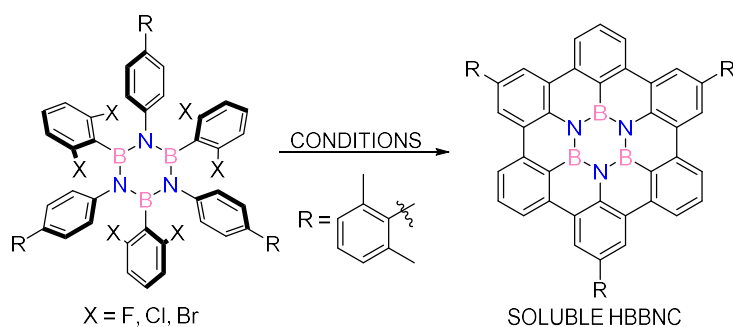


Figure 2A: Strategy towards the synthesis of soluble HBBNC.

In *Chapter III* a complete structural and opto-electronic characterization of the BN-doped materials previously obtained is reported. This is enriched by the comparison with tailored reference compounds, leading to an unequivocal assessment of the effect of doping on the molecule properties. The results displayed in this chapter represent an exhaustive characterization of a borazine-doped hexabenzocoronene, thus filling an important gap in the literature on the topic by proving the ability of borazine doping to widen the HOMO-LUMO gap of PAHs.

Chapter IV presents the preparation and study of extended borazine precursors (multi-borazines) which can be used for the synthesis of borazine-doped nanoribbons. The synthesis is enriched by a complete study on the stability and properties of these unprecedented molecules. The results of these investigations allowed us to synthesise a fluorinated dimeric multi-borazine system which can be used in a future synthesis of borazine-doped extended graphene systems.

Finally, in *Chapter V*, an approach towards borazine-doped polymeric materials is developed relying on the use of ethynyl functionalised borazines undergoing [4+2] cycloadditions with dimeric cyclopentadienone reagents. The result of this reaction is the formation of a borazine-doped polymeric polyphenylene, which was extensively studied using solid state NMR. The material proved to form gels efficiently in chlorinated solvents and due to the presence of the borazine rings and the high thermal and chemical stability, was used as a support material in solid state electrolytes.

LIST OF ABBREVIATIONS

°	Degrees
ϵ	Molar extinction coefficient
λ	Wavelength
σ	Conductivity
Φ_f	Quantum yield of fluorescence
μ	Dipolar moment
$\tau_{f/ph}$	Fluorescence/phosphorescence lifetime
t_{Li}^+	Lithium transference number
A	Absorbance
Å	Angstrom
[A]	Concentration of molecule A
Abs	Absorption
ACID	Anisotropy of the Induced Current Density
Ar	Aryl
a.u.	Arbitrary unit
ATR	Attenuated total reflectance
BET	Brunauer Emmett Teller
Bu	Butyl
°C	Celsius degrees
CDHC	Cyclo-dehydrochlorination
cm	Centimetres
COF	Covalent organic framework
CP/MQ/MAS	Cross Polarization/Multi quantum/Magic angle spinning
CV	Cyclic voltammetry
CVD	Chemical vapour deposition
D	Debye
DDQ	2,3-Dichloro-5,6-dicyano-1,4-benzoquinone
DFT	Density functional theory
DMF	Dimethylformamide
DSC	Differential scanning calorimetry
ΔE	Energy gap

List of abbreviations

Eq.	Equivalent
Em.	Emission
ESI	Electrospray ionisation
ESP	Electrostatic surface potential
FT	Fourier transform
eV	electron volt
rec-GPC	Recycling gel permeation chromatography
GIAO	Gauge independent atomic orbitals
GO	Graphene oxide
GQD	Graphene quantum dots
h	hour
$t_{1/2}$	half-life
HBBNC	Hexa- <i>peri</i> -hexabenzoborazinocoronene
HBC	Hexa- <i>peri</i> -hexabenzocoronene
<i>h</i> -BN	Hexagonal Boron-Nitride
HOMO/LUMO	Highest occupied molecular orbital/Lowest occupied molecular orbital
HR	High resolution
K	Kelvin degrees
KHMDS	Potassium hexamethyldisilazide
LDA	Lithium diisopropylamide
LF-NMR	Low frequency NMR
LSV	Linear sweep voltammetry
LR	Low resolution
IR	Infra-red
min	Minutes
MALDI	Matrix-assisted laser desorption/ionisation
MAS	Magic angle spinning
Me	Methyl
Mes	Mesityl/(2,4,6-trimethylphenyl)
mp	Melting point
MQMAS NMR	Multi quantum magic angle spinning NMR
MS	Mass spectrometry

List of abbreviations

<i>m/z</i>	Mass-to-charge ratio
NICS	Nucleus independent chemical shift
nm	Nanometres
NMR	Nuclear magnetic resonance
Nu ⁻	Nucleophile
ns	Nanoseconds
ODCB	<i>Ortho</i> -dichlorobenzene
OTIPS	O-Tri-isopropylsilyl
PAHs	polycyclic aromatic hydrocarbons
Ph	Phenyl
PIFA	(Bis(trifluoroacetoxy)iodo)benzene
ppm	Parts per million
Py	Pyridine
pXRD	Powder X-ray diffraction
Pa	Pascal
RMSD	Root mean square deviation
r.t.	Room temperature
S	Siemens
SCC	Silica column chromatography
SC-XRD	Single crystal X-Ray diffraction
SEM	Scanning electron microscopy
SSE	Solid state electrolyte
SSS	Short stress sweep
STM	Scanning tunnelling microscopy
t	Time
TADF	Thermally activated delayed fluorescence
TBAF	tetrabutylammoniumfluoride
TCB	trichlorobenzene
TEGDME	Tetraethylene glycol dimethyl ether
TEM	Transmission electron microscopy
TGA	Thermal gravimetric analysis
THF	Tetrahydrofuran
TIPS	Triisopropylsilane

List of abbreviations

TLC Thin layer chromatography

TMS Trimethylsilane

TOF Time of flight

UHV Ultra high vacuum

UV-Vis Ultraviolet-visible light

V Volt

vdW van der Waals

WCA Weakly coordinating anion

w/w weight on weight

wt Weight

CHAPTER 1

INTRODUCTION

1.1 Graphene: an overview

Carbon is one of the most studied elements in the periodic table, not only because it represents the core of organic chemistry, but even because it is able to generate an incredible chemical diversity through its valency.^[1] Due to this, in its elemental form, carbon can be found in many different allotropes which span from diamond to graphite.^[2,3] Amongst all these possible allotropes, great attention has been devoted in the last 30 years to the so-called carbon nanoforms,^[4] represented by fullerenes,^[5,6] nanotubes,^[7-10] nanohorns,^[11] nanodiamonds,^[12,13] nanorods^[14] and graphene.^[15,16] The large amount of studies, both theoretical and experimental, conducted on these materials is driven by the potential technological applications arising from a set of very appealing properties, which largely depend on the material structure.^[17] From this point of view, graphene is certainly one of the most investigated carbon allotropes and it has been the subject of many theoretical studies in the last decades.^[18] Due to the predicted thermodynamic instability of this material,^[19] its possible existence as one atom thick crystalline layer has been matter of debate among the scientific community until its isolation by Geim and Novoselov in 2004, who managed to mechanically exfoliate graphite leading to the first identification of free-standing graphene sheets.^[16]

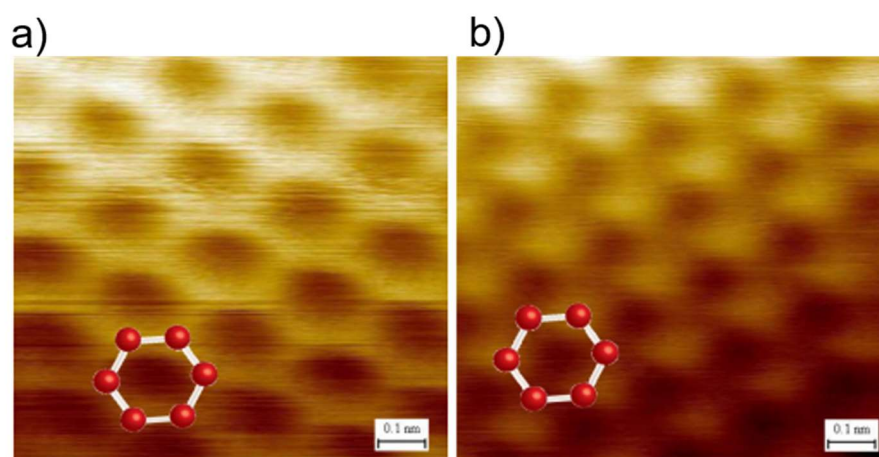


Figure 1.1: a): STM images of single layer graphene with model of the underlying structure reported; b): STM image of multilayer portion of graphene.^[20]

After its successful isolation, experimental proof of the nature of this material was obtained, confirming the predicted structure constituted by sp^2 hybridized carbon atoms arranged in a periodic honeycomb structure, with CC distances of 1.42 Å.^[15] This peculiar arrangement is determined by the three sp^2 orbitals of each atom, which are involved in sigma bonds with neighbour carbons originating the honeycomb σ scaffold,

while the remaining p_z orbitals are engaged in a π system extended over the whole lattice (Figure 1.1).^[21]

Graphene's most interesting properties arise from its peculiar structure and constitute the main reason for the huge interest towards this material. In this regard, outstanding mechanical, thermal and electrical properties have been highlighted in many studies performed on this material. Graphene presents a very high thermal conductivity ranging from 2000 to 6000 W m K^{-1} ^[22,23] along with a stability up to 500 °C in air^[24] which, coupled with a high Young modulus of 1.0 ± 0.1 TPa,^[25] make this material very promising for applications that require mechanical and thermal resistance. The electronic structure and properties of graphene are perhaps the most interesting features of this material, which presents room temperature quantum Hall effect^[26] and behaves like a semi-metallic conductor with a very high charge carrier mobility, spanning from around 1×10^4 up to 4×10^4 $\text{cm}^2 \text{V}^{-1} \text{s}^{-1}$ with a maximum theoretical value of 2×10^5 $\text{cm}^2 \text{V}^{-1} \text{s}^{-1}$ depending on quality of sample and experimental conditions.^[27,28] Furthermore, temperature-independent carrier mobility between 10 K and 100 K was observed in the material.^[29] These outstanding electronic properties contributed to create great expectations around graphene, due to its potential use in a new class of ultra-thin high-performance devices, which could lead to a revolution in the field of miniaturized electronics.^[21,30] Moreover, properties such as quantum Hall effect, are of high interest in the growing field of spintronics, with potential applications in quantum devices.^[31] The ability of graphene to behave like a semi-metallic conductor can be explained by observing the structure of the valence and conducting band, which present contact points (Dirac Points) at the vertices of the Brillouin zone (Figure 1.2).^[32]

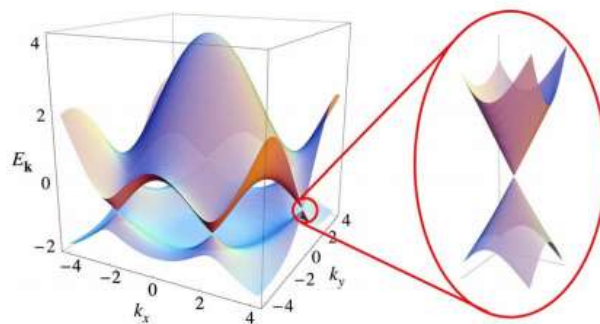
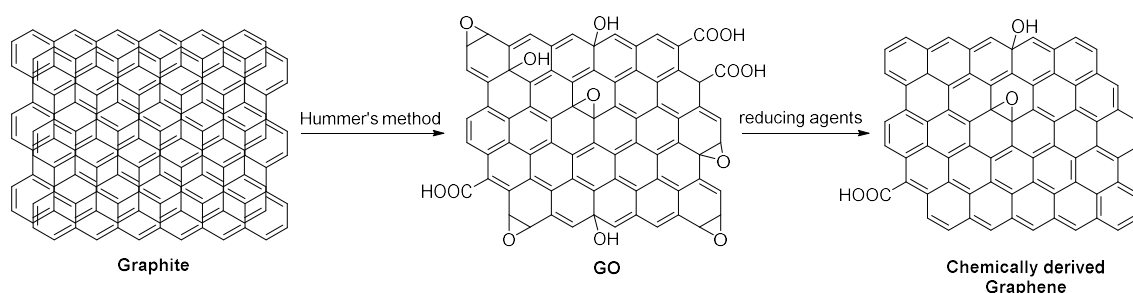


Figure 1.2: Structure of the energy bands of graphene with zoom on the Dirac points. k_x k_y reported in \AA^{-1} .^[32]

This electronic feature results in a semi-metallic conductor behaviour and in a pronounced ambipolar field effect, allowing for a continuous change from holes to electrons, depending on the applied electric field. The properties of graphene are

heavily influenced by the quality of the layer, in fact, the presence of Stone-Wales defects, vacancies or irregular edge morphologies are all factors that can result in variable properties.^[15] From this point of view, one of the major challenges towards future applications is the ability to prepare high quality sheets in a reproducible way. Consequently, various production methods have been investigated in the last decades, following the first synthesis using mechanical exfoliation.^[16,33,34] Generally, graphene is prepared by top-down approaches in which sheets of the material are obtained starting from graphite or surface based methods such as epitaxial growth by annealing suitable gases on metallic substrates (substrate-based methods). The latter resulting in extended sheets that are then cut down to the desired dimensions using techniques such as photolithography. The first synthesis of graphene involved a micromechanical cleavage of graphite with cellophane tape and still represents an excellent example of top-down strategy, as it can produce high quality sheets with dimensions bigger than $100 \mu\text{m}^2$. The main limit of this approach lies in the small amounts of graphene that can be obtained, which precludes the mass production needed for device applications. A possible solution is represented by the synthesis of chemically derived graphene using graphene oxide (GO).^[35,36] In this strategy, graphite is oxidized, and the resulting GO layers are then suspended by applying mechanical force (sonication) relying on the strong interactions between the epoxide, hydroxy and carboxy groups on GO and the water medium. Subsequent reduction of GO sheets with hydrazine produces the desired graphene in a cheap and scalable manner (Scheme 1.1).^[36]



Scheme 1.1: Chemical synthesis of graphene starting from graphite *via* Hummer's method.

Despite the obvious advantages of this method, many problems can arise; amongst all, the tendency to aggregate after reduction, leading to multiple layers and the possible defects due to incomplete reactions, which result in oxygenated graphene.^[34] Another common top-down method is the epitaxial growth of graphene sheets. In this method pioneered by De Heer, graphene is formed by heating silicon carbide at $1300 \text{ }^\circ\text{C}$ in UHV.^[37] Photolithography can then be used in order to pattern the sheets, obtaining material of the desired size for use in devices. The most used substrate-based graphene synthesis is based on chemical vapor deposition (CVD). In this technique, gases such as methane or other hydrocarbons are passed on a transition metal

surface at high temperature under vacuum, leading to the formation of extended graphene sheets. Both this method and the epitaxial growth allow the obtainment of high quality large area layers that can be recovered and transferred after etching/photolithography and used in devices.^[38] However, many challenges remain, in particular the difficult control of the layering during the synthesis of the sheets, which results in materials composed by two or more layers, affecting the properties of the resulting graphene.^[21]

1.2 Towards semiconducting graphene

Along with the above presented synthetic challenges, one of the major limitations in the use of this material in electronic devices is the absence of a bandgap. As previously stated, graphene presents contacts between the valence and conducting band, resulting in a semi-metallic conductor behaviour. This determines a poor I_{on}/I_{off} ratio in graphene-based devices, resulting in the impossibility of turning off the device completely. This phenomenon is due to the presence of carrier populations at any temperature, which make this material not suitable for many promising applications, such as transistors and “logic” applications. To convert graphene into a semiconductor, different strategies based on both physical and chemical methods, have been studied.

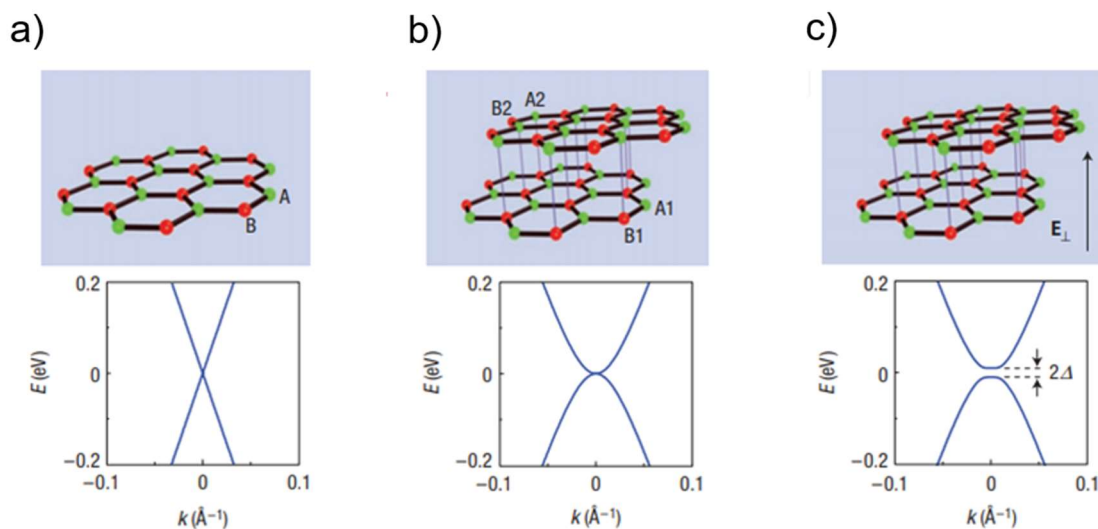


Figure 1.3: a,b) Schematic representations of monolayer and bilayer graphene with respective bandgap structure; c) Biased bilayer graphene with resulting open bandgap structure.^[39]

Physical methods present the advantage of using graphene without the need to modify it, thus avoiding problems related to side reactions or undesired variations in its properties and morphology.

In this context, some of the most valuable results have been obtained by biasing graphene bilayers as reported by Vandersypen and co-workers. This method relies on

stacking two layers of graphene and then applying an electric field perpendicular to the stack, resulting in the opening of a bandgap (Figure 1.3).^[39]

Another method predicted to open a bandgap in this material, is the application of uniaxial strain on graphene sheets, as shown by calculations reported in a work of Shen et al. In this study, the application of a 1% strain on graphene is predicted to open a 0.3 eV bandgap in the material due to the breaking of the sublattice symmetry.^[40,41] Finally, another promising approach is the growth of graphene layers on substrates able to induce a bandgap by interacting with its valence and conducting bands. Theoretical calculations suggest that growing graphene on a high bandgap insulator substrate like boron-nitride (*h*-BN) should result in the presence of a bandgap in the former.^[42,43] Despite these promising results, physical methods suffer from many drawbacks such as the difficulty in obtaining a fine control of the properties and the low versatility, related to the necessity to induce a bandgap in the material using external stimuli or substrates, often resulting in difficult setups. An optimum solution to this problem could be the development of graphene-based materials which are intrinsically semiconducting and from this point of view, the easiest solution is to physically constrain large sheets into smaller units: nanoribbons and nanodots.

1.3 Physically constrained graphene: nanoribbons

In the last years, many different groups have devoted huge efforts towards the study and development of graphene nanoribbons, proving that the electronic characteristics of these materials are largely dependent on the topology of the edges and the size of the molecules. In fact, a different edge structure can determine a change from a semi-metallic conductor behaviour (zig-zag edges) to the desired semiconducting one (armchair edges, Figure 1.4).^[44]

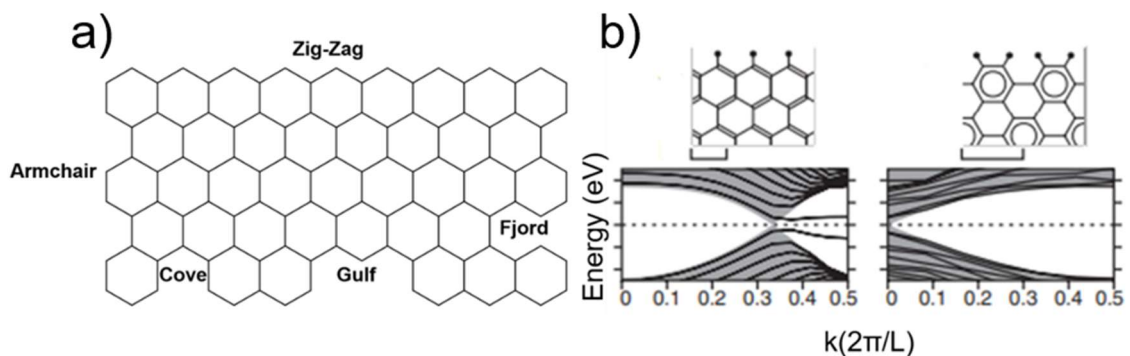


Figure 1.4: a): different edge topologies in graphene; b): band structure depending on edge topology in graphene nanoribbons.^[44]

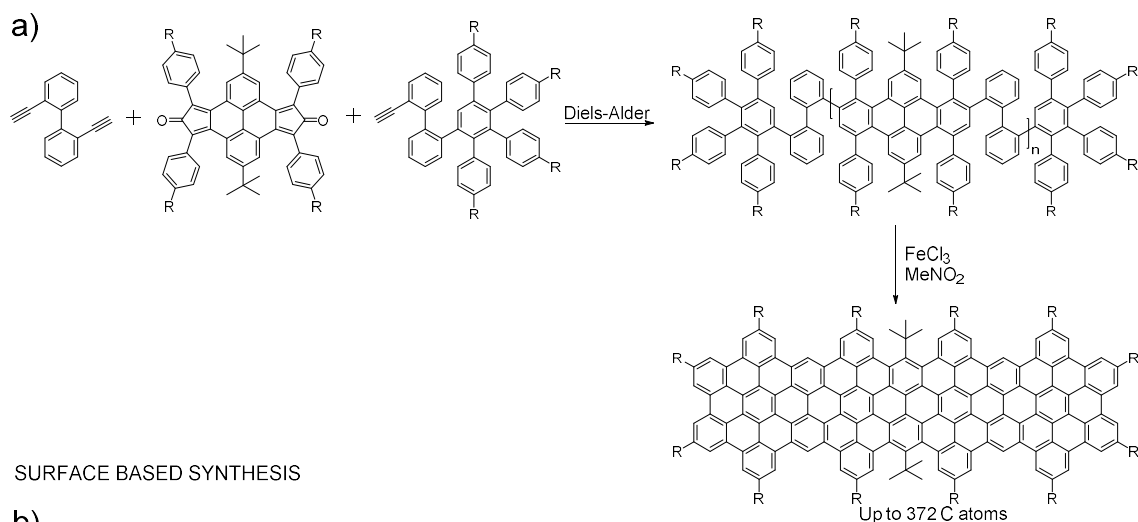
Even the size of the nanoribbons is important in determining the electronic properties: in general, as the size increases a general decrease in the bandgap is observed. From this point of view, to tailor the properties of the nanoribbons, a precise control of size and edges is required. Furthermore, when the dimensions of the nanoribbons get close to those of 0D molecules, a progressive loss in the peculiar properties of graphene is observed, with increased similarities to PAHs.^[45]

Therefore, to produce nanoribbons with tailored bandgaps retaining most of the properties of graphene, a precise synthesis resulting in an exact edge topology and size is required. From this point of view, a top-down approach consisting in cutting down large graphene sheets using photolithography or opening nanotubes has been employed.^[46] By using such methods the actual presence of a bandgap dependent on the ribbon width was proved,^[47] however, the preparation of nanoribbons presenting precisely designed edge topologies still remains challenging, thus limiting the control on the resulting bandgaps.^[48] In order to obtain chemically precise nanoribbons with a defined edge topology, a bottom-up approach, in which small molecules are used to form the desired nanographenes, would be recommended.^[49]

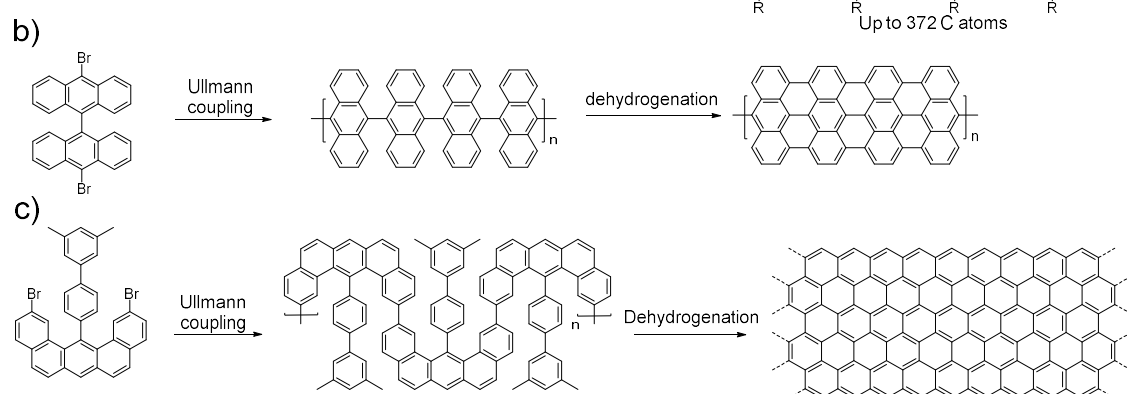
In this context, the pioneering work carried out by Müllen and co-workers represents a milestone in the field and is essentially based on the synthesis of extended nanographene flakes *via* Scholl reactions performed on polyphenylenes.^[50,51] In this strategy, relatively simple starting dienes and dienophiles are polymerized using [4+2] cycloaddition reactions to form tailored polyphenylenes in solution. The following cyclodehydrogenation reaction leads to the formation of nanographenes with high control on both the size and edge morphology (Scheme 1.2 a).^[52]

This strategy, however, suffers from the common drawbacks of solution phase chemistry, such as low solubility of the final products, high yield of reactions required to avoid by-products and difficult purifications. Another possible bottom-up strategy, which has been used extensively, relies on surface chemistry to induce an Ullmann coupling of halogen functionalised building blocks followed by surface mediated cyclodehydrogenation.^[53,54] This strategy has been used by the groups of Fasel and Feng (Scheme 1.2 b, c) to synthesise extended nanographenes with chemically precise edge topology.^[51,55] This resulted in an interesting study of the effects of morphology and substrates on the nanoribbon properties.

SOLUTION BASED SYNTHESIS



SURFACE BASED SYNTHESIS



Scheme 1.2: examples of a) Synthesis in solution as reported by Mullen and co-workers^[52]; b) and c) Surface assisted synthesis of graphene nanoribbons.^[55,56]

Despite the great advantage of providing a chemically precise synthesis of graphene-based materials with relative ease, the surface assisted synthesis suffers of severe limitations, in particular the low scalability and the fact that interactions between the surface (generally transition metals) and the material are present, thus providing results that are dependent on the substrate used.

1.4 Graphene heteroatom doping

It would be desirable to obtain semiconducting graphene without being limited to certain dimensions or topologies and thus being able to fully exploit the potential of this material. Furthermore, it would be preferable to create the desired bandgap in a graphene sheet by changing only one parameter, as this would allow the design and synthesis of materials with controlled properties. This concept is at the roots of the heteroatom doping, which is extensively used in the semiconductors industry to precisely determine the electronic properties of materials by varying the dopant type and amount. This approach can be extended to the graphene case by introducing in the crystal lattice heteroatoms able to change the electronic properties, thus resulting in materials with precisely designed characteristics. In this context, a great amount of

work has been performed using various techniques in order to introduce atoms such as boron, nitrogen, phosphorus, oxygen and sulphur into graphene layers.^[57] The best results overall have been obtained preparing doped graphene *via* CVD, ball milling, thermal annealing, wet chemical methods and plasma/arc-discharge.

1.4.1 Boron doped graphene

Due to the similar dimensions between boron and carbon atoms, the inclusion of the former in graphene leads to a small deviation in the lattice parameters due to a slightly different bond length (1.50 Å for C-B vs 1.42 Å in graphene) whereas the electronic properties of the material are affected importantly. In fact, the presence of the boron atom (electronegativity: 2.0) induces a polarization in the C-B bonds and the presence of the vacant p orbital leads to an electronic depletion accountable for the p-type behaviour and bandgap widening in the materials.^[57]

CVD represents probably the most used technique in the synthesis of boron doped graphene and indeed has been successfully employed by Liu and co-workers using phenyl boronic acid as feedstock.^[58] In this procedure a flow of H₂ containing the C and B source was passed on a copper substrate at 1030 °C leading to the formation of the desired material. XPS analysis on the resulting boron containing graphene proved the inclusion of the boron atoms in the material lattice, which resulted to be a p-type semiconductor with a good carrier mobility of 800 cm² V⁻¹ s⁻¹. Comparable results were obtained by Shen and co-workers with a similar strategy, using polystyrene and boric acid in different ratios as feedstock, again obtaining a p-type behaviour for the resulting material.^[59] Thermal annealing has been used in the successful synthesis of B-doped graphene by heating GO in a furnace at 800°C in the presence of BCl₃.^[60] The resulting material presented a 0.88% doping percentage and was used as anode in lithium ion batteries.

1.4.2 Nitrogen doped graphene

When nitrogen is considered as a dopant, again similar dimensions to carbon are found, however, due to the different valency, nitrogen atoms can be included in graphene in various ways, resulting in different effects and ultimately in a greater deviation from the morphology of pristine graphene compared to the boron case.^[57] In general, the amount of the different nitrogen types depends on the conditions of the synthesis: higher temperatures and longer annealing times result in more abundant graphitic sites, while lower temperatures favour pyridinic and pyrrolic domains, in accordance with the expected thermal stability: graphitic N > pyridinic N > pyrrolic N (Figure 1.5).^[57,61] The presence of differently bound nitrogen atoms heavily affects the properties of the material. In fact, the presence of pyridinic nitrogen is often associated

with a p-type behaviour whereas the presence of graphitic domains results in a n-type material.^[62] A polarization of the CN bonds is present due to the higher electronegativity of nitrogen (3.0 vs 2.5 for C), thus resulting in polarized bonds that can influence the electronic properties of the material and can be active reaction sites.

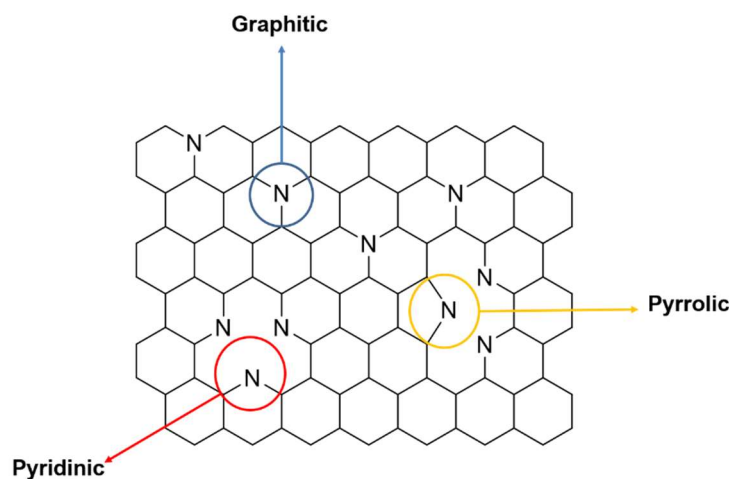


Figure 1.5: Different possible inclusion of nitrogen atoms in graphene lattice.^[63]

Good results have been obtained using nitrogen as dopant; in particular, Ajayan et al. and Yu and co-workers used CVD to synthesize nitrogen doped graphene on copper substrates.^[63,64] In the first case, the synthesis was performed at 950°C using hexane and CH₃CN in a H₂/Ar flow while in the second CH₄ and NH₃ were used with similar conditions leading to the formation of materials presenting n-type semiconducting behaviour and charge mobilities between 200 and 450 cm² V⁻¹ s⁻¹. In another interesting work, Usachov et al. reported the synthesis of N doped graphene using CVD on nickel substrates at 540-635 °C, employing *s*-triazine as feedstock. As a result, graphene presenting 0.4% of graphitic nitrogen was obtained, corresponding to a 0.2 eV widening of the bandgap.^[65]

Along with CVD techniques, thermal annealing has been successfully used to prepare nitrogen doped graphene by heating GO or chemically produced graphene in the presence of various dopant sources such as N₂, NH₃, aniline, pyrrole, melamine etc.^[66,67] In this case, the desired materials were obtained with doping percentages up to 10% and with a good control on the doping type by choosing carefully the reaction temperature and doping precursors. Furthermore, wet chemical methods have been used to produce nitrogen doped graphene by treating GO in the presence of urea, ammonia or hydrazine.^[68] This method presents the advantage of using lower temperatures, resulting in a more scalable and simple synthesis. Another valuable example of this approach is presented by the work of Sun et al. in which a solvothermal approach has been used to achieve high nitrogen percentages starting from GO by

treatment with urea in water at 180 °C. Despite the clear advantages, this method is limited by a difficult control of the doping percentage, which largely depends on the functionalization degree of the starting GO.^[69]

1.4.3 Oxygen doped graphene

Oxygen doping of graphene is mostly related to the synthesis and production of GO. As previously reported this material is obtained by oxidation of graphite in solution using H₂SO₄, KMnO₄ and NaNO₂. The resulting material presents epoxy, hydroxy and carboxy groups and can be considered as an oxygen doped graphene. Since the degree of oxidation varies greatly depending on conditions, the properties of GO can vary from poorly conductive to non-conductive depending on the amount of sp³ carbons formed in the oxidation step. Despite these evident limitations, GO has been used in devices and as a starting material for further functionalization or graphene chemical synthesis.^[70,71]

1.4.4 Phosphorus and Sulphur doped graphene

When third row elements such as P^[72] and S are used, a greater distortion of the graphene sheets is observed due to their size and longer carbon-heteroatom bonds. Moreover, the insertion of large heteroatoms in the graphene lattice is energetically unfavourable, thus resulting in low doping percentages located especially at defect sites or edges.^[57] A successful example of S-doped graphene using CVD technique has been reported by Ajayan using a sulphur solution in hexane as precursor. In this case doping percentages around 0.6% were detected, presenting p-type semiconducting characteristics.^[73] Ball milling has been used by Jeon et al. to produce sulphur doped graphene which was used for catalysis. In this approach however, the functionalization of the material was limited to the edges of the sheets.^[74]

1.4.5 Boron-Nitrogen doped graphene

A potential strategy towards the improvement of the properties of doped graphene materials, is represented by co-doping. This approach should allow the introduction of different heteroatoms at the same time, resulting in synergistic effects and enhanced bandgap widening compared to singly doped graphene.^[57] From this point of view, since boron and nitrogen are the heteroatoms that produced the best results in converting graphene into a semiconductor, a lot of work has been performed towards the synthesis of BN-doped graphene.^[75] The doping of graphene with *h*-BN is advantageous due to the properties of the BN bonds, which are isoelectronic and isosteric with CC bonds and thus can be included in the material lattice maintaining the sp² honeycomb morphology of graphene.^[75] This feature avoids the problems related to different types of bonding of the heteroatoms leading to different properties as

highlighted when nitrogen is used as dopant. Furthermore, the BN bonds are highly polarized (1.844 D)^[76] thus leading to an active surface chemistry and to great variations in the electronic properties of the resulting materials. From this point of view, since *h*-BN is an insulator with high bandgap (5.971 eV)^[77] its inclusion in the graphene lattice should result in the opening of a bandgap dependent on the doping percentage.^[78]

As in the previous cases, the most important results towards the synthesis of BN-doped graphene have been obtained using CVD techniques. In the ground-breaking work of Ajayan and co-workers, extended sheets of graphene doped with *h*-BN were obtained by flowing ammonia borane and methane on a copper surface at 900-1000°C using H₂/Ar as carrier gas.^[79] The ratio between C, N and B can be controlled by regulating the amount of the respective precursors, although since the precursor for B and N is ammonia borane (NH₃-BH₃) the ratio between the two components will always be one. As a result, large sheets mostly composed of 2/3 layers of BN hybridised graphene were obtained with percentages of BN up to 90%. XPS studies performed on the material proved that the BN atoms are arranged in boron-nitride islands segregated from the graphene lattice.

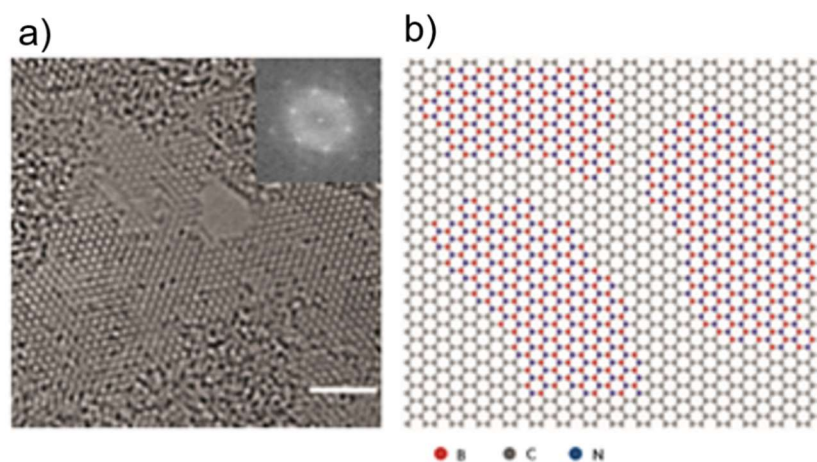


Figure 1.6: a) HRTEM image of a single layer region; b) atomic model of the *h*-BNC film obtained.^[79]

This result is related to the larger binding energy of BN and CC bonds compared to BC and NC ones that are thus confined to the edges of the *h*-BN islands (Figure 1.6b).^[79] As expected, the materials present semiconducting behaviour, as an example, an increase in the optical bandgap is observed moving from samples containing 26% *h*-BN (3.85 eV, 1.51 eV) to the ones containing 35% *h*-BN (4.48 eV, 1.62 eV) with intermediate values between the ones of graphene and pure *h*-BN. The presence of two absorption edges, resulting in two values of bandgap, is due to the segregation between the *h*-BN islands (higher value) and graphene domains (lower value). This

factor is ascribable to a dimension of the *h*-BN islands in the nanometre size and thus ultimately producing a segregated rather than a uniform material. The presence of these islands results in irregular properties, with local discrepancies, that are not optimal when the materials are used in devices.

A possible solution to this problem comes from the work of Bepete et al. in which a CVD using boric acid, N₂ and CH₄ as sources of B, N and C respectively was performed on a copper substrate heated at 995 °C under a flow of 7% H₂ in N₂ gas.^[80] As a result, a large area of uniform graphene was obtained. XPS data suggested the presence of C, B and N in 98%, 1.38% and 0.62% respectively, inserted in a uniform system with no *h*-BN islands present, thus suggesting the efficient creation of BNC domains (Figure 1.7). This result suggests that the segregation of *h*-BN only occurs at high concentrations of BN, limiting the ability of CVD methods to form uniform BN graphene to low doping percentages. A possible alternative synthesis of BN-doped graphene relies on the thermal annealing of glucose, urea and boron oxide at 1250°C under a NH₃ atmosphere as performed by Huang et al. The resulting material presented a 2.72 eV bandgap with a uniform composition without *h*-BN islands; however, only multiple layers of folded material were obtained with various amounts of impurities absorbed on surface.^[81]

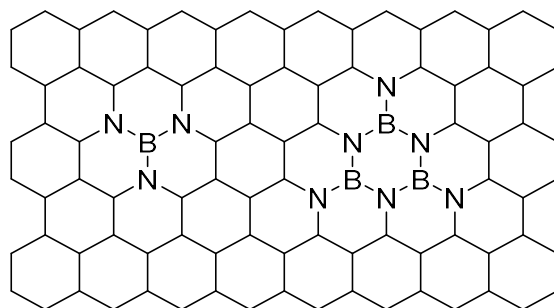
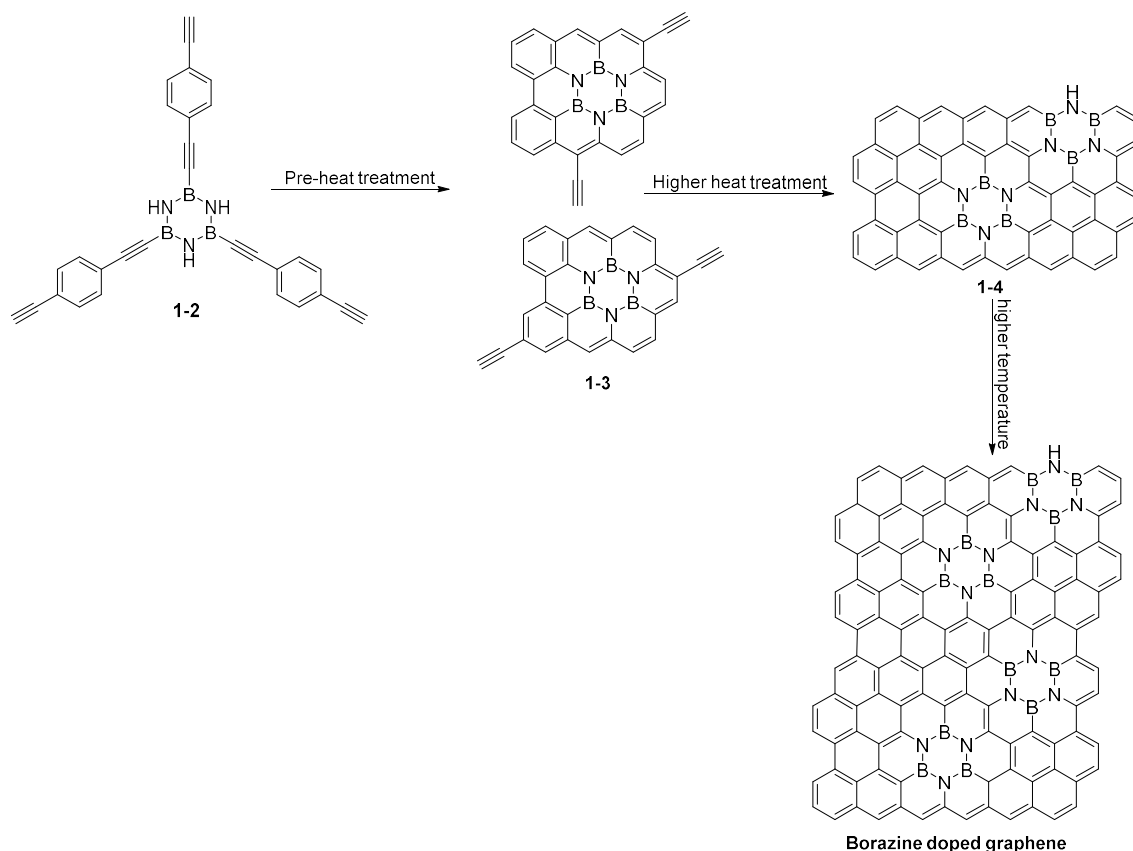


Figure 1.7: Schematic representation of a uniform doping with BN domains in the graphene lattice.^[80]

Another interesting approach has been used recently by Chen et al. to form BN-doped graphene layers using acetylene functionalized borazines as starting materials.

In this approach molecule **1-2** is annealed at 1000°C, 1200°C and 1500°C leading to the formation of doped graphene sheets (Scheme 1.3). The resulting material proved to be a n-type semiconductor; however, the properties of the obtained graphene were largely dependent on the annealing temperature and a precise chemical control on the doping was not possible.^[82]



Scheme 1.3: Preparation of BN-doped graphene using borazine derivatives as feedstock.^[82]

A possible solution to the problems related to the CVD and annealing method is represented by the segregation of the lattices itself by using a CVD heteroepitaxial growth of hybrid materials. In this approach *h*-BN islands are first grown on the substrate followed by the carbon part on the uncovered surface or vice versa^[83,84]. This leads to a possibility of controlling the size of the *h*-BN and graphene islands by limiting the growth time; however, even in this case, a material presenting clear interfaces between *h*-BN and graphene is formed even if with a higher control on the doping percentage. Finally, another strategy is represented by the work of Levendorf et al. in which a patterned growth of hybrid materials is performed.^[85] In this strategy, the semiconducting properties of the materials are obtained by growing precise patterns of *h*-BN into a graphene layer. First, a layer of graphene is formed with CVD on the metallic substrate. Photolithography or reactive ion etching is then used to remove part of the graphene, resulting in precise patterns where the metallic substrate is exposed. *h*-BN is then grown by annealing ammonia borane in the empty spaces, leading to different bandgap sizes depending on the patterns. This approach allows the preparation of atomically precise materials; however, it is based on very complicated setups that are suitable only for small scale production.

1.5 Top-down synthesis limits

All the top-down methods presented in the previous paragraphs, rely on the synthesis of large sheets of BN-doped graphene using CVD or thermal annealing techniques (on pre-formed graphene oxide). These approaches suffer from a difficult control of the doping concentration and segregation between *h*-BN and graphene domains, especially at high concentrations of dopant. This results in a poor control of the material properties that can often be synthesised only in small amounts. The possible solutions to these problems rely on keeping low BN concentrations or in using complex techniques and expensive methods to obtain regular doping patterns. Despite this, obtaining atomically precise doped materials in large scale still represents a major challenge in the field.^[57]

When the precise doping of graphene is considered, it is convenient to introduce two doping parameters: the doping concentration (ρ) and the doping vector (d). ρ is defined as the number of carbon units (aryl rings or CC bonds) substituted by BN units. d defines the position of each doping unit in a cartesian coordinates system where the reference doping unit is defined as (0,0). This allows for the description of the doping position using vectors defined by the number of aryl rings separating the two doping units.^[86]

An important limitation of the previously mentioned methods is the lack of control on the d parameter. In fact, being able to control the relative position d of the doping units in the material lattice is very important in determining how the doping will affect the aromaticity and electronic properties of the system. In a theoretical study by Karamanis et al., the effect of doping with B₃N₃ (borazine) units in nanographenes has been linked to the position in which the substitution is occurring in the relevant Clar resonant structure. If full aromatic sextets are substituted by B₃N₃ units, a widening of the bandgap occurs, instead, when the substitution affects non-sextet rings, an opposite effect is observed (Figure 1.9).^[87,88]

This fact results in the irregular widening of the bandgap (Figure 1.9a) often visible in the previous examples in which, however, a widening is always observed due to loss in lattice symmetry associated with the random doping patterns.^[89] The control of the two parameters d and ρ is therefore necessary to precisely govern the effect of doping on the bandgap of graphene, resulting in reproducible properties.

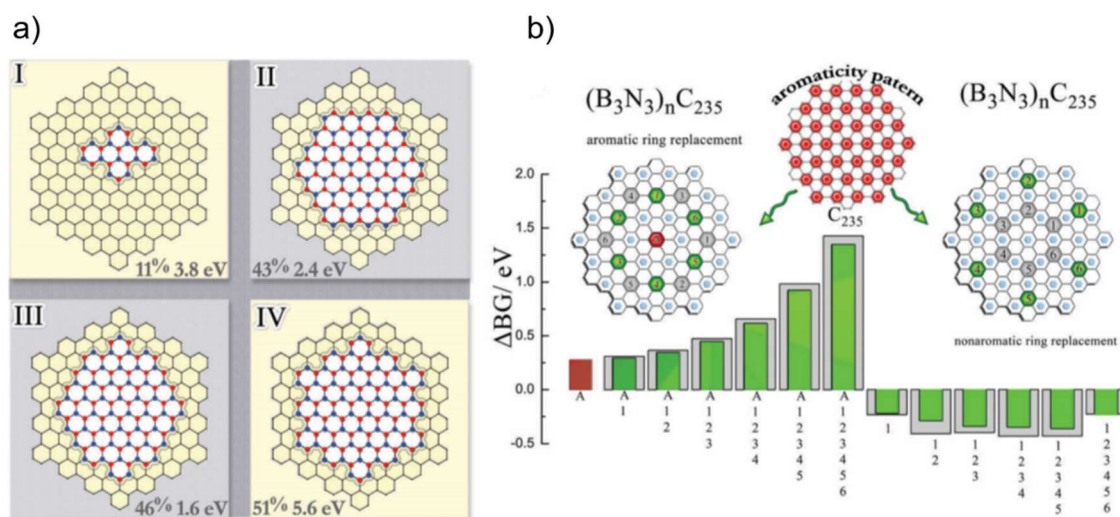


Figure 1.9: a) Bandgap differences in respect to doping concentration in a model C222 graphene flake patched with *h*-BN segments of different sizes. Level of theory: CAM-B3LYP/6-31G(d); b) Column plots representing the computed band gap differences, between a series of B_3N_3 -doped graphene flakes and their pristine counterpart. Every (green or grey) column presents the effect arising from the substitution of the reported rings (green or grey) with B_3N_3 . The red column represents the bandgap of the fragment with only the central ring substituted by B_3N_3 .^[88]

The important effect of *d* highlighted by Karamanis et al. is related to how the substitution affects the relevant Clar resonance structure of the graphene material (Figure 1.10).

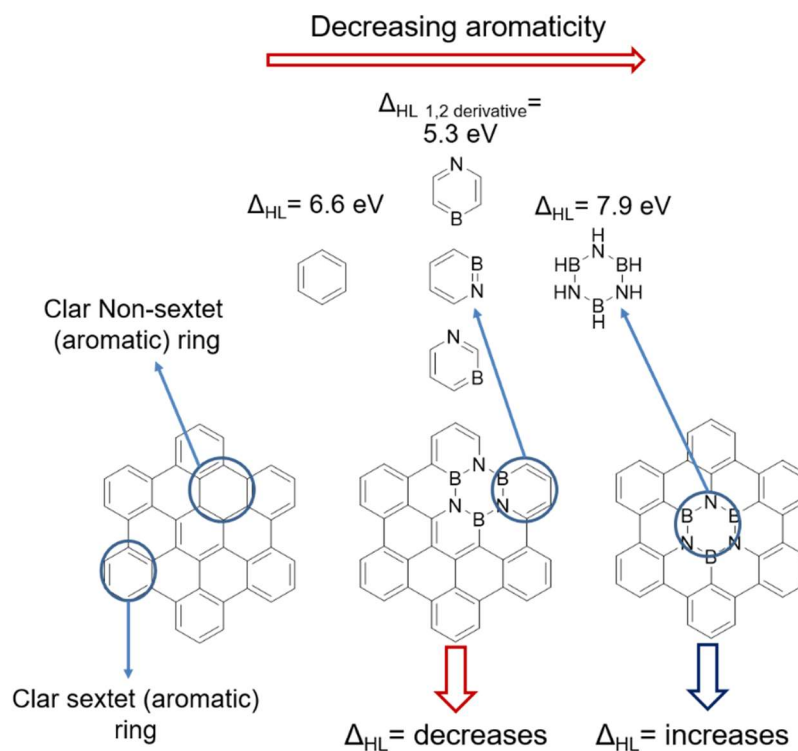


Figure 1.10: Effect of the doping in different positions on the bandgap depending on the kind of BN rings formed.

Substitution of an aromatic sextet ring with a non-aromatic borazine moiety (HOMO-LUMO gap 7.9 eV compared to benzene 6.6 eV, Figure 1.10)^[90] results in an overall widening of the material bandgap and in general, in more localized sextets in the neighbouring aromatic rings due to a decrease in delocalization. On the other hand, the substitution of a non Clar-sextet ring results in the rupture of the aromaticity of the three neighbouring aromatic sextets which are converted in BNC_4 (azaborine) units presenting a narrower HOMO-LUMO gap compared to benzene (5.3 eV vs 6.6 eV), which ultimately results in a shrinking of the bandgap (Figure 1.10).^[90] As a general rule, the presence of partially substituted aromatic sextets is associated with non-monotonic bandgap variations.

When single BN bonds are used instead of borazine, similar assumption can be made. In fact, when the substitution of CC bonds with BN bonds intersects aromatic sextets of the Clar resonance structure, it results in the formation of lower HOMO-LUMO gap species such as azaborine or pyridine and borabenzene (Figure 1.11).^[90,91] As for the previous case, the effect that this substitution has on the material bandgap depends on the position of the doping and in particular on how this affects the Clar resonance structure of the material.

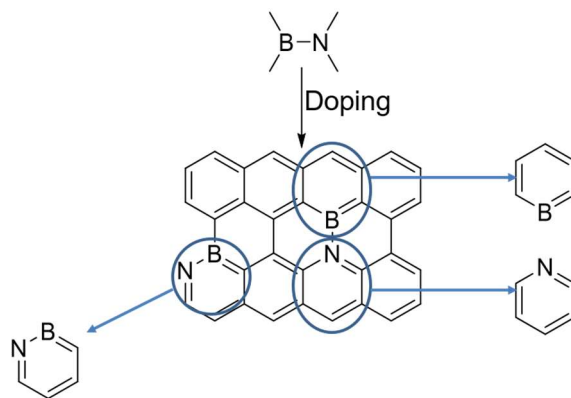
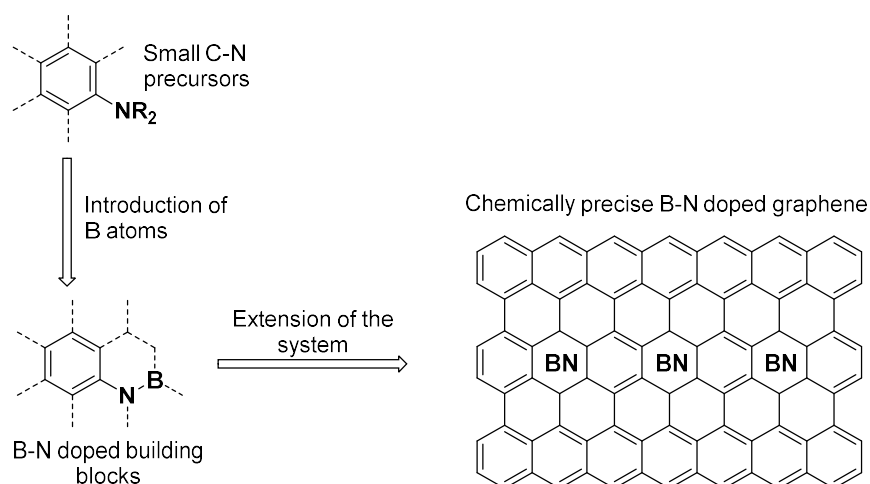


Figure 1.11: Effect of doping with single BN bonds on the aromaticity.

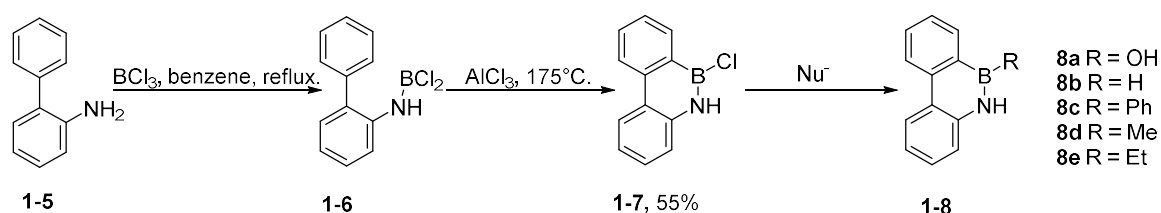
Altogether, these studies confirm that to finely tune the bandgap of BN-doped graphene, it is necessary to precisely control not only parameter ρ but also d . A bottom-up preparation of graphene materials relying on organic synthesis should present the optimal solution to the problem, leading to the formation of chemically precise BN-doped graphene starting from molecular precursors (Scheme 1.4). The synthesis of designed molecular precursors and the study of their properties is therefore fundamental to produce doped graphene presenting tailored bandgaps.



Scheme 1.4: Bottom-up strategy towards precisely doped nanographenes *via* extension of BN-doped building blocks.

1.6 Bottom-up approach: Synthesis of BN-doped PAHs

One of the first steps towards the bottom-up synthesis of BN-doped graphene is represented by the effective preparation of doped PAHs, which can be considered as building blocks of extended graphene systems. This passage is of central importance for the development of experimental procedures that can be used to introduce the dopant atoms in aromatic scaffolds. The study of BN-doped PAHs goes back to the 1950s with the pioneering work by Dewar and co-workers, which led to the synthesis of the first BN-doped phenanthrene.^[92] In this first approach, the introduction of the boron atom was achieved by treating **1-5** with BCl_3 leading to the formation of adduct **1-6**. BN-doped phenanthrene **1-7** was then obtained by electrophilic aromatic substitution by treating **1-6** with AlCl_3 . Various substituents were introduced on the boron atom by treatment of **1-7** with nucleophiles (Scheme 1.5).



Scheme 1.5: Synthesis of BN-doped phenanthrene **1-8**.^[92]

Derivative **1-8b** presents a 15–20 nm blueshift in the absorption and emission spectra when compared to parent phenanthrene, indicative of a larger HOMO-LUMO gap for the doped analogue. In fact, in **1-8b**, the aromatic sextet rings are unaffected by doping and the result is a hypsochromic shift caused by reduced conjugation and enhanced sextet localization.^[93] This first example of a BN-doped PAH triggered a great interest in the scientific community in the following decades, leading to the synthesis and study

of many different BN-doped PAHs. A whole family of doped phenanthrene derivatives has been prepared, highlighting the effective importance of the doping position on the properties of PAHs (Figure 1.12).^[94] Differently from **1-8b**, when the BN-doping is intersecting the aromatic sextet rings of the relevant Clar resonance structure a general bathochromic shift of the emission is observed. However, the magnitude of this effect varies greatly depending on the relative position of the dopant unit in the phenanthrene molecule. This fact is highlighted by the great variation in emission wavelengths in derivatives with similar doping patterns such as **1-10e** and **1-10b** presenting a difference of 153 nm in the λ_{em} . When derivative **1-10a** is examined, the doping is affecting both the sextet rings in the molecule. This results in the formation of borabenzene, pyridine and azaborine systems, resulting in a lowest energy absorption at 446 nm and an emission centred at 450 nm. This data points out an important decrease of the HOMO-LUMO gap for this derivative compared to parent **1-9**.

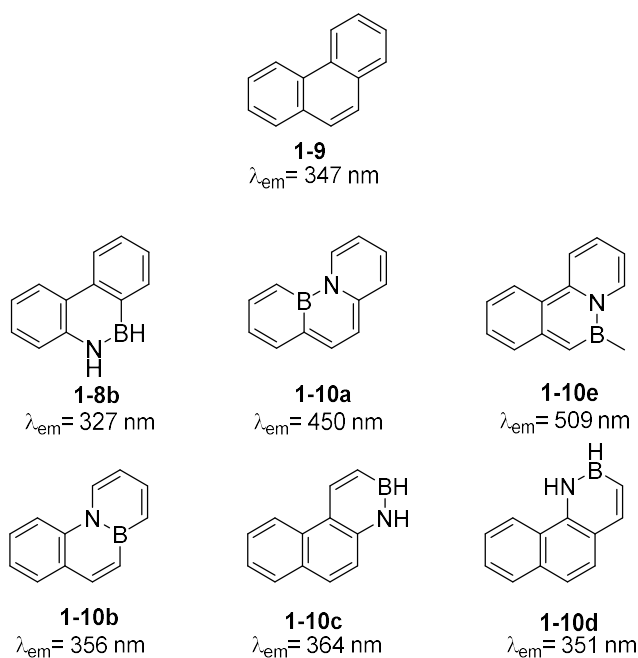
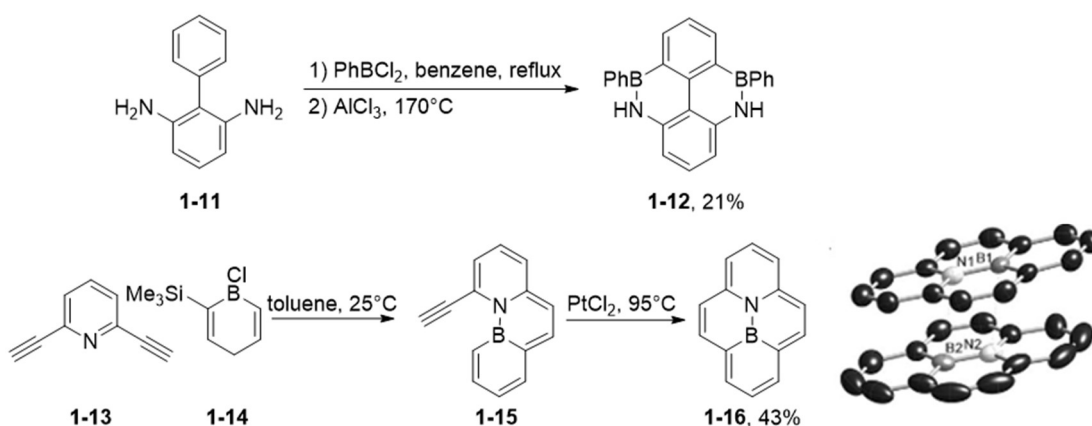


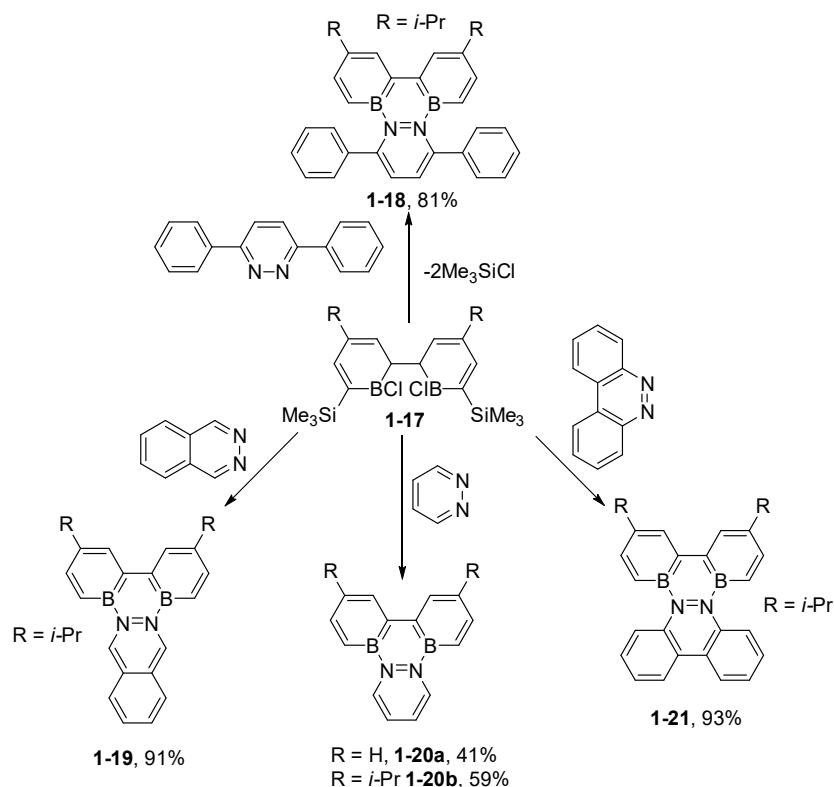
Figure 1.12: Absorption and emission maxima of BN-doped phenanthrene congeners.^[94]

Along with phenanthrenes, other valuable examples of doped PAHs were proposed again by Dewar in 1960^[95] and by Piers and co-workers in 2007^[96] with the synthesis of BN-doped pyrene derivatives. The synthesis of **1-12** was performed with conditions similar to those used for doped phenanthrene **1-8b**, whereas the synthesis of derivative **1-16** relied on the cyclization of acetylene groups using a $PtCl_2$ catalyst (Scheme 1.6).^[95,96] The lowest energy transition for **1-12** is visible at 335 nm suggesting a very small effect on the absorption energy (Pyrene $\lambda_{abs} = 333$ nm). This result is very similar to the one observed for **1-8b**, suggesting that even in this case the preservation of the Clar aromatic sextets is at the roots of this outcome.



Scheme 1.6: Synthesis of BN-doped pyrene derivatives as reported by Dewar and Piers.^[95,96]

On the other hand, the lowest energy absorption for derivative **1-16** appears at 443 nm with an emission maximum at 480 nm. This confirms the important effect determined by the substitution of the two Clar aromatic rings resulting in lower HOMO-LUMO gap species, in analogy with derivative **1-10a**. Interestingly, the polar BN bond in derivative **1-16** imparts a self-assembly behaviour to the derivative visible in the crystal structure, with the boron atom sitting on top of the nitrogen of the nearby molecule.

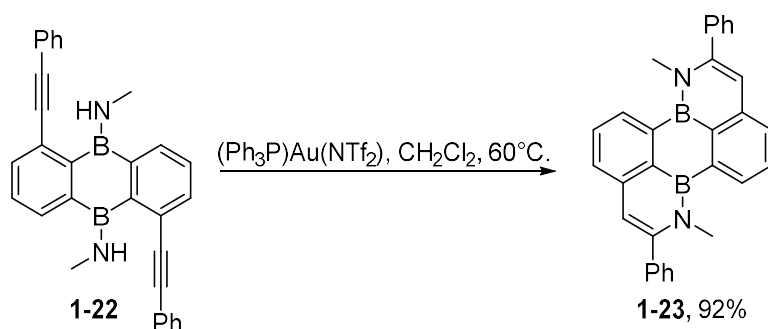


Scheme 1.7: Synthesis of BN-doped triphenylene derivatives.^[97,98]

More extended $B_2N_2C_2$ doped triphenylene analogues were prepared by Piers et al. in a subsequent work, by reacting chloro borane **1-17** with various pyridazine derivatives (Scheme 1.7). In this case, due to the presence of the $B_2N_2C_2$ system instead of the

central, non-sextet ring of triphenylene, pyridazine and borabenzene rings are obtained in place of the outer Clar aromatic sextets. Therefore, a redshift was observed in the absorption and emission energy when derivative **1-20a** ($\lambda_{\text{abs}}= 546 \text{ nm}$, $\lambda_{\text{em}}= 558 \text{ nm}$) was compared to parent triphenylene ($\lambda_{\text{abs}}= 335 \text{ nm}$ $\lambda_{\text{em}}= 355 \text{ nm}$) pointing out an important decrease in the HOMO-LUMO gap.^[97,98] In this case, however, the great bathochromic shift in the absorption and emission is associated with the presence of a charge-transfer transition from the central $\text{B}_2\text{N}_2\text{C}_2$ to the borabenzene rings, which is accountable for the great (1.5 eV) difference in the transition energy.

Another addition to the BN-doped PAHs, came from Kaehler et al. with the synthesis of a doped perylene analogue including two BN bonds (Scheme 1.8). The lowest energy transition for derivative **1-23** appears at 416 nm, blue-shifted compared to perylene ($\lambda_{\text{abs}}= 438 \text{ nm}$), instead emission maxima are localized at 440 nm and 445 nm respectively, corresponding to a widening of the HOMO-LUMO gap of **1-23** (2.84 eV vs 2.77 eV).^[99] This is consistent with the retention of the two fully aromatic sextets of perylene Clar resonance structure.



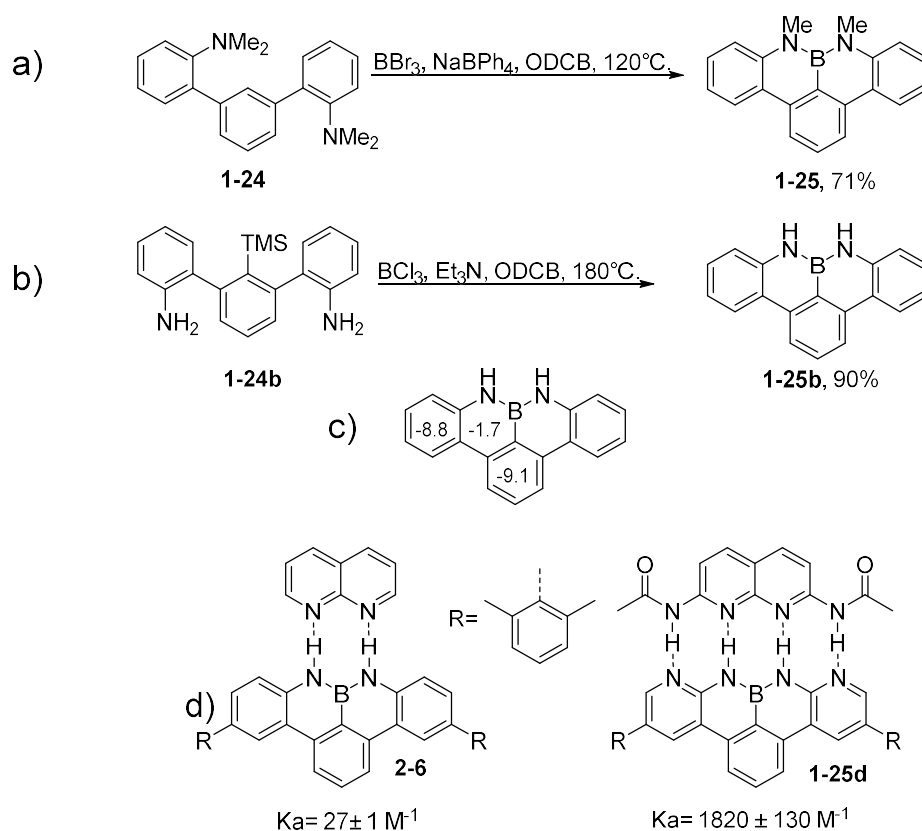
Scheme 1.8: Synthesis of BN-doped perylene derivatives.^[99]

The synthesis of NBN-doped systems has been reported in the work of Hatakeyama, and Feng (Scheme 1.9).^[100,101] In these derivatives, the doping intersects the non-sextet rings of the Clar resonance structure of the hypothetical full carbon derivative.

NICS calculations showed that, while the azaborine derived rings present non-aromatic character (-1.4 ppm), the Clar aromatic rings retain their aromaticity (from -8 to -10 ppm). This data suggests that the doped derivatives should present a wider HOMO-LUMO gap compared to the full carbon, however, in this case a direct comparison is not possible due to the open shell nature of the latter.

The presence of the boron atom connected to the two N-H groups results in acidic protons, which can act as hydrogen bond donors. This feature has been recently exploited leading in the formation of DD-AA and ADDA-DAAD hydrogen bonded systems with **1-25c** and NAP (naphthyridine) in the first case and **1-25d** and DAN

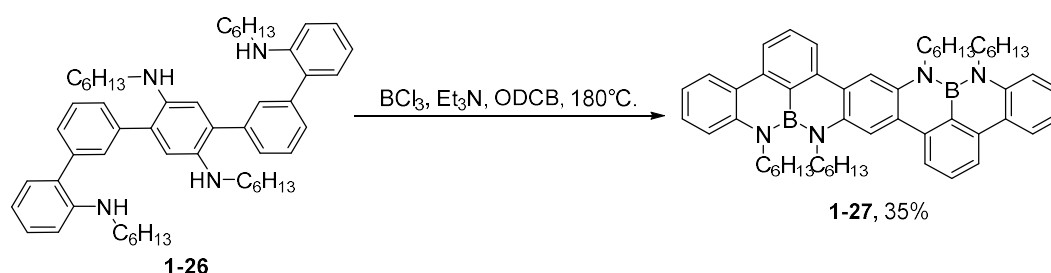
(diacetyl-2,7-diaminonaphthyridine) in the second (Scheme 1.9d). This result represents a valuable example of how peripheral BN-doping of zig-zag edges can be used to induce self-assembly between PAHs.^[102]



Scheme 1.9: Synthesis of NBN-doped derivatives as reported by a) Hatakeyama; b) Feng; c) NICS(1) values calculated for **1-25b**. d) DD-AA and ADDA-DAAD hydrogen bonded systems obtained using NBN-doped PAHs.^[102]

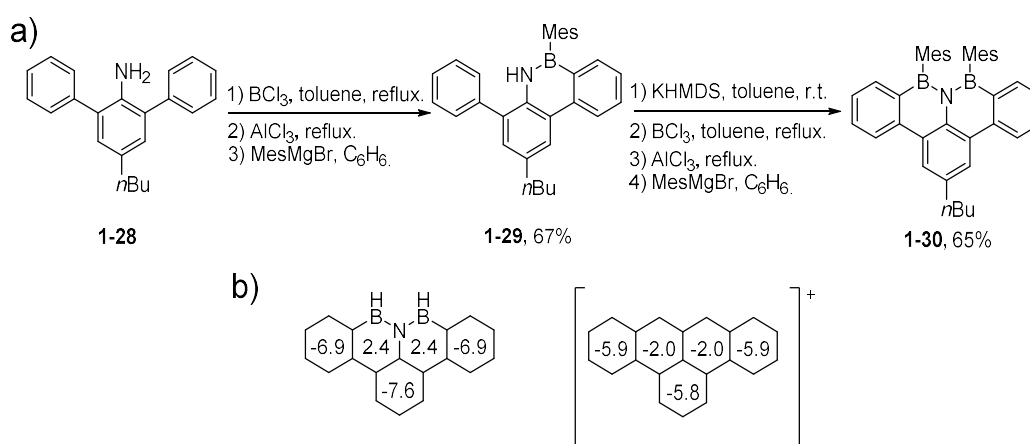
In the group of Feng, the synthesis of the extended NBN derivative **1-27** was carried out as well, showing a good example of how large doped systems can be obtained with a bottom-up approach through electrophilic substitution reactions (Scheme 1.10).

The UV-Vis spectra of this NBN molecule presents narrow Stokes shift suggesting a rigid structure in line with the previous observations for similar derivatives.^[101] Moreover, compared to **1-25b** derivative **1-27** displays redshifted absorption and emission spectra due to the increased conjugation of the system ($\lambda_{\text{abs}} = 435 \text{ nm}$ vs 351 nm ; $\lambda_{\text{em}} = 448 \text{ nm}$ vs 369 nm).



Scheme 1.10: Synthesis of extended NBN derivative **1-27**.

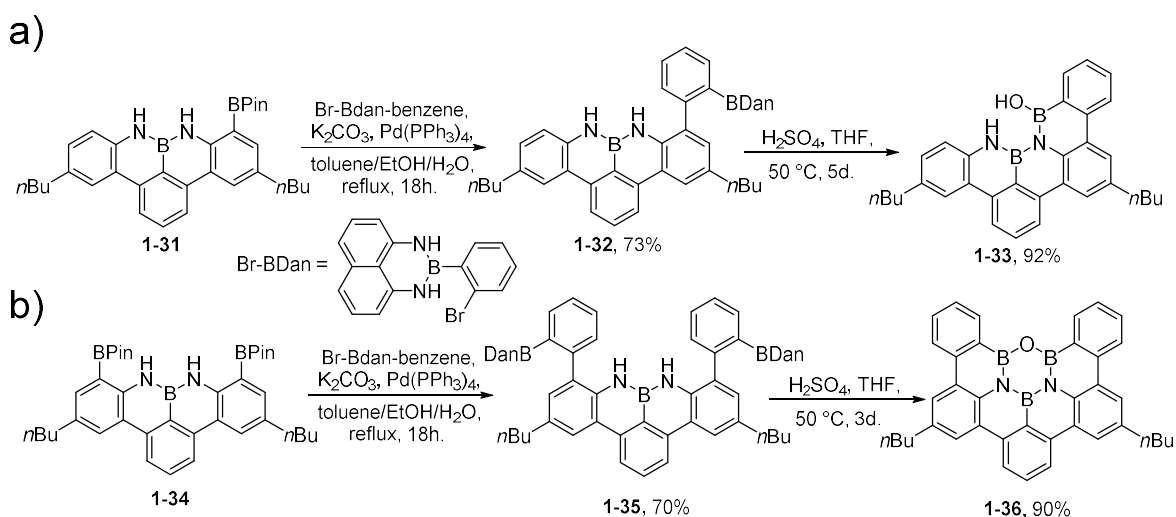
Building on these results, Bettinger and co-workers used a multi-step approach to synthesise the complementary PAH featuring the BNB-doping motif (Scheme 1.11). In this synthesis KHMDS was used to deprotonate the NH group of **1-29** followed by a second electrophilic borylation to give **1-30**. Notably mesityl groups are introduced to avoid the reaction of boron centres with water.^[103] The study of this derivative highlighted a wide stokes shift compared to NBN derivative **1-25b** (47 nm vs 18 nm) and a redshifted emission (λ_{em} = 413 nm vs 369 nm). These differences compared to **1-25b** are likely caused by the twisting of the structure imposed by the bulky mesityl protecting groups.



Scheme 1.11: a) Synthesis of BNB-doped derivative **1-30**; b) NICS(1) values for the doped and full carbon scaffolds.^[103]

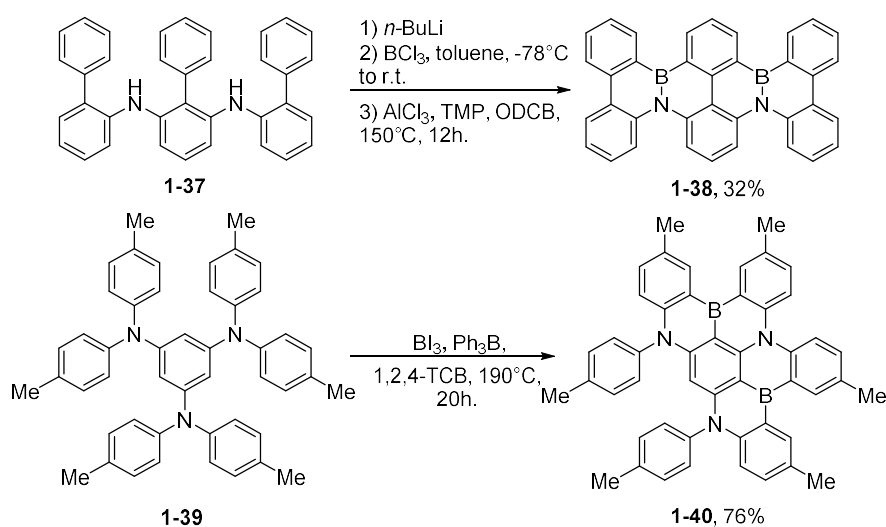
In the same group, derivatives of **1-25b** were used as starting materials in the synthesis of molecules **1-33** and **1-36**. Singly and doubly borylated derivatives **1-31** and **1-34** were functionalized with aryl-BDan groups *via* Suzuki coupling, which was followed by deprotection of the dansyl group in the presence of H_2SO_4 leading to the formation of **1-33** and **1-36** (notably, **1-36** was published after the initial report from our group presented in chapter 2).

For both molecules, narrow stokes shifts and blue emissions were observed (λ_{em} = 404 and 370 nm) with high Φ_{em} of 84% and 58% respectively.^[104,105]



Scheme 1.12: Synthesis of extended BN-doped PAHs as reported by Bettinger and co-workers.^[104,105]

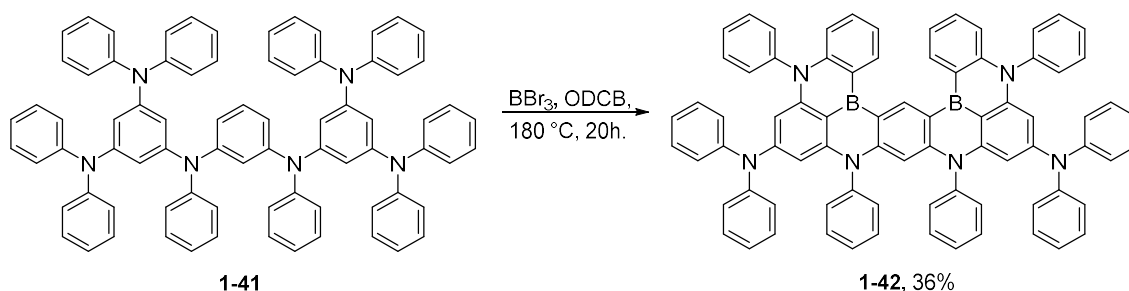
Electrophilic substitution reactions on aromatic scaffolds have been effectively used in the synthesis of extended aromatic systems, which represent important steps towards the bottom-up preparation of BN-doped graphene. One of the most important contributions in the field is represented by the synthesis of extended BN-doped nanographenes from Hatakeyama group, who prepared molecules **1-38** and **1-40** starting from amino functionalized polyphenylenes and by treating them with BCl_3 or BI_3 (Scheme 1.13).^[106,107] Derivative **1-38** displays an electrochemical HOMO-LUMO gap of 1.67 eV and an enhanced hole mobility that the authors address to the presence of the BN bonds. Together with a remarkable stability (no decomposition visible up to 358 °C) this features make this molecule very attractive for organic electronics.



Scheme 1.13: Synthesis of nanographenes **1-32** and **1-34**.

When **1-40** is considered, narrow blue emission centred at 455 nm is found in a poly(methylmethacrylate) (PMMA) film along with a $\Phi_{em} = 53\%$. The presence of phosphorescence centred at 488 nm (at 77 K in PMMA film) highlighted a small energy difference between singlet and triplet states (0.15-0.18 eV) suggesting efficient TADF (Thermally activated delayed fluorescence) for this molecule, which was used as emitter in OLEDs, yielding a pure blue emission with high quantum external efficiency (EQE) of 12.6% at 100 cd/m².^[106]

The same group synthesised extended system **1-42** which again presents energetically close singlet and triplet states and was used in TADF OLEDs. In this paper these properties were linked to the localization of the HOMO and LUMO orbitals imposed by the presence of the boron and nitrogen atoms. This results in a decrease in the vibronic coupling, vibrational relaxation and in a small singlet/triplet gap. As a result, pure narrow blue emission ($\lambda_{em} = 469$ nm with 18 nm full width at half maximum) and efficient TADF were obtained from the devices with a 32.8% EQE at 100 cd/m², much improved compared with devices based on **1-40**.^[108]

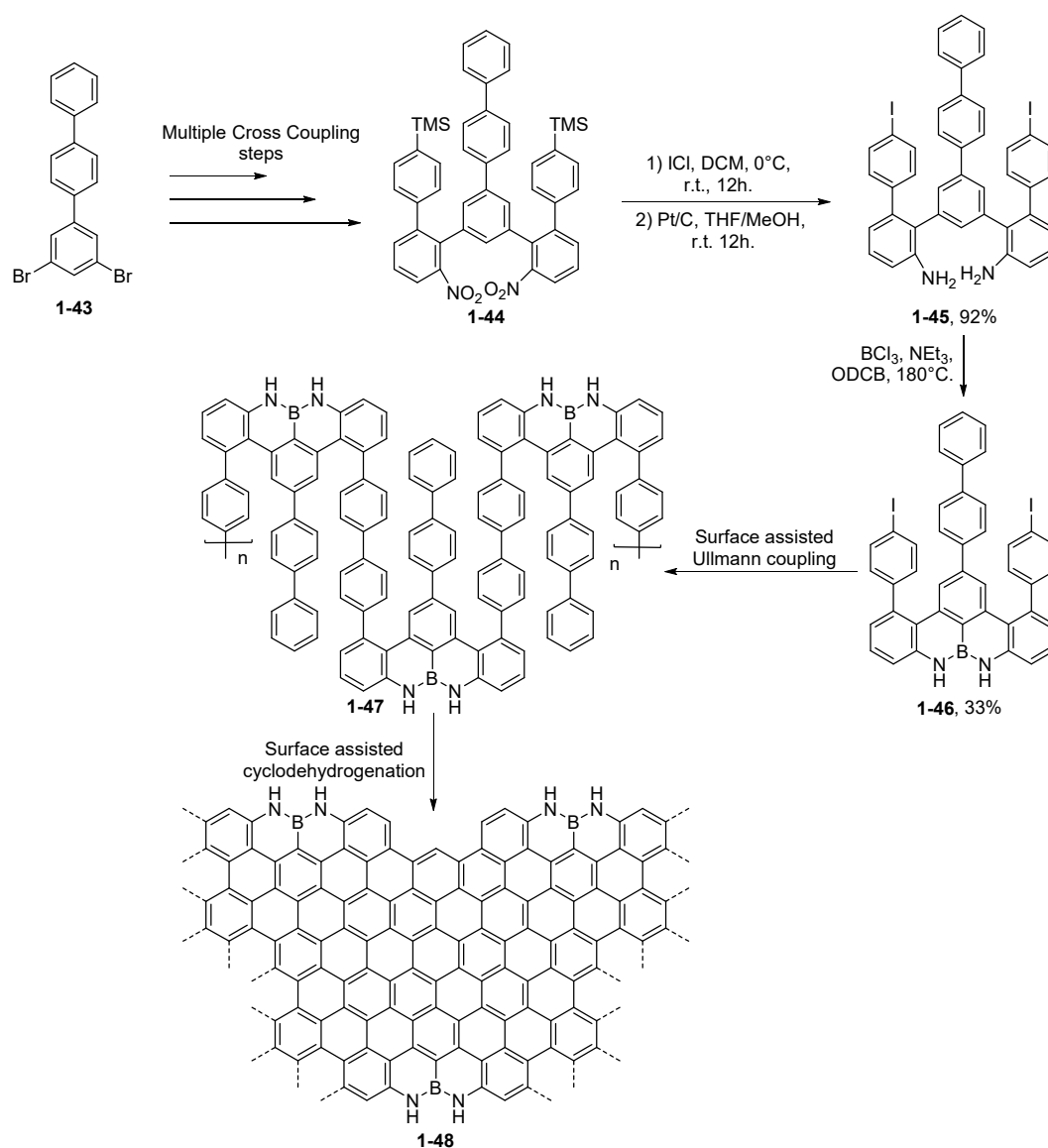


Scheme 1.14: Synthesis of BN-doped derivative **1-42** as reported by Hatakeyama and co-workers, this derivative presenting narrow blue emission was used as active material in TADF OLEDs.

One of the most interesting examples of the use of doped PAHs in the synthesis of BN-doped graphene comes again from the work of Feng and co-workers (Scheme 1.15). In this approach, precisely designed NBN-doped monomers are polymerized on surface using an Ullmann coupling, followed by dehydrogenation reaction resulting in precisely doped nanoribbons which were studied using STM and nc-AFM (non-contact atomic force microscopy) in UHV conditions. DFT calculations highlighted an increased bandgap for **1-48** compared to the pristine counterpart (0.90 eV vs 0.27 eV).^[109]

In the previously reported examples, the doping units are isolated BN, NBN or BNB moieties selectively placed either at the peripheries or in the core of aromatic precursors bearing amino groups at specific positions. Strategies relying on multiple electrophilic aromatic substitutions, allowed for the preparation of extended BN-doped PAHs. As expected, the result of the doping on the molecule's HOMO-LUMO gap is

largely dependent on the CC bonds that are substituted and on how this affects aromaticity and the Clar resonant structure of the PAHs



Scheme 1.15: Synthesis of NBN-doped precursor **1-46** and its use in the synthesis of nanoribbon **1-48**.^[109]

Another possibility to obtain BN-doped nanographenes and then graphene, consists in the use of preorganized doping units, in which the BN bonds are clustered in six-membered rings (borazines) and used to replace benzenoid rings in graphitic materials, leading to an increase of the bandgap due to the higher HOMO-LUMO gap of borazine compared to benzene. In this strategy, borazine derivatives are used as precursors in the synthesis of nanographenes.

1.7 BN clusters: borazines

Borazine has often been dubbed as “inorganic Benzene” due to the similarities of this BN-based cycle with the most famous aromatic compound. Borazine presents a similar bond length (1.44 Å) to benzene (1.40 Å) and as in the latter, this distance is an average between the ones of a single and double bond (Figure 1.13).^[110]

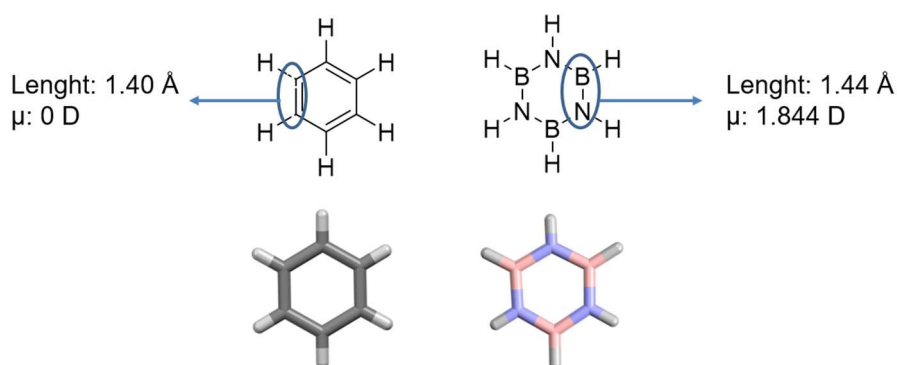


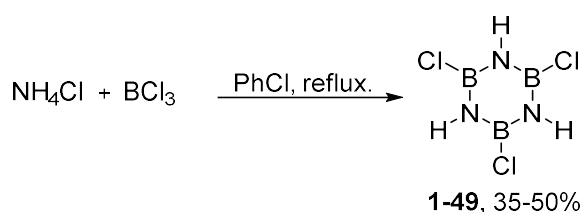
Figure 1.13: Molecular and crystal structures of benzene and borazine.^[111,112]

This fact, along with the planarity of borazine derivatives, led to hypothesize the presence of an aromatic ring current in this molecule. Despite this, many theoretical studies indicate only a weak aromatic character for borazine, which is in line with the experimental properties of this molecule, such as the afore mentioned high susceptibility towards hydrolysis and the tendency to undergo addition reactions.^[113] This difference in aromaticity and chemical behaviour, can be ascribed to the strongly polarized BN bonds in borazine, resulting in more localized electron densities on the more electronegative nitrogen atoms.^[114] This results in delocalization only on isolated BNB fragments^[113] ultimately opposing the presence of ring currents and widening the HOMO-LUMO gap with respect to benzene (7.9 eV vs 6.6 eV).^[90] Due to these peculiar properties, borazine represents the ideal candidate for graphene doping in order to obtain a widening of the bandgap.^[88] In order to synthesise borazine-doped nanographenes, the preparation of functionalized borazine derivatives that can subsequently undergo planarization reactions is required.

1.7.1 Borazine synthesis

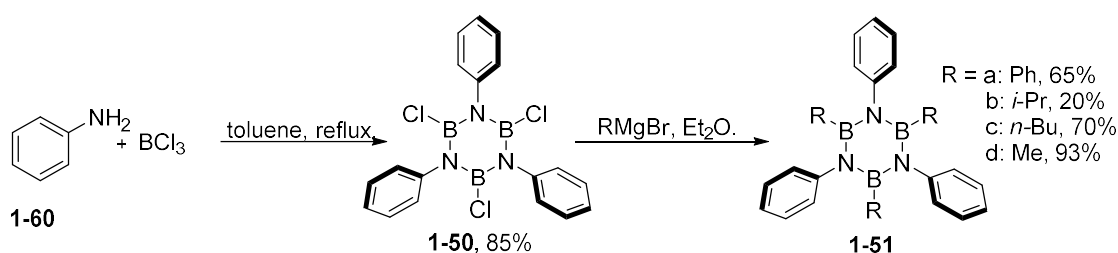
Many different approaches have been developed for the synthesis of borazine and its derivatives, starting from the original work by Stock and Pohland in 1926 involving the thermal dehydrogenation of $\text{NH}_3 \cdot \text{BH}_3$ at 200°C.^[115] This was followed by many variations involving the use of high pressure, lower temperatures or different precursors. In particular, the use of BH_3 adducts with alkyl amines led to the synthesis of N-Alkyl borazines in high yields (>90%).^[116] Along with borane adducts, ammonium

salts in the presence of lithium or sodium borohydride^[117,118] have been used successfully and even nitriles proved to be valid precursors when reacted with diborane in dimethoxyethane at 85°C.^[119] Dehydrogenation reactions leading to borazine derivatives were performed at low temperature using transition metal complexes as reported by Manner and co-workers who treated $\text{CH}_3\text{NH}_2 \cdot \text{BH}_3$ with $[\text{Rh}(1,5\text{-cod})(\mu\text{-Cl})]_2$ at 45°C leading to the formation of N,N',N'' -trimethylborazine in a 95% yield.^[120] A breakthrough in the synthesis of borazine derivatives was achieved in 1955 by Brown and Laubencayer using boron halides as precursors. In this procedure, BCl_3 was reacted with NH_4Cl in refluxing PhCl leading to the formation of B,B',B'' -trichloro borazine (Scheme 1.16).^[121]



Scheme 1.16: Synthesis of B,B',B'' -trichloroborazine **1-49**.

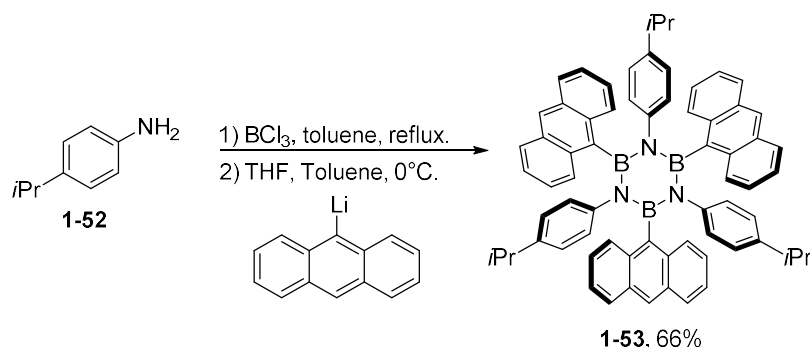
A further development of this synthesis came from the work of Groszos and Stafiej who prepared B,B',B'' -trichloro- N,N',N'' -triphenyl borazole (chloro-borazole) using a modified protocol based on the seminal work of Kinney and Jones.^[122] In this procedure, aniline was reacted with BCl_3 in refluxing toluene and the resulting chloro-borazole functionalized on the boron atoms using a substitution reaction with Grignard reagents.^[123,124] This new versatile approach allowed functionalisation of borazines on all the boron and nitrogen atoms, with the possibility of placing different substituents on different positions (Scheme 1.17).



Scheme 1.17: Synthesis of hexa-functionalised borazines.^[123]

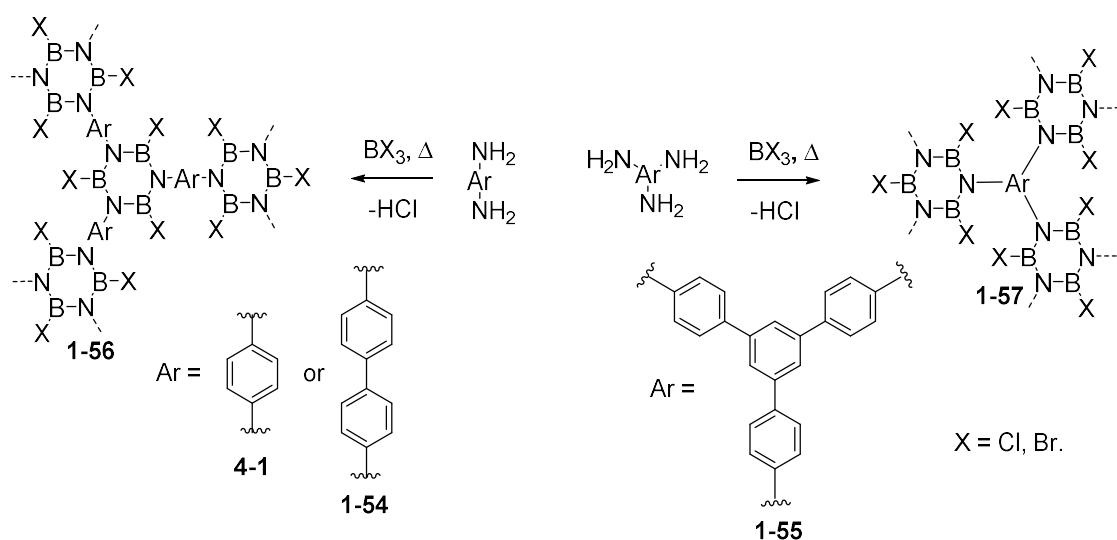
After the development of this synthetic strategy, the synthesis of borazines presenting six phenyl groups bonded to the borazine was achieved. The aryl rings could be functionalized in different ways as far as functional groups stable to the synthetic conditions were used. As an example of the versatility of this approach, Yamaguchi and co-workers obtained the formation of “molecular bundles” by reacting an *i*-Pr

functionalised chloro-borazole with the lithium reagent derivative of anthracene resulting in borazine **1-53** (Scheme 1.18).^[125]



Scheme 1.18: Synthesis of derivative **1-53**.^[125]

The same approach, relying on condensation reactions between boron halides and aniline derivatives, has been successfully used by El-Kaderi and co-workers in the synthesis of COFs presenting high surface area for gas absorption applications. To obtain the formation of the frameworks, **4-1**, **1-54** or **1-55** were treated with boron halides (BCl_3 or BBr_3) *via* a solvothermal approach. This resulted in the formation of the desired covalent networks (Scheme 1.19) and represents a valuable example of the synthesis of extended borazine-doped dendrimeric systems using these methods.^[126,127]

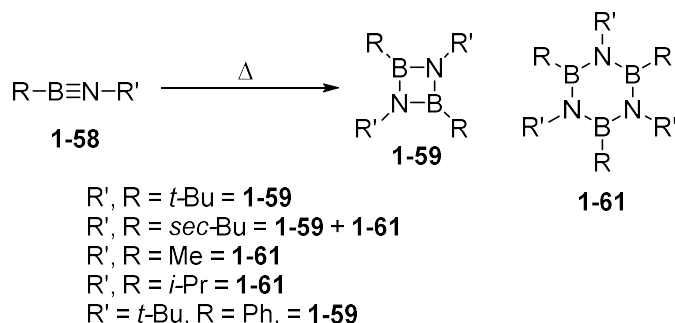


Scheme 1.19: Synthesis of borazine containing porous materials *via* condensation reaction as reported by El-Khaderi and co-workers.

1.7.2 Mechanism of formation

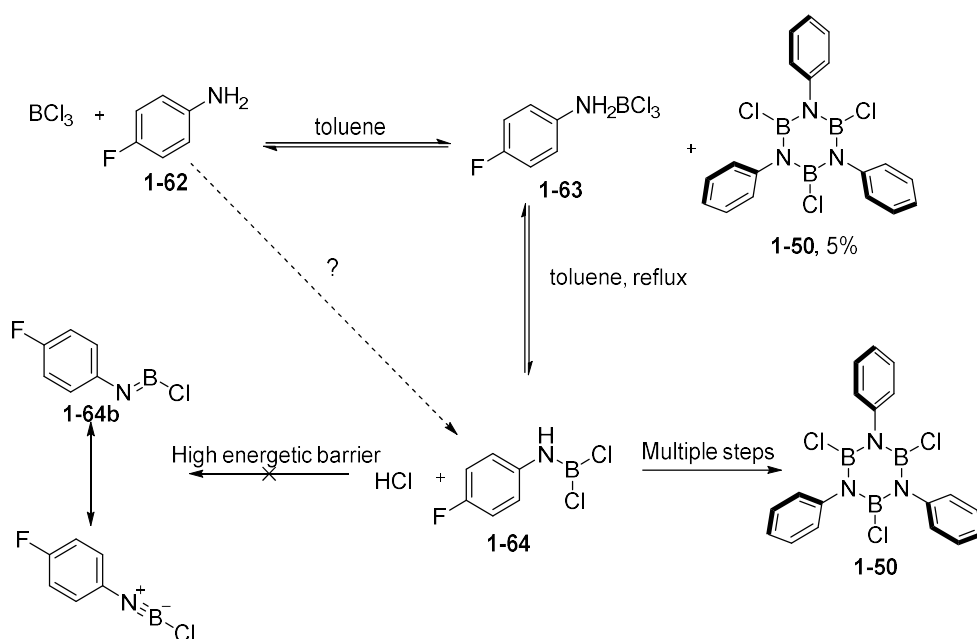
From the mechanistic point of view, various studies have been performed on the borazine synthesis to understand the key intermediates in the formation of this heterocycle. A 1+1+1+1+1+1 hexamerisation (*via* condensation or dehydrogenation) and a 2+2+2 trimerization have been proposed as possible mechanisms leading to the

formation of borazine rings. While the latter has been proposed by Paetzold and co-workers^[128] as the leading mechanism starting from dialkyliminoboranes (**1-58**, Scheme 1.20), the former seems to be more reliable for the thermal synthesis of borazines starting from amine-boron halide adducts.



Scheme 1.20: [2+2+2] mechanism involving iminoboranes.^[128]

In a paper published by Bettinger and co-workers the formation of borazine is elegantly studied by using 4-fluoro aniline as starting material and monitoring its reaction with BCl_3 using ^{19}F -NMR (Scheme 1.21).^[129]



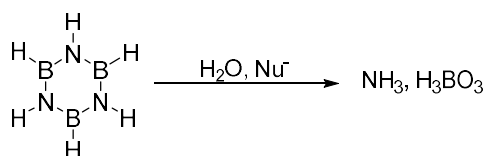
Scheme 1.21: Plausible mechanism of formation of borazine derivatives based on recent studies by Bettinger and co-workers.

These investigations confirmed the presence of the adduct **1-63** and borazine **1-50** after mixing at 0°C the two reagents. The formation of **1-50** in this step is still matter of debate and the role of trace impurities could not be ruled out. After heating at reflux, NMR studies confirmed the formation of anilindichloroborane (**1-64**), however, computational studies ruled out the elimination of HCl from this derivative to give iminoborane **1-64b** due to a very high energetic barrier associated to this step. No

evidence for intermediates between **1-64** and **1-50** was obtained, thus making impossible to draw conclusions for the conversion of **1-64** to **1-50**, however, free aniline arising from the first equilibrium seems to be involved in the formation of the final product.^[129]

1.7.3 Stability of borazine derivatives

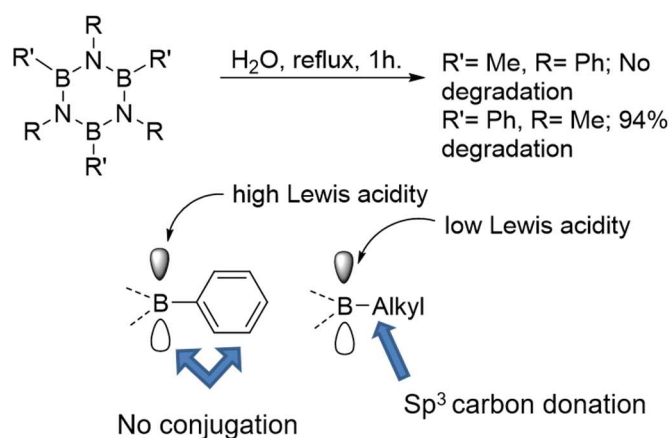
As previously reported, borazine is particularly reactive toward nucleophiles. This is related to the Lewis acidity of the boron atoms which are susceptible to nucleophilic attack, resulting in the hydrolysis of the borazine ring to ammonia and boric acid.^[110] This sensitive nature explains borazine tendency to hydrolyse in presence of atmospheric moisture (Scheme 1.22). The same characteristics are present in borazines functionalized with electron withdrawing groups on the boron atoms as in chloro-borazole derivatives. In this case, the presence of the chlorine further increases the Lewis acidity of the boron atom resulting in fast hydrolysis in presence of water.^[122]



Scheme 1.22: Hydrolysis of borazine in presence of moisture.

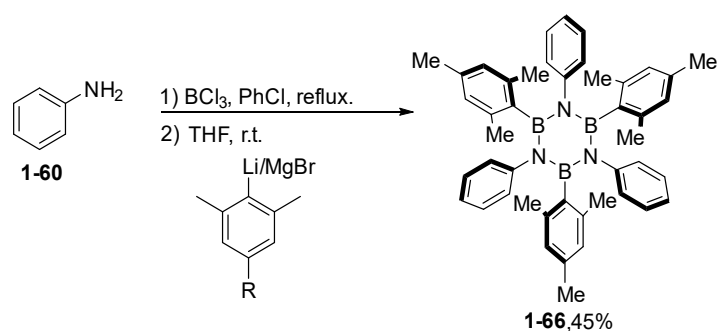
The introduction of substituents on boron and nitrogen atoms importantly affects the stability of borazines and this was already noticed in the 1950s by Groszos and Stafiej, who reported that B,B',B''-trialkyl-N,N',N''-triphenyl borazines display remarkable stability to moisture.^[124] This is related to a diminished Lewis acidity of the boron centres due to the electron donating nature of the sp³ carbon to which they are bonded. Borazines presenting alkynyl substituents on the boron atoms have been studied extensively by Nakagawa and co-workers, who proved that B,B',B''-trialkynyl borazines present half-lives of days in an 80% dioxane/water mixture and thus are more stable than the parent borazine and chloro-borazoles.^[130] Despite this, B,B',B''-trialkynyl borazines still undergo hydrolysis in the presence of water. An interesting observation comes from the work of Brotherton and McCloskey, who studied the rate of hydrolysis of different borazines in 90% acetone/water mixtures, concluding that, in general, alkyl groups on boron atoms increase the stability of the borazine ring, whereas phenyl groups decrease it.^[131] This result is highlighted by the comparison of the stability in boiling water between B,B',B''-trimethyl-N,N',N''-triphenyl borazine and B,B',B''-triphenyl-N,N',N''-trimethyl borazine; in the first case, after boiling in water for 1 h the borazine was recovered quantitatively, whereas in the second a 94% degradation was observed (Scheme 1.23).^[124] When hexaphenyl-borazines are considered, the same

rules apply. In this case, parent hexaphenyl-borazine is prone to hydrolysis ($t_{1/2} = 1.37$ h in acetone/water 90%) in the presence of moisture even if to a lesser extent compared to chloro-borazole derivatives.^[132] This susceptibility to hydrolysis for B,B',B''-triphenyl borazines, arises from the out-of-plane arrangement of the phenyl π system and boron empty p orbital, resulting in the absence of conjugation between the two. As a result, boron atoms in B,B',B''-triphenyl borazines present a quite high Lewis acidity, resulting in instability towards nucleophiles (Scheme 1.21).



Scheme 1.23: Different stabilities between B-Alkyl and -Aryl borazines.

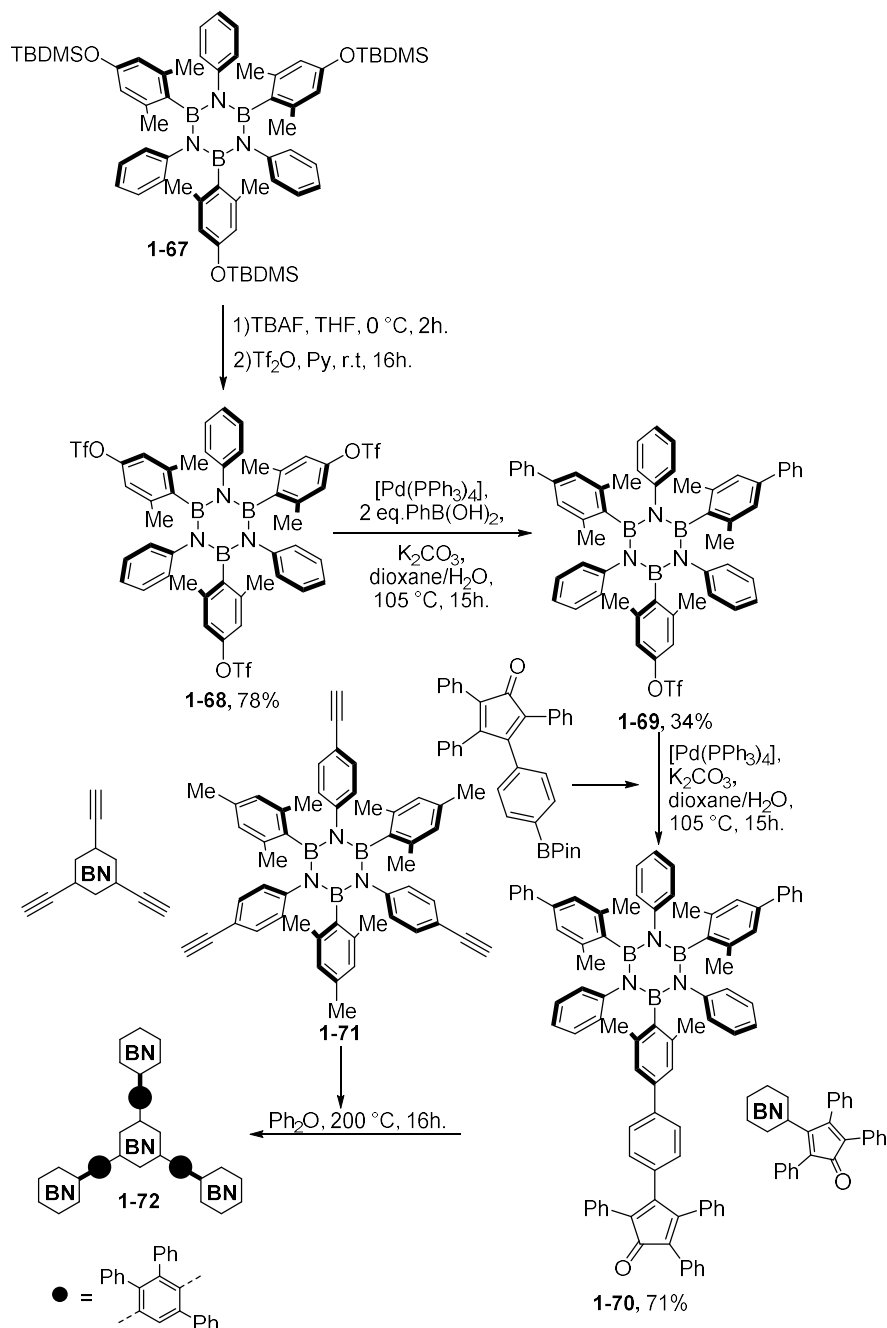
As reported by Nagasawa et al., in order to obtain hexaaryl-borazines completely stable to hydrolysis, it is necessary to introduce *ortho*-substituents on the boron bonded phenyl rings.^[133]



Scheme 1.24: Synthesis of hydrolysis stable borazine derivatives.

This results in a steric protection of the boron centres and thus in borazines completely stable towards hydrolysis. The most famous example of hydrolysis stable borazine is represented by the B,B',B''-trimesityl-N,N',N''-triphenyl borazine **1-66**, which has been synthesised by many groups and even used in optoelectronic applications (Scheme 1.24).^[134]

Borazines presenting mesityl or xylyl groups bonded to the boron atoms, proved to be resistant to cross-coupling reaction conditions, organometallics (RLi, RMgX), bases (TBAF, K_2CO_3), oxidants ($FeCl_3$) and reductants ($NaBH_4$, Fe, H_2 , Pd/C).^[110]



Scheme 1.25: Synthesis of borazine-doped polyphenylenes.^[86]

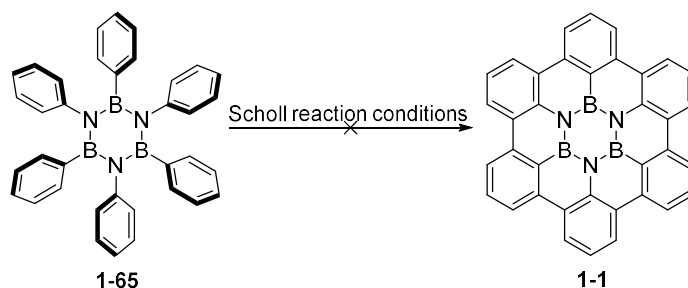
This stability allowed for the development of a rich chemistry on *ortho*-substituted hexaaryl-borazines, often resulting in very complex architectures. A notable example is represented by the work performed in our group, where the synthesis of complex borazine-based dendrimeric structures was obtained capitalizing on [4+2]

cycloadditions on B,B',B''-trimesityl/xylyl-N,N',N''-triphenyl borazine derivatives bearing acetylene and cyclopentadienone groups in specific positions (Scheme 1.25).^[86]

1.8 Borazines as precursors in the synthesis of nanographenes

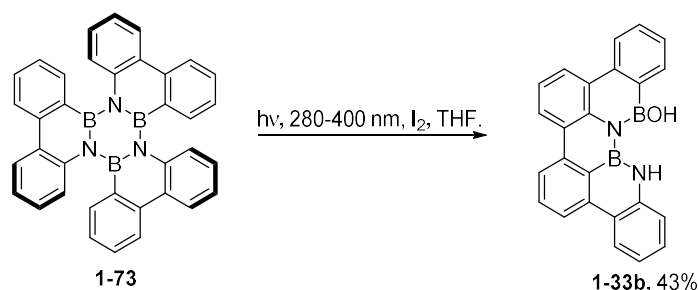
To use hexaphenyl-borazines as starting materials in nanographene synthesis, it is necessary to induce the formation of CC bonds among the phenyl substituents leading to the desired 2D structures. Many efforts have been dedicated to the conversion of hexaphenyl-borazine **1-65** into hexa-*peri*-hexabenzoborazinocoronene **1-1** which can be considered as the smallest unit of a borazine-doped graphene. Cyclodehydrogenations in the presence of various oxidants such as FeCl₃ in CH₃NO₂, MoCl₅ in CH₂Cl₂ and PIFA with BF₃·OEt₂ in CH₂Cl₂, led to the formation of intractable mixtures with no indication of the formation of the desired product (Scheme 1.26).^[135] Since all these attempts rely on oxidative conditions, oxidation of nitrogen atoms leading to degradation of the borazine rings can possibly explain the inability to form molecule **1-1**.

When AlCl₃ with CuCl₂ in CS₂ was used, an insoluble polymeric material was obtained, suggesting a preference for intermolecular bond formation with these reaction conditions. Analyses performed on the product revealed the presence of the borazine ring, indicating that this feature was not destroyed during the reaction.^[135]



Scheme 1.26: Attempted synthesis of HBBNC **1-1** with Scholl reactions.

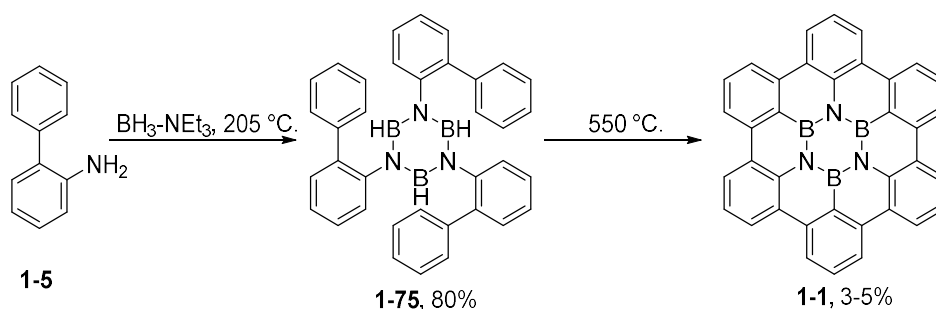
Another valuable attempt was carried out in the group of Bettinger by irradiation of BN doped hexabenzotriphenylene **1-73** with I₂ under UV irradiation at 280-400 nm (Scheme 1.27). This strategy is based on a similar procedure that proved to be very successful on stilbenes and polyphenylenes. However, in this case, the presence of the borazine ring dramatically reduces the CC bond formation yield, resulting in the exclusive formation of incomplete cyclization product **1-33b**.^[136]



Scheme 1.27: Attempted photophysical synthesis of **1-1**.

In a following study, Bettinger group used fs, ns and μs time-resolved spectroscopy to study the effect of the presence of the borazine ring compared to that of benzene on the excited state properties of the derivatives. From this study, the presence of the borazine ring essentially leads to a faster decay of hexaphenyl-borazine excited state compared to the full carbon analogue (3 ps vs 428 ps). Furthermore, the decrease in the conjugation determined by the increased electronic localization in the borazine ring results in a higher diradical character of the cyclized intermediates, with a low energetic barrier for bond fission, leading to very low CC bond formation yields.^[137]

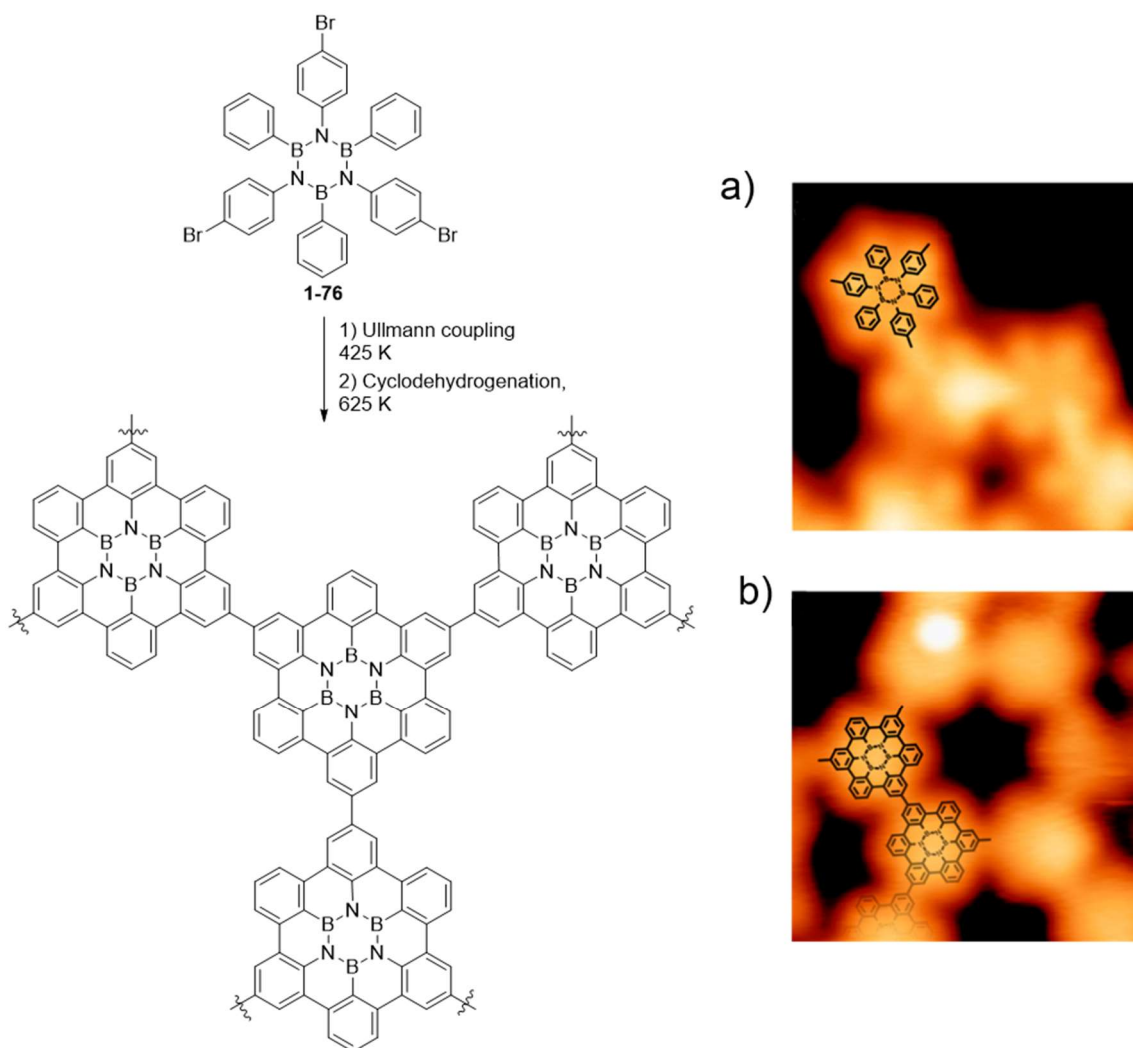
One of the most interesting results in the field was obtained again by Bettinger and co-workers, who used a thermolysis approach relying on the high thermal stability of BN-based materials to induce CC bond formation. In this strategy, biphenyl aniline **1-5** was treated with $\text{Et}_3\text{N}\cdot\text{BH}_3$ giving borazine **1-75**, which by subsequent treatment at 550°C under an inert atmosphere resulted in the formation of desired derivative **1-1** as a very insoluble material with a 3-5% yield (Scheme 1.28).



Scheme 1.28: Thermolytic synthesis of **1-1** as reported by Bettinger and co-workers.^[138]

Due to the insolubility of **1-1**, characterization was limited to solid state NMR techniques along with LR-MS and pXRD, which however presented two different phases in the pattern, one of which arising from an impurity.^[138,139] A very important result in the use of hexaphenyl-borazines as precursors for nanographene synthesis was obtained by Casu and Sanchez-Sanchez groups, who managed to synthesise molecule **1-1** and a borazine-doped PAH network using surface-assisted Ullmann coupling and dehydrogenation.^[140,141] In the work of Sanchez-Sanchez an Ullmann

coupling on derivative **1-76** was induced on a Ag(111) substrate at 425 K under UHV conditions. The resulting covalent network was then annealed at 625 K resulting in the formation of a precise network consisting of **1-1** units connected by covalent bonds (Scheme 1.29). The resulting material was formed only in small amounts and confined on surface, leading to an influence of the metallic substrate on the properties of the material.



Scheme 1.29: Synthesis of HBBNC network using surface chemistry.

1.9 Outlines of the dissertation

In this doctoral work our objective was the development of a solution phase synthesis of soluble HBBNC derivatives. Since all previous approaches only produced very insoluble **1-1** using surface chemistry or thermolytic procedures, it has been impossible to study in detail the properties of this derivative. The synthetic strategy for the preparation of such molecule is reported in *Chapter II* and represents the first example of a soluble borazine-doped nanographene. In this chapter, the synthesis and

planarization of bromo, chloro and fluoro hexaaryl-borazines was carried out resulting in the formation of soluble HBBNC using a silylium ion promoted reaction on fluoro hexaaryl-borazines.

Unveiling the optoelectronic properties of HBBNC represents a fundamental step in extending the knowledge on doping effects and towards the preparation of borazine-doped graphene presenting a tailored bandgap. For these reasons, an extensive study on the properties of this derivative has been carried out in *Chapter III* by comparison with tailored reference compounds. The results of these studies confirmed the ability of borazine doping to widen the HOMO-LUMO gap of PAHs, resulting in materials with blue emissions and high quantum yields.

Aiming at a successive synthesis of extended nanographenes, borazine-doped polyphenylene precursors (multi-borazines) were synthesised and these results are reported in *Chapter IV*. The resulting multi-borazines displayed doping concentrations between 12% and 18% and optoelectronic properties confirming the ability of borazine rings to break the conjugation of the polyphenylene backbone.

Finally, decarbonylative [4+2] cycloadditions were used to produce a borazine-doped polymeric material using B,B',B''-triethynyl-N,N',N''-triphenyl borazine as starting material. The synthesis and complete characterization of the resulting polymer are reported in *Chapter V*. This unprecedented material formed gels in chlorinated solvents and thanks to its remarkable thermal and chemical stability, was used as support in solid state electrolytes (SSEs).

1.10 References

- [1] J. Emsley, *Nature's Building Blocks: An AZ Guide to the Elements*, Oxford University Press, **2011**.
- [2] A. Hirsch, *Nat. Mater.* **2010**, *9*, 868–871.
- [3] R. Hoffmann, A. A. Kabanov, A. A. Golov, D. M. Proserpio, *Angew. Chemie Int. Ed.* **2016**, *55*, 10962–10976.
- [4] J. L. Delgado, M. Á. Herranz, N. Martín, *J. Mater. Chem.* **2008**, *18*, 1417–1426.
- [5] H. W. Kroto, J. R. Heath, S. C. O'Brien, R. F. Curl, R. E. Smalley, *Nature*, **1985**, *318*, 162–163.
- [6] P. R. Buseck, S. J. Tsipursky, R. Hettich, *Science*, **1992**, *257*, 215–217.
- [7] V. M. Radushkevich, L. V. Lukyanovich, *Zhurnal Fiz. Khimii* **1952**, *26*, 88–95.
- [8] S. Iijima, *Nature* **1991**, *354*, 56–58.
- [9] D. S. Bethune, C. H. Kiang, M. S. de Vries, G. Gorman, R. Savoy, D. S. Bethune, C. H. Klang, J. Vazquez, R. Beyers, *Nature* **1993**, *363*, 605–607.
- [10] S. Iijima, T. Ichihashi, *Nature* **1993**, *363*, 603–605.

- [11] S. Iijima, M. Yudasaka, R. Yamada, S. Bandow, K. Suenaga, F. Kokai, K. Takahashi, *Chem. Phys. Lett.* **1999**, *309*, 165–170.
- [12] V. N. Mochalin, O. Shenderova, D. Ho, Y. Gogotsi, *Nat. Nanotechnol.* **2012**, *7*, 11–23.
- [13] V. V. Danilenko, *Phys. Solid State* **2004**, *46*, 595–599.
- [14] Y. Liu, W. Hu, X. Wang, C. Long, J. Zhang, D. Zhu, D. Tang, S. Xie, *Chem. Phys. Lett.* **2000**, *331*, 31–34.
- [15] M. J. Allen, V. C. Tung, R. B. Kaner, *Chem. Rev.* **2010**, *110*, 132–145.
- [16] K. S. Novoselov, A. K. Geim, S. V. Morozov, D. Jiang, Y. Zhang, S. V. Dubonos, I. V. Grigorieva, A. A. Firsov, *Science*, **2004**, *306*, 666–669.
- [17] V. Georgakilas, J. A. Perman, J. Tucek, R. Zboril, *Chem. Rev.* **2015**, *115*, 4744–4822.
- [18] M. Taghioskoui, *Mater. Today* **2009**, *12*, 34–37.
- [19] S. Y. Zhou, Ç. Ö. Girit, A. Scholl, C. J. Jozwiak, D. A. Siegel, P. Yu, J. T. Robinson, F. Wang, A. Zettl, A. Lanzara, *Phys. Rev. B* **2009**, *80*, 121409.
- [20] E. Stolyarova, T. R. Kwang, S. Ryu, J. Maultzsch, P. Kim, L. E. Brus, T. F. Heinz, M. S. Hybertsen, G. W. Flynn, *Proc. Natl. Acad. Sci. U. S. A.* **2007**, *104*, 9209–9212.
- [21] W. Choi, I. Lahiri, R. Seelaboyina, Y. S. Kang, *Crit. Rev. Solid State Mater. Sci.* **2010**, *35*, 52–71.
- [22] J. H. Seol, I. Jo, A. L. Moore, L. Lindsay, Z. H. Aitken, M. T. Pettes, X. Li, Z. Yao, R. Huang, D. Broido, N. Mingo, S. R. Ruoff, L. Shi, *Science* **2010**, *328*, 213–216.
- [23] A. Alofi, G. P. Srivastava, *Phys. Rev. B* **2013**, *87*, 115421.
- [24] H. Y. Nan, Z. H. Ni, J. Wang, Z. Zafar, Z. X. Shi, Y. Y. Wang, *J. Raman Spectrosc.* **2013**, *44*, 1018–1021.
- [25] C. Lee, X. Wei, J. W. Kysar, J. Hone, *Science* **2008**, *321*, 385–388.
- [26] K. S. Novoselov, Z. Jiang, Y. Zhang, S. V. Morozov, H. L. Stormer, U. Zeitler, J. C. Maan, G. S. Boebinger, P. Kim, A. K. Geim, *Science* **2007**, *315*, 1379.
- [27] S. V. Morozov, K. S. Novoselov, M. I. Katsnelson, F. Schedin, D. C. Elias, J. A. Jaszczak, A. K. Geim, *Phys. Rev. Lett.* **2008**, *100*, 11–14.
- [28] J. H. Chen, C. Jang, S. Xiao, M. Ishigami, M. S. Fuhrer, *Nat. Nanotechnol.* **2008**, *3*, 206–209.
- [29] K. S. Novoselov, A. K. Geim, S. V. Morozov, D. Jiang, M. I. Katsnelson, I. V. Grigorieva, S. V. Dubonos, A. A. Firsov, *Nature* **2005**, *438*, 197–200.
- [30] A. K. Geim, K. S. Novoselov, *Nat. Mater.* **2007**, *6*, 183–191.
- [31] W. Han, R. K. Kawakami, M. Gmitra, J. Fabian, *Nat. Nanotechnol.* **2014**, *9*, 794–807.
- [32] A. H. Castro Neto, F. Guinea, N. M. R. Peres, K. S. Novoselov, A. K. Geim, *Rev. Mod. Phys.* **2009**, *81*, 109–162.
- [33] D. Wei, Y. Liu, *Adv. Mater.* **2010**, *22*, 3225–3241.
- [34] J. Zhu, *Nat. Nanotechnol.* **2008**, *3*, 528–529.

- [35] W. S. Hummers, R. E. Offeman, *J. Am. Chem. Soc.* **1958**, *80*, 1339.
- [36] S. Park, J. An, I. Jung, R. D. Piner, S. J. An, X. Li, A. Velamakanni, R. S. Ruoff, *Nano Lett.* **2009**, *9*, 1593–1597.
- [37] W. A. de Heer, C. Berger, X. Wu, P. N. First, E. H. Conrad, X. Li, T. Li, M. Sprinkle, J. Hass, M. L. Sadowski, M. Potemski, G. Martinez, *Solid State Commun.* **2007**, *143*, 92–100.
- [38] R. Muñoz, C. Gómez-Aleixandre, *Chem. Vap. Depos.* **2013**, *19*, 297–322.
- [39] J. B. Oostinga, H. B. Heersche, X. Liu, A. F. Morpurgo, L. M. K. Vandersypen, *Nat. Mater.* **2008**, *7*, 151–157.
- [40] Z. H. Ni, T. Yu, Y. H. Lu, Y. Y. Wang, Y. P. Feng, Z. X. Shen, *ACS Nano* **2008**, *2*, 2301–2305.
- [41] S. M. Choi, S. H. Jhi, Y. W. Son, *Phys. Rev. B* **2010**, *81*, 23–26.
- [42] G. Giovannetti, P. A. Khomyakov, G. Brocks, P. J. Kelly, J. Van Den Brink, *Phys. Rev. B* **2007**, *76*, 2–5.
- [43] J. Jung, A. M. DaSilva, A. H. Macdonald, S. Adam, *Nat. Commun.* **2015**, *6*, 6308.
- [44] T. Wassmann, A. P. Seitsonen, A. M. Saitta, M. Lazzeri, F. Mauri, *Phys. Rev. Lett.* **2008**, *101*, 1–4.
- [45] L. Li, G. Wu, G. Yang, J. Peng, J. Zhao, J. J. Zhu, *Nanoscale* **2013**, *5*, 4015–4039.
- [46] L. Ma, J. Wang, F. Ding, *ChemPhysChem* **2013**, *14*, 47–54.
- [47] Y. W. Son, M. L. Cohen, S. G. Louie, *Phys. Rev. Lett.* **2006**, *97*, 1–4.
- [48] K. A. Ritter, J. W. Lyding, *Nat. Mater.* **2009**, *8*, 235–242.
- [49] J. F. Morin, A. Jolly, D. Miao, M. Daigle, *Angew. Chemie Int. Ed.* **2020**, *59*, 4624–4633.
- [50] J. Wu, L. Gherghel, M. D. Watson, J. Li, Z. Wang, C. D. Simpson, U. Kolb, K. Müllen, *Macromolecules* **2003**, *36*, 7082–7089.
- [51] A. Narita, X. Feng, Y. Hernandez, S. A. Jensen, M. Bonn, H. Yang, I. A. Verzhbitskiy, C. Casiraghi, M. R. Hansen, A. H. R. Koch, G. Fytas, O. Ivasenko, B. Li, K. S. Mali, T. Balandina, S. Mahesh, S. De Feyter, K. Müllen, *Nat. Chem.* **2014**, *6*, 126–132.
- [52] Y. Fogel, L. Zhi, A. Rouhanipour, D. Andrienko, H. J. Räder, K. Müllen, *Macromolecules* **2009**, *42*, 6878–6884.
- [53] L. Talirz, P. Ruffieux, R. Fasel, *Adv. Mater.* **2016**, *28*, 6222–6231.
- [54] J. Cai, P. Ruffieux, R. Jaafar, M. Bieri, T. Braun, S. Blankenburg, M. Muoth, A. P. Seitsonen, M. Saleh, X. Feng, K. Müllen, R. Fasel, *Nature* **2010**, *466*, 470–473.
- [55] P. Ruffieux, S. Wang, B. Yang, C. Sanchez-Sanchez, J. Liu, T. Dienel, L. Talirz, P. Shinde, C. A. Pignedoli, D. Passerone, T. Dumslaff, X. Feng, K. Müllen, R. Fasel, *Nature* **2016**, *531*, 489–492.
- [56] A. Narita, X. Y. Wang, X. Feng, K. Müllen, *Chem. Soc. Rev.* **2015**, *44*, 6616–6643.

- [57] X. Wang, G. Sun, P. Routh, D. H. Kim, W. Huang, P. Chen, *Chem. Soc. Rev.* **2014**, *43*, 7067–7098.
- [58] H. Wang, Y. Zhou, D. Wu, L. Liao, S. Zhao, H. Peng, Z. Liu, *Small* **2013**, *9*, 1316–1320.
- [59] T. Wu, H. Shen, L. Sun, B. Cheng, B. Liu, J. Shen, *New J. Chem.* **2012**, *36*, 1385–1391.
- [60] Z. S. Wu, W. Ren, L. Xu, F. Li, H. M. Cheng, *ACS Nano* **2011**, *5*, 5463–5471.
- [61] T. V. Khai, H. G. Na, D. S. Kwak, Y. J. Kwon, H. Ham, K. B. Shim, H. W. Kim, *J. Mater. Chem. C* **2012**, *3*, 17992–18003.
- [62] T. Schiros, D. Nordlund, L. Pálková, D. Prezzi, L. Zhao, K. S. Kim, U. Wurstbauer, C. Gutiérrez, D. Delongchamp, C. Jaye, D. Fischer, H. Ogasawara, L. G. M. Pettersson, D. R. Reichman, P. Kim, M. S. Hybertsen, A. N. Pasupathy, *Nano Lett.* **2012**, *12*, 4025–4031.
- [63] D. Wei, Y. Liu, Y. Wang, H. Zhang, L. Huang, G. Yu, *Nano Lett.* **2009**, *9*, 1752–1758.
- [64] A. Leela, M. Reddy, A. Srivastava, S. R. Gowda, H. Gullapalli, M. Dubey, P. M. Ajayan, *ACS Nano* **2010**, *4*, 6337–6342.
- [65] D. Usachov, O. Vilkov, A. Grüneis, D. Haberer, A. Fedorov, V. K. Adamchuk, A. B. Preobrajenski, P. Dudin, A. Barinov, M. Oehzelt, C. Laubschat, D. V. Vyalikh, *Nano Lett.* **2011**, *11*, 5401–5407.
- [66] Z. H. Sheng, L. Shao, J. J. Chen, W. J. Bao, F. Bin Wang, X. H. Xia, *ACS Nano* **2011**, *5*, 4350–4358.
- [67] G. H. Jun, S. H. Jin, B. Lee, B. H. Kim, W. S. Chae, S. H. Hong, S. Jeon, *Energy Environ. Sci.* **2013**, *6*, 3000–3006.
- [68] P. Wu, Z. Cai, Y. Gao, H. Zhang, C. Cai, *Chem. Commun.* **2011**, *47*, 11327–11329.
- [69] L. Sun, L. Wang, C. Tian, T. Tan, Y. Xie, K. Shi, M. Li, H. Fu, *RSC Adv.* **2012**, *2*, 4498–4506.
- [70] K. A. Mkhoyan, A. W. Contryman, J. Silcox, D. A. Stewart, G. Eda, C. Mattevi, S. Miller, M. Chhowalla, *Nano Lett.* **2009**, *9*, 1058–1063.
- [71] D. R. Dreyer, S. Park, C. W. Bielawski, R. S. Ruoff, *Chem. Soc. Rev.* **2010**, *39*, 228–240.
- [72] Z. W. Liu, F. Peng, H. J. Wang, H. Yu, W. X. Zheng, J. Yang, *Angew. Chemie Int. Ed.* **2011**, *50*, 3257–3261.
- [73] H. Gao, Z. Liu, L. Song, W. Guo, W. Gao, L. Ci, A. Rao, W. Quan, R. Vajtai, P. M. Ajayan, *Nanotechnology* **2012**, *23*, 1–7.
- [74] I. Y. Jeon, S. Zhang, L. Zhang, H. J. Choi, J. M. Seo, Z. Xia, L. Dai, J. B. Baek, *Adv. Mater.* **2013**, *25*, 6138–6145.
- [75] M. Kan, Y. Li, Q. Sun, *WIREs Comput. Mol. Sci.* **2016**, *6*, 65–82.
- [76] M. Sugie, H. Takeo, C. Matsumura, *Chem. Phys. Lett.* **1979**, *64*, 573–575.
- [77] K. Watanabe, T. Taniguchi, H. Kanda, *Nat. Mater.* **2004**, *3*, 404–409.
- [78] L. Liu, Z. Shen, *Appl. Phys. Lett.* **2009**, *95*, 252104.

- [79] L. Ci, L. Song, C. Jin, D. Jariwala, D. Wu, Y. Li, A. Srivastava, Z. F. Wang, K. Storr, L. Balicas, F. Liu, P. M. Ajayan, *Nat. Mater.* **2010**, *9*, 430–435.
- [80] G. Bepete, D. Voiry, M. Chhowalla, Z. Chiguvare, N. J. Coville, *Nanoscale* **2013**, *5*, 6552–6557.
- [81] C. Huang, C. Chen, M. Zhang, L. Lin, X. Ye, S. Lin, M. Antonietti, X. Wang, *Nat. Commun.* **2015**, 7698.
- [82] C. Chen, K. Guo, Y. Zhu, F. Wang, W. Zhang, H. Qi, *Appl. Mater. Interfaces* **2019**, *11*, 33245–33253.
- [83] Y. Gao, Y. Zhang, P. Chen, Y. Li, M. Liu, T. Gao, D. Ma, Y. Chen, Z. Cheng, X. Qiu, W. Duan, Z. Liu, *Nano Lett.* **2013**, *13*, 3439–3443.
- [84] L. Liu, J. Park, D. A. Siegel, K. F. McCarty, K. W. Clark, W. Deng, L. Basile, J. C. Idrobo, A. Li, G. Gu, *Science* **2014**, *343*, 163–167.
- [85] M. P. Levendorf, C. J. Kim, L. Brown, P. Y. Huang, R. W. Havener, D. A. Muller, J. Park, *Nature* **2012**, *488*, 627–632.
- [86] D. Marinelli, F. Fasano, B. Najjari, N. Demitri, D. Bonifazi, *J. Am. Chem. Soc.* **2017**, *139*, 5503–5519.
- [87] N. Otero, C. Pouchan, P. Karamanis, *J. Mater. Chem. C* **2017**, *5*, 8273–8287.
- [88] N. Otero, K. E. El-Kelany, C. Pouchan, M. Rérat, P. Karamanis, *Phys. Chem. Chem. Phys.* **2016**, *18*, 25315–25328.
- [89] H. I. Sirikumara, E. Putz, M. Al-Abboodi, T. Jayasekera, *Sci. Rep.* **2016**, *6*, 19115.
- [90] A. J. V. Marwitz, M. H. Matus, L. N. Zakharov, D. A. Dixon, S. Y. Liu, *Angew. Chemie Int. Ed.* **2009**, *48*, 973–977.
- [91] X. Zheng, G. E. Herberich, *Organometallics* **2000**, *19*, 3751–3753.
- [92] M. J. S. Dewar, V. P. Kubba, R. Pettit, *J. Chem. Soc.* **1958**, 3073–3076.
- [93] M. J. D. Bosdet, C. A. Jaska, W. E. Piers, T. S. Sorensen, M. Parvez, *Org. Lett.* **2007**, *9*, 1395–1398.
- [94] A. Abengózar, D. Sucunza, P. García-García, D. Sampedro, A. Pérez-Redondo, J. J. Vaquero, *J. Org. Chem.* **2019**, *84*, 7113–7122.
- [95] S. S. Chissick, M. J. S. Dewar, P. M. Maitlis, *Tetrahedron Lett.* **1960**, *1*, 8–10.
- [96] M. J. D. Bosdet, W. E. Piers, T. S. Sorensen, M. Parvez, *Angew. Chem. Int. Ed.* **2007**, *46*, 4940–4943.
- [97] D. J. H. Emslie, W. E. P. Piers, M. Parvez, *Angew. Chem. Int. Ed.* **2003**, *42*, 1251–1255.
- [98] C. A. Jaska, D. J. H. Emslie, M. J. D. Bosdet, W. E. Piers, T. S. Sorensen, M. Parvez, *J. Am. Chem. Soc.* **2006**, *128*, 10885–10896.
- [99] T. Kaehler, M. Bolte, H. Lerner, M. Wagner, *Angew. Chem. Int. Ed* **2019**, *131*, 11501–11506.
- [100] M. Numano, N. Nagami, S. Nakatsuka, T. Katayama, *Chem. A Eur. J.* **2016**, *22*, 11574–11577.
- [101] X. Wang, F. Zhang, K. S. Schellhammer, P. Machata, F. Ortmann, G. Cuniberti, Y. Fu, J. Hunger, R. Tang, A. A. Popov, R. Berger, K. Müllen, X. Feng, *J. Am.*

- Chem. Soc.* **2016**, *138*, 11606–11615.
- [102] J. Tasseroul, M. M. Lorenzo-Garcia, J. Dosso, F. Simon, S. Velari, A. De Vita, P. Tecilla, D. Bonifazi, *J. Org. Chem.* **2020**, *85*, 3454–3464.
- [103] M. Fingerle, C. Maichle-Mössmer, S. Schundelmeier, B. Speiser, H. F. Bettinger, *Org. Lett.* **2017**, *19*, 4428–4431.
- [104] M. Fingerle, H. F. Bettinger, *Chem. Commun.* **2020**, *56*, 3847–3850.
- [105] M. Fingerle, S. Stocker, H. F. Bettinger, *Synthesis* **2019**, *51*, 4147–4152.
- [106] K. Matsui, S. Oda, K. Yoshiura, K. Nakajima, N. Yasuda, T. Hatakeyama, *J. Am. Chem. Soc.* **2018**, *140*, 1195–1198.
- [107] T. Hatakeyama, S. Hashimoto, S. Seki, M. Nakamura, *J. Am. Chem. Soc.* **2011**, *133*, 18614–18617.
- [108] Y. Kondo, K. Yoshiura, S. Kitera, H. Nishi, S. Oda, H. Gotoh, Y. Sasada, M. Yanai, T. Hatakeyama, *Nat. Photonics* **2019**, *13*, 678–682.
- [109] Y. Fu, H. Yang, Y. Gao, L. Huang, R. Berger, J. Liu, H. Lu, Z. Cheng, S. Du, H.-J. Gao, X. Feng, *Angew. Chemie Int. Ed.* **2020**, *59*, 8873–8879.
- [110] D. Bonifazi, F. Fasano, M. M. Lorenzo-garcia, D. Marinelli, J. Tasseroul, *Chem. Commun.* **2015**, *51*, 15222–15236.
- [111] R. Boese, A. H. Maulitz, P. Stellberg, *Chem. Ber.* **1994**, *127*, 1887–1889.
- [112] A. Katrusiak, M. Podsiadło, A. Budzianowski, *Cryst. Growth Des.* **2010**, *10*, 3461–3465.
- [113] R. Islas, E. Chamorro, J. Robles, T. Heine, J. C. Santos, G. Merino, *Struct. Chem.* **2007**, *18*, 833–839.
- [114] R. A. Iwaki, T. Udagawa, *Chem. Phys. Lett.* **2020**, *745*, 137271.
- [115] A. Stock, E. Pohland, *Berichte der Dtsch. Chem. Gesellschaft* **1926**, *59*, 2215–2223.
- [116] A. Meller, E. Schaschel, *Inorg. Nucl. Chem. Lett.* **1966**, *2*, 41–43.
- [117] T. Wideman, L. G. Sneddon, *Inorg. Chem.* **1995**, *34*, 1002–1003.
- [118] G. W. Schaeffer, R. Schaeffer, H. I. Schlesinger, *J. Am. Chem. Soc.* **1951**, *73*, 1612–1614.
- [119] A. J. Leffler, *Inorg. Chem.* **1964**, *3*, 145–146.
- [120] C. A. Jaska, K. Temple, A. J. Lough, I. Manners, *J. Am. Chem. Soc.* **2003**, *125*, 9424–9434.
- [121] C. A. Brown, A. W. Laubengayer, *J. Am. Chem. Soc.* **1955**, *77*, 3699–3700.
- [122] R. G. Jones, C. R. Kinney, *J. Am. Chem. Soc.* **1939**, *61*, 1378–1381.
- [123] J. H. Smalley, S. F. Stafiej, *J. Am. Chem. Soc.* **1959**, *81*, 582–586.
- [124] S. J. Groszos, S. F. Stafiej, *J. Am. Chem. Soc.* **1958**, *80*, 1357–1360.
- [125] A. Wakamiya, T. Ide, S. Yamaguchi, *J. Am. Chem. Soc.* **2005**, *127*, 14859–14866.
- [126] T. E. Reich, S. Behera, K. T. Jackson, P. Jena, H. M. El-Kaderi, *J. Mater. Chem.* **2012**, *22*, 13524–13528.

- [127] T. E. Reich, K. T. Jackson, S. Li, P. Jena, H. M. El-Kaderi, *J. Mater. Chem.* **2011**, *21*, 10629–10632.
- [128] P. Paetzold, *Phosphorus. Sulfur. Silicon Relat. Elem.* **1994**, *93*, 39–50.
- [129] J. Hahn, M. Krieg, C. Keck, C. Maichle-Mössmer, R. F. Fink, H. F. Bettinger, *Dalt. Trans.* **2018**, *47*, 17304–17316.
- [130] H. Watanabe, T. Totani, T. Yoshizaki, *Inorg. Chem.* **1965**, *4*, 657–660.
- [131] R. J. Brotherton, A. L. McCloskey, *Adv. Chem.* **1964**, *42*, 131–138.
- [132] I. B. Atkinson, D. C. Blundell, D. B. Clapp, *J. Inorg. Nucl. Chem.* **1972**, *34*, 3037–3041.
- [133] K. Nagasawa, *Inorg. Chem.* **1966**, *5*, 442–445.
- [134] S. Kervyn, O. Fenwick, F. Di Stasio, Y. S. Shin, J. Wouters, G. Accorsi, S. Osella, D. Beljonne, F. Cacialli, D. Bonifazi, *Chem. Eur. J.* **2013**, *19*, 7771–7779.
- [135] C. Tönshoff, M. Müller, T. Kar, F. Latteyer, T. Chassé, K. Eichele, H. F. Bettinger, *ChemPhysChem.* **2012**, *13*, 1173–1181.
- [136] M. Müller, S. Behnle, C. Maichle-Mössmer, H. F. Bettinger, *Chem. Commun.* **2014**, *50*, 7821–7823.
- [137] J. A. Snyder, P. Grüninger, H. F. Bettinger, A. E. Bragg, *J. Phys. Chem. A* **2017**, *121*, 8359–8367.
- [138] M. Krieg, F. Reicherter, P. Haiss, M. Ströbele, K. Eichele, M. J. Treanor, R. Schaub, H. F. Bettinger, *Angew. Chemie Int. Ed.* **2015**, *54*, 8284–8286.
- [139] S. Biswas, M. Müller, C. Tönshoff, K. Eichele, C. Maichle-Mössmer, A. Ruff, B. Speiser, H. F. Bettinger, *Eur. J. Org. Chem.* **2012**, *24*, 4634–4639.
- [140] C. Sánchez-Sánchez, S. Brüller, H. Sachdev, K. Müllen, M. Krieg, H. F. Bettinger, A. Nicolai, V. Meunier, L. Talirz, R. Fasel, P. Ruffieux, *ACS Nano* **2015**, *9*, 9228–9235.
- [141] F. Ciccullo, A. Calzolari, M. Krieg, H. F. Bettinger, E. Magnano, T. Chasse, M. B. Casu, *J. Phys. Chem. C* **2016**, *120*, 17645–17651.

CHAPTER 2

BORAZINE-DOPED NANOGRAPHENES: SYNTHESIS OF HEXA-*PERI*-HEXABENZOBORAZINOCORONENE

This chapter describes the synthesis of the first soluble borazine-doped nanographene (**2-1**), focusing on the various attempts made to synthesize this long-sought molecule. With the aim of obtaining the desired product, various carbon-carbon (CC) sp² bond forming reactions have been tested on different halogen-functionalized borazines. Ultimately, the development of *ortho* functionalized borazines presenting two fluorine atoms on the boron bonded aryl rings allowed us to perform a Friedel-Crafts like CC bond formation using a silylium ion as reported by Siegel et al. This approach produced the desired product in a 5% yield along with partially cyclized by-product **2-33**. Theoretical studies gave an insight on the reaction mechanism and allowed for the design of a borazine derivative presenting one fluorine on each aryl ring (**2-34**) leading to increased yields and to the isolation of unprecedented B₃N₂O doped PAH **2-38**. Finally, different silylium ion reagents were tested and the suitability of the reaction conditions for different functional groups was investigated offering a complete set of tools for the synthesis of borazine-doped nanographenes.

The chapter is divided in 14 main sections: *i*) section 2.1 presents the aim of the project; *ii*) section 2.2 describes previous approaches towards the synthesis of a soluble derivative of hexa-*peri*-hexabenzoborazinocoronene (**2-1**); *iii*) section 2.3 describes the use of *ortho*-functionalized borazines as precursors in the synthesis of **2-1**; *iv*) section 2.4 describes the CC bond forming reactions that can be used to obtain **2-1** starting from halogen hexaaryl-borazines *v*) Section 2.5 displays the retrosynthetic approach towards **2-1** using halogen *ortho*-functionalized borazines; *vi*) section 2.6 contains the synthesis of bromo hexaaryl-borazines; *vii*) section 2.7 contains the synthesis and planarization attempts on chloro hexaaryl-borazines; *viii*) section 2.8 contains the synthesis and planarization attempts on fluoro hexaaryl-borazines; *ix*) Section 2.9 presents theoretical studies on reaction mechanism along with an optimization of reaction conditions; *x*) Section 2.10 contains the synthesis of non-functionalised HBBNC **1-1**; *xi*) Section 2.11 presents studies on the effect of different weakly coordinating anions (WCA) on the reaction outcome; *xii*) Section 2.12 presents planarization attempts on fluoro hexaaryl-borazines presenting different functional groups; *xiii*) Section 2.13 presents some conclusions and perspectives for future work; *xiv*) Section 2.14 contains references for the chapter.

Chapter 2

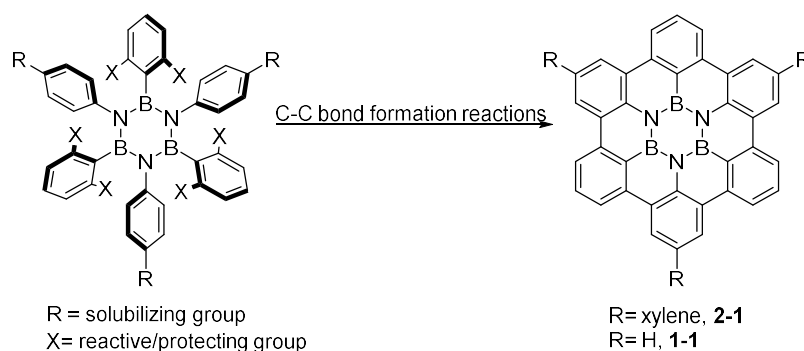
The research work described in sections 2.1-2.12 was carried out at Cardiff university. X-Ray analysis was performed by D. Marinelli and N. Biot (Cardiff University) and N. Demitri (Elettra-Sincrotrone, Basovizza, Trieste, Italy). Photophysical characterization was carried out by Dr. A. Fermi and T. Battisti. (Cardiff University) Computational investigations were performed by T. Battisti and B. D. Ward (Cardiff University), powder X-Ray diffraction was performed by K. D. M. Harris and C. Hughes (Cardiff University).

Part of the work reported in this chapter has been published in the following articles: **Dosso, J.**; Tasseroul, J.; Fasano, F.; Marinelli, D.; Biot, N.; Fermi, A.; Bonifazi, D. Synthesis and Optoelectronic Properties of Hexa-*peri*-hexabenzoborazinocoronene. *Angew. Chem., Int. Ed.* **2017**, 56, 4483–4487.

Dosso, J.; Battisti T.; Ward B. D.; Demitri, N.; Hughes C.; Williams P.A.; Harris K. D. M.; Bonifazi, D. Boron-nitrogen-doped nanographenes: a synthetic tale from borazine precursors. *Chem. A Eur. J.* **2020**, 26, 6608-6621.

2.1 Aim of the project

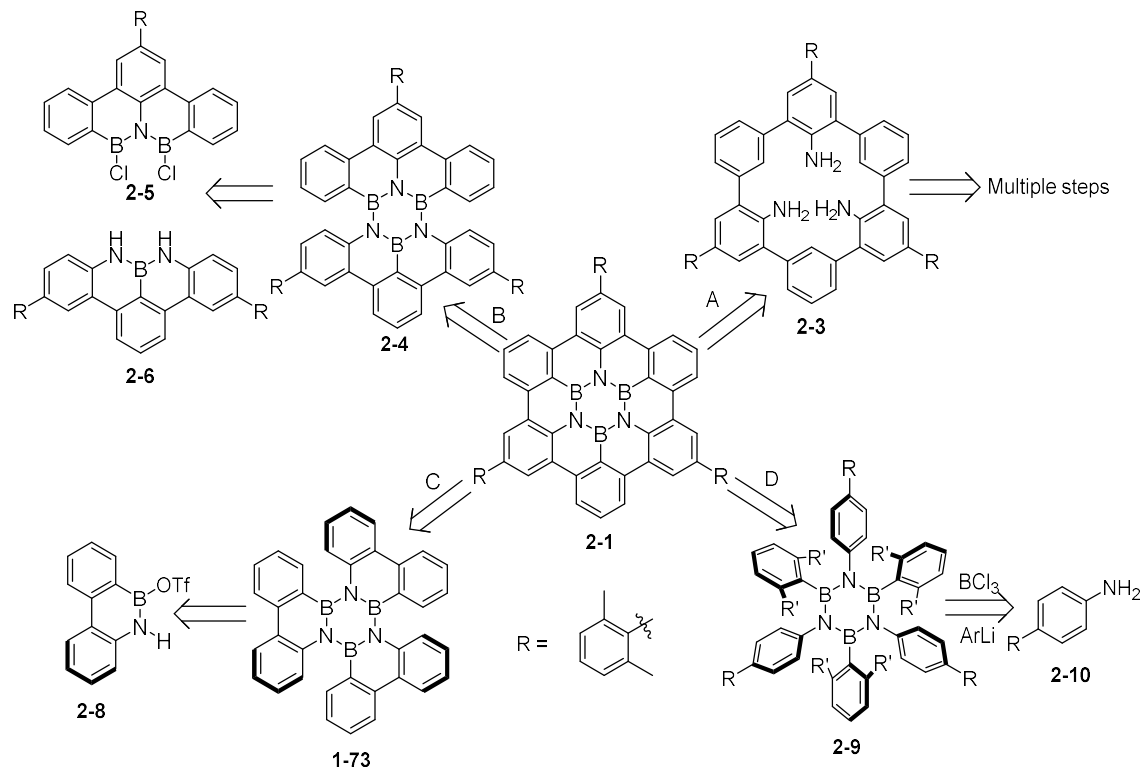
Representing the archetypal borazine-doped nanographene and the smallest unit of a borazine-doped graphene, elusive *hexa-peri-hexabenzoborazinocoronene* (**1-1**) has been at the centre of an extensive synthetic effort. To the best of our knowledge, the synthesis of this molecule has been achieved only with surface chemistry and a thermolytic approach, in both cases using hexaphenyl-borazine (**1-65**) derivatives as starting materials. The low yields and unpractical syntheses together with the very low solubility of **1-1**, contributed to the low amount of experimental data available for this molecule. This work aims at the obtainment of a soluble and thus fully characterizable derivative of **1-1**, resulting in an experimental confirmation of theoretical studies performed on this molecule. To form the desired soluble **2-1** using a solution-based synthesis, different strategies involving borazines as starting materials need to be investigated. From this point of view, borazines bearing *ortho*-functional groups able to undergo CC bond formation under the right conditions, represent the best approach towards a solution-based synthesis of **2-1** derivatives (Scheme 2.1). Consequently, a thorough study on the stability and reactivity of *ortho*-functionalized borazines needs to be carried out since many of these derivatives have never been prepared before. Theoretical investigations will be carried out to understand the reaction mechanisms and different starting materials, reagents and functional groups will be tested to reach a reliable procedure towards the synthesis of **2-1**, **1-1** and various functionalized derivatives. The result of this work will be a complete investigation of the reaction conditions to form HBBNC derivatives.



Scheme 2.1: General scheme towards the synthesis of soluble **2-1**.

2.2 Previous work towards the synthesis of 2-1

In order to synthesise a soluble derivative of HBBNC (**2-1**) different approaches relying on the formation of BN, BC and CC bonds have been attempted in our group as well as others, as highlighted in Scheme 2.2.



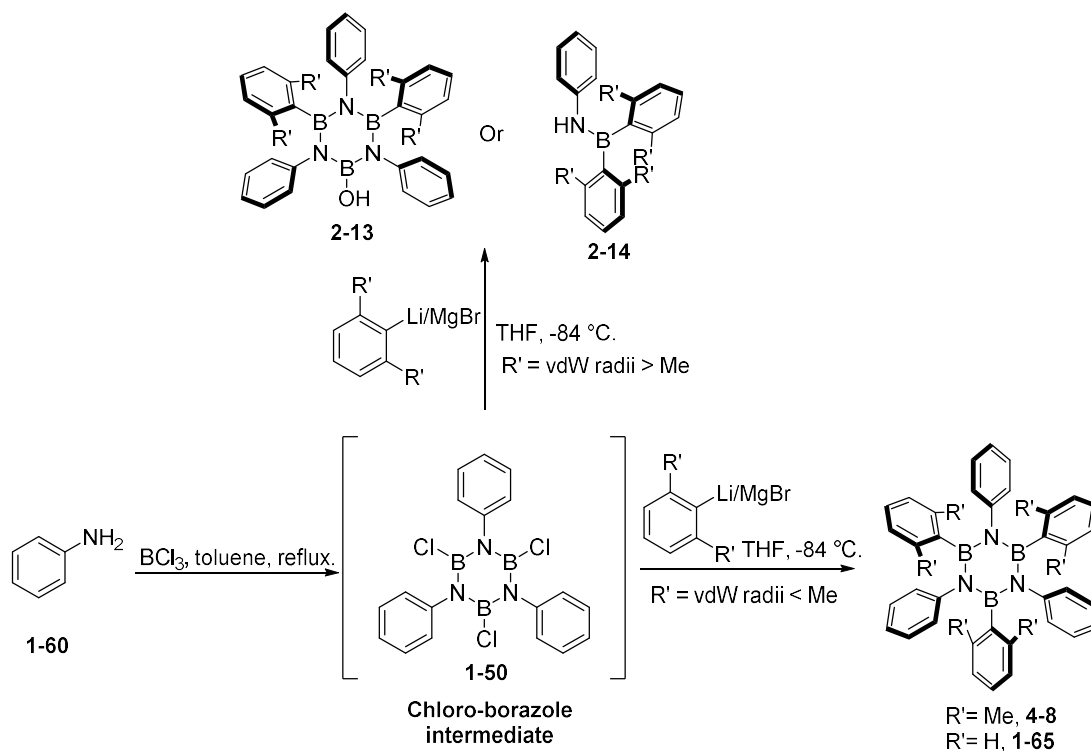
Scheme 2.2: Previous solution-based attempts towards synthesis of **2-1**.

In our group, the synthesis of amino-spherand derivative **2-3** was initially attempted (Path A), relying on a final electrophilic borylation to give **2-1**. Despite some initial success in the synthesis of various intermediate products, the extremely complicated synthesis of **2-3**, based on multiple cross-coupling reactions and protection/deprotection steps, resulted in very low yields, ultimately making impossible to obtain desired **2-3**. This result required a change in the synthetic strategy and a synthesis involving the coupling of NBN and BNB fragments **2-6** and **2-5** (Path B) was attempted. This strategy relied on the formation of two BN and two CC bonds to give the final **2-1**. However, despite the successful synthesis of fragment **2-6**, the difficulties encountered in the synthesis of BNB derivative **2-5** along with the difficult coupling between the poorly reactive N-H moieties and the hydrolysis prone BCl made impossible to obtain **2-1**. At this point, the only options remaining were represented by the formation of three (Path C) or six (Path D) CC bonds on a preformed borazine derivative. In path A, an attempt to form the missing three CC bonds on a borazino triphenylene derivative was carried out by Bettinger and co-workers. In this case, the

strained starting material **2-7** is prone to hydrolysis and all attempts involving irradiation failed, leading only to partially planarized derivatives. To avoid the use of strained starting materials, the formation of six CC bonds starting from *ortho* functionalized hexaaryl-borazine derivatives (**2-9**) can be envisaged (pathway D). In this approach, borazines bearing *ortho* functional groups able to undergo CC bond formation reactions are used as starting materials for the synthesis of HBBNC derivatives. A careful choice of the *ortho* functional groups is necessary, since a balance between reactivity in the planarization reaction and stability of the borazine is required. To address these points, an investigation on the synthesis and planarization of *ortho* functionalised borazines needs to be carried out.

2.3 *Ortho*-functionalized borazines as precursors in the BN-doped nanographenes synthesis

To obtain the desired soluble **2-1** a careful design of the starting borazines is required. Generally, hexaaryl-borazine derivatives are synthesized following the synthetic route displayed in Scheme 2.3. In this synthesis, aniline **1-60** is treated with BCl_3 in refluxing toluene to give chloro-borazole **1-50**. Subsequent treatment of **1-50** with an organometallic reagent (ArLi or ArMgX) results in a substitution reaction on the boron atoms giving the desired hexaaryl-borazines.



Scheme 2.3: General synthesis towards stable *ortho*-functionalized hexaaryl-borazine derivative **4-8**. Effects of steric parameters on reaction outcome are also reported.

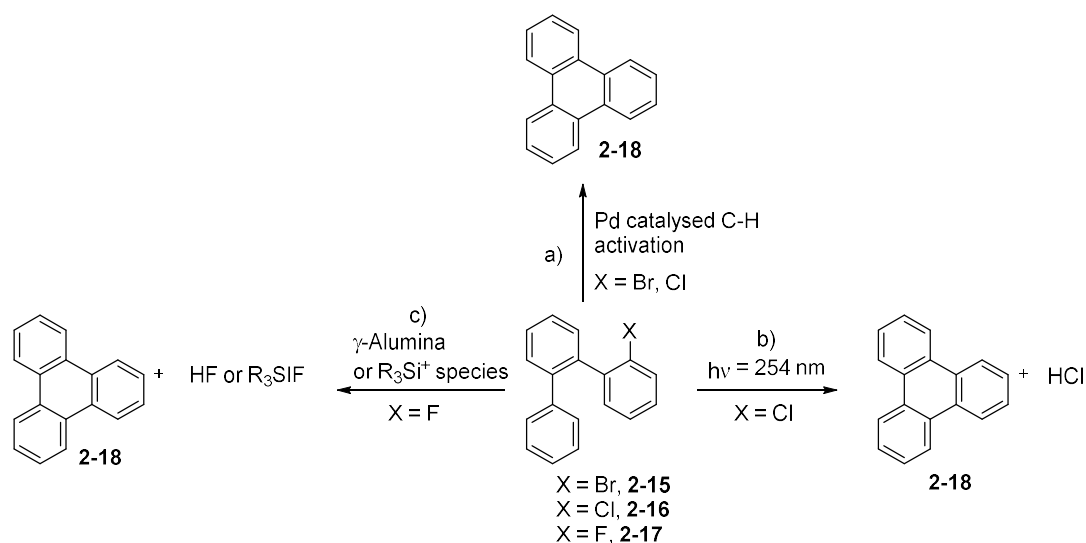
To obtain moisture stable easy to handle hexaaryl-borazines, it is necessary to sterically shield the boron centres. In fact, parent molecule **1-65** ($R' = H$) is known to undergo nucleophilic attack at the boron resulting in degradation of the BN ring with formation of phenyl boronic acid and aniline.^[1,2] The instability of **1-65** arises from the lack of conjugation between the π system of the phenyl rings and the empty p orbital on boron, resulting in a quite high Lewis acidity that makes the latter prone to nucleophilic attack.

Further confirmation of this, comes from the pioneering work of Groszos and Stafiej,^[3] who showed that stable borazines are obtained when electron donating groups such as alkyl chains are bonded to the boron instead of phenyl groups. This is due to the diminished Lewis acidity of the boron atoms determined by the sp^3 carbon electron donating effect, resulting in borazines stable enough to be handled in air without moisture-free techniques. Oppositely, steric protection of boron is necessary to obtain stable derivatives of hexaaryl-borazines. Consequently, it is necessary to synthesize hexaaryl-borazines presenting *ortho* substituents (R' , Scheme 2.3) able to protect the boron centres and at the same time act as leaving groups during the CC bond formation leading to **2-1**.

Focusing on the size of the *ortho* substituents, it is important to underline that too bulky groups ($R' = i\text{-Pr}$, $t\text{-Bu}$, scheme 2.3) will not allow the formation of the borazine core due to the impossibility for six large groups to fit on the borazine together. As a general rule, *ortho* substituents presenting a steric hindrance equal or lower than the methyl group (Van der Waals radius = ca. 2.0 Å)^[4] lead to the formation of hexaaryl-borazines. When the steric hindrance is higher, hydroxyl borazine **2-13** can be formed, but only if four groups can fit on the core, otherwise only N-phenyl boramines would be obtained (**2-14**, Scheme 2.3). Knowing this, to obtain stable borazines with *ortho* substituents able to act as leaving groups in CC bond formation reactions, it was decided to attempt the synthesis of hexaaryl-borazines presenting halogens as *ortho* functional groups. We considered that the van der Waals radii of bromine, chlorine and fluorine (vdW radii of 1.92 Å, 1.77 Å and 1.47 Å respectively),^[5] which are less than the reported value for the methyl group, should result in the formation of stable borazines.^[6] Moreover, the presence of the halogens (in particular chlorine and bromine) allows for the use of many different reaction conditions able to give CC bond formation. Indeed, several reactions have been exploited to form PAHs using chlorinated, brominated, and fluorinated precursors, which could be used to obtain **2-1** starting from halogenated borazines.

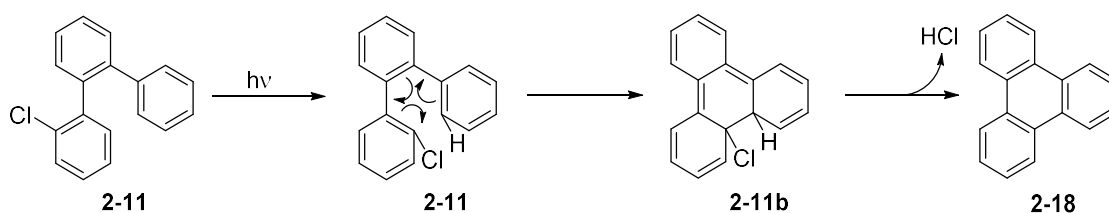
2.4 Synthetic strategies for planarization of *ortho*-halo borazines

When halogen precursors are considered, strategies involving different conditions and halogens have been used to form CC bonds. The use of Pd-catalysed reactions starting from C-X bonds (X = Cl, Br) and un-functionalized C-H bonds is very promising (Scheme 2.4a).^[7,8] This approach has been extensively used in the synthesis of PAHs (Scheme 2.4a) and generally combines high yields with controlled reaction conditions. This approach could be used on bromo and chloro hexaaryl-borazines to form **2-1** with high yields and in a scalable manner.



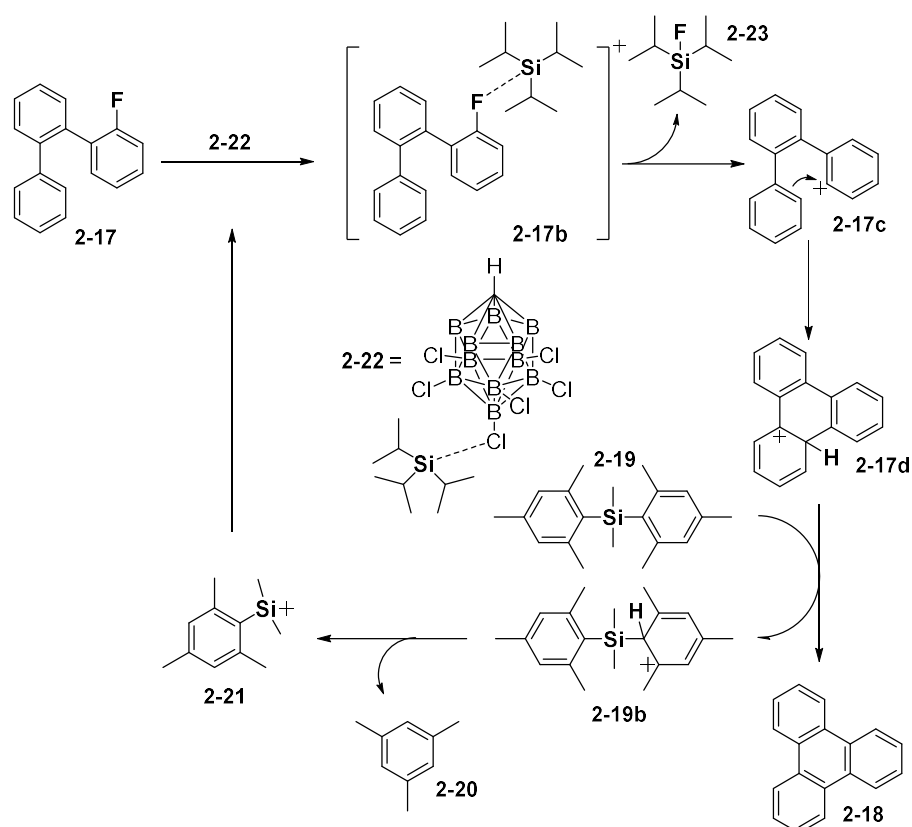
Scheme 2.4: examples of reactions able to induce CC bond on triphenylene model with synthetic potential in the synthesis of **2-1** using *ortho*-halogenated borazines.

Another possible approach relies on photoreactions, since different conditions have been developed on halogenated polyphenylene systems leading to PAH formation. From this point of view, notable work has been performed by Morin and co-workers who developed a cyclodehydrochlorination (CDHC) reaction under UV light irradiation on various chlorine-functionalized polyphenylenes, yielding the corresponding PAHs in very high yields (Scheme 2.4b).^[9] This reaction is reported as a 6 e⁻ electrocyclization followed by elimination of HCl (Scheme 2.5) and it should avoid problems related to radical pathways such as rearrangements with formation of complex mixtures.



Scheme 2.5: Mechanism of CDHC reaction as reported by Morin et al.^[10]

When fluoro-functionalized borazines are considered, the lower reactivity of the C-F bond contributes to make this option the most challenging. However, in the last decade, the branch of chemistry concerning C-F bonds has flourished, leading to many new reactions. In particular, CC sp^2 bonds have been obtained starting from fluorinated polyphenylenes with various approaches, usually involving Friedel-Crafts like reactions using strong Lewis acids such as activated γ -alumina^[11] and silylium ions^[12] (Scheme 2.4c). A silylium ion induced Friedel-Crafts like cyclisation of C-F bonds has been developed by Siegel and co-workers. In this reaction, triphenylene **2-18** is obtained in almost quantitative yield by treating **2-17** with silylium ion reagent **2-22** (Scheme 2.6).

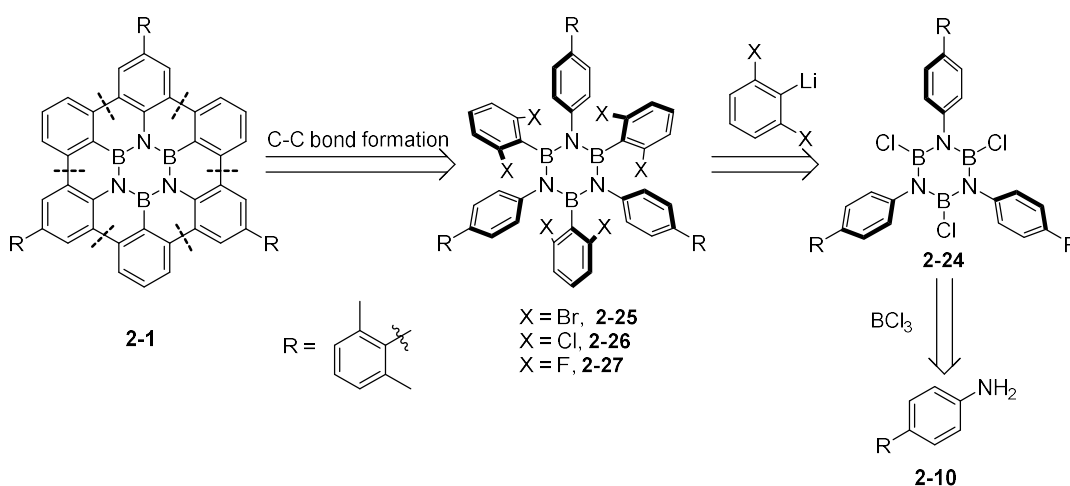


Scheme 2.6: Reaction mechanism for silylium ion induced Friedel-Crafts like CC bond formation starting from fluoro-arenes.^[13]

In the mechanism, the C-F bond is activated by carborane stabilized silylium ion **2-22** leading to the formation of Wheland intermediate **2-17d**. The latter undergoes rearomatization leading to the formation of CC sp^2 bonds in **2-18** as displayed in Scheme 2.6.^[13] In this procedure dimethyldimesitylsilane **2-19** is used as a Brønsted base to scavenge the acidic proton on **2-17d** and thus rearomatizing the system to give **2-18**. Furthermore, the resulting protonated dimethyldimesitylsilane **2-19b** in turn rearomatizes by breaking the weaker C-Si bond regenerating silylium ion **2-21**, allowing the use of catalytic amounts of the expensive and difficult to synthesise **2-22**.

2.5 Retrosynthetic approach towards 2-1

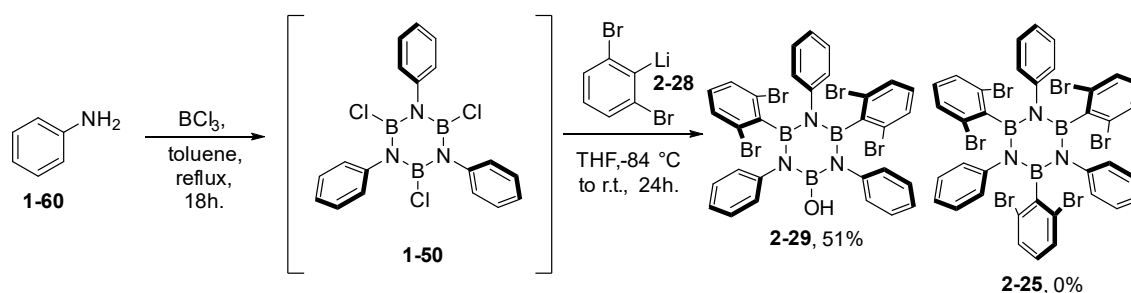
A retrosynthetic strategy towards **2-1** was then designed and is presented in Scheme 2.7. In this strategy, target molecule **2-1** can be synthesised by planarizing *ortho* halogen hexaaryl-borazines using CC bond forming reactions involving halogen substituents (see paragraph 2.4). The desired halogenated hexaaryl-borazines can be in turn obtained by treating chloro-borazole **2-24** with suitable organolithium reagents. Finally, **2-24** can be synthesised by reacting aniline **2-10** bearing a xylene solubilizing moiety with BCl_3 in refluxing toluene.



Scheme 2.7: Retrosynthetic plan towards soluble HBBNC derivative **2-1**.

2.6 Bromo Hexaaryl-borazine

The synthesis of the bromo hexaaryl-borazine **2-25** was then started (Scheme 2.8). In this procedure, LDA in THF at $-84\text{ }^\circ\text{C}$ was used to obtain organolithium reagent **2-28** starting from 1,3-dibromobenzene.^[14] Notably, the use of LDA instead of the more common *n*-BuLi was necessary to avoid the halogen-lithium exchange with bromine and therefore obtaining the desired metalation with formation of **2-28**. Low temperature with no excess of LDA was required to avoid rearrangements such as halogen-dance reactions, and LiBr elimination resulting in benzyne derivatives.^[14,15] In order to obtain a less hindered system and more general results, instead of aniline **2-10**, **1-60** was used in this reaction. **1-60** was then treated with BCl_3 in refluxing toluene and the resulting chloro-borazole **1-50** reacted with aryl-lithium derivative **2-28**. Hydroxyborazine **2-29** was obtained from the reaction as the only product in a 51% yield and its structure confirmed by SC-XRD (Figure 2.1).



Scheme 2.8: Synthesis of borazines **2-25**.

The absence of **2-25** or degradation products in the mixture suggests that this result is plausibly due to steric hindrance effects, which make impossible to place six bromine atoms on the borazine core. Since van der Waals values suggest that six bromine atoms should fit on the borazine core, this result might be related to the steric hindrance of the lithium reagent. Indeed, coordination and formation of aggregates is a common feature of organolithium derivatives and in this case, **2-28** might be forming bulky aggregates with diisopropylamine and THF resulting in the exclusive formation of hydroxy-borazine **2-29**.

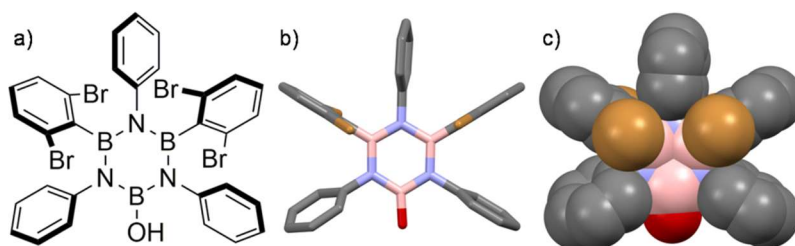
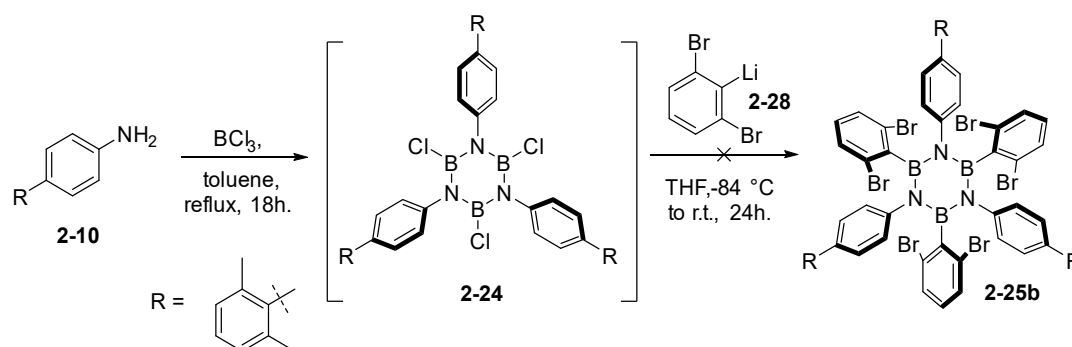


Figure 2.1: Crystal structure of derivative **2-29**; a) molecular structure, b) capped sticks crystal structure, c) spacefill crystal structure. Space group: P-1. Crystals obtained from slow evaporation of a CH_2Cl_2 solution. Colour code: grey: C, pink: B, blue: N, red: O and brown: Br. H atoms omitted for clarity.

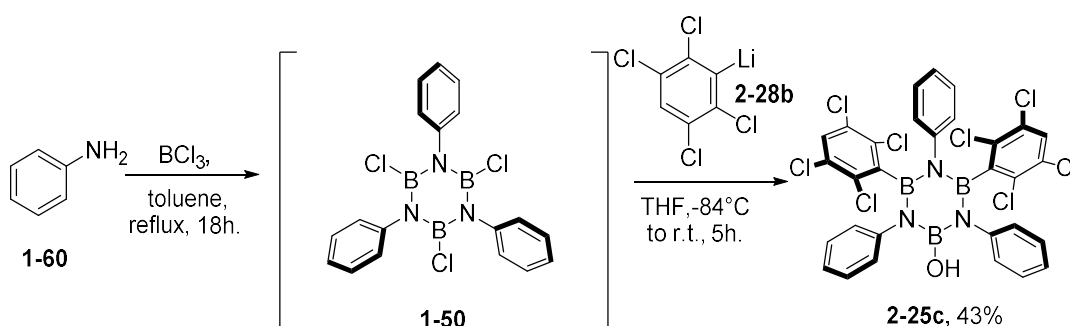
In order to establish whether the use of LDA was accountable for the formation of **2-29** and to obtain the desired borazine **2-25b**, aniline **2-10**, was refluxed with BCl_3 and the resulting chloro-borazole reacted with aryl-lithium **2-28**, obtained by treating 1-iodo-2,6-dibromobenzene with *t*-BuLi at -84°C .



Scheme 2.9: Synthesis of borazines **2-25** using *t*-BuLi.

As a result, no borazine was formed suggesting an inefficient halogen-lithium exchange (Scheme 2.9). At this point, a final reaction to assess the effect of LDA on borazine formation was carried out (Scheme 2.10). In this case the metalation with LDA was carried out on 1,2,4,6-tetrachlorobenzene to understand if the formation of hydroxy borazine was ascribable to the use of LDA or to the presence of the bromine atoms on **2-28**.

Lithium reagent **2-28b** was then formed by treating 1,2,4,6-tetrachlorobenzene with LDA at $-84\text{ }^{\circ}\text{C}$ for 30 min. Aniline **1-60** was refluxed with BCl_3 in toluene forming chloro-borazole **1-50** which was then reacted with **2-28b**. Again, only the hydroxy-borazine derivative **2-25c** was obtained in a 43% yield.

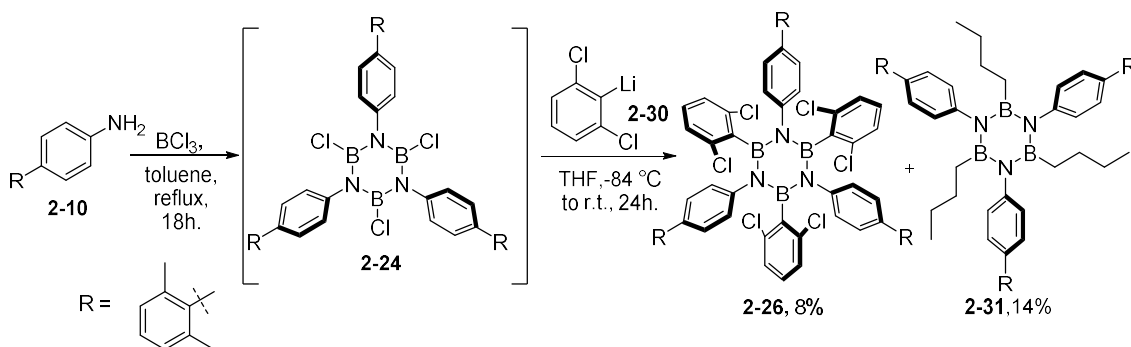


Scheme 2.10: Synthesis of borazines **2-25c** using LDA.

This result strengthens the hypothesis that in the case of borazine **2-25** the selective formation of hydroxy-derivative **2-29** is related to the use of LDA and possibly to the formation of aggregates involving diisopropylamine. Altogether, these results prompted us to move towards the synthesis of chloro-borazine derivative **2-26**.

2.7 Chloro Hexaaryl-borazine

Since all the attempted strategies to form bromo-functionalized borazines failed, we decided to synthesize chloro-derivative **2-26** (Scheme 2.11).



Scheme 2.11: Synthesis of borazine **2-26**.

Aniline **2-10** was reacted with BCl_3 in refluxing toluene and the resulting chloro-borazole treated with aryl-lithium derivative **2-30** which had been obtained *via* halogen-

lithium exchange using *n*-BuLi on 1-bromo-2,6-dichlorobenzene in THF at -84 °C (Scheme 2.11). Temperature control is extremely important in order to avoid nucleophilic substitution reactions on carbons bearing Cl substituents, which are known to occur above -45 °C.^[16] The reaction resulted in the formation of desired product **2-26**, although with a modest 8% yield due to the formation of unexpected derivative **2-31**. Crystal structure analysis confirmed the structure of borazine **2-26**, displaying an orthogonal arrangement of the peripheral aryl groups with respect to the borazine ring, with tilting angles of almost 90 ° for both nitrogen and boron bonded aryl rings (87.37 ° and 88.47° average, Figure 2.2).

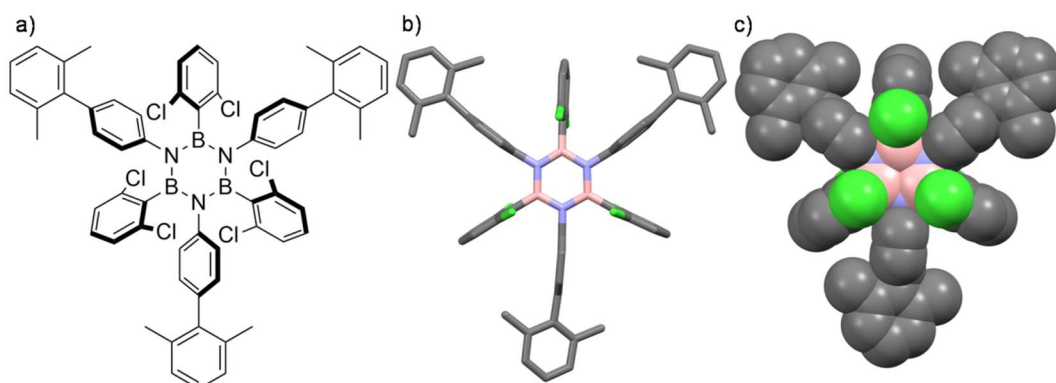


Figure 2.2: Crystal structure of derivative **2-26**; a) molecular structure, b) capped sticks crystal structure, c) spacefill crystal structure. Space group: P-1. Crystals obtained from MeOH diffusion in CH₂Cl₂. Colour code: grey: C, pink: B, blue: N, red: O and green: Cl. H atoms omitted for clarity.

As previously stated, while purifying borazine **2-26**, derivative **2-31** (Figure 2.3) was also isolated as the only other product in a 14% yield, which can be linked to the low yield observed for **2-26**.

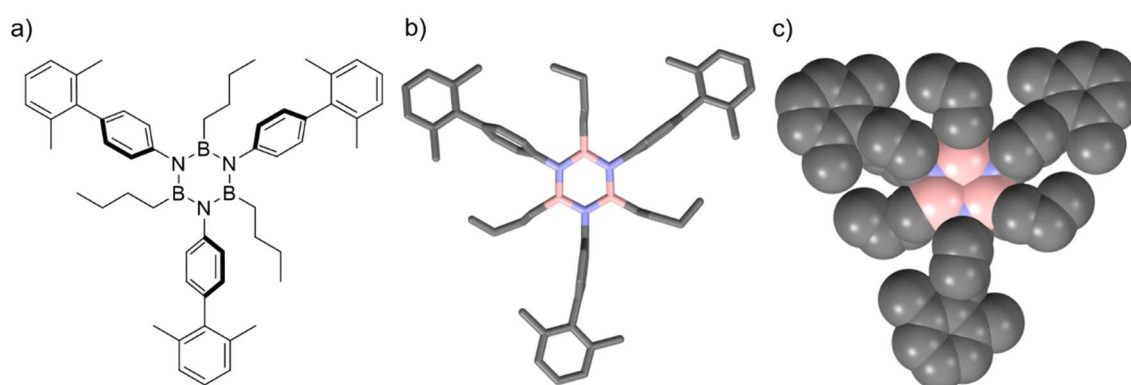
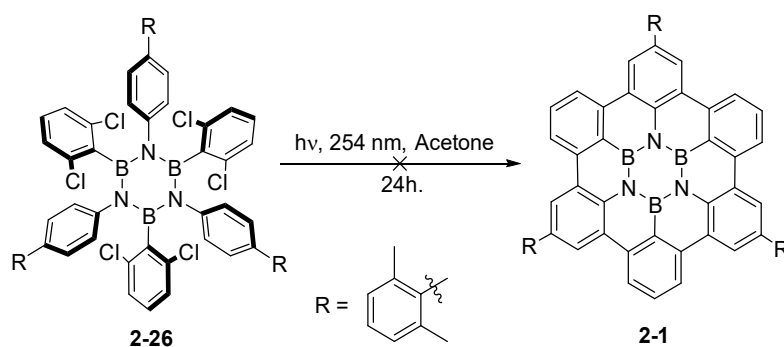


Figure 2.3: Crystal structure of derivative **2-31**; a) molecular structure, b) capped sticks crystal structure, c) spacefill crystal structure. Space group: P 2₁/c. Crystals obtained from MeOH diffusion in CHCl₃. Colour code: grey: C, pink: B, blue: N, red: O and green: Cl. H atoms omitted for clarity.

The formation of unexpected derivative **2-31** might be attributed to the low reactivity of organolithium **2-30**. In fact, the presence of the two chlorine atoms *ortho* to the C-Li

bond determines a decrease in the overall nucleophilicity of the reagent, resulting in a competition between unreacted *n*-BuLi and **2-30**.

Having managed to synthesise **2-26**, the planarization of this derivative was then attempted using the CDHC reaction under UV irradiation. Since **2-26** was poorly soluble in decaline and acetonitrile (the most common solvents for this reaction), dry degassed acetone was used (scheme 2.12).



Scheme 2.12: Attempted synthesis of **2-1** using UV irradiation (254 nm) to induce a CDHC reaction as reported by Morin et al.

The resulting solution of **2-26** in acetone was irradiated in a sealed quartz tube at 254 nm for 48 h in a Luzchem[®] reactor. TLC analysis of the reaction showed a very complex mixture of products, which was analysed with MALDI mass spectroscopy (Figure 2.4).

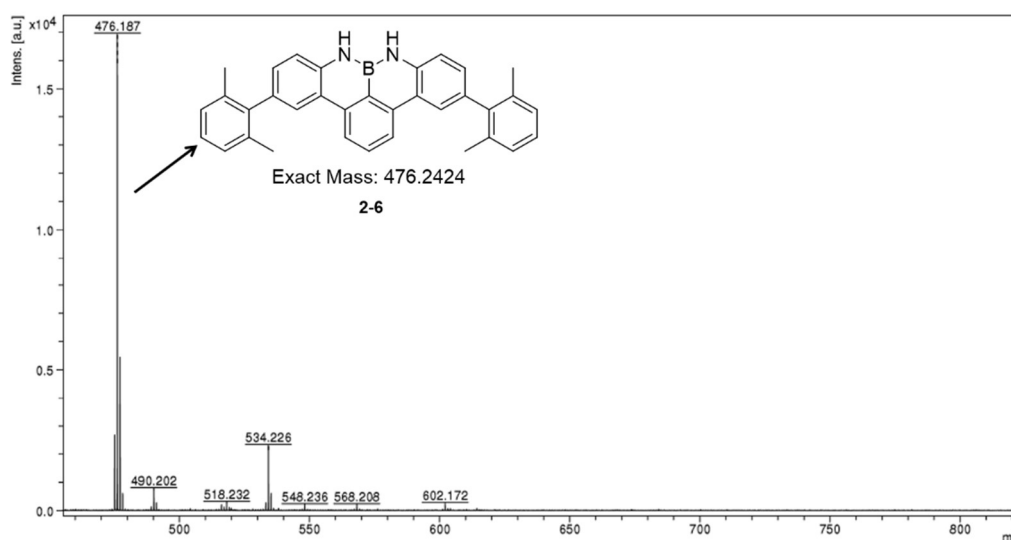
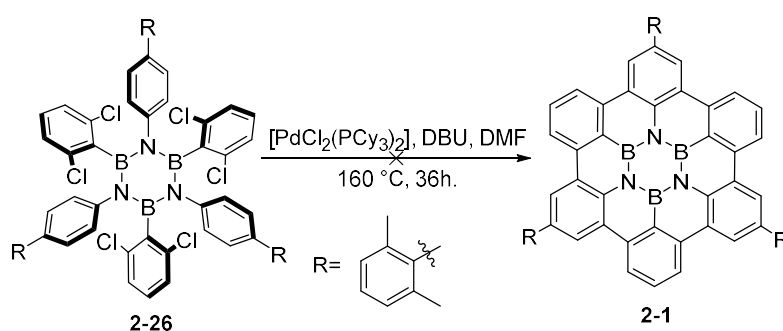


Figure 2.4: LR-MALDI mass analysis spectrum of reaction mixture after 48 h irradiation of **2-26** at 254 nm.

From the mass spectrum it is clearly visible the formation of partially planarized derivative **2-6**, however, no trace of **2-1** was observed. Despite the inability to form the desired product, the formation of two CC bonds suggests that the reaction is working to some extent but, probably due to a low quantum yield of bond formation, it does not

lead to the final product. This ultimately results in hydrolysis of the partially planarized intermediates upon quenching. Furthermore, the presence of acetone as sensitizing solvent, which is in a triplet state at 254 nm, could result in a different mechanism of reaction, possibly a radical one, arising from a homolytic cleavage of C-Cl bonds. This would be consistent with the complex reaction mixture observed. These considerations, along with the low solubilities of borazine derivatives in the solvents required by this kind of reactions led to a change of strategy. The synthesis of **2-1** was then attempted by palladium catalysed C-H bond activation, which is a valuable option to form aromatic CC bonds starting from aromatic C-Cl and C-H bonds (Scheme 2.13).



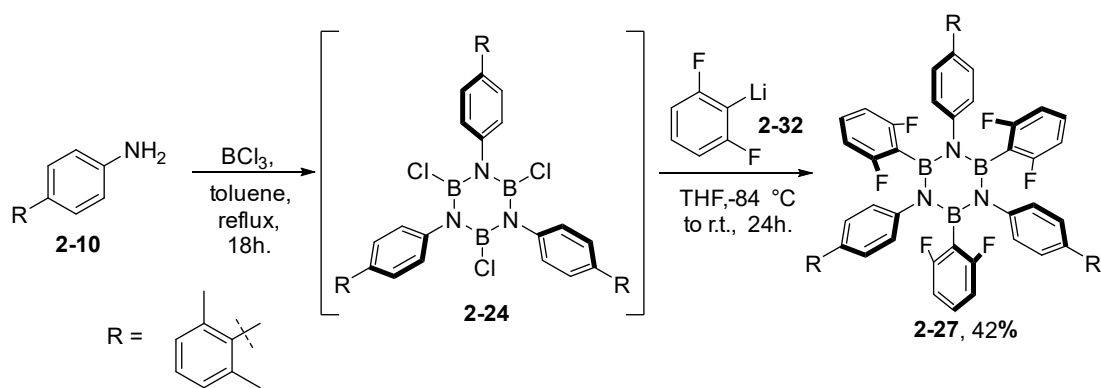
Scheme 2.13: Attempted synthesis of **2-1** using Pd catalysed C-H activation reaction on borazine **2-26**.

Borazine **2-26** was then treated with $[\text{PdCl}_2(\text{PCy}_3)_2]$ and DBU in dry DMF under N_2 at 160 °C for 36 h. Even in this case, the target molecule was not obtained and only starting material or degradation products were visible from TLC analysis. This outcome is probably determined by an inefficient oxidative addition, while the presence of DBU and high temperature can be linked to the degradation of part of the starting material due to nucleophilic attack on the boron atom.

This initial set of attempts suggested that UV promoted C-Cl bond activation and cross-coupling conditions are not suitable for the synthesis of **2-1** prompting us to move on C-F bonds.

2.8 Fluoro Hexaaryl-borazine

Since all attempts to planarize derivative **2-26** failed, we decided to attempt the synthesis and planarization of fluoro hexaaryl-borazine **2-27** (Scheme 2.14). Xylyl aniline **2-10** was reacted with BCl_3 and the resulting chloro-borazole intermediate treated with aryl-lithium **2-32** resulting in the formation of borazine **2-27** in a 42% yield. Notably, it is necessary to keep low temperatures (-84 °C) during both the lithium-halogen exchange and the subsequent reaction of **2-32** with the chloro-borazole to avoid the formation of undesired benzyne intermediates, which would result in the formation of triphenylenes.



Scheme 2.14: Synthesis of borazine **2-27**.

As for the previous cases, the molecular structure of molecule **2-27** was confirmed by SC-XRD, as shown in Figure 2.5. When the crystal structure of **2-27** is compared to the one of **2-26**, a smaller tilting of the side rings (67.10° to 80.16°) is visible, resulting in a “propeller-like” arrangement of the fluorine atoms. Borazine **2-27** is stable in solution or when stored under air, probably because of the high electronegativity of the fluorine atoms, which generate a hydrophobic pocket on the borazine ring shielding boron atoms from moisture. However, when derivative **2-27** is treated with strong bases, fluoride sources or, more in general, nucleophiles, degradation of the borazine occurs, thus restricting possible planarization reactions to Lewis acid conditions.

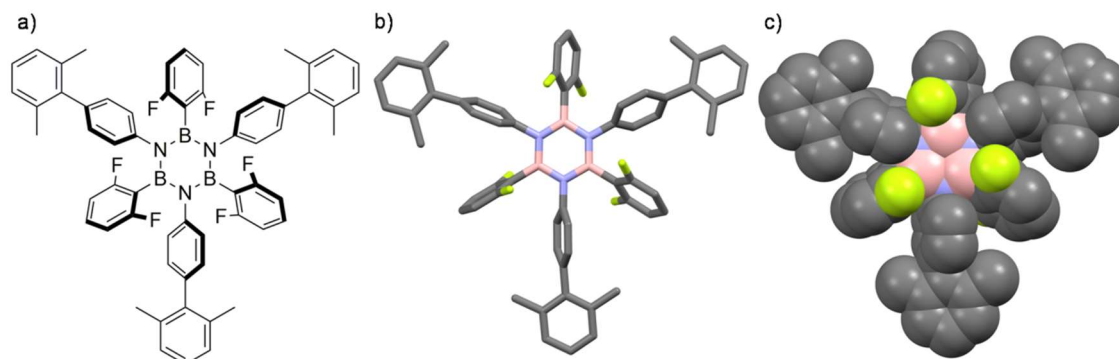
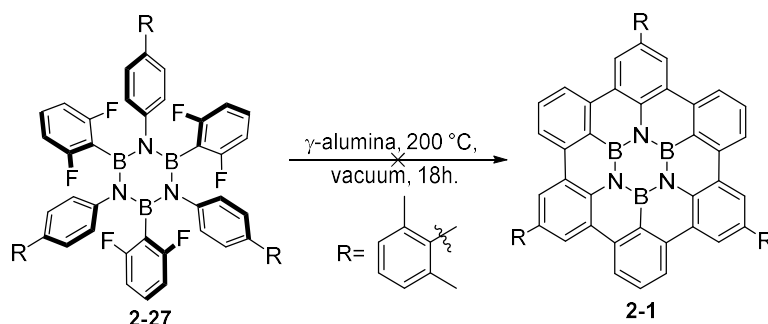


Figure 2.5: Crystal structure of derivative **2-27**; a) molecular structure, b) capped sticks crystal structure, c) spacefill crystal structure. Space group: $P2_1/c$. Crystals obtained from MeOH diffusion in CH_2Cl_2 . Colour code: grey: C, pink: B, blue: N, red: O and yellow: F. H atoms omitted for clarity.

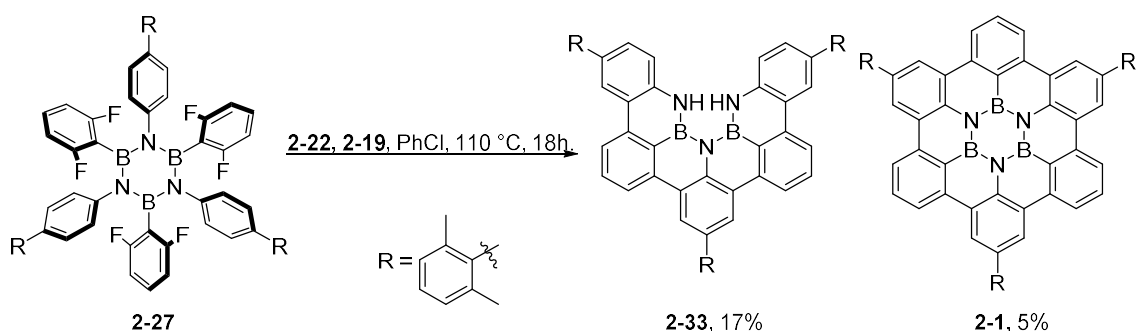
Having obtained desired borazine **2-27**, the synthesis of HBBNC **2-1** was attempted using activated γ -alumina as reported by K.Y. Ashmarov and co-workers (Scheme 2.15).^[11] In this procedure the strong Lewis acidity and fluorophilicity of the Aluminium active sites on the surface of γ -alumina is used to cleave C-F bonds leading to the formation of CC bonds and consequent elimination of HF. γ -alumina was then activated by heating at 250°C under air for 10 min. followed by 370°C for 2 h under vacuum. Borazine **2-27** was added to activated alumina and reacted at 200°C under vacuum for 18 h. Despite the harsh reaction conditions and high Lewis acidity of γ -alumina, even in

this case only starting **2-27** was recovered. A stronger activation of γ -alumina at 550 °C under N_2 flow did not improve the reaction outcome. This result can be probably related to quenching of the active sites by the nitrogen of the borazine ring *via* its adsorption on the surface of alumina. An indication of this comes from the exclusive use of this reaction for PAH scaffolds, which suggests a possible incompatibility with molecules bearing Lewis basic sites.



Scheme 2.15: Attempted synthesis of **2-1** using activated γ -alumina as Lewis acid.

Given these results, we decided to attempt the synthesis of **2-1** using the procedure developed by Siegel et al. employing silylium ions as strong Lewis acids with high fluorophilicity and low affinity for nitrogen in a homogeneous phase reaction (Paragraph 2.4). Borazine **2-27** was then treated with carborane stabilized silylium ion **2-22** in the presence of dimethyldimesitylsilane **2-19** in anhydrous PhCl at 110 °C, leading to the formation of the desired **2-1** in a 5% yield (61% per CC bond formation, Scheme 2.16) as a white powder soluble in CH_2Cl_2 .^[17]



Scheme 2.16: Synthetic procedure towards the formation of **2-1** and by-product **2-33**.

HBBNC derivative **2-1** was characterized with NMR, UV-Vis (Chapter 3), SC-XRD (Figure 2.6) and HRMS. In particular, the latter led to the first identification of the molecule due to the peak corresponding to the molecular ion at m/z 837.3652 ($C_{60}H_{42}B_3N_3^+$, calc.: 837.3658).

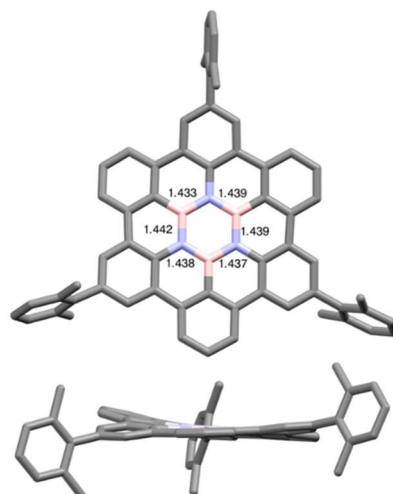


Figure 2.6: Crystal structure of derivative **2-1**; Space group: $I2/a$. Crystals obtained from *i*-PrOH diffusion in C_6H_6 . Colour code: grey: C, pink: B, blue: N. H atoms omitted for clarity.

When the crystal structure of **2-1** is considered, the presence of the central borazine is confirmed along with an almost planar structure, with some distortion visible probably due to the presence of the xylene groups. The BN bonds present lengths from 1.433(3) to 1.442(2) Å, slightly shorter than the ones found in *h*-BN (1.446 Å). Along with **2-1**, incomplete cyclisation product **2-33** was also isolated in a 17% yield (scheme 2.16). As for **2-1**, confirmation of the structure of by-product **2-33** came from NMR, HRMS and especially SC-XRD (Figure 2.7), with the latter showing a distorted structure consistent with the presence of a cove region constituted by the incomplete BN ring.

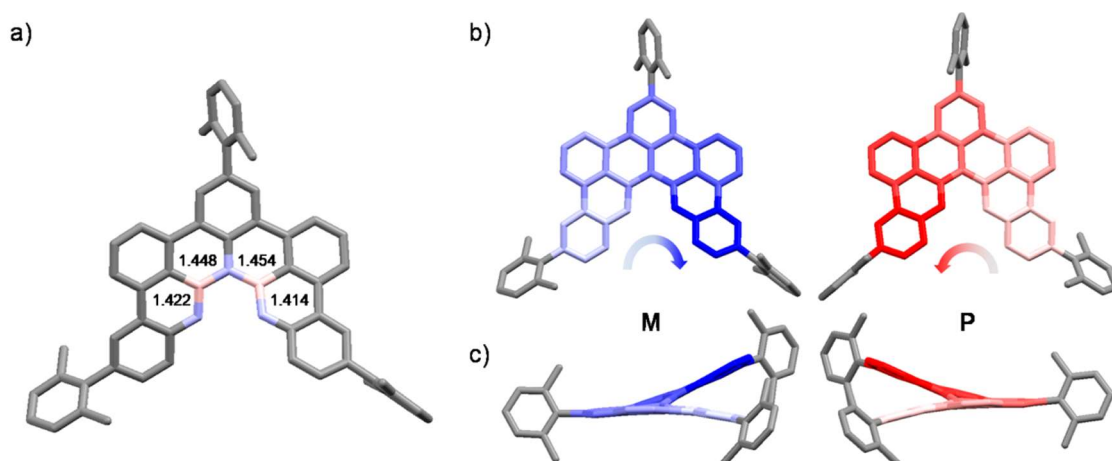


Figure 2.7: Crystal structure of derivative **2-33**; a) Front view of **2-33** with BN distances b), c) front view and side view with axial enantiomers (M and P highlighted) of **2-33**. Crystals obtained from *i*-PrOH diffusion in CH_2Br_2 . Colour code: pink B, blue N, gray C; space group: $P2_1/n$.

The free N-H groups at the edge of the BN system determine the steric hindrance leading to the distortion of the structure with a resulting 37° tilt between the two sides of the molecule. This distortion leads to the presence of two axial enantiomers in the crystal structure (Figure 2.7b, c). The observed BN bond lengths for **2-33** are 1.414(4)-

1.422(3) Å for the BNH couple and 1.448(3)-1.454(4) Å for the NBN fragment respectively, thus reflecting an effect of the distortion on the bond lengths in the BN system.

To explain the formation of **2-33** as major product and the low yield of **2-1** it was decided to perform computational studies to figure out the lowest energy intermediates for each step of the reaction (Figure 2.8). The structures and energies of the intermediates were computed using B3LYP hybrid functional^[18] with a 6-31(d,p) basis set^[19] on all centres with Gaussian 09.^[20] The solvent (THF) was incorporated using the polarized continuum model, in which the molecular cavity is defined by the united atom model that incorporates hydrogen into the parent heavy atom.^[21]

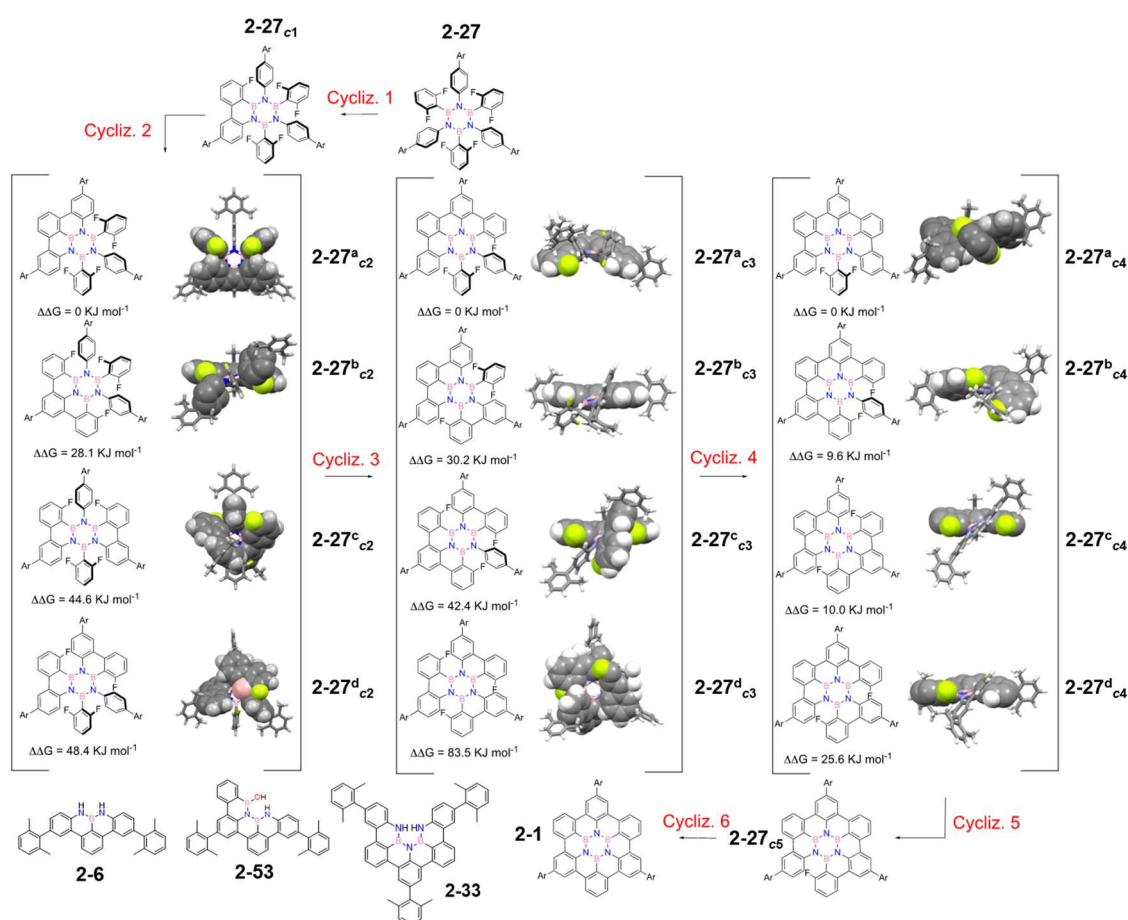


Figure 2.8: Step wise Friedel-Crafts-based planarization mechanism according to route A. Calculated Gibbs free energies ($\Delta\Delta G$) for the possible intermediates formed at each cyclization step [B3LYP/6-31G(d,p)].

For the sake of clarity, the different intermediates are named **2-27ⁿ_{cx}** where ⁿ refers to the intermediate within the cyclization subset whereas _{cx} corresponds to the cyclization step. After the first cyclization step only derivative **2-27_{c1}** can be formed, presenting a phenanthrene portion. The following three steps in the cyclization reaction lead to 4

possible intermediates each (subsets c_2 , c_3 and c_4) finally giving the single intermediate **2-27** _{c_5} for cyclization 5 and the final product **2-1** for cyclization 6.

When the first set of intermediates (c_2) is considered, it is possible to see that the lowest energy intermediate is represented by **2-27**^a _{c_2} which is formed by reaction of the most conjugated part of **2-27** _{c_1} with one of the neighbouring rings, further extending the π system. The presence of intermediate **2-27**^a _{c_2} was confirmed by the isolation of the resulting hydrolysis product **2-6**. Similarly, in the third cyclization step, the lowest energy intermediate **2-27**^a _{c_3} is again generated by reaction of the most extended π system with the neighbouring ring and in this case the presence of the hydrolysis product **2-53** arising from **2-27**^a _{c_3} was visible when the reaction mixtures were analysed by mass spectroscopy. When the fourth cyclization is considered, the most favoured intermediate is again the one with the most extended π system corresponding to **2-27**^a _{c_4} , in which a ring with two fluorine atoms is left to planarize generating a strained intermediate. Hydrolysis of **2-27**^a _{c_4} leads to the formation of **2-33**, thus giving a theoretical explanation for the formation of this by-product in the reaction. Since evidence for the presence of **2-27** _{c_5} was never observed, cyclization six is probably very fast and this, along with the relatively high yield of **2-33**, confirms the suspected rate determining nature of cyclization five.

The higher stability of the more conjugated systems is quite intuitive; however, a more precise explanation can be achieved by using Natural Bond Orbital (NBO) analysis of starting borazine **2-27**. From this point of view the presence of 3-centre 4-electron hyperbonds is noticed in the B_3N_3 core of **2-27**, each centred on a NBN unit and described as a combination of a N-centred p orbital and a BN π bond as $NB:N \leftrightarrow N:BN$ (Figure 2.9a) which describe a strongly delocalized structure.

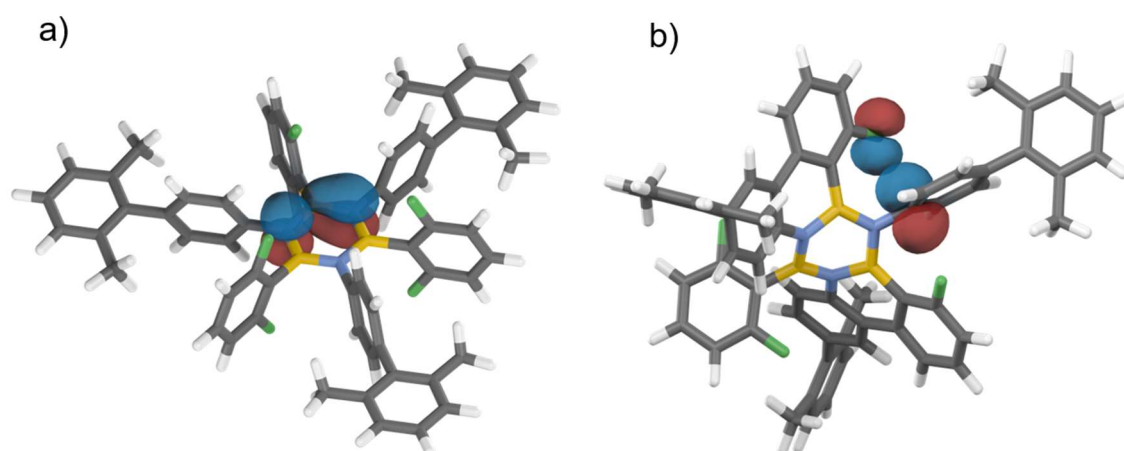
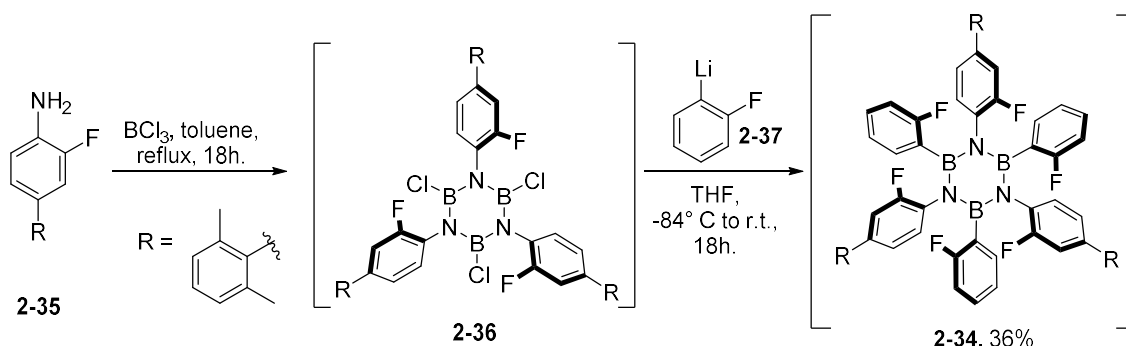


Figure 2.9: a) A 3-centre, 4-electron bond described by NBO analysis of precursor 5; b) NBO-derived donor-acceptor interaction between a fluorine lone pair and an ipso carbon of the aryl group [B3LYP/6-31G(d,p)].

When a deviation from planarity occurs in the B_3N_3 core, less delocalized structures are obtained due to a loss of the hyperbonds, which are substituted by donor-acceptor interactions that involve the N-based occupied p orbitals and the B-based vacant p orbitals, thereby indicating a lesser degree of delocalization. It must be said that, however, deviation of the borazine ring from planarity does not always directly correlate with their relative free energies. As an example, intermediate **2-27^c_{c2}** (figure 2.9b) presents the greatest deviation from planarity (RMSD = 0.294 Å; $\Delta\Delta G = 44.6 \text{ kJ mol}^{-1}$) in the **2-27^a_{c2}**–**2-27^d_{c2}** series but the higher energy intermediate in the subset is represented by **2-27^d_{c2}** (RMSD = 0.250 Å; $\Delta\Delta G = 48.4 \text{ kJ mol}^{-1}$). This result arises from a stabilizing effect relating to the unlinked non-fluorinated aryl group in **2-27^c_{c2}** via two donor-acceptor interactions from the proximal fluorine lone pairs to a lone valence (vacant p orbital) on the ipso-carbon of the aryl moiety (Figure 2.9b). These analyses give an overall picture of the BN delocalization being the dominant factor in determining stability, but where comparatively minor stereoelectronic factors can have a significant contribution to the overall stability of intermediate species in the reaction process.

2.9 Optimization of the reaction conditions

Since the rate determining step for the previous mechanism proved to be the reaction of intermediate **2-27^a_{c4}**, a good strategy towards an increased yield was to design a new borazine precursor which would avoid the formation of strained **2-27^a_{c4}**. It was then decided to prepare a borazine with a different distribution of fluorine atoms on the aryl rings possibly resulting in different intermediates. Borazine **2-34**, bearing one fluorine atom on each aryl ring was then prepared (Scheme 2.17). From the synthetic point of view, aniline **2-35** was treated with BCl_3 in refluxing toluene and the resulting chloro-borazole **2-36** reacted with **2-37** forming **2-34** as mixture of atropoisomers in a 36% yield.



Scheme 2.17: Synthesis of borazine derivative **2-34** which is obtained as a mixture of atropoisomers.

Final product **2-34** is composed by a mixture of 10 atropoisomers. This is determined by the fact that steric hindrance blocks rotation of the aryl moieties, resulting in

configurations presenting different fluorine arrangements on each side of the borazine ring.

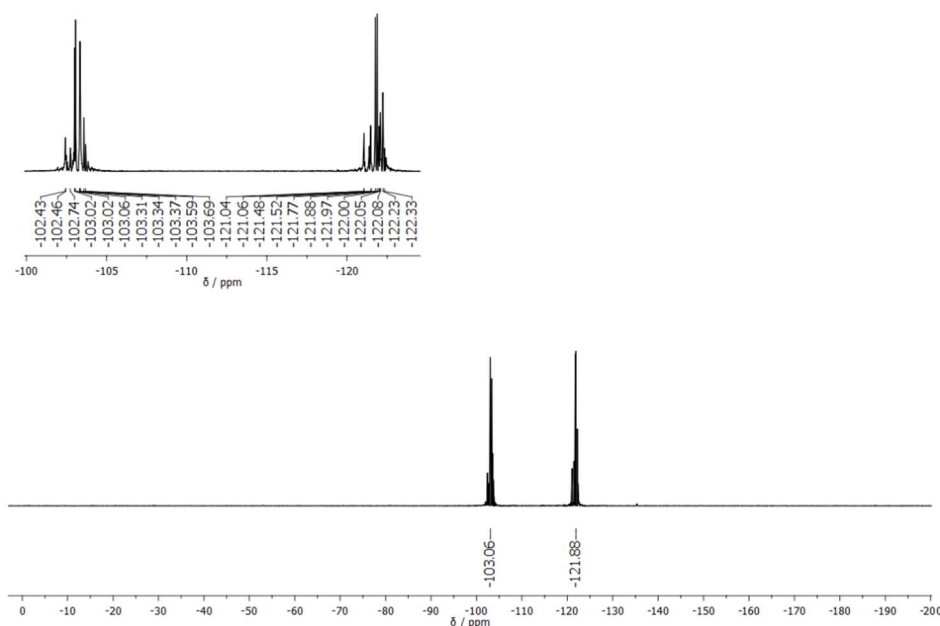
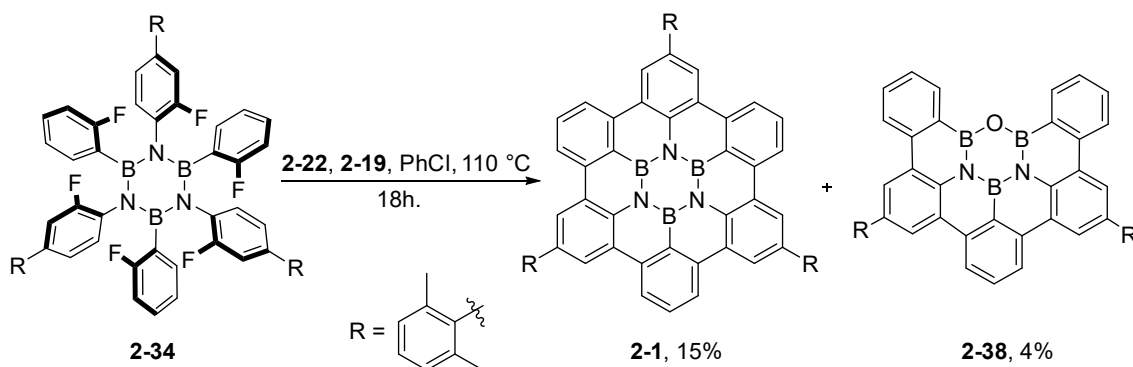


Figure 2.10: 376 MHz ^{19}F -NMR of derivative **2-34** in CDCl_3 .

Evidence for this comes from the ^{19}F -NMR of **2-34** reported in Figure 2.10, which shows two main groups of signals, corresponding to the fluorine substituents on the nitrogen bonded ring and to those on the boron ring, respectively. These two blocks of signals are constituted by multiple peaks with small variations in the chemical shift, ascribable to the different atropoisomers present in the mixture. Separation of the single atropoisomers of **2-34** was not possible with SCC, especially because the mixture proved to be somehow unstable if exposed to moisture for long periods of time.



Scheme 2.18: Planarization reaction performed on **2-34** leading to the formation of derivatives **2-1** and **2-38**.

This difference from **2-27** might arise from different degrees of steric protection of the borazine ring in the different atropoisomers, leading to degradation of the least stable

ones. Consequently, the cyclization reaction was performed directly on the isomeric mixture using the previously reported conditions. Borazine **2-34** was treated with silylium ion **2-22** in the presence of dimethyldimesitylsilane **2-19** in degassed PhCl at 110 °C (Scheme 2.18) giving **2-1** in a 15% yield.

Along with **2-1**, molecule **2-38** was obtained as well in a low 4% yield and fully characterized. From the crystal structure of **2-38** the presence of the gulf region arising from the oxygen in the B₃N₂O ring is highlighted along with an almost planar structure with an average RMSD of 0.13(9) Å. The BN bond lengths are comprised between 1.437(4) and 1.441(4) Å while BO bond lengths are comprised between 1.386(4) and 1.375(4) Å, very close to the distances measured for boric acid and phenyl boroxine^[22] thus suggesting a small degree of π character for these bonds (Figure 2.11).

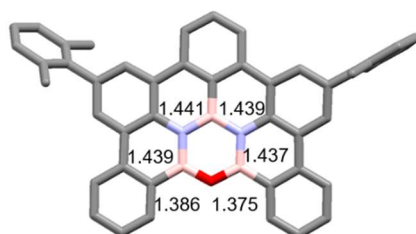


Figure 2.11: Crystal structure of derivative **2-38**; a) Front view of **2-38** with BN and BO distances. Colour code: pink B, blue N, gray C, red O. space group: P2₁/n, crystals obtained via diffusion of *i*-PrOH in CH₂Br₂ solution.

The presence of this by-product, which is different from the ones obtained in cyclization of **2-27**, suggests that this reaction follows a mechanism involving different intermediates compared to the one of **2-27**. Moreover, **2-38** represents the first example of a B₃N₂O doped PAH, which plausibly arises from the insertion of an oxygen atom with loss of an aniline molecule from one of the intermediates of the reaction. To shed some light in the cyclization mechanism even in this case computational studies were performed (Figure 2.12).

In this investigation, due to the high number of possible intermediates for cyclizations c2 (8) and c3 (14), only the last two cyclization steps c4 and c5 were analysed. Again, it can be hypothesized that the reaction proceeds stepwise with extension of the π system. This finds confirmation in the fact that **2-34**^{a_{c4}} is the lowest energy intermediate for c4 and indeed constitutes the intermediate with the biggest π system between the different options. Furthermore, **2-34**^{a_{c4}} is the intermediate that most probably leads to **2-38** via hydrolysis and loss of the fluorine atom still attached to the π system. However, further investigations are needed to unravel the possible source of hydride yielding the fluoride-hydrogen exchange reaction. When c5 is considered, two different intermediates are possible: **2-34**^{a_{c5}} and **2-34**^{b_{c5}}, where the remaining fluorine is present either on a boron bonded ring or on the nitrogen bonded one. However, again, it was

not possible to find evidence for these intermediates in any analysis, suggesting a fast reaction towards **2-1**.

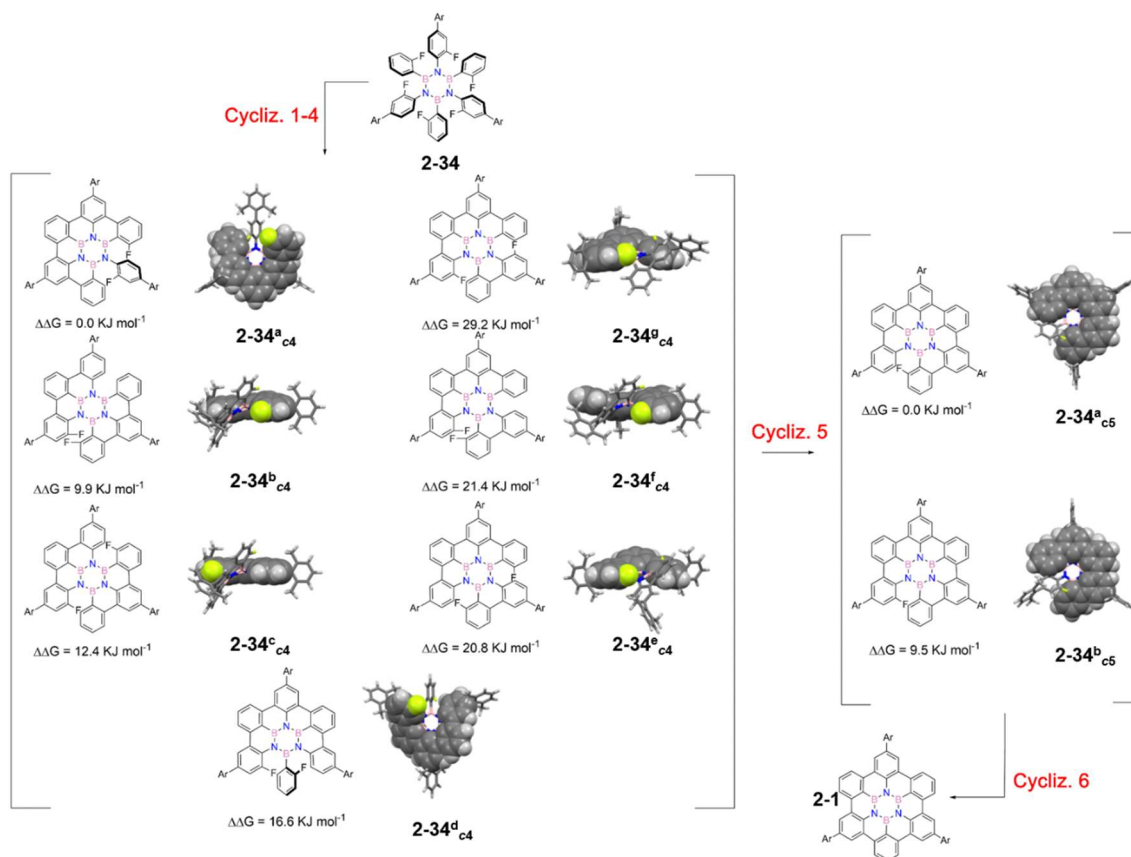
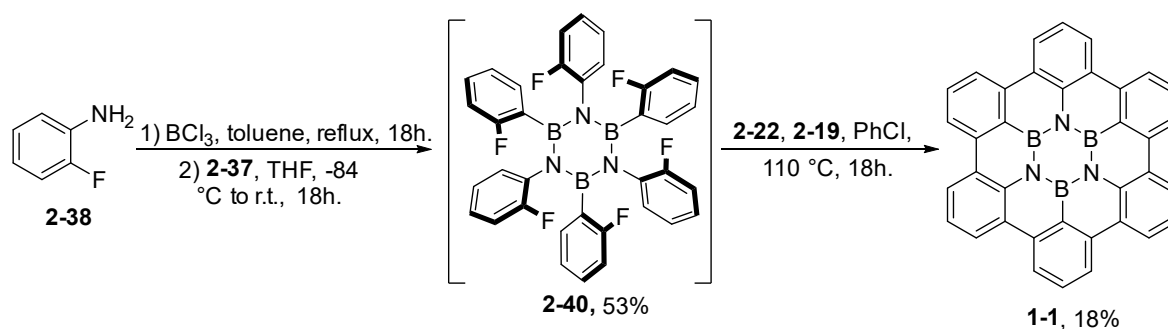


Figure 2.12: Friedel-Crafts-based stepwise planarization mechanism according to route B. In this case, the calculated Gibbs free energies ($\Delta\Delta G$) of the intermediates intervening in the fourth and fifth cyclization steps are considered. The presence of different isomers in steps 1-3 deterred us from tackling the calculation of all steps [B3LYP/6-31G(d,p)].

As a result of these studies it was confirmed that the cyclization reaction of **2-34** occurs with a different mechanism from that of **2-27**. This difference in the mechanism could explain the higher yield of **2-1** and the presence of **2-38** as by-product in place of **2-33**.

2.10 Synthesis of unsubstituted HBBNC 1-1

To prove the versatility of this new strategy, it was decided to perform the reaction on borazine **2-40** obtaining HBBNC **1-1**. This system was chosen due to the low solubility of the final product which should determine a simple purification by consecutive washings of the final molecule, allowing for an easier assessment of the effects of different conditions on the reaction outcome.



Scheme 2.19: Planarization reaction performed on derivative **2-40**.

The synthesis started with the preparation of borazine **2-40** which was obtained by treating 2-fluoroaniline **2-38** with BCl_3 in refluxing toluene, followed by treatment of the resulting chloro-borazole with lithium derivative **2-37** (Scheme 2.19). As for **2-34** even **2-40** was obtained as a mixture of atropisomers. Separation of the different isomeric components was not possible using SCC and thus the following cyclization reaction was performed on the mixture (Scheme 2.19).

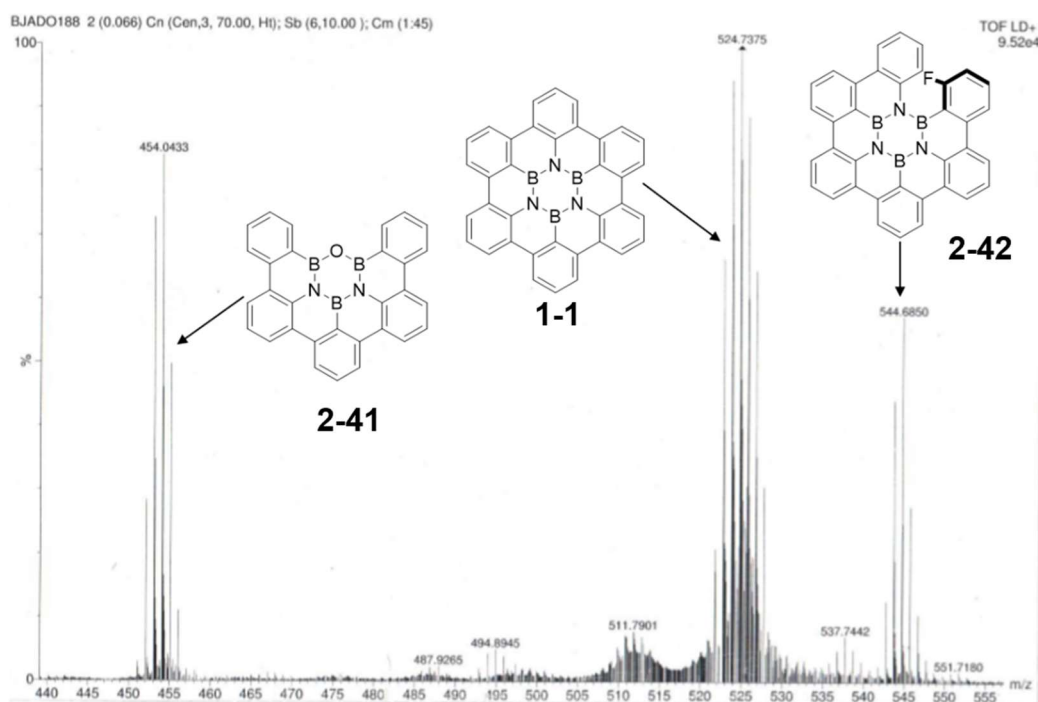


Figure 2.13: LR-MS LD⁺ of planarization of derivative **2-40**.

Even in this case, **1-1** was formed along with fragments originated by the rupture of the BN core such as B₃N₂O derivative **2-41** and the last cyclization intermediate **2-42**, which was never found in previous reactions. Since the latter was never observed when soluble derivatives were formed, the presence of **2-42** in this case might be related to the low solubility of the system, resulting in the precipitation of part of **2-42** before the last cyclization could occur. This result represents another important proof of the stepwise mechanism predicted by computational studies.

After multiple cycles of sonication and washing with various solvents (ODCB, PhCl, EtOAc etc...) desired clean product **1-1** was obtained in a 18% yield as a grey solid. This result is comparable with the yield obtained for **2-1** within experimental error. Mass analysis of the sample showed only one peak corresponding to the desired product at *m/z* 525.1763 (C₃₆H₁₈B₃N₃⁺, calc.: 525.1780), as previously reported by Bettinger et al. for the same derivative.^[23] To further confirm the structure of the obtained material, powder-XRD (pXRD) analysis was carried out. A previous pXRD study^[23] has been reported for **1-1** by Bettinger et al. involving a profile-fitting using the Le Bail technique of the pXRD pattern recorded for a two-phase sample comprising **1-1** together with another crystalline phase arising from an impurity. The Le Bail fitting showed that the unit cell of **1-1** closely matches the unit cell in the reported crystal structure^[24,25] of hexa-peri-hexabenzocoronene. However, in their work only the preliminary profile-fitting was carried out and no structure solution and refinement were performed. The pXRD pattern of **1-1**, which was prepared using the reaction depicted in scheme 2.19, closely matches the one previously reported but, in this case, since **1-1** was pure and presented a single phase in the sample, structure determination was possible using the pXRD pattern.

Profile fitting and unit cell refinement from the pXRD data were carried out using the Le Bail technique^[26] implemented in the program GSAS^[27], starting from a unit cell (*a* = 12.929 Å, *b* = 5.119 Å, *c* = 17.9983 Å, β = 108.984 °) and space group (P2₁/n) that were derived from the reported^[25] unit cell of HBC by transformation to the conventional setting (which has the shortest lengths of the *a*- and *c*-axes and the value of β closest to 90°). A good-quality Le Bail fit was achieved (Figure 2.15a; Rwp = 0.57%, Rp = 0.44%), with the following refined unit cell parameters: *a* = 12.921(5) Å, *b* = 5.0996(7) Å, *c* = 18.002(5) Å, β = 109.151(16)°. The fact that this unit cell accounts for all peaks observed in the experimental pXRD data confirms the purity of **1-1** which is constituted by a single phase. From the unit cell volume and density considerations, it is deduced that there are two molecules of **1-1** in the unit cell, and therefore the asymmetric unit for space group P2₁/n comprises one half molecule of **1-1**. Structure solution of **1-1** was

carried out using the direct-space strategy,^[28,29] implemented using a genetic algorithm (GA) in the program EAGER.^[30–37] In the direct-space structure solution calculations, the molecular model was derived from the molecule in the crystal structure of HBC, but with the central C6 ring replaced by a central B₃N₃ ring. The asymmetric unit comprised the whole molecule of **1-1** with half occupancy of all atoms, and with the centre of the molecule fixed at a crystallographic inversion centre. Clearly, the inversion symmetry operation creates disorder in the positions of the B and N atoms in the central ring, resulting in an occupancy of B0.5 N0.5 for each atomic site in the central ring.

In the GA structure solution calculations, each trial structure was defined by three structural variables $\{\theta, \phi, \psi\}$, which specify the overall orientation of the molecule relative to the unit cell. In total, 40 independent GA calculations were carried out, with each GA calculation involving the evolution of a population of 100 trial structures for 100 generations. In each generation, 10 mating operations and 50 mutation operations were applied. All 40 independent GA calculations produced essentially the same structure giving best fit to the experimental pXRD data (i.e., lowest Rwp). This trial structure was used as the initial structural model for Rietveld refinement. In the Rietveld refinement, restraints were applied to bond lengths and bond angles (derived from the known molecular geometry^[25] of the carbon analogue), and a planar restraint was applied to the whole molecule. As in the structure solution, the asymmetric unit comprised a whole molecule of **1-1** with half occupancy of all atoms, with the centre of the molecule fixed at an inversion centre. A common isotropic displacement parameter was refined for all non-hydrogen atoms, and the value for hydrogen atoms was set at 1.2 times this value.

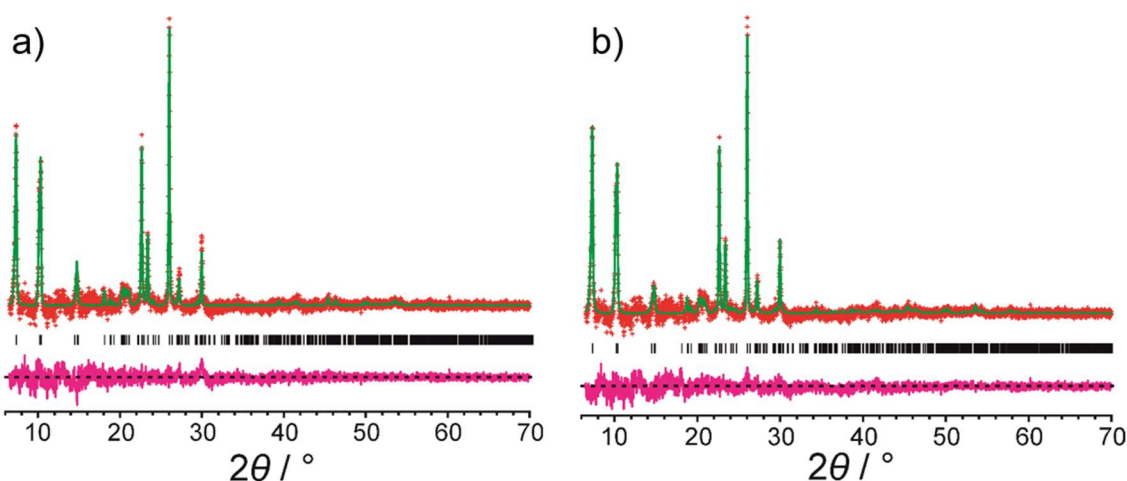


Figure 2.15: a) Le Bail fitting of the powder XRD pattern of **1-1**. Red + marks, experimental data (background subtracted); green line, calculated data; magenta line, difference plot; black tick marks, predicted peak positions b) Final Rietveld refinement for **1-1**. Red + marks, experimental data (background subtracted); green line, calculated data; magenta line, difference plot; black tick marks, predicted peak positions.

The final Rietveld refinement produced a good-quality fit (Figure 2.15; $R_{wp} = 0.60\%$, $R_p = 0.45\%$), comparable to the quality of fit obtained in the Le Bail fitting procedure (Figure 2.15a), with the following refined unit cell parameters: $a = 12.934(5) \text{ \AA}$, $b = 5.1022(8) \text{ \AA}$, $c = 18.009(5) \text{ \AA}$, $\beta = 109.188(17)^\circ$, $V = 1122.4(7) \text{ \AA}^3$.

The crystal structure of **1-1**, shown in Figure 2.16a and 2.16b, is essentially isostructural to the crystal structure of the carbon analogue as demonstrated by the overlay of the two structures shown in Figure 2.16c. According to the classification of aromatic hydrocarbon crystal structures,^[38] the structure is assigned to the γ packing type. The molecules are arranged in "slabs" parallel to the ab -plane; all molecules in a given slab are related by translation and hence have the same orientation. Adjacent slabs are related by the 2_1 screw axis (parallel to the b -axis), and the molecules in adjacent slabs have different orientations. As discussed above, the crystal structure of **1-1** is disordered, with each atomic site in the central ring represented as $B_{0.5} N_{0.5}$. This representation of the average structure may be readily interpreted in terms of the molecule of **1-1** adopting two orientations with equal probability (the two orientations differ by 60° rotation about an axis perpendicular to the plane of the molecule). In the average structure, the positions of the C and H atoms for the two molecular orientations occupy the same set of sites.

To assess whether there is any significant energy difference between the two molecular orientations in the disordered (average) structure, periodic DFT-D calculations were carried out for two ordered structures, in each case containing only one of the two molecular orientations. To generate these ordered structures, the crystallographic inversion centre was removed to give space group $P2_1$ (with one molecule in the asymmetric unit), and the central ring was an ordered B_3N_3 ring (i.e., with each atomic site occupied by only B or only N, and with the B and N atoms alternating around the ring). The two ordered structures differ by 60° rotation about an axis perpendicular to the plane of the molecule. Each structure was subjected to DFT-D geometry optimization (with fixed unit cell). The resulting geometry optimized structures are very similar (except regards the assignment of B and N atoms to the atomic sites of the central ring); the largest displacement between atomic sites in the two structures is 0.111 \AA , with an RMSD of 0.072 \AA . The energy difference between the two optimized structures is only $4 \times 10^{-4} \text{ kJ mol}^{-1}$. This very small energy difference is fully compatible with the existence of disorder involving equal populations of the two molecular orientations in the average crystal structure determined from pXRD data.

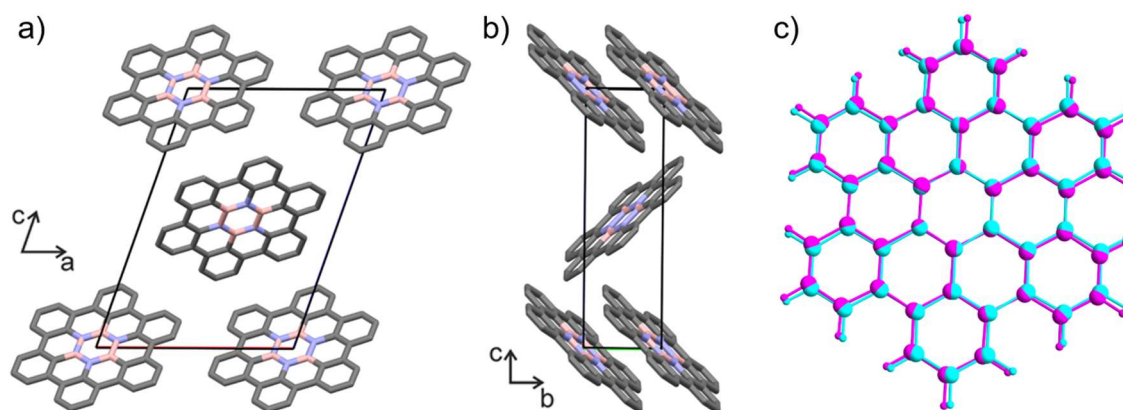


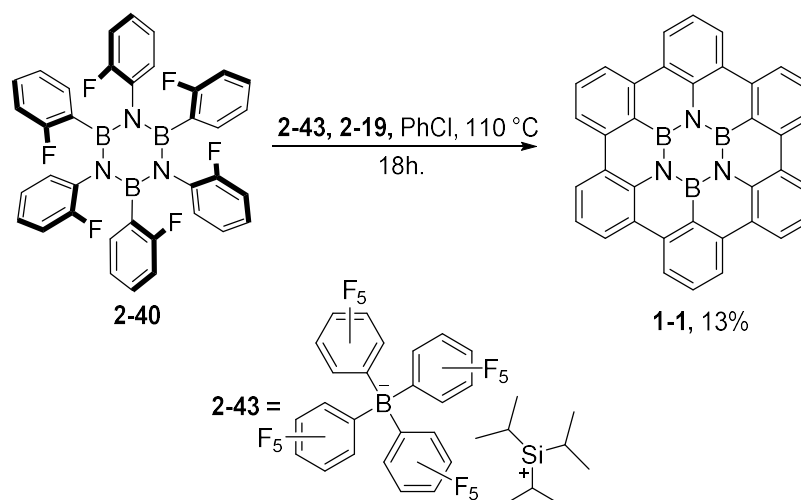
Figure 2.16: Crystal structure of **1-1** viewed a) along the b-axis and b) along the a-axis. In this disordered structure, the occupancy of each atomic site in the central ring is $B_{0.5} N_{0.5}$. The slabs of molecules discussed in the text are parallel to the ab-plane, which is horizontal in both (a) and (b). c) Overlay of the crystal structures of **1-1** (magenta) and the carbon analogue of **1-1** (cyan). The overlay was constructed by matching the unit cell axes (not shown) of the two structures.

The outcome of this crystallographic study confirmed the successful formation of derivative **1-1**, although with similar yields to **2-1**, thus ruling out any effect of the xylly groups on the reaction outcome. At this point the focus was moved on the investigation of the effect of different WCA on the reaction to access a broader set of silylium reagents.

2.11 Effects of different WCAs on the reaction outcome

Due to the difficult multistep synthesis, the commercial availability of carborane **2-22** is limited to few companies, resulting in a high price per gram of this compound. This fact, along with the strong influence of WCA on the reactivity of silylium ions, has led us to the decision to study the effect of different WCA on the reaction outcome. The synthesis was then repeated on **2-40** using tetrakis pentafluorophenyl borate stabilized silylium ion **2-43** as reagent (Scheme 2.20). Tetrakis pentafluorophenyl borate is known to be a more coordinating anion than the previously used carborane present in **2-22**, thus resulting in less ionic silicon centres. The ionic degree of silylium ions is usually assessed using ^{29}Si -NMR in which low field values suggest a more ionic nature of the silicon centre. When this analysis is performed on **2-22**, a value of 115 ppm is found, whereas, for **2-43**, a shift of 107 ppm is obtained,^[39,40] thus confirming a slightly less ionic nature for the latter, which should result in a lower reactivity. Despite this, the easier preparation, and the lower price per gram of tetrakis pentafluorophenyl borate make it very appealing in this reaction when compared to carborane reagents. The reaction was then performed with the new reagent and when **2-40** was treated with **2-43** and **2-19** in PhCl at 110 °C the desired product **1-1** was again formed. However, in

this case, a 13% yield was obtained, which is lower than the one achieved in previous attempts.



Scheme 2.20: Planarization reaction involving **2-40** and silylium ion **2-43**. Structure of **2-43** reported.

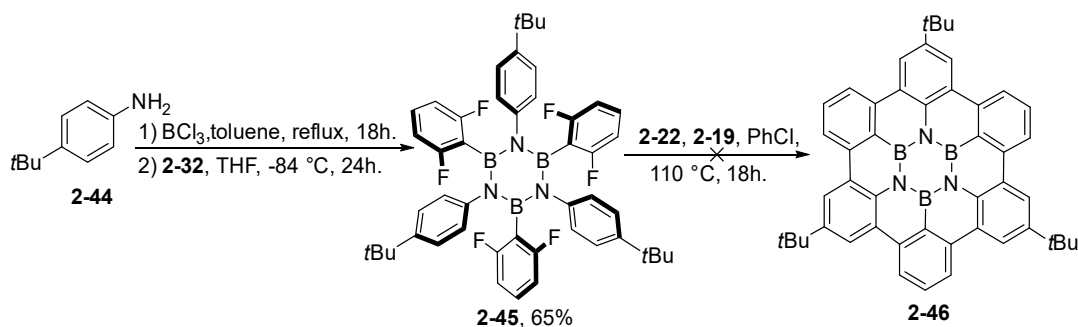
This result is quite interesting since it shows that the use of the more accessible **2-43** in the reaction is an available option, even if providing generally lower yields compared to **2-22**.

The reaction was then repeated using TMSOTf ($^{29}\text{Si-NMR} = 44 \text{ ppm}$ close to the ones reported for $\text{TMSClO}_4 = 47 \text{ ppm}$)^[41] and in this case the silicon reagent was used as solvent in the presence of $\text{P}(o\text{-tolyl})_3$ as Bronsted base at $140 \text{ }^\circ\text{C}$ for 18 h. These harsh conditions were used to overcome the much lower ionic degree of this silicon reagent but, despite these modifications, no products were formed and only starting borazine was visible. This result confirms that the silicon reagent must be a strong Lewis acid with high ionicity to obtain the desired CC bond formation, thus limiting the viable WCA to ones presenting a very low coordination ability.

From the obtained results, it appears that the removal of the xylene groups does not increase the reaction yield and results in the formation of insoluble products which led to the first identification of **2-42**, representing an important proof of the stepwise mechanism of cyclization. Furthermore, when **2-43** was used in place of **2-22** the reaction still worked producing the desired product even if with a lower yield.

2.12 Synthesis of functionalized HBBNC derivatives

To synthesise functionalized HBBNC derivatives, different starting fluoro hexaarylborazines had to be prepared. Since the yield was not the focus of this study, borazines bearing two fluorine atoms on the boron bonded aryl ring were used to avoid mixtures of atropoisomers resulting in difficult characterizations. As a first test, the xyllyl solubilizing group was substituted with a *t*-Bu moiety by using aniline **2-44** as starting material in the borazine synthesis (Scheme 2.21).



Scheme 2.21: Synthetic pathway towards *t*-Bu derivatives **2-45** and **2-46**.

Aniline **2-44** was then treated with BCl_3 in refluxing toluene followed by reaction of resulting chloro-borazole with organolithium **2-32** giving molecule **2-45** in a 65% yield. Derivative **2-45** structure was confirmed by SC-XRD (Figure 2.16). As previously seen for molecule **2-27** the fluorine atoms in the crystal structure are arranged in a “gear like” fashion and as for the previous case even **2-45** is stable to normal handling conditions.

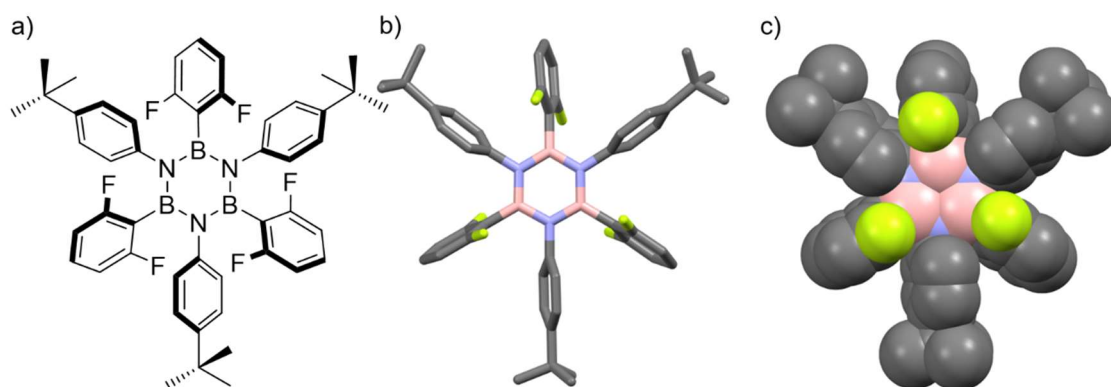


Figure 2.16: Crystal structure of derivative **2-45**; a) molecular structure, b) capped sticks crystal structure, c) spacefill crystal structure. Space group: $P2_1/c$. Crystals obtained from MeOH diffusion in CH_2Cl_2 . Colour code: grey: C, pink: B, blue: N, red: O and yellow: F. H atoms omitted for clarity.

The planarization reaction conditions involving carborane **2-22** were then applied to **2-45** to obtain *t*-Bu functionalized **2-46**. However, a black insoluble material was obtained from the reaction, which after various washings gave a grey insoluble powder.

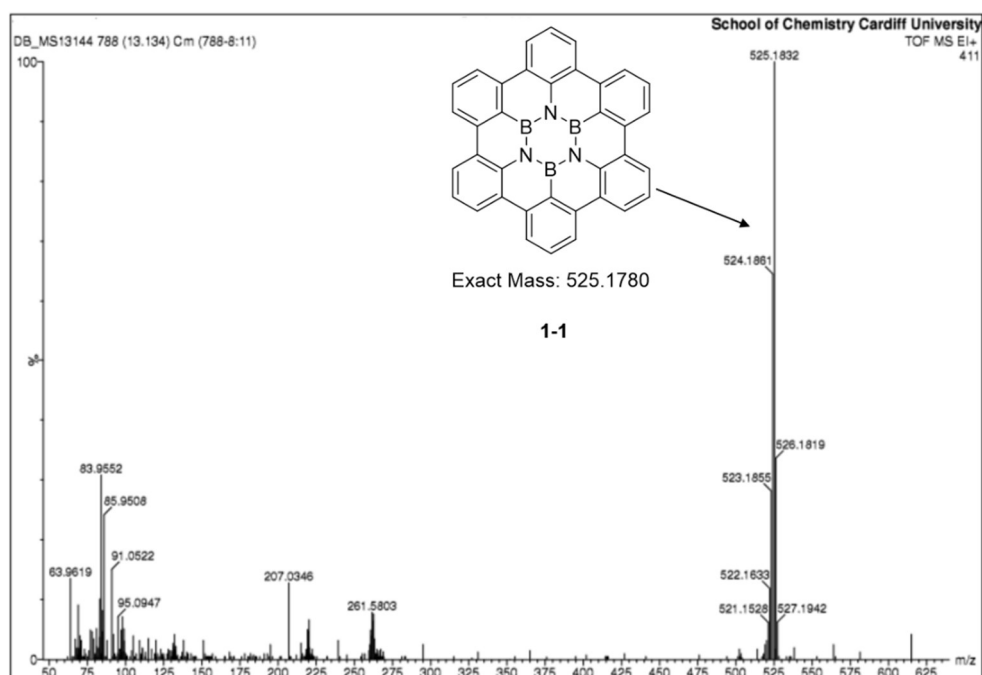
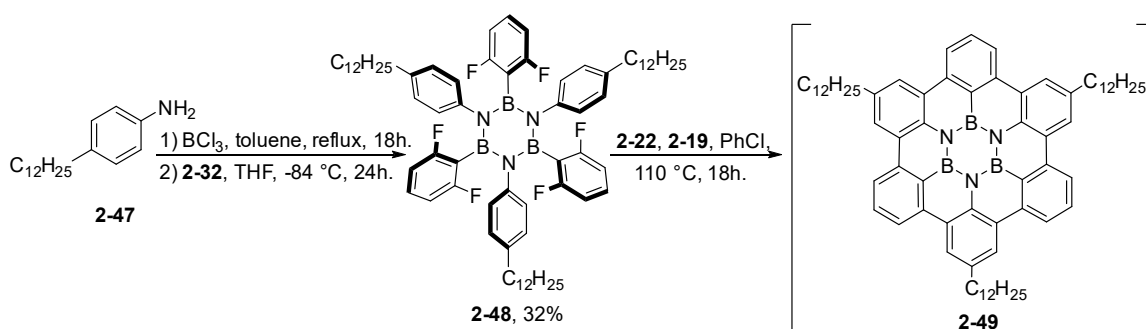


Figure 2.17: LR-MS EI⁺ mass spectra of insoluble material obtained from cyclization of **2-45**.

The insoluble material was then studied with LR-MS and in the spectra only one peak at m/z : 525.1832 was visible, corresponding to **1-1** (Figure 2.17). This evidence suggests that the cyclization is occurring successfully on **2-45**, but the strong acidic conditions induce the loss of the *t*-Bu groups, leading to the formation of the non-functionalized **1-1**.

At this point, it was decided to substitute the *t*-Bu group with a dodecyl moiety ($-C_{12}H_{25}$) to disfavour the formation of carbocations resulting in loss of the functional groups. The synthesis of **2-48** was then started by refluxing dodecyl aniline **2-47** with BCl_3 in toluene (Scheme 2.22).



Scheme 2.22: Synthetic strategy towards dodecyl derivatives **2-48** and **2-49**.

The resulting chloro-borazole intermediate was then treated with the lithium derivative **2-32** giving borazine **2-48** in a good 32% yield. Treatment of **2-48** with silylium

carborane **2-22** and dimethyldimesitylsilane **2-19** led to the formation of a mixture of products that proved to be soluble only in hot toluene.

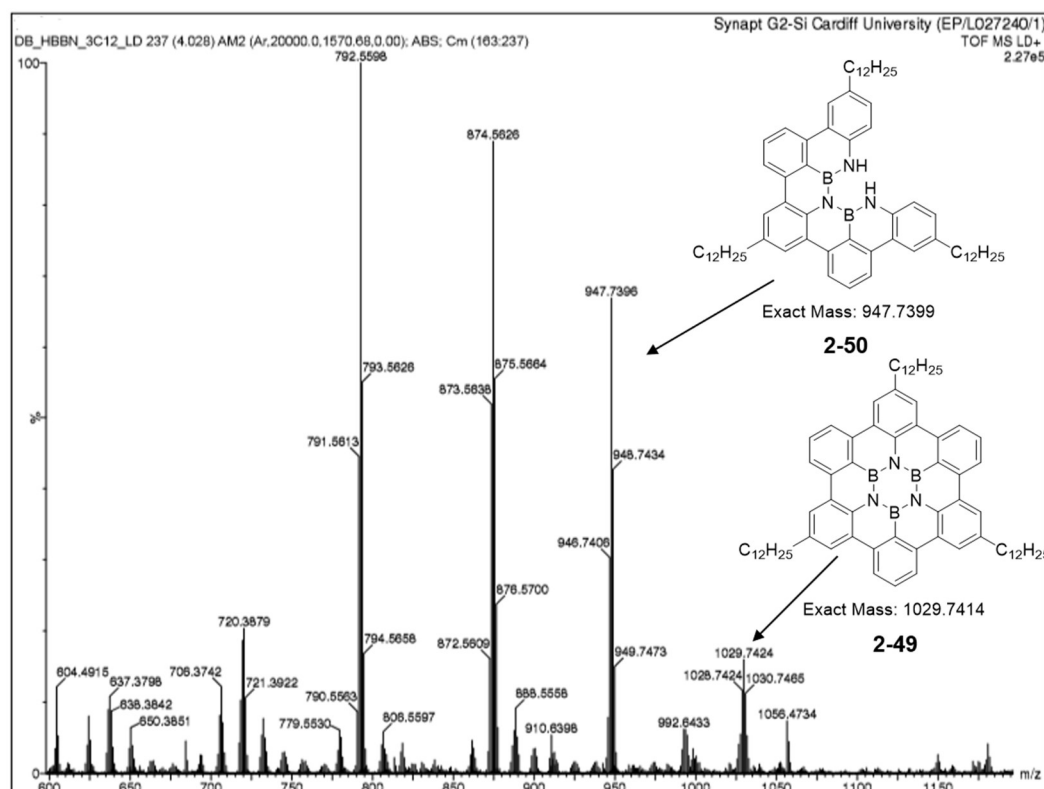
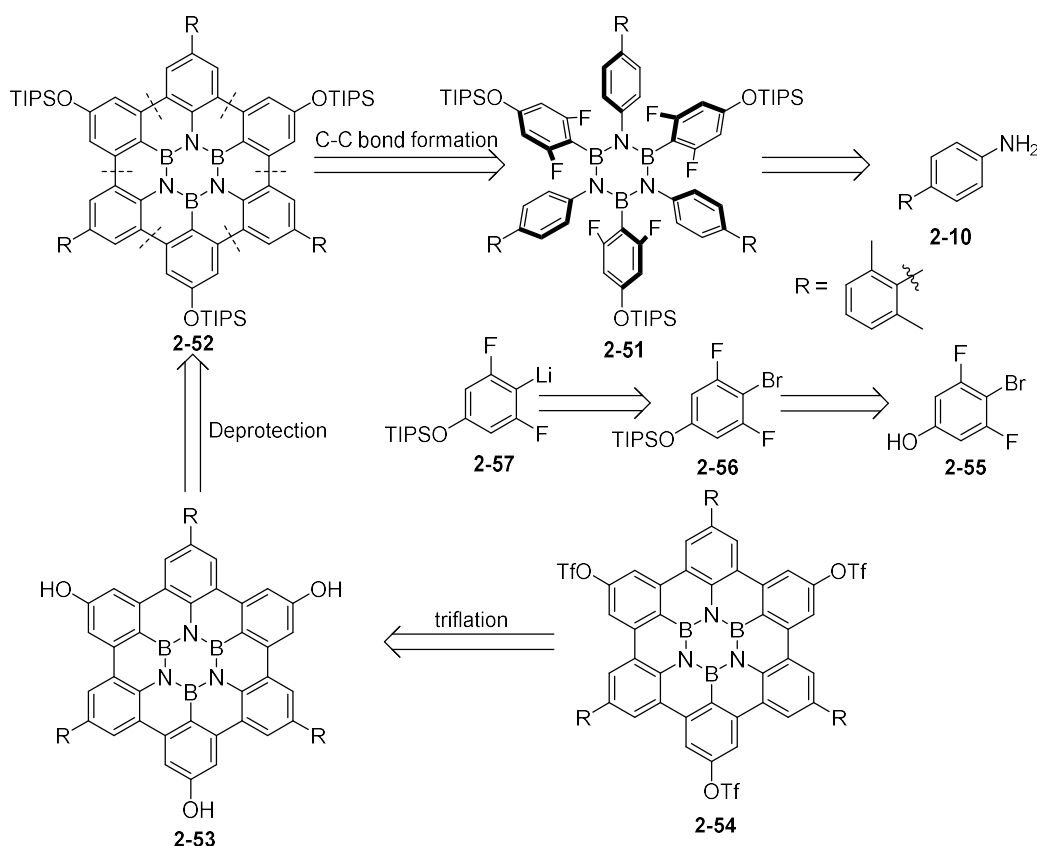


Figure 2.18: HR-MS LD⁺ of reaction mixture obtained from cyclization of **2-48**.

As a result of the low solubility it was not possible to separate the different components of the mixture, limiting the characterization to HR-MS (Figure 2.18). The presence of target molecule **2-49** was confirmed by the peak corresponding to the molecular ion m/z 1029.7424 ($C_{72}H_{90}B_3N_3^+$, calc.: 1029.7414). However, the incomplete cyclization product **2-50** was present as well at m/z 947.7396, whereas the two main peaks at m/z 874.5626 and 792.5596 are due to fragmentations of the $C_{12}H_{25}$ chains during ionization of the molecules.

After these results, it is evident that xylene moieties provide the best solution to impart solubility to the final product while preserving its stability to the reaction conditions. Consequently, to obtain soluble products that could undergo further functionalization, it is necessary to synthesize borazines bearing both xylene groups as solubilizing moieties and protected functional groups stable to the cyclization conditions. The use of the OH group represents the best option, since it can be protected in many ways and is quite versatile. For instance, it can easily undergo conversion to triflate which can be in turn employed in cross-coupling reactions.

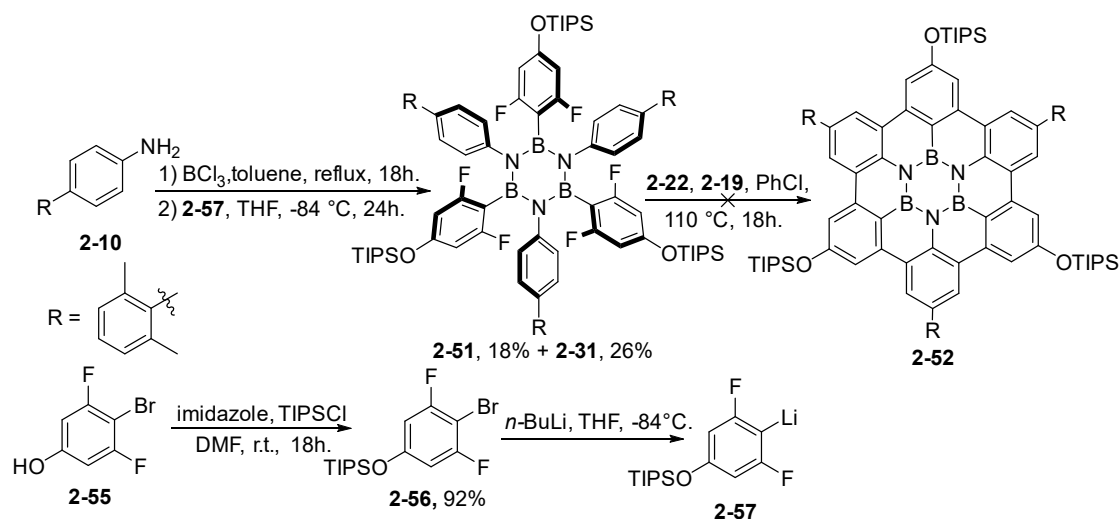
The retrosynthetic approach towards the derivative bearing triflate groups is reported in Scheme 2.23.



Scheme 2.23: Retrosynthetic approach towards molecule **2-54**.

According to this plan, the final product **2-54**, should be obtained by triflation of hydroxy derivative **2-53**. In the outlined strategy, hydroxy derivative **2-53** can be in turn obtained by deprotection with fluoride of TIPS protected **2-52**. The TIPS protecting group represent the best choice due to its bulkiness, which should be able to avoid reaction of the hydroxy moieties with the silylium ion. At this point, **2-52** could be formed applying the silylium ion cyclization on borazine **2-51** which should be obtained starting from **2-10** and lithium derivative **2-57** obtained *via* lithium-halogen exchange on TIPS protected 4-bromo-3,5-difluorophenol **2-56**. The latter can be formed by treatment of **2-55** with TIPSCl (Scheme 2.23).

The synthesis started with treatment of **2-10** with BCl_3 in refluxing toluene. The resulting chloro-borazole intermediate was reacted with lithium derivative **2-57** leading to the formation of desired borazine **2-51** in a 18% yield (Scheme 2.24). The side product *n*-butyl derivative **2-31** was formed as well in a 26% yield, suggesting a competition between *n*-BuLi and lithium derivative **2-57**.



Scheme 2.24: Preparation of **2-56**, synthesis and attempted planarization of borazine **2-51**.

At this point, planarization of molecule **2-51** was performed using **2-22** and **2-19** in PhCl at 110 °C. However, in this case, TLC analysis highlighted the formation of a complex mixture of very polar products. This result suggests that, although being very bulky, TIPS is not effectively protecting the hydroxy groups and a deprotection/reaction is occurring in the reported conditions. This results in reactions between the silylium ion and the hydroxy moieties, possibly leading to polymerized materials.

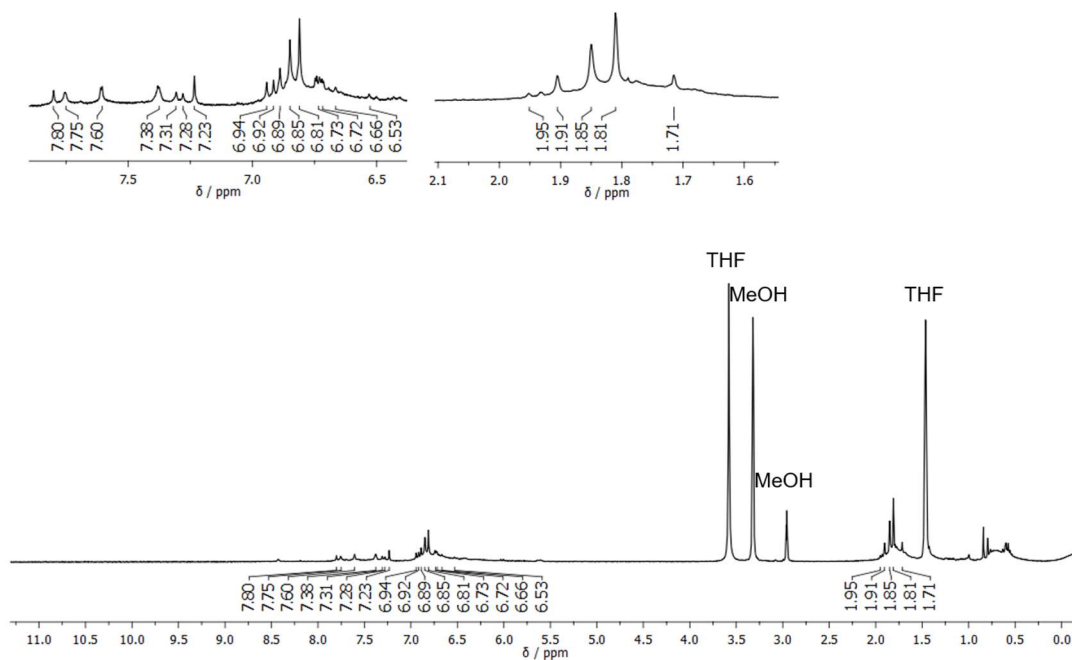


Figure 2.19: 300 MHz $^1\text{H-NMR}$ in THF/MeOH of mixture of products obtained from cyclization of **2-51**.

To shed light on the reaction outcome, the obtained mixture was analysed with $^1\text{H-NMR}$ (Figure 2.19). In the obtained spectra, aromatic signals are present between 7.80 and 6.52 ppm, compatibly with a planarized system presenting donor OH groups. Absence of the TIPS signals in the region comprised between 0.50 ppm and 0.00 ppm confirms the loss of the protective groups. Furthermore, the presence of multiple signals ascribable to the xylene methyl groups between 1.95 ppm and 1.71 ppm suggests the presence of different products, possibly resulting from reactions of the unprotected OH groups (Figure 2.19).

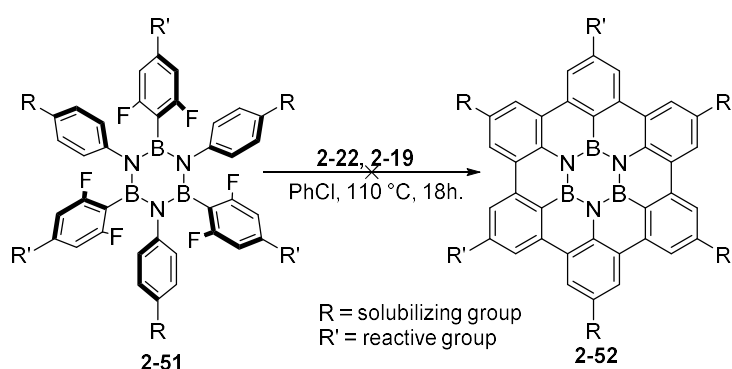
This result points out that the reaction is not suitable for molecules containing functional groups different from aromatic scaffolds and primary alkanes due to the strong Lewis acid nature of the silylium ion. Since it was impossible to introduce functional groups that could allow further functionalization and extension of the system, the focus was moved on the characterization of the obtained derivatives to shed light on the BN-doping effects.

2.13 Conclusions and perspectives

In conclusion, to obtain the desired target molecule various unprecedented halogen-functionalized borazines have been synthesized, extending the knowledge on this class of derivatives. The use of a silylium ion induced Friedel-Crafts like reaction on fluoro-borazine **2-27** led to the formation of the desired soluble **2-1** in a 5% yield along with derivative **2-33** as major product. To improve the reaction conditions and understand the formation of **2-33**, theoretical studies were performed, confirming a stepwise mechanism in which the low energy intermediates are constituted by the structures presenting the most extended and less distorted conjugate structure. Consequently, a new synthesis involving a fluoro-borazine bearing one fluorine atom on each ring was designed. Planarization of this borazine led to the formation of the desired product in a 15% yield along with unprecedented $\text{B}_3\text{N}_2\text{O}$ doped **2-38**. Computational studies on this reaction confirmed the presence of different intermediates in the stepwise mechanism possibly accounting for the higher yield and formation of **2-38**. The versatility of the reaction was proved by synthesising HBBNC **1-1**, which was obtained in a 18% yield and characterized by pXRD and HR-MS. To widen the scope of the reaction, fluorine functionalized borazines bearing other functional and solubilizing groups have been synthesized and the planarization reaction attempted. However, these studies pointed out that only aromatic scaffolds and primary alkyl chains can survive the harsh reaction conditions of the silylium ion induced C-F bond activation reaction. This result excluded the possibility of using functionalized borazines in the cyclization reaction to obtain functionalized HBBNC derivatives, which could be further functionalized and possibly

used to construct extended nanographene systems (Scheme 2.25). Therefore, the production of nanoribbon systems will have to rely on the preparation of extended dendrimeric systems that can be planarized straightaway.

Furthermore, a complete characterization of derivatives **2-1** and **2-38** will be performed and all-carbon reference compounds for derivatives **2-1** and **2-38** will be synthesised as well to assess the differences imparted on the derivatives by the borazine based rings. The outcome of this work will provide a useful base of experimental data for the future design of doped nanographenes presenting tailored bandgap and properties.



Scheme 2.25: Attempted synthesis of functionalized derivative **2-52**.

2.14 References

- [1] I. B. Atkinson, D. C. Blundell, D. B. Clapp, *J. Inorg. Nucl. Chem.* **1972**, *34*, 3037–3041.
- [2] D. Bonifazi, F. Fasano, M. M. Lorenzo-garcia, D. Marinelli, J. Tasseroul, *Chem. Commun.* **2015**, *51*, 15222–15236.
- [3] S. J. Groszos, S. F. Stafiej, *J. Am. Chem. Soc.* **1958**, *80*, 1357–1360.
- [4] L. Pauling, *The Nature of the Chemical Bond* **1960**, 260.
- [5] A. Bondi, *J. Phys. Chem.* **1964**, *68*, 441–451.
- [6] K. Nagasawa, *Inorg. Chem.* **1966**, *5*, 442–445.
- [7] K. Ota, T. Tanaka, A. Osuka, *Org. Lett.* **2014**, *16*, 2974–2977.
- [8] X. H. Cheng, S. Höger, D. Fenske, *Org. Lett.* **2003**, *5*, 2587–2589.
- [9] M. Daigle, A. Picard-lafond, E. Soligo, J. F. Morin, *Angew. Chem. Int. Ed* **2016**, *55*, 2042–2047.
- [10] J. F. Morin, A. Jolly, D. Miao, M. Daigle, *Angew. Chemie Int. Ed.* **2020**, *59*, 4624–4633.
- [11] K. Y. Amsharov, M. A. Kabdulov, M. Jansen, *Angew. Chemie Int. Ed.* **2012**, *124*, 4672–4675.
- [12] H. F. T. Klare, *ACS Catal.* **2017**, *7*, 6999–7002.
- [13] O. Allemann, S. Duttwyler, P. Romanato, K. K. Baldridge, J. S. Siegel, *Science* **2011**, *332*, 574–577.

- [14] S. Luliński, J. Serwatowski, *J. Org. Chem.* **2003**, *68*, 5384–5387.
- [15] M. Schnürch, M. Spina, A. F. Khan, M. D. Mihovilovic, P. Stanetty, *Chem. Soc. Rev.* **2007**, *36*, 1046–1057.
- [16] A. Saednya, H. Hart, *Synthesis* **1996**, *1*, 1455–1458.
- [17] J. Dosso, J. Tasseroul, F. Fasano, D. Marinelli, N. Biot, A. Fermi, D. Bonifazi, *Angew. Chem. Int. Ed.* **2017**, *56*, 4483–4487.
- [18] T. Yanai, D. P. Tew, N. C. Handy, *Chem. Phys. Lett.* **2004**, *393*, 51–57.
- [19] W. J. Hehre, R. Ditchfield, J. A. Pople, *J. Chem. Phys.* **1972**, *52*, 2257–2561.
- [20] W. C. M. J. Frisch, G. W. Trucks, H. B. Schlegel, G. E. Scuseria, M. A. Robb, J. R. Cheeseman, G. Scalmani, V. Barone, B. Mennucci, G. A. Petersson, H. Nakatsuji, M. Caricato, X. Li, H. P. Hratchian, A. F. Izmaylov, J. Bloino, G. Zheng, J. L. Sonnenberg, M. Had, *Gaussian 09, Revis. D.01, Gaussian Inc., Wallingford CT* **2010**.
- [21] J. Tomasi, B. Mennucci, R. Cammi, *Chem. Rev.* **2005**, *105*, 2999–3093.
- [22] D. K. Straub, *J. chem. educ.* **1995**, *72*, 494–497.
- [23] M. Krieg, F. Reicherter, P. Haiss, M. Ströbele, K. Eichele, M. J. Treanor, R. Schaub, H. F. Bettinger, *Angew. Chemie Int. Ed.* **2015**, *54*, 8284–8286.
- [24] J. M. Robertson, J. Trotter, *J. Chem. Soc* **1961**, 1280–1284.
- [25] R. Goddard, M. W. Haenel, W. C. Herndon, C. Krueger, M. Zander, *J. Am. Chem. Soc.* **1995**, *117*, 30–41.
- [26] A. Le Bail, H. Duroy, J. L. Fourquet, *Mat. Res. Bull.* **1988**, *23*, 447–452.
- [27] A. C. Larson, R. B. Von Dreele, *Los Almos Natl. Lab. Los Almos, NM* **2004**, *LAUR*, 86–748.
- [28] K. D. M. Harris, M. Tremayne, P. Lightfoot, P. G. Bruce, *J. Am. Chem. Soc.* **1994**, *116*, 3543–3547.
- [29] K. D. M. Harris, *Adv. X-Ray Crystallogr.*, Springer, **2011**, pp. 133–177.
- [30] K. D. M. Harris, S. Habershon, E. Y. Cheung, R. L. Johnston, *Z. Krist.* **2004**, *219*, 838–846.
- [31] B. M. Kariuki, P. Calcagno, K. D. M. Harris, D. Philp, R. L. Johnston, *Angew. Chem. Int. Ed* **1999**, *38*, 831–835.
- [32] B. M. Kariuki, K. Psallidas, K. D. M. Harris, R. L. Johnston, R. W. Lancaster, S. E. Staniforth, S. M. Cooper, *Chem. Commun.* **1999**, 1677–1678.
- [33] D. Albesa-jove, B. M. Kariuki, S. J. Kitchin, L. Grice, E. Y. Cheung, K. D. M. Harris, *ChemPhysChem* **2004**, *5*, 414–418.
- [34] F. Guo, J. Martí, Z. Pan, C. E. Hughes, K. D. M. Harris, *J. Phys. Chem. C* **2008**, *112*, 19793–19796.
- [35] P. A. Williams, C. E. Hughes, G. K. Lim, B. M. Kariuki, K. D. M. Harris, *Cryst. Growth Des.* **2012**, *12*, 3104–3113.
- [36] C. E. Hughes, G. N. M. Reddy, S. Masiero, S. P. Brown, P. A. Williams, K. D. M. Harris, *Chem. Sci.* **2017**, *8*, 3971–3979.
- [37] O. Al Rahal, C. E. Hughes, P. A. Williams, A. J. Logsdail, Y. Diskin-posner, K. D.

- M. Harris, *Angew. Chem. Int. Ed* **2019**, *131*, 18964–18968.
- [38] G. R. Desiraju, A. Gavezzotti, *J. Am. Chem. Soc.* **1989**, *26*, 621–623.
- [39] T. A. Kochina, D. V Vrazhnov, E. N. Sinotova, M. G. Voronkov, *Russ. Chem. Rev.* **2006**, *75*, 95–110.
- [40] J. B. Lambert, S. Zhang, S. M. Ciro, *Organometallics* **1994**, *13*, 2430–2443.
- [41] M. Arshadi, D. Johnels, U. Edlund, C. H. Ottosson, D. Cremer, *J. Am. Chem. Soc.* **1996**, *118*, 5120–5131.

CHAPTER 3

BN vs CC: EFFECTS OF BORAZINE DOPING ON PROPERTIES OF PAHs.

In this chapter an extensive study of the optoelectronic properties of borazine-doped derivatives **2-1** and **2-38** has been carried out. To compare the effect of doping on the different derivatives, tailored reference compounds have been synthesised. Hexabenzocoronene **3-2** has been compared with HBBNC **2-1** highlighting an important widening of the HOMO-LUMO gap resulting from the substitution of the central ring in **3-2** with a borazine ring. In a similar fashion, unprecedented B₃N₂O doped derivative **2-38** has been compared with the corresponding full carbon **3-13** and pyrilium analogue **3-27^{BF}** again proving the ability of borazine based rings to widen the HOMO-LUMO gap and lead to increased rigidity of the structures of PAHs. Along with the optoelectronic properties, the aromaticity of the different derivatives has been studied as well. Finally, since the inclusion of the B₃N₂O based system leads to the formation of a gulf region in the PAH, a comparison between hexabenzocoronene based derivatives (**2-1**, **3-2**) and the gulf presenting ones (**2-38**, **3-13**) allowed us to understand the effect of the topological element in these aromatics.

This chapter is divided in 13 main sections: *i*) Section 3.1 defines the aim of the project *ii*) Section 3.2 presents the synthesis of derivative **3-2**; *iii*) Section 3.3 describes the synthesis of gulf full-carbon derivative **3-13**; *iv*) Section 3.4 reports the synthesis of pyrilium reference compound **3-27^{BF}**; *v*) Section 3.5 presents crystal structure comparisons between doped (**2-1** and **2-38**) and full carbon derivatives (**3-2** and **3-13**); *vi*) Section 3.6 presents a comparison between ESP plots of molecules; *vii*) Section 3.7 presents a study on solvates of **2-1** with different aromatic solvents. *viii*) Section 3.8 displays a study on the aromaticity of the derivatives; *ix*) Section 3.9 displays a full comparison between the optical properties of the molecules; *x*) Section 3.10 presents electrochemical studies on the derivatives; *xi*) Section 3.11 presents and HOMO-LUMO calculations on derivatives; *xii*) Section 3.12 draws some conclusions and perspectives; *xiii*) Section 3.13 contains references for the chapter.

The research work described in sections 3.1 to 3.11 was carried out at Cardiff university. X-Ray analysis were performed by N. Demitri (Elettra-Sincrotrone, Basovizza, Trieste, Italy), N. Biot and D. Romito (Cardiff University). Photophysical characterization was carried out by T. Battisti, computational studies were performed by T. Battisti (Cardiff University).

The results reported in this chapter have been published in the following articles:

Dosso, J.; Tasseroul, J.; Fasano, F.; Marinelli, D.; Biot, N.; Fermi, A.; Bonifazi, D. Synthesis and Optoelectronic Properties of Hexa-*peri*-hexabenzoborazinocoronene. *Angew. Chem., Int. Ed.* **2017**, 56, 4483–4487.

Dosso, J.; Battisti T.; Ward B. D.; Demitri, N.; Hughes C.; Williams P.A.; Harris K. D. M.; Bonifazi, D. Boron-nitrogen-doped nanographenes: a synthetic tale from borazine precursors. *Chem. A Eur. J.* **2020**, 26, 6608-6621.

3.1 Aim of the Project

As previously reported in chapter 2, the synthesis of molecule **2-1** represents a very important result since it constitutes the first example of a soluble PAH presenting a borazine ring as a dopant unit. To assess the effect of the borazine doping on this system, the synthesis of reference hexa-*peri*-hexabenzocoronene **3-2** (Scheme 3,1 bottom left) will be carried out, thus allowing for a direct comparison between **2-1** and **3-2**. Since the effect of the substitution of a full aromatic ring in PAHs with a borazine was investigated only by theoretical means in the literature, an in-depth study on the borazine-doped derivative and corresponding reference involving UV-Vis absorption emission spectroscopy, Cyclic voltammetry (CV) and computational studies will be carried out. Furthermore, the formation of **2-38** obtained by planarizing borazine **2-34** bearing one fluorine on each ring, represents an important breakthrough since no examples of B₃N₂O doped PAHs are known in the literature (a paper reporting a similar derivative by Bettinger and co-workers was published immediately after our contribution, see Chapter 1). Differently from **2-1**, in the case of **2-38** the presence of the oxygen atom results in a gulf region (Figure 3.1, top row). It was anticipated that this topological element along with the presence of the almost unknown B₃N₂O system would have almost certainly led to variations in the properties compared to **2-1** and could be important for the future development of doped materials and PAHs. While a direct comparison with **2-1** is possible, this would not distinguish between the topological and doping contributions to the properties of **2-38**. The only way to determine the unknown effects of the B₃N₂O ring on the properties of PAHs is to compare the properties of **2-38** with tailored reference compounds (Figure 3.1 top left and right). From this point of view, the gulf full carbon analogue of **2-38** (Scheme 3.1 top left) will be synthesised together with heteroatom doped pyrilium derivative (Scheme 3.1, top right) in order to have a comparison with a system presenting an aromatic oxygen doped ring. After assessing the effect of the different borazine based rings on the properties of PAHs, the cross comparison between the coronene and gulf derivatives will clarify the effect of the edge topology difference between the two classes of PAHs (Figure 3.1). The synthesis and study of these reference compounds will give a clear picture on the effects of the doping and topology on the aromaticity and spectroscopic properties of this class of PAHs, resulting in an important fundamental contribution to the field.

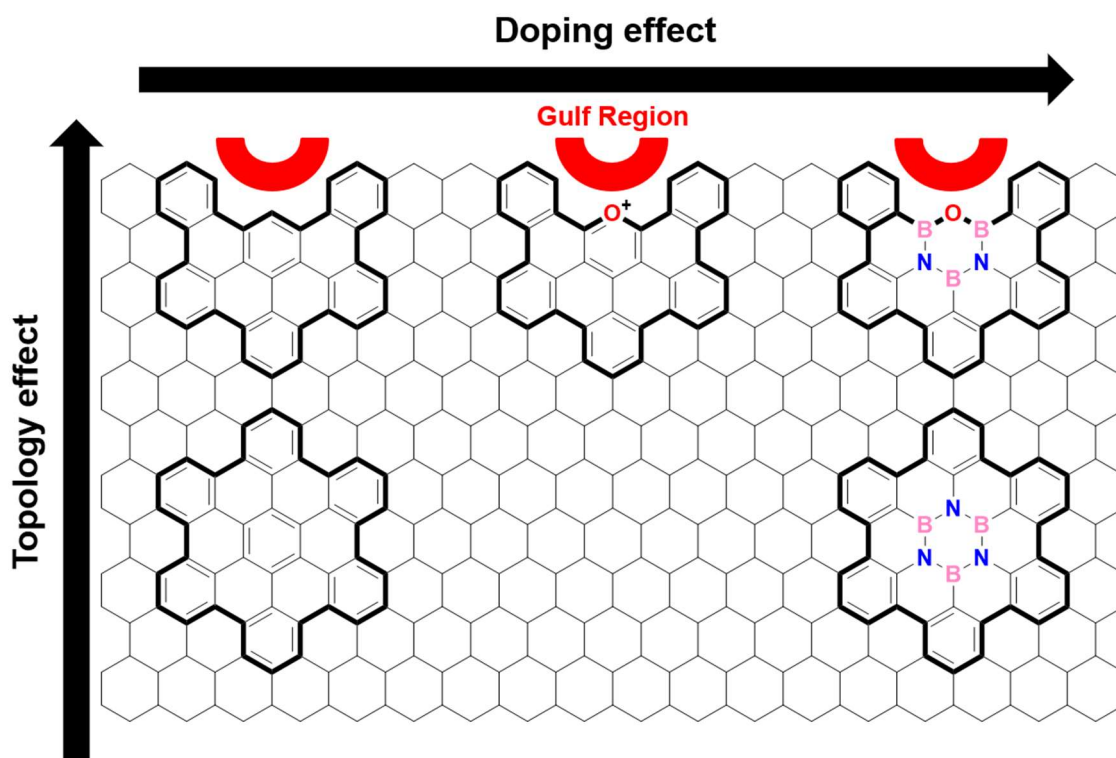
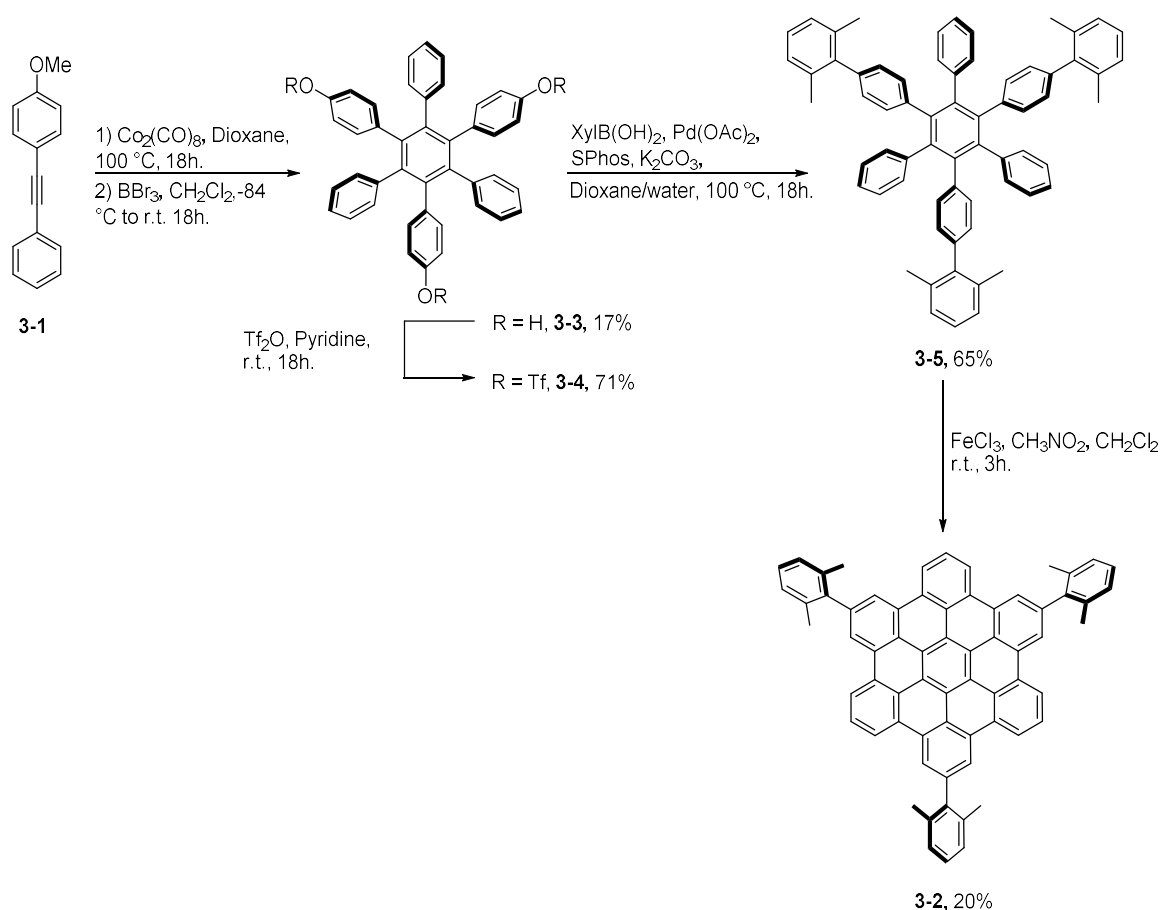


Figure 3.1: Nanographenes model compounds used to study the effects of doping and topology.

3.2 Synthesis of soluble hexa-*peri*-hexabenzocoronene

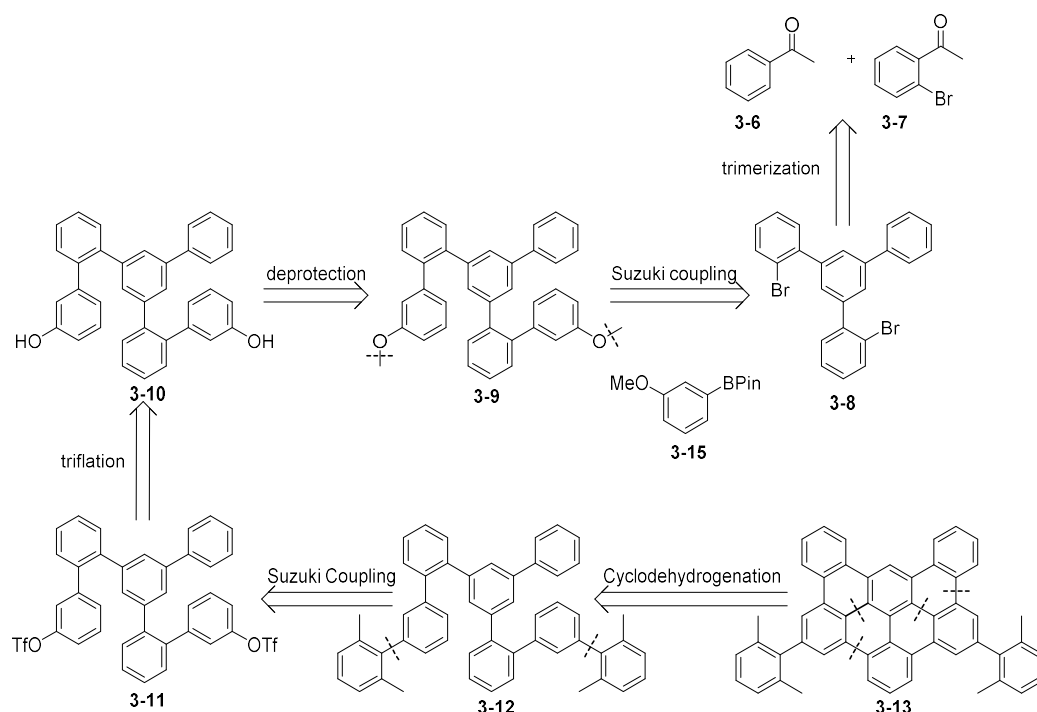
To understand the effect of the substitution of a benzene ring with a borazine in a hexabenzocoronene scaffold, the full carbon analogue HBC **3-2** was synthesized in accordance with the synthesis reported in Scheme 3.1, based on literature procedures for similar derivatives. The first step in the synthesis consisted in the trimerization of the methoxy alkyne derivative **3-1** in the presence of $[\text{Co}_2(\text{CO})_8]$ to give a mixture of 1,3,5 and 1,2,4 trimethoxy hexaphenyl isomers, which were subjected to deprotection in the presence of BBr_3 . Separation of the two isomers was performed by silica gel column chromatography (SCC) affording **3-3** in a 17% yield. **3-3** was then triflated using Tf_2O in pyridine and the resulting **3-4** was cross coupled with xylyl boronic acid in the presence of $\text{Pd}(\text{OAc})_2$, SPhos and K_2CO_3 yielding polyphenylene **3-5** in a 65% yield. Finally, a Scholl reaction with FeCl_3 in $\text{CH}_3\text{NO}_2/\text{CH}_2\text{Cl}_2$ with N_2 bubbling gave the desired **3-2** in a 20% yield after multiple purifications on preparative TLC.



Scheme 3.1: synthetic pathway towards reference compound **3-2**.

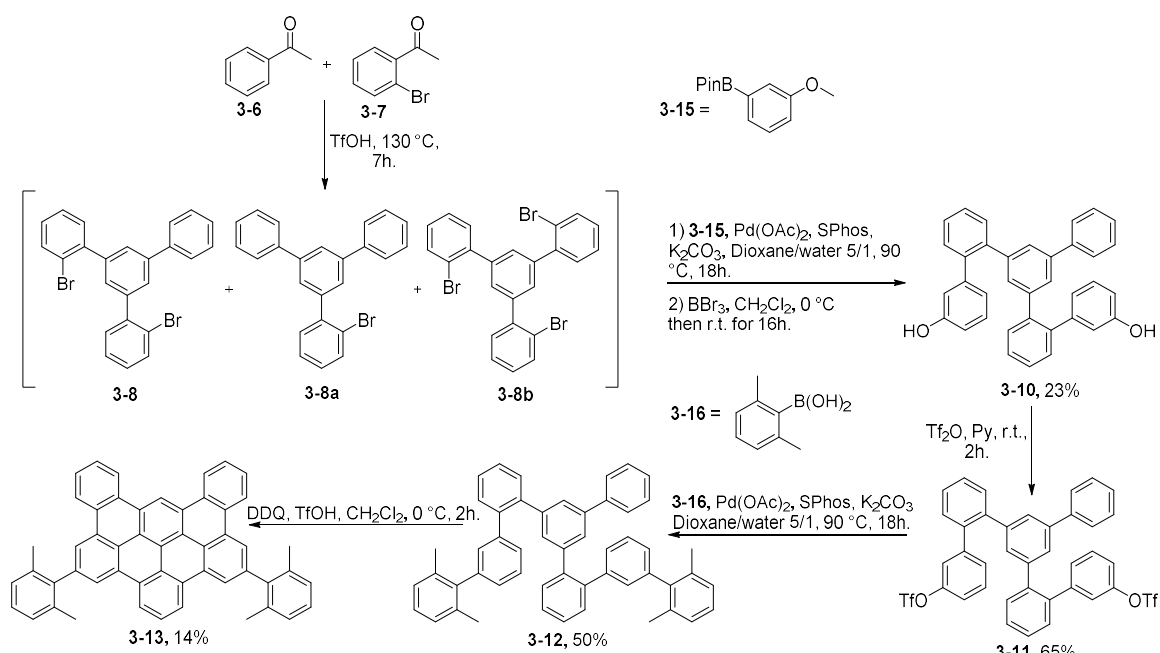
3.3 Synthesis of all-carbon gulf derivative

At this point, a suitable retrosynthetic approach towards full-carbon analogue **3-13** was designed (Scheme 3.2). According to this strategy, target molecule **3-13** can be obtained with a Scholl reaction starting from polyphenylene derivative **3-12**, in which the solubilizing moieties could be inserted by Suzuki cross coupling with triflate derivative **3-11**. The latter can be in turn formed by triflation of di-hydroxy functionalized **3-10**, derived from **3-9** by deprotection of the methoxy groups with BBr_3 (Scheme 3.2). Derivative **3-9** can be prepared by Suzuki coupling of dibromo **3-8** with **3-15**, where the former can be obtained by trimerization of acetophenone **3-6** and **3-7** in the presence of triflic acid.



Scheme 3.2: Retrosynthetic approach towards derivative **3-13**.

The synthesis started with the trimerization reaction of **3-6** and **3-7** in the presence of triflic acid at 130 °C (Scheme 3.3) to give a mixture of brominated derivatives containing **3-8** along with mono-bromo **3-8a** and tri-bromo **3-8b**. Molecule **3-15** was prepared by Miyaura coupling on 3-bromoanisole **3-14** with B_2Pin_2 , $[\text{Pd}(\text{dppf})\text{Cl}_2]$ and KOAc in dry degassed DMF at 90 °C giving molecule **3-15** in an 81% yield. Since products **3-8**, **3-8a** and **3-8b** presented very similar polarities it was impossible to purify them with SCC and the mixture was directly used in the following Suzuki cross-coupling with **3-15** (Scheme 3.3).



Scheme 3.3: Synthesis of full carbon **3-13**.

The resulting mixture of methoxy derivatives containing **3-9** was directly dissolved in CH_2Cl_2 and BBr_3 was added at $0\text{ }^\circ\text{C}$ followed by stirring at r.t. for 18 h. This resulted in a mix of hydroxy derivatives easily separated using SCC giving dihydroxy derivative **3-10** in a 23% yield (over two steps). The hydroxy groups of **3-10** were converted to triflates using Tf_2O in pyridine (Scheme 3.3) and a Suzuki cross coupling of **3-11** with 2,6-dimethylphenyl boronic acid **3-16** in the presence of $\text{Pd}(\text{OAc})_2$, SPhos and K_2CO_3 gave **3-12** in a 50 % yield. The final step of the synthesis involved a Scholl reaction on **3-12** but, when the standard conditions with FeCl_3 in CH_3NO_2 and CH_2Cl_2 were used, complex mixtures of products were formed without regard for temperature and reaction time. This can be due to the formation of chlorinated by-products which is a common feature of this kind of reactions.^[1] For this reason, we attempted the synthesis using DDQ and TfOH in degassed CH_2Cl_2 at $0\text{ }^\circ\text{C}$ (Scheme 3.3). The resulting reaction mixture was purified with a preparative TLC affording desired product **3-13** in a low 14% yield. **3-13** could be identified *via* $^1\text{H-NMR}$ (Figure 3.2), $^{13}\text{C-NMR}$, HR-MS and SC-XRD, with results comparable to the ones reported for similar derivatives described in previous works.^[2,3]

From the reported $^1\text{H-NMR}$ all the signals expected for **3-13** are visible, in particular the highly deshielded singlet at 10.54 ppm corresponding to proton H_a along with singlets H_f and H_g (8.99 and 8.86 ppm) represent a good proof of the formation of the polycyclic system.

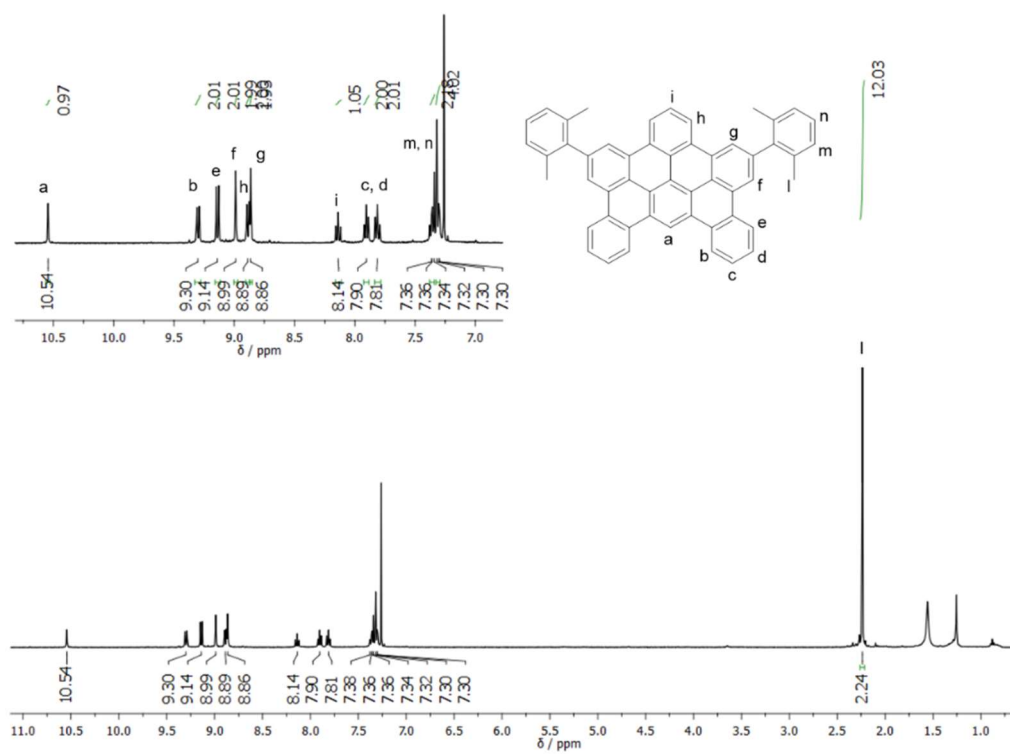
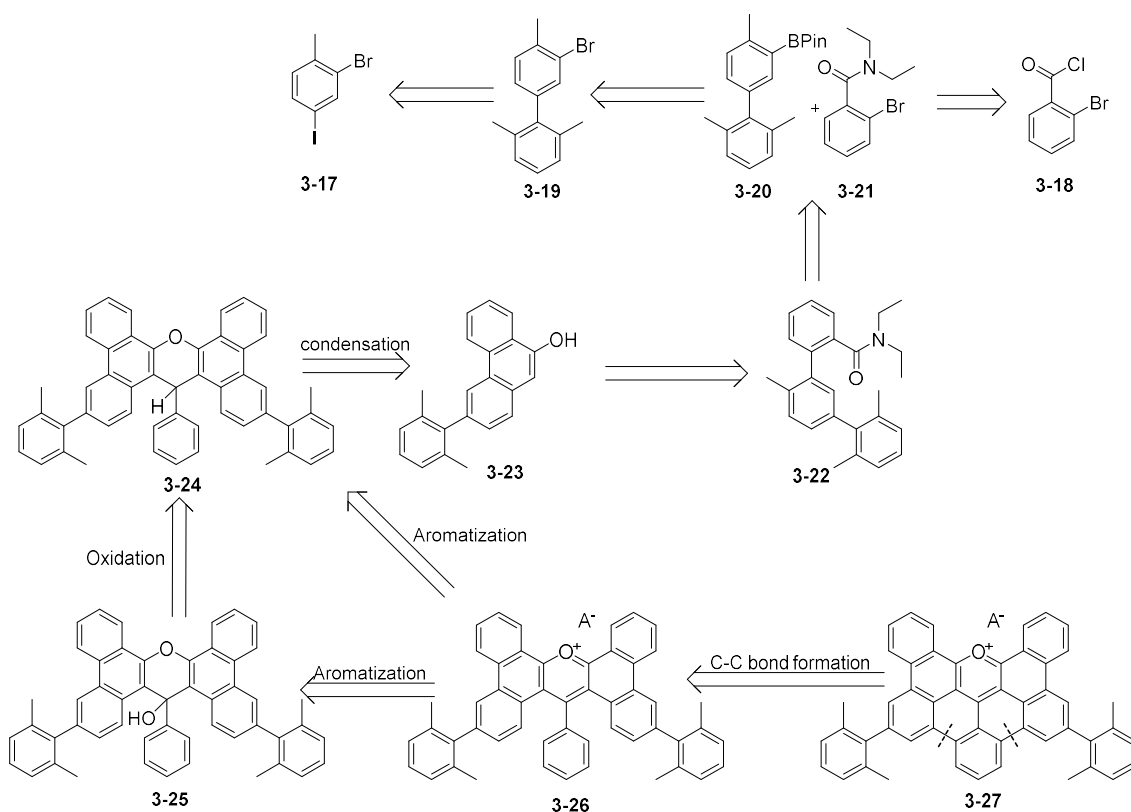


Figure 3.2: 400 MHz $^1\text{H-NMR}$ of **3-13** in CDCl_3 structure and assigned protons reported.

3.4 Synthesis of pyrilium gulf derivative

After **3-13** was obtained, a strategy towards pyrilium reference compound **3-27** was designed. The retrosynthetic approach reported in Scheme 3.4 is partially based on the work by Müllen and co-workers on similar derivatives.^[4] In accordance with the planned strategy, the final molecule **3-27** can be obtained *via* irradiation of **3-26**, with consequent formation of two CC bonds within the molecule. Aromatization of the central xanthenone ring to form **3-26** can be obtained in two ways: *i*) starting from **3-24** by treatment with Br₂ to form **3-26** as salt with Br⁻ as counterion or *ii*) by oxidation of **3-24** with PbO₂ to obtain **3-25**, which is then dehydrated with a mineral acid leading to **3-26** as a salt with a counterion dependant on the acid used (for the sake of simplicity we will identify the molecule with the relative counterion with the following nomenclature: N^{xx} N = molecule number, xx = Br for bromide and xx = BF for tetrafluoroborate).

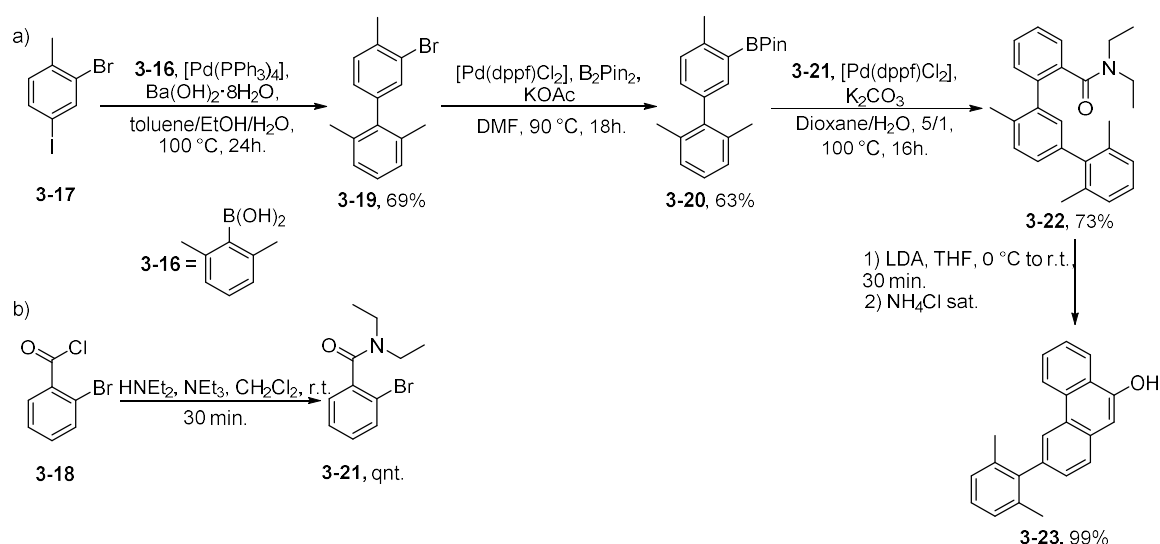


Scheme 3.4: Retrosynthetic approach towards derivative **3-27^{Br}** and **3-27^{BF}**.

At this point, derivative **3-24** can be formed *via* an acid catalysed aldolic condensation of phenanthrol derivative **3-23**. To obtain the latter, a metalation of the methyl group of **3-22** followed by intramolecular addition of the resulting lithium reagent on the amide can be performed. Finally, **3-22** can be obtained by cross coupling reaction between **3-20** and **3-21**, where the former could be obtained by two consecutive cross coupling reactions starting from **3-17** while the latter is obtained *via* an amidation of acyl chloride **3-18**.

The synthesis started with the preparation of **3-21**, which was obtained in quantitative yield by treating acyl chloride **3-18** with diethylamine and triethylamine in CH_2Cl_2 . At this point, **3-17** was cross coupled with boronic acid **3-16** (Scheme 3.5) in the presence of $[\text{Pd}(\text{PPh}_3)_4]$ and $\text{Ba}(\text{OH})_2 \cdot 8\text{H}_2\text{O}$ in a 5/2/1 mixture of toluene/EtOH/ H_2O at 100°C . Notably $\text{Ba}(\text{OH})_2$ had to be used due to the best results of this base when sterically hindered substrates are present.^[5]

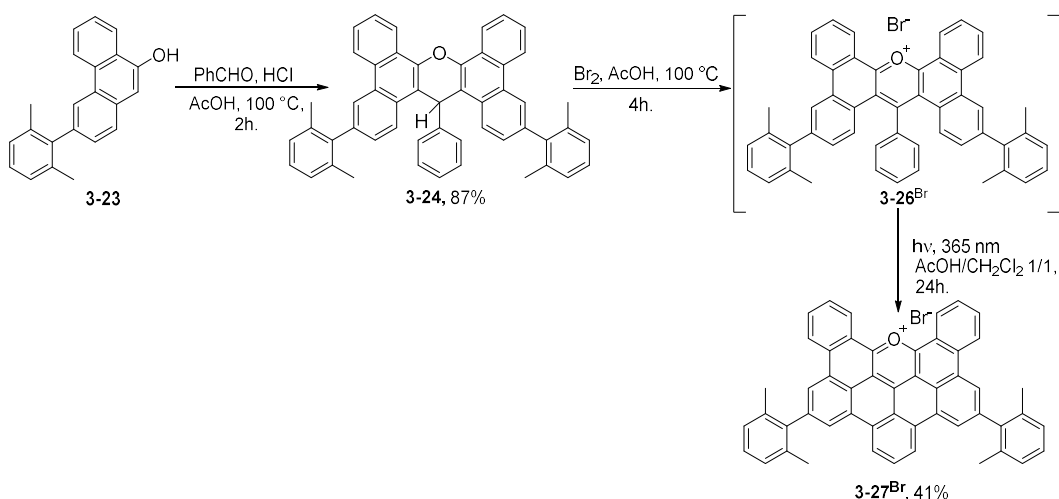
As a result, the desired **3-19** was formed in a 69% yield and subsequently converted in the boronic ester derivative **3-20** via a Miyaura coupling giving the desired product in a 63% yield. The coupling between **3-20** and **3-21** was performed using $[\text{Pd}(\text{dppf})\text{Cl}_2]$ as catalyst and K_2CO_3 in Dioxane/ H_2O 5/1 at 100°C as reported by Jorgensen et al.^[6] giving **3-22** in a good yield (73%, Scheme 3.5).



Scheme 3.5: Synthesis of derivative **3-23**.

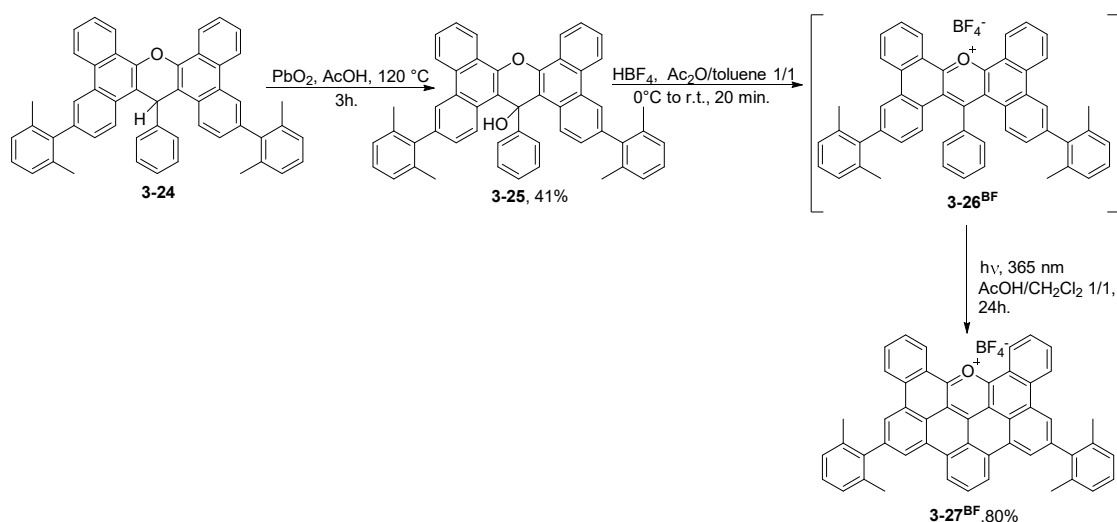
The protocol developed by Snieckus and co-workers was then followed in order to perform an amide directed metalation using LDA on the methyl bonded to the central ring of **3-22**. This resulted in the attack of the lithium derivative on the amide carbonyl and elimination of diethyl amine giving derivative **3-23**.^[7] The successful synthesis of derivative **3-23** was confirmed with ^1H , ^{13}C -NMR and HR-MS, proving the formation of the desired material. Molecule **3-23** exists as an equilibrium with the keto-form, which results in the presence of a strong carbonyl signal at 1674 cm^{-1} in the IR spectra.

At this point, derivative **3-23** was used in an aldolic condensation in the presence of benzaldehyde, HCl and AcOH giving xanthene **3-24** as the major product with an 87% yield (Scheme 3.6).



Scheme 3.6: Synthesis of derivatives **3-24** and **3-27^{Br}**.

Derivative **3-24** was then treated with Br₂ in AcOH at 100 °C to obtain derivative **3-26^{Br}**. However, when purification of the latter was attempted, formation of violet material occurred, suggesting that derivative **3-26^{Br}** is light-sensitive resulting in formation of **3-27^{Br}**. For this reason, the reaction mixture from the previous step was directly irradiated at 365 nm to form the desired product **3-27^{Br}** as a deep purple solid in a 41% yield. When the product was analysed, a low solubility resulting in aggregation and broad ¹H-NMR signals was observed. To obtain a more soluble product, an alternative synthesis was performed to form **3-27^{BF}** presenting tetrafluoro borate as counterion (Scheme 3.7). In this synthetic pathway, derivative **3-24** was treated with PbO₂ in AcOH at 120 °C leading to the formation of **3-25** with a 41% yield.^[4] The low yield derives from the fact that **3-25** is unstable when purified on silica, resulting in the formation of coloured materials probably due to dehydration resulting in the formation of charged species. Molecule **3-25** was then treated with an Et₂O solution of HBF₄ using a 1/1 Ac₂O/toluene mixture as solvent, leading to the formation of an orange precipitate.



Scheme 3.7: Synthesis of derivatives **3-25** and **3-27^{BF}**.

Due to the light sensitivity of this derivative, the reaction mixture was washed with anhydrous Et₂O, centrifuged and the resulting orange powder (**3-26^{BF}**) was immediately dissolved in an AcOH/CH₂Cl₂ 1/1 mixture and irradiated at 365 nm. The resulting bright red solution was evaporated to give **3-27^{BF}** as a purple solid in an 80% yield. In this case **3-27^{BF}** did not show much aggregation and it was possible to record a good quality ¹H-NMR in CD₂Cl₂ (Figure 3.3).

The lower tendency to aggregate resulted in the possibility of fully characterizing the derivative, however, despite all the attempts made, no crystals of **3-27^{BF}** were ever grown. From the ¹H-NMR spectrum reported it is possible to see all the signals expected for the system, in particular the presence of singlets *H_f* and *H_e* at 9.30 and 9.23 ppm indisputably proof the formation of the two CC bonds in the last step of the synthesis. Furthermore, the presence of tetrafluoro borate as counterion was proved by ¹¹B-NMR and ¹⁹F-NMR with signals at -1.21 ppm and -153.14 ppm respectively, in both cases consistent with literature reports for this anion.^[8]

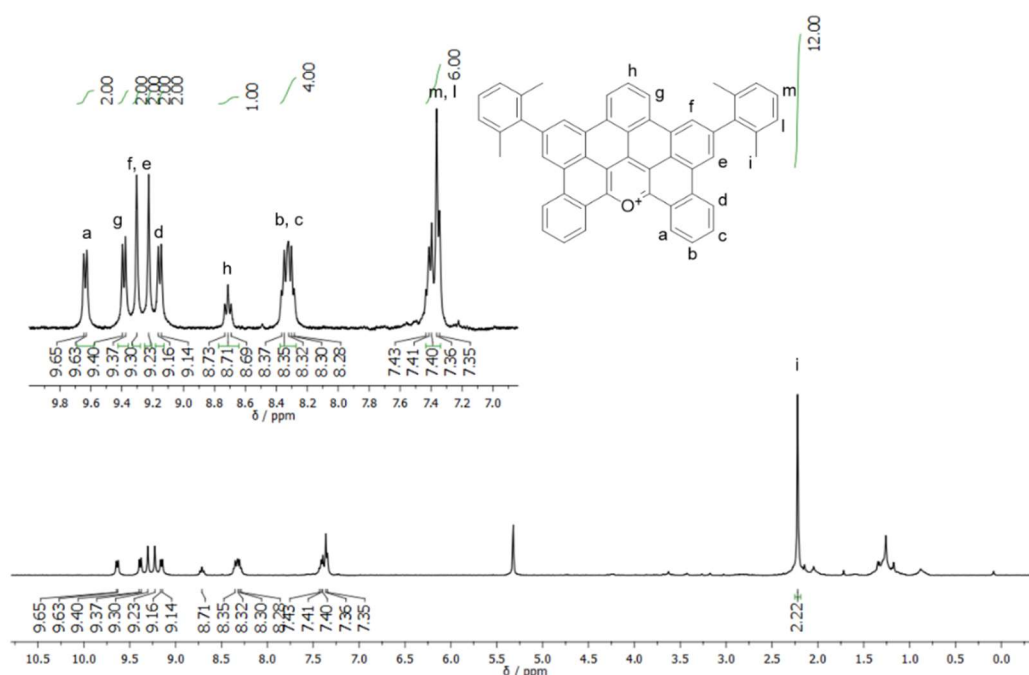


Figure 3.3: 400 MHz ¹H-NMR of derivative **3-27^{BF}** in CD₂Cl₂.

3.5 Crystal structure comparison

The crystal structures of obtained molecules were then compared, starting from hexabenzocoronene derivatives **2-1** and **3-2** (Figure 3.4).

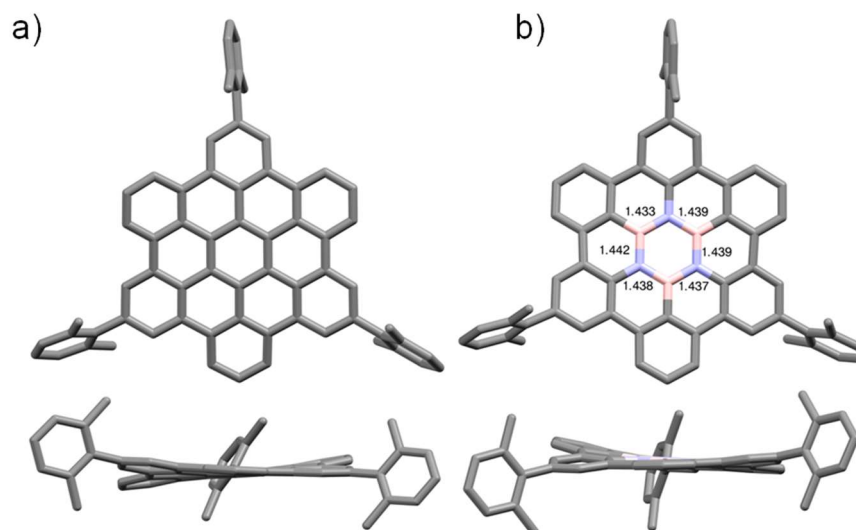


Figure 3.4: a) front (top) and side (bottom) view of the X-Ray crystal structure of **3-2** space group: *P*-1; b) front (top) and side (bottom) view of **2-1**, bond lengths reported, space group: *I*2/a. Colour code: grey: C, pink: B, blue: N. H atoms omitted for clarity. **2-1** was obtained from diffusion of *i*-PrOH in a C₆H₆ solution.

From the crystal structures of **3-2** and **2-1** it is evident that the molecular morphology is not altered by the substitution of the central benzene ring with a borazine. Both molecules present a certain degree of distortion, probably ascribable to the presence of the xylene moieties, since previous pXRD characterization on derivative **1-1** provided a completely flat structure.

When **3-13** and **2-38** were analysed, it could be further confirmed that BN-doped systems retain the morphology of the pristine PAHs (Figure 3.5). In fact, both structures are almost planar and present a small degree of distortion, with an average RMSD of the atoms in the aromatic scaffold from their mean plane of 0.13(9) Å for **2-38** and 0.15(12) Å for **3-13** (Figure 3.5 a, b). In both cases, a similar columnar packing is observed (Figure 3.5 c, d) with the molecules undergoing π - π stacking interactions and with antiparallel units arranged into columns with average distances of 3.52(20) Å and 3.43(16) Å for **3-13** and **2-38**, respectively. In the case of **2-38**, a distance between boron and oxygen between consecutive molecules smaller than the vdW sum of radii is observed (distance = 3.31 Å vdW = 3.35). This result seems to suggest that in **2-38** a certain degree of donation from the electronegative oxygen to the empty p orbital of boron might be present in the solid state. However, this feature seems to be more a

consequence of π - π stacking interactions than a factor influencing the assembly of the molecules in the solid state.

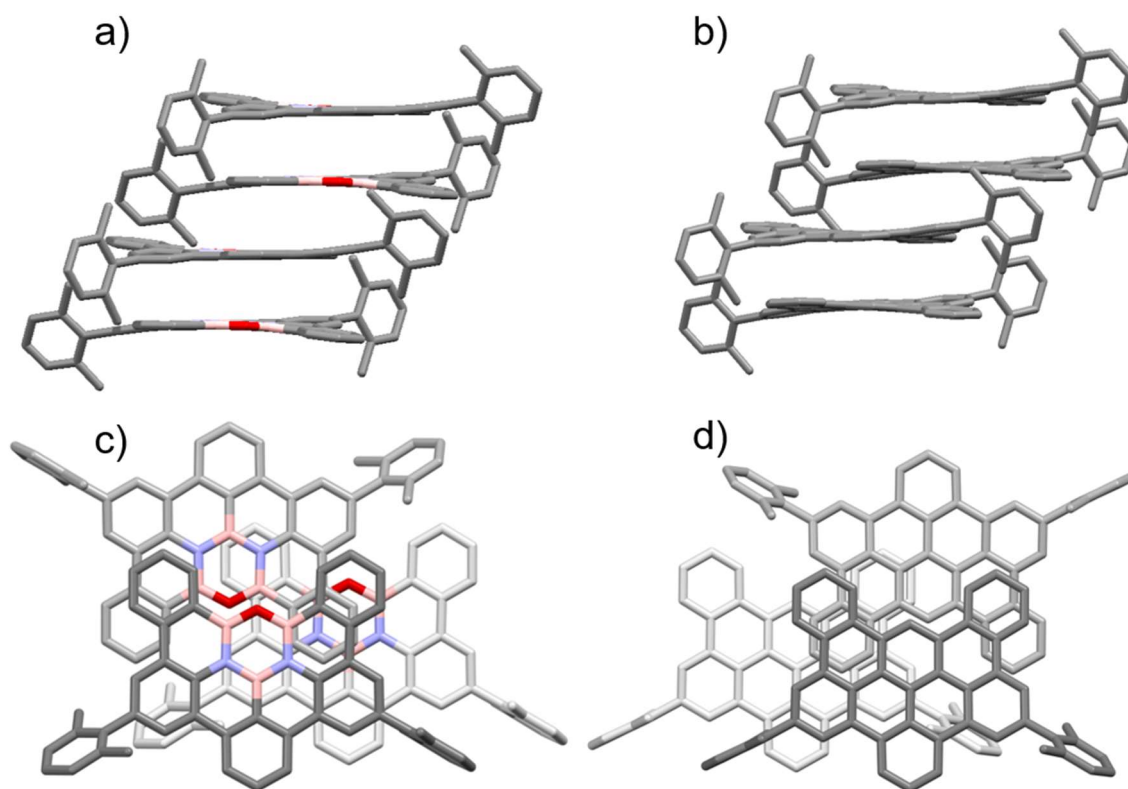


Figure 3.5: a) Side and c) top (bottom) view of the packing of **2-38**, b) Side and d) top view of the packing of **3-13**. Atom colors: pink B, blue N, red O, gray C. Space groups: $P 2_1/c$ and $P-1$. **2-38** was obtained from diffusion of *i*-PrOH in a CH_2Br_2 solution.

3.6 ESP Plots

Having confirmed the retention of the molecular morphology in derivative **2-1** and **2-38**, ESP plots (Figure 3.6) were calculated on the previously reported crystal structures to understand the electronic effects of the borazine doping in these derivatives.

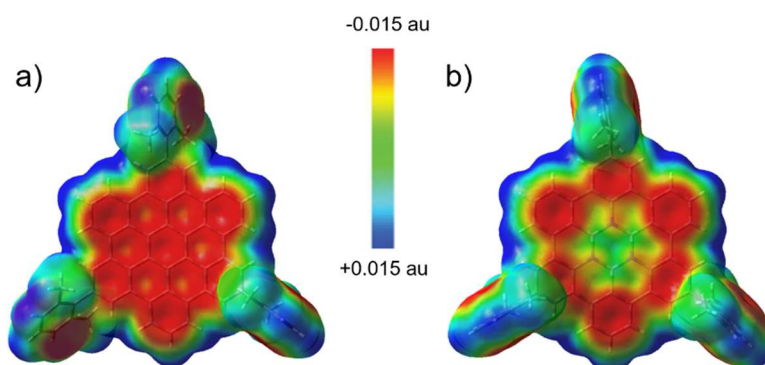


Figure 3.6: ESP mapped on the vdW surface up to an electron density of 0001 electron bohr⁻³. Calculation performed with Gaussian 09 at B3LYP/6-31G-(d,p) level of theory.

When **2-1** and **3-2** are considered, the ESP plots appear visibly different for the two structures, with **3-2** (Figure 3.6a) showing an extended negatively charged π system

occupying most of the structure surface (as expected for this kind of enlarged PAHs). When the charge distribution of **2-1** is considered (Figure 3.6b), charge polarization corresponding to the BN bonds is clearly visible in the central part of the molecule, with negatively charged nitrogen and positively charged boron atoms. These results point out that the substitution of a benzene ring with a borazine in nanographene molecules represents a valuable method to change the electronic properties of materials without affecting the morphology.

ESP surfaces were computed as well (mapped on the vdW surface up to an electron density of 0.05 electron/bohr⁻³) for molecules **3-13** and **2-38** to assess the electronic effects of doping with B₃N₂O (Figure 3.7)

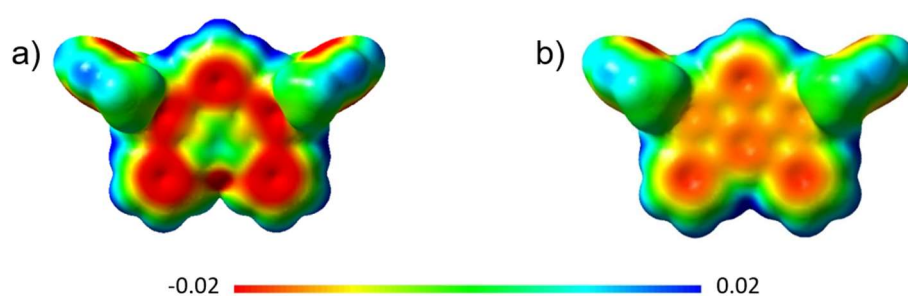


Figure 3.7: ESP surfaces mapped on the vdW surface up to an electron density of 0.05 electron/bohr⁻³ for molecules a) **2-38** and b) **3-13**.

Similarly to **2-1** and **3-2**, even in this case an important difference is induced by the presence of the borazine derived ring. While **3-13** presents an extended negatively charged surface due to the π electrons, **2-38** presents an evident polarization of the central part of the molecule with slightly negative nitrogen and positively charged boron atoms. Oxygen results more negative than the other heteroatoms due to the higher electronegativity. Similarly to **2-1**, the fully aromatic benzenoid rings in **2-38** are more negative than the corresponding ones in **3-13** and this effect can be ascribed to the enhanced localization of this sextets, resulting in higher electron density in these regions. This effect has been predicted in BN-doped systems where a fully benzenoid ring is substituted by a borazine based ring.^[9]

3.7 HBBNC solvates

The presence of the polarized BN bonds in **2-1** is expected to enable dipolar surface interactions in the BN-doped derivatives and thus potential interactions with polarized species, which are of great interest towards various applications, from sensing to catalysis. When **2-1** is considered, both boron and nitrogen atoms are confined in a sp^2 hybridization, which cannot convert to a sp^3 one as requested for any kind of covalent interaction, limiting potential interactions to non-covalent ones. If the borazine ring

resonance is considered, the boron formally presents only a partially empty p orbital and similarly, nitrogen atoms present a decreased nucleophilic nature due to the electron withdrawing effect of the attached boron atoms. Despite this, a strong polarization of the BN bonds is still present as highlighted in the ESP plots (Paragraph 3.6) and suggests that weak electrostatic interaction might occur with spatially close polarized groups.

To prove the recognition capabilities of this system, we decided to grow crystals of both **2-1** and **3-2** in solvents presenting highly polarized groups, ideally resulting in solvates showing interactions in the solid state. Firstly, **2-1** and **3-2** were crystallized in fluorobenzene (PhF). The choice of this solvent is due to the presence of the highly electronegative fluorine atom which results in a strongly polarized C-F bond and thus in a highly negative potential on the fluorine atom, which should be able to interact with the positive potential present on boron (Figure 3.8).

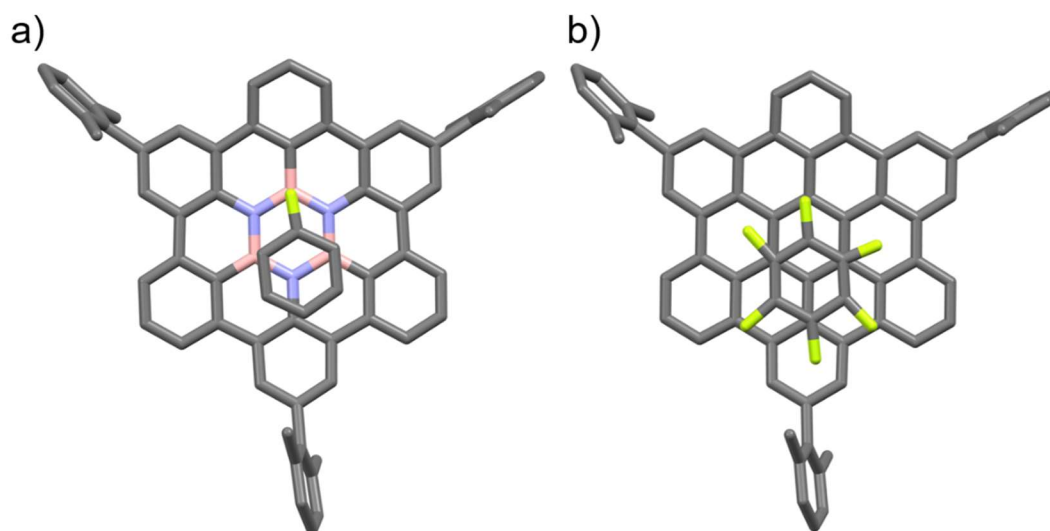


Figure 3.8: a) Crystal structure of **2-1**, space group: *P*-1; b) Crystal structure of **3-2**, space group: *P*-1. Both structures measured at 150(2) K. Crystals obtained *via* diffusion of *i*-PrOH in PhF.

From the crystal structures reported in Figure 3.8 it is quite clear that, in the case of **2-1**, the molecule of PhF presents one preferred orientation in the solvate, with the negative fluorine atom sitting atop of the positive boron. The presence of a recognition is further confirmed when the solvate of **3-2** is considered, in which no preferential position of the fluorine atom on the π structure (1/6 occupancy of the fluorine for each position) is evidenced. Moreover, distances calculated on the crystal structure give further confirmation of this effect, with values well below the vdW sum of radii for **2-1** (3.28 vs 3.39 Å) and above for **3-2** (3.34 vs. 3.17 Å). When the distance between the hexabenzocoronene plane and PhF is considered, it emerges that in **2-1** the fluorine atom is closer to the plane (3.28 Å) than the phenyl ring (3.34 Å). This suggests that

the interaction between fluorine and boron is not merely a consequence of π - π interactions. On the other hand, when the solvate of **3-2** is considered, an almost identical distance between the fluorine and the phenyl ring of PhF from **3-2** plane is found (3.36 vs 3.38 Å) suggesting a π stack driven association.

We then decided to repeat the same experiment using chlorobenzene (PhCl), which presents a less hard and negative nature compared to PhF. The resulting crystal structures for **2-1** and **3-2** in PhCl are reported in Figure 3.9 a, b.

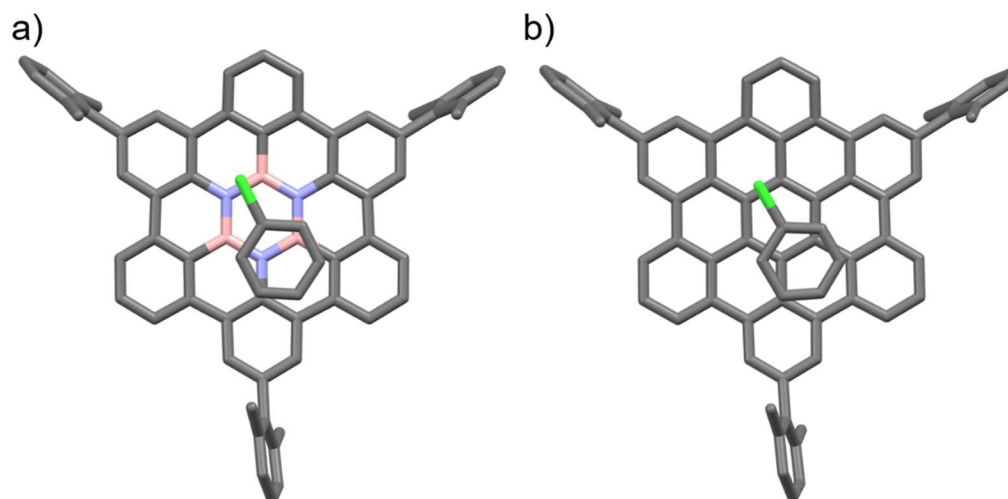


Figure 3.9: a) Crystal structure of **2-1** PhCl, space group: *P*-1; b) Crystal structure of **3-2** in PhCl, space group: *P*-1. Both structures measured at 150(2) K. Crystals obtained *via* diffusion of *i*-PrOH in PhCl.

In this case, the same identical disposition of the PhCl molecules is found in both structures, with the chlorine atom sitting in the middle of the BN bond in the case of **2-1** and of a CC bond of the central benzene in **3-2**. This suggests that there is no noticeable recognition between chlorine and boron. This is probably due to the less electronegative nature and worse overlap provided by the 3p orbitals of chlorine compared to the 2p of boron and fluorine. The proximity between the chlorine atom and the central ring of the two derivatives (3.43 and 3.46 Å) is probably ascribable to the presence of π - π interactions between the phenyl ring of PhCl and the π system of **2-1** and **3-2** resulting in the observed solvate structure. This is highlighted by a higher distance from **2-1** and **3-2** of the chlorine atom (3.43 and 3.46 Å) compared to the phenyl ring (3.37 and 3.40 Å), suggesting that indeed π - π interaction are driving the association between PhCl and the hexabenzocoronene cores.

From these results, recognition is limited to highly electronegative second row elements and, for this reason, we envisaged that oxygen should be able to undergo recognition. Solvates of **2-1** were then grown in anisole (Figure 3.10).

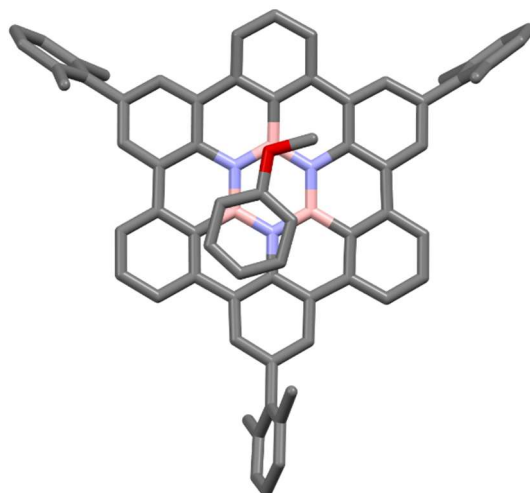


Figure 3.10: Crystal structure of **2-1** PhOMe, space group: *P*-1, measured at 150(2) K. Crystals obtained *via* diffusion of MeOH in PhOMe.

In this case, the recognition between the electronegative oxygen and the positive boron atom is again present, with a distance between boron and oxygen of 3.32 Å, well below the sum of vdW radii (3.44 Å). This result confirms the previous hypothesis of the ability of **2-1** to give recognition of highly electronegative second row elements, which paves the way for a potential use of these materials in sensing devices. At the present time, an assessment of the nature and energy of this interaction is still being carried out and will be the focus of future investigations.

3.8 Aromaticity of heteroatom doped nanographenes

When the aromaticity and NMR properties of derivative **2-1** are considered, many different theoretical studies have been carried out during the last decades. In general, the substitution of a full aromatic sextet in **3-2** with a borazine ring (thus generating **2-1**) is expected to result in an aromaticity decrease in the central part of the molecule and in more localized sextets.^[9] In other words, **2-1** and consequently **2-38** should present more localised ring currents and a generally less electron rich nature (as already introduced in ESP studies). To investigate experimentally the effect of the doping on the ring currents, we compared the aromatic regions of the ¹H-NMR of hexabenzocoronene derivatives (Figure 3.11). From the ¹H-NMR it is possible to assign the different protons to the corresponding signals, thus obtaining further confirmation of the structure of **2-1**. Coupled *Ha* and *Hb* appear as a triplet (8.02 ppm) and doublet (8.50 ppm) respectively, while *Hc* is instead a singlet at 8.56 ppm. This pattern of signals is very similar to the one observed for **3-2**, however, in the case of **2-1**, the signals appear at higher fields due to a decrease in the magnetic anisotropy of the system. Furthermore, the inversion in the position of the chemical shifts for the signals corresponding to *Hc* and *Hb* in molecule **2-1** compared to the corresponding ones in

the full carbon, can be linked to the presence of boron and nitrogen bonded to the rings, with the boron determining a lower chemical shift for proton *Hb* compared to *Hc*.

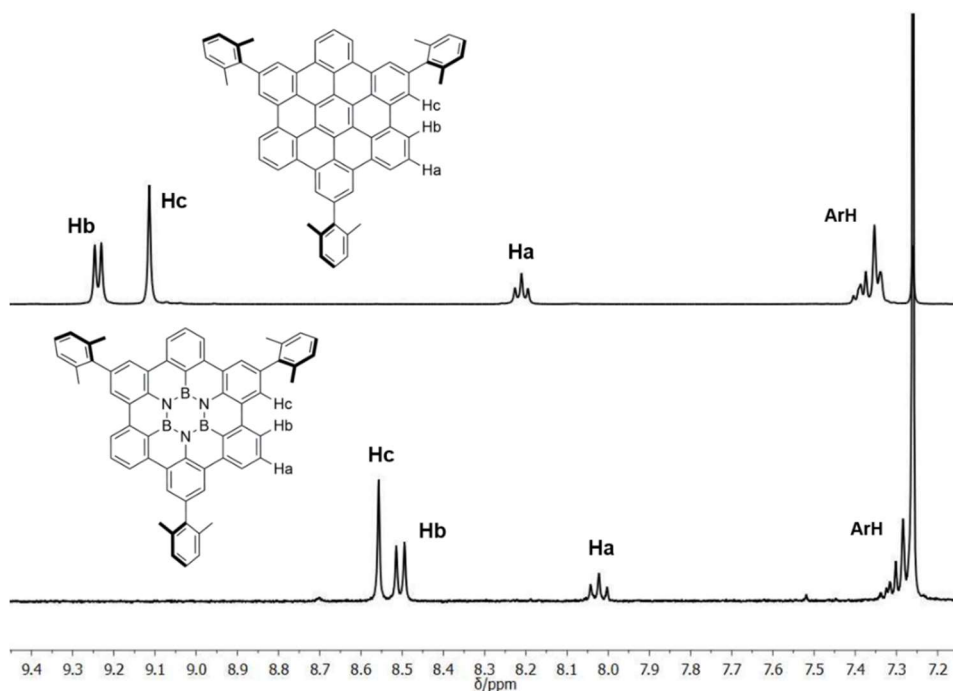


Figure 3.11: Exerts of the ^1H -NMR spectra of aromatic region recorded at 400 MHz in CHCl_3 for **3-2** (above) and **2-1** (below).

When the gulf derivatives were studied, a similar decrease in the ring currents could be expected (Figure 3.12). Since, no computational studies were ever performed on these derivatives, we decided to perform NICS(1) and ACID calculations on the gulf molecules in order to compare the experimental results with the theoretical ones.

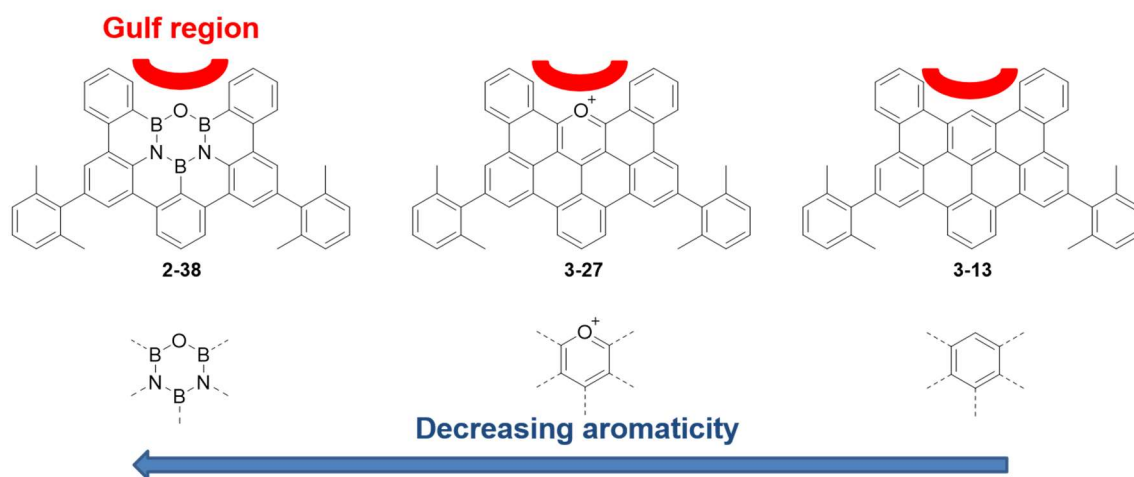


Figure 3.12: Derivatives **2-38**, **3-27** and **3-13** with gulf region and doping moieties highlighted.

We started by calculating the NICS(1) and ACID plots for derivatives **2-38**, **3-13** and **3-27^{BF}**, thus confronting the effect on aromaticity of the substitution of the central ring of

3-13 with the B_3N_2O system and with an oxygen-containing heteroaromatic ring (Figure 3.13).

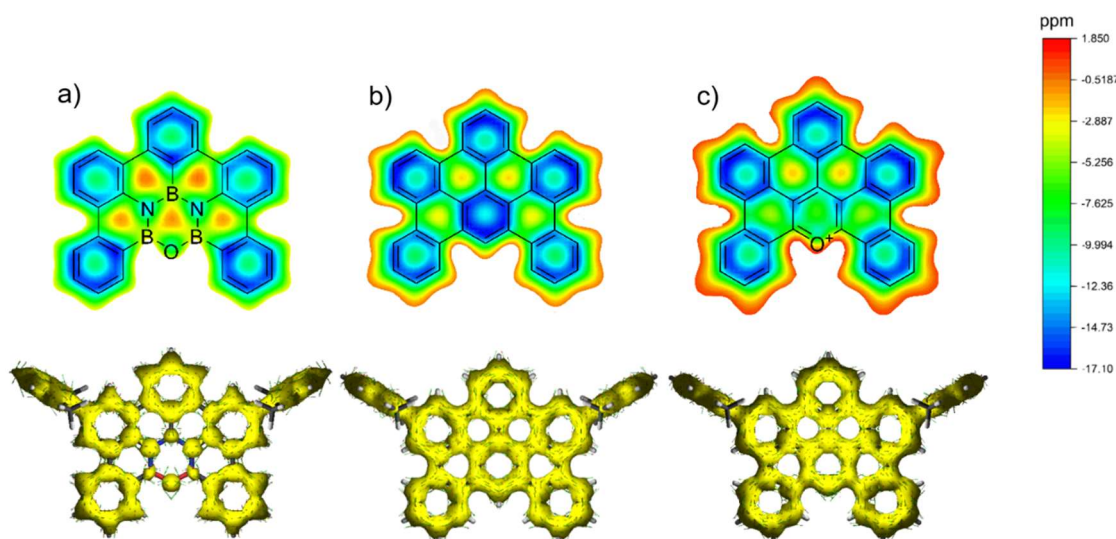


Figure 3.13: top: NICS(1)-GIAO surfaces for a) **2-38**, b) **3-13**, and c) **3-27^{BF}** calculated from the B3LYP/6-31+G** optimized geometry in vacuum; bottom: ACID Surfaces calculated for a) **2-38**, b) **3-13** and c) **3-27^{BF}**.

From the results of this calculation, a strong decrease in aromaticity is evident in the central part of **2-38** with values for the B_3N_2O ring falling in the non-aromatic region (-0.95 ppm, Figure 3.13a, top). This result is further confirmed by ACID calculations (Figure 3.13a, bottom), in which an absence of ring currents in the central ring of **2-38**, resulting in electronic localization on the single atoms, is visible. On the other hand, similar aromaticity values (-17 ppm) in the outer rim of aromatic rings are noticed when compared to **3-13**. This is in line with previous computational studies and this effect is ascribed to a higher localization of the sextets resulting from the substitution of the central ring.^[9] This is again confirmed by ACID studies displaying a higher localization of the ring currents on the single benzenoid rings in **2-38** when compared to **3-13**, in which delocalization is occurring on the whole structure (Figure 3.13b, bottom). Interestingly, the aromaticity of the non-sextet rings of the Clar resonance structure in **2-38** is further decreased by the substitution of the central ring when compared to **3-13** (0 ppm vs -3 ppm). When **3-27^{BF}** is considered (Figure 3.13c top and bottom), an intermediate situation is visible. As expected, the NICS(1) values of the central ring are comprised between the previous ones (-8 ppm) suggesting an intermediate degree of aromaticity. At the same time ACID measurements for this derivative evidence a similar situation to **3-13** with ring currents involving the full aromatic surface and delocalization occurring on the entire π surface. This result is reflected in the similar situation between the Clar-sextet and non-sextet rings of **3-27^{BF}** compared to **3-13**.

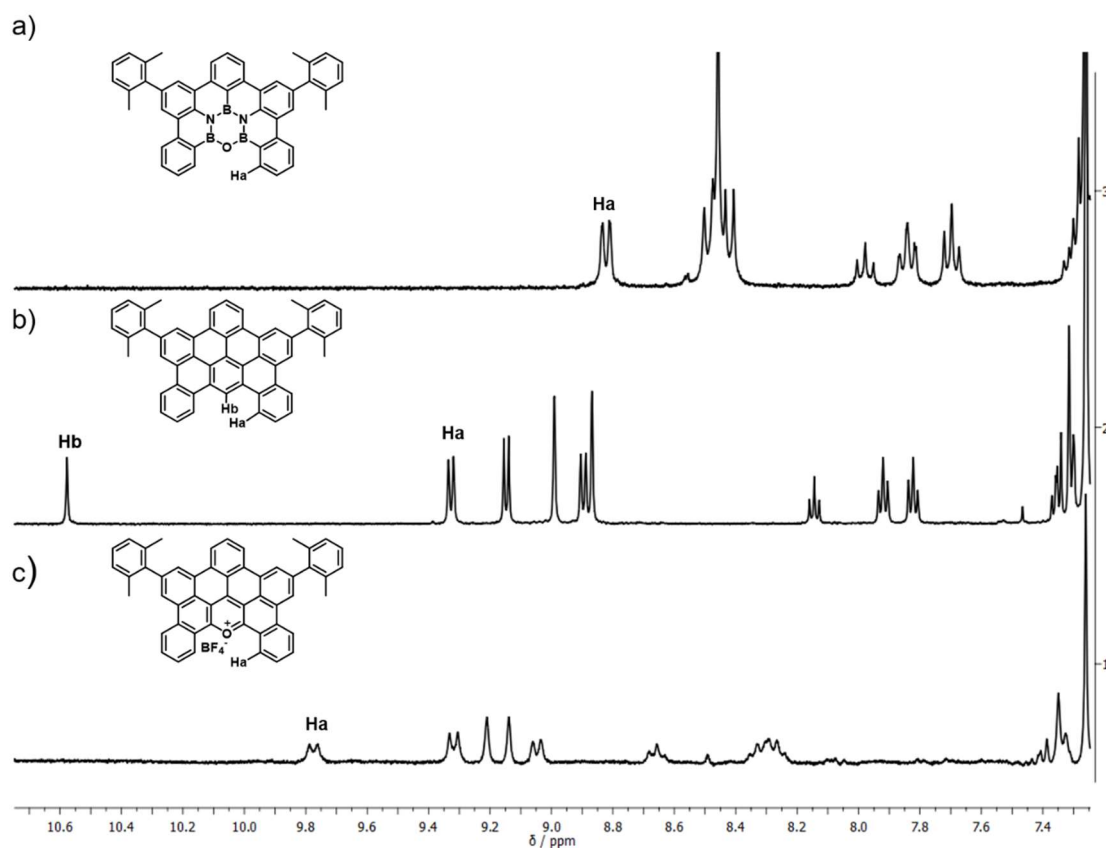


Figure 3.14: Excerpts of the ^1H -NMR spectra (400 MHz, CDCl_3) in the aromatic region for a) **2-38**, b) **3-13** and c) **3-27^{BF}**.

As previously performed for hexabenzocoronene derivatives, a comparison between the NMR spectra of the three derivatives was carried out (Figure 3.14 a, b, c). From this analysis a strong high field shift is observed for proton H_a in **2-38** (8.82 ppm) compared to the same proton in **3-13** (9.30 ppm). This result is related to the overall decrease in the magnetic anisotropy of the system arising from the loss of aromaticity in the central part of the molecule in accordance with results obtained from **2-1** and **3-2**. Surprisingly, **3-27^{BF}** does not present the halfway situation expected, instead, the H_a proton of this molecule is the most deshielded in the series (9.77 ppm). This result however should not be related to aromaticity, but instead could be the result of the presence of the charged oxygen in the system. Indeed, when resonance structures of **3-27^{BF}** are considered, it results that a partial positive charge is present on the α carbon, which is accountable for the low field shift of the H_a proton.

The results obtained from these studies highlight a quite similar situation for the substitution of the central benzene ring in both HBC **3-2** and gulf derivative **3-13**. In general, the substitution of the central aromatic ring with a $\text{B}_3\text{N}_n\text{O}_o$ based system results in a decrease in the aromaticity in the central part of the molecule. This results in more localised aromatic sextets and ring currents as highlighted by ACID calculations on the gulf derivatives. This effect is exposed nicely in the excerpts of the

$^1\text{H-NMR}$ spectra of the different derivatives in which a decrease of the magnetic anisotropy is always associated to the introduction of the borazine based systems.

3.9 UV-Vis Comparison

To assess the effect of borazine doping on the optical properties of PAHs, absorption and emission spectra were recorded for hexabenzocoronene and gulf derivatives (Figure 3.15, table 3.1). From these measurements **2-1** presents strongly blue-shifted absorption and emission when compared with **3-2**, particularly when absorption is considered. The lowest energy transition for **2-1** appears at 375 nm while in **3-2** it is found at 446 nm, resulting in a 71 nm blueshift. In addition, the absorption bands of **2-1** show noticeable vibrational substructures, evidencing a high degree of rigidity of the molecular skeleton. Fluorescence and 77 K phosphorescence follow a similar behaviour with λ_{em} at higher energies ($\lambda_{\text{fl}} = 404$ nm, $\lambda_{\text{ph}} = 492$ nm) for **2-1** and lower ones ($\lambda_{\text{fl}} = 485$ nm, $\lambda_{\text{ph}} = 570$ nm) for **3-2**. Both these results are in line with theoretical predictions for these systems, suggesting an efficient widening of the HOMO-LUMO gap induced by the borazine doping, which results in an increase of 0.53 eV in the optical bandgap moving from **3-2** to **2-1**. Interestingly, the quantum yield of fluorescence (Φ_{fl}) increases dramatically moving from **3-2** (3%) to **2-1** (43%).

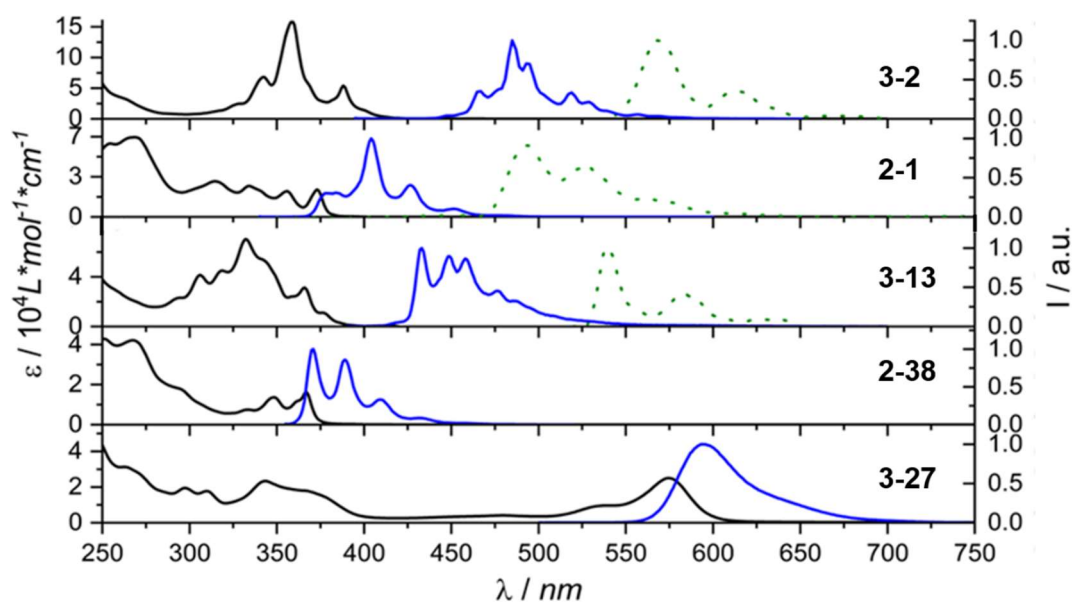


Figure 3.15: Absorption (—), fluorescence (—) in aerated CH_2Cl_2 solutions at r.t., phosphorescence (---) at 77 K in a 1:1 $\text{CH}_2\text{Cl}_2:\text{CHCl}_3$ glassy matrix of **3-2** ($\lambda_{\text{ex}} = 355$ nm), **2-1** ($\lambda_{\text{ex}} = 315$ nm), **3-13** ($\lambda_{\text{ex}} = 265$ nm), **2-38** ($\lambda_{\text{ex}} = 265$ nm), and **3-27^{BF}** ($\lambda_{\text{ex}} = 267$ nm).

This effect can be probably ascribed to the higher HOMO-LUMO gap, which can help preventing non-radiative decay of the excited state. Notably, when the measure is performed in degassed CH_2Cl_2 , the Φ_{fl} increases to 77%.

At this point, the steady-state UV-Vis absorption and emission properties of gulf derivatives **2-38**, **3-13** and **3-27^{BF}** were also studied in order to assess the effect of doping on the electronic properties of the gulf molecules. The results of these studies are reported in table 3.1 and figure 3.15. Derivative **3-13** presents a lowest energy transition at 430 nm ($\epsilon < 1000 \text{ cm}^{-1}\text{M}^{-1}$) whereas the maximum of absorption is localized at 332 nm ($\epsilon = 70400 \text{ cm}^{-1}\text{M}^{-1}$). When the central ring is substituted with the $\text{B}_3\text{N}_2\text{O}$ moiety a blueshift of 59 nm in the absorption occurs with the lowest energy transition appearing at 367 nm and the maximum of absorption at 292 nm ($\epsilon = 18500 \text{ cm}^{-1}\text{M}^{-1}$) with a much lower ϵ than its all-carbon congener.

These results are in line with what observed moving from **3-2** to **2-1**. As for **2-1**, even in the case of **2-38** the absorption is well structured suggesting a high degree of rigidity for the system. When the absorption of **3-27^{BF}** is taken in consideration, a broad unstructured band is observed at 575 nm ($\epsilon = 25027 \text{ cm}^{-1}\text{M}^{-1}$) strongly redshifted with respect to **3-13**, this result is most likely due to the presence of the charged oxygen in the system.

Focusing on emission spectra, **2-38** presents the most blueshifted fluorescence ($\lambda_{\text{max}} = 371 \text{ nm}$, $\tau_{\text{fl}} = 3.37 \text{ ns}$, $\Phi_{\text{fl}} = 0.90$) followed by **3-13** ($\lambda_{\text{max}} = 408 \text{ nm}$, $\tau_{\text{fl}} < 1 \text{ ns}$, $\Phi_{\text{fl}} = 0.11$) and finally **3-27^{BF}** ($\lambda_{\text{max}} = 595 \text{ nm}$, $\tau_{\text{fl}} = 8.1 \text{ ns}$, $\Phi_{\text{fl}} = 0.48$). Both **2-38** and **3-27^{BF}** present narrow Stokes shifts as already seen for derivative **2-1**, again confirming the rigid nature of these derivatives. Interestingly, Φ_{fl} increases nine-fold moving from **3-13** to **2-38**. This can be due to the increased band gap of this derivative and the higher rigidity imposed by the BN system as previously noticed for the case of **2-1** and **3-2**. No phosphorescence was detected for **2-38** in a frozen matrix at 77 K and this result can possibly be a consequence of the highly efficient radiative singlet deactivation which results in a low population of the triplet state that possibly undergoes non-radiative relaxation.

Table 3.1. Photophysical data in aerated CH₂Cl₂ and in glassy matrix for molecules **3-5**, **3-18**, **3-32^{BF}**, **2-2** and **2-1**.

Molecule	Absorption		Emission				
	λ [nm] (ϵ , L mol ⁻¹ cm ⁻¹) ^{a)}	$\lambda_{\max,fl}$ [nm] ^{a)}	E_{opt} [eV]	τ_{fl} [ns]	Φ_{fl}	$\lambda_{\max,ph}$ [nm] ^{e)}	τ_{ph} [s] ^{e)}
3-2	446 (1000) 388 (53800) 358 (159100)	485	2.76	16.4	0.03	570	0.8
2-1	375 (24000) 314 (31200)	404	3.29	8.2	0.43	492	4.0
2-38	367 (16250) 362 (11860) 348 (13600) 292 (18500)	371 389 409 430	3.36 ^{b)}	3.37	0.90	-	-
3-13	430 (800) 377 (10900) 366 (31300) 332 (70400) 319 (45000) 306 (41500)	408 433 449 458 476	3.11 ^{c)}	<1.0	0.11 ^{d)}	540 584 634	2.7
3-27^{BF}	575 (25027) 539 (9635) 480 (4117) 364 (18116) 343 (23378)	595	2.12 ^{b)}	8.1	0.48	-	-

^{a)} Recorded in an aerated CH₂Cl₂ solution at r.t. ^{b)} Calculated from the lowest energy intersection between absorption and emission spectra normalized on the lowest energy peak (E_{opt} [eV] = $1240.5/\lambda_{\text{cross}}[\text{nm}]$). ^{c)} Calculated from the average between the energies of the lowest emission and absorption peak. ^{d)} 9,10-Diphenylanthracene was used as reference standard (0.97 in aerated Cyclohexane). ^{e)} Recorded at 77 K in a 1:1 CH₂Cl₂:CHCl₃ glassy matrix.

Among the examined molecules, only **3-13** presented phosphorescence emission with a λ_{\max} at 540 nm and a τ_{fl} = 2.7 s. Altogether these data allowed us to estimate an increase of 0.25 eV in the optical HOMO-LUMO gap when the central ring of **3-13** is substituted with the boroxadiazine system. This result is again consistent with the data reported for **2-1** (ΔE_{opt} = 0.53 eV), however this time a smaller increase in the gap is observed.

A general comparison with derivatives **2-1** and **3-2** was performed as well to compare the effects induced by the presence of the gulf region on the absorption/emission properties of nanographenes. When the results obtained for derivatives **2-38** and **3-13** are compared to those for **2-1** and **3-2** it is possible to see that the presence of the gulf region results in a blueshift in both absorption and emission. This difference is however

of small proportion for **2-38** and **2-1** ($\Delta_{\text{abs}} = 0.07$ eV) whereas is more marked for **3-13** and **3-2** ($\Delta_{\text{abs}} = 0.10$ eV). This fact is probably related to the more localized nature of the sextets in the doped derivatives, resulting in a less important effect on the absorption and emission properties related to the removal of one aromatic ring. The Stokes shift for derivatives **2-1** and **2-38** are very narrow and this, along with the structured absorptions observed for both systems, suggests a high rigidity of the molecular scaffolds. Since these features are not observed in **3-2** and **3-13** this effect is most probably related to the presence of the BN bonds. When quantum yields are considered, it emerges that the removal of one ring from the system results in an increase of the Φ_{fl} from 43% to 90% between **2-1** and **2-38** and from 3% to 11% between **3-2** and **3-13**; this effect is related to the absence of phosphorescence emission for **2-38**, which was instead observed for **2-1**.

3.10 Electrochemistry

To establish the HOMO and LUMO energy levels for the different derivatives, cyclic voltammetry (CV) was performed. We started with the experiments on both **2-1** and **3-2** (Figure 3.16).

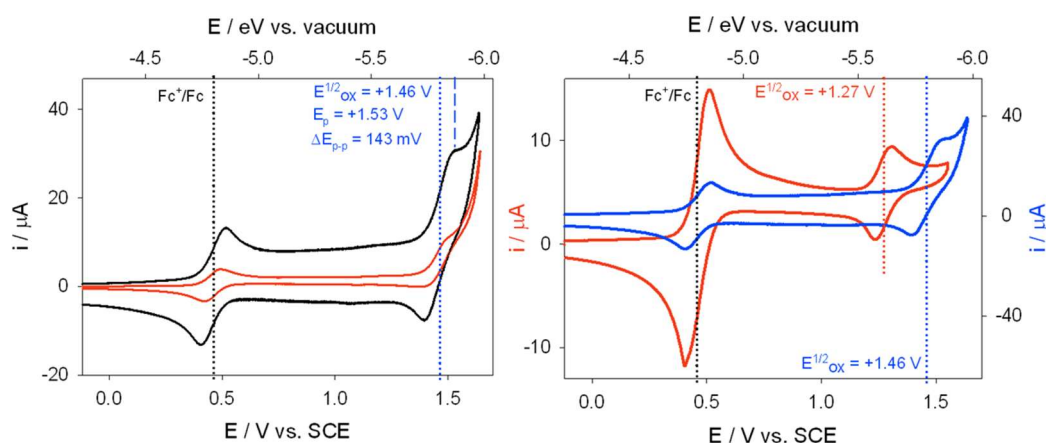


Figure 3.16: a) cyclic voltammograms of **2-1** in CH_2Cl_2 (ca. 0.70 mM). Scan rates: 0.5 V s^{-1} (black line), 0.05 V s^{-1} (red line). B) Comparison between cyclic voltammograms of **2-1** (blue line, scan rate 0.5 V s^{-1}) and **3-2** (red line, scan rate 0.05 V s^{-1}) in CH_2Cl_2 . TBAPF_6 (0.08 M) is used as a supporting electrolyte; ferrocene (Fc) is introduced as internal reference ($E_{\text{Fc}^+/\text{Fc}} = 0.46 \text{ V vs SCE}$; $-4.8 \text{ eV vs vacuum}$).

From the data obtained, it emerges that **2-1** presents a quasi-reversible first oxidation wave at 1.46 V vs SCE in CH_2Cl_2 , which is higher in energy than the one observed for **3-2** ($E_{1/2\text{ox}} = 1.27 \text{ V vs SCE}$). This can be translated in a more difficult oxidation of **2-1**, which is consistent with a less electron rich nature of this derivative. On the other hand, no reduction peaks were observed for the two molecules at any scan rate under the same conditions. HOMO and LUMO energies calculated from the data obtained for the two derivatives are respectively -5.80 eV and -2.51 eV for **2-1** and -5.61 eV and -2.85

eV for **3-2**. These data underline that the 0.53 eV extension of the HOMO-LUMO gap of **2-1** is emerging from both a decrease in the HOMO energy and an increase in the LUMO one (Figure 3.17).

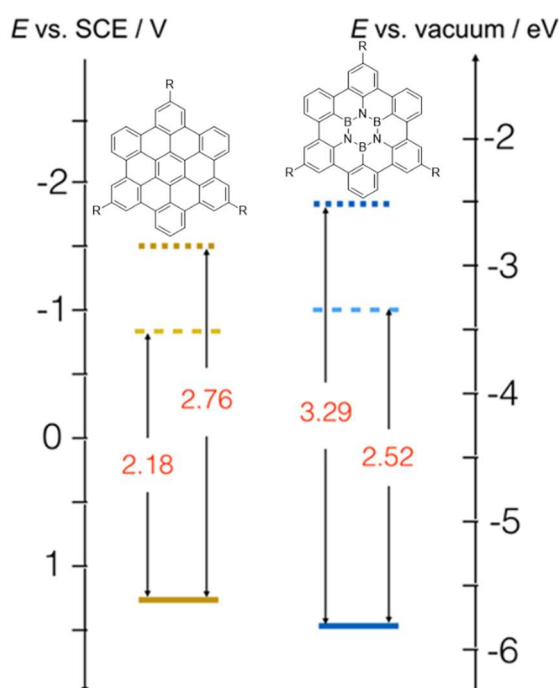


Figure 3.17: Frontier orbital energies estimated from the CV and photophysical data for **3-2** and **2-1**. Reduction potentials of the triplet excited states are evidenced by the narrower optical energy gaps ($ET^* = E^{1/2}_{ox} - E^{opt}_T$). $Fc^+/Fc = 0.46$ V vs SCE; -4.8 eV vs vacuum.

When the same electrochemical studies were performed on the gulf series of derivatives, only quasi reversible oxidation waves were detected for **2-38** and **3-13** and irreversible oxidative events for **3-27^{BF}** with no reduction waves visible for any of the derivatives at any scan rate. Moreover, all the oxidative events took place between 0.8 and 1.2 V vs Fc^+/Fc at a $0.2 \text{ V} \cdot \text{s}^{-1}$ scan rate. In this analysis, **2-38** presented the highest energy oxidation at 1.09 V followed by **3-13** with 1.01 V, again confirming the electron depleting effect of the BN based ring systems. When **3-27^{BF}** is considered, a value of 0.50 V is observed for the first oxidation wave, thus making this derivative the more oxidizable in the series (Figure 3.18), this oxidation however results in degradation of the species. The CV studies along with the values of the optical HOMO-LUMO gaps previously reported, allowed us to estimate the energies of the frontier orbitals for the gulf derivatives. As expected, the HOMO of **2-38** (-6.19 eV) is lower in energy compared to **3-13** (-6.11 eV) and the LUMO levels of **2-38** and **3-13** are quite different in energy (-2.83 eV and -3.00 eV), with the latter at lower potentials. Therefore, the variation in energy of the HOMO-LUMO gap is due to the variation in both the energy levels as previously observed for derivative **2-1**.

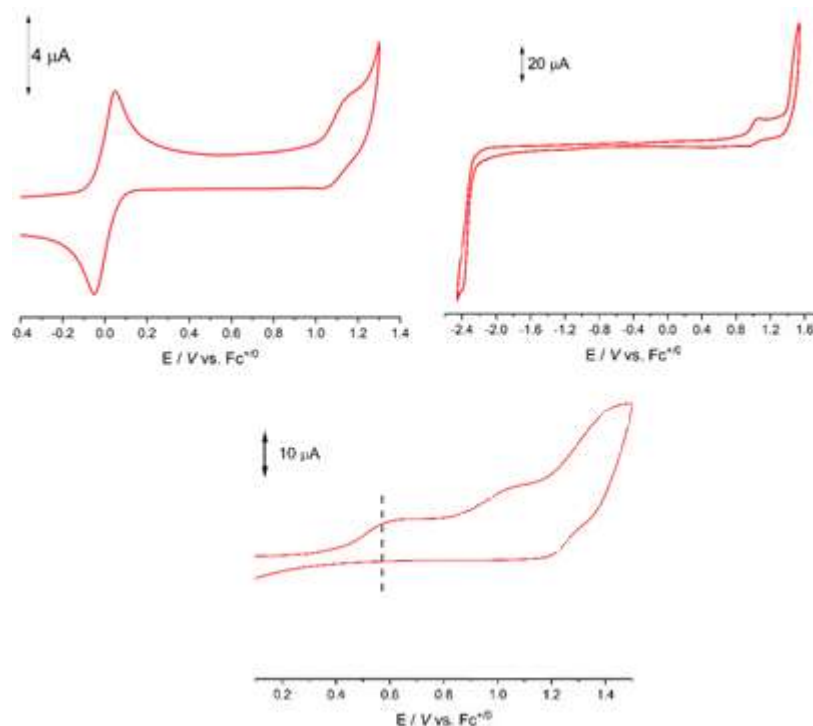


Figure 3.18: CV of **2-38** (top, left), **3-13** (top, right), **3-27^{BF}** (bottom) recorded in CH_2Cl_2 solutions at room temperature under N_2 . Scan rate 0.1 V s^{-1} . TBAPF_6 was used as supporting electrolyte. The couple $\text{Fc}^{+/0}$ has been used as internal standard.

When **3-27^{BF}** is considered, the HOMO level obtained from CV is placed at -5.6 eV while the LUMO is found at -3.48 eV . A much smaller optical gap between the orbitals is found (2.12 eV), and this can be attributed to the presence of charge separation states in this derivative, which is related to the great difference in the energy levels compared to the other derivatives in the series (Figure 3.19).

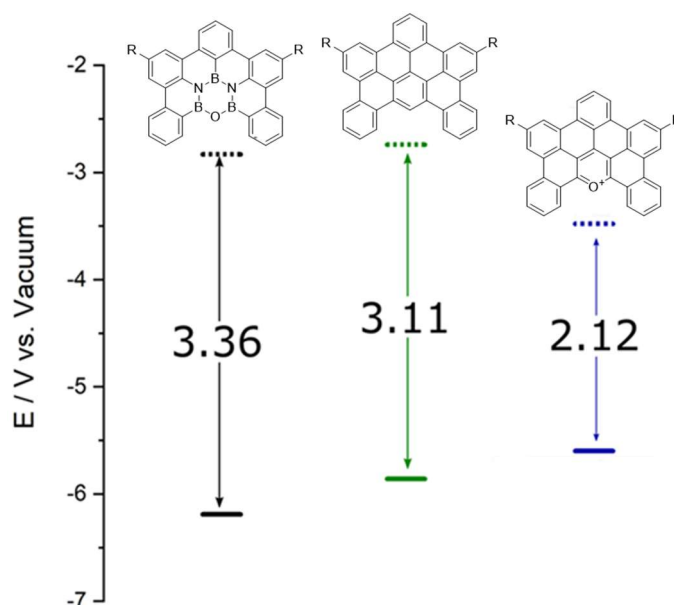


Figure 3.19: Frontier orbital energies estimated from the CV and photophysical data for **2-38**, **3-13** and **3-27^{BF}**.

3.11 HOMO-LUMO calculations

To shed light on the electrochemistry results and give a theoretical confirmation to the experimental data, the HOMO and LUMO orbitals for the derivatives were calculated in vacuum at B3LYP/6.31G (d,p) level of theory (GAUSSIAN09) (Figure 3.20) and at the B3LYP/6-31+G** level of theory (Figure 3.21). From the calculation, clearly the presence of the borazine ring in **2-1** induces a different arrangement of the HOMO and especially the LUMO orbitals. While in **3-2** both these orbitals are distributed on all the π surface, in the case of **2-1** the orbitals are more irregular and the LUMO is sitting exclusively on the hexaphenylene ring. This result provides further evidence on the important effects determined by the substitution of a phenyl ring with a borazine in PAHs. The calculated values of the HOMO and LUMO levels for derivatives **3-2** and **2-1** are reported as well in Figure 3.20 and show a good agreement with the results obtained experimentally. Furthermore, as in the experimental results, the extension of the computational HOMO-LUMO gap is arising from both a decrease in HOMO energy and increase in the LUMO one, resulting in a 0.48 eV widening of the gap, in very good agreement with the observed one (0.53 eV).

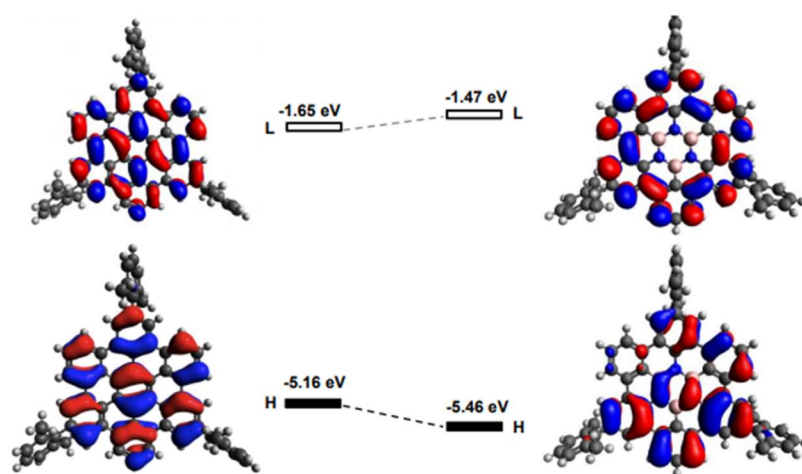


Figure 3.20: HOMO and LUMO profiles for **2-1** and **3-2** at B3LYP/6-31G(d,p) level of theory (GAUSSIAN09), calculated values for HOMO LUMO levels vs vacuum are reported as well.

At this point, the HOMO-LUMO profiles for the gulf derivatives were calculated as well (figure 3.21). From these data it is possible to see that, similarly to the previous case, the presence of the B_3N_2O system determines a change in the distribution of the HOMO and LUMO orbitals compared to **3-13**. In fact, the HOMO of **2-38** is distributed evenly on the structure except for the two rings of the gulf region, whereas the LUMO is distributed on the outer rim of the molecule and not on the central B_3N_2O ring very similarly to what observed for **2-1**.

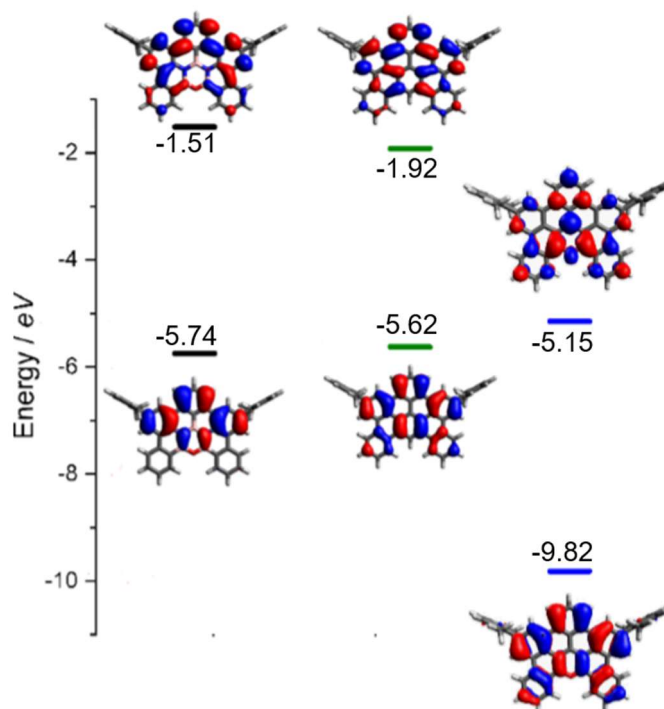


Figure 3.21: HOMO and LUMO energy levels calculated for molecules **2-38**, **3-13** and **3-27^{BF}** at the B3LYP/631+G** level of theory.

On the other hand, the orbitals in **3-13** appear uniformly distributed on all the π surface again in a similar fashion to what reported for **3-2**. Finally, derivative **3-27^{BF}** presents a less uniform distribution compared to **3-13** especially for the LUMO, which might be related to the presence of the charge in the system. The values of the computational HOMO-LUMO gap for **2-38** and **3-13** (4.31 eV and 3.71 eV) are generally in agreement with the experimentally obtained ones (3.36 eV, 3.11 eV) despite presenting some overestimation. When **3-27^{BF}** is considered, the biggest discrepancy from the experimental value is found (4.67 eV vs 2.12 eV) probably due to the presence of the charged system and a charge transfer state, which is not considered in the calculation.

3.12 Conclusions and perspectives

As a result of the work described in this chapter an extensive characterization of BN-doped derivatives **2-1** and **2-38** is now available. Moreover, the synthesis of reference compounds **3-2**, **3-13** and **3-27^{BF}** allowed for a comparison between the doped derivatives and full-carbon/heteroaromatic ones. From this study, the ability of borazine doping to widen the HOMO-LUMO gap of PAHs is highlighted along with an increased rigidity and quantum yield. The comparison between gulf derivatives (**2-38**, **3-13** and **3-27^{BF}**) and the hexabenzocoronene ones (**2-1** and **3-2**) allowed the identification of the effect of the different edge topology on the properties of the PAHs. In particular, the presence of the gulf region results in higher quantum yields for derivatives **2-38** and **3-**

13 compared to **2-1** and **3-2**. Computational studies highlighted a decrease in aromaticity in the central part of the molecule for the doped systems, indirectly confirmed by analysis of $^1\text{H-NMR}$ spectra, in which a strong decrease of the magnetic anisotropy is visible for derivatives **2-1** and **2-38**. This fact is correlated with the expected decrease in the ring current associated with a higher localization of full aromatic sextets in these derivatives. CV studies show a general decrease in the electron abundance of borazine-doped derivatives with first oxidation waves at higher voltages compared to full carbon analogues. This work provides exhaustive experimental evidence of the effect of borazine doping on PAHs, confirming the theoretically predicted ability of borazine based systems to increase the HOMO-LUMO gap of PAHs and consequently the bandgap of graphene systems.

3.13 References

- [1] L. Zhai, R. Shukla, R. Rathore, *Org. Lett.* **2009**, *11*, 3474–3477.
- [2] C. Kübel, K. Eckhardt, V. Enkelmann, G. Wegner, K. Müllen, *J. Mater. Chem.* **2000**, *10*, 879–886.
- [3] M. Daigle, A. Picard-lafond, E. Soligo, J. F. Morin, *Angew. Chem. Int. Ed* **2016**, *55*, 2042–2047.
- [4] D. Wu, W. Pisula, M. C. Haberecht, X. Feng, K. Müllen, *Org. Lett.* **2009**, *11*, 5686–5689.
- [5] A. Suzuki, *Pure appl. Chem.* **1994**, *66*, 213–222.
- [6] K. B. Jørgensen, T. Rantanen, T. Dörfler, V. Snieckus, *J. Org. Chem.* **2015**, *80*, 9410–9424.
- [7] X. Cai, S. Brown, P. Hodson, V. Snieckus, *Can. J. Chem.* **2004**, *205*, 195–205.
- [8] D. Moser, Y. Duan, F. Wang, Y. Ma, M. J. O'Neill, J. Cornella, *Angew. Chemie Int. Ed.* **2018**, *57*, 11035–11039.
- [9] N. Otero, K. E. El-Kelany, C. Pouchan, M. Rérat, P. Karamanis, *Phys. Chem. Chem. Phys.* **2016**, *18*, 25315–25328.

CHAPTER 4

SYNTHESIS OF MULTI-BORAZINE SYSTEMS: TOWARDS
EXTENDED BORAZINE-DOPED NANOGRAPHENES.

In this chapter the synthetic efforts towards multi-borazine derivatives are reported. These BN-doped polyphenylene dendrimers are of central importance as starting materials for the synthesis of extended borazine-doped nanographenes. To prepare fluoro-multiborazine derivatives able to undergo the planarization reaction presented in chapter 2, a study on model compounds presenting xylyl moieties bonded to the boron atom of the borazine ring was carried out. The study of these derivatives highlighted the central importance of steric hindrance on the stability of the multi-borazine systems and led to the development of a synthesis resulting in the formation of the first fluoro-functionalized multi-borazine. Despite the success and complete characterization of this derivative, the subsequent cyclization reaction could not be carried out due to low yields and partial instability of the molecule.

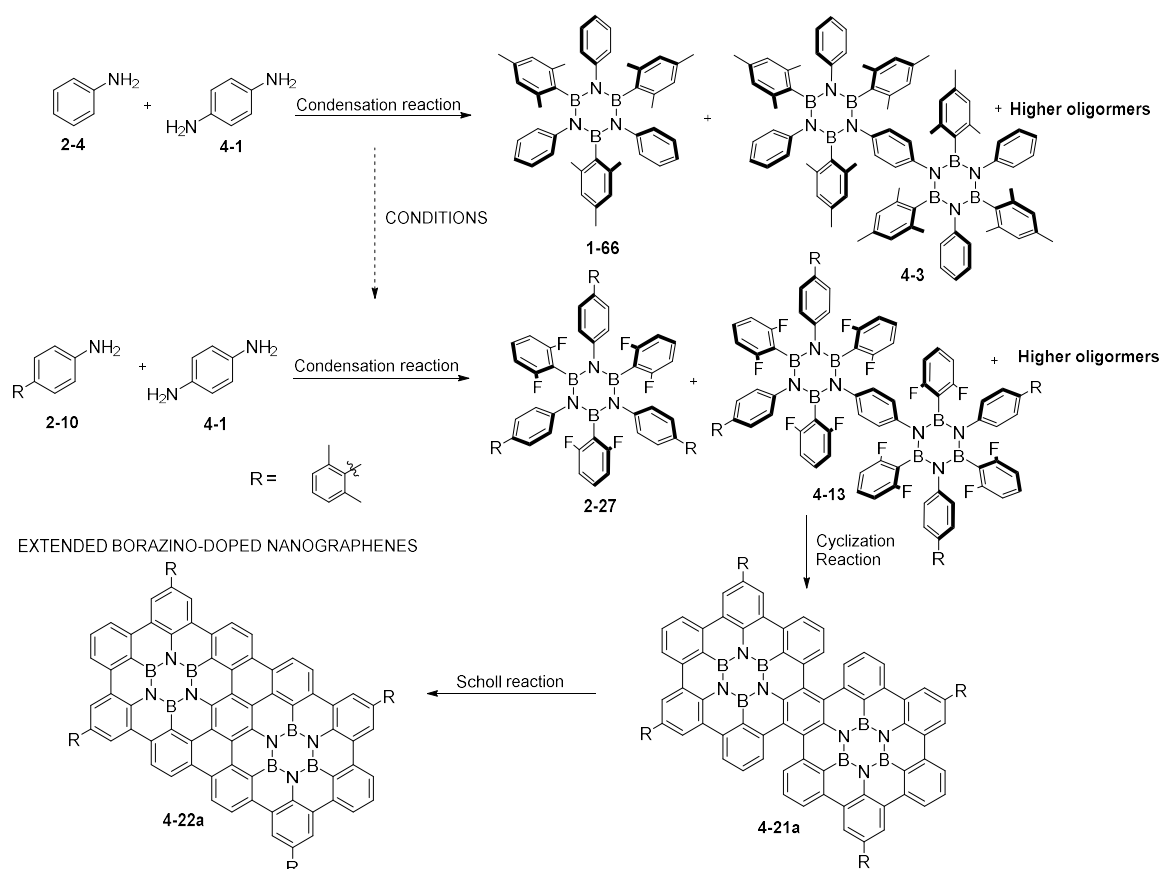
This chapter is divided in six main sections: *i*) section 4.1 presents the aim of the project; *ii*) Section 4.2 describes the synthesis of multi-borazine derivatives *via* condensation reactions along with their spectroscopic properties; *iii*) Section 4.3 presents a study on the UV-Vis properties of the multiborazine derivatives; *iv*) Section 4.4 presents the synthesis of fluoro-functionalized multi-borazine **4-19**. *v*) Section 4.5 draws some conclusions and perspectives from the obtained results; *vi*) Section 4.6 contains the references for the chapter.

The research work described in sections 4.2 and 4.3 was carried out jointly with D. Marinelli at Cardiff university. X-Ray analysis were performed by N. Demitri (Elettra-Sincrotrone, Basovizza, Trieste, Italy). Photophysical characterization was carried out by T. Battisti (Cardiff university).

The results reported in sections 4.2 and 4.3 have been published in the following article: **J. Dosso**, D. Marinelli, N. Demitri, D. Bonifazi, *ACS Omega* **2019**, *4*, 9343–9351.^[1]

4.1 Aim of the project

The aim of the work described in this chapter is the development of a suitable synthesis towards polyphenylenic borazine-doped systems, namely multi-borazines. These derivatives consist in multiple borazine cores bonded by a bridging moiety, represented by a diamine unit such as *p*-phenylenediamine (**4-1**). The synthetic strategy towards these molecules will rely on a condensation reaction involving aniline and **4-1**, followed by treatment of the resulting chloro-borazoles with suitable organolithium reagents (scheme 4.1). The presence of the bridging **4-1** will allow the formation of the dendrimeric systems leading to multidispersed mixtures of products. As a first step, the synthesis of model compounds presenting mesityl groups bonded on the boron atoms of the borazine ring needs to be carried out to optimize the reaction conditions and study the stability of such derivatives. The choice of the mesityl group is due to its ability to effectively shield the boron atoms from nucleophilic attack, thus leading to stable derivatives which can be studied and fully characterized.^[2,3] Once suitable conditions have been developed, the synthesis of fluoro-functionalized multi-borazines will be performed, leading to derivatives that can be used in planarization reactions to form borazine-doped nanoribbons (Scheme 4.1).

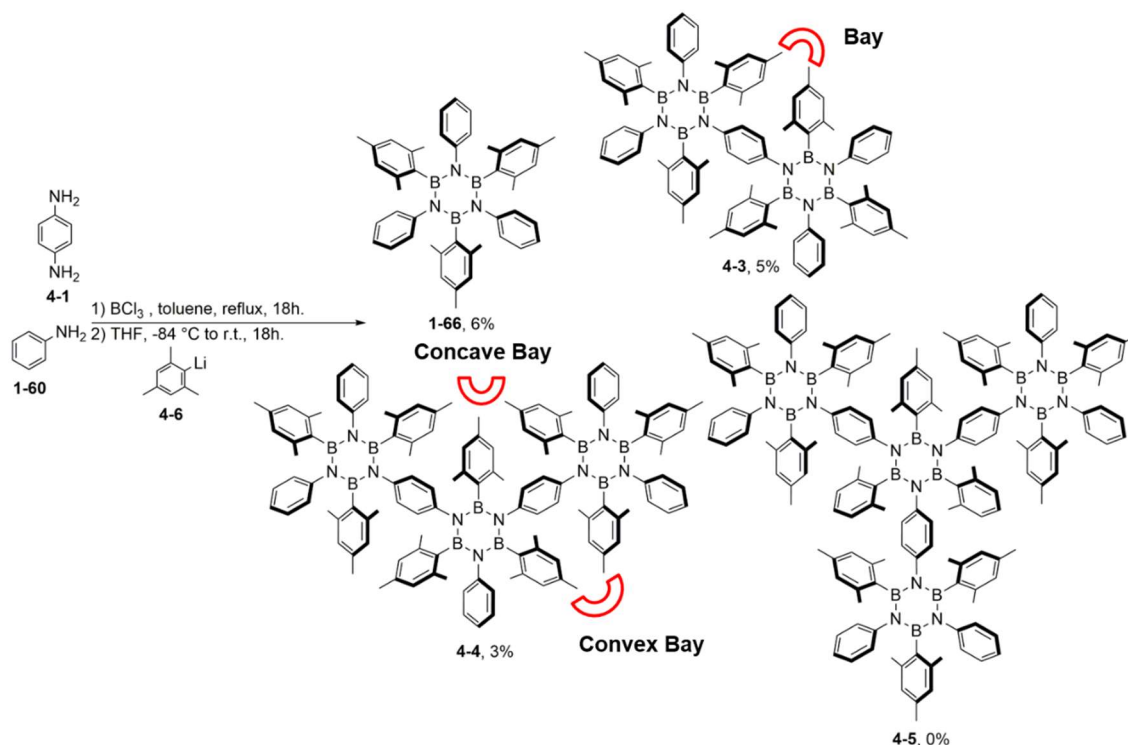


Scheme 4.1: Synthetic strategy towards fluoro-multiborazine derivatives and their use as precursors in borazine-doped nanographene synthesis.

Furthermore, model compounds themselves represent interesting derivatives which will be of central importance in understanding the effect of high doping percentages (16-18%) on polyphenylene systems. This will allow a comparison with previous results obtained in our group with similar derivative with a lower doping percentages (0-8%)^[4].

4.2 Synthesis of test Multi-borazine derivatives

To synthesize the desired mesityl multi-borazino derivatives a synthetic route involving a condensation polymerization was followed (Scheme 4.2).



Scheme 4.2: Synthetic route towards mesityl multi-borazino derivatives.

As a first attempt, a 4:1 mixture of **1-60** and **4-1** was reacted with BCl_3 in refluxing toluene. The resulting chloro-borazole mixture was then treated with mesityl lithium (**4-6**) leading to a statistical distribution of products. Notably, addition of BCl_3 was performed at $80\text{ }^\circ\text{C}$ to increase the solubility of **4-1** in toluene. Purification of the mixture with SCC led to the isolation of **1-66** and **4-3** in 10% and 2% yield, respectively. Aiming at the synthesis of more extended BN polyphenylene derivatives, the reaction was repeated using a higher amount of the bridging diamine and thus a 2:1 ratio between **1-60** and **4-1** was used. After quenching with **4-6**, a mixture of products was obtained. Again, **1-66** was isolated by SCC in 6% yield along with a quite complex mixed fraction. Purification of this last part was carried out using rec-GPC (Figure 4.1) leading to the isolation of **4-3** (5% yield) and **4-4** (3% yield).

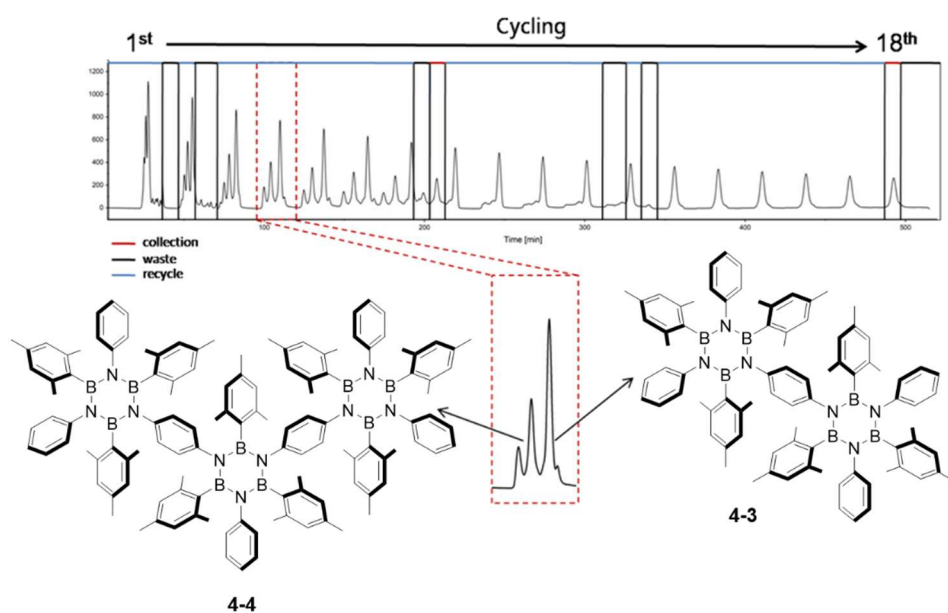


Figure 4.1: Rec-GPC trace of the crude mixture after silica gel column chromatography, showing the waste (black), recycle (blue) and collection (red) sequence. Inset: zoom of the chromatogram of 4th cycle.

Despite the high ratio of **4-1** used, it was not possible to isolate oligomeric products suggesting that this could be due to stability issues of derivatives. This hypothesis was confirmed when degradation of both **4-3** and particularly **4-4** was noticed in presence of moisture, resulting in the impossibility to isolate **4-4** in pure form. Despite the partial instability, **4-3** was isolated and completely characterized suggesting that the observed instability could be directly correlated with the increase in molecular weight. Crystals of **4-3** suitable for SC-XRD were obtained by slow evaporation of a solution of CHCl_3 . Examination of the resulting crystal structure (Figure 4.2) gives a valuable explanation of the reactivity of this system, which arises from the high steric hindrance in the bay regions of the molecule (Scheme 4.2). This effect is due to the presence of the *para*-methyl groups of the mesityl rings belonging to different borazine units. The steric clash between the mesityl groups in the bay area of **4-3** develops in a deviation from the arrangement between the aryl substituents and the borazine ring observed in **1-66**, resulting in an interplanar angle between 55.5 to 77.3 degrees in **4-3**. Furthermore, the central BN core in **4-3** displays a significant structural deformation, with a RMSD of 0.14 Å of the core BN atoms from the average plane. The result of these steric effects in **4-3** is a distorted arrangement of the borazine cores that are forced in shifted parallel planes with no rotation (interplanar distance of 0.14 Å, Figure 4.2b). This ultimately results in a decreased steric shielding of the boron atoms by the methyl groups, leading to an enhanced susceptibility of the BN cores towards hydrolysis, which is otherwise unexpected in borazine derivatives presenting mesityl groups bonded on boron atoms.

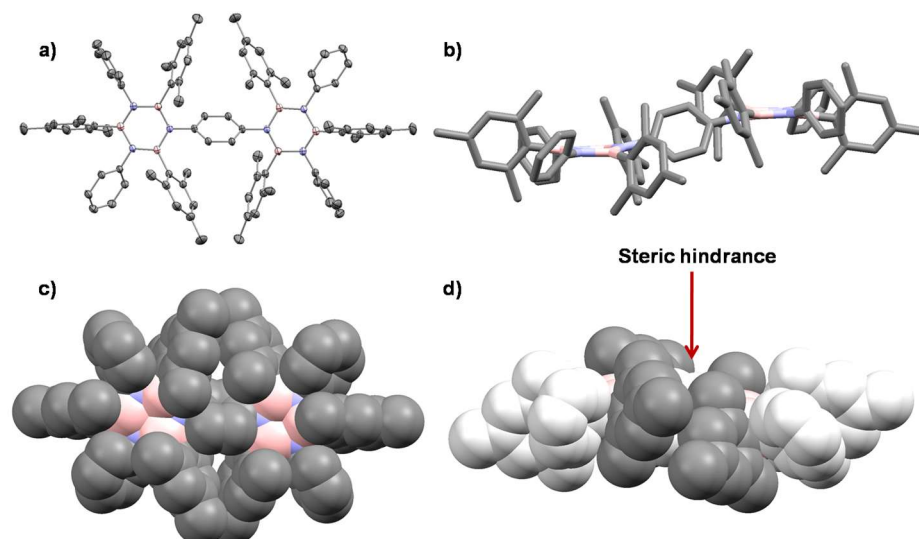
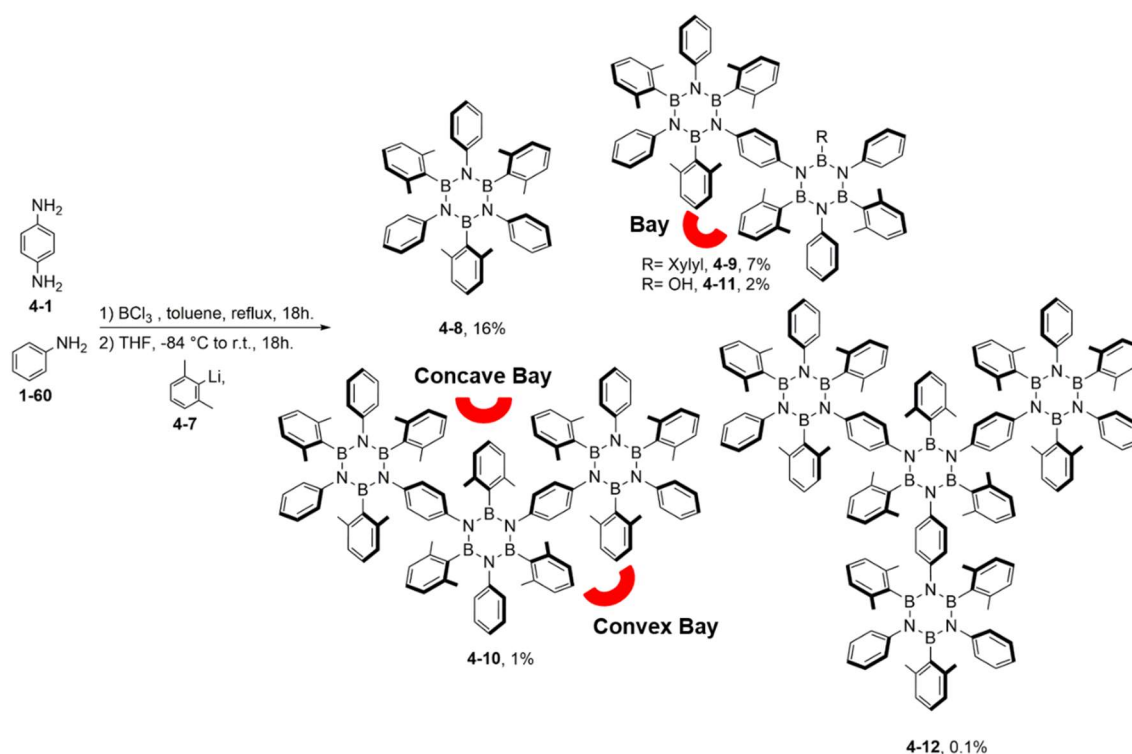


Figure 4.2: Crystal structure of **4-3** a) front view ellipsoids representation of ASU contents (50% probability). b) side view (stick representation) it is visible how steric hindrance between neighbour BN cores is minimized with shifting. c) front view (spacefill representation) d) side view (spacefill representation) steric hindrance between neighbour mesityl groups highlighted.

To reduce the structural strain and therefore obtaining more stable derivatives, the synthesis of derivatives with decreased steric hindrance in the bay regions should be envisaged. Since the *para*-methyl of the mesityl groups is the major source of steric hindrance, the most efficient approach should be the replacement of mesityl lithium **4-6** with xylyl lithium **4-7** (Scheme 4.3). The resulting xylyl multi-borazine derivatives should present a much lower steric hindrance in the bay regions of the molecules, leading to increased stability towards nucleophilic attack and possibly to the isolation of high molecular weight oligomers (Scheme 4.3). The reaction of Scheme 4.2 was then repeated refluxing a 2:1 ratio between **1-60** and **4-1** with BCl_3 and the resulting mixture of chloro-borazoles was treated with **4-7** in THF, leading to the formation of a quite complex statistical mixture. Multiple chromatographic purifications involving both SCC and preparative TLCs allowed us to isolate **4-8** (16% yield), **4-9** (7% yield), **4-10** (1% yield), **4-11** (2% yield) and **4-12** (0.1% yield) along with an inseparable mixture of oligomeric products. The structural identity of the monodispersed fractions was firstly demonstrated by HR-MS spectrometry, which confirmed the molecular mass for all oligomers (**4-8**, $[\text{C}_{42}\text{H}_{43}\text{B}_3\text{N}_3]^+$, calc.: 622.3736, found: 622.3766; **4-9**, $[\text{C}_{78}\text{H}_{78}\text{B}_6\text{N}_6]^+$, calc.: 1164.6846, found: 1164.6812; **4-10**, $[\text{C}_{114}\text{H}_{114}\text{B}_9\text{N}_9]^+$, calc.: 1708.0035, found: 1707.9987; **4-11**, $[\text{C}_{70}\text{H}_{70}\text{B}_6\text{N}_6\text{O}]^+$, calc.: 1076.6169, found: 1076.6207; and **4-12**, $[\text{C}_{150}\text{H}_{150}\text{B}_{12}\text{N}_{12}]^+$, calc.: 2251.3223, found: 2251.3375).



Scheme 4.3: Synthetic route towards xylyl multi-borazino derivatives.

The single components of the final multi-dispersed fraction were not separable *via* SCC and thus the mixture was analysed using size exclusion chromatography calibrated on a series of poly(methylmethacrylate) standards. The result of this analysis proved that this fraction was composed by oligomers up to 10^4 Da (corresponding to 16-18 borazine units), with an average molecular weight of 1900 Da and a dispersity of 1.97 (Figure 4.3).

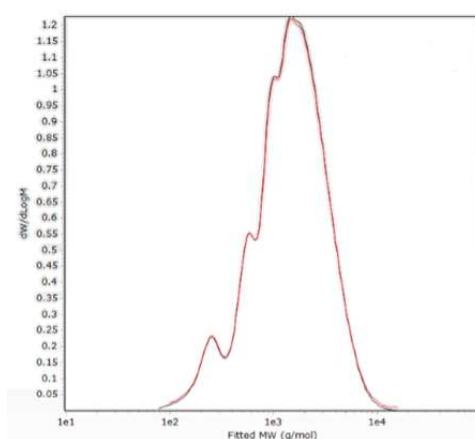


Figure 4.3: Molecular weight distribution of oligomeric fraction.

To understand better the nature of the mixture, ^{11}B -NMR and FT-ATR analyses were carried out. The ^{11}B -NMR spectrum shows a peak at 37.5 ppm, indicative of the

borazine core, along with a smaller peak at 25.2 ppm indicating presence of boron linked to oxygen (Figure 4.4).

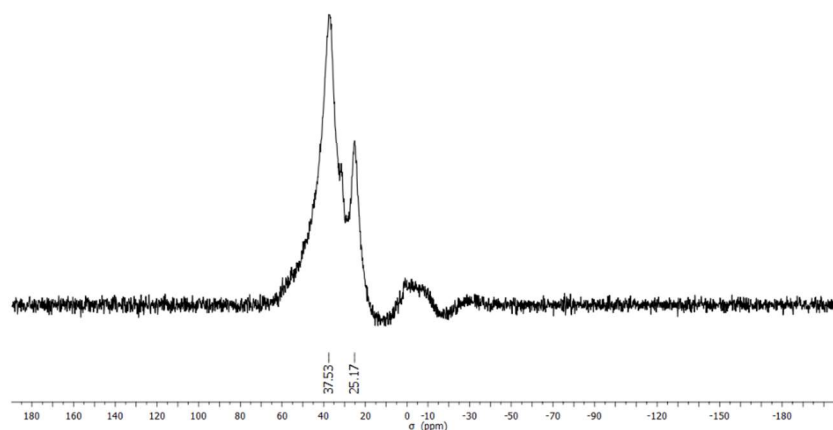


Figure 4.4: 160 MHz ^{11}B -NMR of oligomeric fraction in CDCl_3 (probe residual signal visible from 10 to -10 ppm).

The presence of B-OH groups in the mixture finds further confirmation in the FT-ATR spectrum of these oligomers, which closely resembles that of **4-11**, with an OH-stretching absorption band centred at 3612 cm^{-1} which suggests that at least a part of the higher oligomers is composed of hydroxylated species (Figure 4.5).

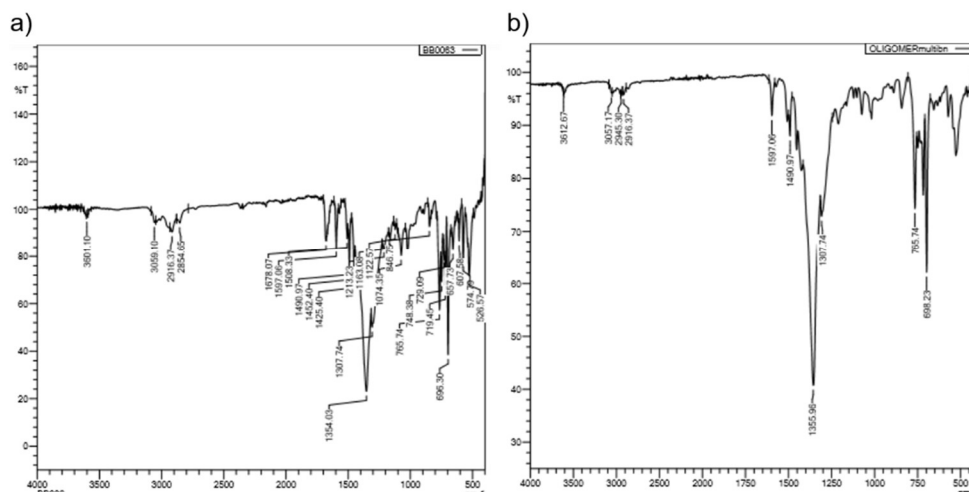


Figure 4.5: a) FT-ATR spectra of **4-11**. b) FT-ATR spectra of oligomeric fraction.

This result points out that, despite the decrease in the steric hindrance, the high molecular weight derivatives are to some extent instable and thus partially hydrolysable. Another possible explanation could be that the increased steric hindrance hinders the nucleophilic attack of **4-7** on some boron atoms, leading to unreacted B-Cl groups that are hydrolysed during workup. Both these explanations are plausible and

further investigation is required to assess the exact mechanism resulting in the instability of the higher oligomers. Moving on the monodispersed fractions, derivatives from **4-8** to **4-10** were fully characterized with ^1H , ^{13}C -NMR and UV-Vis spectroscopy. Furthermore, suitable crystals for SC-XRD were obtained for **4-8** (slow evaporation of CHCl_3 solution, Figure 4.6), **4-9**, **4-10**, (diffusion of pentane in a CHCl_3 solution, Figure 4.7 and 4.10) and **4-11**, (slow evaporation of a 1:1 CH_2Cl_2 :petroleum ether mixture, Figure 4.8 and 4.9).

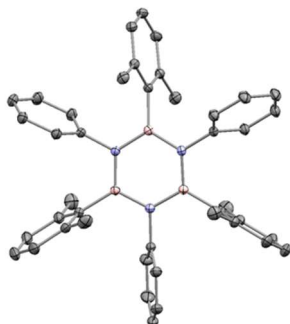


Figure 4.6: **4-8** front view ellipsoids representation of ASU contents (50% probability), crystals obtained by slow evaporation of CHCl_3 solution.

From the obtained structures it is possible to see that in the case of **4-8** the crystal structure is very similar to previously reported examples of **1-66**, which is expected due to the very similar chemical structure.^[5]

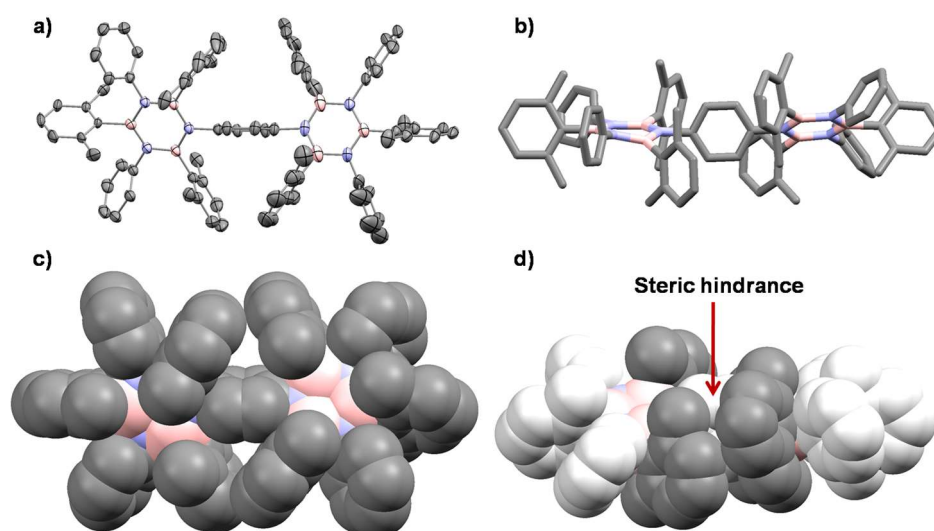


Figure 4.7: Crystal structure of **4-9** a) front view ellipsoids representation of ASU contents (50% probability). b) side view (stick representation) it is visible how steric hindrance between neighbour BN cores is drastically reduced with xylol groups. c) front view (spacefill representation) d) side view (spacefill representation) some steric hindrance between neighbour xylol groups is still present.

In the case of **4-9** important differences emerge when compared with **4-3** (Figure 4.7). Firstly, a relevant suppression of the strain in bay regions of the system (Figure 4.7b) with a more homogeneous protection of the reactive boron centres (Figure 4.7c) is visible in **4-9**. No shifting on different planes of the borazine cores is visible, although a tilting of 32° between the two cores is present, suggesting that a certain level of steric hindrance is still present in the bay regions of the molecule. Despite this, **4-9** appears to be indefinitely stable upon storage in the presence of atmospheric moisture just as **4-8**, thus confirming that most of the strain present in **4-3** has been successfully removed.

When crystals of **4-11** are considered, two different polymorphs are observed, one with rod shaped crystals α ($P 21/c$ unit cell: $a = 18.861(4) \text{ \AA}$; $b = 22.390(4) \text{ \AA}$; $c = 14.820(3) \text{ \AA}$ $\beta = 104.44(3)^\circ$), the other with plate shaped ones β ($P 21/c$ $a = 11.350(2) \text{ \AA}$; $b = 16.679(3) \text{ \AA}$; $c = 32.207(6) \text{ \AA}$ $\beta = 99.29(3)^\circ$).

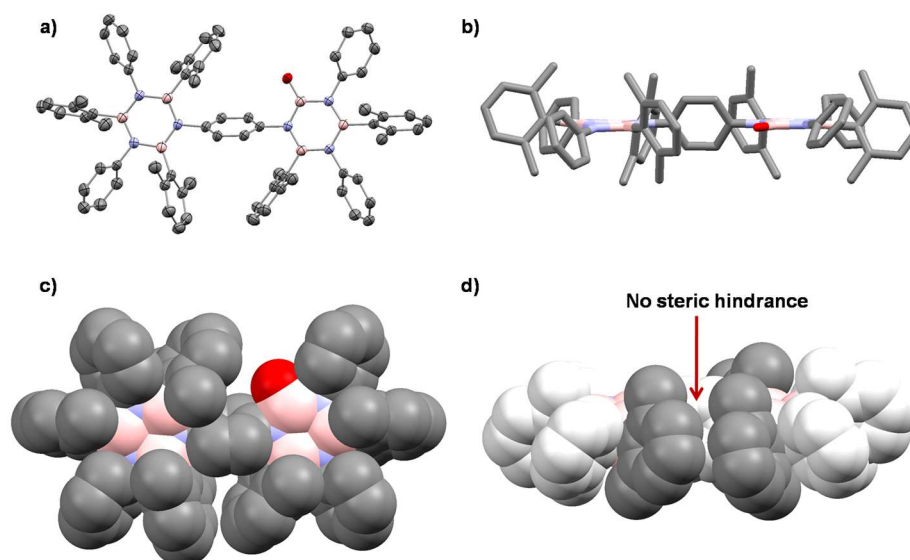


Figure 4.8: Crystal structure of the β polymorph of **4-11** a) front view ellipsoids representation of ASU contents (50% probability). b) side view (stick representation) it is visible how steric hindrance between neighbour BN cores is eliminated with substitution of a xylyl group with a hydroxyl. c) front view (spacefill representation) d) side view (spacefill representation).

In both polymorphs the substitution of a xylyl group with a hydroxyl one is observed, and this change leads to a further suppression of the residual strain between neighbour xylyl moieties in the bay regions compared to **4-9** (Figure 4.8d and 4.9d).

In the β crystals this results in a flat structure, with coplanar borazine cores (1.5° tilting, Figure 4.8b). In the α crystals (Figure 4.9), a tilt angle of 39° is present between the two different BN cores. The tilting between the cores in this case does not arise from strain in the molecule but is related to a greater degree of flexibility, due to the reduced

hindrance, which allows a different arrangement of the BN cores in the solid state, ultimately resulting in the two different polymorphs.

Moreover, **4-11** resulted to be stable towards moisture just as **4-9**, thus confirming the presence of an effective steric shielding on the boron atoms. Since **4-9** is stable under normal handling conditions, it is unlikely that **4-11** is formed by degradation of **4-9**. Considered that the OH derivatization was observed only in boron atoms close to the bridging position, one can hypothesize that the nucleophilic attack of xyllyl-lithium in that position is more difficult due to steric hindrance. This possibly results in the previously reported formation of hydroxyl multi-borazino derivatives in the oligomeric fraction. In fact, it could be inferred that the increase in molecular weight leads to a higher strain in the bay positions of the derivatives that results in higher percentages of hydroxylated derivatives.

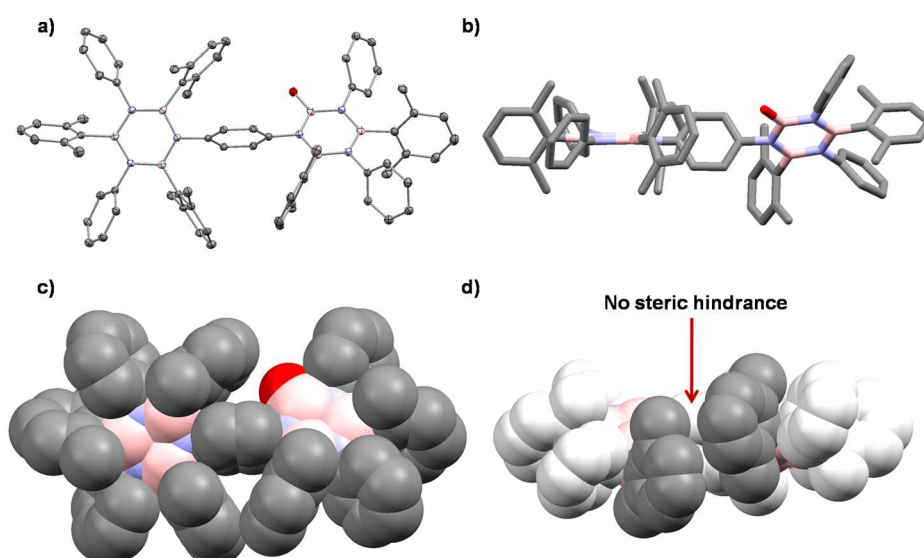


Figure 4.9: Crystal structure of the polymorph α of **4-11** a) front view ellipsoids representation of ASU contents (50% probability). b) side view (stick representation) c) front view (spacefill representation) d) side view (spacefill representation).

When the crystal structure of **4-10** (Figure 4.10a) is considered, an increased strain in the concave bay region comprised between the three BN cores is visible as previously postulated (Figure 4.10c).

This leads to a distortion of the structure resulting in a helicoidally fashioned distribution of the xylene moieties (figure 4.10 b-d). In Figure 4.10b it is clearly visible a 53.0-53.5 ° tilting of the peripheric borazine centres with respect to the central one, which allows the structure to release some of the strain arising from the crowded concave bay area of the molecule.

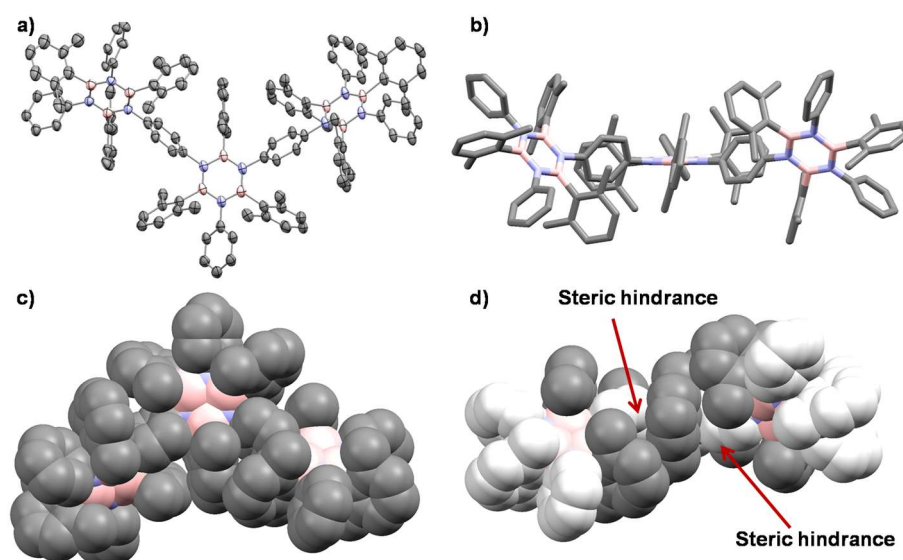


Figure 4.10: Crystal structure of **4-10** a) front view ellipsoids representation of ASU contents (15% probability). b) side view (stick representation) it is visible how steric hindrance between neighbour BN cores leads to a tilting of the borazine cores xylyl. c) front view (spacefill representation) d) side view (spacefill representation), helicoidally distribution of xylyl groups in evidence.

This distortion could be a valid explanation for the low yield of the high molecular weight derivatives despite the relatively high ratio between **2-4** and **4-1**.

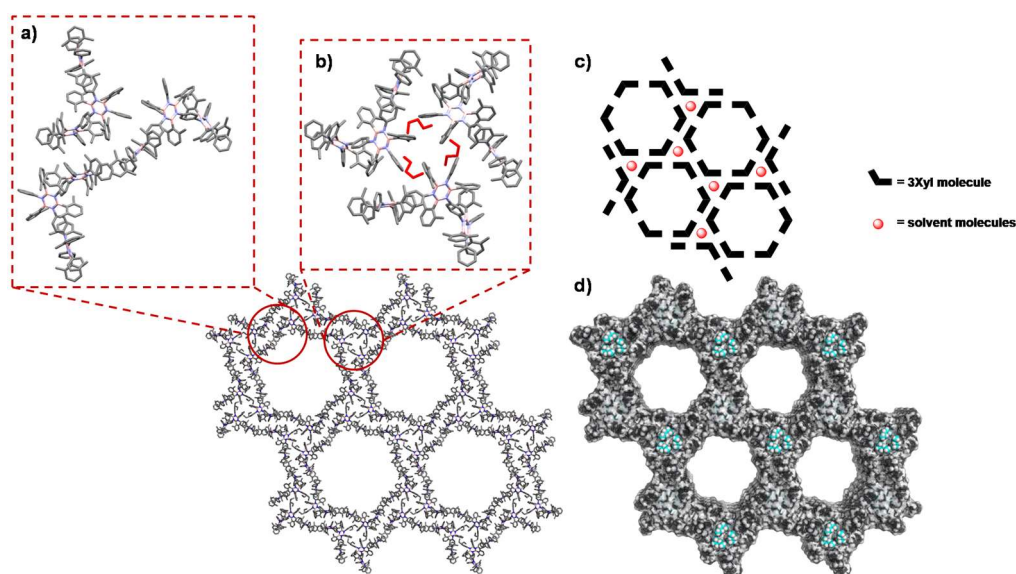


Figure 4.11: a) Detail (stick representation) of crystal structure showing CH- π interactions between xylyl groups b) detail (stick representation) of solvent position in the crystal c) Scheme representing molecules arrangement and solvent position in the crystal d) highlight of pores and solvent (spacefill representation).

When looking at the crystal packing, molecule **4-10** forms an hexagonal porous network in which each pore is formed by six molecules of **4-10** (Figure 4.11c) held together by CH- π interactions resulting from the interdigitation of peripheral phenyl rings (Figure 4.11 a). Three molecules of the solvent are included in the structure in specific positions (Figure 4.11 b, d), with non-covalent interactions that stabilize the crystal. The

pores present in the crystal structure have a diameter of 32 Å and are filled with disordered pentane molecules.

As previously stated, trace amounts of **4-12** were obtained as well (0.1% yield). Due to the very low yield of this derivative only a limited characterization was possible, and the identification of this molecule relied mostly on the HR-MS analysis (Figure 4.12).

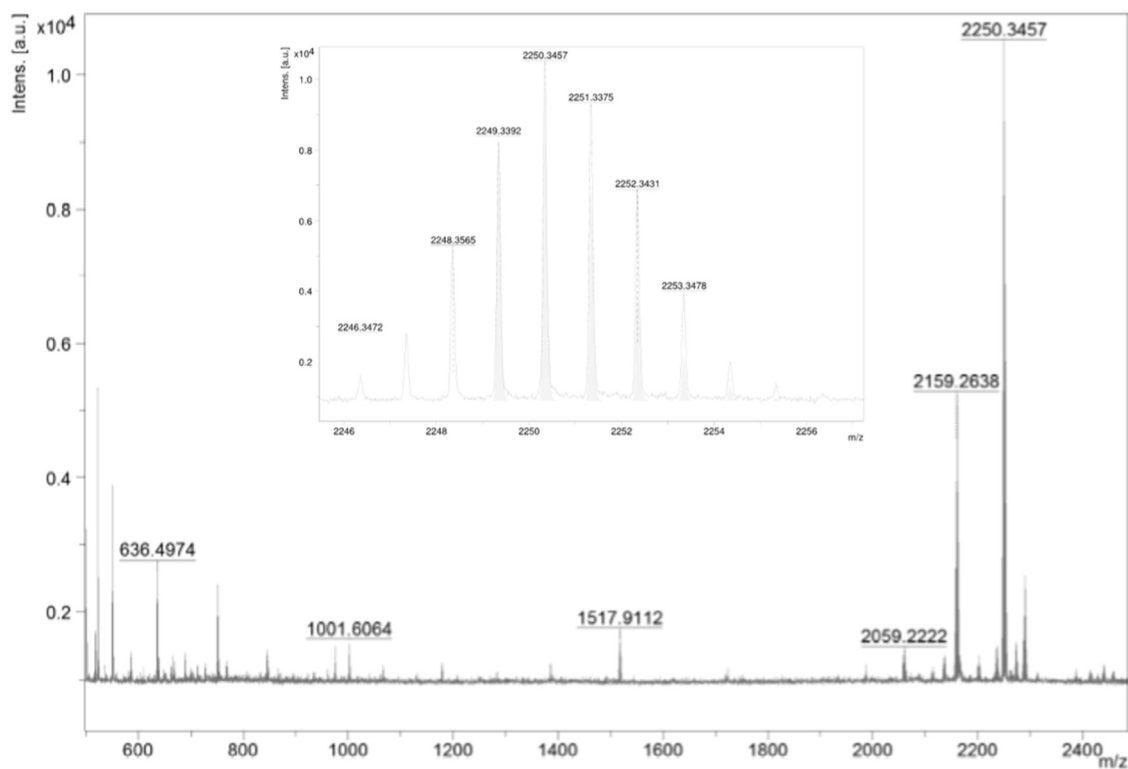
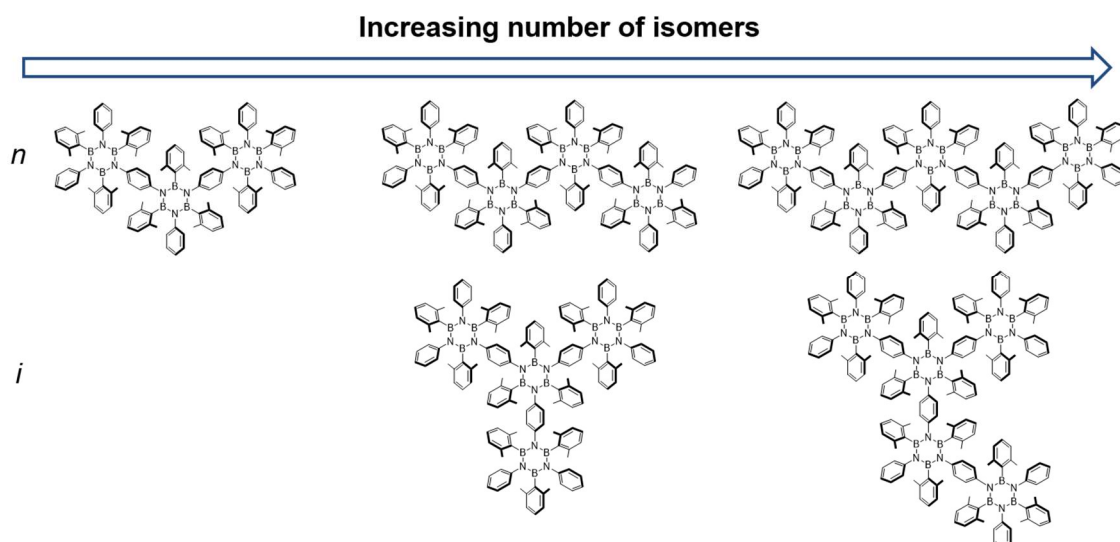


Figure 4.12: MALDI⁺ HR-MS spectrum of **4-12** derivative: [C₁₅₀H₁₅₀B₁₂N₁₂]⁺, calc.: 2251.3223, found: 2251.3375.

Despite various attempts using different solvent mixtures it was never possible to grow crystals of **4-12**. The low yield can be ascribed to the increased steric hindrance for the larger multi-borazino derivatives, as it leads to the preferential formation of hydroxyl multi-borazines. In analogy with alkanes, the four-unit multi-borazine **4-12** presents two possible isomers which can be identified with the nomenclature *n-4-12* and *i-4-12* (Scheme 4.4).

The two isomers were not separable and no attempts using rec-GPC were carried out due to the very small amount obtained. Oligomers longer than **4-12** are expected to be formed as mixtures of isomers, which above the pentamer, could include even cyclic structures.



Scheme 4.4: Representation of the possible isomers up to the 5-unit derivatives.

4.3 UV-Vis properties of multi-borazine derivatives

To study the effect of high doping dosages on the optoelectronic properties of borazine-polyphenylenes, the steady-state UV-Vis absorption and emission properties of **4-8**, **4-9**, **4-10** and **4-12** (both isomers) were studied (Figure 4.13).

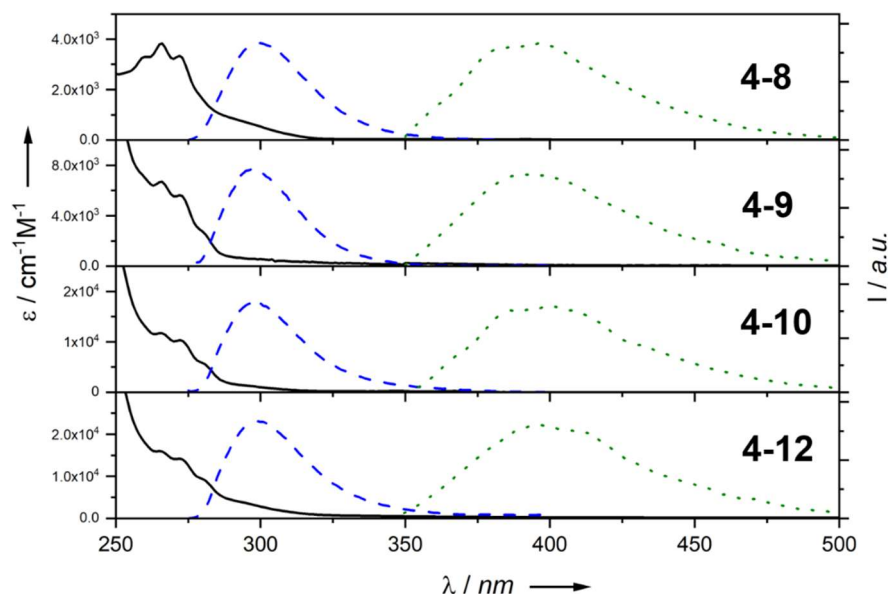


Figure 4.13: Absorption (solid line) at r.t., fluorescence at r.t. (black dashed line) and fluorescence at 77 K (red dashed line), and phosphorescence at 77 K (dotted line) of **4-8** ($\lambda_{\text{exc}} = 265$ nm), **4-9** ($\lambda_{\text{exc}} = 265$ nm), **4-10** ($\lambda_{\text{exc}} = 267$ nm) and **4-12** ($\lambda_{\text{exc}} = 267$ nm) in an aerated CH_2Cl_2 solution.

When the emissive properties of air-equilibrated CH_2Cl_2 solutions of all borazine derivatives are considered, significant radiative UV emission profiles ($\lambda_{\text{max}} = 300, 297, 298$ and 299 nm, Table 4.1) and very short lifetimes, ($\tau_{\text{fl}} = 1.24 - 1.66$ ns, Table 4.1) consistent with the presence of excited singlet radiative deactivation, are observed for

all molecules. These observations suggest that the absorption properties of these oligomers are additive, and that no significant π -conjugation occurs upon extension of the oligomers. All solutions showed very low quantum yields ($\Phi_{em} = 2\% - 7\%$; Table 4.1) suggesting that the borazine core leads to a quenching of the fluorescence compared to less doped polyphenylene derivatives.^[4] From these data, a confirmation that high BN dosages enhance the deactivation rate of the singlet excited state is obtained. When cooled to 77 K, non-negligible phosphorescence emission has been also observed (Figure 4.13) showing very similar emission profiles for the different derivatives, all placed at ca. 390 nm. The presence of this phosphorescence emission is also in line with previously reported borazino-polyphenylenes.^[4] Representative phosphorescence lifetime measurements showed long-lasting emission profiles (τ_{ph} ca. $\sim 1.11 - 1.56$ s).

Table 4.1: UV-Vis Absorption and emission properties of derivatives **4-8**, **4-9**, **4-10** and **4-12**.

Molecule	Absorption			Emission			
	λ [nm] (ϵ , Lmol ¹ cm ⁻¹) a)	$\lambda_{max,fl}$ ^{a)} [nm]	E_{opt} ^{b)} [eV]	τ_{fl} [ns]	Φ_{fl}	$\lambda_{max,ph}$ ^{e)} [nm]	τ_{ph} ^{e)} [s]
4-8	260 (3300)	300	4.31	1.24	0.02	383	1.11(single)
	266 (3831)						1.42 (76%)
	272 (3342)						0.37 (24%)
4-9	266 (6702)	297	4.18	1.66	0.02	389	1.49 (single)
	272 (5630)						1.70 (88%)
	280 (2755)						0.27 (12%)
4-10	266 (11747)	298	4.16	1.39	0.06	386	1.56(single)
	272 (10300)						1.71 (88%)
	280 (5813)						0.14 (12%)
4-12	266 (15669)	299	4.15	1.36	0.07	393	1.46(48%)
	272 (13949)						0.26 (52%)
	280 (9100)						

^{a)}Recorded in an aerated CH₂Cl₂ solution at r.t. ^{b)} Calculated from the lowest energy crossing point between the absorption and emission spectra normalised on the lowest energy peak (E_{opt} [eV] = $1240.5/\lambda_{cross}$ [nm]). ^{c)} 9,10-Diphenylanthracene was used as reference standard (0.97 in Cyclohexane). ^{d)} Recorded at 77K in a 1:1 CH₂Cl₂:CHCl₃ glassy matrix.

The only parameter that changes consistently among the different derivatives is the extinction coefficient, which regularly increases from **4-8** to **4-12**. This effect plausibly arises from the increasing number of phenyl rings in the system, which leads to a linear increase in the absorption for the molecules, since each derivative increases by the same number of rings compared with the previous one (Figure 4.14). This confirms the additive nature of the observed effects in these derivatives, which is related only to the number of units in each molecule and rules out any kind of extended conjugation between the different sub-units.

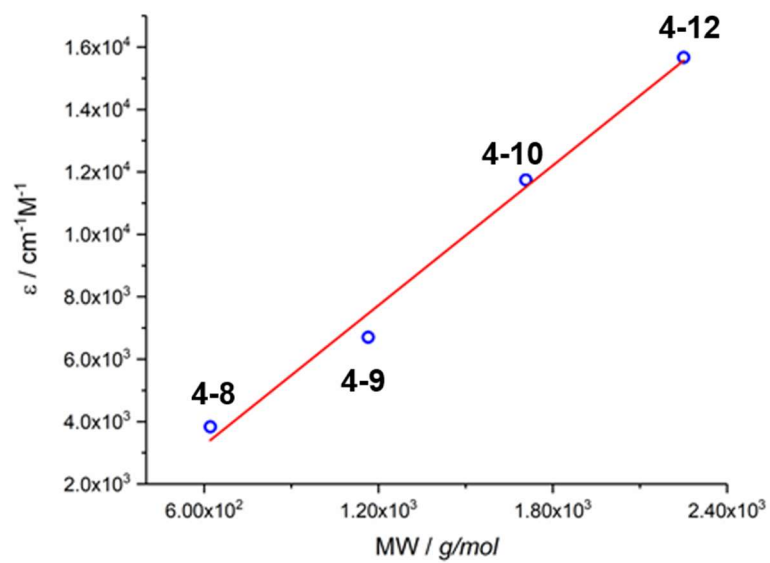
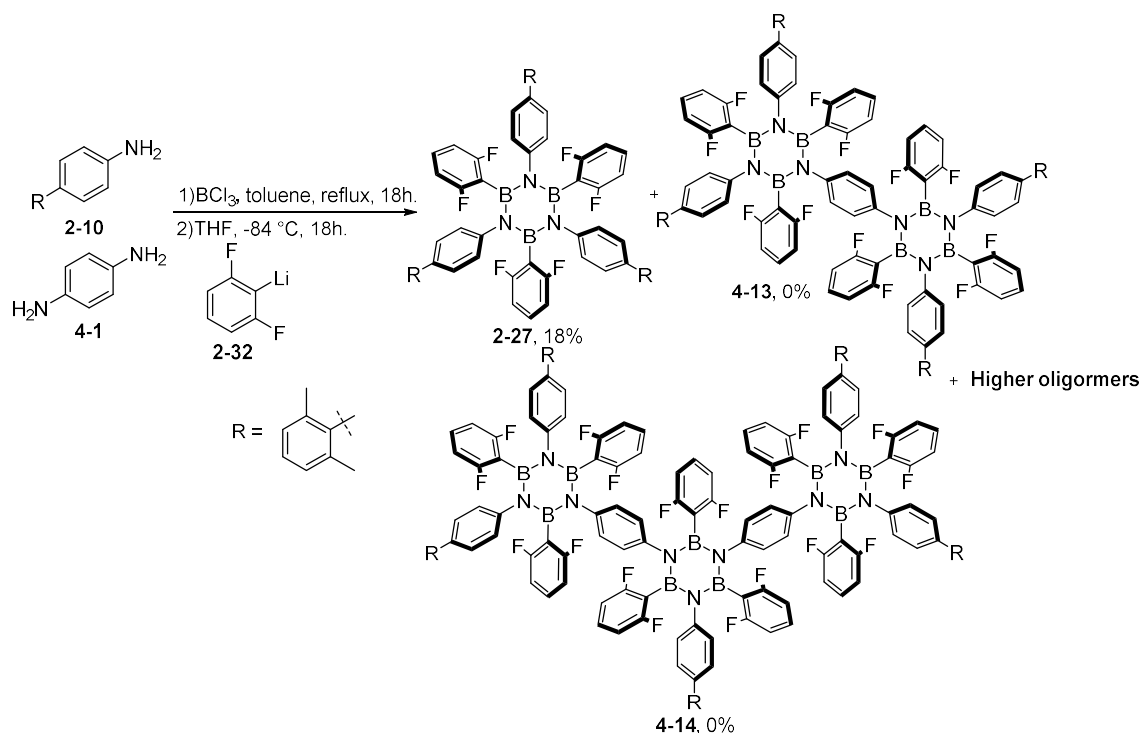


Figure 4.14: graph reporting the linear correlation between MW of the derivatives and molar extinction coefficient.

4.4 Synthesis of fluorine-functionalized multi-borazine derivatives

The synthesis of multi-borazine derivatives bearing fluorine atoms in *ortho* position on the boron bonded aryl rings was then attempted. To avoid the formation of mixtures of atropoisomers, the synthesis was initially performed using lithium derivative **2-32** (Scheme 4.5). Moreover, to obtain soluble nanographenes after the final planarization reaction, aniline **2-10** was used in place of aniline **1-60**. A 4:1 mixture of **2-10** and **4-1** was used to achieve a higher yield of the lower molecular weight derivatives **4-13** and **4-14**, avoiding isomeric products. The mixture of **2-10** and **4-1** was then suspended in dry toluene and heated at 80°C until complete solubilization before adding BCl₃ and refluxing for 18 h. The resulting suspension of chloro-borazoles was then treated with lithium derivative **2-32**, in turn obtained *via* halogen-lithium exchange using *n*-BuLi in THF at -84°C.

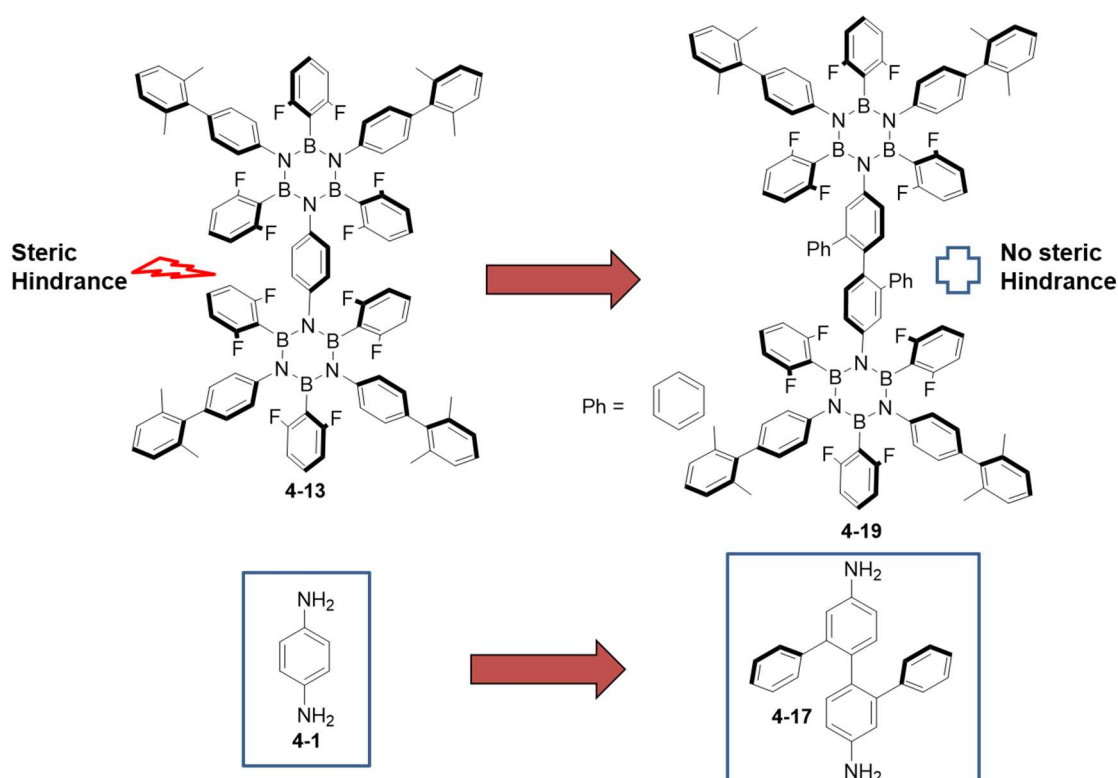


Scheme 4.5: Synthetic route towards fluorine-functionalised multi-borazino derivatives.

When purification was attempted, only borazine **2-27** was successfully isolated in a 18% yield, whereas the other derivatives underwent rapid degradation on silica and when exposed to atmospheric moisture. The only possible explanation for this result is related to the much smaller size of the fluorine atoms compared to that of the methyl groups of the previous derivatives. In fact, in the xylyl derivatives the methyl groups are bulky enough to protect the boron atoms despite the presence of some residual strain in the systems. In the case of **4-13** instead, the residual strain plausibly leads to a

deviation of the fluorine atoms positions away from the boron atom. This results in unprotected boron centres which easily undergo nucleophilic attack leading to the observed rapid degradation.

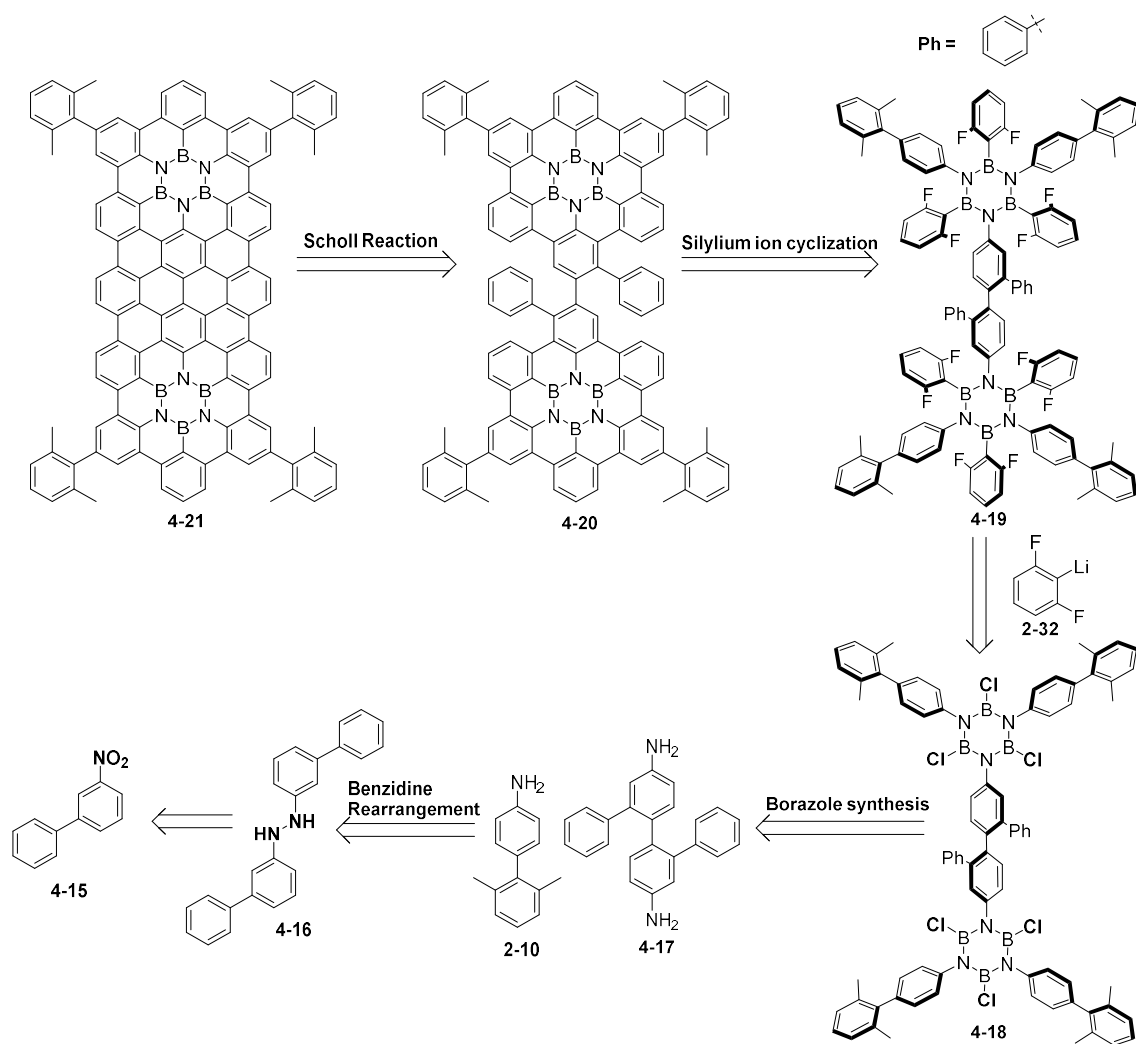
Given these results, a new strategy to further reduce the steric hindrance arising in the bay and concave bay regions of the molecules was needed. Aiming at this, it was decided to increase the distance between the neighbouring borazine cores, and this could be achieved by using a substituted benzidine **4-17** instead of phenylenediamine **4-1** (Scheme 4.6).



Scheme 4.6: Strategy towards stable fluorine-functionalised multi-borazines using a benzidine ligand in place of **4-1**.

In fact, one phenyl ring more in the bridging unit would work as a spacer between the borazine units, thus resulting in their independent behaviour and consequently in stable derivatives.

The new retrosynthetic strategy towards extended nanographenes is reported in scheme 4.7.

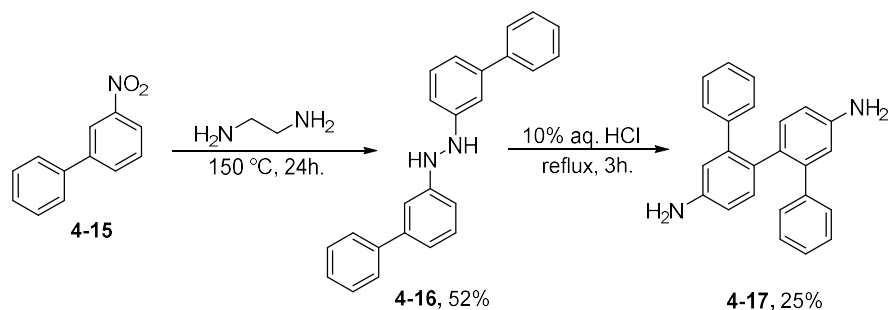


Scheme 4.7: Retrosynthetic strategy towards nanographene **4-21** using fluorine-functionalised multi-borazine systems.

According to this approach the final nanographene molecule **4-21** should be obtained from a Scholl reaction on partially planarized derivative **4-20** which can be formed using the silylium ion induced cyclization reaction employing silylium carborane **2-22** and dimethyldimesitylsilane **2-19** on multi-borazine derivative **4-19**. The desired multi-borazine **4-19** should be formed by reaction of chloro-borazole **4-18** with the lithium derivative **2-32**. **4-18** can be obtained by reacting **2-10** and **4-17** in the presence of BCl_3 in refluxing toluene. Aniline **2-10** can be used to introduce the solubilizing groups necessary to obtain soluble nanographenes. Finally, the desired benzidine derivative **4-17** should be formed by benzidine rearrangement of hydrazobenzene **4-16** which can be in turn obtained from *meta*-nitrobiphenyl **4-15** by reduction with ethylene diamine.

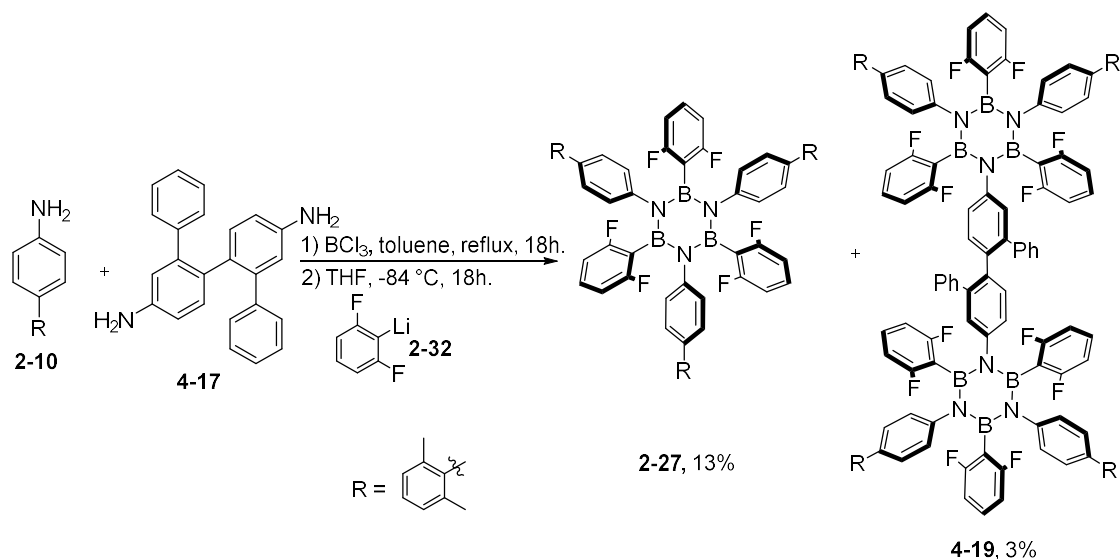
The synthesis started with the reduction of commercially available **4-15** (Scheme 4.8) using ethylenediamine as solvent in a sealed vessel under vacuum at 150°C which resulted in the formation of the desired hydrazobenzene **4-16** in a 52% yield after precipitation from petroleum ether.

Derivative **4-16** was then subjected to a benzidine rearrangement by refluxing in 10% aq. HCl under N₂, resulting in the formation of a mixture of products which was purified *via* column chromatography, giving the desired benzidine derivative **4-17** in a 25% yield (Scheme 4.8).



Scheme 4.8: Benzidine rearrangement of **4-16** resulting in formation of **4-17**.

At this point a mixture of **4-17** and 4 equivalents of aniline **2-10** were reacted with BCl₃ in refluxing toluene and the resulting chloro-borazoles mixture was treated with lithium derivative **2-32** (Scheme 4.9).



Scheme 4.9: Synthesis of fluorine-functionalised multi-borazine **4-19**.

Purification of the reaction mixture on a silica gel plug using petroleum ether/CH₂Cl₂ (90:10 to 60:40) as eluents led to the isolation of both **2-27** and **4-19** in a 13% and 3% yield, respectively. This result proves that indeed the use of **4-17** as bridging unit in the synthesis increases the stability of the multi-borazine derivatives by further reducing the residual strain in the molecules. The structure of **4-19** was proved by both ¹H-NMR and HR-MS (Figure 4.15) with identification of the molecular ion peak at *m/z* 1856.7334 (C₁₁₆H₈₆B₆N₆F₁₂⁺, calc: 1856.7281) leading to the unambiguous identification of this derivative.

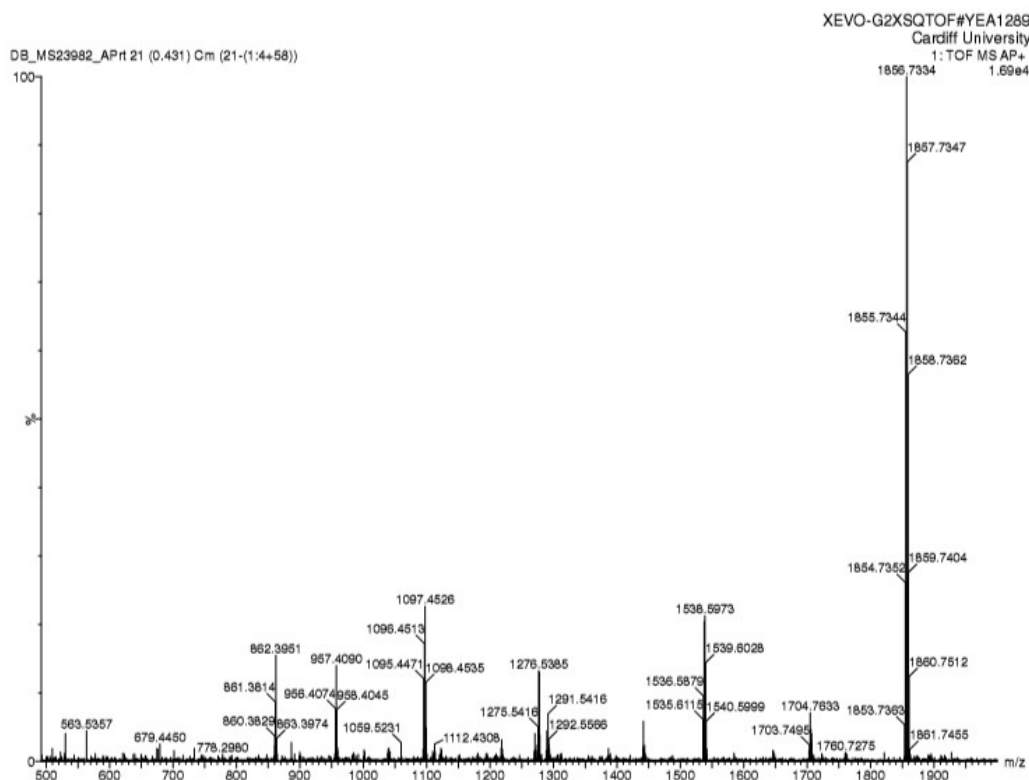


Figure 4.15: AP⁺ HR-MS spectrum of derivative **4-19** with molecular ion visible at m/z 1856.7334 ($C_{116}H_{86}B_6N_6F_{12}^+$, calc: 1856.7281).

During the characterization of **4-19** some degradation of the material was visible, especially if left in solution for long periods of time. This seems to suggest that, despite the great improvement in the molecule stability due to the increased distance between the borazine units, the boron atoms are still susceptible to nucleophilic attack in this molecule. This result can be linked with both the very low yield obtained for **4-19** and the absence of higher oligomers, which can be due to partial degradation of these compounds during purification. This reactivity observed for **4-19** suggests that, despite all efforts, the small dimensions of fluorine are not able to completely shield the boron, especially in large systems in which many steric contributions are present. Furthermore, it is plausible that despite the reduction of the steric hindrance in the bay region, the two borazine units are not behaving as independent parts but are still influenced by the presence of each other, leading to deviations from the stable conformation observed in **2-27**.

Considering these results and the low overall yield of the synthesis, it was not possible to perform the cyclization reaction on derivative **4-19**, leading to the consideration that in order to obtain extended nanographene systems a different approach could be more effective.

4.5 Conclusions

The synthesis through a condensation reaction of borazine-doped polyphenylene derivatives displaying high doping dosages (16%-18%) was reported. This work represents a steppingstone towards the synthesis of starting materials for the preparation of extended borazine-doped nanographenes. To assess the stability and to find the best conditions towards multi-borazino derivatives, model mesityl and xylyl compounds were prepared. The use of mesityl lithium **4-6** yielded strained mesityl multi-borazines, which revealed to be unstable in the presence of moisture. However, when **4-6** was substituted with xylyl lithium **4-7**, chemically stable xylyl multi-borazines derivatives were obtained, with a maximum degree of oligomerization of 16-18 units. While dimer **4-9**, trimer **4-10** and tetramer **4-12** were isolated as pure products, higher oligomers could be only obtained as mixtures with various degrees of hydroxylation and characterized by GPC. SC-XRD studies on **4-9** and **4-3** highlighted the paramount importance of steric hindrance in the stability of this derivatives. When the synthesis of planarisable fluorine functionalized derivatives was carried out, only degradation compounds were obtained, indicating that the smaller dimensions of the fluorine atoms were not enough to counteract the distortion induced by the strain in the system. The use of a longer benzidine spacer between the borazine cores led to the isolation of **4-19**, which despite being stable enough to be isolated still proved to be sensitive towards moisture. This result, along with the consequent lower yields, led to the impossibility of using **4-19** in the planarization reaction. In summary, these findings suggest that a different approach is required to successfully synthesise extended borazine-doped nanographenes, possibly relying on different polymerization reactions or planarization reactions. From this point of view the work will focus mainly in finding new ways to polymerize borazine cores exploiting cycloaddition reactions. Furthermore, efforts are currently dedicated to finding alternative ways towards the planarization of borazine derivatives with higher yields, which could possibly lead to efficient synthetic pathways for the formation of borazine-doped nanographenes in such amounts that would allow their application in electronic devices.

4.6 References

- [1] J. Dosso, D. Marinelli, N. Demitri, D. Bonifazi, *ACS Omega* **2019**, *4*, 9343–9351.
- [2] K. Nagasawa, *Inorg. Chem.* **1966**, *5*, 442–445.
- [3] D. Bonifazi, F. Fasano, M. M. Lorenzo-garcia, D. Marinelli, J. Tasseroul, *Chem. Commun.* **2015**, *51*, 15222–15236.
- [4] D. Marinelli, F. Fasano, B. Najjari, N. Demitri, D. Bonifazi, *J. Am. Chem. Soc.*

2017, 139, 5503–5519.

- [5] S. Kervyn, O. Fenwick, F. Di Stasio, Y. S. Shin, J. Wouters, G. Accorsi, S. Osella, D. Beljonne, F. Cacialli, D. Bonifazi, *Chem. Eur. J.* **2013**, 19, 7771–7779.
- [6] K. Suzuki, A. Kobayashi, S. Kaneko, K. Takehira, T. Yoshihara, H. Ishida, Y. Shiina, S. Oishi, S. Tobita, *Phys. Chem. Chem. Phys.* **2009**, 11, 9850–9860.

CHAPTER 5

**BORAZINE-DOPED POLYPHENYLENIC POLYMERS:
SYNTHESIS AND APPLICATIONS.**

In this chapter the synthesis of a novel borazine-doped polyphenylene material *via* an unprecedented [4+2] cycloaddition reaction on ethynyl borazines is reported. This approach led to the formation of a borazine-doped polymeric material in a simple and scalable manner. The material was characterized by comparison with its monomeric unit *via* ATR-IR, Solid state ^{13}C and ^{11}B -NMR. Furthermore, the polymer formed gels in chlorinated solvents and a gel composed by 4% w/w of the material in CHCl_3 was thoroughly characterized and studied, showing rheological properties comparable to those of polyacrylamide gels with low crosslinker percentage. Finally, due to its high thermal and chemical stability, the material was studied as potential support for SSEs (solid state electrolytes) proving to have properties comparable to those of PEG based electrolytes, thus opening up for the application of this new class of materials in lithium ion batteries.

This chapter is divided in 10 main sections: *i*) section 5.1 presents an introduction on the topic; *ii*) Section 5.2 contains the aim of the project; *iii*) Section 5.3 presents the synthesis of borazine **5-2** and monomer **5-4**; *iv*) Section 5.4 displays the synthesis of polymeric material **5-1**; *v*) Section 5.5 presents the solid state NMR characterization of **5-1** and **5-4**; *vi*) section 5.6 displays the pXRD analysis of **5-4**; *vii*) Section 5.7 reports the rheological studies performed on gels obtained from **5-1** in chlorinated solvents. *viii*) Section 5.8 presents the application of **5-1** as solid-state electrolyte. *ix*) Section 5.9 draws some conclusions and perspective for this new class of materials; *x*) Section 5.10 contains the references for the chapter.

X-Ray analysis were performed by N. Demitri (Elettra-Sincrotrone, Basovizza, Trieste, Italy). Rheological characterization was performed by M. Abrami and M. Grassi (University of Trieste). SSE preparation and related studies was performed by H. Oubaha (University of Louvain), solid state NMR analysis was performed by K.D.M Harris and C. E. Hughes (Cardiff University), BET measurements were performed by M. Carta at Swansea University, NMR analysis of **5-4** in C_6D_6 was performed at Vienna University by Dr. K. Hanspeter.

5.1 Introduction

In the last decades polyphenylene based materials have been the object of extensive research efforts.^[1,2] This interest is related to the many different applications of these derivatives, spanning from precursors in graphene synthesis^[3,4] to antennae systems,^[5-7] proton exchange membranes,^[8,9] optoelectronic devices,^[10] and self-assembling materials.^[11] Doping with heteroatoms^[12,13] along with the tailored addition of functional groups,^[14,15] are possible strategies employed to further widen the range of applications of polyphenylenes. In particular, polar BN bonds have been used to replace CC sp^2 couples in polymeric materials^[16-18] leading to variations in the optoelectronic properties largely dependent on the number and position of bonds replaced.^[13,19] The complete replacement of a phenyl ring with a borazine has been exploited as well to generate BN-doped polyphenylenes and the multi-borazine derivatives reported in chapter 4.^[20] This strategy proved to be particularly effective in breaking the conjugation of the materials, leading to blueshifted emissions and lower quantum yields when compared to the all carbon counterparts.^[20,21] Furthermore, the presence of borazine rings and in general, of polar BN bonds can impart a different reactivity to the materials, especially when interactions between these peculiar bonds and polar or charged species are envisaged.^[22,23] This is particularly true for gas adsorption/storage applications^[23,24] and for solid state electrolytes (SSEs), in which the presence of doping units can lead to improved performances.^[25-27] The potential use of BN-doped polyphenylene materials in SSEs is mostly related to the high local dipole of the BN bonds which is expected to be able to interact with charged species. This ability of rings presenting high local dipoles, has been highlighted in polyethylene oxide (PEO) based systems presenting boroxine rings as reported by Fujinami and co-workers.^[25] In this work, an improvement of the lithium transfer number associated with the presence of the boroxine rings was observed, due to the ability of the B_3O_3 ring to interact with the anions thus increasing the mobility of the Li^+ ions (Figure 5.1).

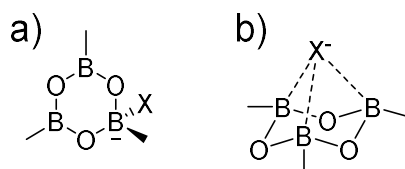
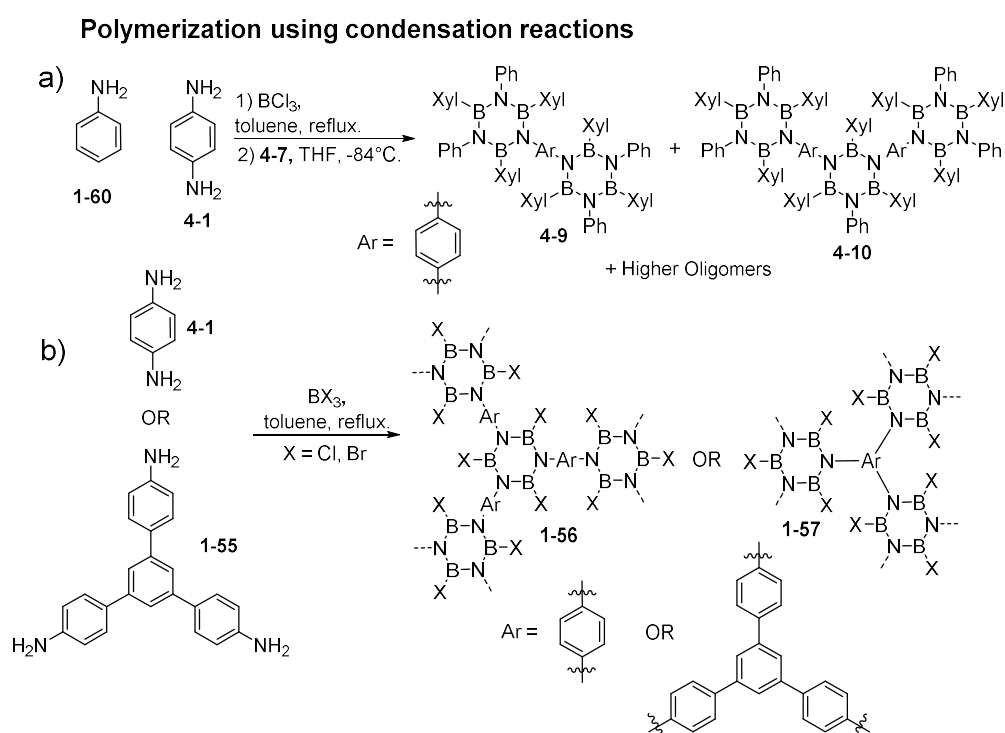


Figure 5.1: Plausible interactions between anions and boroxine rings in SSEs; a) Interaction with one boron; b) interaction with three boron atoms.

From the synthetic point of view, the careful design is of central importance when preparing polyphenylene materials, especially when the resulting product presents characteristics that make purification or processing particularly challenging. In the design and synthesis of borazine-doped polyphenylene materials, one of the limiting

factors is the stability of borazines, which dictates the presence of groups able to shield the boron atom from nucleophilic attack in order to have easy to handle materials.^[28,29] Most of the work on borazine-doped polyphenylenic materials consists in forming them using directly the borazine core formation reaction (Scheme 5.1). In this strategy, a diamine or triamine unit such as **4-1** or **1-55** is used to induce the polymerization, which occurs with condensation reactions in presence of boron halides resulting in the formation of borazine rings connected by bridging units. This strategy has been used successfully in Chapter 4 to obtain multi-borazine derivatives. However, the increased steric hindrance in the higher oligomers resulted in a difficult reaction of the chloro-borazole intermediates with xyllyl-lithium, causing low yields and the formation of B-OH moieties.



Scheme 5.1: Polymerization through condensation reactions; a) Multiborazine oligomers as reported in chapter 4; b) Borazine based porous networks for gas adsorption applications by El-Khadri e co-workers.

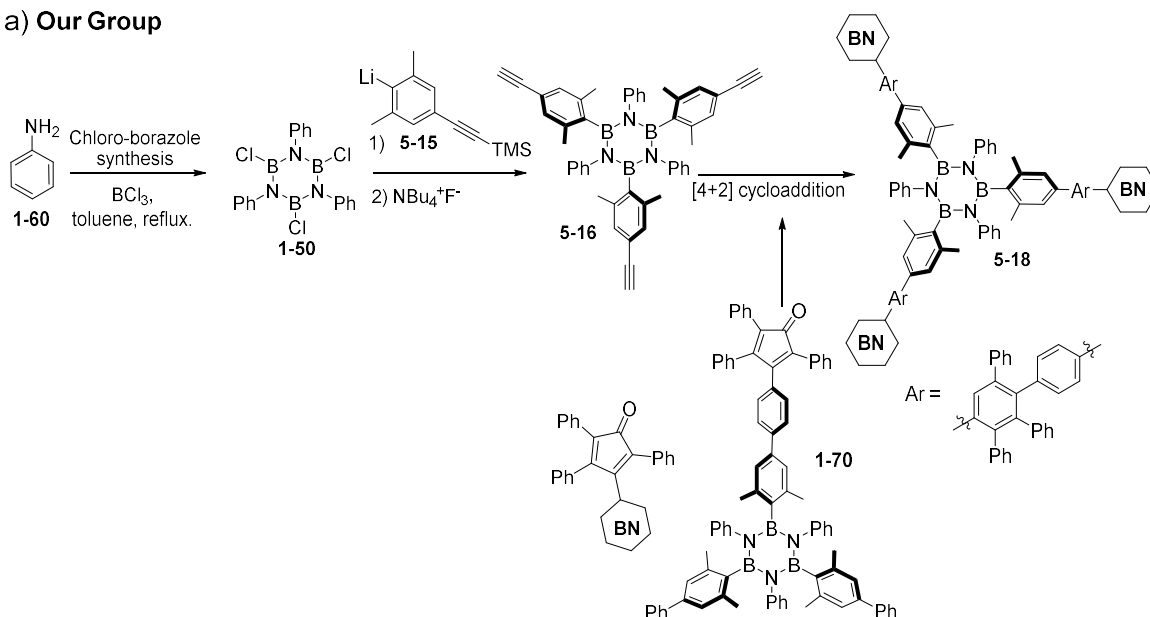
In the work of El-Kaderi (Figure 5.1b) the same approach relying on condensation reactions is employed. In this case, the polymeric chloro-borazoles are used directly as the active material for gas absorption thus avoiding the difficult functionalization of the polymeric chloro-borazoles. However, this limits the use of such materials to moisture-free conditions in order to avoid the hydrolysis of the sensitive B-Cl and B-Br groups.

[23,24,30]

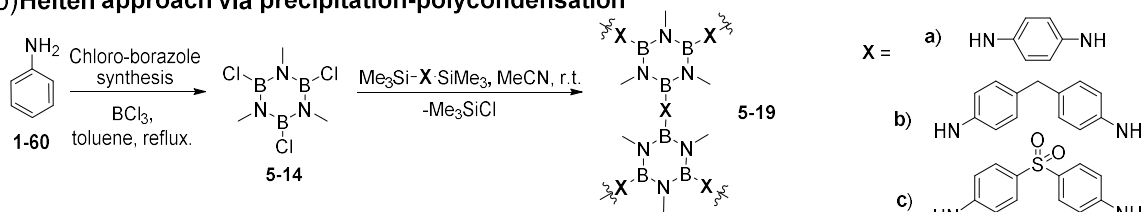
Other possible strategies towards borazine-doped polymeric materials are the polymerization of pre-formed hexaphenyl-borazine units or chloro-borazole derivatives

(Scheme 5.2a, b).^[21,31] The use of functionalized hexaphenyl-borazines requires the synthesis of complex systems, bearing functional groups that can induce the polymerization. At the same time, protection of the boron atoms from nucleophilic attack is required to avoid moisture sensitive materials and thus be able to perform the reactions without degradation (Scheme 5.2a). The presence of the protective methyl groups allows the use of this building blocks without moisture-free conditions in a variety of reactions. Nevertheless, the introduction of the protecting groups tames the ability of the borazine rings to interact with polar species, thus limiting the effects of the doping to the optoelectronic properties.

a) Our Group



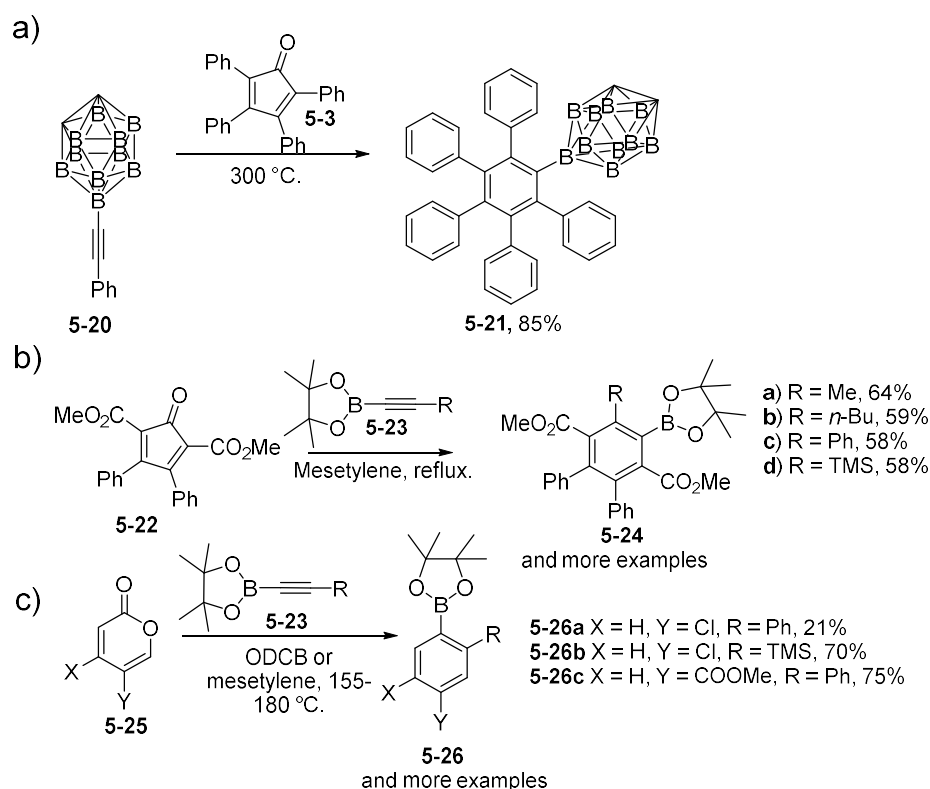
b) Helten approach via precipitation-polycondensation



Scheme 5.2: Polymerization *via* reaction of pre-formed borazine units. a) Borazine-doped polyphenylenes obtained by [4+2] cycloadditions of hexaphenyl-borazine derivatives; b) Polymeric materials formed *via* precipitation-polycondensation of chloro-borazoles.

Another strategy is represented by the polymerization of monomeric chloro-borazoles (Scheme 5.2b). In the work by Helten and co-workers, chloro-borazole **5-14** was polymerized using silicon/boron exchange reactions involving silylamine derivatives of linker units (X, Scheme 5.2b). With this strategy, it is possible to use linkers presenting various degrees of functionalization, thus introducing more functional groups in the material (Scheme 5.2b). However, the main drawback of this approach consists in the necessity to deal with the highly moisture sensitive nature of the chloro-borazoles, which limits their manipulation to moisture-free techniques (Scheme 5.2b).

[4+2] cycloadditions are of paramount importance in the preparation of both all-carbon and borazine-doped polyphenylenes.^[17,32] In particular, the pioneering work by Müllen and co-workers has heavily contributed in highlighting the potential of carefully designed dienes and alkyne functionalized moieties in forming chemically precise polyphenylenes.^[33] Consequently, to synthesise borazine-doped materials, it would be highly desirable to have ethynyl functionalized borazines able to undergo [4+2] cycloadditions without the need of protecting groups or complex syntheses. From this point of view, the most interesting starting materials are B,B',B''-triethynyl-N,N',N''-triphenyl borazines, which despite being reported as moisture sensitive in solution,^[34] are known to be bench stable, differently from chloro-borazoles.^[35] When polymerization of ethynyl borazines is envisaged, [4+2] cycloadditions on the alkynes directly bonded to the boron atom of the borazine core are required. Due to the high synthetic potential of [4+2] cycloadditions on boron bonded alkynes, various examples of these reactions are reported.^[36,37] A [4+2] cycloaddition of tetraphenylcyclopentadienone (**5-3**) on a phenyl alkyne bonded to a *o*-carborane (Figure 5.3a) was reported by Craciun et al., leading to the formation of polyphenyl-functionalized *o*-carboranes.

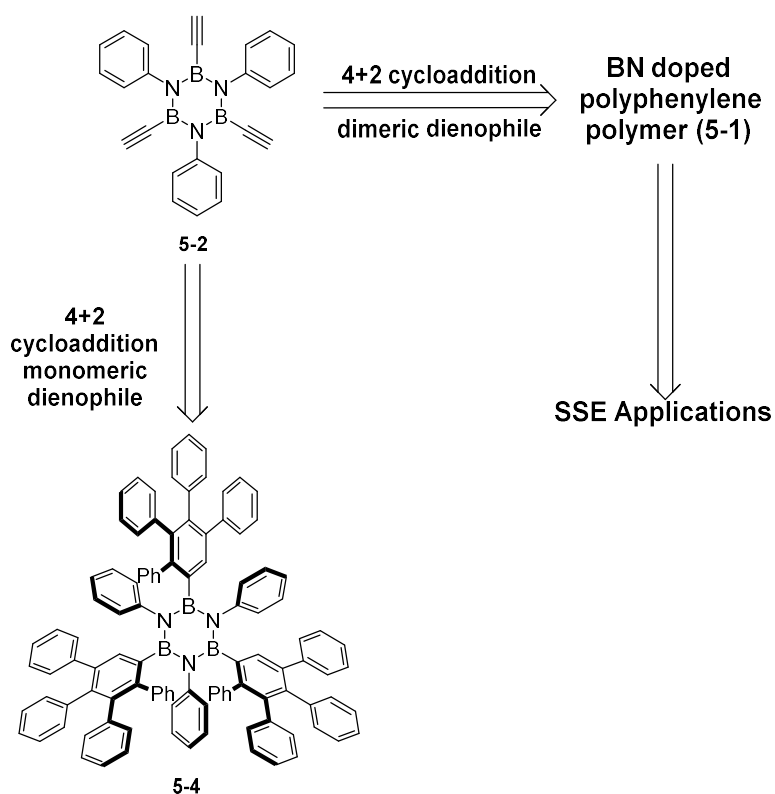


Scheme 5.3: Previous examples of reactions involving boron bonded acetylenes. a) [4+2] cycloaddition on a carborane bonded acetylene as reported by Craciun et al. b) and c) [4+2] cycloaddition on acetylene groups bonded to boronic ester as reported in the group of Harrity.^[38,39]

Other interesting examples came from the group of Harrity, in which functionalised borylated benzenes were obtained using [4+2] cycloaddition reactions involving cyclopentadienone derivative **5-22** or Pyrone derivative **5-25** and various alkyne derivatives bonded to a boronic ester. This resulted in the formation of functionalized benzene derivatives **5-24** and **5-26** bearing boronic ester functionalities together with different functional groups (Scheme 5.3b, c).^[38,39] When alkynes bonded to borazines are considered, no examples of [4+2] cycloaddition reactions were ever reported to the best of our knowledge. Consequently, before using this approach to form polymeric materials, a study of the cycloaddition reaction on alkynyl borazines is required.

5.2 Aim of the project

The aim of this chapter is to prepare borazine-doped polymeric materials. To obtain a clean and efficient reaction, an unprecedented [4+2] cycloaddition on ethynyl borazines will be performed using tetraphenyl cyclopentadienone leading to the formation of monomeric unit **5-4** (Scheme 5.1).



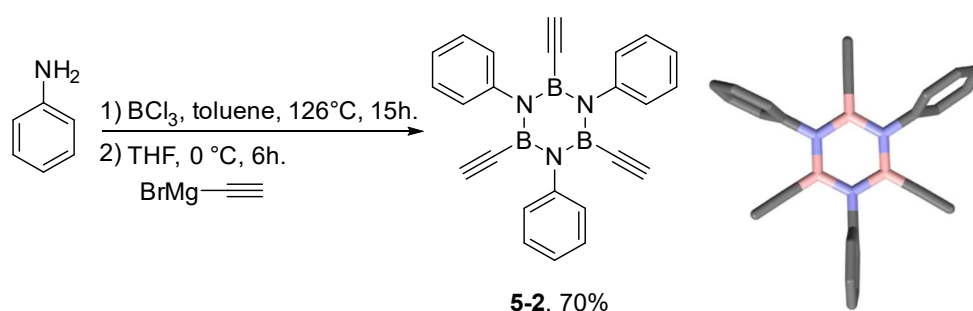
Scheme 5.4: General approach towards the synthesis of borazine-doped polymers using [4+2] cycloadditions.

If this approach will be successful, suitable dimeric dienes will be prepared and used to induce the polymerization of ethynyl borazine **5-2** resulting in the formation of polymeric material **5-1**. After the synthesis of the desired polymer, extensive characterization will be carried out to determine the structure and composition of the material. Due to the

expected thermal stability of **5-1** and the presence of polar BN bonds possibly able to interact with charged species^[25,26], this material could be a good support component in Li⁺ containing SSEs. For these reasons, the use of **5-1** as support in SSEs will be investigated as well.

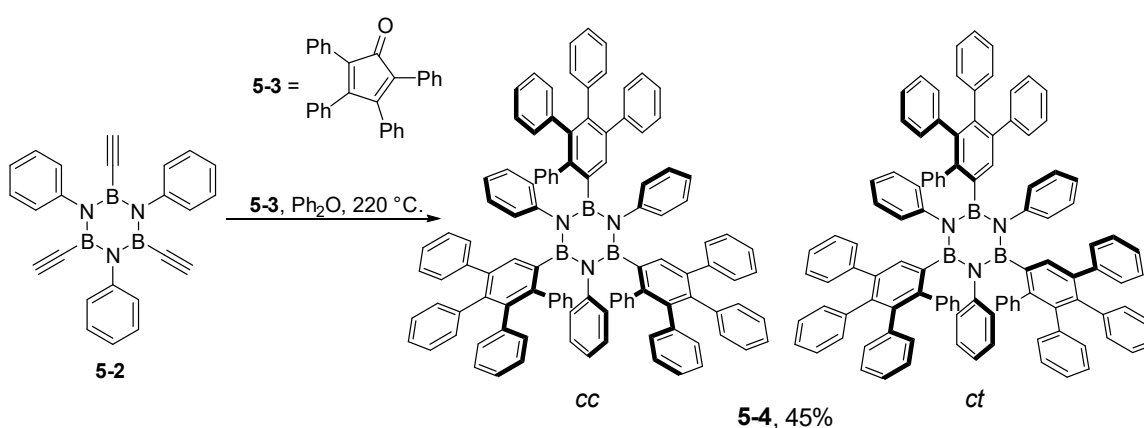
5.3 Synthesis of Monomer 5-4

B,B',B''-triethynyl-N,N',N''-triphenyl borazine **5-2** was synthesized based on a modified procedure derived from the original work by Groszos and Stafiej^[40] and Yamaguchi.^[41] Following this protocol, aniline **1-60** was reacted with BCl₃ in refluxing toluene and the resulting chloro-borazole treated with a solution of ethynyl magnesium bromide at 0 °C giving **5-2** in a 70% yield (Scheme 5.4).



Scheme 5.5: Left: Synthetic approach towards derivative **5-2**; Right: Crystal structure of derivative **5-2** obtained from slow evaporation of a 1/1 solution of petroleum ether/CH₂Cl₂. Space group: R-3.

The resulting product proved to be moisture sensitive, especially when in solution, resulting in aniline formation. Despite this, **5-2** was found to be stable for months when kept dry,^[34] thus allowing for an easy handling and storage of the material.



Scheme 5.6: Synthetic approach towards derivative **5-4** using borazine **5-2** as starting material. The [4+2] cycloaddition reaction was then performed on **5-2** using commercially available tetraphenylcyclopentadienone **5-3** in dry degassed Ph₂O at 220 °C (Scheme 5.6), leading to the formation of desired product **5-4** in a 45% yield (77% yield for single

reaction) as a mixture of *cc* and *ct* atropoisomers. The formation of two atropoisomers is expected since the attack of the diene can occur on both sides of the borazine ring. This results in two possible configurations arising from three reactions on the same side of the molecule (*cc*) or two on one side and one on the other (*ct*). Confirmation of the structure of the two isomers was achieved *via* SC-XRD (Figure 5.2). Since separation of the two isomers proved impossible, crystallization of the mixture was carried out, resulting in a combination of 2 different crystals, each arising from one of the two different atropoisomers. It was then possible to diffract each type of crystal by manually selecting them from the mixture, allowing for structure solution of the two atropoisomers (Figure 5.2). From SC-XRD analysis the *cc* isomer presents the innermost rings of the pentaphenyl system on the same side of the borazine ring. Whereas, in the *ct* atropoisomer, two rings are on the same side of the borazine system, while one is on the opposite.

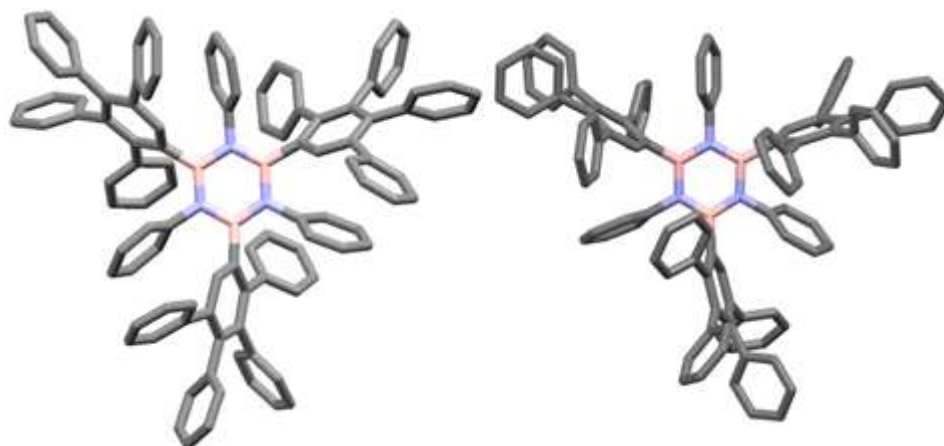


Figure 5.2: Crystal structure for both *cc* and *ct* isomers of **5-4** are reported. Space groups: $P 6_3$ and: $P-1$ respectively. Crystals obtained from slow diffusion of *i*-PrOH in CH_2Br_2 .

To understand the relative ratio between the two isomers a multidimensional NMR analysis was carried out in C_6D_6 . From the ^1H -NMR spectrum of the atropisomeric mixture three singlets are visible at 7.52, 7.45 and 7.32 ppm, integrating for 1, 2 and 0.3 protons, respectively. As the only protons visible as singlets are those on the aryl group bonded on the boron atom (H_{ct} and H_{cc}), it is reasonable to assume that the proton resonances in a 1:2 ratio (at 7.52 and 7.45 ppm) derive from *ct* atropoisomer, whereas the peak at 7.32 ppm is that of the *cc* isomer. To confirm this assignment, ^{13}C -DEPTq, ^1H - ^{13}C HSQC and HMBC were performed. From the HSQC experiment the protons visible at 7.52 and 7.45 ppm correlate with ^{13}C signals at 136.41 and 135.82 ppm, whereas the signal at 7.32 ppm correlates with the carbon atom visible at 135.75 ppm.

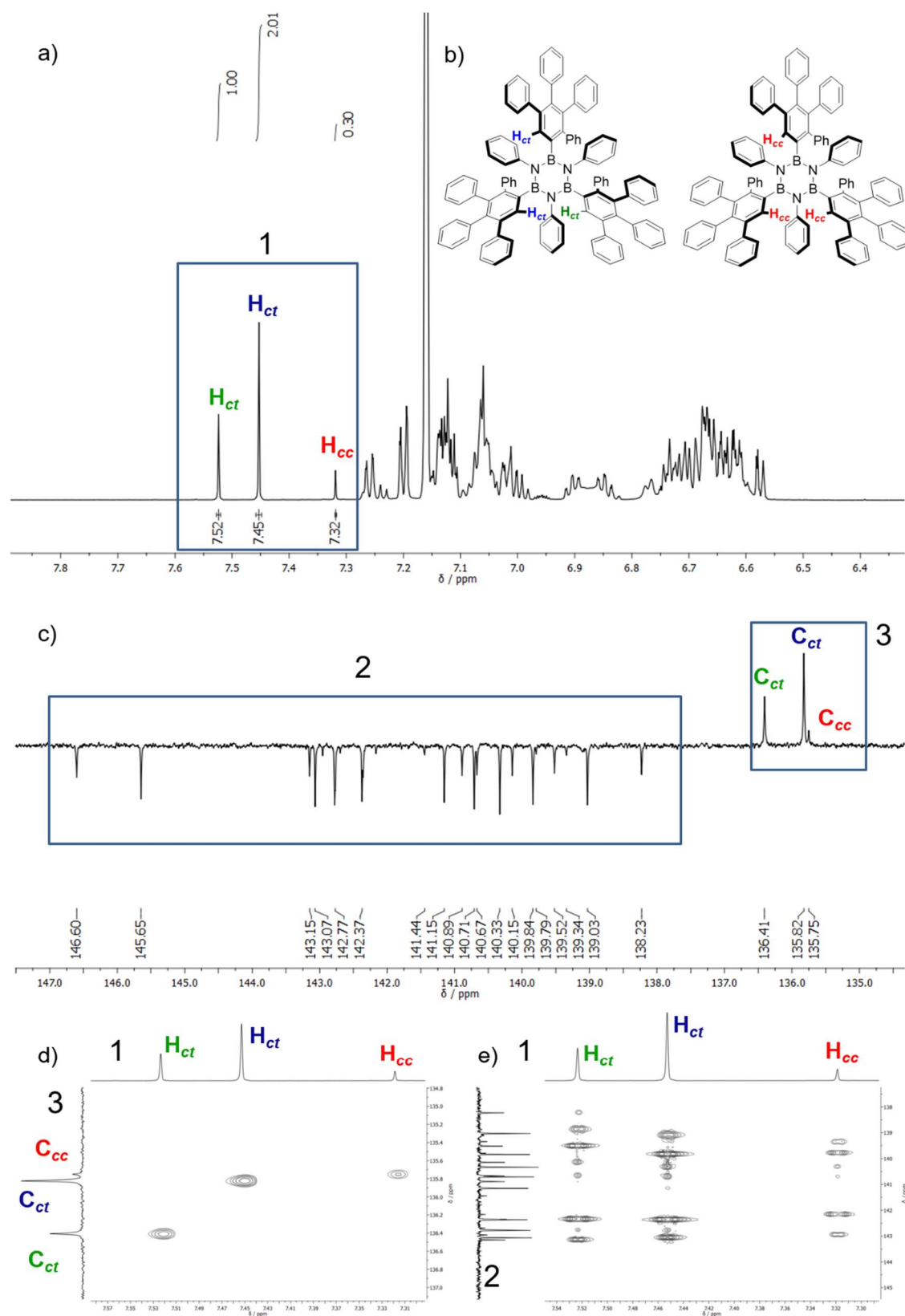


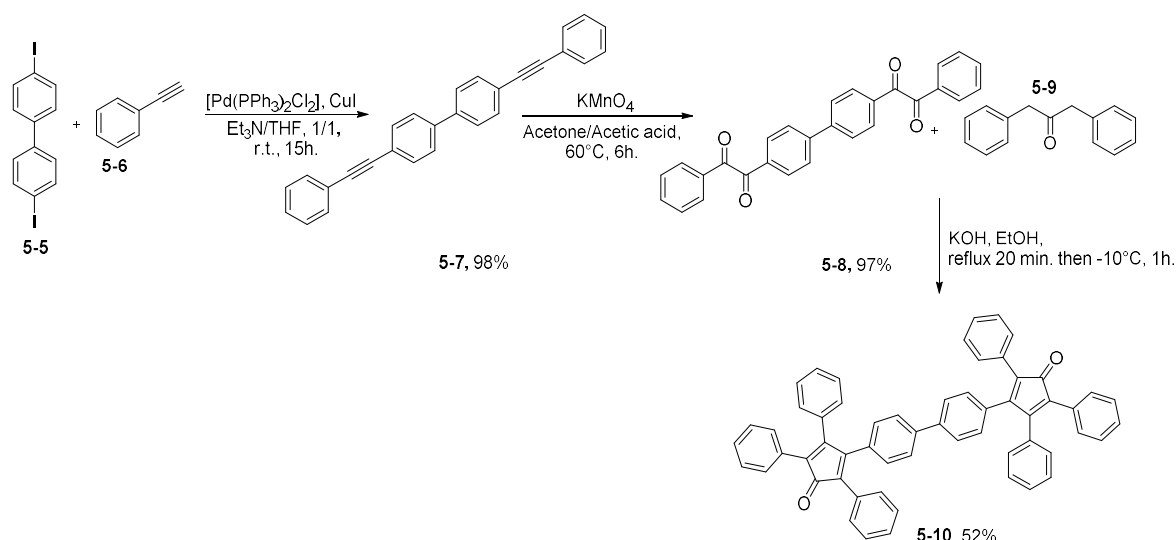
Figure 5.3: a) Zoom of the aromatic signal of 700 MHz ^1H -NMR of **5-4**; b) Chemical structure of atropoisomers *ct* and *cc* of **5-4** with diagnostic protons highlighted; c) 176 MHz ^{13}C DEPTq-NMR of **5-4**; d) Detail of ^1H - ^{13}C HSQC-NMR for protons H_{ct} and H_{cc} ; e) Detail of ^1H - ^{13}C HMBC-NMR for protons H_{ct} and H_{cc} ; All spectra were performed in C_6D_6 .

The DEPTq spectra confirms that these carbons are indeed bonded to protons and not quaternary. The fact that in the HMBC experiment the protons at 7.52, 7.45 and 7.32

ppm correlate only with quaternary carbons confirms the correct assignment for the singlets. In fact, the only protons depicting an exclusive correlation with quaternary carbons are those on the B-aryl ring (Figure 5.3). Since the ratio between integrals of signals at 7.52 and 7.45 ppm is 1:2, these signals must be those related to the *ct* atropoisomer. This result suggests a *ct*:*cc* ratio of ca. 10:1 in the mixture (90% *ct*-atropoisomer. excess).

5.4 Synthesis of Polymer 5-1

To use this novel approach to prepare borazine-doped polyphenylenic polymers, it was necessary to design a new dimeric diene able to induce the polymerization between the ethynyl borazine units. The synthesis of the dimeric diene started with a double Sonogashira coupling of phenylacetylene **5-6** with 4,4'-diiodobiphenyl **5-5** which led to bis alkyne derivative **5-7** in almost quantitative yield.

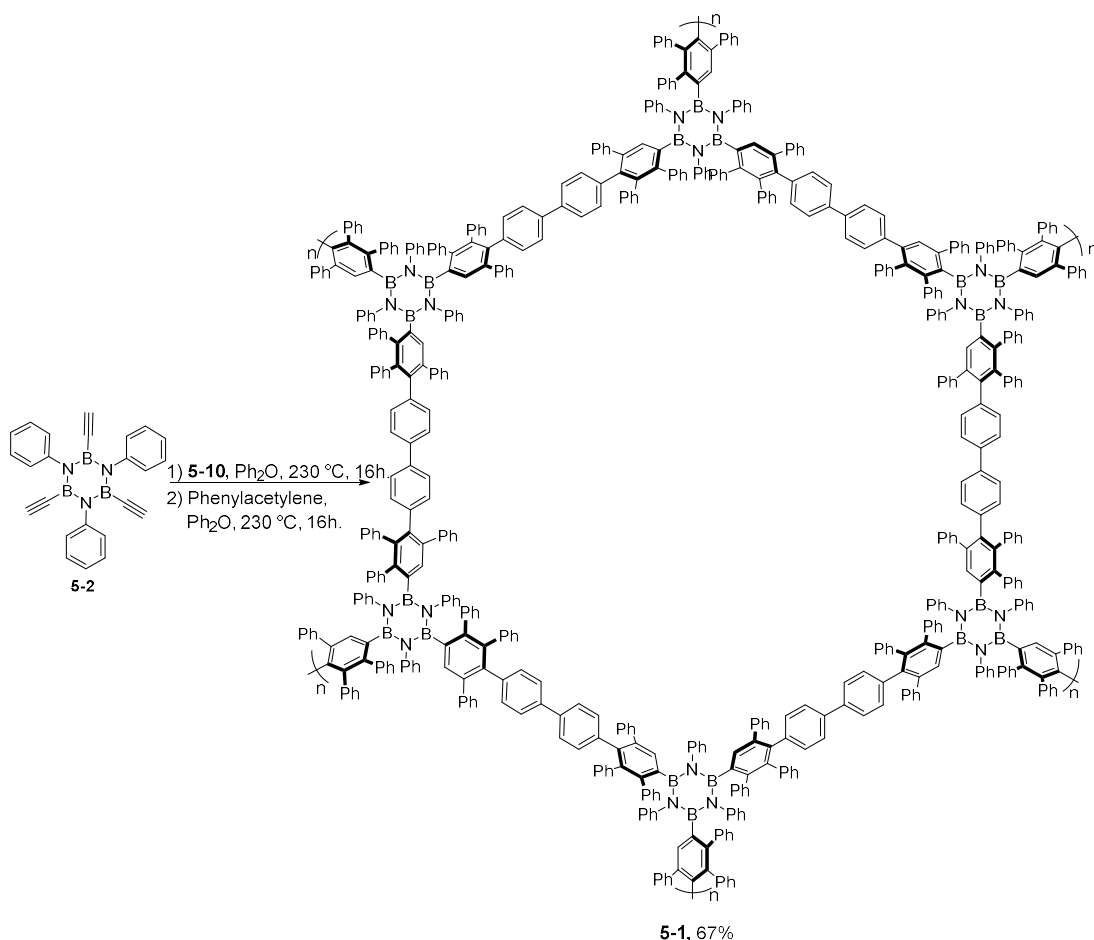


Scheme 5.7: Synthesis of derivative **5-10**.

Oxidation of **5-7** at 60 °C in the presence of KMnO_4 gave tetracarbonyl derivative **5-8** in a 97% yield, which was in turn subjected to an aldolic condensation with **5-9** producing the desired dimeric diene **5-10** in a 52% yield.

The cycloaddition reaction on borazine **5-2** with **5-10** was then performed in degassed Ph_2O at 230 °C and a strong evolution of CO was observed when the reaction mixture reached 220 °C (Scheme 5.8). A red solid material was formed after ca. 3 h, which very interestingly led to the gelification of Ph_2O despite the high temperature conditions (230 °C). After 18 h the reaction mixture was dropped in cold petroleum ether, filtered and subjected to 3 cycles of sonication-centrifugation in petroleum ether/ CH_2Cl_2 mixtures. The resulting reddish material was formed in a 67% yield and reacted with phenylacetylene in dry degassed Ph_2O at 230 °C to end-cap the unreacted

cyclopentadienone units. The resulting pale-yellow solid was precipitated in petrol, filtered, and subjected to various sonication-centrifugation cycles using different solvents (petroleum ether/ CH_2Cl_2 , Acetone, MeOH and Et_2O) giving desired **5-1** quantitatively compared to the previous step (no trace of unreacted cyclopentadienone visible, see following characterisations).



Scheme 5.8: Synthesis of polymer **5-1**.

Due to the insolubility of the product in organic solvents, its characterization was performed by FT-ATR and solid-state NMR techniques. The spectra were compared to those of monomeric unit **5-4**. In particular, ATR-IR analysis (Figure 5.3) evidences similar signals in the spectra in both cases, with the presence of intense peaks at ca. 1355 cm^{-1} and 1321 cm^{-1} assignable to the BN stretching, suggesting the retainment of the borazine core in both materials. Notably for both **5-4** and **5-1** no signals related to C=O bonds are visible implying an effective end-capping reaction. The main difference between the spectra is the presence of a peak ascribable to the stretching of OH moieties (3211 cm^{-1}) in the polymeric material. A possible explanation for this signal could be the presence of trapped MeOH which was used in the purification of the polymer.

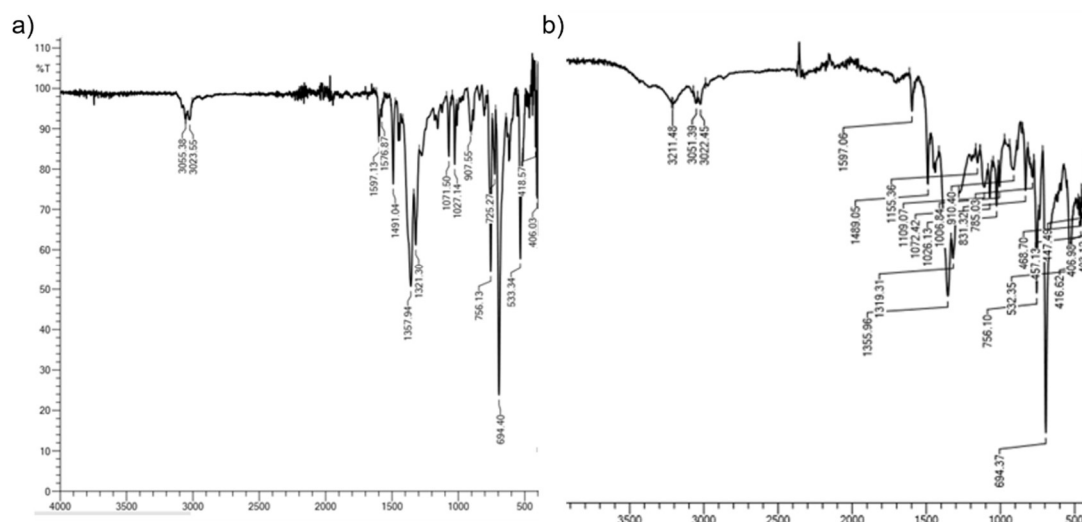


Figure 5.4: a) FT-ATR of monomer **5-4** (mixture of isomers). b) FT-ATR of **5-1**.

This assumption was confirmed by a TGA experiment performed under N_2 , in which a ca. 10% weight loss is occurring at around 100 °C, suggesting that solvent is entrapped within the material. A high thermal stability of the polymer was evidenced by the presence of a second 50% weight loss corresponding to degradation of the polymeric material appearing only above 400 °C and reaching a maximum at 550 °C. This was followed by a final loss of ca. 5% occurring between 650 to 900 °C, which can be linked to more extensive degradation of the organic component. (Figure 5.4).

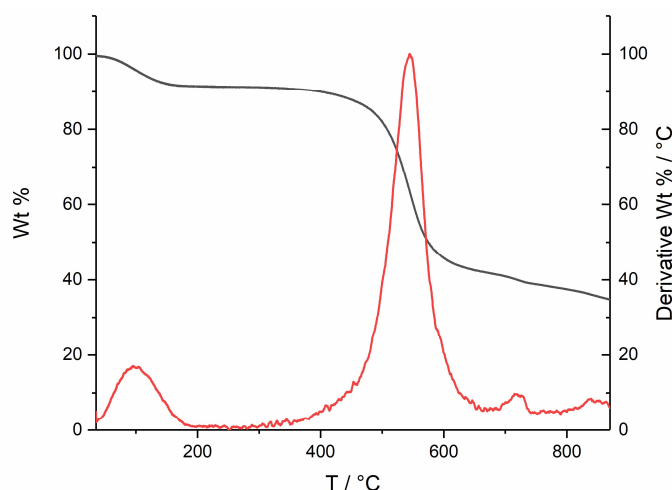


Figure 5.5: TGA trace of BN-Polymer performed under N_2 .

5.5 Solid state NMR studies

The high-resolution solid-state ^{13}C -NMR spectra recorded (using the $^1H \rightarrow ^{13}C$ CPMAS technique) for **5-2**, **5-4** and **5-1** are shown in Figure 5.6a, b and c, respectively. The solid-state ^{13}C -NMR spectrum of **5-2** displays resonances at 84 and 101 ppm and 125 to 150 ppm due to ethynyl and aromatic environments, respectively. The fact that the

peaks due to ethynyl groups are absent from the solid-state ^{13}C -NMR spectra of **5-4** and **5-1** is consistent with complete conversion of starting material **5-2** in the reactions.

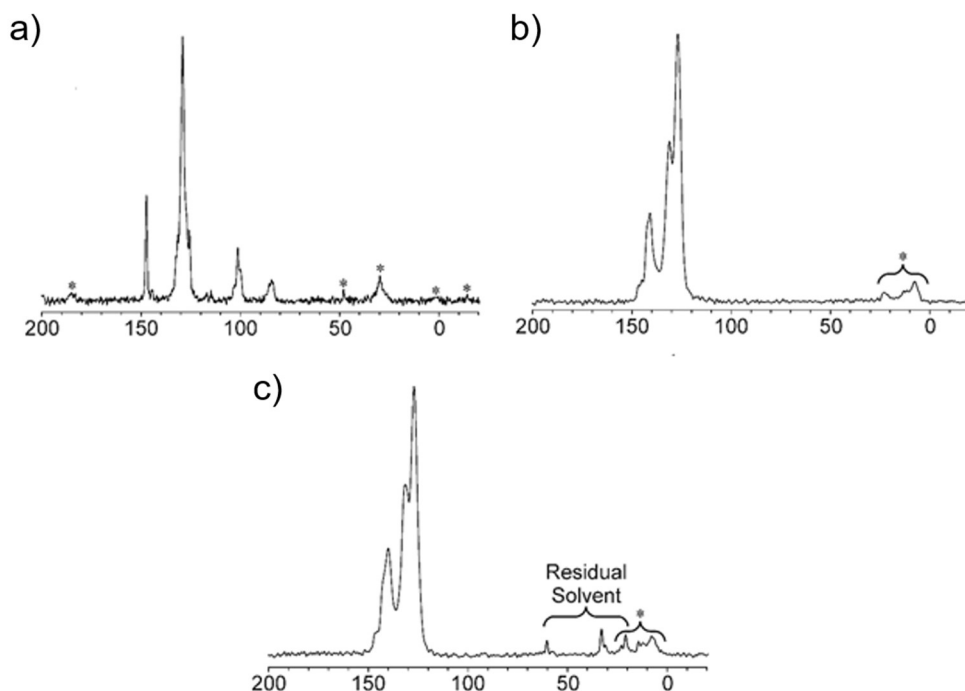


Figure 5.6: 100 MHz $^1\text{H}\rightarrow^{13}\text{C}$ CP MAS NMR spectra recorded for (a) **5-2**, (b) **5-4**, and (c) **5-1**. Peaks marked with asterisks are spinning sidebands.

The solid-state ^{13}C -NMR spectra of **5-4** and **5-1** contain multiple overlapped peaks between 120 and 150 ppm, corresponding to the aromatic ^{13}C environments in these materials. The fact that the ^{13}C -NMR spectra of the monomer and polymer are virtually identical in this region (see the overlay of the spectra in Figure 5.7) strongly suggests that the local structure around the central aromatic ring (including the conformations of the substituents) is very similar in these materials. Low intensity peaks between ca. – 15 ppm and 60 ppm are assigned to residual solvent (sharp low-intensity peaks for the polymer sample MeOH, Acetone or grease) or spinning sidebands, as annotated on the spectra in Figure 5.6.

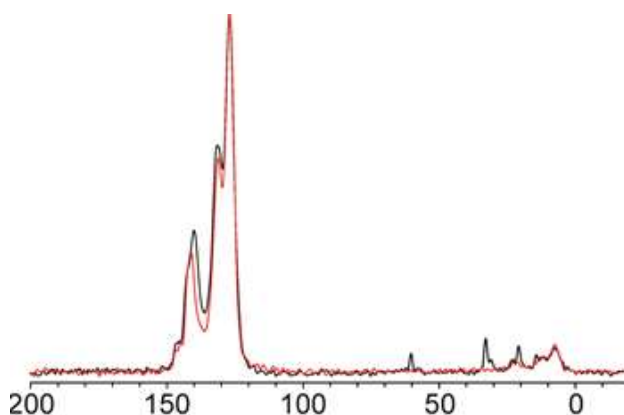


Figure 5.7: Overlay of the 100 MHz $^1\text{H} \rightarrow ^{13}\text{C}$ CPMAS NMR spectra recorded for **5-4** (red) and **5-1** (black).

The sample was then analysed using solid-state ^{11}B MQMAS-NMR. MQMAS is a solid-state 2D NMR experiment used to obtain high resolution spectra of quadrupolar nuclei. This procedure allows the suppression of the dipolar-dipolar interaction and chemical shift anisotropy by using MAS while the use of MQ (multi quantum) coherence allows the disentanglement of quadrupolar and isotropic interactions.^[42] The result is a 2D spectra in which peaks otherwise overlapped (due to the quadrupolar coupling) are separated along the indirect (isotropic) dimension (y axis), whereas the quadrupolar broadening is still present on the direct (anisotropic) one (x axis). The projection of the contours on the indirect dimension is the high-resolution spectra for the atom, allowing the identification of the number of species and relative intensities. The projection on the direct dimension instead corresponds to the spectra presenting the second order quadrupolar interaction, containing information on the quadrupolar coupling constant (Q) and asymmetry of electric field (η) for the quadrupolar atoms (Figure 5.9).

Solid-state ^{11}B MQMAS-NMR spectra recorded for **5-4** and **5-1** are shown in Figure 5.8, and one-dimensional projections of these spectra onto the direct dimension (horizontal in Figure 5.8) are shown in Figure 5.9.

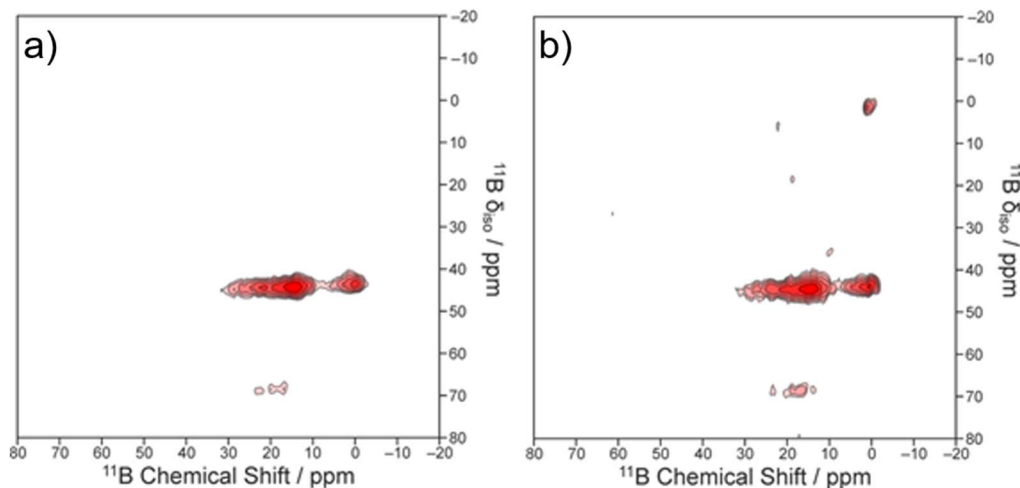


Figure 5.8: 128 MHz ^{11}B MQMAS NMR spectra for (a) **5-4** and (b) **5-1**. The contours are on a logarithmic scale using a factor of 1.3 between adjacent contours.

The projections in Figure 5.9 were obtained from the ^{11}B MQMAS-NMR spectra by summation of all data between 39 and 49 ppm along the indirect dimension (vertical in Figure 5.8). The ^{11}B MQMAS-NMR spectra for both **5-4** and **5-1** contain two broad peaks with shifts in the indirect dimension between 40 and 50 ppm (the peak at 0 ppm in both dimensions in the spectrum of the polymer is a diagonal artefact, which may be ignored).

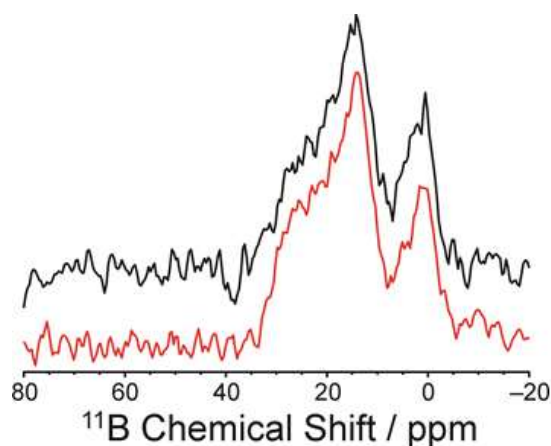


Figure 5.9: Projection of the ^{11}B MQMAS NMR spectra onto the direct dimension (by summation of the data between 39 and 49 ppm along the indirect dimension) for **5-4** (red) and **5-1** (black).

The shapes of the peaks are very similar for the monomer and polymer samples, as clearly evident both from the two-dimensional contour plots in Figure 5.8 and from the projections onto the direct dimension shown in Figure 5.9, indicating that **5-4** and **5-1** have similar values of the quadrupolar parameters and isotropic chemical shifts for the ^{11}B environments. Again, this observation suggests that the local structure in the vicinity of the central B_3N_3 rings (including the conformations of the substituents bonded to the B atoms) is very similar in the monomer and polymer materials.

5.6 PXRD on 5-4 Sample

PXRD data recorded for **5-4** and **5-1** obtained directly from the chemical reaction indicate that both materials are amorphous. In order to gain insights into the stereochemistry of the chemical reaction (for example, to establish whether the spatial distribution of the substituents bonded to the boron atoms of the B_3N_3 rings corresponds to the *cc* isomer, the *ct* isomer, or a mixture of the *cc* and *ct* isomers), sample **5-4** was crystallized from CH_2Br_2 . The structural properties of the bulk crystallized monomer phase were then investigated using pXRD.

Figure 5.10 shows the results from Le Bail fitting^[43] of the pXRD data for the crystallized **5-4** sample, starting from the unit cell of the triclinic form of the monomer determined from SC-XRD data, which contains the *ct* isomer of the monomer as a solvate with CH_2Br_2 . The Le Bail fitting procedure led to a good-quality fit, with final refined unit cell parameters: $a = 12.4760(12) \text{ \AA}$, $b = 16.3471(15) \text{ \AA}$, $c = 21.5362(20) \text{ \AA}$, $\alpha = 71.848(5)^\circ$, $\beta = 88.747(7)^\circ$, $\gamma = 83.658(7)^\circ$, $V = 4147.7(9) \text{ \AA}^3$. The unit cell volume is larger by ca. 0.7% than the unit cell determined for the same material from SC-XRD data (the SC-XRD data collection was carried out 100 K whereas the pXRD data were recorded at 294 K).

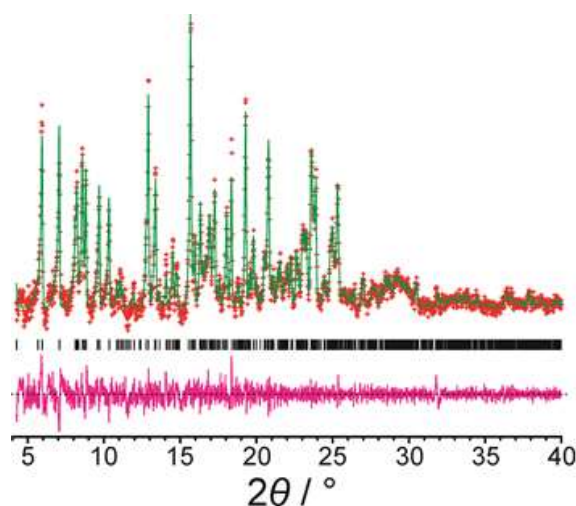


Figure 5.10: Le Bail fitting of the pXRD data (background subtracted) recorded for the crystallized **5-4** sample (red + marks, experimental data; green line, calculated data; magenta line, difference plot; black tick marks, predicted peak positions).

From the good quality of the Le Bail fit (Figure 5.10), we conclude that the only crystalline phase present in the crystallized sample of **5-4** contains the *ct* isomer of the monomer as a solvate with CH_2Br_2 . The minor discrepancies evident in the difference plot in Figure 5.10 may be attributed to small errors in the baseline and line shape, and there is no evidence for the presence of any other crystalline phase (for example, containing the *cc* isomer of the substituted B_3N_3 ring). This result suggests that, accordingly with the NMR results the *cc* isomer is formed only in a low amount compared to the *ct* one (probably less than 10%). Given the very close agreement between the solid-state NMR data (both high-resolution ^{13}C -NMR spectra and ^{11}B MQMAS-NMR spectra) for **5-4** and **5-1** samples, and given that the pXRD study indicates that the crystallized monomer sample contains mainly the *ct* isomer of the substituted B_3N_3 ring, it is a reasonable inference that the polymer sample also contains mainly the *ct* isomer of the substituted B_3N_3 ring.

5.7 Gel formation and rheological studies

As previously mentioned, gelification of Ph_2O occurred at $230\text{ }^\circ\text{C}$ during the cycloaddition polymerization, which suggested that **5-1** could form gels. To assess if the material was able to form gelled systems in solvents different from Ph_2O , **5-1** was suspended in different solvents and swelling, resulting in gel formation, was observed in chlorinated ones. CHCl_3 and CH_2Cl_2 gave the best results with a critical gelification concentration of 4% w/w for CHCl_3 . The rheology of the gel was then studied in CHCl_3 due to the higher boiling point of this solvent which leads to an easier handling and characterization of the material. In order to understand the interactions between the solvent and the polymeric material in the gel, low field NMR (LF-NMR) was performed at three different concentrations (2, 4 and 8% w/w) of **5-1** in CHCl_3 , thus obtaining data

from a sub-gelated system (2%) to a super-gelated one (8%). LF-NMR detects the response of the solvent hydrogen atoms in magnetic fields, focusing on the FID decay, which is related to the spin-spin relaxation time T_2 . Since T_2 not only depends on B_0 intensity and temperature, but also on the presence of solid surfaces (such as those of polymeric chains of a polymeric solution or gel) the values of T_2 for the solvent hydrogens can be used to obtain information on the material. Indeed, solvent hydrogens near the solid surface relax faster than those in the bulk as the surface behaves as magnetization absorber.^[44] Hence, the higher the concentration of “solid” part, the faster the relaxation process is. This, in turn, reflects in a smaller T_2 and a more rapid FID decay. In the case of not homogeneous systems such as gels, where meshes of different size can exist, the average T_2 depends on the relaxation time pertaining to each mesh size. Since the smaller the mesh size, the faster the hydrogens relaxation is, deconvolution of the exponential FID decay signal allows for identification of different T_2 values arising from the various mesh sizes present in the material.

Table 5.1: LF-NMR T_2 times for various concentrations of polymer in CHCl_3 .

	T_{21} (ms)	A_1 (%)	T_{22} (ms)	A_2 (%)	T_{23} (ms)	A_3 (%)	T_{24} (ms)	A_4 (%)
CHCl_3	2531	100						
5-1 2%	2373	81	1350	19				
5-1 4%	1927	73	981	18	108	9		
5-1 8%	1537	51	635	20	133	11	23	17

The results for our system are reported in Table 5.1; as expected, a decrease in T_2 occurs when the polymer concentration increases. More interestingly, when moving from 2% to 8% concentration, an increasing number of relaxation times (T_{2i} numbers) are detected, reflecting a higher heterogeneity of the system network that indicates the existence of meshes of different size (with small T_{2i} times corresponding to small cavity size).

From the rheological point of view, only the 4% w/w gel was analysed by short stress sweep (SSS) and frequency sweep (FS) measures. The two measures are performed on a sample using two metallic plates to apply different shear force at the same frequency (SSS) or a shear force at different frequencies (FS). Short stress sweep tests were performed in the stress (τ) range spanning from 0.33 Pa to 12 Pa at 1 Hz. Then, frequency sweep tests, were performed inside the linear viscoelastic region ($\tau = 1$ Pa), allowing the determination of the systems mechanical spectra (dependence of the elastic (G') and viscous (G'') moduli on pulsation $\omega=2\pi f$) in the frequency range spanning from 0.1 to 10 Hz. Elastic modulus G' is determined by the solid component

in the gelified system, which is able to store mechanical energy and release it when the external mechanical stimulus is removed (returning to the pre-stress situation). Whereas G'' is the viscous component of the system arising from the liquid part of the material, which is dissipative in nature resulting in inelastic behaviour. Gelified systems present a G' modulus \gg of G'' , instead emulsions or dispersions present the opposite behaviour, similar to viscous liquids.^[45] Consequently, the determination of parameters G' and G'' is important to determine the mechanical properties and processability of materials. Moreover, the fitted plots obtained from FS measurements can be used to calculate Shear modulus (G), cross linking (ρ_x) and the mesh size (ξ_{RHEO}) of the material. From SSS measure (Figure 5.11) the presence of an elastic module G' much greater than viscous module G'' was observed confirming the presence of a gelified system for 4% polymer **5-1** in CHCl_3 .

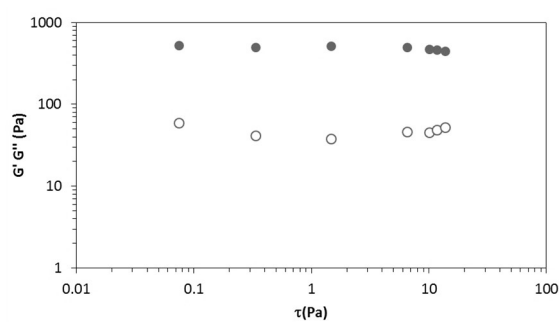


Figure 5.11: SSS plot for 4% w/w gel in CHCl_3 .

FS measure (Figure 5.12c) along with Maxwell best fitting (solid lines) allowed us to estimate the Shear modulus (G), cross linking (ρ_x) and the mesh size (ξ_{RHEO}) of the gel resulting in a G of 667 ± 54 Pa, ρ_x of $2.7 \times 10^{-7} \pm 2.2 \times 10^{-8}$ and ξ_{RHEO} of 23.0 ± 0.6 nm, suggesting that the material has a G comparable with that of a polyacrilamide gel with a low crosslinking percentage.^[46]

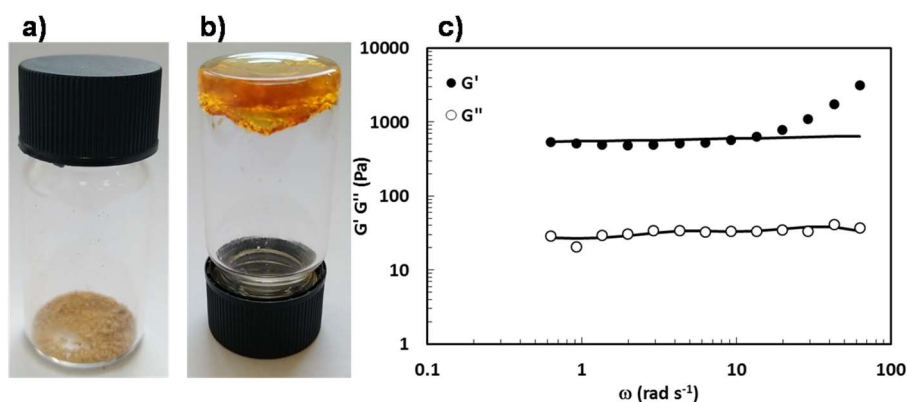


Figure 5.12: a) dry xerogel; b) gel obtained mixing polymer with CHCl_3 ; c) FS plot (dotted line) and Maxwell fitting (solid line) for 4% w/w gel in CHCl_3 .

The mesh size is compatible with that of a mesoporous material, however, the isotherm of N₂ adsorption at 77 K measured on the xerogel indicates a macroporous/non-porous material with a calculated apparent Brunauer-Emmett-Teller (BET) surface area of 62 m²/g. This seems to suggest that probably the polyphenyl structure is folding when dry, whereas when gelified the unfolding of the phenyl groups lead to mesoporous size cavities in the gel.

5.8 BN-Polymer as support in solid state electrolytes (SSE)

5-1/TEGDME (Tetraethylene glycol dimethyl ether)-LiClO₄ based solid state electrolytes were prepared following the process depicted in Figure 5.13 and tested. Polymer **5-1** was first suspended in CH₂Cl₂ (2 mL) under ultra-sonication at 35 °C for 2 h followed by a vigorous stirring at r.t. for 12 h.

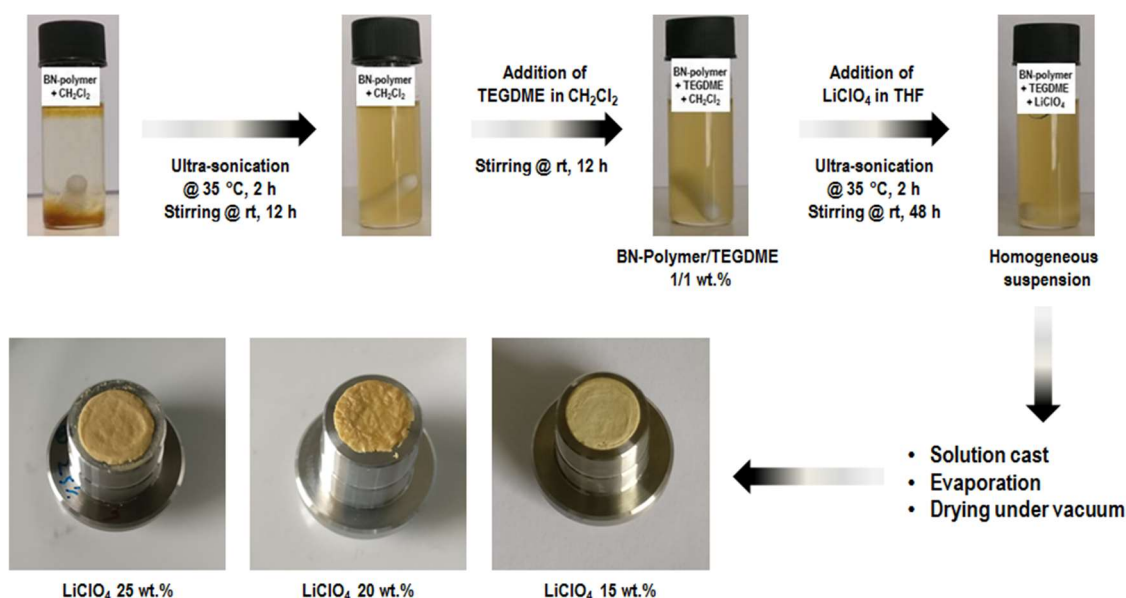


Figure 5.13: Preparation methodology for **5-1**/TEGDME-LiClO₄ based solid state electrolytes.

Then the TEGDME solution in CH₂Cl₂ (0.5 mL) was added and the obtained mixtures stirred at r.t. for 12 h. Finally, the LiClO₄ solutions at different concentrations (15, 20 and 25 wt.%) in THF (0.5 mL) were added to the **5-1**/TEGDME suspensions and ultra-sonicated at 35 °C for 2 h followed by vigorous stirring at r.t. for 48 h, so that homogeneous suspensions were obtained. The solid-state electrolytes were deposited by solution cast on stainless steel discs adapted for Swagelok cells and dried at r.t. for 18 h followed by drying under vacuum at 70 °C for 2 h (Figure 5.13).

The ion transport behaviour of the obtained SSEs was investigated by electrochemical impedance spectroscopy (EIS) at r.t., using TEGDME/15 wt.% LiClO₄ liquid electrolyte as reference (Figure 5.14a and table 5.2). Impedance is a measure of the ability of a circuit to resist the flow of electrical current. This parameter is much more explicative

than resistance for an AC system since it is not limited by the boundaries of an ideal resistor (Ohm law, resistance independent from frequency and AC current voltage signals though resistor in phase with each other).

Measurements of EIS are usually carried out by applying an alternate potential to an electrochemical cell and then measuring the current flow through it. If a sinusoidal potential excitation is applied, the response will be an AC signal. When the excitation signal is small (mV) the response of the cell will be pseudolinear and as a result the AC signal will be a sinusoid of the same frequency but shifted in phase compared to the excitation potential. This allows to define the impedance as a function of a phase shift (Φ) and magnitude (Z_0 defined as ratio between potential and current at $t = 0$).

$$\text{Eq. 1: } Z(\omega) = \frac{E}{I} = Z_0 e^{(j\Phi)} = Z_0 (\cos\Phi + j\sin\Phi)$$

Since impedance $Z(\omega)$ is composed by a real and an imaginary part (Eq. 1) it is possible to plot the real part on the x axis and the imaginary one on the y axis originating a Nyquist plot, in which each point of the graph represents the impedance at one specific frequency.^[47] From this plot, the bulk resistance of the samples can be calculated from the curves allowing for determination of the ionic conductivity (σ) using the following equation:

$$\sigma = \frac{t}{R_b \cdot A}$$

where σ is the ionic conductivity ($\text{S} \cdot \text{cm}^{-1}$), R_b the bulk resistance, t and A are the thickness and the area of the SSE samples, respectively.

Solid electrolytes containing **5-1** showed a decrease in ionic conductivity with increasing salt content, displaying the highest ionic conductivity of $1.51 \times 10^{-5} \text{ S} \cdot \text{cm}^{-1}$ for the sample containing 15 wt.% of LiClO_4 (Figure 5.14b and table 5.2).

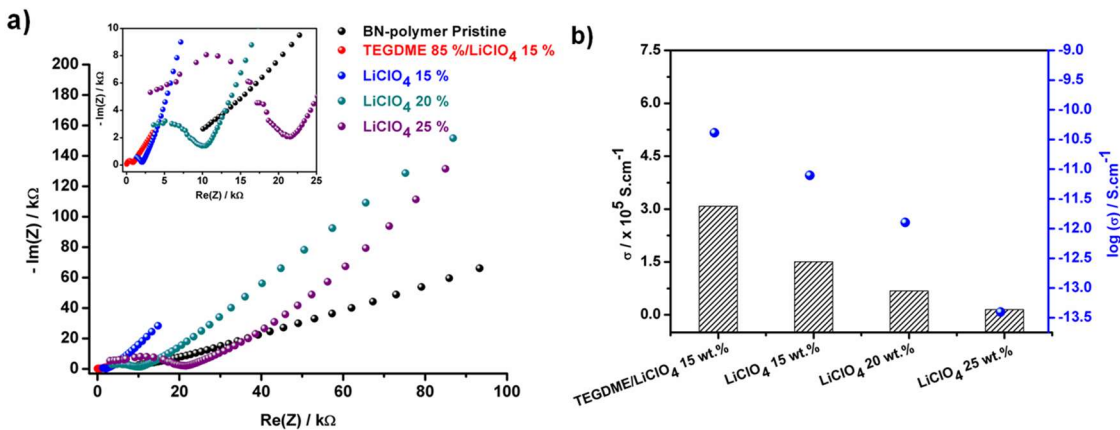


Figure 5.14: a) Nyquist plots of pure **5-1**, TEGDME/15 wt.% LiClO₄ and **5-1**/TEGDME/x wt.% LiClO₄ (x = 15, 20 or 25 wt.% of LiClO₄) at r.t.; b) Ionic conductivity of TEGDME/15 wt.% LiClO₄ reference and **5-1**-based SSEs as a function of LiClO₄ content.

The R_b (resistivity) value increased with increasing lithium salt amount incorporated into **5-1**/TEGDME matrix due to the decrease in the available coordination sites of TEGDME by ion pairing, which is consistent with ether crown ion chelation mechanism.^[48,49] This could be due to a decrease in distance between dissociated ions, enabling the recombination into neutral ion pairs. This in turn leads to the formation of large aggregates of ions which reduces the segmental motion of ethylene oxide sites in the matrix, resulting in a hampering of the polymer motion, essential for fast ion conduction.^[50-54]

Table 5.2: Characteristic properties at r.t. of the prepared SSEs as a function of Lithium salt content.

Sample	wt. %			t[cm]	A[cm ²]	R _b [Ω]	σ[S·cm ⁻¹]
	5-1	TEGDME	LiClO ₄				
0	100	-	-	0.018	1.33	-	-
1	-	85	15	0.02159	1.33	526	3.08×10 ⁻⁵
2	42.5	42.5	15	0.02451	0.79	2060	1.51×10 ⁻⁵
3	40	40	20	0.03	0.79	5580	6.80×10 ⁻⁶
4	37.5	37.5	25	0.036	0.79	20586	1.50×10 ⁻⁶

Since conductivity is influenced by temperature, "σ" was studied as a function of T for pure TEGDME, liquid TEGDME/15 wt.% LiClO₄ and **5-1**/TEGDME/15 wt.% LiClO₄ and the results are reported in the temperature dependent conductivity plots shown in Figure 5.15. The ionic conductivity of **5-1**/TEGDME/15 wt.% LiClO₄ electrolyte increases, up to 2.7 × 10⁻⁴ S·cm⁻¹ at 373 K. Figure 5.15 shows a linear variation of the log (σ) versus 10³/T plots suggesting an Arrhenius type thermally activated process:^[55]

$$\sigma = \sigma_0 e^{-E_a/kT}$$

where σ is the conductivity, E_a, the activation energy associated with conduction, k, the Boltzmann constant, T the temperature, and σ₀ a preexponential term.

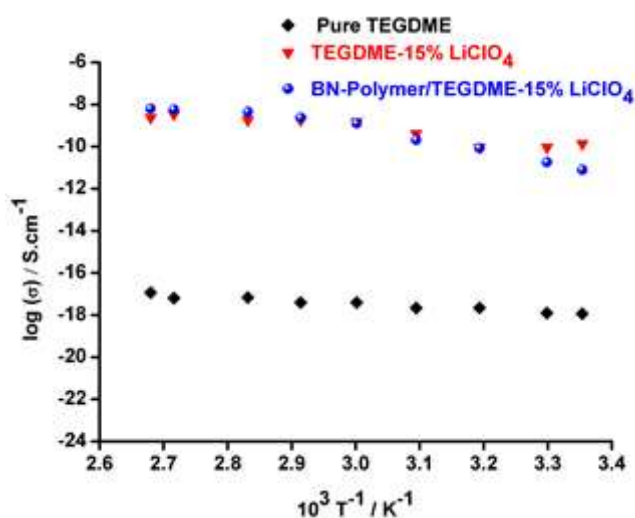


Figure 5.15: Arrhenius plots of ionic conductivity versus reciprocal absolute temperature for pure TEGDME, liquid TEGDME/15 wt.% LiClO₄ and **5-1**/TEGDME/15 wt.% LiClO₄ electrolytes.

At low temperature, the **5-1** based electrolyte exhibits a lower ionic conductivity than the liquid TEGDME/15 % wt. LiClO₄ system. However, it presents a similar behaviour to the liquid TEGDME/15 % wt. LiClO₄ system at high temperatures. The higher conductivity at high temperatures is probably due to the amorphous nature of the polymer which is promoting more free volume in the polymer electrolyte system upon increasing the temperature.^[56,57] In addition, the interaction of Lithium salts with TEGDME helps to weaken the ionic interaction in the salt and thus, the barrier to ion transport is lower and less energy is needed for ion mobility^[58,59]

Table 5.3: Room temperature (25 °C) and 100 °C values of ionic conductivity for the pure TEGDME, liquid TEGDME/15 wt.% LiClO₄, **5-1**/TEGDME/15 wt.% LiClO₄ electrolytes.

Sample	$\sigma/S \cdot \text{cm}^{-1}$ 25 °C	$\sigma/S \cdot \text{cm}^{-1}$ 100 °C
Pure TEGDME	1.62×10^{-8}	4.43×10^{-8}
Liquid TEGDME/15 wt.% LiClO ₄	3.08×10^{-5}	1.18×10^{-4}
5-1 /TEGDME/15 wt.% LiClO ₄	1.51×10^{-5}	2.75×10^{-4}

To investigate how the morphological changes of the **5-1**/TEGDME/LiClO₄ based electrolytes could affect the performances, the films were subjected to scanning electron microscopy (SEM) analysis (Figure 5.16). Pristine **5-1** (see Figure 5.16a) presented a “sponge-like” structure with formation of cavities with an average diameter in the micrometre range (from 1 μm to 20 μm) whereas no pores were visible in **5-1**/TEGDME/LiClO₄ based electrolytes (Figure 5.16b, c, d). For the 15 wt.% LiClO₄ containing sample **5-1**/TEGDME/LiClO₄, the higher conductivity could be attributed to

the relatively homogenous structure, implying a good dispersion of all components in the electrolyte film (Figure 5.16b).

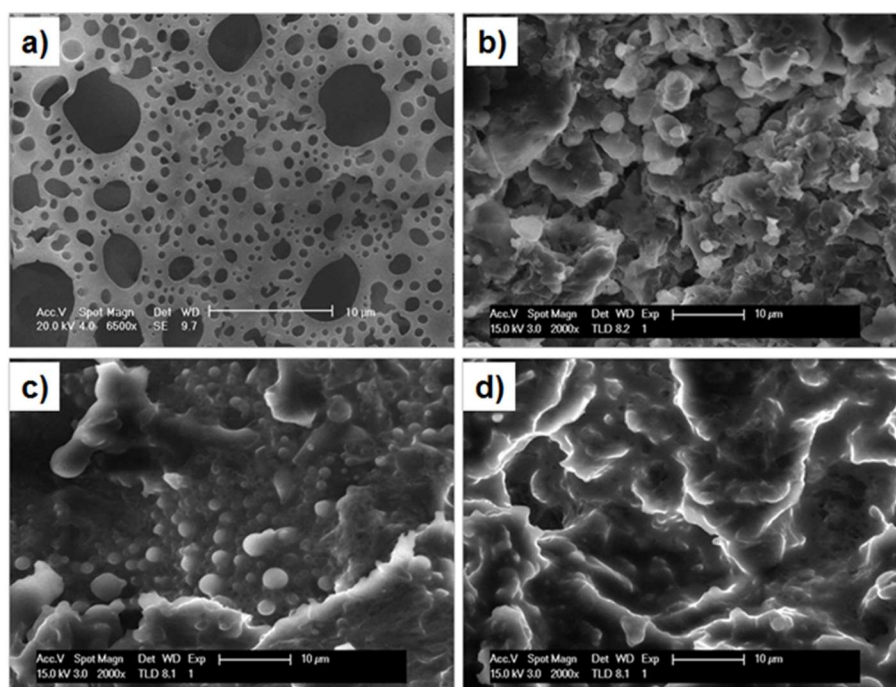


Figure 5.16: SEM images of a) **5-1** pristine and **5-1**/TEGDME/LiClO₄ electrolytes at different wt.% LiClO₄ contents; b) 15 wt.%, c) 20 wt.%, and d) 25 wt.%.

However, the 20 wt.% LiClO₄ sample presents spherical aggregates with an average diameter in the μm range which could be ascribed to the lithium salt not completely dissolving in the polymer matrix (Figure 5.16c). Increasing the amount of the Li salt to 25 wt.% leads to a further decrease in the conductivity of the SSE. This could be attributed to the bigger aggregates formed in the polymer matrix leading to a microstructure that is interspersed with big pores. (Figure 5.16d).

The thermal stability of the obtained **5-1**/TEGDME/LiClO₄ SSEs was studied by TGA, with heating rate of 10 °C/min from r.t. to 1000 °C under N₂ atmosphere, and differential scanning calorimetry (DSC, performed under N₂ flow at a ramp rate of 10 °C/min) on both the single components and the films. As expected, samples of **5-1**/TEGDME/LiClO₄ displayed the same behaviour as the single components (Figure 5.17a). A gradual weight loss of about 5% was observed during the initial heating up to 100 °C, which can be considered as the result of moisture present in the electrolytes. The first significant weight loss (about 45%-55%) is due to the TEGDME evaporation or degradation at 150 °C, followed by a gradual loss of about 5% in the temperature range of 300-450 °C due to LiClO₄. The complete decomposition of the sample takes place between 500 and 600 °C with a weight loss of about 75%, this result is in line with the TGA performed on the pristine **5-1** (Figure 5.5). The DSC thermograms (Figure 5.17b)

obtained for **5-1**/TEGDME/LiClO₄ in the range 30–250 °C showed no endothermic peak associated with a melting temperature. This further demonstrated the amorphous nature of the polymer and the polymer-salt systems. The absence of the temperature of glass transition suggested the high rigidity of **5-1**, possibly related to the blocking of segmental motion which could explain the low conductivity.

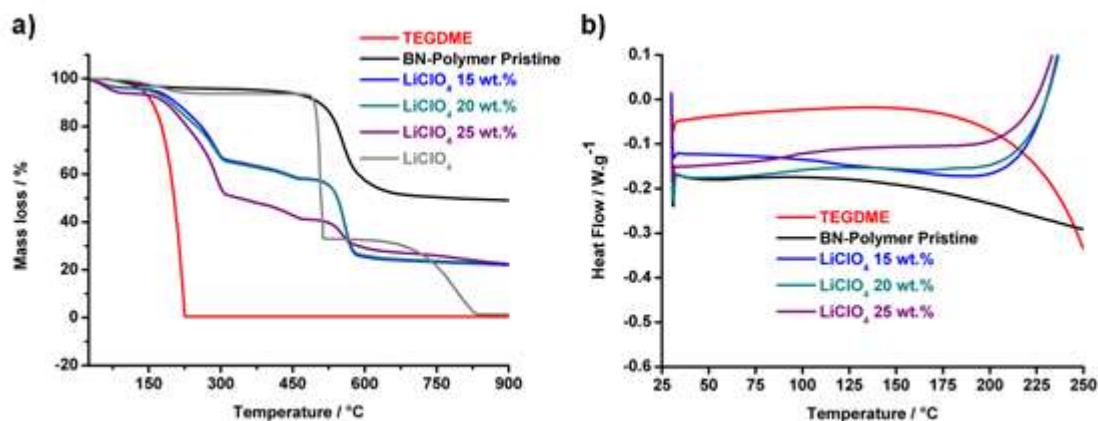


Figure 5.17: a) Thermogravimetric analysis (TGA). b) Differential scanning calorimetry (DSC) thermograms of **5-1**/TEGDME/LiClO₄ based electrolytes.

The electrochemical stability of the highest conducting SSE system was studied as well with linear sweep voltammetry (LSV) and cyclic voltammetry (CV), using stainless steel working electrode and Li metal as reference and counter electrode. The SSE system proved to be electrochemically stable between 1.84 to 3.70 V vs Li/Li⁺ with no decomposition of any of the components in this potential region (Figure 5.18a). CV responses for seven cycles (Figure 5.18b) present redox peaks around 1.55 V and at 3.86 V. No changes in the redox peak voltages were observed during the cycles, furthermore, the overlapping of the sweeps indicates that the charge transfer reaction at the interface between the solid electrolyte and Li metal is reversible. From the CV study the range of electrochemical stability is observed from 2.00 V to 3.60 V which is in very good accordance with LCV results (Figure 5.18a).

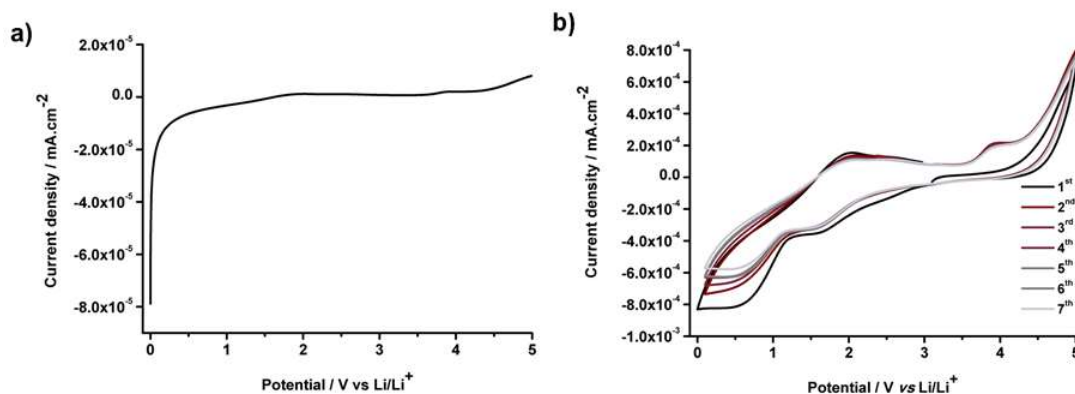


Figure 5.18: a) Linear sweep voltammogram of the **5-1**/TEGDME-15 wt.% LiClO₄ electrolyte at a scan rate of 1.0 mV·s⁻¹ from 0.0 V to 5.0 V at r.t.; b) Cyclic voltammogram of the **5-1**/TEGDME-15 wt.% LiClO₄ electrolyte at a scan rate of 1.0 mV·s⁻¹ in the voltage range of 0.0-5.0 V vs Li/Li⁺ at r.t.

Finally, the Lithium ion transference number (t_{Li^+}) was evaluated following the potentiostatic polarization method. t_{Li^+} describes the relative amount of current transported by the lithium ion compared to the counter ion and is related to the formation of gradients of concentration of the ionic component during operation.^[60] This phenomenon can result in precipitation of dissolved salt at the anode and depletion at cathode especially while operating at high current, possibly resulting in cell failure. High t_{Li^+} values (close to 1) help preventing these effects, resulting in a good high-rate performance and power output from the cell. In our system, the t_{Li^+} measurement was achieved at r.t. by applying a 10 mV DC polarization to a symmetric Li/**5-1**/TEGDME-LiClO₄/Li cell configuration until the current reached a steady state (Figure 5.19). In these conditions, in absence of redox reaction with the anion, the anion current will vanish in the steady state and the total current will be caused by Li⁺ ions. In fact, the initial total current decreased with time from 1.405 μA and reached a steady state value of 0.238 μA after 18 h allowing determination of the t_{Li^+} using the Bruce-Vincent-Evans equation:^[61]

$$t_{Li^+} = \frac{I_s(\Delta V - I_0 R_0)}{I_0(\Delta V - I_s R_s)}$$

where I_0 and I_s are the initial and steady-state currents, R_0 and R_s are the initial and steady-state interfacial resistances and ΔV is the applied polarization voltage.

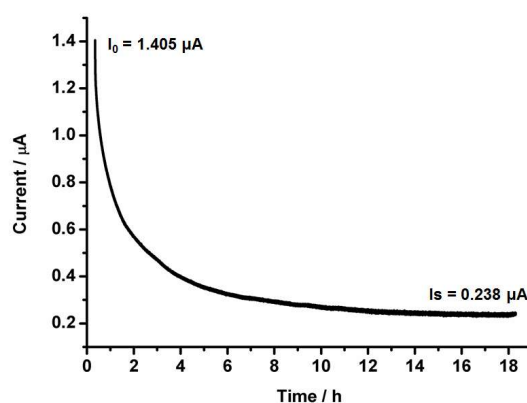


Figure 5.19: Current-time profile of a symmetrical Li/**5-1**/TEGDME/15 wt.% LiClO₄/Li cell configuration after applying a DC voltage of 10 mV on the cell, for determining Li⁺ transfer number.

The interfacial bulk resistance increased from 2260 Ω to 21713 Ω through polarization. From this study it emerged that the **5-1**/TEGDME/15 wt.% LiClO₄ electrolyte presents a

transference number of about 0.2, a value in the range those observed for PEG based electrolytes and in the range of most common solid polymer electrolytes (0.2-0.5).^[60]

5.9 Conclusion

In conclusion a novel BN-doped polymeric material was synthesized using a [4+2] cycloaddition reaction on B,B',B'' triethynyl borazines. The resulting polymer **5-1** was characterized by comparison with monomeric unit **5-4** using solid state ¹³C, ¹¹B-NMR and FT-ATR, allowing the structural determination of **5-1**. The new BN-doped polyphenylenic material formed gels efficiently in chlorinated solvents, producing one of the few examples of a BN-doped gel. From rheological studies it was possible to estimate the shear modulus, the mesh size and the crosslinking in the gel. Due to the high thermal and chemical stability, the polymer was tested for use as a support component in SSE for lithium ion batteries. In particular, the SSE with **5-1**/TEGDME/15 wt.% LiClO₄ composition, presented an *Arrhenius* behaviour and a r.t. ionic conductivity of $1.51 \times 10^{-5} \text{ S} \cdot \text{cm}^{-1}$ with a Li⁺ transference number of about 0.2 comparable with PEG based electrolytes. Furthermore, the σ value increased with T, suggesting an enhanced performance of the 15 wt.% SSE at higher temperatures. This very interesting result represents a steppingstone towards future possible applications of borazine-doped polyphenylenic materials in the field of lithium ion batteries.

5.10 References

- [1] B. A. G. Hammer, K. Müllen, *Chem. Rev.* **2016**, *116*, 2103–21040.
- [2] K. Müllen, *ACS Nano* **2014**, *8*, 6531–6541.
- [3] A. Narita, X. Feng, K. Müllen, *Chem. Rec.* **2015**, *15*, 295–309.
- [4] C. D. Simpson, G. Mattersteig, K. Martin, L. Gherghel, R. E. Bauer, H. J. Räder, K. Müllen, *J. Am. Chem. Soc.* **2004**, *126*, 3139–3147.
- [5] T. Weil, E. Reuther, K. Müllen, *Angew. Chemie - Int. Ed.* **2002**, *41*, 1900–1904.
- [6] L. Chen, Y. Honsho, S. Seki, D. Jiang, *J. Am. Chem. Soc.* **2010**, *132*, 6742–6748.
- [7] D. Liu, S. De Feyter, M. Cotlet, A. Stefan, U. M. Wiesler, A. Herrmann, D. Grebel-Koehler, J. Qu, K. Müllen, F. C. De Schryver, *Macromolecules* **2003**, *36*, 5918–5925.
- [8] M. Adamski, T. J. G. Skalski, B. Britton, T. J. Peckham, L. Metzler, S. Holdcroft, *Angew. Chem. Int. Ed* **2017**, *6*, 9186–9189.
- [9] J. Miyake, R. Taki, T. Mochizuki, R. Shimizu, R. Akiyama, M. Uchida, K. Miyatake, *Sci. Adv.* **2017**, *3*, 1–8.
- [10] C. Li, M. Liu, N. G. Pschirer, M. Baumgarten, K. Müllen, *Chem. Rev.* **2010**, *110*, 6817–6855.

- [11] Y. Huang, Y. Mai, X. Yang, U. Beser, J. Liu, F. Zhang, D. Yan, K. Müllen, X. Feng, *J. Am. Chem. Soc.* **2015**, *137*, 11602–11605.
- [12] D. Bonifazi, F. Fasano, M. M. Lorenzo-Garcia, D. Marinelli, H. Oubaha, J. Tasseroul, *Chem. Commun.* **2015**, *51*, 15222–15236.
- [13] H. Helten, *Chem. Eur. J.* **2016**, *22*, 12972–12982.
- [14] B. A. G. Hammer, Y. Wu, S. Fischer, W. Liu, T. Weil, K. Müllen, *ChemBioChem* **2017**, *18*, 960–964.
- [15] H. John, R. Bauer, P. Espindola, P. Sonar, J. Heinze, K. Müllen, *Angew. Chemie - Int. Ed.* **2005**, *44*, 2447–2451.
- [16] W. M. Wan, A. W. Baggett, F. Cheng, H. Lin, S. Y. Liu, F. Jäkle, *Chem. Commun.* **2016**, *52*, 13616–13619.
- [17] I. C. Y. Hou, Y. Hu, A. Narita, K. Müllen, *Polym. J.* **2018**, *50*, 3–20.
- [18] M. Côté, P. D. Haynes, C. Molteni, *Phys. Rev. B* **2001**, *63*, 125207–125207.
- [19] X. Y. Wang, J. Y. Wang, J. Pei, *Chem. Eur. J.* **2015**, *21*, 3528–3539.
- [20] J. Dosso, D. Marinelli, N. Demitri, D. Bonifazi, *ACS Omega* **2019**, *4*, 9343–9351.
- [21] D. Marinelli, F. Fasano, B. Najjari, N. Demitri, D. Bonifazi, *J. Am. Chem. Soc.* **2017**, *139*, 5503–5519.
- [22] S. Bagheri, H. R. Masoodi, *Chem. Phys. Lett.* **2015**, *629*, 46–52.
- [23] S. Behera, K. T. Jackson, H. M. El-Kaderi, T. E. Reich, P. Jena, *J. Mater. Chem.* **2012**, *22*, 13524–13528.
- [24] T. E. Reich, K. T. Jackson, S. Li, P. Jena, H. M. El-Kaderi, *J. Mater. Chem.* **2011**, *21*, 10629–10632.
- [25] M. A. Mehta, T. Fujinami, *Chem. Lett.* **1997**, *26*, 915–916.
- [26] M. A. Mehta, T. Fujinami, Y. Yang, T. Inoue, *J. Appl. Polym. Sci.* **2002**, *84*, 17–21.
- [27] R. Tao, T. Fujinami, *J. Appl. Electrochem.* **2005**, *35*, 163–168.
- [28] R. Islas, E. Chamorro, J. Robles, T. Heine, J. C. Santos, G. Merino, *Struct. Chem.* **2007**, *18*, 833–839.
- [29] K. Nagasawa, *Inorg. Chem.* **1966**, *5*, 442–445.
- [30] K. T. Jackson, T. E. Reich, H. M. El-Kaderi, *Chem. Commun.* **2012**, *48*, 8823–8825.
- [31] N. A. Riensch, A. Deniz, S. Köhl, L. Müller, A. Adams, A. Pich, H. Helten, *Polym. Chem.* **2017**, *8*, 5264–5268.
- [32] G. Hizal, U. Tunca, A. Sanyal, *J. Polym. Sci.* **2011**, *49*, 4103–4120.
- [33] U. M. Wiesler, A. J. Berresheim, F. Morgenroth, G. Lieser, K. Müllen, *Macromolecules* **2001**, *34*, 187–199.
- [34] H. Watanabe, T. Totani, T. Yoshizaki, *Inorg. Chem.* **1965**, *4*, 657–660.

- [35] Y. Uchimaru, N. Koda, H. Yamashita, *Phosphorus, Sulfur, and Silicon* **2001**, *169*, 231–234.
- [36] L. Craciun, D. M. Ho, M. Jones, R. A. Pascal, *Tetrahedron Lett.* **2004**, *45*, 4985–4987.
- [37] J. E. Moore, M. York, J. P. A. Harrity, *Synlett* **2005**, 860–862.
- [38] J. D. Kirkham, A. G. Leach, E. C. Row, J. P. A. Harrity, *Synthesis* **2012**, *44*, 1964–1973.
- [39] P. M. Delaney, J. E. Moore, J. P. A. Harrity, *Chem. Commun.* **2006**, 3323–3325.
- [40] S. J. Groszos, S. F. Stafiej, *J. Am. Chem. Soc.* **1958**, *80*, 1357–1360.
- [41] A. Wakamiya, T. Ide, S. Yamaguchi, *J. Am. Chem. Soc.* **2005**, *127*, 14859–14866.
- [42] K. Chen, *Int. J. Mol. Sci.* **2020**, *21*, 5666.
- [43] A. Le Bail, H. Duroy, J. L. Fourquet, *Mater. Res. Bull.* **1988**, *23*, 447–452.
- [44] K. R. Brownstein, C. E. Tarr, *Phys. Rev. A* **1979**, *19*, 2446–2453.
- [45] C. Yan, D. J. Pochan, *Chem. Soc. Rev.* **2010**, *39*, 3528–3540.
- [46] C. M. Perrault, D. Juncker, H. E. Park, *AIP Conf. Proc.* **2008**, *1027*, 615–617.
- [47] A. Sacco, *Renew. Sustain. Energy Rev.* **2017**, *79*, 814–829.
- [48] A. M. Stephan, *Eur. Polym. J.* **2006**, *42*, 21–42.
- [49] S. Moins, J. C. Martins, A. Krumpmann, V. Lemaur, J. Cornil, N. Delbosc, A. Decroly, P. Dubois, R. Lazzaroni, J. F. Gohy, et al., *Chem. Commun.* **2017**, *53*, 6899–6902.
- [50] P. H. Huh, M. G. Choi, J. J. Nam, J. K. Lee, J. O. Lee, W. Yang, *Macromol. Res.* **2004**, *12*, 422–426.
- [51] L. C. Rodrigues, P. C. Barbosa, M. M. Silva, M. J. Smith, *Electrochim. Acta* **2007**, *53*, 1427–1431.
- [52] N. A. Stolwijk, C. Heddier, M. Reschke, M. Wiencierz, J. Bokeloh, G. Wilde, *Macromolecules* **2013**, *46*, 8580–8588.
- [53] S. Terada, T. Mandai, S. Suzuki, S. Tsuzuki, K. Watanabe, Y. Kamei, K. Ueno, K. Dokko, M. Watanabe, *J. Phys. Chem. C* **2016**, *120*, 1353–1365.
- [54] N. K. Karan, O. K. Pradhan, R. Thomas, B. Natesan, R. S. Katiyar, *Solid State Ionics* **2008**, *179*, 689–696.
- [55] P. Yang, L. Liu, L. Li, J. Hou, Y. Xu, X. Ren, M. An, N. Li, *Electrochim. Acta* **2014**, *115*, 454–460.
- [56] M. S. Michael, M. M. E. Jacob, S. R. S. Prabakaran, S. Radhakrishna, *Solid State Ionics* **1997**, *98*, 167–174.
- [57] S. G. Rathod, R. F. Bhajantri, V. Ravindrachary, P. K. Pujari, G. K. Nagaraja, J. Naik, V. Hebbar, H. Chandrappa, *Bull. Mater. Sci.* **2015**, *38*, 1213–1221.
- [58] T. S. R. Naiwi, M. M. Aung, A. Ahmad, M. Rayung, M. S. Su'ait, N. A. Yusof, K.

- Z. W. Lae, *Polymers*. **2018**, *10*, 1142.
- [59] L. Carbone, M. Gobet, J. Peng, M. Devany, B. Scrosati, S. Greenbaum, J. Hassoun, *J. Power Sources* **2015**, *299*, 460–464.
- [60] D. Dong, H. Zhang, B. Zhou, Y. Sun, H. Zhang, M. Cao, J. Li, H. Zhou, H. Qian, Z. Lin, et al., *Chem. Commun.* **2019**, *55*, 1458–1461.
- [61] S. Zugmann, M. Fleischmann, M. Amereller, R. M. Gschwind, H. D. Wiemhöfer, H. J. Gores, *Electrochim. Acta* **2011**, *56*, 3926–3933.

CHAPTER 6

EXPERIMENTAL PART

6.1 Instrumentation

Thin layer chromatography (TLC): was conducted on pre-coated aluminium sheets with 0.20 mm Merk Millipore Silica gel 60 with fluorescent indicator F254. **Column chromatography:** was carried out using Merck Gerduran silica gel 60 (particle size 40-63 μm). **Preparative thin layer chromatography** was conducted on UNIPLATE™ analtech silica gel GF TLC plates glass-backed 20 × 20 cm 1500 μm . **Melting points (mp):** were measured on a Gallenkamp apparatus in open capillary tubes and have not been corrected. **Nuclear magnetic resonance (NMR):** spectra were recorded on a Bruker Fourier 300 MHz spectrometer equipped with a dual (^{13}C , ^1H) probe, a Bruker AVANCE III HD 400MHz NMR spectrometer equipped with a Broadband multinuclear (BBFO) SmartProbe™ or a Bruker AVANCE III HD 500MHz Spectrometer equipped with Broadband multinuclear (BBO) Prodigy CryoProbe. ^1H spectra were obtained at 500, 400 or 300 MHz, ^{13}C spectra were obtained at 125, 100 or 75 MHz, ^{19}F spectra were obtained at 376 or 470 MHz and ^{11}B were obtained at 128 MHz or 160 MHz. All spectra were obtained at r.t. if not otherwise stated. Chemical shifts were reported in ppm according to tetramethylsilane using the solvent residual signal as an internal reference (CDCl_3 : $\delta_{\text{H}} = 7.26$ ppm, $\delta_{\text{C}} = 77.16$ ppm; CD_2Cl_2 : $\delta_{\text{H}} = 5.32$, $\delta_{\text{C}} = 54.00$; $\text{DMSO-}d_6$: $\delta_{\text{H}} = 2.50$ ppm, $\delta_{\text{C}} = 39.52$ ppm; CD_3OD : $\delta_{\text{H}} = 3.31$ ppm, $\delta_{\text{C}} = 49.00$ ppm; $\text{Acetone-}d_6$: $\delta_{\text{H}} = 2.05$ ppm, $\delta_{\text{C}} = 29.85$, 206.26 ppm, C_6D_6 : $\delta_{\text{H}} = 7.16$ ppm, $\delta_{\text{C}} = 128.06$ ppm). Coupling constants (J) were given in Hz. Resonance multiplicity was described as s (singlet), d (doublet), t (triplet), dd (doublet of doublets), dt (doublet of triplets), td (triplet of doublets), q (quartet), m (multiplet) and bs (broad signal). Carbon, boron and fluorine spectra were acquired with a complete decoupling for the proton. NMR spectra of monomer **5-4** were recorded at the NMR centre of the Faculty of Chemistry, University of Vienna, on a Bruker AV III HD 700 MHz NMR spectrometer (Bruker BioSpin, Rheinstetten, Germany). The instrument is equipped with a quadruple (^1H , ^{13}C , ^{15}N , ^{19}F) inverse helium cooled cryo probe operating at 700.40 MHz for ^1H , and 176.12 MHz for ^{13}C , respectively. The spectra were acquired at a temperature of 25° C in C_6D_6 as solvent. For all 1D and 2D NMR experiments the appropriate pulse sequences were used as supplied by the manufacturer, e.g. for ^{13}C spectra a DEPTq sequence with a 135° pulse for multiplicity selection, for heteronuclear correlation spectra gradient selected HSQC and HMBC experiments. **Solid state NMR:** Solid-state $^1\text{H} \rightarrow ^{13}\text{C}$ CPMAS NMR and ^{11}B MQMAS NMR spectra were recorded on a Bruker

Avance III HD spectrometer at 9.4 T [Larmor frequencies: 400.2 MHz (^1H), 100.6 MHz (^{13}C), 128.4 MHz (^{11}B)]. Magic-angle spinning was carried out at 12 kHz for the monomer and polymer samples and at 10 kHz for the starting material. $^1\text{H} \rightarrow ^{13}\text{C}$ CPMAS NMR spectra were acquired using ramped CP.^[1] ^{11}B MQMAS NMR spectra were recorded using a four-pulse split- t_1 sequence^[2] with the indirect dimension scaled to have the same contribution from the isotropic shift as the direct dimension.^[3]

Infrared spectra (IR): were recorded on a Shimadzu IR Affinity 1S FTIR spectrometer in ATR mode with a diamond mono-crystal. **Mass spectrometry:** (i) High-resolution ESI mass spectra (HR-MS) were performed on a Waters LCT HR TOF mass spectrometer in the positive or negative ion mode. (ii) High-resolution MALDI mass spectra (HR-MS) was performed on a Bruker Autoflex speed MALDI-TOF. The sample was prepared with a 1:1 ratio of sample to the matrix DCTB (15 mg/mL) in CH_2Cl_2 , all these analyses were carried out at Cardiff university. **Irradiation equipment:** Photochemical reactions were performed in a LZC-ICH2 Luzchem[®] equipped with 8 LZC-UVA lamps centred at approx. 350 nm (8 Watt). **Photophysical analysis:** Absorption spectra were recorded on air equilibrated solutions at room temperature with an Agilent Cary 5000 UV-Vis spectrophotometer, using quartz cells with path length of 1.0 cm. Emission spectra were recorded on an Agilent Cary Eclipse fluorescence spectrofluorometer. Emission lifetime measurements were performed on a JobinYvon-Horiba FluoroHub single photon counting module, using Nano-LED pulsed sources at 372 nm. **Electrochemical measurements:** Cyclic voltammetry (CV) measures were carried out at room temperature in N_2 purged dry CH_2Cl_2 with an AUTOLAB PGSTAT 204. Glassy carbon electrode with a 3 mm diameter has been used as a working electrode, an Ag wire as a pseudo-reference electrode (AgQRE) and a Pt spiral as a counter electrode. Working electrode and AgQRE electrodes were polished on a felt pad with 0.05 or 0.3 μm alumina suspension and then sonicated in deionized H_2O for few minutes before each experiment: the Pt wire was flame-cleaned. Tetrabutylammonium hexafluorophosphate (TBAPF_6) has been exploited as a supporting electrolyte at a concentration around 0.1 M. Ferrocene (Fc) and Decamethylferrocene (FcMe_{10}) have been added as internal reference: $E^{1/2}(\text{Fc}^{+/0}) = 0.46 \text{ V vs SCE in } \text{CH}_2\text{Cl}_2$; $E^{1/2}(\text{FcMe}_{10}^{+/0}) = -0.072 \text{ V vs SCE in } \text{CH}_2\text{Cl}_2$. HOMO and LUMO energies were calculated from the first formal redox potentials (half-wave potentials) using equations (1) and (2):

$$E(\text{HOMO}) = - (5.1 \text{ eV} + E^{1/2}_{\text{ox.1}} \text{ vs Fc}^{+/0}) \quad (1)$$

$$E(\text{LUMO}) = - (5.1 \text{ eV} + E^{1/2}_{\text{red.1}} \text{ vs Fc}^{+/0}) \quad (2)$$

Or

$$E(\text{HOMO}) = -(4.8 \text{ eV} + E^{1/2}_{\text{ox}} \text{ vs Fc}^+/\text{Fc}) \quad (3)$$

$$E(\text{LUMO}) = -(4.8 \text{ eV} + E^{1/2}_{\text{red}} \text{ vs Fc}^+/\text{Fc}) \quad (4)$$

When oxidation or reduction waves were not detected by means of cyclic voltammetry, HOMO or LUMO levels have been calculated using the optical gap ΔE_{0-0} , considering the lowest energy crossing point between normalized absorption and emission spectra $\text{eV} = 1240.5(\text{eV}\cdot\text{nm})/\lambda_{\text{cross}}(\text{nm})$. **Theoretical Calculations:** All the calculations were performed using Gaussian09 including the D.01 revision.^[4] Geometry optimizations and frontier orbitals calculations were carried out in vacuum at the B3LYP/6-31+G** level of theory. When possible, the resolved crystal structure was used as a starting geometry for the optimization. NICS surfaces were calculated using a flat array of ghost atoms separated by 0.1 Å placed 1 Å over the molecular plane and plotted using Originlab 2019b. ESP surfaces were mapped on the van der Waals surface of molecules up to electron density of 0.05 electron/bohr³ and plotted using Gaussianview4. ACID surfaces were calculated using the script kindly provided by the Herges Group^[5] and plotted using POV-Ray software. **Mechanism studies:** Density functional theory calculations were performed using Gaussian 09.^[4] Structures were optimised without geometrical constraints using the B3LYP hybrid functional^[6] with a 6-31(d,p) basis set on all centres.^[7] Solvent (THF) was incorporated using the polarised continuum model, in which the molecular cavity defined by the united atom model that incorporates hydrogen into the parent heavy atom.^[8] Geometry optimisations were followed by frequency calculations to ascertain the nature of the stationary points; none of the structures contained imaginary frequencies. NBO calculations were performed using NBO 6.0, invoked *via* the Gaussian 09 program interface.^[9] **Recycling Gel Permeation Chromatography (GPC):** was performed on a LC-9110G NEXT system equipped with JAIGEL 2HH and 2.5HH columns and a FC-3310 collector. **Multi-borazine oligomeric fraction GPC:** performed at university of Warwick, Polymer Characterization Research Technology Platform, Gibbet Hill Road, Coventry. CV4 7AL. All SEC data was recorded on an Agilent Infinity II MDS instrument equipped with a differential refractive index (DRi), dual angle light scatter (LS) and viscometry (VS) detectors. The system was equipped with 2 × PL gel Mixed C columns (300 × 7.5 mm) and a PL gel 5 µm guard column. The mobile phase was CHCl₃ stabilized with 2 % TEA (triethylamine) and run at a flow rate of 1 mL min⁻¹ at 30 °C. Agilent poly(methylmethacrylate) (PMMA) EasiVials were used to create a third order calibration from DRi data between: 1,568,000 and 550 g mol⁻¹. **LF-NMR:** LF-NMR characterization was performed at 20 °C by means of a Bruker Minispec mq20 (0.47 T, Germany). The determination of the average water protons transverse (spin-spin) relaxation time (T_{2m}) was performed according to the CPMG sequence (Carr–Purcell–Meiboom–Gill)^[10] $\{90^\circ[-\tau-180^\circ-$

$\tau(\text{echo})\}n\text{-TR}$ with a 8.36 μs wide 90° pulse, $\tau = 250 \mu\text{s}$, and TR (sequences repetition rate) equal to 5 s. **Rheology measures:** were performed by a stress controlled rotational rheometer (Haake Mars Rheometer, 379-0200 Thermo Electron GmbH, Karlsruhe, Germany) equipped by parallel plate geometry (PP35, $\phi = 35 \text{ mm}$, serrated surfaces to avoid slippage at the wall). The measuring device was kept at 10°C inside a glass bell at saturated conditions to avoid evaporation effects. To evaluate the extension of the linear viscoelastic range, oscillatory stress sweep tests were performed in the stress (τ) range spanning from 0.33 Pa to 12 Pa at 1 Hz. Then, frequency sweep tests, performed inside the linear viscoelastic region ($\tau = 1 \text{ Pa}$), allowed the determination of the systems mechanical spectra (dependence of the elastic (G') and viscous (G'') moduli on pulsation $\omega=2\pi f$) in the frequency range spanning from 0.1 to 10 Hz. The generalized Maxwell model^[11] was used to fit the experimental mechanical spectra in order to determine the shear modulus G given by the sum of the elastic spring constants (g_i) of all the Maxwell elements^[12]:

$$G' = \sum_{i=1}^n g_i \frac{(\lambda_i \omega)^2}{1 + (\lambda_i \omega)^2} \quad (5)$$

$$G'' = \sum_{i=1}^n g_i \frac{\lambda_i \omega}{1 + (\lambda_i \omega)^2} \quad (6)$$

$$G = \sum_{i=1}^n g_i \quad (7)$$

where λ_i is the relaxation time of the i th Maxwell element. The number, n , of the Maxwell elements was determined by minimizing the product $\chi^{2*(n+1)}$, where χ^2 is the sum of the squared errors and $(n+1)$ represents the number of fitting parameters of eq. (5)-(6). Indeed, following a consolidate strategy,^[11] eq. (5) and (6) fitting to experimental mechanical spectra was performed assuming that relaxation times (λ_i) were scaled by a factor 10 ($\lambda_{i+1} = 10\lambda_i$).

The evaluation of the average network mesh size (ξ_{RHEO}) was performed starting from the Flory theory^[13]:

$$\rho_x = G/RT \quad (8)$$

where ρ_x is the network crosslink density, defined as the moles of crosslinks between different polymeric chains per gel unit volume, T is temperature and R is the universal gas constant. The link between ρ_x and ξ_{RHEO} is provided by the equivalent network theory,^[14] according to which the following relation holds:

$$\xi = \sqrt[3]{6/\pi\rho_x N_A} \quad (9)$$

where N_A is Avogadro number.

6.2 Materials and general methods

Synthesis: Chemicals were purchased from *Sigma Aldrich*, *Acros Organics*, *TCl*, *Apollo Scientific*, *Alfa Aesar*, *Fluorochem* and were used as received. Solvents were purchased from *Fisher scientific*, while deuterated solvents from *Eurisotop* and *Sigma Aldrich*. THF, CH₂Cl₂ and toluene were dried on a Braun MB SPS-800 solvent purification system and further dried over activated 4 Å molecular sieves. PhCl and Hexane were washed with conc. H₂SO₄ and a KMnO₄ solution in 1M NaOH (1 g of KMnO₄ every 50 mL of 1M NaOH solution) and then distilled from CaH₂ or P₂O₅ and stored over 4 Å molecular sieves. Aniline was distilled from CaH₂ under N₂ and stored away from light in a N₂ atmosphere. Aniline, PhCl and hexane were left on CaH₂ overnight prior distillation. Low temperature baths were prepared using different solvent mixtures depending on the desired temperature: -84 °C with Ethyl acetate/liq. N₂, and 0 °C with ice/H₂O. Anhydrous conditions were achieved by drying Schlenk flasks or 2-neck flasks by 3 cycles of flaming with a heat gun under vacuum and purging with N₂. The inert atmosphere was maintained using N₂-filled balloons equipped with a syringe and needle that was used to penetrate the silicon stoppers used to close the flask's necks. Additions of liquid reagents were performed using N₂ purged plastic syringes. Degassing of solutions was performed by bubbling with N₂ while sonicating or *Freeze-pump-thaw* procedure: solutions were frozen using liquid nitrogen and kept under vacuum for 10 min. before thawing. Molecular sieves (4 Å) were activated by heating at 165 °C under vacuum (less than 1 mbar) for 18 h. All reactions were performed in dry conditions and under inert atmosphere unless otherwise stated. **SSE preparation:** LiClO₄ (battery grade) was obtained from *Acros* was used without further purification. TEGDME from *Sigma-Aldrich* was dried under vacuum for 48 h prior to use. CH₂Cl₂ and THF (spectroscopy grade) were purchased from *VWR* and were used as received.

6.3 X-Ray Measurements

CCDC **1523993**, **1523994** and **1523995** contain the supplementary crystallographic data for compounds **2-1**, **3-2** and **2-27**; **1963744**, **1963743**, **1963745** and **1973297** contain the supplementary crystallographic data for compounds **3-13**, **2-33**, **2-38** and **1-1**. CCDC **1873312**, **1873316**, **1873314**, **1873313**, **1873315** and **1873317** contain the supplementary crystallographic data for compounds **4-8**, **4-9**, **4-11 α** , **4-11 β** , **4-3** and **4-10**. These data can be obtained free of charge from The Cambridge Crystallographic Data Centre *via* <https://www.ccdc.cam.ac.uk/structures>.

X-ray diffraction analysis - Structural characterization.

Derivatives 2-1, 3-2, 2-26, 2-29, 2-31, 2-45 and 2-27

Single crystals of **2-1**, **3-2**, **2-27**, **2-26**, **2-45** and **2-31** were grown by slow diffusion of *i*-PrOH in CHCl₃ or C₆H₆ or alternatively MeOH in CH₂Cl₂. **2-29** was obtained from slow evaporation of CH₂Cl₂. Crystallographic studies were undertaken on single crystal mounted in paratone and studied on an Agilent SuperNova Dual three-circle diffractometer using Cu-K α (λ = 1.540598 Å) or Mo-K α (λ = 0.7093187 Å) radiation and a CCD detector. Measurements were typically made at 150(1) K with temperatures maintained using an Oxford Cryostream unless otherwise stated. Data were collected, integrated and corrected for absorption using a numerical absorption correction based on gaussian integration over a multifaceted crystal model within CrysAlisPro.^[15] The structures were solved by direct methods and refined against F2 within SHELXL-2013.^[16]

Derivatives in Chapter 3, 4 and 5

Data collections were performed at the X-Ray diffraction beamline (XRD1) of the Elettra Synchrotron, Trieste (Italy).^[17] The crystals were dipped in NHV oil (Jena Bioscience, Jena, Germany) and mounted on the goniometer head with kapton loops (MiTeGen, Ithaca, USA). Complete datasets were collected at 100 K (nitrogen stream supplied through an Oxford Cryostream 700 - Oxford Cryosystems Ltd., Oxford, UK) through the rotating crystal method. Data were acquired using a monochromatic wavelength of 0.700 Å on a Pilatus 2M hybrid-pixel area detector (DECTRIS Ltd., Baden-Daettwil, Switzerland). The diffraction data were indexed and integrated using XDS.^[18] Scaling have been done using CCP4-Aimless^[19,20]. Two data collections had to be merged for **2-33** and **3-13** crystals to obtain complete data sets. The structures were solved by the dual space algorithm implemented in the SHELXT code.^[16] Fourier analysis and refinement were performed by the full-matrix least-squares methods based on F2 implemented in SHELXL (Version 2018/3). The Coot program was used for modelling.^[21] Anisotropic thermal motion refinement have been used for all atoms with occupancies equal or greater than 50%. Geometric and thermal motion parameters restrains (DFIX, DANG, SIMU) have been applied on disordered solvent molecules. Hydrogen atoms were included at calculated positions with isotropic Ufactors = 1.2·Ueq or Ufactors = 1.5·Ueq for methyl and hydroxyl groups (Ueq being the equivalent isotropic thermal factor of the bonded non hydrogen atom). Pictures were prepared using Ortep3^[22] and Pymol^[23] software. Essential crystal and refinement data are reported below.

None of the **4-10** crystals tested diffracted better than ~1.0 Å: this is consistent with the presence of huge voids in the crystal packing, filled with disordered solvent molecules. Electron content of cavities have been estimated with the SQUEEZE routine of PLATON.^[24] One ordered pentane molecule (with 50% occupancy) has been modelled

in the asymmetric unit (ASU) of **4-10**, while not construable residual density have been squeezed (3103 electrons in 12195 Å³ - 45% of the unit cell volume). The disordered solvent has been estimated as additional 11.5 pentane molecules in the ASU; contributions of these molecules have been included in the properties reported in crystallographic data tables. Anisotropic thermal motion refinement has been used for all non-solvent atoms. Hydrogen atoms were included at calculated positions with isotropic Ufactors = 1.2 Ueq or Ufactors = 1.5 Ueq for methyl groups (Ueq being the equivalent isotropic thermal factor of the bonded non hydrogen atom). Restraints on bond lengths, angles and thermal motion parameters (DFIX, DANG, SIMU and DELU) have been applied on disordered borazine fragments (in **4-9** and **4-10**) and for pentane molecule (in **4-10**). Pictures were prepared using Ortep3^[22] and Pymol^[23] software.

Multiple data collections had to be merged, for triclinic crystals (**5-4-ct**) to obtain complete sets, using CCP4-Aimless^[19,20] code. The structures were solved by the dual space algorithm implemented in the SHELXT code.^[16] Fourier analysis and refinement were performed by the full-matrix least-squares methods based on F2 implemented in SHELXL (Version 2018/3)^[16]. The Coot program was used for modelling.^[21] Anisotropic thermal motion refinement have been used for all atoms with full occupancies. Geometric and thermal motion parameters restraints (DFIX, DANG, SIMU) have been applied on disordered solvent molecules. Hydrogen atoms were included at calculated positions with isotropic Ufactors = 1.2·Ueq or Ufactors = 1.5·Ueq for methyl and hydroxyl groups (Ueq being the equivalent isotropic thermal factor of the bonded non hydrogen atom). Disordered solvent molecules have been modelled in **5-2** (0.16 dichloromethane/ASU), **5-4-cc** (1.75 methanol/ASU + 0.25 water/ASU) and **5-4-ct** (0.35 CH₂Br₂/ASU) structures. An additional disordered solvent contribution has been identified in **5-4-cc**, where methanol and waters fill inner parts of crystal channels without specific intermolecular contacts with the ordered borazine packing scaffold. The corresponding not construable residual electron density couldn't be modelled and has been removed with Platon SQUEEZE^[24] routine (120 e⁻/cell squeezed, corresponding to additional ~5.5 methanol and ~1.5 water molecules/cell in 420 Å³ volume voids). Crystals of **5-2** show merohedral twinning (direct lattice two-fold twinning axis [100]), with a twin fraction of 45%, identified using Platon TWINROTMAT algorithm.^[22] Pictures were prepared using Ortep3^[22] and Pymol^[23] software. Essential crystal and refinement data are reported below.

Crystallographic data tables

	2-26 [C ₆₀ H ₄₈ B ₃ N ₃ Cl ₆]	2-29 [C ₃₀ H ₂₂ B ₃ Br ₄ N ₃ O]	2-31 [C ₅₄ H ₆₆ B ₃ N ₃]	2-45 [C ₄₈ H ₄₈ B ₃ N ₃ F ₆]
Chemical Formula	C ₆₀ H ₄₈ B ₃ N ₃ Cl ₆	C ₃₀ H ₂₂ B ₃ Br ₄ N ₃ O	C ₅₄ H ₆₆ B ₃ N ₃	C ₄₈ H ₄₈ B ₃ N ₃ F ₆
Formula weight (g/mol)	1053.2259	788.8776	789.5536	813.4032
Temperature (K)	293(2)	150(2)	150(2)	283(2)
Wavelength (Å)	1.54184	1.54184	1.54184	1.54184
Crystal system	Triclinic	Triclinic	Monoclinic	Monoclinic
Space Group	<i>P</i> -1	<i>P</i> -1	<i>P</i> 2 ₁ /c	<i>P</i> 2 ₁ /c
Unit cell dimensions	<i>a</i> = 12.1875 (6) Å <i>b</i> = 12.5868 (4) Å <i>c</i> = 20.4846 (9) Å α = 90.539 (3)° β = 94.781 (4)° γ = 118.895 (4)°	<i>a</i> = 11.7497(3) Å <i>b</i> = 16.5362(4) Å <i>c</i> = 18.7461(5) Å α = 90.149(2)° β = 107.676(2)° γ = 110.591(2)°	<i>a</i> = 13.1945(5) Å <i>b</i> = 36.3967(11) Å <i>c</i> = 10.0266(3) Å α = 90° β = 96.071(3)° γ = 90°	<i>a</i> = 10.9244(6) Å <i>b</i> = 20.9184(13) Å <i>c</i> = 19.9847(18) Å α = 90° β = 94.326(6)° γ = 90°
Volume (Å ³)	2737.1 (2)	3224.10 (15)	4788.13	4553.9(6)
Z	12	4	4	20
Density (calculated) (g·cm ⁻³)	1.180	1.720	1.095	1.186
Absorption coefficient (mm ⁻¹)	0.640	7.09	0.060	0.701
F(000)	972	1628	1704.0	1704.0
Crystal habit	Colorless thin rods	Colorless needles	Colorless prisms	Colorless thin rods
Theta range for data collection	4.0 to 74.1°.	3.6 to 74.1°	3.0 to 29.7°	4.1 to 74.4°.
Index ranges	-15 ≤ <i>h</i> ≤ 15 -10 ≤ <i>k</i> ≤ 15 -25 ≤ <i>l</i> ≤ 25	-13 ≤ <i>h</i> ≤ 14 -20 ≤ <i>k</i> ≤ 20 -23 ≤ <i>l</i> ≤ 23	-13 ≤ <i>h</i> ≤ 17 -45 ≤ <i>k</i> ≤ 50 -13 ≤ <i>l</i> ≤ 9	-13 ≤ <i>h</i> ≤ 13 -25 ≤ <i>k</i> ≤ 25 -24 ≤ <i>l</i> ≤ 24
Reflections collected	19619	32017	27688	15787
Independent reflections (data with <i>I</i> > 2σ(<i>I</i>))	9072 [R(int) = 0.040]	11305 [R(int) = 0.0375]	7632 [R(int) = 0.043]	10446 [R(int) = 0.0698]
Data completeness	96.9%	94.1 %	79.1%	97.4%
Refinement method	Full-matrix least-squares on F ²	Full-matrix least-squares on F ²	Full-matrix least-squares on F ²	Full-matrix least-squares on F ²
Data / restraints / parameters	10783 / 0 / 649	12362 / 0 / 790	10692 / 1 / 577	15787 / 228 / 643
Goodness-of-fit on F ²	1.07	1.13	1.042	0.927
Final R indices [<i>I</i> > 2σ(<i>I</i>)]	R ₁ = 0.123, wR ₂ = 0.450	R ₁ = 0.052, wR ₂ = 0.142	R ₁ = 0.079, wR ₂ = 0.235	R ₁ = 0.070, wR ₂ = 0.184
Largest diff. peak and hole (eÅ ⁻³)	1.17 and -0.71	1.47 and -1.68	0.47 and -0.36	0.48 and -0.36

Chapter 6

	2-27 · [C ₆₀ H ₄₈ B ₃ N ₃ F ₆]	2-1 [C ₆₀ H ₄₅ B ₃ N ₃]	3-2 [C ₆₆ H ₄₈]
CCDC Number	1523995	1523993	1523994
Chemical Formula	C ₆₀ H ₄₈ B ₃ N ₃ F ₆	C ₆₀ H ₄₅ B ₃ N ₃	C ₆₆ H ₄₈
Formula weight (g/mol)	957.4142	837.4246	834.3287
Temperature (K)	150(2)	150(2)	150(2)
Wavelength (Å)	1.54184	1.54184	1.54184
Crystal system	Triclinic	Triclinic	Monoclinic
Space Group	<i>P</i> -1	<i>P</i> -1	<i>P</i> 1 2/a
Unit cell dimensions	<i>a</i> = 9.9104(10) Å <i>b</i> = 11.2360(14) Å <i>c</i> = 25.2756(11) Å <i>α</i> = 83.961(6)° <i>β</i> = 85.819(6)° <i>γ</i> = 67.366(10)°	<i>a</i> = 7.8357(4) Å <i>b</i> = 18.8882(8) Å <i>c</i> = 18.9726(10) Å <i>α</i> = 64.191(4)° <i>β</i> = 79.617(4)° <i>γ</i> = 82.496(4)°	<i>a</i> = 25.0707(6) Å <i>b</i> = 16.0942(4) Å <i>c</i> = 26.2129(7) Å <i>α</i> = 90° <i>β</i> = 100.269(2)° <i>γ</i> = 90°
Volume (Å ³)	2581.7(5)	2482.2(2)	10407.3(5)
Z	2	2	8
Density (calculated) (g·cm ⁻³)	1.232	1.277	1.265
Absorption coefficient (mm ⁻¹)	0.702	0.554	0.542
F(000)	996	1002	4176
Crystal size (mm ³)	0.885 x 0.151 x 0.120	0.607 x 0.144 x 0.083	0.452 x 0.116 x 0.045
Crystal habit	Colorless thin rods	Colorless thin rods	yellow thin rods
Theta range for data collection	4.278 to 74.599°	4.401 to 74.153°	3.279 to 74.368°
Index ranges	-12 ≤ <i>h</i> ≤ 11 -13 ≤ <i>k</i> ≤ 12 -24 ≤ <i>l</i> ≤ 31	-9 ≤ <i>h</i> ≤ 9 -23 ≤ <i>k</i> ≤ 18 -20 ≤ <i>l</i> ≤ 23	-30 ≤ <i>h</i> ≤ 19 -18 ≤ <i>k</i> ≤ 19 -31 ≤ <i>l</i> ≤ 32
Reflections collected	16695	17385	20940
Independent reflections (data with I > 2σ(I))	9832 [R(int) = 0.0810]	9795 [R(int) = 0.0375]	10311 [R(int) = 0.0459]
Data completeness	97.4%	99.8%	99.8%
Refinement method	Full-matrix least-squares on F ²	Full-matrix least-squares on F ²	Full-matrix least-squares on F ²
Data / restraints / parameters	9832 / 0 / 655	9795 / 0 / 682	10311 / 0 / 728
Goodness-of-fit on F ²	1.054	1.032	1.032
Final R indices [I > 2σ(I)]	R ₁ = 0.1050, wR ₂ = 0.2626	R ₁ = 0.0565, wR ₂ = 0.1518	R ₁ = 0.0716, wR ₂ = 0.1873
R indices (all data)	R ₁ = 0.1542, wR ₂ = 0.3023	R ₁ = 0.0716, wR ₂ = 0.1697	R ₁ = 0.1072, wR ₂ = 0.2260
Largest diff. peak and hole (eÅ ⁻³)	0.661 and -0.502	0.341 and -0.374	0.355 and -0.388

Chapter 6

	3-13 ^{-1/2} CH ₂ Br ₂ [C ₅₂ H ₃₄ · ^{1/2} CH ₂ Br ₂]	2-33 [C ₅₄ H ₄₃ B ₂ N ₃]	2-38 ^{-1/8} CH ₂ Br ₂ ^{-7/8} CH ₃ OH [C ₄₆ H ₃₃ B ₃ N ₂ O· ^{1/8} CH ₂ Br ₂ ^{-7/8} CH ₃ OH]
CCDC Number	1963744	1963743	1963745
Chemical Formula	C _{52.5} H ₃₅ Br	C ₅₄ H ₄₃ B ₂ N ₃	C ₄₇ H _{36.75} B ₃ B _{0.25} N ₂ O _{1.88}
Formula weight (g/mol)	745.71	755.53	711.94
Temperature (K)	100(2)	100(2)	100(2)
Wavelength (Å)	0.700	0.700	0.700
Crystal system	Triclinic	Monoclinic	Monoclinic
Space Group	<i>P</i> -1	<i>P</i> 2 ₁ / <i>n</i>	<i>P</i> 2 ₁ / <i>c</i>
Unit cell dimensions	<i>a</i> = 7.853(2)Å <i>b</i> = 14.615(3)Å <i>c</i> = 17.556(4)Å <i>α</i> = 65.73(3)° <i>β</i> = 88.99(3)° <i>γ</i> = 89.56(3)°	<i>a</i> = 15.313(3)Å <i>b</i> = 15.891(3)Å <i>c</i> = 16.401(3)Å <i>α</i> = 90° <i>β</i> = 99.82(3)° <i>γ</i> = 90°	<i>a</i> = 14.765(3)Å <i>b</i> = 33.278(7)Å <i>c</i> = 7.612(2)Å <i>α</i> = 90° <i>β</i> = 92.20(3)° <i>γ</i> = 90°
Volume (Å ³)	1836.6(8)	3932.6(14)	3737.4(13)
Z	2	4	4
Density (calculated) (g·cm ⁻³)	1.348	1.276	1.265
Absorption coefficient (mm ⁻¹)	1.115	0.070	0.328
F(000)	770	3674	1486
Crystal size (mm ³)	0.10 x 0.02 x 0.02	0.10 x 0.05 x 0.05	0.08 x 0.03 x 0.02
Crystal habit	Colorless thin rods	Colorless thin rods	Colorless thin rods
Theta range for data collection	1.25° to 28.23°	1.66° to 25.60°	1.20° to 26.66°
Index ranges	-10 ≤ <i>h</i> ≤ 10 -19 ≤ <i>k</i> ≤ 19 -23 ≤ <i>l</i> ≤ 23	-18 ≤ <i>h</i> ≤ 18 -19 ≤ <i>k</i> ≤ 19 -20 ≤ <i>l</i> ≤ 19	-18 ≤ <i>h</i> ≤ 18 -42 ≤ <i>k</i> ≤ 42 -9 ≤ <i>l</i> ≤ 9
Resolution (Å)	0.74	0.81	0.78
Reflections collected	41687	44477	18488
Independent reflections (data with I > 2σ(I))	9283 (4446)	7634 (4634)	7984 (4502)
Data multiplicity (max resltn)	4.39 (4.19)	5.64 (5.51)	2.23 (2.17)
I/σ(I) (max resltn)	4.35 (1.05)	7.13 (2.63)	5.41 (2.13)
R _{merge} (max resltn)	0.0995 (0.6825)	0.0916 (0.3461)	0.0794 (0.3037)
Data completeness (max resltn)	97.8% (96.2%)	98.3% (97.6%)	97.0% (97.3%)
Refinement method	Full-matrix least-squares on F ²	Full-matrix least-squares on F ²	Full-matrix least-squares on F ²
Data / restraints / parameters	9283 / 3 / 501	7634 / 0 / 538	7984 / 36 / 505
Goodness-of-fit on F ²	0.993	1.022	1.003
Δ/σ _{max}	0.000	0.000	0.013
Final R indices [I > 2σ(I)]	R ₁ = 0.0931, wR ₂ = 0.2597	R ₁ = 0.0563, wR ₂ = 0.1432	R ₁ = 0.0865, wR ₂ = 0.2380
R indices (all data)	R ₁ = 0.1735, wR ₂ = 0.3192	R ₁ = 0.1033, wR ₂ = 0.1641	R ₁ = 0.1348, wR ₂ = 0.2820
Largest diff. peak and hole (eÅ ⁻³)	1.496 and -0.868	0.695 and -0.256	0.854 and -0.442
R.M.S. deviation from mean (eÅ ⁻³)	0.103	0.056	0.077

Chapter 6

	4-8 [C ₄₂ H ₄₂ B ₃ N ₃]	4-9 [C ₇₈ H ₇₈ B ₆ N ₆]	4-11α [C ₇₀ H ₇₀ B ₆ N ₆ O]
CCDC Number	1873312	1873316	1873314
Chemical Formula	C ₄₂ H ₄₂ B ₃ N ₃	C ₇₈ H ₇₈ B ₆ N ₆	C ₇₀ H ₇₀ B ₆ N ₆ O
Formula weight (g/mol)	621.21	1164.32	1076.18
Temperature (K)	100(2)	100(2)	100(2)
Wavelength (Å)	0.700	0.700	0.700
Crystal system	Monoclinic	Triclinic	Monoclinic
Space Group	C c	P -1	P 2 ₁ /c
Unit cell dimensions	a = 12.091(2) Å b = 21.639(4) Å c = 13.768(3) Å α = 90° β = 101.26(3)° γ = 90°	a = 12.472(3) Å b = 15.108(3) Å c = 19.725(4) Å α = 80.08(3)° β = 75.32(3)° γ = 68.48(3)°	a = 18.861(4) Å b = 22.390(4) Å c = 14.820(3) Å α = 90° β = 104.44(3)° γ = 90°
Volume (Å ³)	3532.8(13)	3331.8(14)	6061(2)
Z	4	2	4
Density (calculated) (g·cm ⁻³)	1.168	1.161	1.179
Absorption coefficient (mm ⁻¹)	0.064	0.064	0.066
F(000)	1320	1236	2280
Crystal size (mm ³)	0.10 x 0.10 x 0.05	0.05 x 0.03 x 0.02	0.10 x 0.02 x 0.02
Crystal habit	Colorless prisms	Colorless prisms	Colorless rods
Theta range for data collection	1.85° to 30.00°	1.06° to 30.00°	1.10° to 25.27°
Resolution (Å)	0.70	0.70	0.82
Index ranges	-17 ≤ h ≤ 17 -28 ≤ k ≤ 28 -19 ≤ l ≤ 19	-17 ≤ h ≤ 17 -21 ≤ k ≤ 21 -28 ≤ l ≤ 28	-22 ≤ h ≤ 22 -27 ≤ k ≤ 27 -18 ≤ l ≤ 17
Reflections collected	33042	96765	36597
Independent reflections (data with I > 2σ(I))	10445 (10422)	19920 (16202)	11459 (5118)
Data multiplicity (max resltn)	5.53 (4.80)	4.76 (4.21)	3.14 (3.15)
I/σ(I) (max resltn)	38.86 (28.12)	20.50 (9.47)	5.05 (0.98)
R _{merge} (max resltn)	0.0350 (0.0630)	0.0357 (0.1088)	0.1149 (0.6937)
Data completeness (max resltn)	97.1% (93.7%)	97.9% (95.2%)	99.4% (99.1%)
Refinement method	Full-matrix least-squares on F ²	Full-matrix least-squares on F ²	Full-matrix least-squares on F ²
Data / restraints / parameters	10445 / 2 / 440	19920 / 256 / 1079	11459 / 0 / 759
Goodness-of-fit on F ² □/□ _{max}	1.039 0.001	1.067 0.005	0.983 0.000
Final R indices [I > 2σ(I)] ^a	R ₁ = 0.0325, wR ₂ = 0.0898	R ₁ = 0.0615, wR ₂ = 0.1748	R ₁ = 0.0720, wR ₂ = 0.1693
R indices (all data) ^a	R ₁ = 0.0325, wR ₂ = 0.0899	R ₁ = 0.0729, wR ₂ = 0.1866	R ₁ = 0.1760, wR ₂ = 0.2255
Largest diff. peak and hole (e·Å ⁻³)	0.323 and -0.225	0.452 and -0.374	0.271 and -0.218
R.M.S. deviation from mean (e·Å ⁻³)	0.047	0.040	0.054

$$^a R_1 = \frac{\sum ||F_o| - |F_c||}{\sum |F_o|}, wR_2 = \left\{ \frac{\sum [w(F_o^2 - F_c^2)]^2}{\sum [w(F_o^2)]^2} \right\}^{1/2}$$

Chapter 6

	4-11β [C ₇₀ H ₇₀ B ₆ N ₆ O]	4-3 [C ₈₄ H ₉₀ B ₆ N ₆]	4-10 ·12C ₅ H ₁₂ [C ₁₁₄ H ₁₁₄ B ₆ N ₆ ·12C ₅ H ₁₂]
CCDC Number	1873313	1873315	1873317
Chemical Formula	C ₇₀ H ₇₀ B ₆ N ₆ O	C ₈₄ H ₉₀ B ₆ N ₆	C ₁₇₄ H ₂₅₈ B ₆ N ₆
Formula weight (g/mol)	1076.18	1248.47	2573.17
Temperature (K)	100(2)	100(2)	100(2)
Wavelength (Å)	0.700	0.700	0.700
Crystal system	Monoclinic	Orthorhombic	Trigonal
Space Group	<i>P</i> 2 ₁ / <i>c</i>	<i>P</i> <i>bca</i>	<i>P</i> -3
Unit cell dimensions	<i>a</i> = 11.350(2) Å <i>b</i> = 16.679(3) Å <i>c</i> = 32.207(6) Å α = 90° β = 99.29(3)° γ = 90°	<i>a</i> = 21.268(4) Å <i>b</i> = 14.952(3) Å <i>c</i> = 22.475(5) Å α = 90° β = 90° γ = 90°	<i>a</i> = 50.994(7) Å <i>b</i> = 50.994(7) Å <i>c</i> = 12.034(2) Å α = 90° β = 90° γ = 120°
Volume (Å ³)	6017(2)	7147(2)	27101(9)
Z	4	4	6
Density (calculated) (g·cm ⁻³)	1.188	1.160	0.946
Absorption coefficient (mm ⁻¹)	0.066	0.037	0.051
F(000)	2280	2664	8460
Crystal size (mm ³)	0.08 x 0.08 x 0.02	0.50 x 0.12 x 0.08	0.05 x 0.05 x 0.03
Crystal habit	Colorless rods	Colorless prisms	Colorless thin rods
Theta range for data collection	1.26° to 25.94°	1.78° to 30.96°	1.20° to 20.07°
Resolution (Å)	0.80	0.68	1.02
Index ranges	-14 ≤ <i>h</i> ≤ 14 -20 ≤ <i>k</i> ≤ 20 -40 ≤ <i>l</i> ≤ 40	-31 ≤ <i>h</i> ≤ 31 -21 ≤ <i>k</i> ≤ 21 -31 ≤ <i>l</i> ≤ 31	-49 ≤ <i>h</i> ≤ 49 -49 ≤ <i>k</i> ≤ 49 -11 ≤ <i>l</i> ≤ 11
Reflections collected	44465	78255	123980
Independent reflections (data with <i>I</i> > 2σ(<i>I</i>))	12263 (6258)	11797 (10575)	17767 (10193)
Data multiplicity (max resltn)	3.55 (3.54)	6.36 (5.59)	6.98 (7.01)
<i>I</i> /σ(<i>I</i>) (max resltn)	6.89 (1.52)	29.85 (18.18)	15.47 (2.15)
R _{merge} (max resltn)	0.0993 (0.5533)	0.0331 (0.0609)	0.0430 (0.5092)
Data completeness (max resltn)	99.6% (99.7%)	99.3% (98.0%)	99.8% (99.8%)
Refinement method	Full-matrix least-squares on F ²	Full-matrix least-squares on F ²	Full-matrix least-squares on F ²
Data / restraints / parameters	11459 / 0 / 759	11797 / 0 / 443	17767 / 668 / 1098
Goodness-of-fit on F ²	1.007	1.030	1.016
□/□ _{max}	0.002	0.001	0.037
Final R indices [<i>I</i> > 2σ(<i>I</i>)] ^a	R ₁ = 0.0675, wR ₂ = 0.1453	R ₁ = 0.0496, wR ₂ = 0.1474	R ₁ = 0.1044, wR ₂ = 0.2510
R indices (all data) ^a	R ₁ = 0.1497, wR ₂ = 0.1813	R ₁ = 0.0539, wR ₂ = 0.1429	R ₁ = 0.1454, wR ₂ = 0.2857
Largest diff. peak and hole (e·Å ⁻³)	0.230 and -0.237	0.482 and -0.245	0.322 and -0.335
R.M.S. deviation from mean (e·Å ⁻³)	0.055	0.057	0.036

$$^a R_1 = \frac{\sum |F_o| - |F_c|}{\sum |F_o|}, wR_2 = \left\{ \frac{\sum [w(F_o^2 - F_c^2)^2]}{\sum [w(F_o^2)^2]} \right\}^{1/2}$$

	5-2	5-4-cc	5-4-ct
Chemical Formula	C _{24.12} H _{18.25} B ₃ Cl _{0.25} N ₃	C ₁₁₆ H ₁₁₃ B ₃ N ₃ O _{9.5}	C _{108.35} H _{78.7} B ₃ Br _{0.7} N ₃
Formula weight (g/mol)	391.46	1733.52	1511.01
Temperature (K)	100(2)	100(2)	100(2)
Wavelength (Å)	0.700	0.700	0.700
Crystal system	Trigonal	Hexagonal	Triclinic
Space Group	<i>R</i> -3	<i>P</i> 6 ₃	<i>P</i> -1
Unit cell dimensions	<i>a</i> = 33.662(5) Å <i>b</i> = 33.662(5) Å <i>c</i> = 13.762(3) Å <i>α</i> = 90° <i>β</i> = 90° <i>γ</i> = 120°	<i>a</i> = 25.694(4) Å <i>b</i> = 25.694(4) Å <i>c</i> = 9.446(2) Å <i>a</i> = 90° <i>b</i> = 90° <i>g</i> = 120°	<i>a</i> = 12.429(2) Å <i>b</i> = 16.259(3) Å <i>c</i> = 21.464(4) Å <i>a</i> = 71.24(3)° <i>b</i> = 88.86(3)° <i>g</i> = 83.77(3)°
Volume (Å ³)	13505(5)	5400.6(19)	4082.2(16)
Z	24	2	2
Density (calculated) (g·cm ⁻³)	1.155	1.066	1.229
Absorption coefficient (mm ⁻¹)	0.091	0.064	0.395
F(000)	4878	1842	1579
Theta range for data collection	1.19° to 29.97°	2.31° to 30.96°	0.99° to 30.00°
Index ranges	-45 ≤ <i>h</i> ≤ 46 -47 ≤ <i>k</i> ≤ 47 -17 ≤ <i>l</i> ≤ 17	-37 ≤ <i>h</i> ≤ 37 -37 ≤ <i>k</i> ≤ 34 -13 ≤ <i>l</i> ≤ 13	-17 ≤ <i>h</i> ≤ 16 -23 ≤ <i>k</i> ≤ 23 -30 ≤ <i>l</i> ≤ 30
Resolution (Å)	0.70	0.68	0.
Reflections collected	44602	61077	82600
Independent reflections (data with I > 2σ(I))	8874 (6292)	11870 (6997)	23937 (18973)
Data multiplicity (max resltn)	4.88 (4.01)	9.70 (8.32)	3.31 (2.96)
I/σ(I) (max resltn)	12.89 (3.02)	10.41 (2.25)	7.00 (4.76)
R _{merge} (max resltn)	0.0604 (0.3447)	0.1111 (0.6042)	0.0454 (0.1633)
Data completeness (max resltn)	97.2% (92.8%)	99.9% (99.6%)	96.0% (91.9%)
Refinement method	Full-matrix least-squares on F ²	Full-matrix least-squares on F ²	Full-matrix least-squares on F ²
Data / restraints / parameters	8874 / 5 / 328	11870 / 23 / 397	23937 / 17 / 1050
Goodness-of-fit on F ²	1.014	1.000	1.021
D/s _{max}	0.001	0.006	0.000
Final R indices [I > 2σ(I)]	R ₁ = 0.0597, wR ₂ = 0.1407	R ₁ = 0.0683, wR ₂ = 0.1581	R ₁ = 0.0765, wR ₂ = 0.2063
R indices (all data)	R ₁ = 0.0927, wR ₂ = 0.1616	R ₁ = 0.1237, wR ₂ = 0.1861	R ₁ = 0.0932, wR ₂ = 0.2229
Largest diff. peak and hole (eÅ ⁻³)	0.336 and -0.239	0.264 and -0.242	1.105 and -1.140
R.M.S. deviation from mean (eÅ ⁻³)	0.049	0.049	0.075

6.4 PXRD Parameters

High-quality pXRD data were recorded for a powder sample of **1-1** at ambient temperature (294 K) on a Bruker D8 diffractometer (CuKα₁, Ge-monochromated) operating in transmission mode. The powder sample was packed into a glass capillary, which was flame-sealed and attached to the disc sample holder of the pXRD instrument. Data were recorded from 2θ = 4° to 70° (step size, 0.016°; total time, 60h).

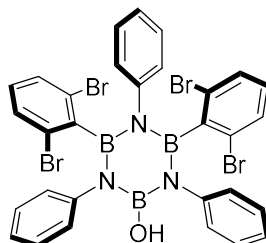
Periodic DFT-D calculations were carried out using CASTEP^[25] (Academic Release Version 19.1). Geometry optimization calculations utilized ultrasoft pseudopotentials,^[26]

the PBE functional,^[27] semi-empirical dispersion correction using the TS correction scheme,^[28] fixed unit cell, preserved space group symmetry, periodic boundary conditions, a basis set cut-off energy of 700 eV and a Monkhorst-Pack grid^[29] of minimum sample spacing $0.05 \times 2\pi \text{ \AA}^{-1}$. Convergence criteria for geometry optimization were 0.01 eV \AA^{-1} for forces, 0.00001 eV per atom for energy, and 0.001 \AA for atomic displacements.

6.5 Synthetic Procedures

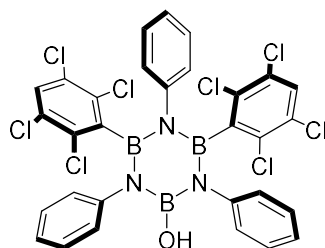
Chapter 2

Synthesis of B,B'-Bis(2,6-dibromophenyl)-B''-hydroxy-N,N',N''-triphenylborazine (2-29)

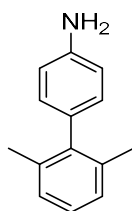


To a solution of aniline (500 mg, 5.37 mmol) in dry toluene (7.0 mL) under N₂, BCl₃ (1.0 M solution in heptanes; 6.4 mL; 6.4 mmol) was added dropwise at 0 °C and the suspension stirred for 10 min. The Schlenk flask was then equipped with a condenser connected to a CaCl₂ trap and the reaction refluxed for 18 h. The condenser was then exchanged with a septum and the resulting white suspension degassed 5 times following the *freeze-pump-thaw* procedure to remove residual HCl. In parallel, 1,3-dibromobenzene (1.38 g, 5.91 mmol) was dissolved in 10.0 mL of anhydrous THF in a flame dried Schlenk flask and LDA (1.0 M in hexane/THF, 7.0 mL, 7.0 mmol) added dropwise at -84 °C. The suspension was stirred for 2 h at the same temperature. The chloro-borazole intermediate was cannulated to the THF solution at -84 °C and allowed to react at this temperature for 30 min., at 0 °C for 30 min. and at r.t. for 24 h. The reaction was quenched with H₂O, diluted in CH₂Cl₂ (50 mL), washed with H₂O (100 mL × 2) and brine (100 mL). The organic layer was dried over MgSO₄, filtered and evaporated under vacuum. Precipitation of the residue in MeOH afforded pure **2-29** as a white solid (923 mg, 51%). mp: 288-290 °C. ¹H NMR (500 MHz, CDCl₃) δ: 7.59 (*d*, *J* = 7.7 Hz, 2 H), 7.46 (*d*, *J* = 7.7 Hz, 4 H), 7.19 (*t*, *J* = 7.7 Hz, 4 H), 7.09-7.04 (*m*, 6 H), 6.87 (*t*, *J* = 7.7 Hz, 2 H), 6.80 (*t*, *J* = 7.3 Hz, 1 H), 6.63 (*t*, *J* = 7.9 Hz, 2 H), 3.58 (*s*, 1 H). ¹³C{¹H} NMR (126 MHz, CDCl₃) δ: 144.87, 143.12, 130.18, 129.84, 128.52, 127.81, 127.35, 127.04, 126.26, 126.02, 125.39. (One signal missing due to ¹¹B quadrupolar relaxation) ¹¹B{¹H} NMR (128 MHz, CDCl₃) δ: 33.49, 25.25. IR (ATR) ν (cm⁻¹): 3564, 3026, 1541, 1491, 1454, 1429, 1398, 1379, 1206, 1138, 1047, 1028, 912, 770, 750, 708, 696, 550. ASAP⁺ HRMS: [M+H]⁺ calc. for [C₃₀H₂₃B₃N₃O⁷⁹Br₄]⁺: 789.8854, found: 789.8884. Crystals suitable for X-Ray diffraction were obtained from slow evaporation of a CH₂Cl₂ solution.

Synthesis of B,B'-Bis(2,3,5,6-tetrachlorophenyl)-B''-hydroxy-N,N',N''-triphenyl-borazine (2-25c)

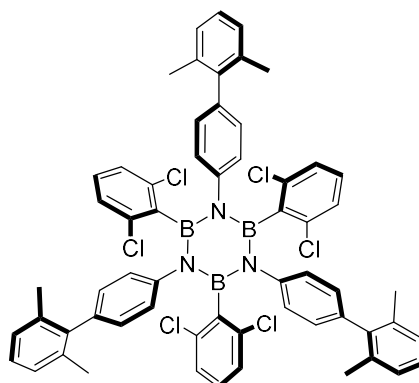


To a solution of aniline (200 mg, 2.15 mmol) in dry toluene (5.0 mL) under N_2 , BCl_3 (1.0 M solution in heptanes; 2.6 mL; 2.6 mmol) was added dropwise at 0 °C and the suspension stirred for 10 min. The Schlenk flask was then equipped with a condenser connected to a $CaCl_2$ trap and the reaction refluxed for 18 h. The condenser was then exchanged with a septum and the resulting white suspension degassed 5 times following the *freeze-pump-thaw* procedure to remove residual HCl. In parallel, 1,2,4,5-tetrachlorobenzene (510 mg, 2.37 mmol) was dissolved in 10.0 mL of anhydrous THF in a flame dried Schlenk flask and LDA (1.0 M in hexane/THF, 2.8 mL, 2.8 mmol) slowly added dropwise at -84 °C. The suspension was stirred for 30 min at the same temperature. The chloro-borazole intermediate was cannulated to the THF solution at -84 °C and allowed to react at this temperature for 30 min followed by for 30 min at 0 °C and then 4 h at r.t.. The reaction was then quenched with H_2O , diluted in CH_2Cl_2 (50 mL), washed with H_2O (100 mL \times 2) and brine (100 mL). The organic layer was dried over $MgSO_4$, filtered and evaporated under vacuum. Precipitation of the residue in MeOH afforded pure **2-25c** as a white solid (230 mg, 43%). mp: >300 °C. 1H NMR (500 MHz, $CDCl_3$) δ : 7.34-7.24 (*m*, 10 H), 7.14 (*s*, 4 H), 6.94-6.88 (*m*, 3 H), 3.63 (*s*, 1 H). $^{13}C\{^1H\}$ NMR (75 MHz, $CDCl_3$) δ : 144.02, 142.47, 132.37, 130.79, 130.49, 128.99, 127.86, 127.18, 126.59, 126.30, 126.16. (One signal missing due to ^{11}B quadrupolar relaxation) $^{11}B\{^1H\}$ NMR (128 MHz, $CDCl_3$) δ : 33.34, 25.06. IR (ATR) ν (cm^{-1}): 1595, 1491, 1375, 1161, 1074, 752, 698, 677, 644, 627, 517. ASAP⁺ HRMS: $[M]^+$ calc. for $[C_{30}H_{18}^{10}B^{11}B_2N_3Cl_8O]^+$: 747.9274, found: 747.9300.

Synthesis of 2',6'-Dimethyl-[1,1'-biphenyl]-4-amine (2-10)

In a Schlenk flask, dioxane (20 mL) and H₂O (4 mL) were degassed 2 times following *freeze-pump-thaw* procedure. 4-Iodoaniline (800 mg, 3.65 mmol), boronic acid (1.02 g, 6.78 mmol), Pd(OAc)₂ (41 mg, 0.18 mmol), K₃PO₄ (1.55 g, 7.30 mmol) and SPhos (150 mg, 0.37 mmol) were then added to the solution that was immediately frozen and degassed two more times with the same procedure. The suspension was then stirred at 90 °C for 18 h under N₂. The reaction was diluted with EtOAc (10 mL), H₂O (10 mL) and extracted with EtOAc (30 mL × 5). The combined organic layers were dried over MgSO₄ and evaporated under vacuum to give a red liquid. The crude product was purified by silica gel column chromatography (Eluents: petroleum ether/EtOAc; gradient from 100% to 70:30) to afford an orange liquid that was distilled under reduced pressure (0.5 mbar, 150°C) to give the desired **2-10** as a pale yellow liquid (337 mg, 47%). ¹H NMR (300 MHz, CDCl₃) δ: 7.19-7.10 (*m*, 3 H), 6.95 (*d*, *J* = 8.5 Hz, 2 H), 6.77 (*d*, *J* = 8.5 Hz, 2 H), 3.70 (*bs*, 2 H), 2.09 (*s*, 6 H). ¹³C{¹H} NMR (75 MHz, CDCl₃) δ: 144.90, 141.99, 136.78, 131.31, 129.98, 127.29, 126.78, 115.24, 21.07. IR (ATR) ν (cm⁻¹): 3368, 3057, 2911, 1622, 1578, 1558, 1508, 1466, 1452, 1271, 1177, 1165, 1123, 1101, 1026, 1005, 964, 827, 787, 775, 766, 750, 716, 621, 579, 563, 532, 525, 519, 498, 484. ESI⁺ HRMS: [M]⁺ calc. for [C₁₄H₁₅N]⁺: 197.1204; found 197.1209.

Synthesis of B,B',B''-Tri[2,6-(dichloro)phenyl]-N,N',N''-tri[4-(2,6-dimethylphenyl)phenyl]borazine (2-26)

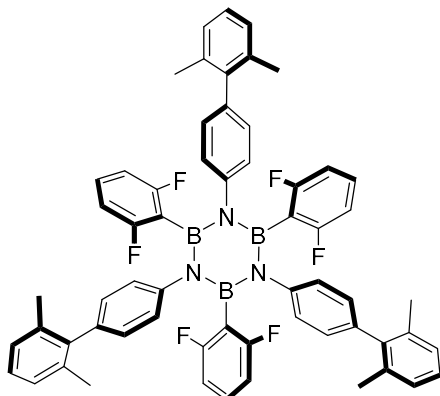


To a solution of aniline **2-10** (300 mg, 1.52 mmol) in dry toluene (2.0 mL) under N₂, BCl₃ (1.0 M solution in heptanes; 1.8 mL; 1.8 mmol) was added dropwise at 0 °C and the suspension stirred for 10 min. The Schlenk flask was then equipped with a condenser connected to a CaCl₂ trap and the reaction refluxed for 18 h. The condenser was then exchanged with a septum and the resulting white suspension degassed 5 times following the *freeze-pump-thaw* procedure to remove residual HCl. In parallel, 2-bromo-1,3-dichlorobenzene (378 mg, 1.67 mmol) was dissolved in 3.0 mL of anhydrous THF in a flame dried Schlenk flask, *n*-BuLi (1.6 M in hexanes, 1.2 mL, 1.9 mmol) added dropwise at -84 °C and the suspension stirred for 10 min. The chloroborazole toluene suspension was then cannulated to the THF solution at -84 °C. The mixture was allowed to react at this temperature for 1 h and then at r.t. for 24 h. The reaction was quenched with H₂O, diluted with CH₂Cl₂ (20 mL) and washed with H₂O (30 mL × 3). The resulting organic layer was dried on MgSO₄, filtered and concentrated under vacuum. Addition of MeOH to the residue resulted in a white precipitate which was filtered. Purification of the resulting white powder by silica gel column chromatography (Eluent: petroleum ether/CH₂Cl₂ 80:20) afforded desired product **2-26** (42 mg, 8%) together with borazine **2-31** (55 mg, 14%) as white solids. mp: >300 °C. ¹H NMR (300 MHz, CDCl₃) δ: 7.51 (*d*, *J* = 8.2 Hz, 6 H), 7.07-6.95 (*m*, 9 H), 6.89-6.78 (*m*, 9 H), 6.66 (*d*, *J* = 8.2 Hz, 6 H), 1.63 (*s*, 18 H). ¹³C{¹H} NMR (75 MHz, CDCl₃) δ: 143.68, 141.77, 138.19, 136.65, 136.11, 129.48, 127.90, 127.06, 126.77, 126.71, 125.96, 20.31. One signal missing due to ¹¹B quadrupolar relaxation. ¹¹B{¹H} NMR (128 MHz, CDCl₃) δ: 36.35. IR (ATR) ν (cm⁻¹): 3032, 2945, 2868, 1628, 1566, 1508, 1385, 1339, 1146, 1007, 841, 766. AP⁺ HRMS: [M+H]⁺ calc. for [C₆₀H₄₉B₃Cl₆N₃]⁺: 1053.2259, found: 1053.2374. Crystals suitable for X-Ray diffraction analysis were obtained from vapor diffusion of MeOH to a CH₂Cl₂ solution.

Borazine **2-31**: mp: 260-262 °C. ¹H NMR (300 MHz, CDCl₃) δ: 7.20 (*d*, *J* = 8.2 Hz, 6 H), 7.16-7.08 (*m*, 15 H), 2.05 (*s*, 18 H), 1.04-0.94 (*m*, 6 H), 0.88-0.77 (*m*, 6 H), 0.53-0.47

(*m*, 15 H). $^{13}\text{C}\{^1\text{H}\}$ NMR (126 MHz, CDCl_3) δ : 146.15, 141.96, 137.70, 136.34, 129.07, 128.95, 127.35, 127.04, 26.70, 26.03, 20.78, 16.32, 13.26. $^{11}\text{B}\{^1\text{H}\}$ NMR (128 MHz, CDCl_3) δ : 36.99. IR (ATR) ν (cm^{-1}): 3026, 2955, 2928, 2853, 1508, 1464, 1429, 1371, 1200, 1163, 1099, 1005, 843, 770, 748, 583, 525. AP⁺-HRMS: $[\text{M}]^+$ calc. for $[\text{C}_{54}\text{H}_{66}^{10}\text{B}_2^{11}\text{BN}_3]^+$: 789.5650, found: 789.5663. Crystals suitable for X-Ray diffraction were obtained from vapor diffusion of MeOH to a CHCl_3 solution.

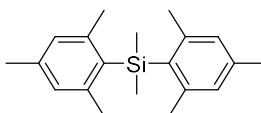
Synthesis of B,B',B''-Tri[2,6-(difluoro)phenyl]-N,N',N''-tri[4-(2,6-dimethylphenyl)phenyl]borazine (2-27)



To a solution of freshly distilled aniline **2-10** (210 mg, 1.06 mmol) in dry toluene (1.82 mL) under N_2 , BCl_3 (1.0 M solution in heptanes; 1.3 mL; 1.3 mmol) was added dropwise at 0 °C and the suspension stirred for 10 min. The Schlenk flask was then equipped with a condenser connected to a CaCl_2 trap and the reaction refluxed for 18 h. The condenser was then exchanged with a septum and the resulting white suspension degassed 5 times following the *freeze-pump-thaw* procedure to remove residual HCl. In parallel, 2-bromo-1,3-difluorobenzene (225 mg, 1.17 mmol) was dissolved in 0.80 mL of anhydrous THF in a flame dried Schlenk flask, *n*-BuLi (1.6 M in hexanes, 0.9 mL, 1.4 mmol) added dropwise at -84 °C and the suspension stirred for 10 min. The chloro-borazole toluene suspension was cannulated to the THF solution at -84 °C and allowed to react at this temperature for 3 h, followed by 3 h at 0 °C and at r.t. for 12 h. The reaction was quenched with H_2O , diluted with CH_2Cl_2 (20 mL) and washed with H_2O (30 mL \times 3). The resulting organic layer was dried on MgSO_4 , filtered and concentrated under vacuum. Addition of MeOH to the residue resulted in a white precipitate which was filtered, affording desired product **2-27** as a white solid (143 mg, 42%). mp: >300 °C. ^1H NMR (300 MHz, CD_2Cl_2) δ : 7.19 (*d*, $J = 7.9$ Hz, 6 H), 7.07-7.02 (*m*, 3 H), 6.98-6.91 (*m*, 9 H), 6.70 (*d*, $J = 8.2$ Hz, 6 H), 6.48 (*t*, $J = 7.6$ Hz, 6 H), 1.63 (*s*, 18 H). $^{13}\text{C}\{^1\text{H}\}$ NMR (75 MHz, CD_2Cl_2) δ : 163.15 (*dd*, $J = 241.2$ Hz, 14.6 Hz), 144.81, 141.90, 138.78, 136.44, 131.08 (*t*, $J = 10.0$ Hz), 128.97, 127.52, 127.44, 127.27, 110.20 (*d*, $J = 26.5$ Hz), 20.42. One signal missing due to ^{11}B quadrupolar relaxation. $^{11}\text{B}\{^1\text{H}\}$ NMR (128 MHz, CDCl_3) δ : 35.59, ^{19}F NMR (276 MHz, CD_2Cl_2) δ : -101.67. IR

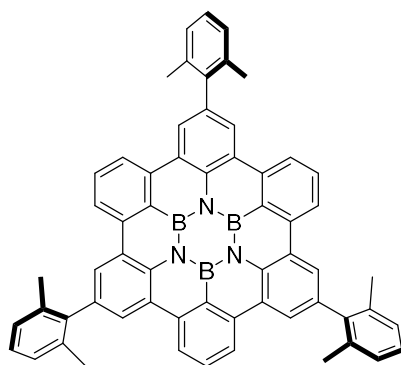
(ATR) ν (cm⁻¹): 3055, 2953, 2920, 1622, 1578, 1508, 1452, 1389, 1256, 1225, 1165, 1146, 1103, 1051, 1024, 1005, 964, 843, 789, 777, 766, 750, 714, 621, 579, 546, 534, 525, 500, 484. ESI⁺ HRMS: [M+H]⁺ calc. for [C₆₀H₄₉B₃F₆N₃]⁺: 958.4136, found: 958.4142. Crystals suitable for X-Ray diffraction analysis were obtained from vapor diffusion of MeOH to a CH₂Cl₂ solution.

Synthesis of Dimethyldimesithylsilane (2-19)



To a solution of 2-bromo mesitylene (4.00 g, 20.0 mmol) in dry THF (13.0 mL) under N₂, *n*-BuLi (1.6 M in hexane, 12.5 mL, 20.0 mmol) was added dropwise at -84 °C. The white suspension was stirred for 1 h at the same temperature and dichlorodimethyl silane (1.2 mL, 10.0 mmol) added. The mixture was stirred at -84 °C for 90 min. followed by r.t. for 18 h. The reaction was quenched with H₂O and extracted with EtOAc (50 mL × 3). The combined organic layers were dried over MgSO₄, filtered and evaporated under vacuum. The crude was purified by silica gel column chromatography (Eluent: petroleum ether 100%) to give product **2-19** as colourless crystals (1.14 g, 38%). Further purification is recommended for the planarization reaction and can be achieved by crystallization from pentane at -25 °C resulting in large colourless prisms. Spectral properties are in agreement with those reported in the literature;^[30] ¹H NMR (300 MHz, CDCl₃) δ : 6.76 (s, 4 H), 2.25 (s, 12 H), 2.24 (s, 6 H), 0.67 (s, 6 H), ¹³C{¹H} NMR (75 MHz, CDCl₃) δ : 143.27, 138.29, 135.13, 129.25, 24.19, 21.09, 6.18.

Synthesis of 2-8-14-Trixylyl-hexaphenyl borazinocoronene (2-1)



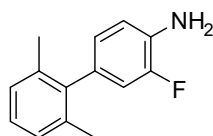
A solution of Triphenylmethinium-1-carba-hexachlorododecaborate (100 mg, 0.17 mmol) in freshly distilled PhCl (0.8 mL) under N₂ was treated with a large excess of anhydrous triisopropylsilane (0.8 mL, 3.9 mmol) and the reaction stirred at r.t. under N₂ for 3 h. The volume of the suspension was then reduced to 20% and the resulting pale-yellow solid washed with anhydrous hexane (3 mL × 4) and dried under vacuum. The resulting silylium carborane **2-22** was dissolved in dry PhCl (4 mL) under N₂ and cannulated to a flame dried Schlenk flask containing dimethyldimesithylsilane **2-19** (490 mg, 1.65 mmol) and borazine **2-27** (98 mg, 0.10 mmol). The resulting solution was diluted with 6 mL of anhydrous PhCl (reaction turns dark) and stirred at 110 °C for 24 h under N₂. After cooling down, the reaction was diluted with CH₂Cl₂ (10 mL), quenched with some drops of H₂O and solvents removed under vacuum. The crude was purified by silica gel column chromatography (Eluent: petroleum ether/CH₂Cl₂ 80:20) giving **2-33** (12.8 mg, 17 %) and **2-1** which was further purified via recycling GPC (Eluent: CHCl₃) to give **2-1** (4.3 mg, 5%) as white solid.

Molecule **2-1**. mp: >300 °C. ¹H NMR (400 MHz, CD₂Cl₂) δ: 8.58 (s, 6 H), 8.55 (d, *J* = 8.0 Hz, 6 H), 8.05 (t, *J* = 8.0 Hz, 3 H), 7.31-7.25 (m, 9 H), 2.25 (s, 18 H). ¹³C{¹H} NMR (75 MHz, CDCl₃) δ: 142.24, 140.04, 137.18, 135.94, 135.75, 133.14, 128.00, 127.89, 126.83, 126.31, 121.36, 21.53. (One signal missing due to ¹¹B quadrupolar relaxation) ¹¹B{¹H} NMR (128 MHz, CDCl₃) δ: 30.64, IR (ATR) ν (cm⁻¹): 3065, 2955, 2909, 1653, 1647, 1636, 1597, 1582, 1555, 1508, 1491, 1466 1439, 1373, 1315, 1250, 1163, 1101, 1072, 1030, 878, 822, 772, 746, 679, 646, 627, 575, 532, 492, 459. MALDI-TOF-HRMS: [M]⁺ calc. for [C₆₀H₄₂B₃N₃]⁺ 837.3658; found: 837.3652. Crystals suitable for X-Ray diffraction were obtained from vapor diffusion of *i*-PrOH to a benzene solution. CCDC: **1523993** contains the supplementary crystallographic data for compound **2-1**.

Molecule **2-33**. mp: >300°C. ¹H NMR (300 MHz, CDCl₃) δ: 8.25-8.17 (m, 9 H), 7.84 (t, *J* = 7.9 Hz, 2 H), 7.63 (s, 2 H), 7.36 (d, *J* = 8.1 Hz, 2 H), 7.24-7.18 (m, 10 H), 2.21 (s, 6 H), 2.17 (s, 12H). ¹³C{¹H} NMR (75 MHz, CDCl₃) δ: 141.89, 141.82, 139.82, 138.83, 138.39, 136.89, 136.80, 134.08, 133.99, 132.04, 129.61, 127.60, 127.56, 127.40,

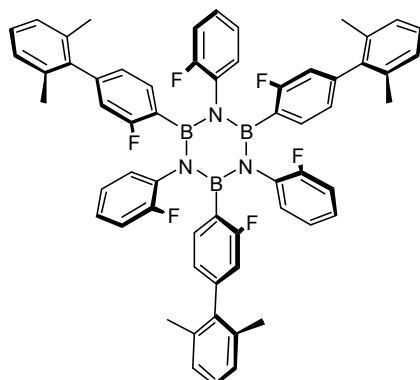
127.30, 126.47, 125.95, 125.03, 122.76, 120.18, 119.92, 119.21, 21.40, 21.31. $^{11}\text{B}\{^1\text{H}\}$ NMR (128 MHz, CDCl_3) δ : 30.79, IR (ATR) ν (cm^{-1}): 3402, 3057, 3015, 2918, 2851, 1595, 1570, 1501, 1460, 1429, 1396, 1344, 1285, 1233, 1190, 1032, 881, 822, 777, 768, 754, 733, 692, 667, 644, 623, 592, 565, 557, 529, 513. ESI $^-$ HRMS: $[\text{M}]^-$ calc. for $[\text{C}_{54}\text{H}_{43}\text{B}_2\text{N}_3]^-$ 755.3649; found: 755.3679.

Synthesis of 3-Fluoro-2',6'-dimethyl-[1,1'-biphenyl]-4-amine (2-35)



In a Schlenk flask, a mixture of dioxane (20 mL) and H_2O (4.0 mL) was added to 2-fluoro-4-bromonitrobenzene (3.00 g, 13.6 mmol), 2,6-dimethylboronic acid (2.30 g, 15.3 mmol), $[\text{Pd}(\text{PPh}_3)_2]$ (628 mg, 0.34 mmol) and K_2CO_3 (5.60 g, 40.8 mmol). The resulting suspension was degassed for 20 min. with N_2 bubbling under sonication and stirred at 90°C under N_2 for 18 h. The reaction was then diluted with EtOAc (10 mL), H_2O (10 mL), extracted with EtOAc (30 mL \times 5) and the combined organic layers dried over MgSO_4 , filtered and concentrated under vacuum. Filtration on silica plug (eluent: Petroleum ether/ CH_2Cl_2 80:20) gave 2.6 g of a white powder that was used straight away in the reduction reaction. The product from the previous step (2.6 g, 10.6 mmol) was added to a suspension of Zn (6.8 g, 104 mmol) in a mixture of AcOH (50 mL) and EtOH (100 mL). The reaction was stirred at r.t. for 30 min. and then filtered on celite, washing thoroughly with EtOAc. The resulting solution was neutralized with sat. K_2CO_3 , washed with H_2O (100 mL \times 2), brine (100 mL), dried over MgSO_4 , filtered and evaporated under reduced pressure to give an orange oil. Distillation under reduced pressure (0.7 mbar, 150°C) afforded **2-35** as a pale-yellow oil (1.8 g, 62%). ^1H NMR (300 MHz, CDCl_3) δ : 7.17-7.07 (*m*, 3 H), 6.87-6.77 (*m*, 2 H), 6.71 (*dd*, $J = 8.2, 2.0$ Hz, 1 H), 3.74 (*bs*, 2 H), 2.05 (*s*, 6 H). $^{13}\text{C}\{^1\text{H}\}$ NMR (75 MHz, CDCl_3) δ : 151.74 (*d*, $J = 239.3$ Hz), 140.90, 136.64, 132.87 (*d*, $J = 12.9$ Hz), 131.85 (*d*, $J = 6.5$ Hz), 127.36, 127.12, 125.18 (*d*, $J = 3.1$ Hz), 117.12 (*d*, $J = 3.9$ Hz), 116.03 (*d*, $J = 18.2$ Hz), 20.93 (*d*, $J = 3.3$ Hz). $^{19}\text{F}\{^1\text{H}\}$ NMR (376 MHz, CDCl_3) δ : -135.34. IR (ATR) ν (cm^{-1}): 3381, 3032, 2922, 1634, 1510, 1391, 768, 413, EI $^+$ HRMS: $[\text{M}]^+$ calc. for $[\text{C}_{14}\text{H}_{14}\text{FN}]^+$: 215.1110; found: 215.1100.

Synthesis of B,B',B''-Tri[2-fluorophenyl]-N,N',N''-tri[2-fluoro-4-(2,6-dimethylphenyl)phenyl]borazine * (2-34)

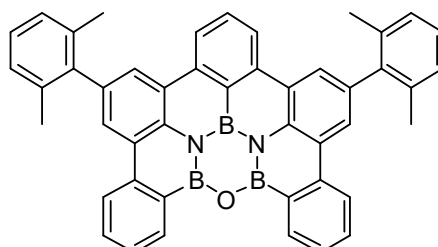


*mixture of atropoisomers

To a solution of freshly distilled aniline **2-35** (500 mg, 2.33 mmol) in dry toluene (2.6 mL) under N₂, BCl₃ (1.0 M solution in heptanes; 2.8 mL; 2.8 mmol) was added dropwise at 0 °C and the resulting suspension stirred for 10 min. The Schlenk flask was then equipped with a condenser connected to a CaCl₂ trap and the reaction refluxed for 18 h. The condenser was then exchanged with a septum and the resulting white suspension degassed 5 times following the *freeze-pump-thaw* procedure to remove residual HCl. In parallel, 1-bromo-2-fluorobenzene (0.3 mL, 2.6 mmol) was dissolved in 3.9 mL of anhydrous THF in a flame dried Schlenk flask, *n*-BuLi (1.6 M in hexanes, 1.9 mL, 3.1 mmol) added dropwise at -84 °C and the reaction stirred for 10 min. at the same temperature. The chloro-borazole toluene suspension was cooled to -84 °C and cannulated to the THF solution at the same temperature. The resulting suspension was allowed to react at -84 °C for 1 h, followed by 1 h at 0 °C and at r.t. for 20 h. The reaction was then quenched with some drops of H₂O, diluted with CH₂Cl₂ (20 mL), washed with H₂O (30 mL × 3), brine (20 mL), dried on MgSO₄ and filtered. The organic layer was then evaporated under vacuum and addition of MeOH to the residue resulted in a white precipitate, which was filtered affording **2-34** as a white powder (270 mg, 36%). mp: >300 °C. ¹H NMR (500 MHz, CDCl₃) δ: 7.18-6.98 (*m*, 18 H), 6.77 (*bs*, 3 H), 6.60 (*bs*, 3 H), 6.52-6.39 (*m*, 6 H), 1.75-1.65 (*m*, 18 H). ¹³C{¹H} NMR (125 MHz, CDCl₃) δ: 164.92, 164.38, 163.90, 163.00, 162.46, 162.00, 159.01, 158.50, 158.15, 157.04, 156.58, 156.20, 140.91, 140.47, 140.07, 139.94, 136.64, 135.91, 133.93, 133.21, 132.94, 132.34, 131.76, 130.83, 130.46, 130.37, 130.23, 129.91, 129.78, 129.72, 127.40, 127.19, 125.26, 124.30, 123.97, 123.11, 122.86, 117.34, 116.14, 115.49, 115.17, 115.06, 114.04, 113.90, 113.76, 113.45, 20.94, 20.25, 20.22, 20.18, 20.15. ¹¹B{¹H} NMR (160 MHz, CDCl₃) δ: 36.99, ¹⁹F{¹H} NMR (276 MHz, CD₂Cl₂) δ: -102.43; -103.69 (*m*), -121.04; -122.33 (*m*). IR (ATR) ν (cm⁻¹): 3061, 3022, 2920, 2857,

1612, 1510, 1439, 1385, 827, 754. ESI⁺ HRMS: [M+H]⁺ calc. for [C₆₀H₄₉B₃F₆N₃]⁺: 958.4136, found: 958.4191.

Synthesis of 6,12-Bis(2,6-dimethylphenyl)-18-oxa-17b1,18a1-diaza-7b2,17b,18a-triboradibenzo[fg,ij]phenanthro[9,10,1,2,3-pqrst]pentaphene (2-38)



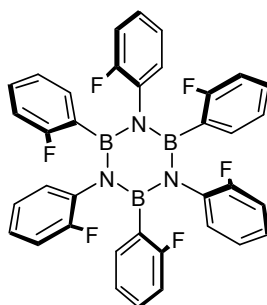
A solution of Triphenylmethinium-1-carba-hexachlorododecaborate (87 mg, 0.15 mmol) in anhydrous PhCl (1.0 mL) under N₂ was treated with a large excess of anhydrous triisopropylsilane (0.86 mL, 4.2 mmol) and the reaction stirred at r.t. under N₂ for 3 h. The volume of the suspension was then reduced to 20%, the resulting pale-yellow solid washed with dry hexane (3 mL × 4) and dried under vacuum. The resulting **2-22** was then dissolved in anhydrous PhCl (1.0 mL), degassed 3 times with *freeze-pump-thaw* procedure and cannulated under N₂ to a flame dried Schlenk flask containing a solution of **2-19** (500 mg, 1.70 mmol) and borazine **2-34** (200 mg, 0.21 mmol) in anhydrous degassed PhCl (8.0 mL). The resulting solution (reaction turns violet) was stirred at 110 °C under N₂ for 24 h, diluted with CH₂Cl₂ (20 mL) and quenched with some drops of H₂O. The organic layer was washed with H₂O (30 mL × 2), brine (30 mL), dried over MgSO₄, filtered and the solvents removed under vacuum. The crude was purified by silica gel column chromatography (eluent: petroleum ether/CH₂Cl₂ 80:20) and preparative TLC (eluent: petroleum ether/CH₂Cl₂ 80:20) to give **2-38** (5 mg, 4%) and **2-1** (26 mg, 15%) as white powders.

Molecule **2-38**. mp: >300 °C. ¹H NMR (300 MHz, CDCl₃) δ: 8.82 (*dd*, *J* = 8.0, 1.2 Hz, 2 H), 8.50-8.41 (*m*, 8 H), 7.98 (*t*, *J* = 8.0 Hz, 1 H), 7.84 (*td*, *J* = 8.0, 1.5 Hz, 2 H), 7.70 (*t*, *J* = 7.3 Hz, 2 H), 7.33-7.28 (*m*, 6 H), 2.21 (*s*, 12 H). ¹³C{¹H} NMR (125 MHz, CDCl₃) δ: 141.92, 141.89, 140.00, 136.86, 135.20, 134.51, 133.39, 133.16, 132.64, 127.69, 127.58, 127.14, 126.09, 125.92, 125.56, 125.43, 123.00, 120.91, 21.39. (two peaks missing due to B-induced quadrupolar relaxation). ¹¹B{¹H} NMR (160 MHz, CDCl₃) δ: 30.96, IR (ATR) ν(cm⁻¹): 3067, 2980, 2884, 1647, 1599, 1456, 1369, 816, 772, 674. EI⁺ HRMS: [M]⁺ calc. for [C₄₆H₃₃B₃N₂O]⁺: 662.2872; found: 662.2891. Crystals suitable for X-Ray diffraction analysis were obtained from vapor diffusion of *i*-PrOH to a CH₂Br₂

solution. CCDC: **1963745** contains the supplementary crystallographic data for compound **2-38**.

Molecule **2-1**: white powder: ^1H NMR (400 MHz, CDCl_3) δ : 8.56 (s, 6 H), 8.50 (d, J = 8.0 Hz, 6 H), 8.02 (t, J = 8.0 Hz, 3 H), 7.35-7.27 (m, 9 H), 2.26 (s, 18 H). UV-Vis, λ_{abs} : 314 nm, 334 nm, 354 nm, 373 nm matching literature data.^[31]

Synthesis of B,B',B''-Tri[2-fluorophenyl]-N,N',N''-tri[2-fluorophenyl]borazine **(2-40)**

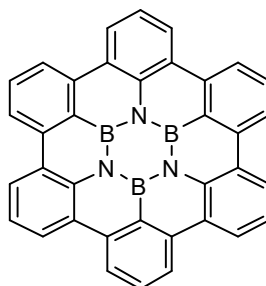


*mixture of atropoisomers

To a solution of freshly distilled 2-Fluoro aniline (500 mg, 4.50 mmol) in dry toluene (5.0 mL) under N_2 , BCl_3 (1.0 M solution in heptanes; 5.4 mL; 5.4 mmol) was added dropwise at 0 °C and the reaction stirred at the same temperature for 10 min. The Schlenk flask was then equipped with a condenser connected to a CaCl_2 trap and the suspension refluxed for 18 h. After exchanging the condenser with a septum, the reaction was allowed to reach r.t. and then degassed 5 times following the *freeze-pump-thaw* procedure to remove residual HCl. In parallel, 1-bromo-2-fluorobenzene (0.54 mL, 4.95 mmol) was dissolved in 7.5 mL of anhydrous THF in a flame dried Schlenk flask, *n*-BuLi (1.6 M in hexanes, 3.7 mL, 5.9 mmol) added dropwise at -84 °C and the suspension stirred for 10 min. at the same temperature. The chloro-borazole toluene suspension was then cooled to -84 °C and cannulated to the THF solution at -84 °C. The resulting suspension was allowed to react at this temperature for 1 h, followed by 1 h at 0 °C and at r.t. for 18 h. The reaction was then quenched with some drops of H_2O , diluted with CH_2Cl_2 (50 mL), washed with H_2O (30 mL \times 3), brine (50 mL), dried on MgSO_4 , filtered and evaporated under vacuum. Precipitation of the residue in MeOH afforded the desired product **2-40** as a white powder (518 mg, 53%). mp: >300 °C. ^1H NMR (300 MHz, CD_2Cl_2) δ : 7.22-6.91 (m, 9 H), 6.84-6.62 (m, 12 H), 6.58-6.53 (m, 3 H). $^{13}\text{C}\{^1\text{H}\}$ NMR (125 MHz, THF-*d*8) δ : 165.31, 165.26, 165.24, 165.16, 165.11, 164.77, 164.75, 164.73, 163.35, 163.29, 163.25, 163.20, 162.87, 162.86, 162.83, 159.70, 159.65, 159.60, 159.38, 159.29, 159.24, 159.20, 157.74, 157.70, 157.64, 157.44, 157.35, 157.30, 157.28, 137.94, 135.05, 135.03, 134.95, 134.93, 134.91, 134.85, 134.83, 134.71, 134.62, 134.13, 134.09, 134.02, 133.89, 133.82,

133.74, 133.66, 133.55, 133.48, 132.57, 132.50, 132.38, 132.29, 132.23, 132.16, 132.05, 131.84, 131.78, 131.63, 131.50, 131.39, 131.28, 131.19, 131.02, 130.94, 130.87, 130.82, 130.72, 130.69, 130.66, 130.57, 128.22, 128.16, 128.14, 128.08, 127.93, 127.88, 127.86, 127.82, 127.80, 127.76, 127.68, 127.62, 127.56, 127.51, 124.43, 124.39, 124.35, 124.31, 123.93, 123.80, 123.56, 123.47, 123.30, 123.23, 116.03, 115.87, 115.70, 115.60, 115.53, 115.44, 115.36, 115.24, 114.83, 114.71, 114.59, 114.52, 114.45, 114.41, 114.31, 114.26, 114.12. $^{11}\text{B}\{^1\text{H}\}$ NMR (160 MHz, CDCl_3) δ : 34.94. $^{19}\text{F}\{^1\text{H}\}$ NMR (276 MHz, CD_2Cl_2) δ : -102.75; -103.99 (*m*), -121.00; -122.23 (*m*). IR (ATR) ν (cm^{-1}): 3075, 3028, 1612, 1589, 1572, 1499, 1439, 1379, 1260, 1206, 1099, 1078, 941, 860, 808, 725, 480. ESI⁺ HRMS: $[\text{M}+\text{H}]^+$ calc. for $[\text{C}_{36}\text{H}_{25}^{10}\text{B}_2^{11}\text{BF}_6\text{N}_3]^+$: 644.2304, found: 644.2311. (adduct with NH_4^+ visible as major peak).

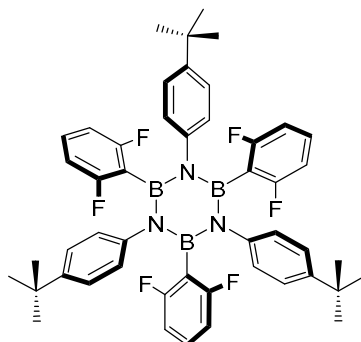
Synthesis of Hexa-*peri*-hexabenzoborazinocoronene (1-1)



A solution of Triphenylmethinium-1-carba-hexachlorododecaborate (89 mg, 0.15 mmol) in freshly distilled PhCl (0.5 mL) under N_2 was treated with a large excess of anhydrous triisopropylsilane (0.70 mL, 3.45 mmol) and the reaction stirred at r.t. under N_2 for 3 h. The volume of the suspension was then reduced to 20% and the resulting pale-yellow solid washed with dry hexane (3 mL \times 4) and dried under vacuum. The resulting **2-22** was then dissolved in anhydrous PhCl (1.0 mL), degassed 3 times following *freeze-pump-thaw* procedure and cannulated under N_2 to a flame dried Schlenk flask containing a solution of **2-19** (368 mg, 1.24 mmol) and borazine **2-40** (100 mg, 0.15 mmol) in degassed PhCl (7.0 mL). The resulting solution (reaction turns violet) was stirred at 110 °C under N_2 for 18 h, cooled, evaporated under reduced pressure and suspended in CH_2Cl_2 under sonication. The dark suspension was transferred in a falcon tube and centrifuged at 5000 rpm for 5 min., the supernatant removed and the procedure repeated with: EtOAc, MeOH, Acetone, ODCB, hot toluene and again CH_2Cl_2 to give **1** as a pale gray solid (14 mg, 18%). mp: >300 °C. IR (ATR) ν (cm^{-1}): 3032, 1628, 1566, 1508, 1383, 1339, 1146, 1101, 1009, 839, 804, 766, 752, 687, 667, 577, 401. LD⁺ HRMS: $[\text{M}]^+$ calc. for $[\text{C}_{36}\text{H}_{18}\text{B}_3\text{N}_3]^+$: 525.1780; found: 525.1763. Crystal structure obtained from X-Ray powder diffraction CCDC: **1973297** contains the

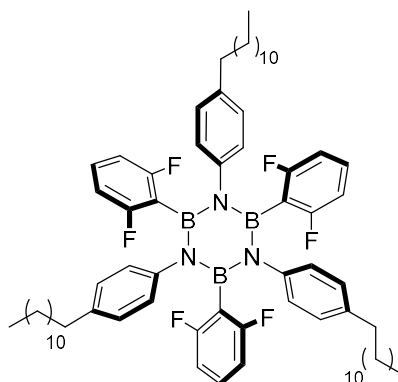
supplementary crystallographic data for compound **1-1**. Data in agreement with previous synthesis of the molecule by Bettinger et al.^[32]

Synthesis of **B,B',B''**-[2,6-(Difluoro)phenyl]-**N,N',N''**-tri[4-(*tert*-butyl)phenyl]-borazine (**2-45**)



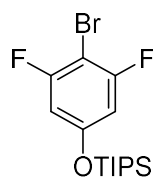
To a solution of freshly distilled 4-*t*-butyl aniline (600 mg, 4.00 mmol) in dry toluene (5.0 mL) under N₂, BCl₃ (1.0 M solution in heptanes; 4.8 mL; 4.8 mmol) was added dropwise at 0 °C and the resulting suspension stirred for 10 min. The Schlenk flask was then equipped with a condenser connected to a CaCl₂ trap and the suspension refluxed for 18 h. After exchanging the condenser with a septum, the reaction was degassed 5 times following the *freeze-pump-thaw* procedure to remove residual HCl. In parallel, 2-bromo-1,3-difluorobenzene (849 mg, 4.42 mmol) was dissolved in 2.9 mL of anhydrous THF in a flame dried Schlenk flask and *n*-BuLi (1.6 M in hexanes, 3.3 mL, 5.3 mmol) added dropwise at -84 °C. The resulting suspension was stirred for 10 min. at the same temperature. The chloro-borazole toluene suspension was then cannulated to the THF solution at -84 °C and allowed to react at this temperature for 3 h, followed by 3 h at 0 °C and at r.t. for 18 h. The reaction was then quenched with water (10 mL), diluted with CH₂Cl₂ (10 mL), washed with H₂O (30 mL × 2) and brine (50 mL). The organic layer was dried over MgSO₄, filtered and evaporated under vacuum. Precipitation of the residue in MeOH afforded the desired product **2-45** as a white solid (707 mg, 65%). mp: >300 °C. ¹H NMR (300 MHz, CDCl₃) δ: 6.96 (*d*, *J* = 8.5 Hz, 6 H), 6.86 (*d*, *J* = 8.5 Hz, 6 H), 6.84-6.78 (*m*, 3 H), 6.38-6.33 (*m*, 6 H), 1.03 (*s*, 27 H). ¹³C{¹H} NMR (75 MHz, CD₂Cl₂) δ: 162.99 (*dd*, *J* = 240.9, 14.8 Hz), 148.55, 143.53, 130.83 (*t*, *J* = 10.0 Hz) 126.78, 124.99, 110.11 (*d*, *J* = 26.9 Hz), 34.47, 31.35. One signal missing due to ¹¹B quadrupolar relaxation. ¹¹B{¹H} NMR (128 MHz, CDCl₃) δ: 34.17. ¹⁹F NMR (276 MHz, CD₂Cl₂) δ: -101.47. IR (ATR) ν (cm⁻¹): 2963, 2870, 1624, 1578, 1508, 1452, 1389, 1269, 1252, 1225, 1115, 1018, 982, 839, 783, 716, 567. ESI⁺ HRMS: [M+H]⁺ calc. for [C₄₈H₄₉¹⁰B¹¹B₂F₆N₃]⁺: 813.4146, found: 813.4162. Crystals suitable for X-Ray diffraction analysis were obtained from vapor diffusion of MeOH to a CH₂Cl₂ solution.

Synthesis of B,B',B''-[2,6-(Difluoro)phenyl]-N,N',N''-tri[4-(dodecyl) phenyl]-borazine (2-48)



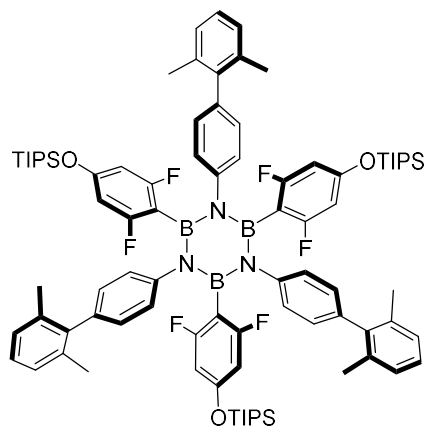
To a solution of 4-dodecyl aniline (300 mg, 1.15 mmol) in dry toluene (1.3 mL) under N_2 , BCl_3 (1.0 M solution in heptanes; 1.4 mL; 1.4 mmol) was added dropwise at 0 °C and the resulting solution stirred for 10 min. The Schlenk flask was then equipped with a condenser connected to a $CaCl_2$ trap and the suspension refluxed for 18 h. After exchanging the condenser with a septum, the reaction was degassed 5 times following the *freeze-pump-thaw* procedure to remove residual HCl. In parallel, 2-bromo-1,3-difluorobenzene (245 mg, 1.27 mmol) was dissolved in 2.0 mL of anhydrous THF in a flame dried Schlenk flask and *n*-BuLi (1.6 M in hexanes, 0.94 mL, 1.50 mmol) added dropwise at -84 °C. The suspension was then stirred for 10 min. at the same temperature. The chloro-borazole toluene suspension was then cannulated to the THF solution at -84 °C and allowed to react at this temperature for 3 h, followed by 3 h at 0 °C and at r.t. for 18 h. The reaction was quenched with H_2O and diluted with CH_2Cl_2 (30 mL). The organic layer was washed with H_2O (30 mL \times 2), brine (50 mL), dried over $MgSO_4$, filtered and evaporated under vacuum. Precipitation of the residue in MeOH afforded the desired product **2-48** as a yellowish pasty solid (143 mg, 32%). mp: 122-124 °C. 1H NMR (300 MHz, $CDCl_3$) δ : 6.96 (*d*, J = 7.8 Hz, 6 H), 6.83-6.80 (*m*, 3 H), 6.67 (*d*, J = 7.8 Hz, 6 H), 6.36 (*t*, J = 7.2 Hz, 6 H), 2.29 (*t*, J = 7.3 Hz, 6 H), 1.33-1.25 (*m*, 54 H), 0.99-0.91 (*m*, 6 H), 0.88 (*t*, J = 6.8 Hz, 9 H). $^{13}C\{^1H\}$ NMR (126 MHz, $CDCl_3$) δ : 162.64 (*dd*, J = 241.5, 14.8 Hz), 143.36, 139.47, 130.17 (*t*, J = 10.1 Hz), 129.28, 127.81, 126.63, 109.70 (*d*, J = 27.3 Hz), 35.10, 32.07, 31.06, 29.85, 29.81, 29.79, 29.76, 29.55, 29.52, 28.71, 22.84, 14.26. $^{11}B\{^1H\}$ NMR (128 MHz, $CDCl_3$) δ : 33.28, $^{19}F\{^1H\}$ NMR (276 MHz, $CDCl_3$) δ : -101.44. IR (ATR) ν (cm^{-1}): 3032, 2920, 2851, 1626, 1566, 1508, 1387, 1339, 1146, 1009, 881, 839, 766, 681. ESI⁺ HRMS: $[M+H]^+$ calc. for $[C_{72}H_{97}^{10}B_2^{11}BF_6N_3]^+$: 1148.7939, found: 1148.7937.

Synthesis of (4-Bromo-3,5-difluorophenoxy)triisopropylsilane (2-56)



In a Schlenk flask 4-bromo-3,5-difluorophenol (1.0 g, 4.8 mmol) was added together with imidazole (980 mg, 14.4 mmol) and DMF (8.0 mL). TIPSCl (1.4 mL, 6.3 mmol) was then added dropwise and the reaction stirred under N₂ at 50 °C for 18 h. The solution was then diluted with CH₂Cl₂ (50 mL), washed with H₂O (100 mL × 2), brine (100 mL), dried over MgSO₄ and evaporated under reduced pressure. Silica column gel chromatography (eluent: Petroleum ether 100 %) gave **2-56** as a transparent oil (1.61 g, 92%). ¹H NMR (300 MHz, CDCl₃) δ: 6.50 (*d*, *J* = 8.0 Hz, 2 H), 1.31-1.19 (*m*, 3 H), 1.10 (*d*, *J* = 6.9 Hz, 18 H). ¹³C{¹H} NMR (101 MHz, CDCl₃) δ 160.24 (*dd*, *J* = 246.7, 7.3 Hz), 156.99 (*t*, *J* = 13.5 Hz), 104.69-104.47 (*m*), 89.26 (*t*, *J* = 24.9 Hz), 17.92, 12.67. ¹⁹F{¹H} NMR (376 MHz, CDCl₃) δ: -105.76. IR (ATR) ν (cm⁻¹): 3082, 2945, 2868, 1613, 1584, 1472, 1369, 1165, 1030, 1009, 881, 845, 795, 569. EI⁺ HRMS: [M]⁺ calc. for [C₁₅H₂₃OBrSiF₂]⁺: 364.0670, found: 364.0670.

Synthesis of B,B',B''-[(3,5-Difluorophenoxy)triisopropylsilane]-N,N',N''-tri[4-(2,6-dimethylphenyl)phenyl]borazine (2-51)

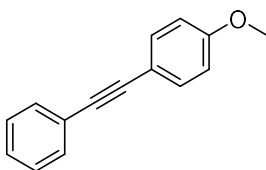


To a solution of aniline **2-10** (400 mg, 2.02 mmol) in dry toluene (3.0 mL) under N₂, BCl₃ (1.0 M solution in heptanes; 3.0 mL; 3.0 mmol) was added dropwise at 0 °C and the resulting solution stirred for 10 min. The Schlenk flask was then equipped with a condenser connected to a CaCl₂ trap and the suspension refluxed for 18 h. After exchanging the condenser with a septum, the reaction was degassed 5 times following the *freeze-pump-thaw* procedure to remove residual HCl. In parallel, **2-56** (850 mg, 2.33 mmol) was dissolved in 4.4 mL of anhydrous THF in a flame dried Schlenk flask and *n*-BuLi (1.6 M in hexanes, 2.3 mL, 3.7 mmol) added dropwise at -84 °C. The suspension was stirred for 10 min. at the same temperature. The chloro-borazole

toluene suspension was cannulated to the THF solution at -84 °C and allowed to react at this temperature for 3 h, followed by 3 h at 0 °C and at r.t. for 18 h. The reaction was quenched with H₂O (5 mL) and diluted with CH₂Cl₂ (10 mL). The organic layer was washed with H₂O (30 mL × 2), brine (50 mL), dried over MgSO₄, filtered and evaporated under vacuum. Silica gel column chromatography (eluent: petroleum ether/CH₂Cl₂ 90:10) afforded **2-51** as a white powder (181 mg, 18%) along with **2-31** (138 mg, 26 %) mp: >300 °C. ¹H NMR (300 MHz, CDCl₃) δ: 7.17-7.02 (*m*, 15 H), 6.75 (*d*, *J* = 7.5 Hz, 6 H), 6.02 (*d*, *J* = 7.5 Hz, 6 H), 1.76 (*s*, 18 H), 1.18-1.11 (*m*, 9 H), 1.00 (*d*, *J* = 6.6 Hz, 54 H). ¹³C{¹H} NMR (126 MHz, CDCl₃) δ: 163.24 (*dd*, *J* = 240.1, 19.2 Hz), 158.30 (*t*, *J* = 14.6 Hz), 144.80, 141.76, 137.76, 136.20, 128.32, 127.42, 127.09, 126.82, 102.05 (*d*, *J* = 29.1 Hz), 20.49, 17.85, 12.58. One peak missing due to ¹¹B-induced quadrupolar relaxation. ¹¹B{¹H} NMR (128 MHz, CDCl₃) δ: 37.15, ¹⁹F NMR (376 MHz, CDCl₃) δ: -101.29. IR (ATR) ν (cm⁻¹): 3030, 2945, 2866, 1628, 1566, 1508, 1464, 1376, 1339, 1146, 1009, 881, 839, 766, 687. ESI⁺-HRMS: [M+H]⁺ calc. for [C₈₇H₁₀₉B₃F₆N₃O₃Si₃]⁺: 1474.7955, found: 1474.8025.

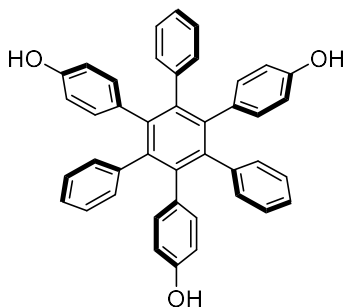
Chapter 3

Synthesis of 1-Methoxy-4-(phenylethynyl)benzene (3-1)



In a Schlenk flask 4-iodoanisole (5.0 g, 21.4 mmol) was added followed by $[\text{Pd}(\text{PPh}_3)_2\text{Cl}_2]$ (155 mg, 0.21 mmol) and CuI (42 mg, 0.21 mmol). A mixture of diisopropylamine (25 mL) and THF (25 mL) was added and the resulting suspension immediately frozen in liquid N_2 . The mixture was degassed by three *freeze-pump-thaw* cycles and phenylacetylene (2.35 mL, 21.4 mmol) added followed by 2 more *freeze-pump-thaw* cycles. The resulting black suspension was then stirred at r.t. for 4 h. The crude solution was diluted with EtOAc (300 mL), washed with H_2O (200 mL) and brine (100 mL). The organic layer was dried over MgSO_4 , filtered and evaporated under reduced pressure. The crude was purified using silica gel column chromatography (Eluents: petroleum ether/ CH_2Cl_2 90:10) to give **3-1** as a white solid (4.30 g, 97%). ^1H NMR (400 MHz, CDCl_3) δ : 7.54-7.48 (*m*, 4 H), 7.37-7.30 (*m*, 3 H), 6.89 (*d*, $J = 8.7$ Hz, 2 H), 3.83 (*s*, 3 H). $^{13}\text{C}\{^1\text{H}\}$ NMR (101 MHz, CDCl_3) δ 159.73, 133.18, 131.58, 128.44, 128.07, 123.71, 115.48, 114.12, 89.50, 88.19, 55.42. ESI⁺ HRMS: $[\text{M}]^+$ calc. for $[\text{C}_{15}\text{H}_{12}\text{O}]^+$: 208.0888; found: 208.0892.

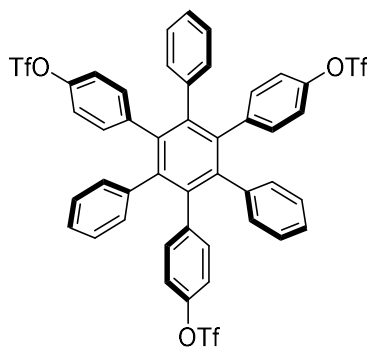
Synthesis of 1,3,5-(4'-Hydroxyphenyl)-2,4,6-phenylbenzene (3-3)



In a Schlenk flask, **3-1** (3.0 g, 14.4 mmol) and $[\text{Co}_2(\text{CO})_8]$ (492 mg, 1.44 mmol) were added and dissolved in dioxane (10 mL). The solution was degassed by 3 *freeze-pump-thaw* cycles and refluxed under N_2 for 18 h. The crude mixture was filtered through a silica gel plug to give a brown solid (2.91 g). This was added to a flame dried Schlenk flask and dissolved in dry CH_2Cl_2 (45 mL). The resulting red solution was cooled to -84 °C and BBr_3 (1.0 M solution in CH_2Cl_2 , 28 mL, 28.0 mmol) slowly added. The mixture was left to react at r.t. for 18 h and then quenched with a few mL of H_2O , diluted with EtOAc (200 mL) washed with H_2O (100 mL \times 3) and brine (100 mL). The yellow organic layer was dried over MgSO_4 , filtered and evaporated under vacuum. The crude was purified using silica gel column chromatography (Eluent: petroleum

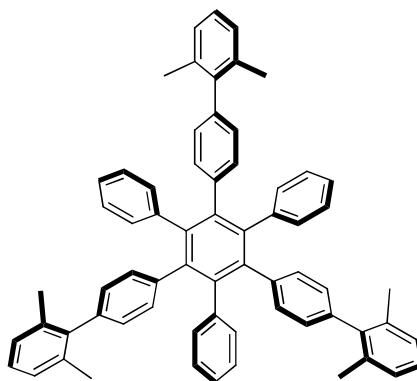
ether/CH₂Cl₂, 90:10) to give **3-3** as a white solid (446 mg, 17%). ¹H NMR (300 MHz, CD₃OD) δ: 6.89-6.79 (*m*, 15 H), 6.61-6.59 (*d*, *J* = 8.7 Hz, 6 H), 6.24 (*d*, *J* = 8.7 Hz, 6 H). ¹³C{¹H} NMR (126 MHz, MeOD) δ: 155.61, 142.71, 142.10, 141.48, 133.62, 132.72, 127.59, 125.97, 114.48. One signal not visible due to overlapping. ESI⁺ HRMS: [M]⁺ calc. for [C₄₂H₃₀O₃]⁺: 582.2195, found: 582.2193.

Synthesis of 1,3,5-(4'-Trifluoromethylsulfonylphenyl)-2,4,6-phenyl benzene (**3-4**)



In a round bottom flask, **3-3** (300 mg, 0.52 mmol) was suspended in dry pyridine (10 mL). The suspension was stirred at 0 °C and Tf₂O (0.87 mL, 5.18 mmol) slowly added. The mixture was stirred for 18 h under N₂ and then the volatiles removed under reduced pressure. The product was purified by silica gel column chromatography (Eluents: petroleum ether/EtOAc, 80:20) affording **3-4** as a white solid (360 mg, 71%). ¹H NMR (300 MHz, CD₂Cl₂) δ: 6.91-6.86 (*m*, 15 H), 6.81 (*d*, *J* = 8.8 Hz, 6 H) 6.75-6.74 (*m*, 6 H). ¹³C{¹H} NMR (126 MHz, CDCl₃) δ: 147.58, 141.04, 140.84, 139.25, 139.04, 132.99, 131.16, 127.41, 126.28, 119.86, 118.74 (*q*, *J* = 321.3 Hz). AP⁺ MS: [M]⁺ calc. for [C₄₅H₂₇F₉O₉S₃]⁺: 978.0673, found: 978.0649.

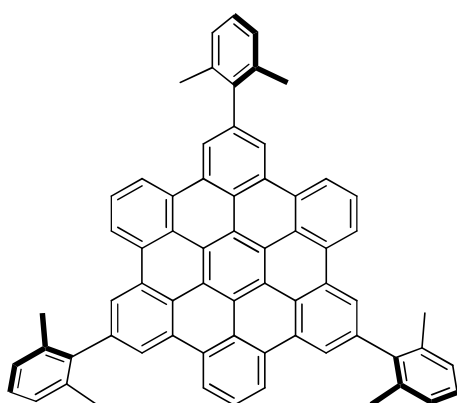
Synthesis of 1,3,5-Tri(4-xylylphenyl)-2,4,6-triphenylbenzene (**3-5**)



In Schlenk flask, **3-4** (200 mg, 0.20 mmol), 2,6-dimethylphenyl boronic acid (123 mg, 0.82 mmol), K₂CO₃ (249 mg, 1.80 mmol), [Pd(OAc)₂] (7 mg, 0.03 mmol), and SPhos (37 mg, 0.09 mmol) were added under N₂ followed by 20 mL of a previously degassed (by N₂ bubbling under sonication) dioxane/H₂O (5:1) mixture. The reaction was then

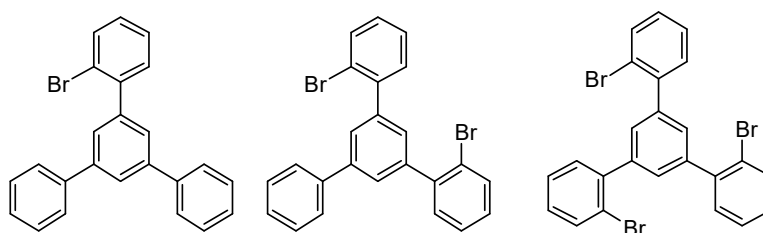
stirred at 100 °C under N₂ for 18 h. The resulting suspension was diluted with CH₂Cl₂ (100 mL), washed with H₂O (50 mL × 3), brine (100 mL) and the solvents removed under reduced pressure. The crude was purified by silica gel column chromatography (Eluents: petroleum ether/CH₂Cl₂, 80:20) affording **3-5** as a white solid (110 mg, 65%). ¹H NMR (400 MHz, CDCl₃) δ: 7.11-7.00 (*m*, 9 H); 6.95-6.87 (*m*, 21 H), 6.65 (*d*, *J* = 8.0 Hz, 6 H) 1.82 (*s*, 18 H); ¹³C{¹H} NMR (75 MHz, CDCl₃) δ: 141.99, 140.79, 140.60, 140.48, 139.37, 137.91, 136.15, 131.88, 131.74, 127.40, 127.10, 126.79, 126.66, 125.20, 20.53. ASAP⁺ HRMS: [M+H]⁺ calc. for [C₆₆H₅₅]⁺: 847.4304, found 847.4287.

Synthesis of 2,8,14-Trixylyl-hexabenzocoronene (3-2)



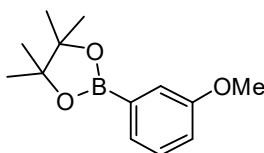
In a Schenk flask, a solution of FeCl₃ (172 mg, 1.06 mmol) in CH₃NO₂ (2 mL) was added dropwise to a stirred solution of **3-5** (30 mg, 0.035 mmol) in anhydrous CH₂Cl₂ (25 mL). The reaction mixture was stirred for 3 h at r.t. with continuous N₂ bubbling through the reaction. The resulting mixture was poured into MeOH, diluted with CH₂Cl₂ (50 mL), washed with H₂O (50 mL × 3) and brine (100 mL). The organic phase was dried over MgSO₄, filtered and evaporated under vacuum. The resulting yellow material was purified by silica gel column chromatography (Eluents: petroleum ether/CH₂Cl₂; 80:20) and preparative TLC (Eluents: petroleum ether/CH₂Cl₂; 80:20). To give **3-2** as a yellow solid (6 mg, 20%). mp: > 300 °C. ¹H NMR (300 MHz, CD₂Cl₂) δ: 9.28 (*d*, *J* = 8.0 Hz, 6 H); 9.14 (*s*, 6 H); 8.25 (*t*, *J* = 8.0 Hz, 3 H); 7.39-7.33 (*m*, 9 H); 2.29 (*s*, 18 H). ¹³C{¹H} NMR (100 MHz, CDCl₃) δ: 142.34, 140.12, 136.78, 131.19, 130.87, 127.83, 127.28, 126.04, 124.53, 123.23, 122.59, 121.78, 121.47, 21.58. IR (ATR) ν (cm⁻¹): 2953, 2918, 2851, 2367, 1610, 1580, 1458, 1437, 1375, 1362, 1269, 1101, 1029, 968, 905, 878, 853, 793, 777, 721. MALDI⁺ HRMS: [M]⁺ calc. for [C₆₆H₄₂]⁺: 834.3287, found 834.3278.

Synthesis of 2,2''-Dibromo-5'-phenyl-1,1':3',1''-terphenyl mixture (3-8, 3-8a, 3-8b)



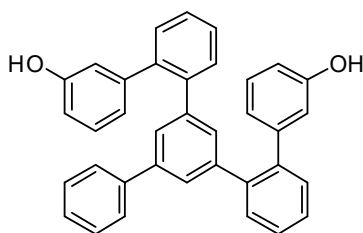
In a round bottom flask 2'-bromoacetophenone (1.60 g, 8.10 mmol) and acetophenone (500 mg, 4.17 mmol) were mixed. TfOH (0.11 mL, 1.25 mmol) was then added dropwise to the mixture and the reaction stirred at 130 °C for 7 h. The resulting black tar was allowed to cool down to r.t., diluted with CH₂Cl₂ (100 mL), washed with H₂O (100 mL × 2), brine (100 mL) and the resulting organic layers dried over MgSO₄, filtered and evaporated under vacuum. The black residue was filtered on a silica plug (eluent: Petroleum ether/CH₂Cl₂ 80:20) to give a mixture of **3-8**, **3-8a**, **3-8b** as a white spongy material (855 mg) that was directly used in the following steps.

Synthesis of 2-(3-Methoxyphenyl)-4,4,5,5-tetramethyl-1,3,2 dioxaborolane (3-15)



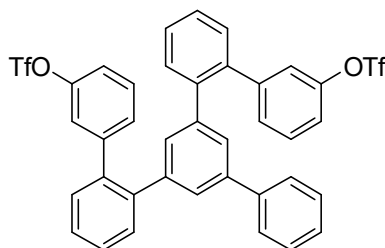
In a Schlenk flask, 3-bromoanisole (2.70 mL, 21.6 mmol) was added together with B₂Pin₂ (6.00 g, 23.7 mmol) and KOAc (6.30 g, 64.5 mmol). Anhydrous DMF (20 mL) was then added and the suspension degassed for 10 min. by bubbling N₂ under sonication. [Pd(dppf)Cl₂·CH₂Cl₂] (878 mg, 1.08 mmol) was added under N₂ and the reaction degassed for further 10 min. The suspension was heated at 90 °C under N₂ for 16 h and then diluted with H₂O (50 mL) and CH₂Cl₂ (100 mL). The organic phase was washed with H₂O (100 mL × 2), brine (100 mL), dried over MgSO₄, filtered and evaporated under vacuum. The resulting black liquid was purified on a silica plug (eluent: Petroleum ether/CH₂Cl₂ from 100% to 50:50) to give **3-15** as a transparent oil (4.1 g, 81%) ¹H NMR (300 MHz, CDCl₃) δ: 7.41 (*dt*, *J* = 7.2 Hz, 1.1 Hz, 1 H), 7.33-7.27 (*m*, 2 H), 7.01 (*ddd*, *J* = 8.2 Hz, 2.8 Hz, 1.2 Hz, 1 H), 3.83 (*s*, 3 H), 1.35 (*s*, 12 H). ¹³C{¹H} NMR (75 MHz, CDCl₃) δ: 159.18, 129.08, 127.33, 118.83, 118.06, 83.97, 55.39, 25.01. One peak missing due to ¹¹B-induced quadrupolar relaxation. IR (ATR) ν (cm⁻¹): 2993, 2977, 2933, 1576, 1490, 1420, 1352, 1313, 1270, 1143, 1045, 964, 851, 772, 706, 422. AP⁺ HRMS: [M]⁺ calc. for [C₁₃H₁₉BO₃]⁺: 233.1464; found: 233.1463.

Synthesis of 5''-Phenyl-[1,1':2',1'':3'',1''':2''',1''''-quinquephenyl]-3,3''''-diol (3-10)

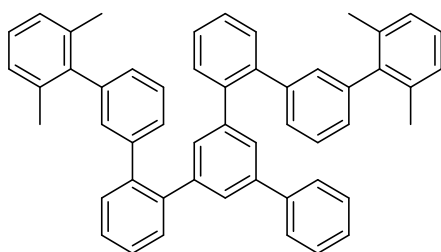


Mixture of products **3-8**, **3-8a**, **3-8b** (500 mg, 1.10 mmol*) was added in a Schlenk flask along with boronic ester **3-15** (557 mg, 2.40 mmol), Pd(OAc)₂ (25 mg, 0.10 mmol), SPhos (133 mg, 0.30 mmol) and K₂CO₃ (896 mg, 6.50 mmol). The Schlenk flask was then evacuated and backfilled with N₂ 3 times. Dioxane (5 mL) and H₂O (1 mL) were added to the mixture and the reaction degassed with N₂ bubbling under sonication for 20 min., followed by heating at 90 °C under N₂ for 18 h. The dark solution was cooled down to r.t., diluted with CH₂Cl₂ (50 mL), washed with H₂O (20 mL × 2), brine (30 mL), dried on MgSO₄, filtered and evaporated under reduced pressure to give a yellow spongy solid (674 mg, 1.3 mmol*). The obtained mixture was added in a round bottom flask under N₂ and dissolved in dry CH₂Cl₂ (50 mL). The solution was then cooled down to 0 °C and BBr₃ (1.0 M in CH₂Cl₂, 7.8 mL, 7.8 mmol) added dropwise. The reaction was allowed to reach r.t. and stirred at this temperature under N₂ for 16 h. The resulting brown solution was cooled to 0 °C, quenched with H₂O (15 mL) and then extracted with CH₂Cl₂ (50 mL × 3). The reunited organic layers were dried over MgSO₄, filtered, evaporated under reduced pressure and the residue purified by silica gel column chromatography (eluent: Petroleum ether/EtOAc 80:20) to give **3-10** as a white spongy material (122 mg, 23%). mp: 71-73 °C. ¹H NMR (300 MHz, CDCl₃) δ: 7.43-7.39 (*m*, 8 H), 7.35-7.28 (*m*, 4 H), 7.17 (*d*, *J* = 1.6 Hz, 2 H), 7.12-7.07 (*m*, 3 H), 7.03 (*dd*, *J* = 7.7 Hz, 1.1 Hz, 2 H), 6.78-6.72 (*m*, 3 H), 6.38 (*dd*, *J* = 2.4 Hz, 1.5 Hz, 2 H), 5.73 (*bs*, 2 H). ¹³C{¹H} NMR (75 MHz, CDCl₃) δ: 154.39, 143.42, 141.61, 140.97, 140.45, 140.25, 140.21, 130.64, 130.59, 130.01, 129.88, 128.66, 127.85, 127.72, 127.63, 127.25, 127.22, 122.66, 117.68, 114.18. IR (ATR) ν (cm⁻¹): 3308, 3056, 2971, 2933, 2870, 1585, 1473, 1412, 1303, 1191, 886, 788, 753, 714, 697, 615, 441, 420. AP⁺ HRMS: [M+H]⁺ calc. for [C₃₆H₂₇O₂]⁺ 491.2011; found: 491.2011.

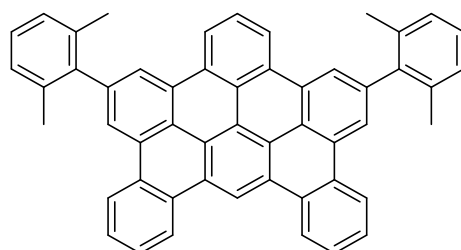
*considered as composed only of dibromo derivative.

Synthesis of 5''-Phenyl-[1,1':2',1'':3'',1'''':2''',1''''-quinquephenyl]-3,3''''-diyl bis(trifluoromethanesulfonate) (3-11)

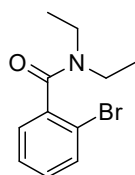
In a single necked round bottom flask, derivative **3-10** (400 mg, 0.82 mmol) was added and purged 3 times with N_2 . Anhydrous pyridine (10 mL) was added and the reaction cooled to 0 °C, followed by dropwise addition of Tf_2O (1.4 mL, 8.34 mmol). The reaction was then allowed to reach r.t. and stirred for 2 h under N_2 . The resulting dark solution was quenched with H_2O (5 mL) and extracted with CH_2Cl_2 (20 mL \times 3). The organic layers were washed with HCl 10% (50 mL \times 2), brine (50 mL), dried over $MgSO_4$, filtered and evaporated under reduced pressure. The residue was purified on a silica plug (eluent: Petroleum ether/ CH_2Cl_2 from 80:20 to 60:40) to give **3-11** as a yellowish powder (405 mg, 65%). mp: 63-64 °C. 1H NMR (300 MHz, $CDCl_3$) δ : 7.46-7.27 (*m*, 12 H), 7.25-7.23 (*m*, 1 H), 7.21-7.16 (*m*, 4 H), 7.13 (*d*, $J = 1.7$ Hz, 2 H), 7.09 (*dt*, $J = 7.5$ Hz, 1.3 Hz, 2 H), 7.06-7.01 (*m*, 3 H). $^{13}C\{^1H\}$ NMR (125 MHz, $CDCl_3$) δ : 149.66, 144.68, 141.07, 140.96, 140.50, 140.29, 138.46, 130.75, 130.46, 130.39, 130.22, 130.10, 129.69, 128.74, 128.68, 128.05, 127.65, 127.49, 127.02, 122.78, 119.54, 118.86 (*q*, $J = 322.6$ Hz). IR (ATR) ν (cm^{-1}): 3060, 3030, 1577, 1420, 1243, 1205, 1129, 900, 802, 755, 694, 602, 508. AP⁺ HRMS: $[M+H]^+$ calc. for $[C_{38}H_{25}O_6F_6S_2]^+$: 755.0997; found: 755.0986.

Synthesis of 5''-Phenyl-[1,1':2',1'':3'',1''':2''',1''''-quinquephenyl]-3,3''''-Xylen (3-12)

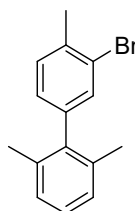
In a Schlenk flask, derivative **3-11** (335 mg, 0.44 mmol) was added together with (2,6-dimethylphenyl) boronic acid (166 mg, 1.11 mmol), Pd(OAc)₂ (11 mg, 0.05 mmol), SPhos (62 mg, 0.15 mmol) and K₂CO₃ (415 mg, 3.01 mmol). The solids were purged 3 times with N₂ and then a mixture of dioxane (10 mL) and H₂O (2 mL) added. The reaction was degassed by bubbling N₂ under sonication for 20 min. then stirred at 100 °C under N₂ for 18 h. The resulting suspension was cooled down to r.t., and CH₂Cl₂ (20 mL) added. The organic phase was washed with H₂O (20 mL × 2), brine (20 mL), dried over MgSO₄, filtered and evaporated under reduced pressure. The resulting residue was purified on a silica plug (eluent: Petroleum ether/CH₂Cl₂ 80:20) to give **3-12** as a white powder (164 mg, 50%) mp: 109-111 °C. ¹H NMR (500 MHz, CDCl₃) δ: 7.42-7.28 (*m*, 10 H), 7.25-7.19 (*m*, 5 H), 7.11-6.97 (*m*, 13 H), 6.95-6.93 (*m*, 2 H), 1.81 (*s*, 12 H). ¹³C{¹H} NMR (125 MHz, CDCl₃) δ: 142.21, 141.81, 141.77, 141.06, 140.97, 140.92, 140.58, 140.37, 136.19, 130.95, 130.70, 130.54, 128.62, 128.14, 127.65, 127.55, 127.35, 127.31, 127.27, 127.24, 127.20, 127.13, 20.90. (two peaks not visible probably due to overlapping). IR (ATR) ν (cm⁻¹): 3068, 3037, 2923, 2847, 1577, 1477, 1420, 1243, 1205, 1129, 900, 837, 802, 754, 715, 694, 420. AP⁺ HRMS: [M+H]⁺ calc. for [C₅₂H₄₃]⁺:667.3365; found: 667.3362.

6,12-bis(2,6-Dimethylphenyl)dibenzo[fg,ij]phenanthro[9,10,1,2,3-pqrst]pentaphene (3-13)

In a flame dried Schlenk flask **3-12** (10 mg, 0.015 mmol) was added under N₂ and dissolved in dry CH₂Cl₂ (3.0 mL). The solution was cooled down to 0 °C and DDQ (34 mg, 0.15 mmol) added under N₂. The reaction was then degassed 3 times using *freeze-pump-thaw* procedure and then cooled to 0 °C. TfOH (0.15 mL, 1.70 mmol) was then added dropwise and the reaction stirred at 0 °C for 1 h and at r.t. for 1.5 h. The resulting black solution was quenched with sat. NaHCO₃ (10 mL) and extracted with CH₂Cl₂ (20 mL × 3). The organic layer was washed with H₂O (20 mL × 2), brine (20 mL), dried over MgSO₄ filtered and evaporated under reduced pressure. The resulting residue was purified with preparative TLC (eluent: Petroleum ether/CH₂Cl₂ 75:25) to give **3-13** as a yellow powder (1.4 mg, 14%). mp: >300°C. ¹H NMR (400 MHz, CDCl₃) δ: 10.54 (s, 1 H), 9.30 (d, *J* = 8.0 Hz, 2 H), 9.14 (d, *J* = 8.0 Hz, 2 H), 8.99 (d, *J* = 1.1 Hz, 2 H), 8.89 (d, *J* = 8.0 Hz, 2 H), 8.86 (d, *J* = 1.1 Hz, 2 H), 8.14 (t, *J* = 8.0 Hz, 1 H), 7.90 (t, *J* = 8.0 Hz, 2 H), 7.81 (t, *J* = 8.0 Hz, 2 H), 7.38-7.34 (*m*, 2 H), 7.32-7.30 (*m*, 4 H), 2.24 (s, 12 H). ¹³C{¹H} NMR (100 MHz, CDCl₃) δ: 142.39, 139.80, 136.73, 130.90, 130.80, 130.78, 130.64, 130.54, 128.11, 128.05, 127.77, 127.09, 127.02, 124.22, 124.13, 123.63, 122.94, 122.75, 122.54, 122.44, 115.46, 21.48. Three peaks not visible due to overlapping. IR (ATR) ν (cm⁻¹): 3065, 2945, 2920, 1558, 1508, 1458, 1404, 1375, 1090, 1015, 866, 789. ASAP⁺ HRMS: [M+H]⁺ calc. for [C₅₂H₃₅]⁺: 659.2739; found: 659.2735. Crystals suitable for X-Ray diffraction were obtained from vapor diffusion of *i*-PrOH to a CH₂Br₂ solution. CCDC **1963744** contains the supplementary crystallographic data for compound **18**.

Synthesis of 2-Bromo-N,N-diethylbenzamide (3-21)

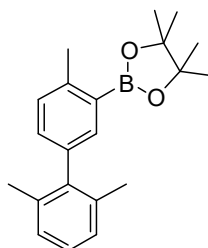
In a two necked flask, diethyl amine (1.60 mL, 15.5 mmol) and triethylamine (2.40 mL, 17.1 mmol) were added and dissolved in CH_2Cl_2 (75 mL). 2-bromobenzoyl chloride (1.80 mL, 13.7 mmol) was then added dropwise and the solution stirred at r.t. for 30 min. The reaction was quenched with 2M HCl (100 mL), extracted with CH_2Cl_2 (100 mL \times 2), washed with H_2O (100 mL \times 3), brine (100 mL), dried on MgSO_4 , filtered and evaporated under reduced pressure to give **3-21** as a transparent oil (3.4 g, quantitative). ^1H NMR (300 MHz, CD_2Cl_2) δ : 7.59-7.56 (*m*, 1 H), 7.40-7.34 (*m*, 1 H), 7.28-7.22 (*m*, 2 H), 3.80-3.69 (*m*, 1 H), 3.37-3.29 (*m*, 1 H), 3.12 (*hept*, $J = 7.2$ Hz, 2 H), 1.24 (*t*, $J = 7.1$ Hz, 3 H), 1.04 (*t*, $J = 7.1$ Hz, 3 H). $^{13}\text{C}\{^1\text{H}\}$ NMR (75 MHz, CD_2Cl_2) δ : 168.60, 139.60, 133.23, 130.41, 128.14, 127.99, 119.56, 43.24, 39.45, 14.24, 12.84. IR (ATR) ν (cm^{-1}): 3055, 2974, 2932, 2874, 1632, 1427, 1292, 1103, 768. ESI⁺ HRMS: $[\text{M}+\text{H}]^+$ calc. for $[\text{C}_{11}\text{H}_{15}\text{NOBr}]^+$: 256.0337; found: 256.0349.

Synthesis of 3'-Bromo-2,4,6-trimethyl-1,1'-biphenyl (3-19)

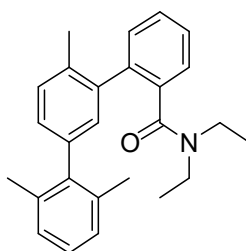
In a Schlenk flask 2-bromo-4-iodo-1-methylbenzene (1.0 g, 3.4 mmol) was added along with 2,6-dimethylboronic acid (556 mg, 3.71 mmol), PPh_3 (100 mg, 0.40 mmol) and $\text{Ba}(\text{OH})_2 \cdot 8\text{H}_2\text{O}$ (3.2 g, 10.1 mmol). The solids were purged 3 times with N_2 and suspended in a toluene/EtOH/ H_2O (10:4:2 mL) mixture. The suspension was degassed for 10 min. with N_2 bubbling under sonication and $[\text{Pd}(\text{PPh}_3)_4]$ (195 mg, 0.2 mmol) added, followed by further 10 min. of degassing. The reaction was heated at 100 °C for 24 h under N_2 , then diluted with H_2O (50 mL) and CH_2Cl_2 (100 mL). The organic layer was washed with H_2O (100 mL \times 2), brine (100 mL), dried over MgSO_4 , filtered and evaporated under reduced pressure. The resulting residue was purified by chromatography on a short silica plug (eluent: Petroleum ether 100%) to give **3-19** as a transparent oil (639 mg, 69%). ^1H NMR (300 MHz, CDCl_3) δ : 7.34 (*d*, $J = 1.5$ Hz, 1 H), 7.29 (*d*, $J = 8.0$ Hz, 1 H), 7.19-7.14 (*m*, 1 H), 7.11-7.08 (*m*, 2 H), 7.00 (*dd*, $J = 7.7$ Hz, 200

1.7 Hz, 1 H), 2.46 (s, 3 H), 2.04 (s, 6 H). $^{13}\text{C}\{^1\text{H}\}$ NMR (75 MHz, CDCl_3) δ : 140.53, 140.38, 136.22, 136.19, 132.84, 130.95, 128.22, 127.48, 127.45, 125.06, 22.79, 20.98. IR (ATR) ν (cm^{-1}): 3057, 3019, 2949, 2920, 2855, 1543, 1464, 1375, 1042, 1024, 883, 824, 768, 712, 677, 606, 434. EI^+ HRMS: $[\text{M}]^+$ calc. for $[\text{C}_{15}\text{H}_{15}\text{Br}]^+$: 274.0357; found: 274.0363.

Synthesis of 4,4,5,5-Tetramethyl-2-(2',4,6'-trimethyl-[1,1'-biphenyl]-3-yl)-1,3,2-dioxaborolane (3-20)

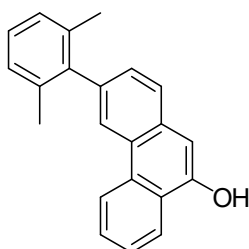


In a Schlenk flask **3-19** (639 mg, 2.33 mmol) was added along with B_2Pin_2 (650 mg, 2.56 mmol), KOAc (686 mg, 7.00 mmol), $[\text{Pd}(\text{dppf})\text{Cl}_2 \cdot \text{CH}_2\text{Cl}_2]$ (98 mg, 0.12 mmol) and suspended in dry DMF (5 mL). The mixture was degassed for 20 min. with N_2 bubbling under sonication and then heated at 90 °C for 18 h under N_2 . The resulting black suspension was diluted with H_2O (50 mL) and CH_2Cl_2 (100 mL). The organic layer was washed with H_2O (50 mL \times 3), brine (50 mL), dried over MgSO_4 , filtered and evaporated under reduced pressure. The residue was purified by chromatography on a short silica plug (eluent: Petroleum ether/ CH_2Cl_2 80:20) to give **3-20** as transparent crystals (470 mg, 63%). mp: 106-108 °C. ^1H NMR (300 MHz, CDCl_3) δ : 7.52 (*d*, $J = 1.9$ Hz, 1 H), 7.22 (*d*, $J = 7.7$ Hz, 1 H), 7.16-7.06 (*m*, 4 H), 2.58 (s, 3 H), 2.03 (s, 6 H), 1.34 (s, 12 H). $^{13}\text{C}\{^1\text{H}\}$ NMR (75 MHz, CDCl_3) δ : 143.08, 141.95, 137.43, 136.47, 136.41, 131.47, 129.99, 127.28, 126.93, 83.56, 25.06, 22.11, 21.15. One peak missing due to ^{11}B -induced quadrupolar relaxation. IR (ATR) ν (cm^{-1}): 2974, 2928, 1408, 1389, 1373, 1335, 1304, 1269, 1254, 1242, 1165, 1146, 1069, 964, 876, 849, 829, 779, 737, 679. ESI^+ HRMS: $[\text{M}+\text{H}]^+$ calc. for $[\text{C}_{21}\text{H}_{28}\text{BO}_2]^+$: 323.2182; found: 323.2186.

Synthesis of N,N-Diethyl-2'',6'',6''-trimethyl-[1,1':3',1''-terphenyl]-2-carboxamide (3-22)

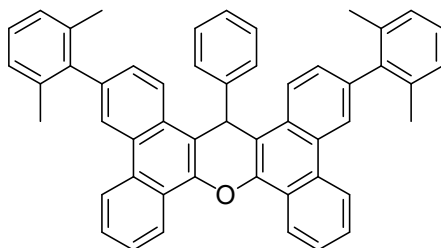
In a Schlenk flask **3-21** (442 mg, 1.73 mmol) was added followed by **3-20** (465 mg, 1.44 mmol) and K_2CO_3 (600 mg, 4.35 mmol). The solids were suspended in a dioxane/ H_2O (10 mL/2 mL) mixture and the suspension degassed for 10 min. with N_2 bubbling under sonication. $[Pd(dppf)Cl_2 \cdot CH_2Cl_2]$ (60 mg, 0.07 mmol) was then added under N_2 , the reaction further degassed for 10 min. and then stirred at 95 °C under N_2 for 16 h. The resulting mixture was diluted with CH_2Cl_2 (30 mL). The organic layer was washed with H_2O (50 mL \times 3), brine (50 mL), dried on $MgSO_4$, filtered and evaporated under reduced pressure. The crude product was purified by chromatography on a short silica plug (eluent: Petroleum ether/EtOAc 80:20) to give **3-22** as white flakes (468 mg, 74%). mp: 148-150 °C. 1H NMR (300 MHz, $CDCl_3$) δ : 7.45-7.28 (*m*, 5 H), 7.16-7.02 (*m*, 5 H), 3.51-2.90 (*bt*, 4 H), 2.28 (*s*, 3 H), 2.08 (*s*, 6 H), 0.92 (*t*, $J = 7.0$ Hz, 6 H). $^{13}C\{^1H\}$ NMR (75 MHz, $CDCl_3$) δ : 170.24, 141.49, 139.90, 138.43, 137.79, 137.00, 136.15, 130.49, 130.25, 128.47, 127.40, 127.31, 126.97, 126.48, 42.78, 38.35, 21.02, 20.20, 13.84, 12.62. Three peaks not visible probably due to overlapping. IR (ATR) ν (cm^{-1}): 3044, 2965, 2918, 1616, 1595, 1431, 1375, 1267, 1080, 827, 775, 748, 625. AP⁺ HRMS: $[M+H]^+$ calc. for $[C_{26}H_{30}NO]^+$: 372.2327; found: 372.2330.

Obtained following a procedure developed by Rantanen *et al.*^[33]

Synthesis of 3-(2,6-Dimethylphenyl)phenanthren-9-ol (3-23)

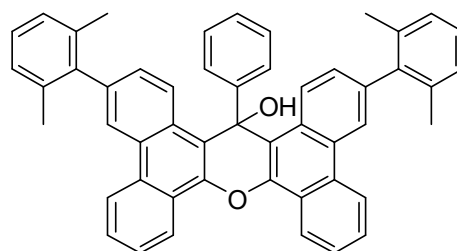
To a solution of LDA (1.0 M in THF, 3.0 mL, 3.0 mmol) in dry THF (4 mL) at 0 °C under N₂, a 0.25 M solution of **3-22** (370 mg, 1.00 mmol) in dry THF was added. The resulting mixture was stirred at r.t. under N₂ for 30 min. and then quenched with a NH₄Cl saturated solution. The aqueous layer was extracted with Et₂O (20 mL × 3) and the organic phase dried over MgSO₄, filtered and evaporated under reduced pressure to give pure **3-23** as a fluffy brown solid (295 mg, 99%). mp: 64-66 °C. ¹H NMR (400 MHz, CDCl₃) δ: 8.62-8.60 (*m*, 1 H), 8.38 (*s*, 1 H), 8.34-8.32 (*m*, 1 H), 7.77 (*d*, *J* = 8.0 Hz, 1H), 7.69-7.64 (*m*, 2 H), 7.34 (*dd*, *J* = 8.0 Hz, 1.5 Hz, 1 H), 7.25-7.21 (*m*, 1 H), 7.18-7.16 (*m*, 2 H), 7.08 (*s*, 1H), 2.09 (*s*, 6 H). (1H from OH not visible). ¹³C{¹H} NMR (125 MHz, CDCl₃) δ: 149.65, 142.27, 137.18, 136.63, 131.70, 131.45, 128.41, 127.52, 127.39, 127.30, 127.00, 126.63, 125.83, 123.02, 122.91, 122.57, 106.09, 21.19. One peak not visible probably due to overlapping. IR (ATR) ν (cm⁻¹): 3341, 3063, 3013, 2951, 1674, 1593, 1277, 1227, 768. EI⁺ HRMS: [M]⁺ calc. for [C₂₂H₁₈O]⁺: 298.1358; found: 298.1360.

Obtained following a procedure developed by Cai *et al.*^[34]

Synthesis of 3,15-Bis(2,6-dimethylphenyl)-18-phenyl-18H-tetrabenzo[a,c,h,j]xanthenes (3-24)

In a single necked round bottom flask, **3-23** (299 mg, 1.00 mmol) was added with benzaldehyde (48 μ L, 0.50 mmol) and the mixture suspended in AcOH (2.0 mL). Conc. HCl (36 μ L) was then added and the reaction stirred at 100 °C until a yellow precipitate formed. The reaction was then filtered, and the residue purified by chromatography on a short silica plug (eluent: Petroleum ether/ CH_2Cl_2 60:40) to give **3-24** as a faint yellow powder (291 mg, 87%). mp: 224-226 °C. ^1H NMR (300 MHz, CDCl_3) δ : 8.97 (*dd*, J = 8.2 Hz, 1.1 Hz, 2 H), 8.68 (*d*, J = 8.2 Hz, 2 H), 8.62 (*d*, J = 8.2 Hz, 2 H), 8.52 (*d*, J = 1.5 Hz, 2 H), 7.86 (*t*, J = 8.2 Hz, 2 H), 7.79-7.71 (*m*, 4 H), 7.52 (*dd*, J = 8.4 Hz, 1.6 Hz, 2 H), 7.23-7.18 (*m*, 8 H), 7.08 (*t*, J = 7.4 Hz, 1 H), 6.65 (*s*, 1 H), 2.12 (*s*, 6 H), 2.06 (*s*, 6 H). $^{13}\text{C}\{^1\text{H}\}$ NMR (75 MHz, CDCl_3) δ : 144.77, 144.71, 141.91, 138.01, 136.66, 136.55, 130.91, 129.07, 128.78, 128.75, 128.58, 127.58, 127.54, 127.42, 127.38, 127.25, 126.72, 125.49, 123.74, 123.62, 122.93, 122.70, 114.82, 38.45, 21.36, 21.16. IR (ATR) ν (cm^{-1}): 3059, 3021, 2951, 2916, 1597, 1439, 1265, 1184, 1134, 1026, 764, 702. AP⁺ HRMS: $[\text{M}+\text{H}]^+$ calc. for $[\text{C}_{51}\text{H}_{39}\text{O}]^+$: 667.3001; found: 667.2996.

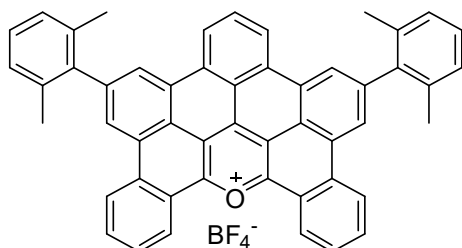
Obtained following a procedure developed by Wu *et al.*^[35]

Synthesis of 3,15-bis(2,6-dimethylphenyl)-18-phenyl-18H-tetrabenzo[a,c,h,j]xanthen-18-ol (3-25)

In a round bottom flask equipped with a condenser, **3-24** (50 mg, 0.08 mmol) was added with PbO_2 (27 mg, 0.11 mmol) and suspended in AcOH (2 mL). The reaction was refluxed for 3 h, poured onto crushed ice, extracted with EtOAc (20 mL \times 3) and the resulting organic phase washed with brine (30 mL), dried on MgSO_4 , filtered and evaporated under reduced pressure. The resulting orange solid was purified with preparative TLC (eluent: Petroleum ether/ CH_2Cl_2 70:30) to give **3-25** as a white powder (21 mg, 41%). mp: 202-204 °C. ^1H NMR (300 MHz, CD_2Cl_2) δ : 9.19 (*d*, $J = 8.7$ Hz, 2 H), 8.98 (*dd*, $J = 8.2$ Hz, 1.1 Hz, 2 H), 8.65 (*d*, $J = 8.2$ Hz, 2 H), 8.46 (*d*, $J = 1.7$ Hz, 2 H), 7.95 (*d*, $J = 8.4$ Hz, 2 H), 7.86 (*t*, $J = 8.2$, 2 H), 7.79-7.73 (*m*, 2 H), 7.32 (*dd*, $J = 8.7$ Hz, 1.8 Hz, 2 H), 7.29-7.20 (*m*, 3 H), 7.20-7.07 (*m*, 6 H), 3.55 (*s*, 1 H), 2.09 (*s*, 6 H), 2.01 (*s*, 6 H). $^{13}\text{C}\{^1\text{H}\}$ NMR (100 MHz, CD_2Cl_2) δ : 147.37, 142.46, 142.20, 138.25, 136.86, 136.76, 132.07, 129.73, 128.81, 128.63, 128.57, 128.30, 127.92, 127.90, 127.84, 127.72, 126.92, 125.13, 123.85, 123.78, 123.18, 116.13, 74.72, 21.37, 21.30. IR (ATR) ν (cm^{-1}): 3059, 2955, 2920, 1597, 1369, 1304, 764, 721, 702, 640. ESI-HRMS: $[\text{M}-\text{H}]^-$ calc. for $[\text{C}_{51}\text{H}_{37}\text{O}_2]^-$ 681.2794; found: 681.2789.

Obtained following a procedure developed by Wu *et al.*^[35]

Synthesis of 6,12-Bis(2,6-dimethylphenyl)dibenzo[*c,h*]benzo[5,6]tetraceno[1,12,11,10-*ijklmna*]xanthen-18-ium tetrafluoro borate (3-27^{BF}**)**

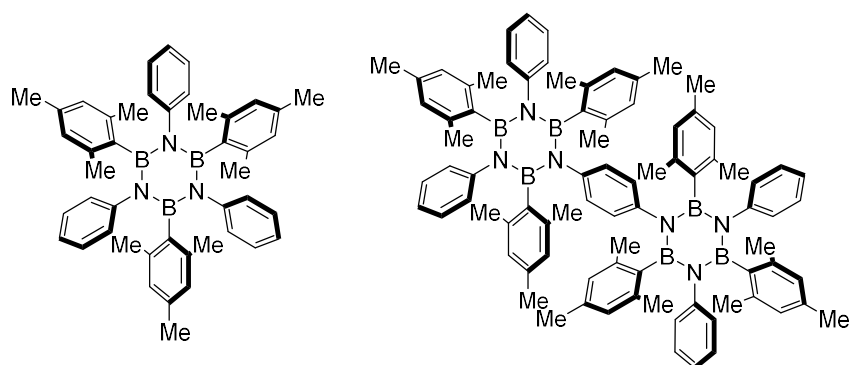


In a round bottom flask **3-25** (20 mg, 0.03 mmol) was added and suspended in 0.8 mL of a 1:1 mixture of Ac₂O and toluene. HBF₄·Et₂O (excess) was added dropwise at 0 °C to give the formation of an orange precipitate. The suspension was then diluted with anhydrous Et₂O (5 mL), transferred into a falcon tube and centrifuged (5000 rpm, 5 min.). After removal of the supernatant, the orange solid was again suspended in Et₂O and centrifuged. This procedure was repeated one more time for a total of 3 washings. The resulting orange powder was then dissolved in a 1:1 mixture of AcOH and CH₂Cl₂ and irradiated for 24 h at 365 nm. The resulting deep red solution was evaporated under reduced pressure to give **3-27^{BF}** as a deep purple powder (18 mg, 80%). mp: 258-260 °C. ¹H NMR (400 MHz, CD₂Cl₂) δ: 9.64 (*d*, *J* = 8.0 Hz, 2 H), 9.39 (*d*, *J* = 8.0 Hz, 2 H), 9.30 (*s*, 2 H), 9.23 (*s*, 2 H), 9.15 (*d*, *J* = 8.0 Hz, 2 H), 8.71 (*t*, *J* = 8.0 Hz, 1 H), 8.37-8.28 (*m*, 4 H), 7.43-7.35 (*m*, 6 H), 2.22 (*s*, 12 H). ¹³C{¹H} NMR (75 MHz, MeOD/CD₂Cl₂ 1:1) δ: 144.97, 141.23, 136.78, 136.59, 136.27, 135.76, 131.48, 130.87, 129.81, 129.11, 128.60, 128.14, 127.95, 126.08, 125.76, 125.42, 123.72, 119.74, 21.43. (five peaks not visible probably due to low solubility). ¹¹B{¹H} NMR (160 MHz, CD₂Cl₂) δ: -1.21. ¹⁹F{¹H} NMR (376 MHz, CD₂Cl₂) δ: -153.14. IR (ATR) ν (cm⁻¹): 3063, 3024, 2916, 2851, 1721, 1582, 1558, 1516, 1493, 1462, 1427, 1400, 1342, 1312, 1049, 1030, 841, 768, 718, 671, 621, 521, 413. ESI⁺ HRMS: [M]⁺ calc. for [C₅₁H₃₃O]⁺: 661.2531; found: 661.2518.

Obtained following a modified procedure based on the work of Wu *et al.*^[35]

Chapter 4

Synthesis of Mesityl multi-borazines 1-66 and 4-3



In a flame dried Schlenk flask, freshly distilled aniline (0.26 mL, 2.85 mmol), *p*-phenyldiamine (0.15 g, 1.39 mmol) and dry toluene (6 mL), were added. The mixture was heated at 80 °C under Argon and BCl₃ (1.0 M in heptane, 6.0 mL, 6.0 mmol) added dropwise and the resulting suspension stirred for 10 min. at r.t. The Schlenk flask was then equipped with a condenser connected to a CaCl₂ trap and the suspension refluxed for 18 h. After exchanging the condenser with a septum, the reaction was degassed 5 times following the *freeze-pump-thaw* procedure to remove residual HCl. In parallel, to a solution of 2-bromomesitylene (0.71 mL, 4.70 mmol) in dry THF (15 mL), *t*-BuLi (1.7 M in hexanes, 5.8 mL, 9.9 mmol) was added dropwise at -84 °C. The solution was allowed to warm at 0 °C and stirred for 10 min. the degassed toluene suspension was thus transferred to the THF solution at 0 °C and allowed to react for 18 h at r.t.. The final mixture was diluted with EtOAc (90 mL) and washed with H₂O (3 × 100 mL) and brine (50 mL). The organic layer was dried over MgSO₄, filtered and evaporated under reduced pressure. The products were purified by silica gel column chromatography (eluent: Petroleum ether/CH₂Cl₂ 80:20) affording **1-66** (36 mg, 6%) as white powder. Additionally, a mixture of other products was obtained. These were separated by Rec-GPC using CHCl₃ as eluent to afford **4-3** (40 mg, 5%) as white powder.

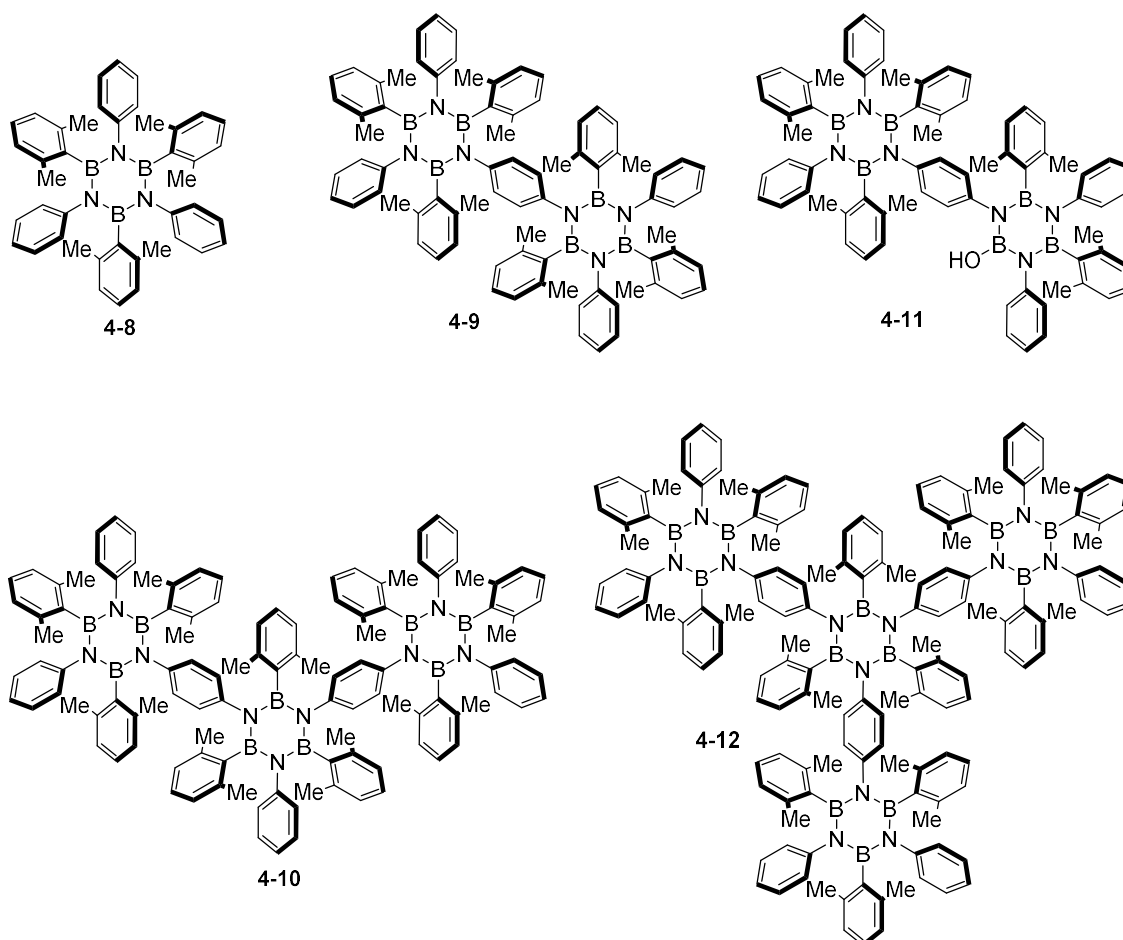
1-66 (data according to literature)^[36]: ¹H NMR (400 MHz, CDCl₃) δ: 6.84-6.70 (*m*, 15 H), 6.33 (*s*, 6 H), 2.23 (*s*, 18 H), 1.97 (*s*, 9 H). ¹³C{¹H} NMR (126 MHz, CD₂Cl₂) δ 146.42, 137.35, 136.17, 127.12, 126.81, 126.28, 124.27, 23.12, 21.15. ¹¹B{¹H} NMR (128 MHz, CDCl₃) δ: 37.02.

4-3: mp: >300 °C. ¹H NMR: (400 MHz, CDCl₃) δ: 6.69 (*s*, 20 H), 6.39 (*s*, 8 H), 6.29 (*s*, 4 H), 6.12 (*s*, 4 H), 2.15 (*s*, 12 H), 2.10 (*s*, 12 H), 1.95 (*s*, 6 H), 1.89 (*s*, 24 H). ¹³C{¹H} NMR (100 MHz, CDCl₃) δ: 146.25, 141.97, 137.45, 137.33, 136.61, 136.10, 135.52, 127.24, 126.55, 126.39, 126.20, 125.83, 124.05, 22.87, 22.58, 21.30, 21.15. ES⁺

HRMS: $[M+Na]^+$ calc. for $[C_{84}H_{90}B_6N_6Na]^+$ 1271.7678; found: 1271.7729. CCDC 1873315 contains the supplementary crystallographic data for compound 4-3.

Synthesis of Xylyl multi-borazines 4-8, 4-9, 4-10, 4-11 and 4-12*

*mixture of isomers



In a flame dried Schlenk flask, freshly distilled aniline (0.49 mL, 5.37 mmol), *p*-phenyldiamine (0.29 g, 2.68 mmol) and dry toluene (12 mL), were added. The mixture was heated at 80 °C under N_2 and BCl_3 (1.0 M in heptane, 11.5 mL, 11.5 mmol) added dropwise. The reaction was cooled down to 0 °C and stirred for 10 min. The Schlenk flask was then equipped with a condenser connected to a $CaCl_2$ trap and the suspension refluxed for 18 h. After exchanging the condenser with a septum, the reaction was degassed 5 times following the *freeze-pump-thaw* procedure to remove residual HCl. In parallel, to a solution of 2-bromo-1,3-dimethylbenzene (2.16 mL, 16.08 mmol) in dry THF (40 mL), *n*-BuLi (1.6 M in hexanes, 10.7 mL, 17.1 mmol) was added dropwise at -84 °C. The solution was allowed to warm at 0 °C and stirred for 10 min. the degassed toluene suspension was thus transferred to the THF solution at 0 °C and allowed to react for 18 h at r.t.. The final mixture was diluted with EtOAc (150 mL) and washed with H_2O (2×100 mL) and brine (2×100 mL). The organic layer was dried

over MgSO₄, filtered and evaporated under reduced pressure. The solid residue was precipitated from cold MeOH and filtered. The resulting white solid was purified by silica gel column chromatography (eluent: Petroleum ether/CH₂Cl₂ 70:30) to afford **4-8** (182 mg, 16%) and **4-9** (107 mg, 7%) as white powders. Additionally, 3 fractions composed by mixtures of products were obtained. The first 2 fractions were purified by Rec-GPC using CHCl₃ as eluent. Purification of the first fraction afforded **4-10** (19 mg, 1%) and **4-11** (22 mg, 2%) as white powders. Purification of the second fraction gave **4-12**, which was further purified with preparative TLC (eluent: Petroleum ether/CH₂Cl₂ 60:40) to give the desired product (2 mg, 0.1%). The third fraction was analysed by GPC at Warwick university and resulted in a mixture of hydroxylated oligomers.

4-8: mp: >300 °C. ¹H NMR (300 MHz, CDCl₃) δ: 6.87-6.84 (*m*, 6 H), 6.80-6.70 (*m*, 12 H), 6.53 (*d*, *J* = 7.5 Hz, 6 H) 2.30 (*s*, 18 H). ¹³C{¹H} NMR (75 MHz, CDCl₃) δ: 146.09, 137.50, 127.14, 126.98, 126.91, 125.39, 124.62, 23.29. One carbon missing due to ¹¹B induced quadrupolar relaxation. ¹¹B NMR (160 MHz, CDCl₃) δ: 36.43. IR (ATR) ν (cm⁻¹): 3061, 3009, 2947, 2916, 2855, 1595, 1489, 1427, 1356, 1288, 1072, 1026, 766, 748, 727, 696, 567, 529, 519. AP⁺ HRMS: [M+H]⁺ calc. for [C₄₂H₄₃B₃N₃]⁺: 622.3736, found: 622.3766. Crystals suitable for X-Ray diffraction were obtained from slow evaporation of CHCl₃.CCDC **1873312** contains the supplementary crystallographic data for compound **4-8**.

4-9: mp: >300 °C. ¹H NMR (500 MHz, CDCl₃) δ: 6.85 (*s*, 4 H), 6.73 (*s*, 22 H), 6.59-6.51 (*m*, 12 H), 6.24 (*s*, 4H), 2.20 (*s*, 12 H), 1.99 (*s*, 24 H). ¹³C{¹H} NMR (125 MHz, CDCl₃) δ: 145.94, 142.09, 137.57, 137.50, 127.09, 126.79, 126.65, 125.86, 125.63, 125.34, 124.40, 23.06, 22.94. Two carbon atoms missing due to ¹¹B induced quadrupolar relaxation. ¹¹B{¹H} NMR (160 MHz, CDCl₃) δ: 37.13. IR (ATR) ν (cm⁻¹): 3057, 2943, 2914, 2859, 1595, 1489, 1452, 1352, 1288, 1070, 1018, 766, 698. MALDI⁺ HRMS: [M]⁺ calc. for [C₇₈H₇₈B₆N₆]⁺: 1164.6846, found: 1164.6812. Crystals suitable for X-Ray diffraction were obtained from slow diffusion of pentane in CHCl₃.CCDC **1873316** contains the supplementary crystallographic data for compound **4-9**.

4-10: mp: >300 °C. ¹H NMR (500 MHz, CDCl₃) δ: 6.91 (*t*, *J* = 7.5 Hz, 1 H), 6.83-6.75 (*m*, 7 H), 6.70-6.68 (*m*, 21 H), 6.61-6.60 (*m*, 3 H), 6.57-6.52 (*m*, 12 H), 6.50-6.47 (*m*, 8 H), 6.13 (*d*, *J* = 8.7 Hz, 4 H), 6.04 (*d*, *J* = 8.7 Hz, 4 H), 2.16 (*s*, 12 H), 1.95 (*s*, 12 H), 1.94 (*s*, 12 H), 1.80 (*s*, 12 H), 1.62 (*s*, 6 H). ¹³C{¹H} NMR (126 MHz, CDCl₃) δ: 145.97, 145.94, 141.97, 141.92, 137.58, 137.55, 137.48, 127.13, 127.07, 126.76, 126.68, 126.63, 126.51, 126.39, 126.00, 125.64, 125.60, 125.51, 125.32, 124.39, 124.20, 23.07, 22.97, 22.95, 22.75, 22.52. ¹¹B{¹H} NMR (160 MHz, CDCl₃) δ: 40.69. IR (ATR) ν

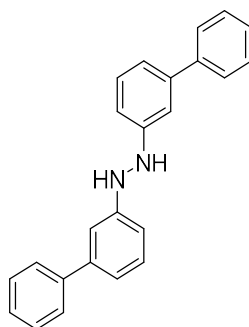
(cm^{-1}): 3040, 2916, 2855, 1597, 1425, 1352, 1302, 1288, 764, 698. MALDI⁺ HRMS: $[\text{M}]^+$ calc. for $[\text{C}_{114}\text{H}_{114}\text{B}_9\text{N}_9]^+$ 1708.0035; found: 1707.9987. Crystals suitable for X-Ray diffraction were obtained from slow diffusion of pentane in CHCl_3 . CCDC **1873317** contains the supplementary crystallographic data for compound **4-10**.

4-11: mp: >300 °C. ^1H NMR (500 MHz, CDCl_3) δ : 7.07 (*t*, $J = 7.7$ Hz, 1 H), 7.00-6.96 (*m*, 2 H), 6.79-6.78 (*m*, 4 H), 6.76-6.64 (*m*, 16 H), 6.60-6.56 (*m*, 2 H), 6.53-6.48 (*m*, 10 H), 6.43 (*t*, $J = 8.1$ Hz, 3 H), 6.33 (*d*, $J = 8.5$ Hz, 1 H), 3.49-3.17 (*m*, 1 H), 2.23 (*s*, 6 H), 2.19 (*s*, 9 H), 2.06 (*bs*, 6 H), 1.98 (*s*, 6 H), 1.90 (*s*, 3 H). $^{13}\text{C}\{^1\text{H}\}$ NMR (126 MHz, CDCl_3) δ : 146.13, 146.04, 145.95, 144.32, 143.54, 142.87, 140.14, 139.55, 137.56, 137.52, 137.41, 137.25, 127.96, 127.48, 127.45, 127.19, 127.07, 126.97, 126.91, 126.87, 126.85, 126.80, 126.67, 125.89, 125.86, 125.56, 125.41, 125.38, 125.30, 125.10, 124.61, 124.56, 124.38, 23.17, 23.12, 22.92, 22.83. $^{11}\text{B}\{^1\text{H}\}$ NMR (160 MHz, CDCl_3) δ : 36.59, 26.27. IR (ATR) ν (cm^{-1}): 3601, 3059, 2916, 2855, 1678, 1597, 1508, 1491, 1452, 1425, 1354, 1308, 1213, 1163, 1123, 1074, 847, 766, 748, 729, 719, 696, 658, 608, 575, 527. ASAP⁺ HRMS: $[\text{M}]^+$ calc. for $[\text{C}_{70}\text{H}_{70}\text{B}_6\text{N}_6\text{O}]^+$: 1076.6169, found: 1076.6207. Crystals suitable for X-Ray diffraction were obtained from slow evaporation of petroleum ether CH_2Cl_2 mixture. CCDC **1873314**, **1873313** contain the supplementary crystallographic data for compound **4-11**.

4-12: mp: >300 °C. ^1H NMR (500 MHz, CD_2Cl_2) δ : 6.93-6.44 (*m*, 69 H), 6.21 (*d*, $J = 8.7$ Hz, 1 H), 6.15-6.13 (*m*, 3 H), 6.06-6.03 (*m*, 3 H), 5.99 (*d*, $J = 0.7$ Hz, 2 H), 2.26-2.12 (*m*, 18 H), 1.97-1.95 (*m*, 18 H), 1.81 (*s*, 9 H), 1.80 (*s*, 3 H), 1.62 (*s*, 6 H), 1.52 (*s*, 18 H). IR (ATR) ν (cm^{-1}): 3055, 2920, 2854, 1597, 1493, 1454, 1427, 1358, 1304. MALDI⁺ HRMS: $[\text{M}]^+$ calc. for $[\text{C}_{150}\text{H}_{150}\text{B}_{12}\text{N}_{12}]^+$ 2251.3223; found: 2251.3375.

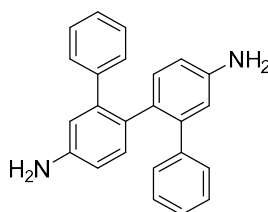
Oligomeric fraction: IR (ATR) ν (cm^{-1}): 3613, 3057, 2945, 2916, 1597, 1491, 1356, 1308, 766, 698. $^{11}\text{B}\{^1\text{H}\}$ NMR (160 MHz, CDCl_3) δ : 37.53, 25.17.

Synthesis of 1,2-Di([1,1'-biphenyl]-3-yl)hydrazine (4-16)



In a pressure vessel *m*-nitrobiphenyl (2.0 g, 10.0 mmol) was added followed by ethylenediamine (6.7 mL, 100.0 mmol). The resulting suspension was frozen with liquid N₂ and the flask evacuated until a pressure below 1 mbar was reached. The flask was sealed, and the reaction heated at 150 °C for 24 h. The resulting mixture was then allowed to cool down, diluted with EtOAc (100 mL) washed with H₂O (50 mL × 3) and brine (50 mL). The resulting organic layer was dried over MgSO₄, filtered and evaporated. The resulting residue was then precipitated with petroleum ether affording compound **4-16** as a yellow powder (908 mg, 52%). mp: 130-132 °C. ¹H NMR (300 MHz, CDCl₃) δ: 7.58-7.55 (*m*, 4 H), 7.43-7.38 (*m*, 4 H), 7.35-7.27 (*m*, 4 H), 7.13-7.12 (*m*, 2 H), 7.09 (*ddd*, *J* = 7.6 Hz, *J* = 1.7 Hz, *J* = 1.0 Hz, 2 H), 6.88 (*ddd*, *J* = 8.0 Hz, *J* = 2.3 Hz, *J* = 1.0 Hz, 2 H) 5.75 (*s*, 2 H). ¹³C{¹H} NMR (75 MHz, CDCl₃) δ: 149.44, 142.68, 141.43, 129.94, 128.80, 127.45, 127.32, 119.21, 111.49, 111.27. IR (ATR) ν (cm⁻¹): 3352, 3325, 3036, 1601, 1584, 1570, 1474, 1439, 1398, 1310, 1273, 1209, 1182, 1161, 1076, 1049, 1026, 989, 924, 872, 856, 791, 754, 696, 640, 615, 515, 457. ES⁺ HRMS: [M+H]⁺ calc. for [C₂₄H₂₁N₂]⁺: 337.1705, found: 337.1711.

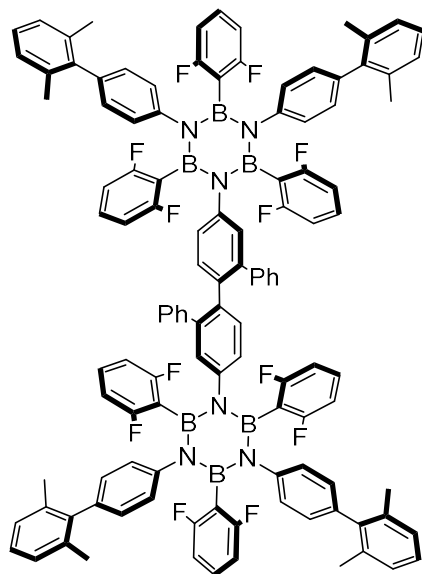
Synthesis of [1,1':2',1'':2'',1'''-quaterphenyl]-4'',5'-diamine (4-17)



In a round bottom flask **4-16** (1.0 g, 3.0 mmol) was added and suspended in 34 mL of degassed 10% aq. HCl. The reaction was then equipped with a condenser closed with a rubber septum connected to a N₂ filled balloon and refluxed for 3 h. The reaction was neutralized using a sat. K₂CO₃ aq. solution and the resulting aqueous layers extracted with EtOAc (50 mL × 3). The resulting organic solution was washed with brine (50 mL), dried on MgSO₄, evaporated and the residue purified on a silica gel plug (eluent: Petroleum ether/EtOAc gradient from 90:10 to 90:20) to give **4-17** as a brown solid (252 mg, 25%). ¹H NMR (300 MHz, CDCl₃) δ: 7.12 (*d*, *J* = 8.1 Hz, 2 H), 7.06-7.02 (*m*, 3

H), 6.99-6.97 (*m*, 3 H), 6.66-6.63 (*m*, 6 H), 6.49 (*d*, $J = 2.5$ Hz, 2 H), 3.63 (*bs*, 4 H). $^{13}\text{C}\{^1\text{H}\}$ NMR (75 MHz, CDCl_3) δ : 145.22, 142.09, 141.64, 132.96, 130.81, 129.22, 127.49, 125.81, 116.80, 114.18. IR (ATR) ν (cm^{-1}): 3460, 3360, 3215, 3026, 1620, 1568, 1477, 1452, 1389, 1315, 1265, 1225, 984, 870, 829, 816, 772, 733, 698, 623, 569, 554, 529, 457, 447, 430, 424, 417, 403. EI^+ HRMS: $[\text{M}]^+$ calc. for $[\text{C}_{24}\text{H}_{20}\text{N}_2]^+$: 336.1626, found: 336.1633.

Synthesis 2,6-Difluoro aryl multi-borazine (4-19)



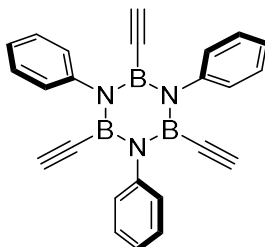
In a flame dried Schlenk flask, **2-10** (473 mg, 2.40 mmol), **4-17** (200 mg, 0.60 mmol) and dry toluene (8.0 mL) were added. The mixture was heated at 80 °C under N_2 and BCl_3 (1.0 M in heptane, 3.6 mmol, 3.6 mL) added dropwise. The reaction was cooled down to 0 °C and stirred for 10 min. The Schlenk flask was then equipped with a condenser connected to a CaCl_2 trap and the reaction refluxed for 18 h. The condenser was then exchanged with a septum and the resulting white suspension degassed 5 times following the *freeze-pump-thaw* procedure to remove residual HCl. In parallel, to a solution of 1-bromo-2,6-difluorobenzene (0.41 mL, 3.66 mmol) in dry THF (10 mL), *n*-BuLi (1.6 M in hexanes, 2.3 mL, 3.7 mmol) was added dropwise at -84 °C and the solution allowed to warm at 0 °C and stirred for 10 min. The degassed toluene suspension was transferred to the THF solution at -84 °C and allowed to react for 3 h at the same temperature followed by 15 h at r.t.. The final mixture was diluted with EtOAc (10 mL), washed with water (2 × 100 mL) and brine (2 × 100 mL). The organic layer was dried over MgSO_4 , filtered and evaporated under reduced pressure. The solid residue was purified with silica gel plug (eluent: Petroleum ether/ CH_2Cl_2 gradient from 90:10 to 80:20) to afford **2-27** (100 mg, 13%) and **4-19** (30 mg, 3%) as white powders

4-19: mp: >300 °C. ^1H NMR (300 MHz, CDCl_3) δ : 7.37-7.32 (*m*, 2 H), 7.15-6.93 (*m*, 34 H), 6.75-6.63 (*m*, 12 H), 6.59-6.41 (*m*, 12 H), 6.20 (*d*, $J = 7.2$ Hz, 2 H) 1.63-1.59 (*m*, 24 H). $^{13}\text{C}\{^1\text{H}\}$ NMR (126 MHz, CD_2Cl_2) δ : 164.31, 164.17, 164.05, 162.40, 162.26, 162.12, 157.86, 145.35, 144.79, 141.96, 141.94, 140.84, 140.78, 138.85, 137.08, 136.52, 136.49, 136.45, 132.04, 131.43, 131.40, 131.31, 131.22, 131.15, 131.07, 130.99, 130.94, 130.32, 129.07, 128.99, 127.99, 127.47, 127.31, 126.02, 125.82, 123.81, 119.39, 110.42, 110.30, 110.09, 20.50, 20.44, 20.40. $^{19}\text{F}\{^1\text{H}\}$ NMR (376 MHz, CDCl_3) δ : -101.69, -101.75. IR (ATR) ν (cm^{-1}): 3042, 2955, 2853, 1622, 1580, 1510, 1452, 1383, 1317, 1254, 1225, 1101, 1005, 984, 843, 787, 777, 768, 750, 716, 696, 596, 575, 534, 525, 498, 480. AP⁺ HRMS: $[\text{M}+\text{H}]^+$ calc. for $[\text{C}_{116}\text{H}_{87}\text{B}_6\text{N}_6\text{F}_{12}]^+$: 1856.7281, found: 1856.7334.

Chapter 5

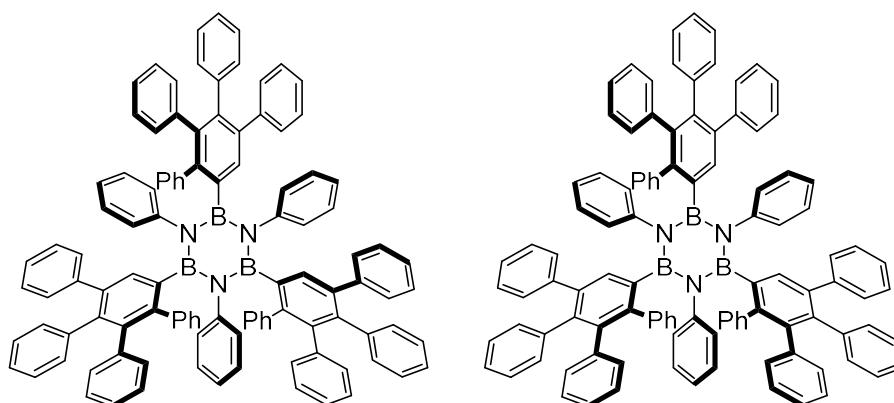
Synthesis of B,B',B''-Triethynyl-N,N',N''-tri(phenyl)-borazine (5-2)

The product is moisture sensitive and slowly degrades if exposed to water

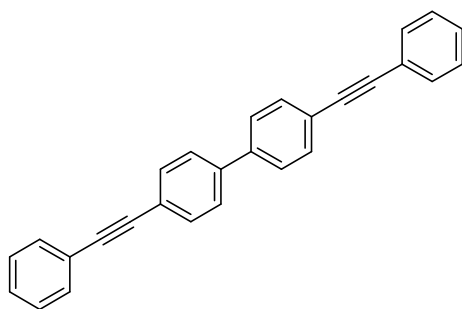


In a flame dried 20 mL Schlenk flask, freshly distilled aniline (0.49 mL, 5.37 mmol) and dry toluene (7.0 mL) were added. The solution was then cooled to 0 °C, BCl₃ (1.0 M in heptane, 6.4 mL, 6.4 mmol) added dropwise and the resulting suspension stirred for 10 min. The Schlenk flask was then equipped with a condenser connected to a CaCl₂ trap and the reaction refluxed for 18 h. The condenser was then exchanged with a septum and the white suspension degassed 5 times following the *freeze-pump-thaw* procedure to remove residual HCl. The degassed mixture was cooled to 0°C and Ethynyl-MgBr (0.5 M in THF, 12.0 mL, 6.0 mmol) added dropwise. The resulting pale-yellow solution was allowed to reach r.t. and stirred for 3 h, dry CH₂Cl₂ (50 mL) added and the reaction mixture filtered on a silica plug washing thoroughly with dry CH₂Cl₂. Evaporation of the solvent gave **5-2** as a pale-yellow powder (478 mg, 70%). mp: 260-262 °C. ¹H NMR: (300 MHz, CD₂Cl₂) δ: 7.38-7.33 (*m*, 6 H), 7.28-7.22 (*m*, 9 H), 2.47 (*s*, 3 H). ¹³C{¹H} NMR (126 MHz, CDCl₃) δ: 147.00, 128.75, 126.26, 98.31. Signal at 128.75 consists of signals overlapped, 1 ethynyl signal missing due to ¹¹B quadrupolar relaxation. ¹¹B{¹H} NMR (128 MHz, CDCl₃) δ: 26.26. IR (ATR) ν (cm⁻¹): 3056, 3032, 2355, 1420, 1204, 1129, 900, 754, 694, 411, 408, 404. EI⁺ HRMS: [M]⁺ calc. for [C₂₄H₁₈B₃N₃]⁺: 381.1780; found: 381.1756. Crystals suitable for X-Ray diffraction analysis were obtained from slow evaporation of a **5-2** solution in 1/1 petroleum ether/CH₂Cl₂.

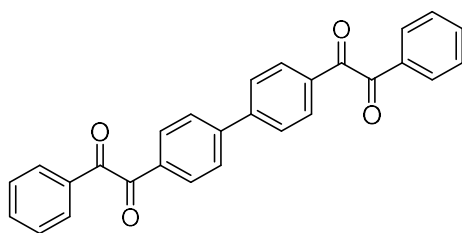
Synthesis of B,B',B''-Tri(3',4'-diphenyl-1,1':2',1''-terphenyl)-N,N',N''-tri(phenyl)-borazine (5-4, *cc* and *ct* isomers).



In a flame dried two necked flask, borazine **5-2** (50 mg, 0.13 mmol) was added along with 2,3,4,5-tetraphenylcyclopenta-2,4-dien-1-one (201 mg, 0.52 mmol). The solids were suspended in dry Ph₂O (1 mL) and the resulting black suspension degassed with N₂ bubbling under sonication for 30 min. The mixture was heated under N₂ at 220 °C for 18 h. The resulting black solution was precipitated from cold petrol and filtered to give a light purple solid. Silica gel column chromatography (eluent: petroleum ether/CH₂Cl₂ 80:20 to 60:40) gave **5-4** as a white fluffy powder (91 mg, 47%). mp: >300 °C. ¹H NMR: (500 MHz, CDCl₃) δ: 7.17-7.05 (*m*, 22 H), 6.92-6.65 (*m*, 43 H), 6.65-5.97 (*m*, 13 H). ¹³C{¹H} NMR (126 MHz, CDCl₃) δ: 146.18, 146.10, 145.10, 142.84, 142.65, 142.45, 142.19, 142.11, 142.06, 141.74, 141.64, 141.54, 141.10, 140.79, 140.56, 140.44, 140.42, 140.34, 139.51, 139.20, 138.96, 138.89, 138.59, 138.42, 138.26, 137.46, 135.63, 135.19, 135.02, 132.01, 131.68, 131.65, 131.59, 131.47, 131.41, 131.34, 131.14, 131.10, 130.18, 129.96, 129.87, 128.74, 128.53, 127.35, 127.31, 127.09, 126.97, 126.77, 126.56, 126.50, 126.42, 126.34, 126.30, 126.10, 125.88, 125.76, 125.68, 125.28, 125.23, 125.02, 124.97, 124.34, 124.04, 123.71. ¹¹B{¹H} NMR (160 MHz, C₆D₆) δ: 37.71. IR (ATR) ν (cm⁻¹): 3055, 3024, 1597, 1577, 1491, 1358, 1321, 1072, 1027, 908, 756, 725, 694, 533, 419, 406. AP⁺ HRMS: [M+H]⁺ calc. for [C₁₀₈H₇₉B₃N₃]⁺: 1450.6548; found: 1450.6578. Crystals suitable for X-Ray diffraction analysis were obtained from slow diffusion of MeOH in a CH₂Br₂ solution. Spectra in C₆D₆ are reported as well in appendix A.

Synthesis of 4,4'-Bis(phenylethynyl)-1,1'-biphenyl (5-7)

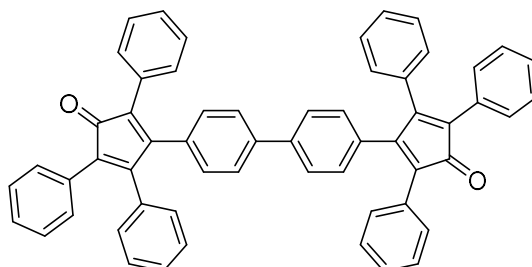
4,4'-diiodo-1,1'-biphenyl (4.00 g, 9.86 mmol) was added in a Schlenk flask along with $[\text{Pd}(\text{PPh}_3)\text{Cl}_2]$ (138 mg, 0.20 mmol) and CuI (38 mg, 0.20 mmol). The solids were then suspended in 50 mL of a 1/1 THF/Triethylamine mixture and the resulting suspension degassed 3 times using *freeze-pump-thaw* procedure. Phenylacetylene (2.40 mL, 21.7 mmol) was then added and the reaction stirred at r.t. for 3 h. The resulting suspension was filtered on a glass frit and washed with MeOH to give **5-7** as a grey powder (3.45 g, 99 %). mp: 246-248 °C. ^1H NMR: (300 MHz, CDCl_3) δ : 7.61 (s, 8 H), 7.58-7.54 (m, 4 H), 7.39-7.35 (m, 6 H). $^{13}\text{C}\{^1\text{H}\}$ NMR (100 MHz, CDCl_3) δ : 140.19, 132.27, 131.79, 128.53, 128.50, 127.04, 123.38, 122.74, 90.53, 89.37. IR (ATR) ν (cm^{-1}): 3086, 3051, 2965, 2359, 2218, 1593, 1499, 1439, 1069, 1024, 1001, 918, 822, 750, 718, 689, 538, 515, 471. ASAP⁺ HRMS: $[\text{M}+\text{H}]^+$ calc. for $[\text{C}_{28}\text{H}_{19}]^+$: 355.1487; found: 355.1481.

Synthesis of 2,2'-([1,1'-Biphenyl]-4,4'-diyl)bis(1-phenylethane-1,2-dione) (5-8)

In a 500 mL round bottom flask **5-7** (1.00 g, 2.82 mmol) was added and suspended in an acetone/AcOH (200 mL/2 mL) mixture. KMnO_4 (2.20 g, 14.12 mmol) was then added in one portion. The reaction was then equipped with a condenser and stirred at 60 °C for 6 h. The solvent was removed under reduced pressure and the resulting solid filtered on a silica plug (eluent: CH_2Cl_2 100%). Evaporation of the solvent gives **5-8** (1.14 g, 97 %) as a bright yellow solid. mp: 196-198 °C. ^1H NMR: (300 MHz, CDCl_3) δ : 8.09 (d, $J = 8.5$ Hz, 4 H), 8.02-7.99 (m, 4 H), 7.76 (d, $J = 8.5$ Hz, 4 H), 7.68 (t, $J = 7.5$ Hz, 2 H), 7.53 (t, $J = 7.5$ Hz, 4 H). $^{13}\text{C}\{^1\text{H}\}$ NMR (75 MHz, CDCl_3) δ : 194.37, 193.98, 145.83, 135.18, 133.03, 132.85, 130.77, 130.12, 129.23, 128.14. IR (ATR) ν (cm^{-1}): 3084, 3067, 1661, 1593, 1553, 1447, 1400, 1317, 1300, 1209, 1169, 1001, 872, 824,

793, 748, 719, 704, 685, 648 634, 490. ASAP⁺ HRMS: [M+H]⁺ calc. for [C₂₈H₁₉O₄]⁺: 419.1283; found: 419.1284.

Synthesis of 4,4'-([1,1'-Biphenyl]-4,4'-diyl)bis(2,3,5-triphenylcyclopenta-2,4-dien-1-one) (5-10)



In a 50 mL round bottom flask equipped with a condenser, **5-8** (1.00 g, 2.39 mmol) was added and dissolved in refluxing EtOH (10 mL). 1,3-Diphenylacetone (1.10 g, 5.24 mmol) was then added portion-wise to the yellow solution at reflux. A KOH solution (135 mg in 2 mL of EtOH) was then added and after 10 min. a brownish suspension was formed. The flask was cooled to -10 °C for 1 h and the reaction mixture filtered on a glass frit and washed with cold MeOH to give the desired product **5-10** as a brown solid (960 mg, 52 %). mp: >300 °C. ¹H NMR: (300 MHz, CDCl₃) δ: 7.40 (*d*, *J* = 8.4 Hz, 4 H), 7.25-7.18 (*m*, 26 H), 6.97 (*dd*, *J* = 8.4 Hz, 1.6 Hz, 8 H). ¹³C{¹H} NMR (126 MHz, CDCl₃) δ: 200.27, 154.39, 153.98, 140.07, 133.28, 132.50, 130.94, 130.82, 130.32, 130.29, 130.21, 129.49, 128.69, 128.26, 128.24, 128.18, 127.69, 127.65, 126.35, 125.70, 125.67. IR (ATR) ν (cm⁻¹): 3055, 3030, 2911, 1707, 1601, 1490, 1443, 1354, 1304, 693, 419, 412. AP⁺ HRMS: [M+H]⁺ calc. for [C₅₈H₃₉O₂]⁺: 767.2950; found: 767.2959.

Synthesis of BN-polymer (5-1)*

* The quality of the starting borazine and dry conditions are fundamental to form the polymeric material, if the borazine is partially degraded or moisture is present only soluble material is formed.

In a flame dried 3 necked flask **5-2** (300 mg, 0.79 mmol) was added along with **5-10** (905 mg, 1.18 mmol) and the flask purged 3 times with N₂. Anhydrous Ph₂O (12 mL) was then added and the resulting brown suspension degassed with N₂ bubbling under sonication for 20 min. The reaction was then stirred under N₂ at 230°C (as soon as the reaction reaches 220°C a strong evolution of CO takes place). After approximately 1 h the reaction turns into a red gel and is stirred for further 16 h. The gelified solution is then allowed to reach room temperature, dropped into cold petroleum ether and filtered. The resulting material was transferred to a falcon tube, suspended in CH₂Cl₂

and sonicated for 10 min., followed by addition of petroleum ether and centrifugation at 5000 rpm for 5 min. This procedure was repeated for further 2 times. The reddish powder (800 mg, 67%) was then added in a flame dried microwave vial and suspended in Ph₂O (7 mL). The vial was sealed, and the solution degassed with N₂ bubbling under sonication for 10 min. (forms a gel). Phenylacetylene (1.15 mL, 10.5 mmol) was then added and the reaction heated under N₂ at 230 °C for 4 h (red colour disappears). After this time, the reaction is again poured into cold petroleum ether and washed 3 times by centrifugation with CH₂Cl₂ (as reported in the previous step) and 1 time each with acetone, MeOH and Et₂O. After drying under vacuum, **5-1** was isolated as a beige solid (600 mg, quantitative yield, some loss of material occurred during washings). IR (ATR) ν (cm⁻¹): 3211, 3051, 3022, 1597, 1489, 1356, 1319, 1155, 1109, 1072, 1026, 1007, 910, 831, 785, 756, 694, 532, 469, 457, 447, 417, 407, 403.

References

- [1] G. Metz, X. Wu, S. O. Smith, *J. Magn. Reson. Ser. A* **1994**, *110*, 219–227.
- [2] S. P. Brown, S. J. Heyes, S. Wimperis, *J. Magn. Reson. - Ser. A* **1996**, *119*, 280–284.
- [3] Y. Millot, P. P. Man, *Solid State Nucl. Magn. Reson.* **2002**, *21*, 21–43.
- [4] M. J. Frisch, G. W. Trucks, H. B. Schlegel, G. E. Scuseria, M. A. Robb, J. R. Cheeseman, G. Scalmani, V. Barone, B. Mennucci, G. A. Petersson, et al., *GAUSSIAN 09 (Revision D.01)* **2013**.
- [5] R. Herges, D. Geuenich, *J. Phys. Chem. A* **2001**, *105*, 3214–3220.
- [6] A. D. Becke, *J. Chem. Phys.* **1993**, *98*, 5648–5652.
- [7] W. J. Hehre, R. Ditchfield, J. A. Pople, *J. Chem. Phys.* **1972**, *56*, 2257–2261.
- [8] J. Tomasi, B. Mennucci, R. Cammi, *Chem. Rev.* **2005**, *105*, 2999–3093.
- [9] E. D. Glendening, J. K. Badenhoop, A. E. Reed, J. E. Carpenter, J. A. Bohmann, C. M. Morales, C. R. Landis, F. Weinhold, *NBO 6.0, Theor. Chem. Institute, Univ. Wisconsin, Madison*, **2013**.
- [10] S. Meiboom, D. Gill, *Rev. Sci. Instrum.* **1958**, *29*, 688–691.
- [11] R. Lapasin, S. Prici, in *Rheol. Ind. Polysaccharides Theory Appl. Springer, Boston, MA*, **1995**, pp. 250–494.
- [12] M. Abrami, I. D'Agostino, G. Milcovich, S. Fiorentino, R. Farra, F. Asaro, R. Lapasin, G. Grassi, M. Grassi, *Soft Matter* **2014**, *10*, 729–737.
- [13] P. J. Flory, *Principles of Polymer Chemistry*, Cornell University Press, **1953**.
- [14] G. Schurz, Springer, Dordrecht, **1991**, pp. 391–437.
- [15] V. CrysAlisPro, *Agil. Technol.* **2014**.
- [16] G. M. Sheldrick, *Acta Crystallogr.* **2015**, *71*, 3–8.
- [17] A. Lausi, M. Polentarutti, S. Onesti, J. R. Plaisier, E. Busetto, G. Bais, L. Barba, A. Cassetta, G. Campi, D. Lamba, et al., *Eur. Phys. J. Plus* **2015**, *130*, 2–8.

- [18] W. Kabsch, A. T. Brünger, K. Diederichs, P. A. Karplus, K. Diederichs, S. McSweeney, R. B. G. Ravelli, P. Evans, S. French, K. Wilson, et al., *Acta Crystallogr. Sect. D Biol. Crystallogr.* **2010**, *66*, 125–132.
- [19] P. R. Evans, G. N. Murshudov, *Acta Crystallogr. Sect. D Biol. Crystallogr.* **2013**, *69*, 1204–1214.
- [20] M. D. Winn, C. C. Ballard, K. D. Cowtan, E. J. Dodson, P. Emsley, P. R. Evans, R. M. Keegan, E. B. Krissinel, A. G. W. Leslie, A. McCoy, et al., *Acta Crystallogr. Sect. D Biol. Crystallogr.* **2011**, *67*, 235–242.
- [21] P. Emsley, K. Cowtan, *Acta Crystallogr. Sect. D Biol. Crystallogr.* **2004**, *60*, 2126–2132.
- [22] L. J. Farrugia, *J. Appl. Crystallogr.* **2012**, *45*, 849–854.
- [23] L. L. C. Schrodinger, *PyMOL Mol. Graph. Syst. Schrodinger, LLC.* **2015**, <http://www.pymol.org>.
- [24] A. L. Spek, *Acta Crystallogr. Sect. C Struct. Chem.* **2015**, *71*, 9–18.
- [25] S. J. Clark, M. D. Segall, C. J. Pickard, P. J. Hasnip, M. I. J. Probert, K. Refson, *Z. Krist.* **2005**, *220*, 567–570.
- [26] D. Vanderbilt, *Phys. Rev. B* **1990**, *41*, 7892–7895.
- [27] J. P. Perdew, K. Burke, M. Ernzerhof, *Phys. Rev. Lett.* **1996**, *77*, 3865–3868.
- [28] A. Tkatchenko, M. Scheffler, *Phys. Rev. Lett.* **2009**, *102*, 1–4.
- [29] H. J. Monkhorst, J. D. Pack, *Phys. Rev. B* **1976**, *13*, 5188–5192.
- [30] O. Allemann, S. Duttwyler, P. Romanato, K. K. Baldrige, J. S. Siegel, *Science* **2011**, *332*, 574–577.
- [31] J. Dosso, J. Tasseroul, F. Fasano, D. Marinelli, N. Biot, A. Fermi, D. Bonifazi, *Angew. Chem. Int. Ed.* **2017**, *56*, 4483–4487.
- [32] M. Krieg, F. Reicherter, P. Haiss, M. Ströbele, K. Eichele, M. J. Treanor, R. Schaub, H. F. Bettinger, *Angew. Chemie Int. Ed.* **2015**, *54*, 8284–8286.
- [33] T. Rantanen, V. Snieckus, *J. Org. Chem.* **2015**, 9410–9424.
- [34] X. Cai, S. Brown, P. Hodson, V. Snieckus, *Can. J. Chem.* **2004**, *205*, 195–205.
- [35] D. Wu, W. Pisula, M. C. Haberecht, X. Feng, K. Müllen, *Org. Lett.* **2009**, *11*, 5686–5689.
- [36] S. Kervyn, O. Fenwick, F. Di Stasio, Y. S. Shin, J. Wouters, G. Accorsi, S. Osella, D. Beljonne, F. Cacialli, D. Bonifazi, *Chem. Eur. J.* **2013**, *19*, 7771–7779.

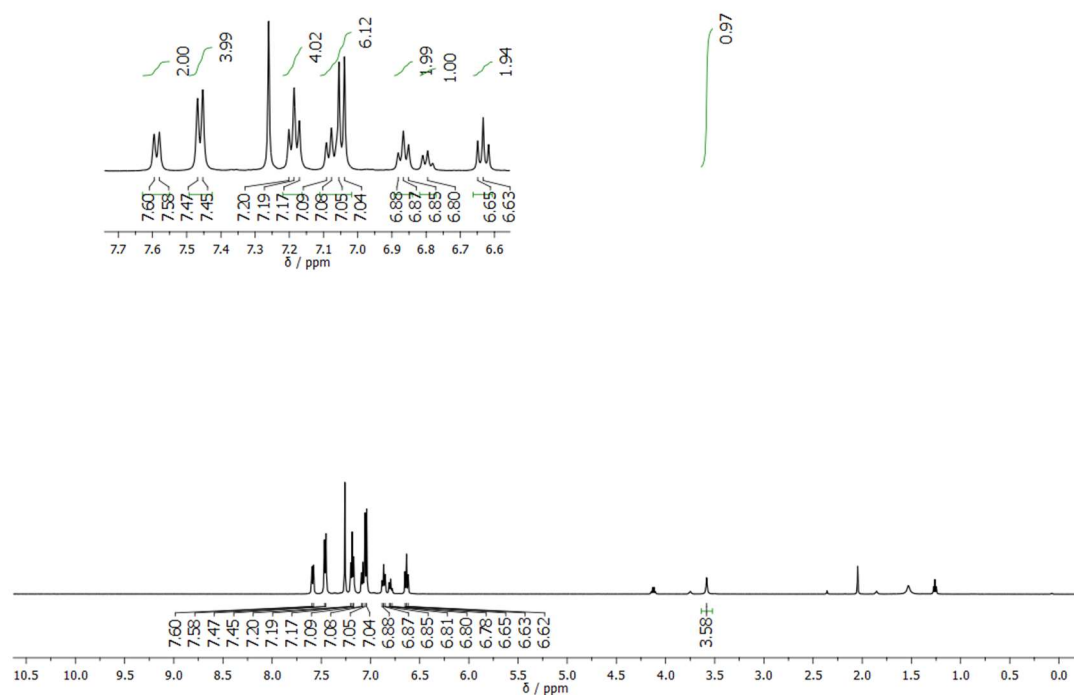
APPENDIX A: ^1H , ^{13}C , ^{11}B -NMR AND HRMS SPECTRA OF SELECTED MOLECULES**Chapter 2****1) B,B'-Bis(2,6-dibromophenyl)-B''-hydroxy-N,N',N''-triphenyl-borazine. (2.29)**

Figure A.1: 500 MHz ^1H -NMR of **2-29** in CDCl_3 . Residual peaks of ethyl acetate visible (4.12, 2.05 and 1.26 ppm).

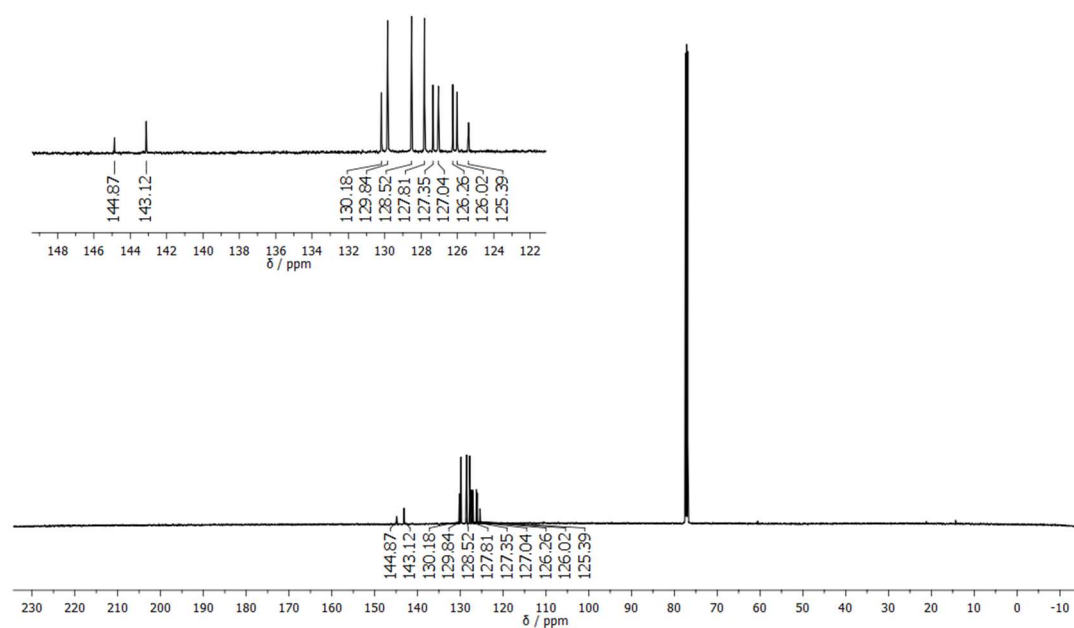


Figure A.2: 126 MHz ^{13}C -NMR of **2-29** in CDCl_3 .

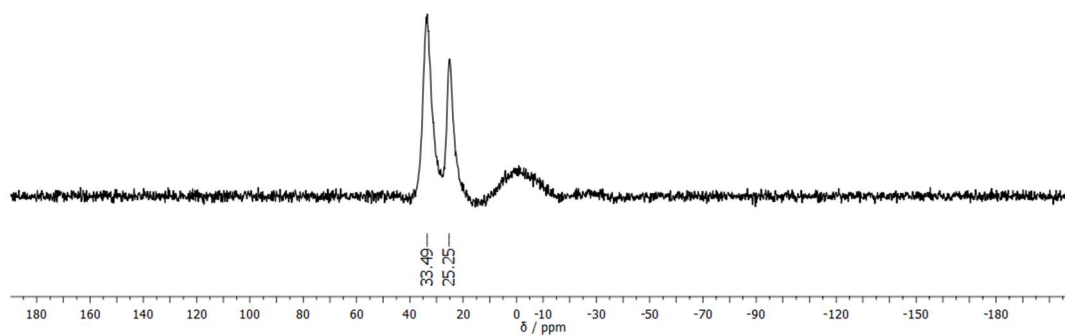


Figure A.3: 160 MHz ^{11}B -NMR of **2-29** in CDCl_3 (probe residual signal present from 10 to -10 ppm).

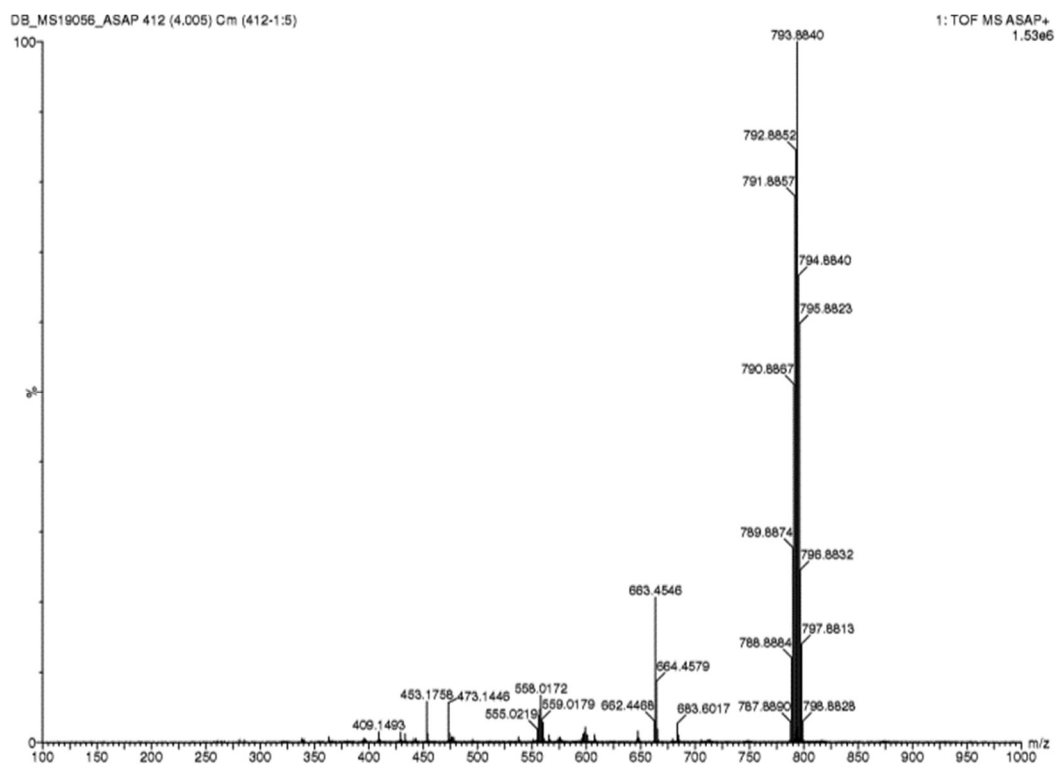


Figure A.4: ASAP⁺ HR-MS of **2-29**.

Appendix A

2) B,B'-Bis(2,3,5,6-tetrachlorophenyl)-B''-hydroxy-N,N',N''-triphenylborazine (2-25c)

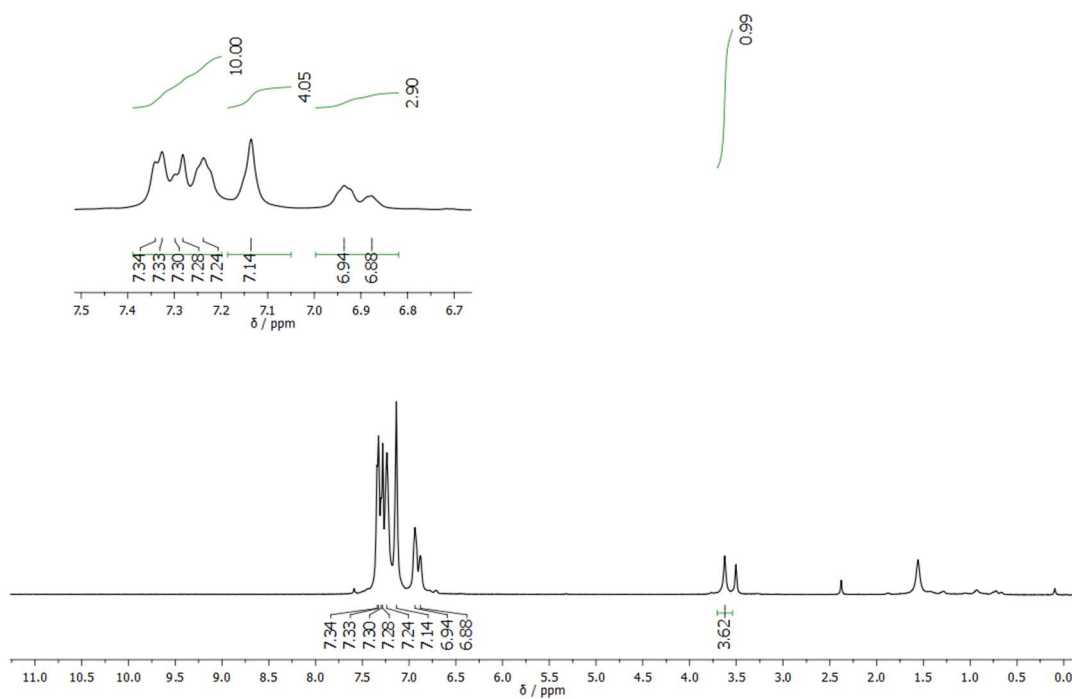


Figure A.5: 500 MHz ^1H NMR of **2-25c** in CDCl_3 .

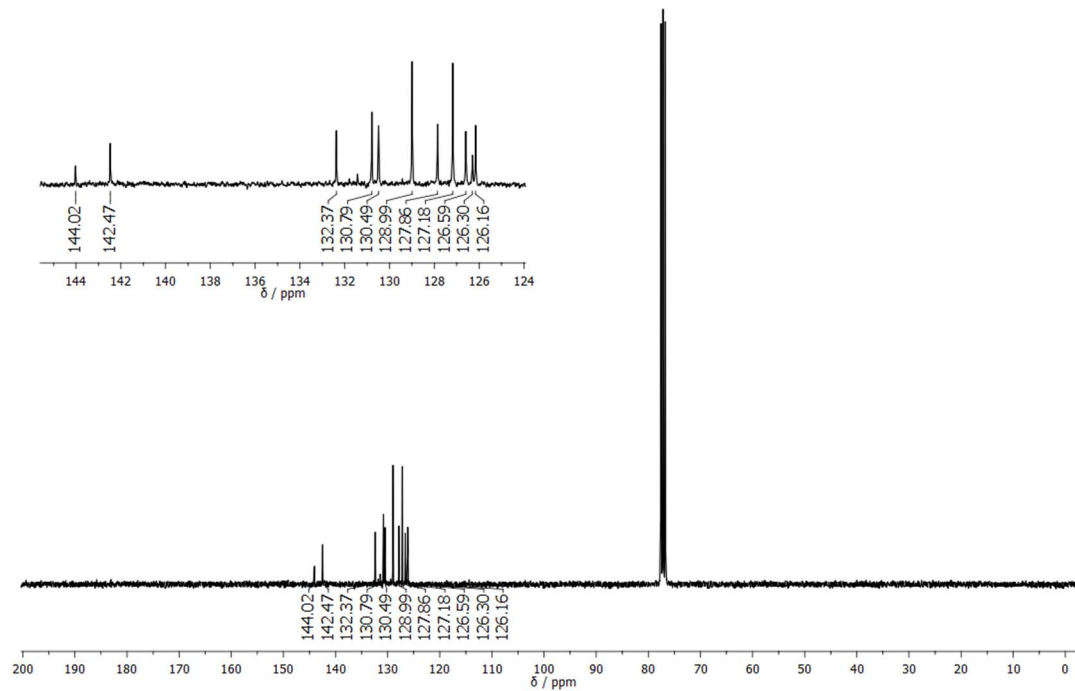


Figure A.6: 75 MHz ^{13}C NMR of **2-25c** in CDCl_3 .

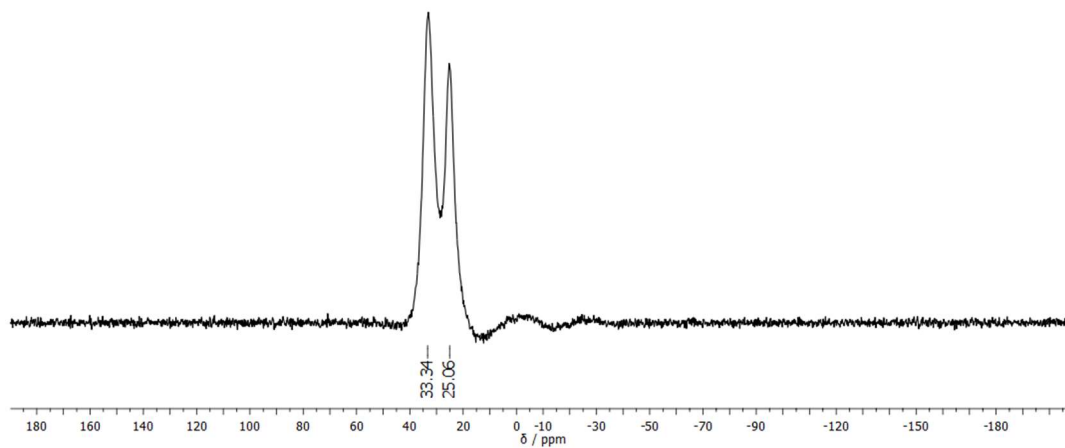


Figure A.7: 160 MHz ^{11}B NMR of **2-25c** in CDCl_3 .

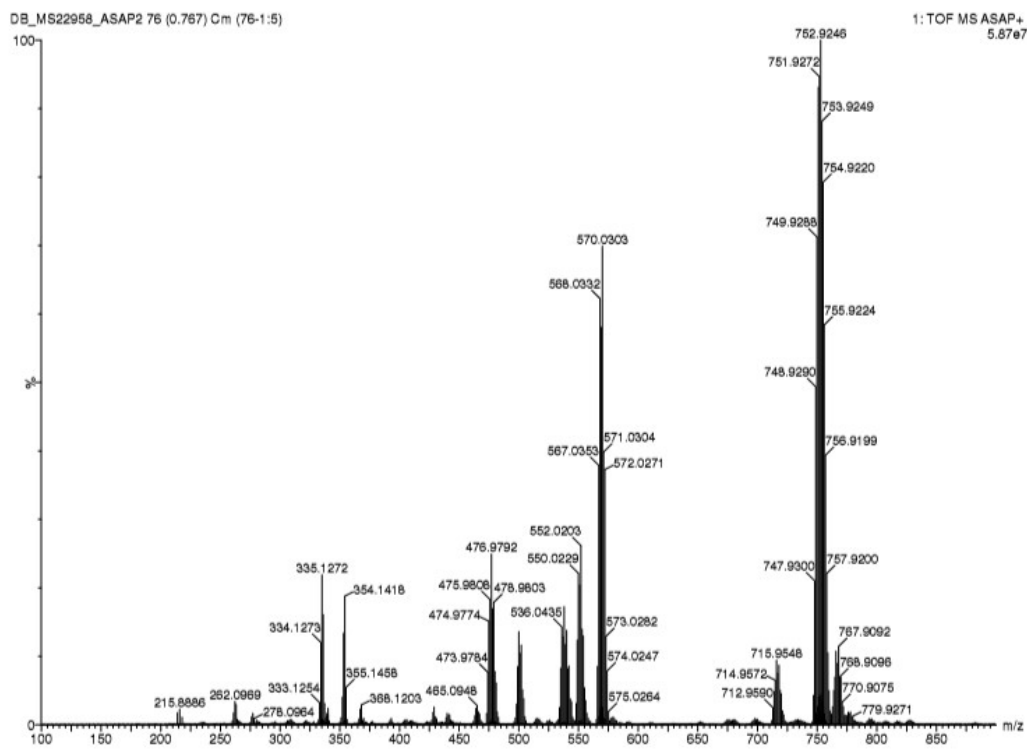


Figure A.8: ASAP⁺ HR-MS of **2-25c**.

Appendix A

3) 2',6'-Dimethyl-[1,1'-biphenyl]-4-amine (2-10)

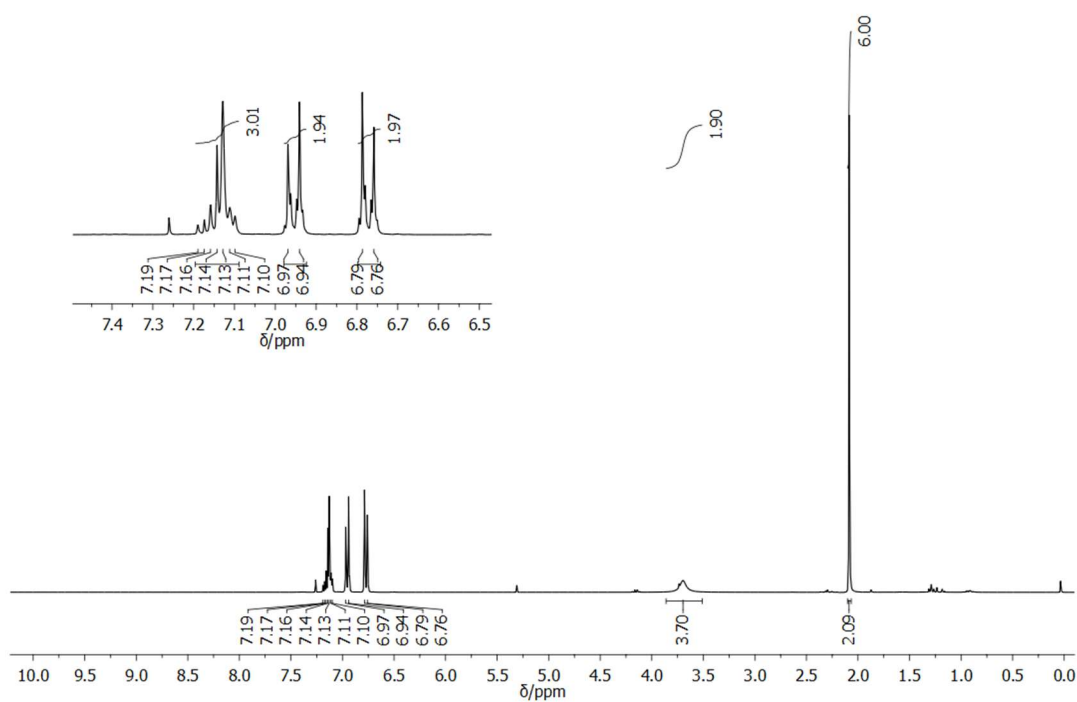


Figure A.9: 300 MHz ¹H-NMR of **2-10** in CDCl₃.

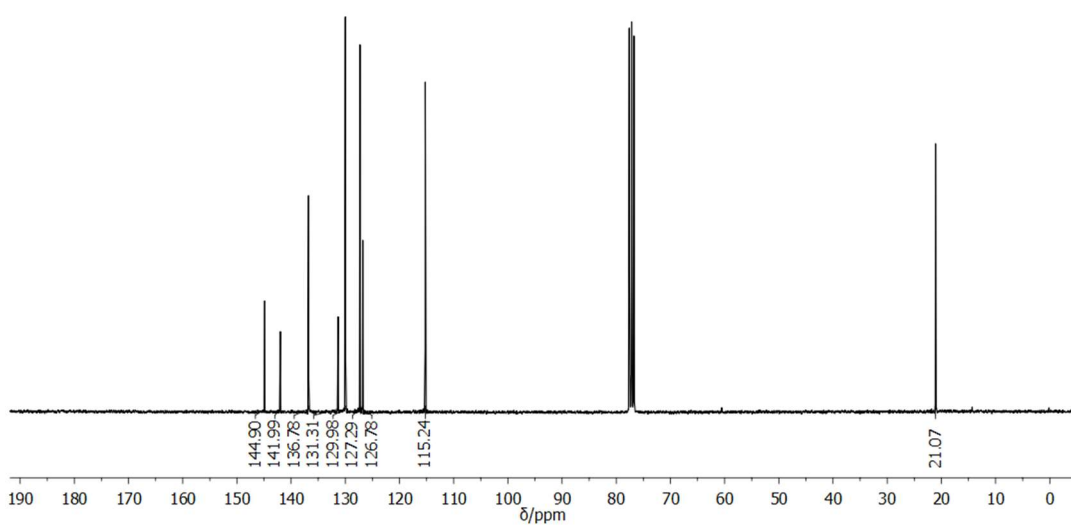


Figure A.10: 75 MHz ¹H-NMR of **2-10** in CDCl₃.

Appendix A

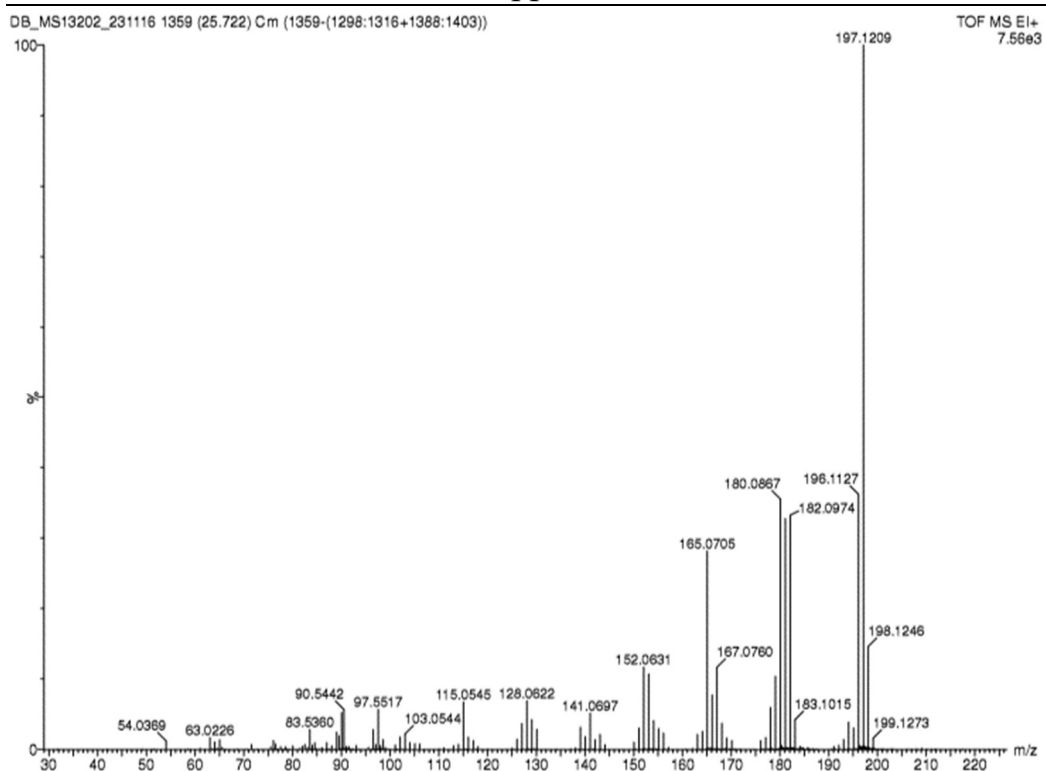


Figure A.11: EI⁺ HR-MS of 2-10.

Appendix A

4)B,B',B''-Tri[2,6-(dichloro)phenyl]-N,N',N''-tri[4-(2,6-dimethylphenyl)phenyl]borazine (2-26)

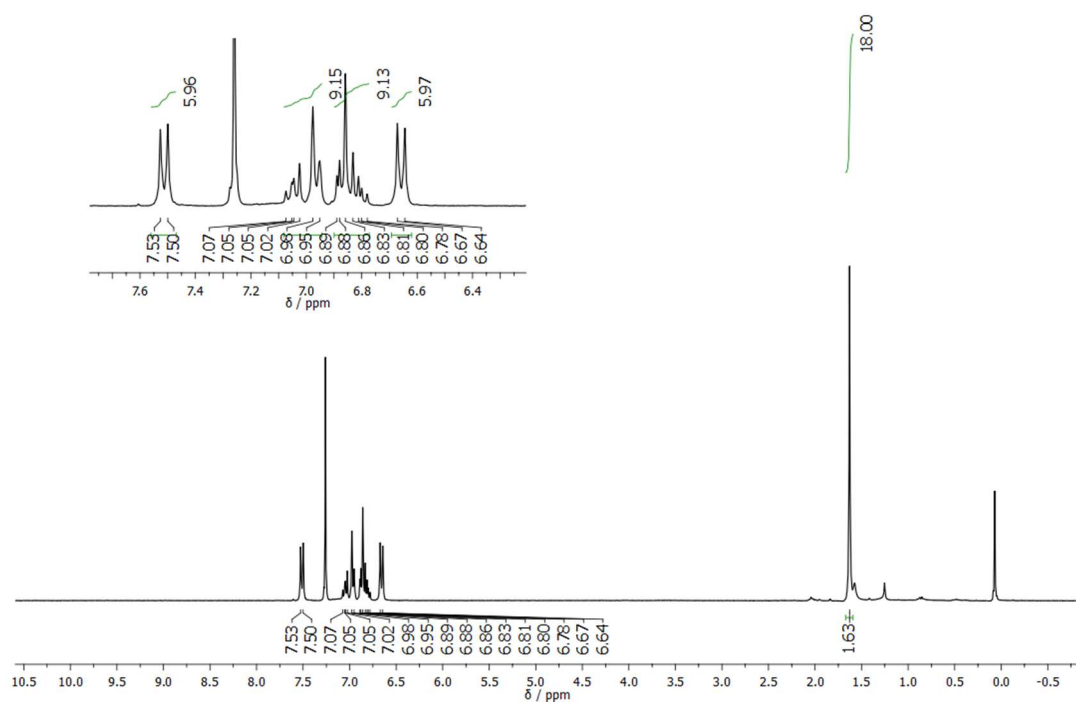


Figure A.12: 300 MHz ¹H-NMR of 2-26 in CDCl₃.

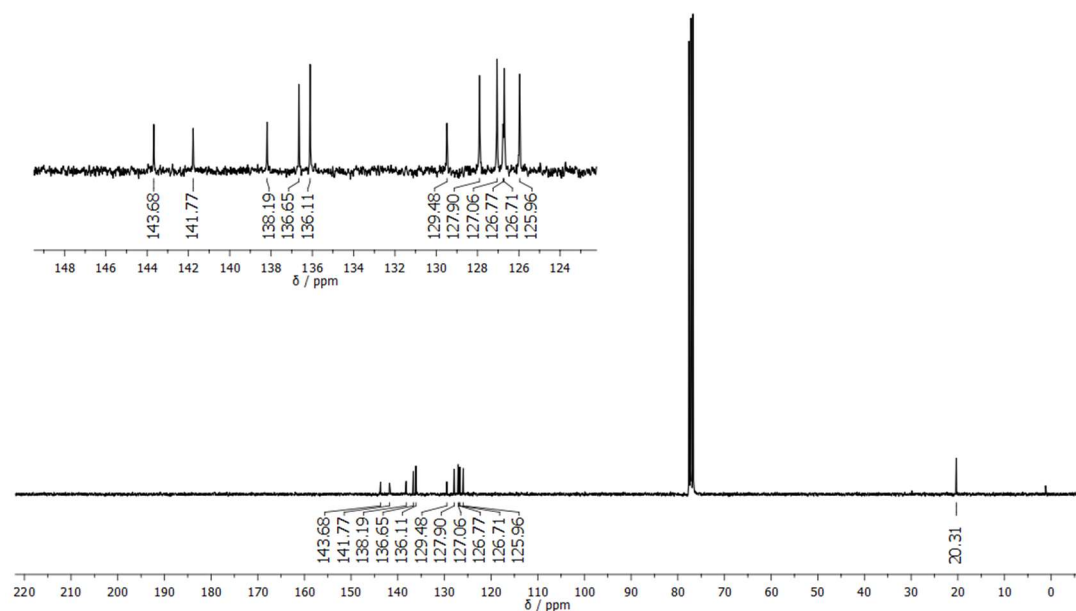


Figure A.13: 75 MHz ¹³C-NMR of 2-26 in CDCl₃.

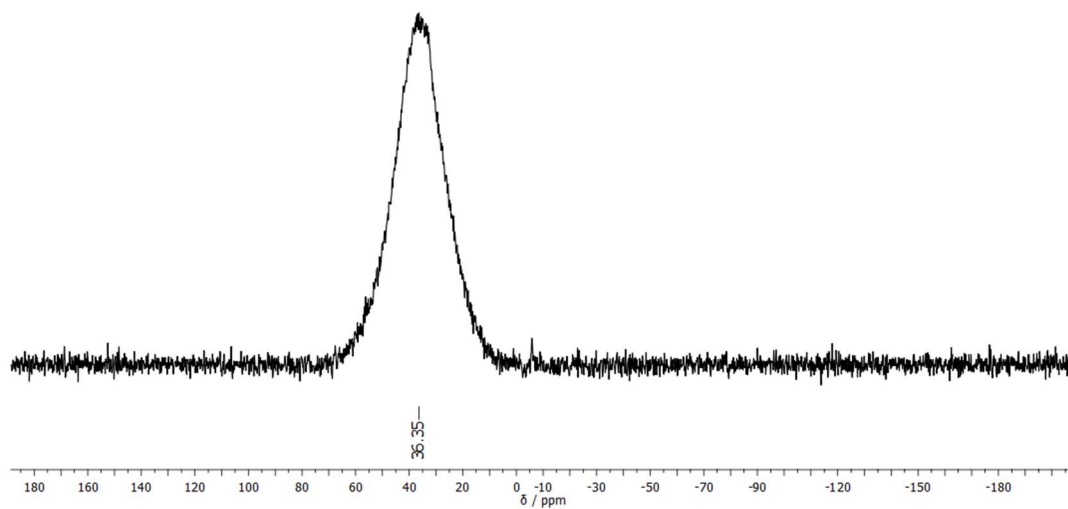


Figure A.14: 128 MHz ^{11}B -NMR of **2-26** in CDCl_3 .

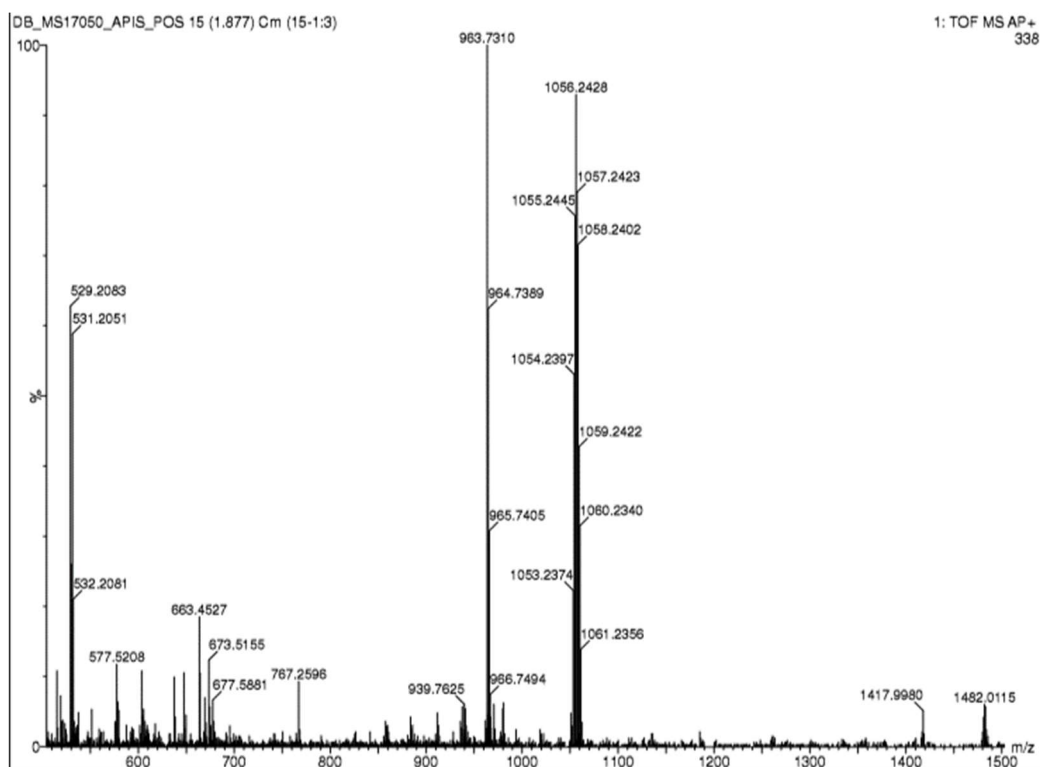


Figure A.15: AP⁺ HR-MS of **2-26**.

Appendix A

5) B,B',B''-Tri n-butyl-N,N',N''-tri[4-(2,6-dimethylphenyl)phenyl]borazine (2-31)

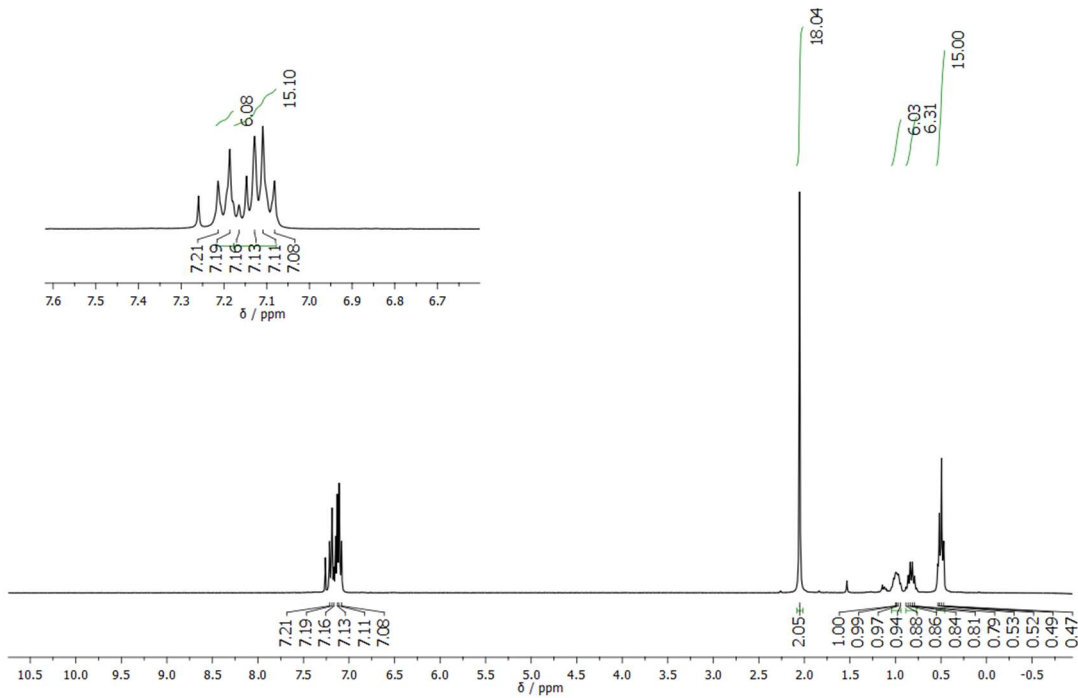


Figure A.16: 300 MHz ¹H-NMR of 2-31 in CDCl₃.

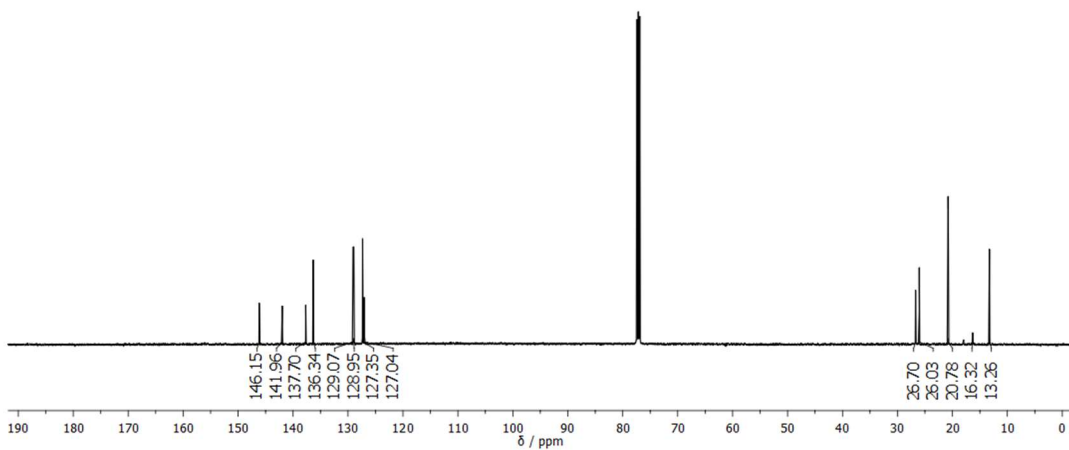


Figure A.17: 126 MHz ¹³C-NMR of 2-31 in CDCl₃.

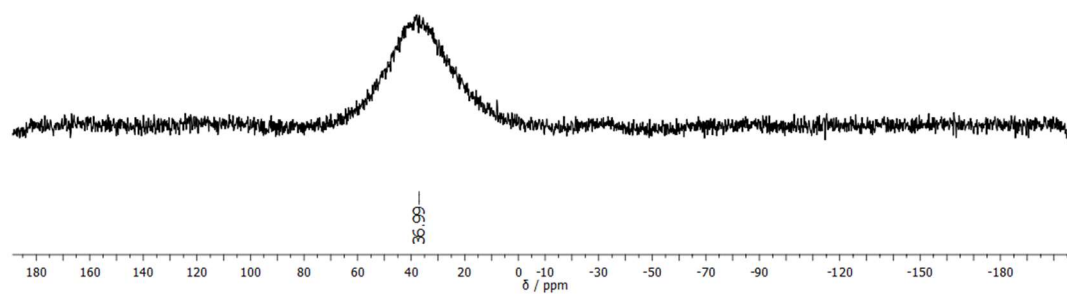


Figure A.18: 160 MHz ^{11}B -NMR of 2-31 in CDCl_3 .

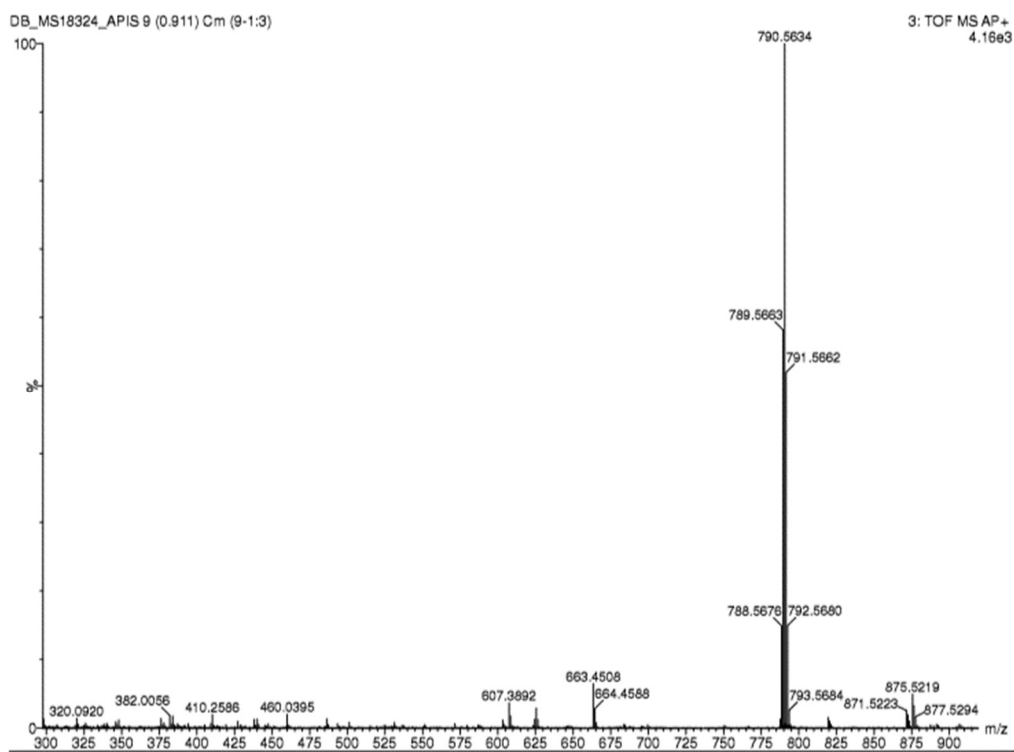
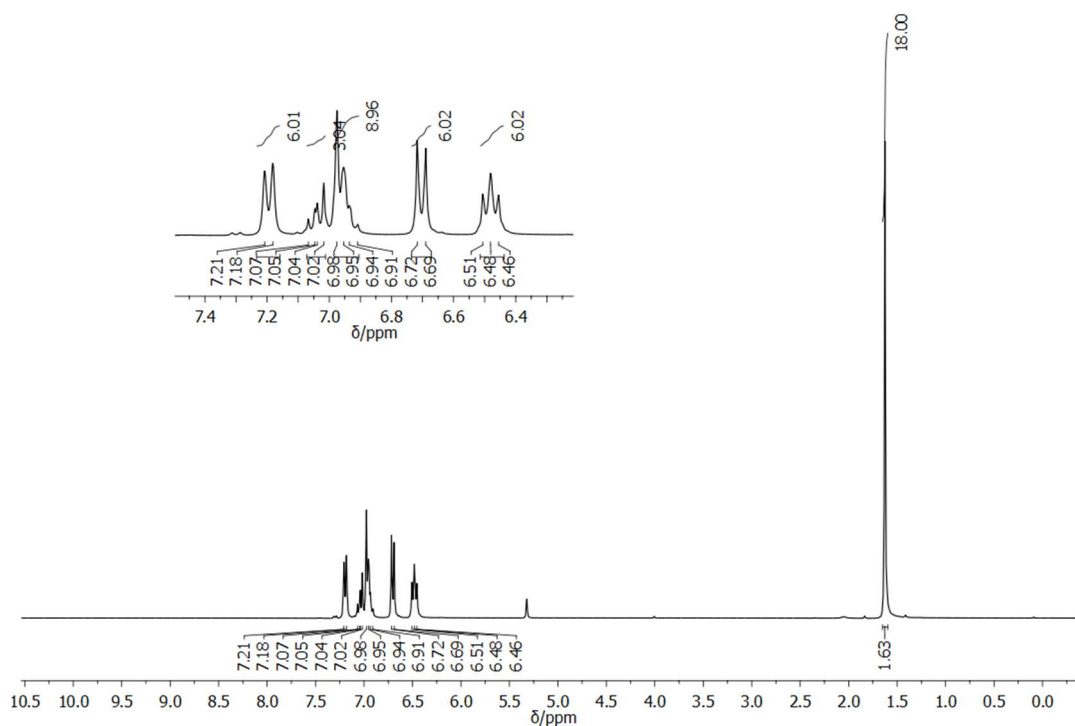
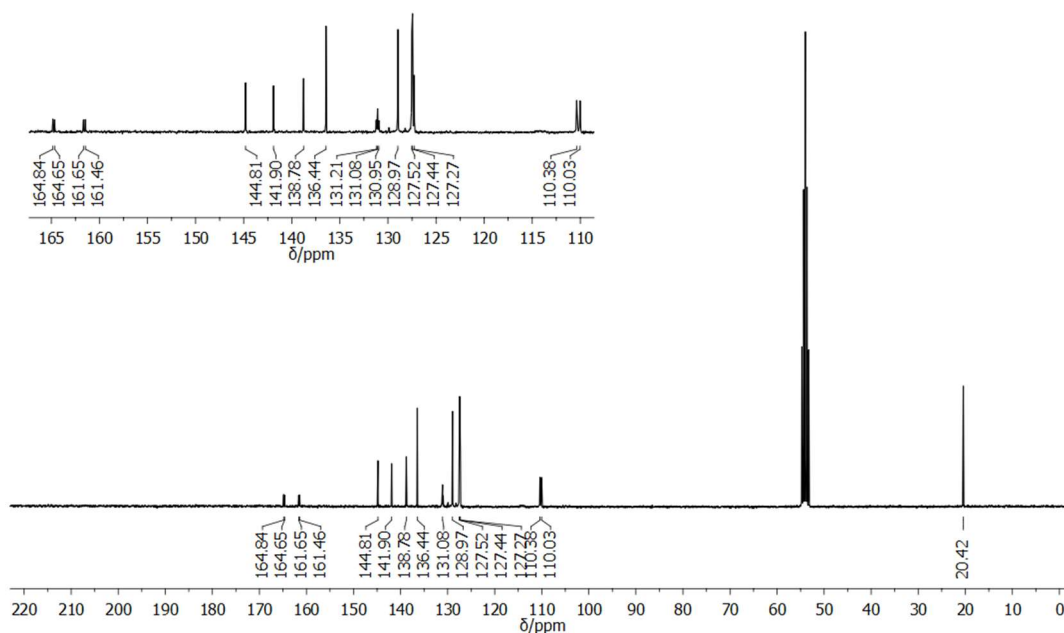


Figure A.19: AP⁺ HR-MS of 2-31.

6) Synthesis of B,B',B''-Tri[2,6-(difluoro)phenyl]-N,N',N''-tri[4-(2,6-dimethylphenyl)phenyl]borazine (2-27)**Figure A.20:** 300 MHz $^1\text{H-NMR}$ of **2-27** in CD_2Cl_2 .**Figure A.21:** 75 MHz $^{13}\text{C-NMR}$ of **2-27** in CD_2Cl_2 .

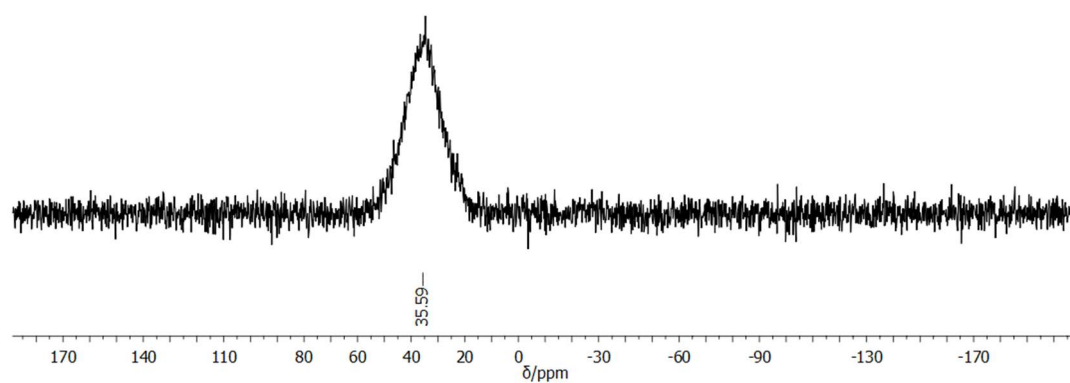


Figure A.22: 128 MHz ^{11}B -NMR of **2-27** in CD_2Cl_2 .

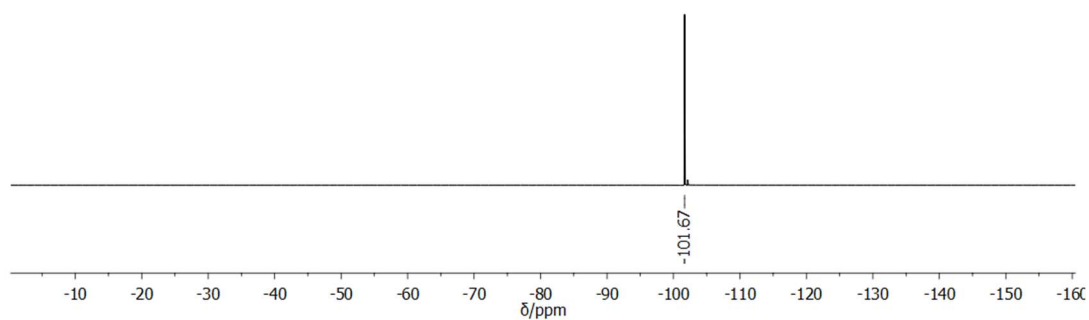


Figure A.23: 376 MHz ^{19}F -NMR of **2-27** in CD_2Cl_2 .

Appendix A

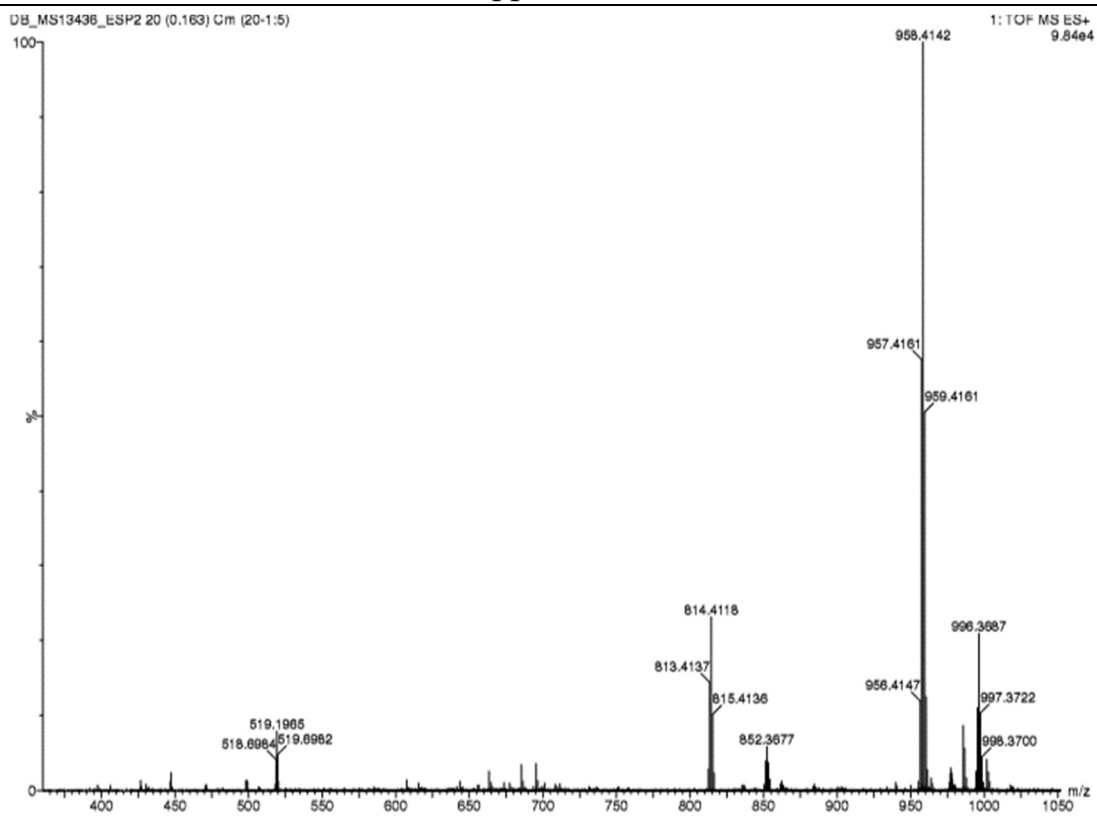
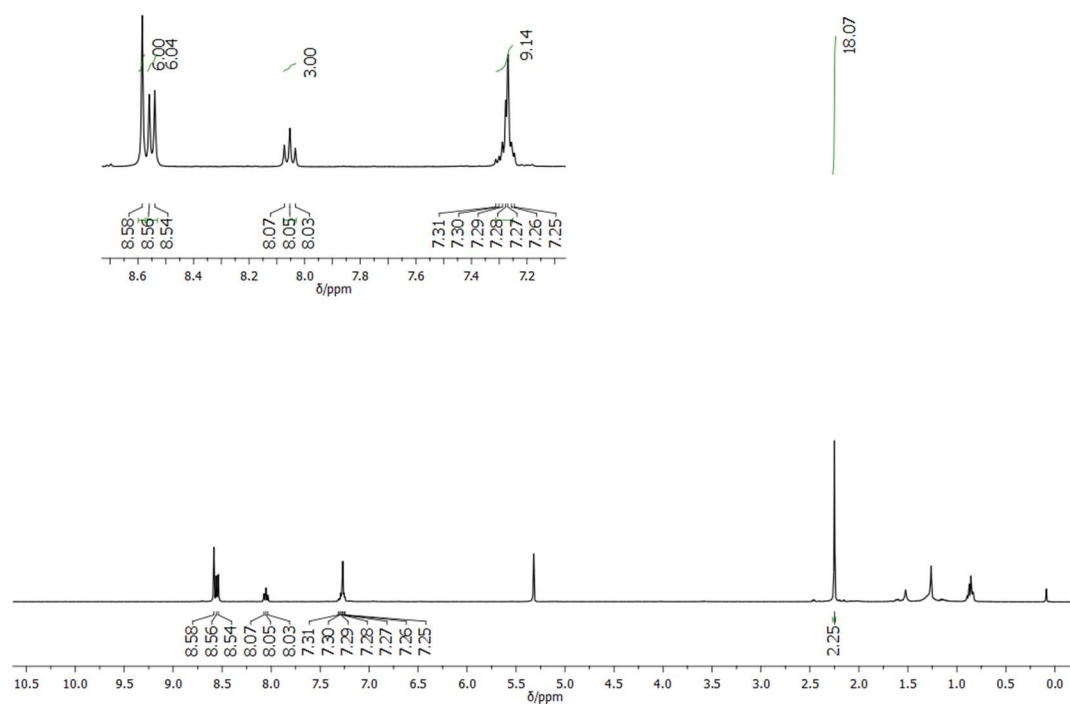
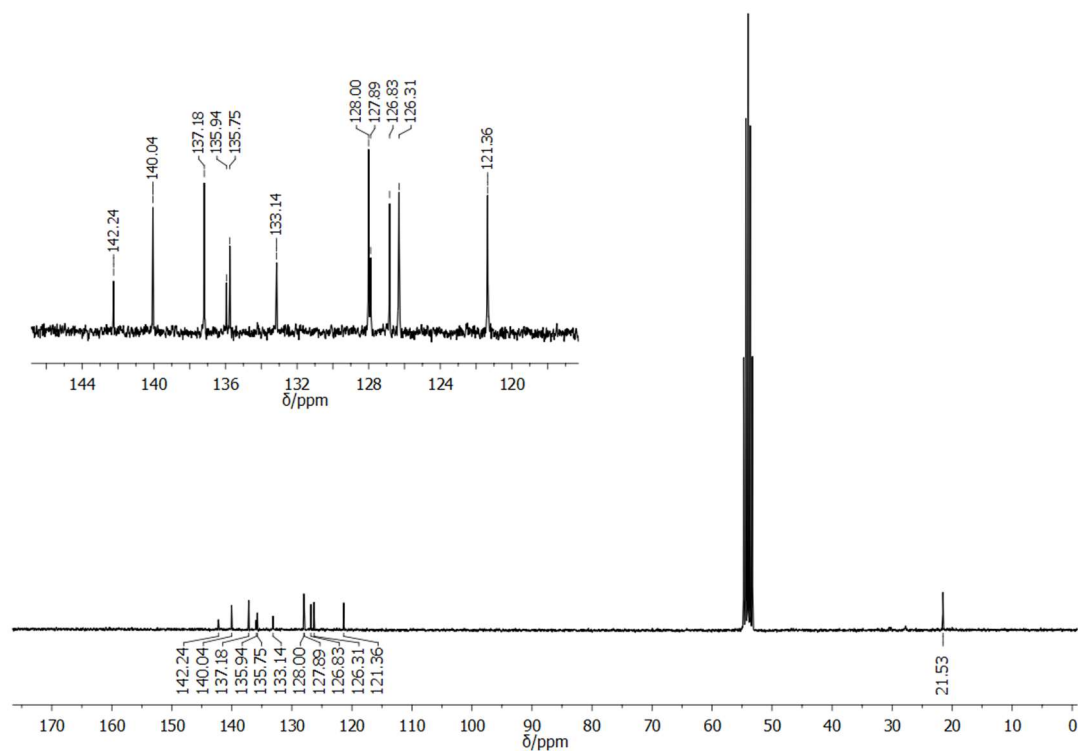


Figure A.24: ES⁺ HR-MS of 2-27.

7) 2-8-14-Trixylyl-hexaphenyl borazinocoronene (2-1)

Figure A.25: 400 MHz ^1H -NMR of 2-1 in CD_2Cl_2 .Figure A.26: 75 MHz ^{13}C -NMR of 2-1 in CD_2Cl_2 .

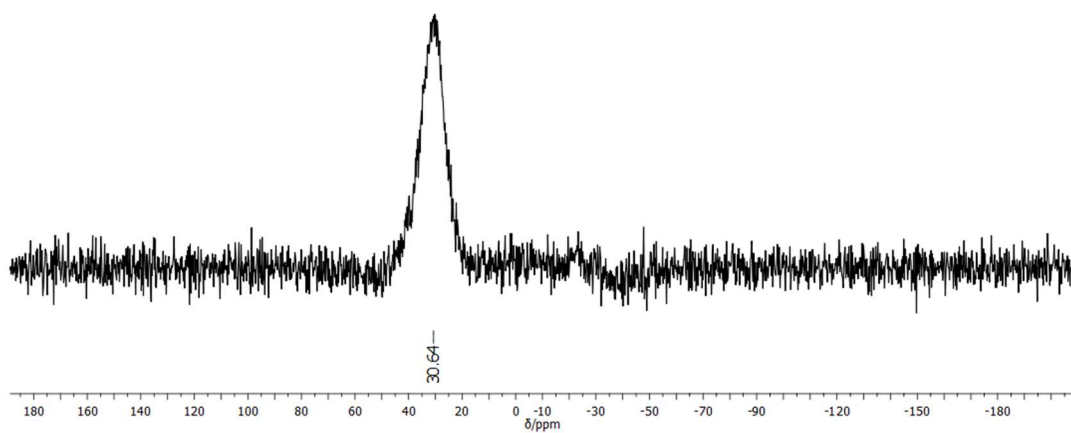


Figure A.27: 128 MHz ^{11}B -NMR of **2-1** in CD_2Cl_2 .

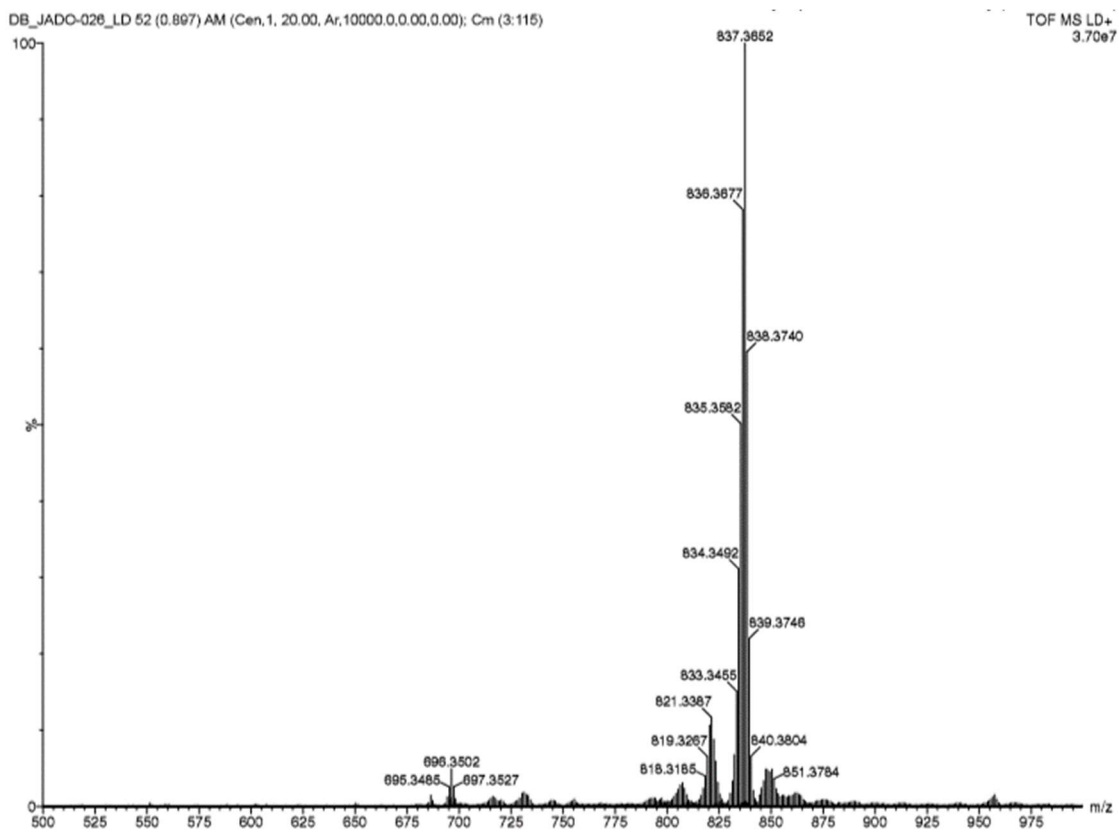
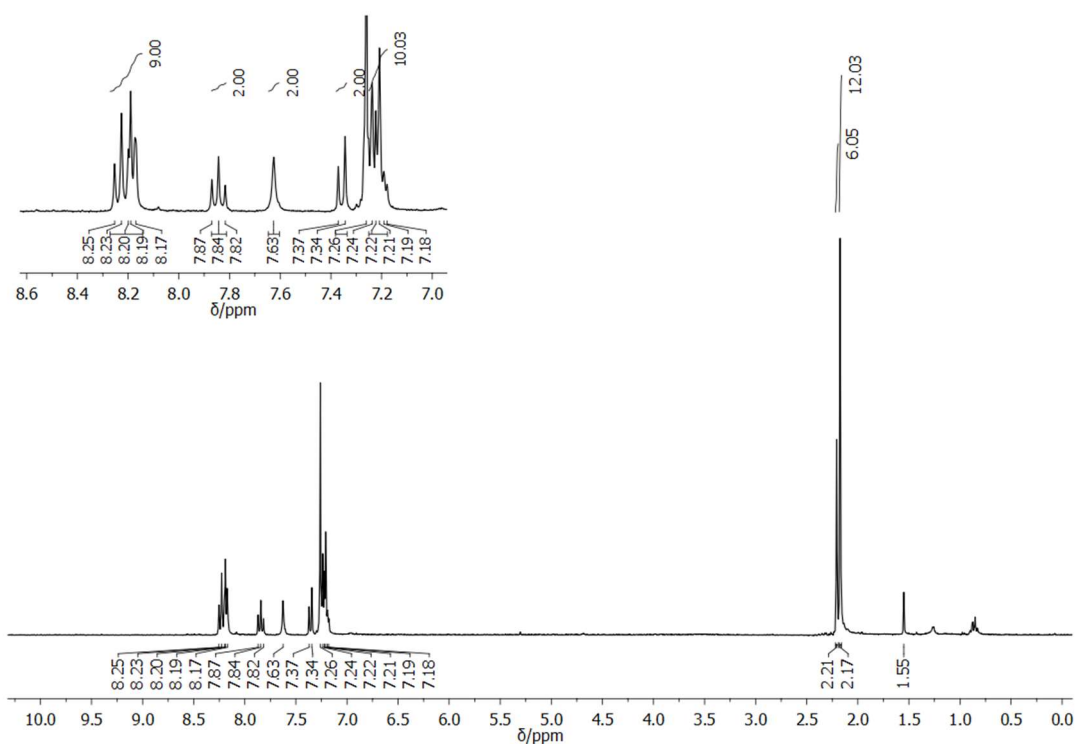
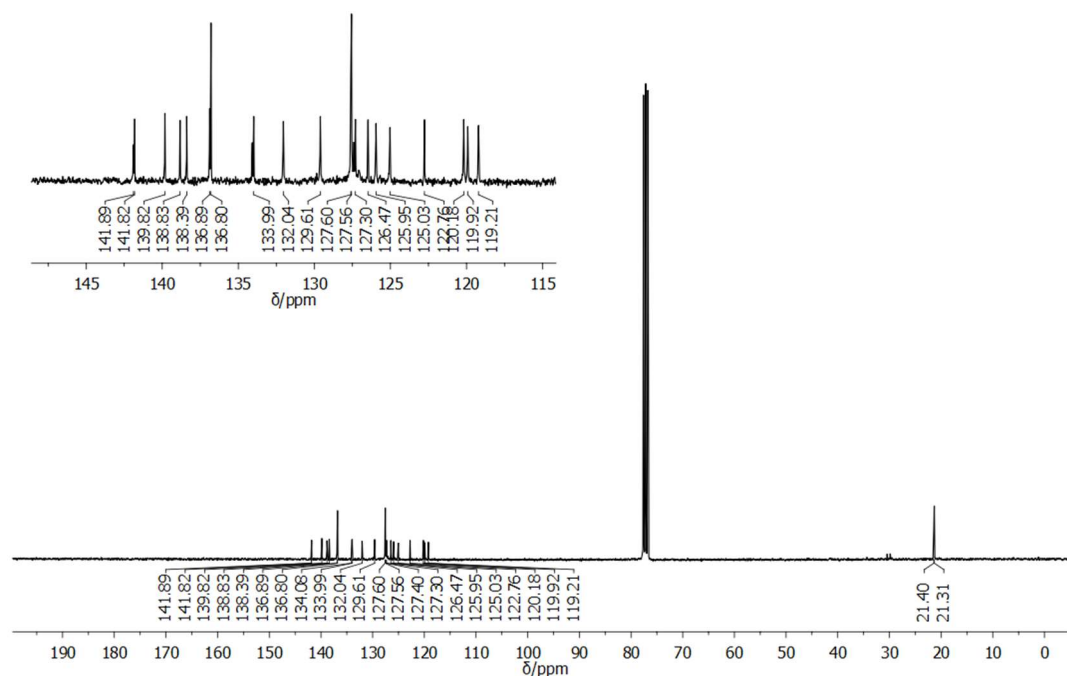


Figure A.28: LD⁺ HR-MS of **2-1**.

8) Aminoboranylboranediamine phenanthro[9,10,1,2,3-pqrst]pentaphene (2-33)**Figure A.29:** 300 MHz $^1\text{H-NMR}$ of 2-33 in CDCl_3 .**Figure A.30:** 75 MHz $^{13}\text{C-NMR}$ of 2-33 in CDCl_3 .

Appendix A

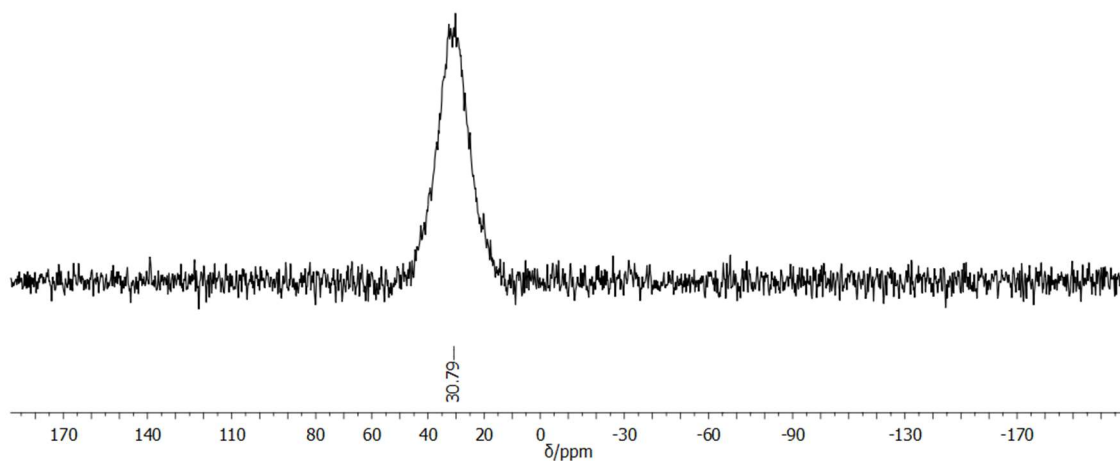


Figure A.31: 128 MHz ^{11}B -NMR of **2-33** in $\text{THF-}d_8$.

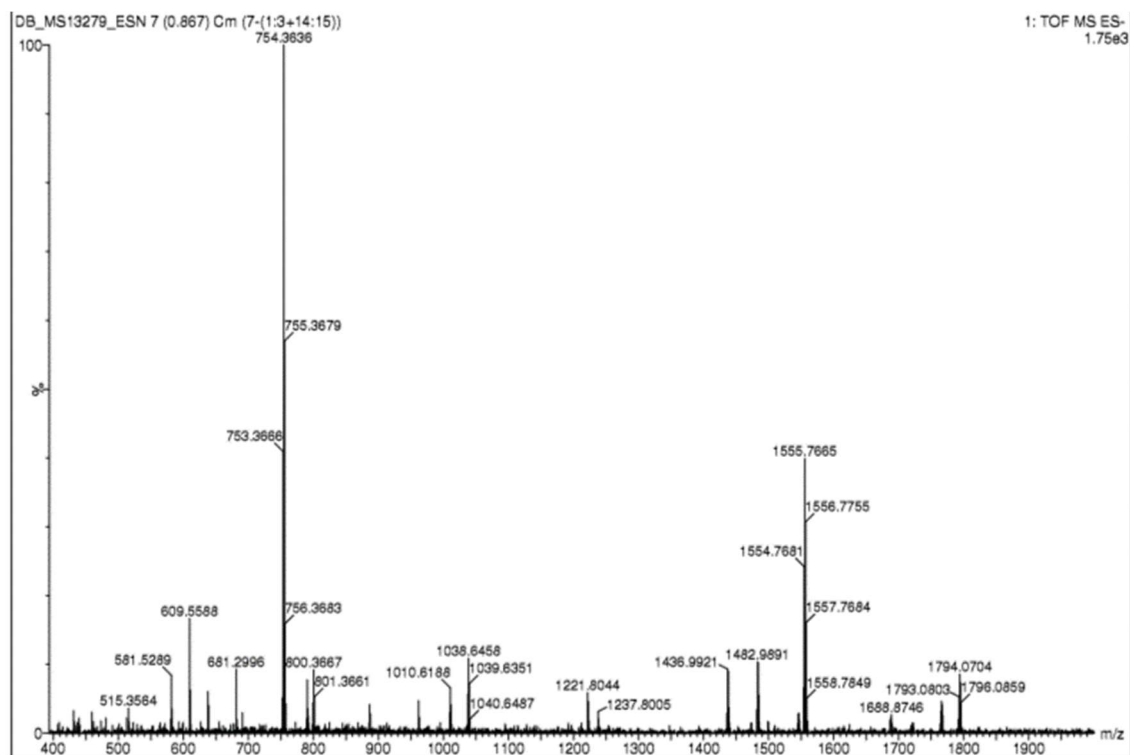


Figure A.32: ES- HR-MS of **2-33**.

Appendix A

9) 3-Fluoro-2',6'-dimethyl-[1,1'-biphenyl]-4-amine (2-35)

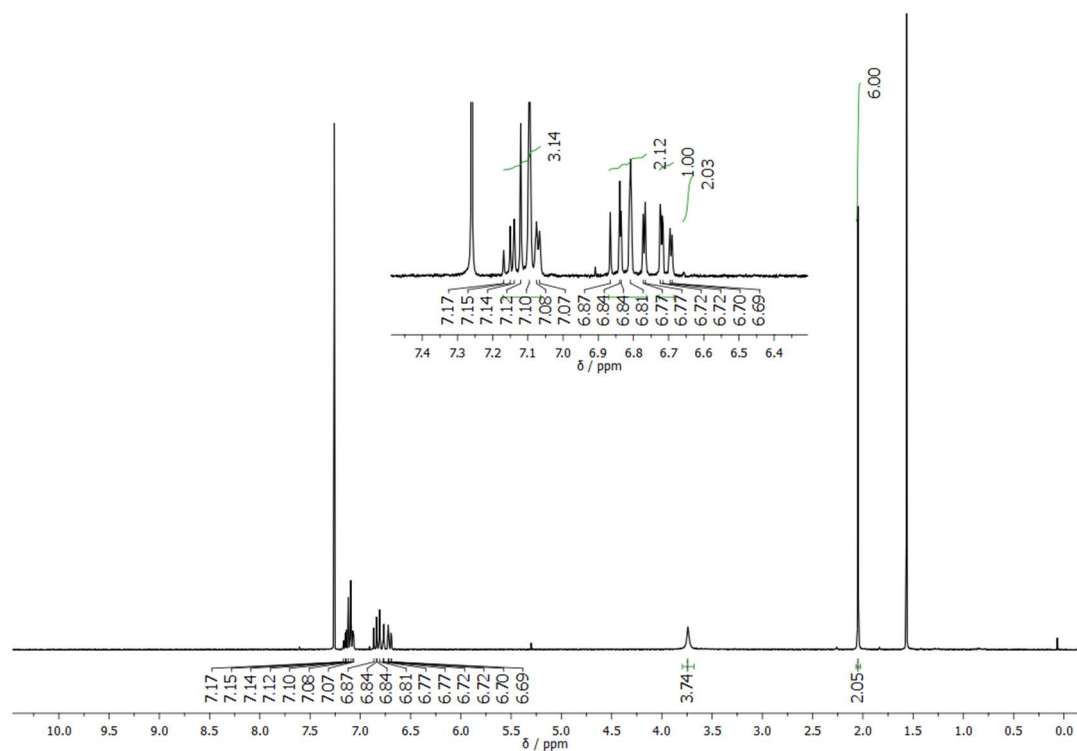


Figure A.33: 300 MHz $^1\text{H-NMR}$ of 2-35 in CDCl_3 .

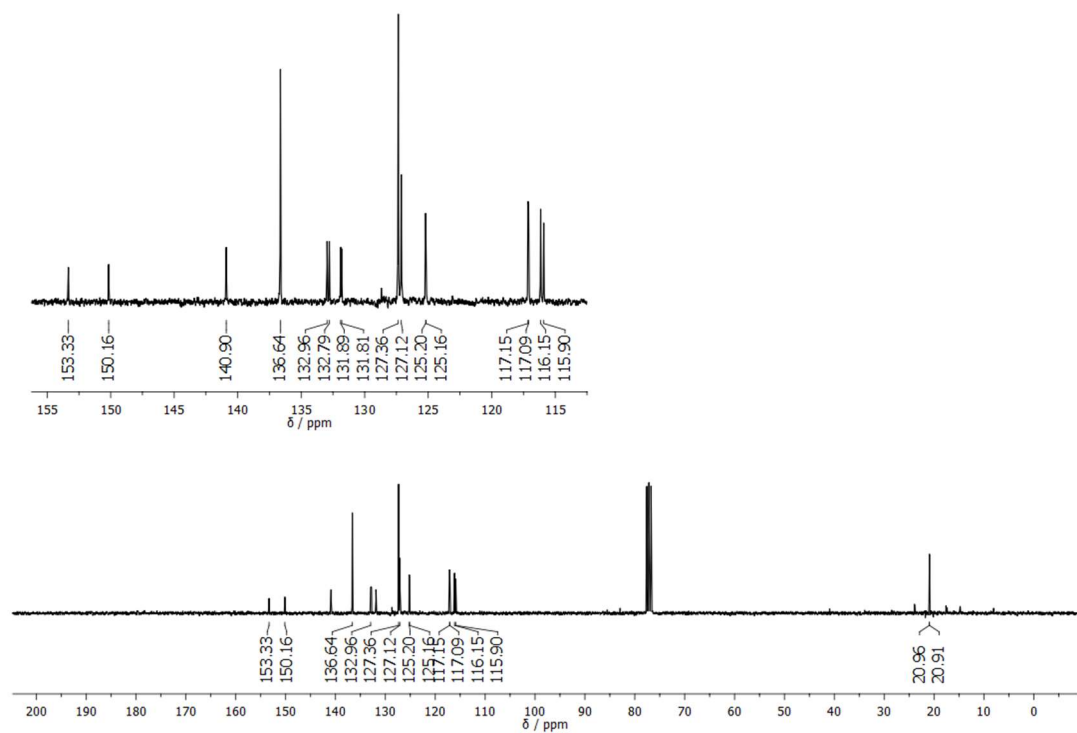


Figure A.34: 75 MHz $^{13}\text{C-NMR}$ of 2-35 in CDCl_3 .

Appendix A

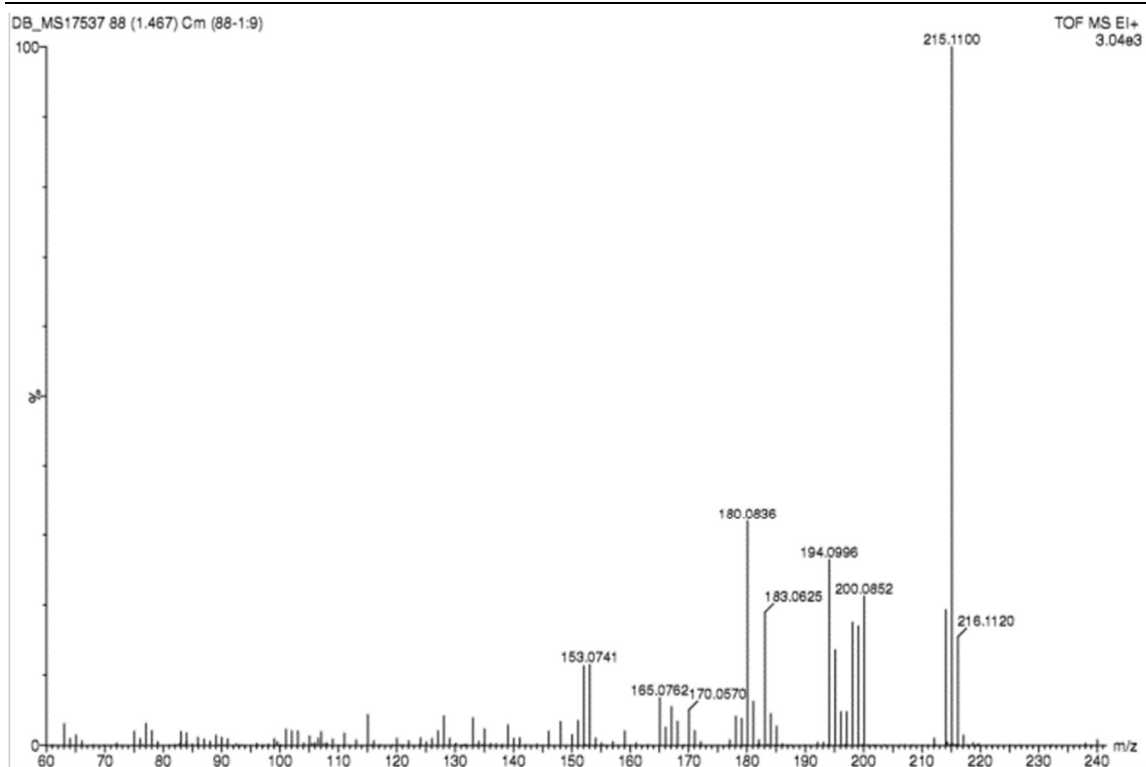
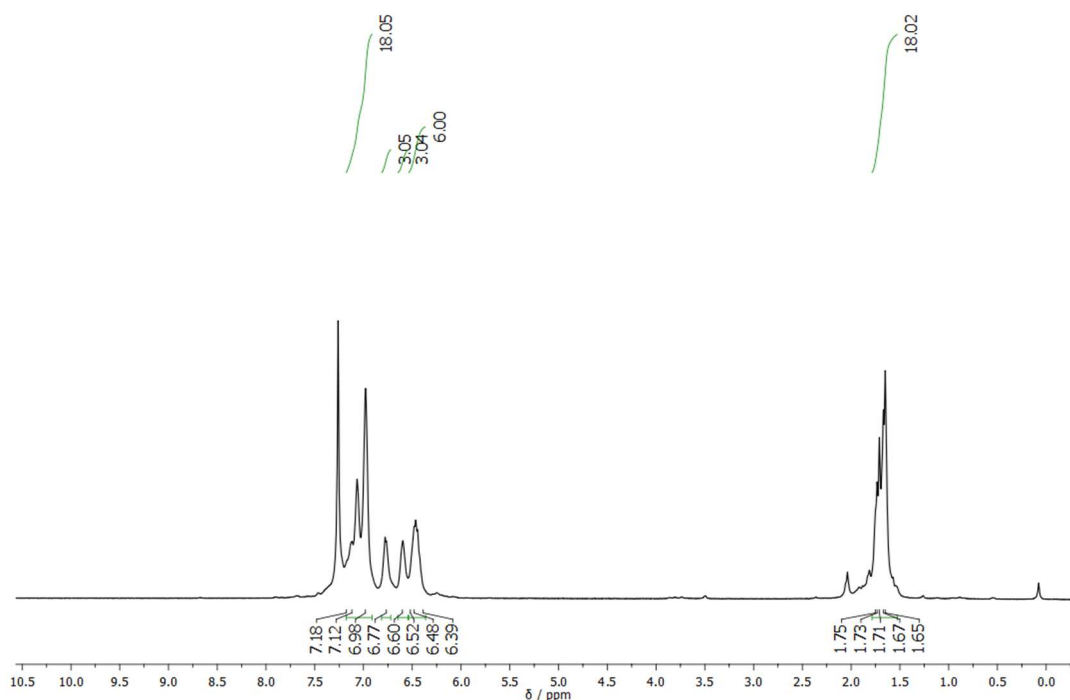
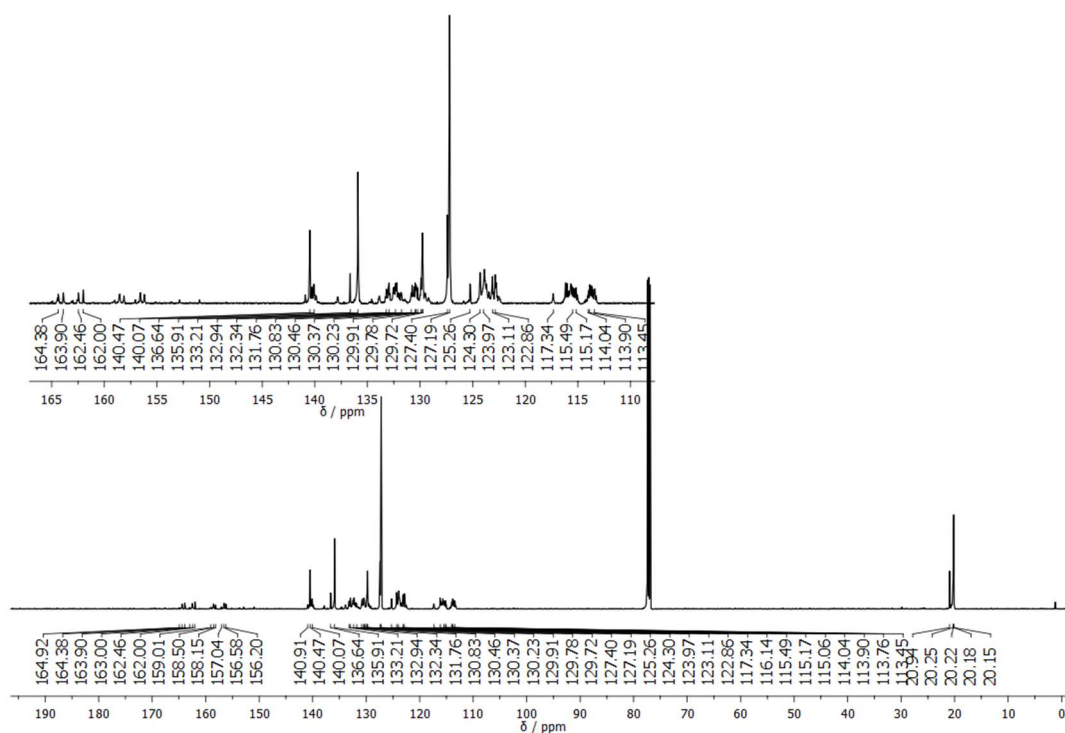


Figure A.35: EI⁺ HR-MS of 2-35.

10) Synthesis of B,B',B''-Tri[2-fluorophenyl]-N,N',N''-tri[2-fluoro-4-(2,6-dimethylphenyl)phenyl]borazine (2-34)**Figure A.36:** 500 MHz $^1\text{H-NMR}$ of **2-34** in CDCl_3 .**Figure A.37:** 125 MHz $^{13}\text{C-NMR}$ of **2-34** in CDCl_3

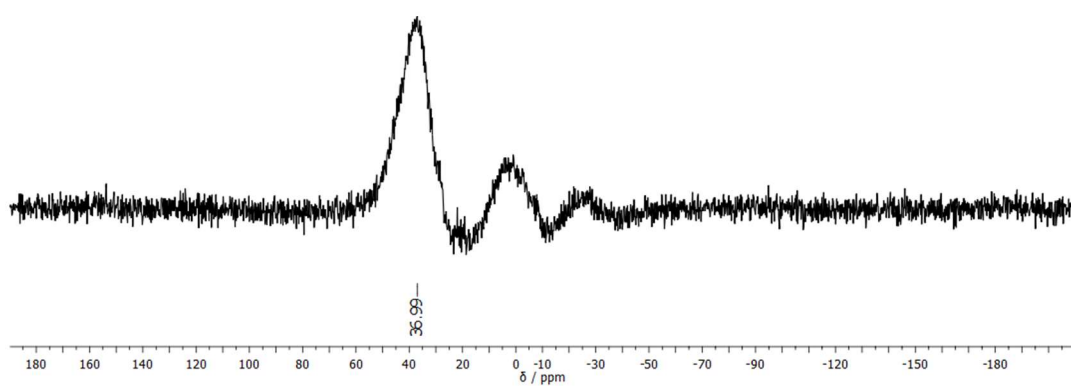


Figure A.38: 160 MHz ^{11}B -NMR of **2-34** in CDCl_3 (probe residual signal present from 10 to -10 ppm).

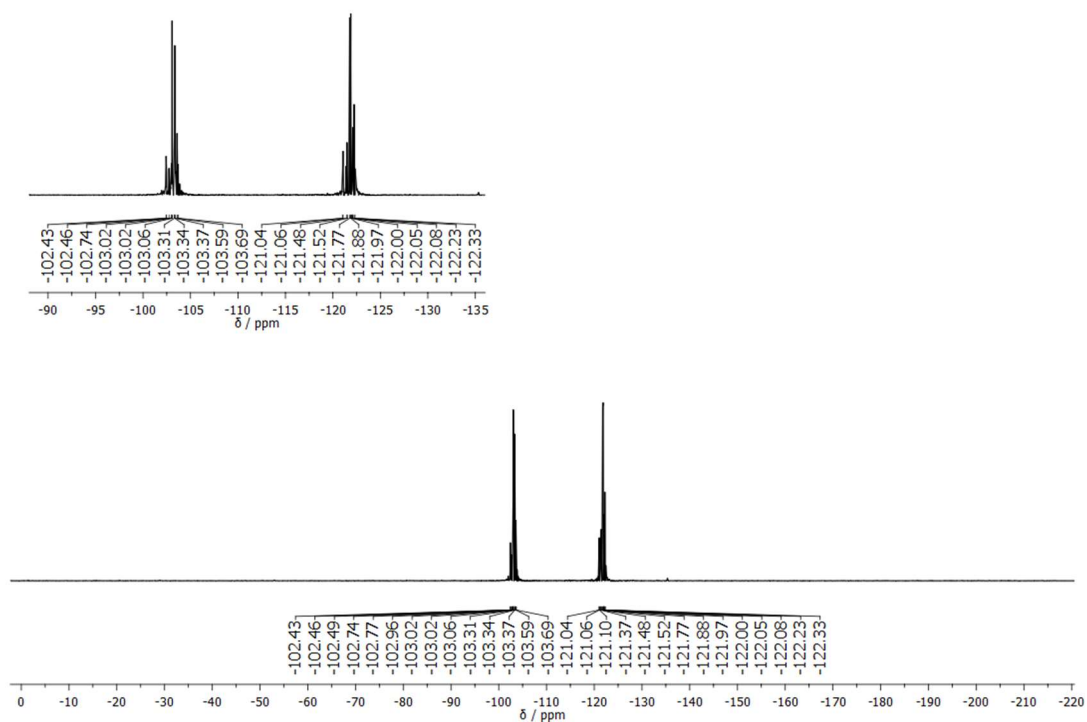


Figure A.39: 376 MHz ^{19}F -NMR of **2-34** in CDCl_3 .

Appendix A

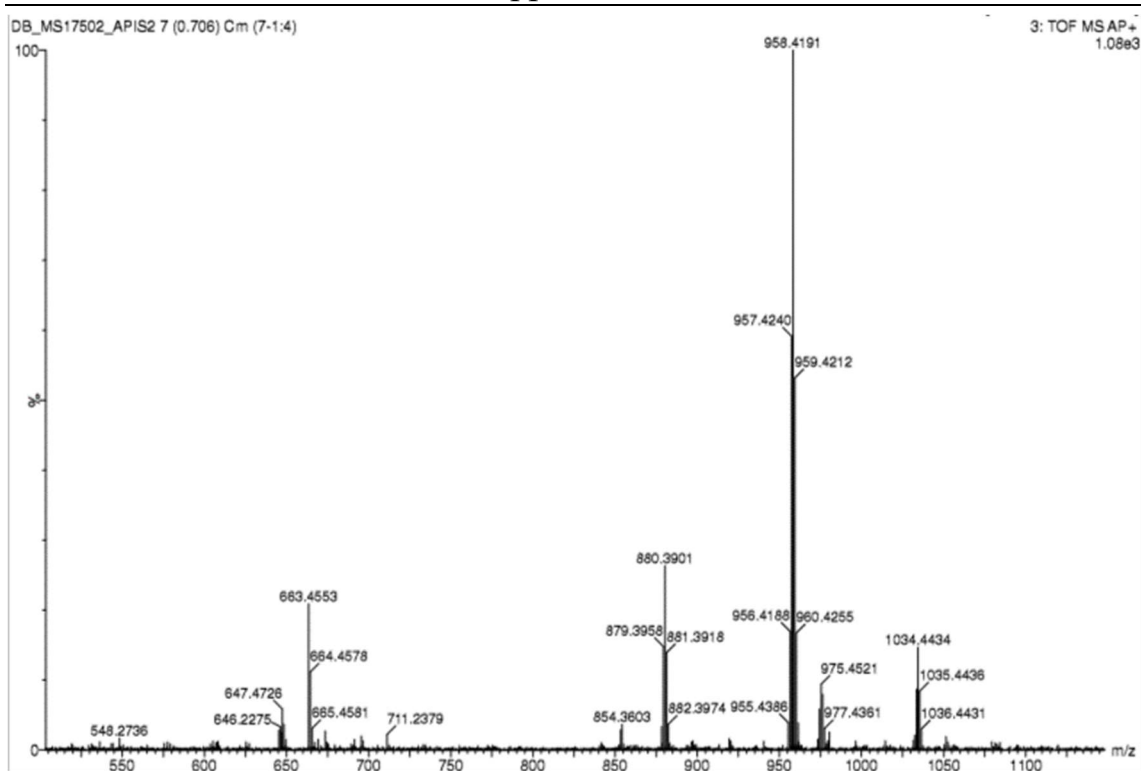


Figure A.40: AP⁺ HR-MS of 2-34.

Appendix A

11) 6,12-Bis(2,6-dimethylphenyl)-18-oxa-17b1,18a1-diaza-7b2,17b,18a-triboradibenzo[fg,ij]phenanthro[9,10,1,2,3-pqrst]pentaphene (2-38)

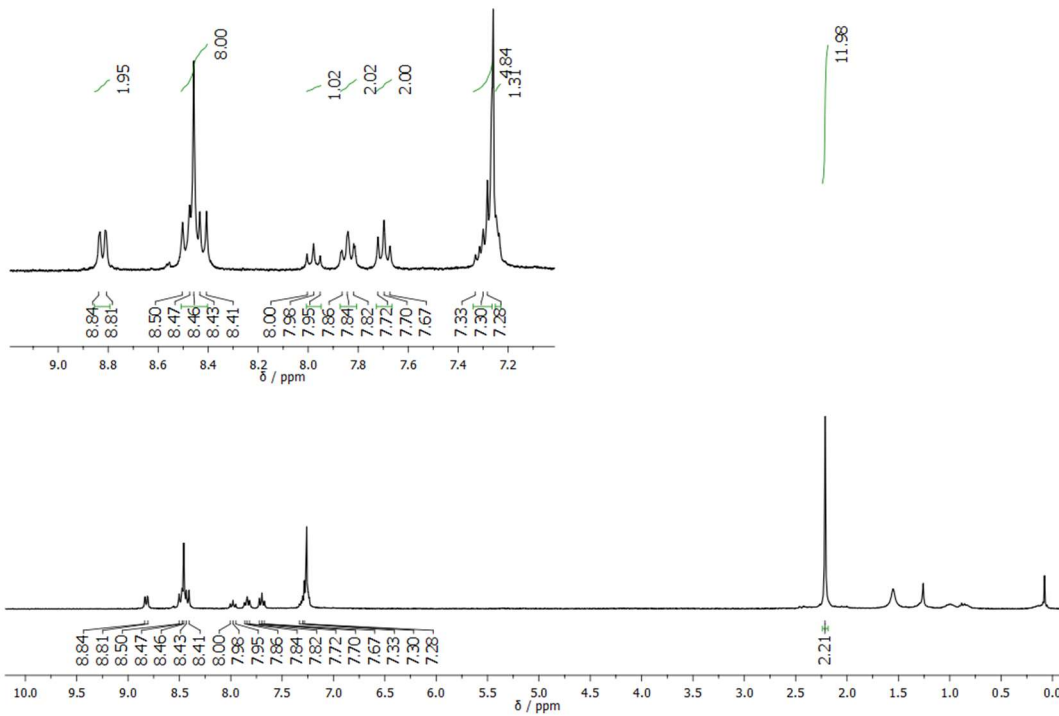


Figure A.41: 300 MHz ¹H-NMR of 2-38 in CDCl₃.

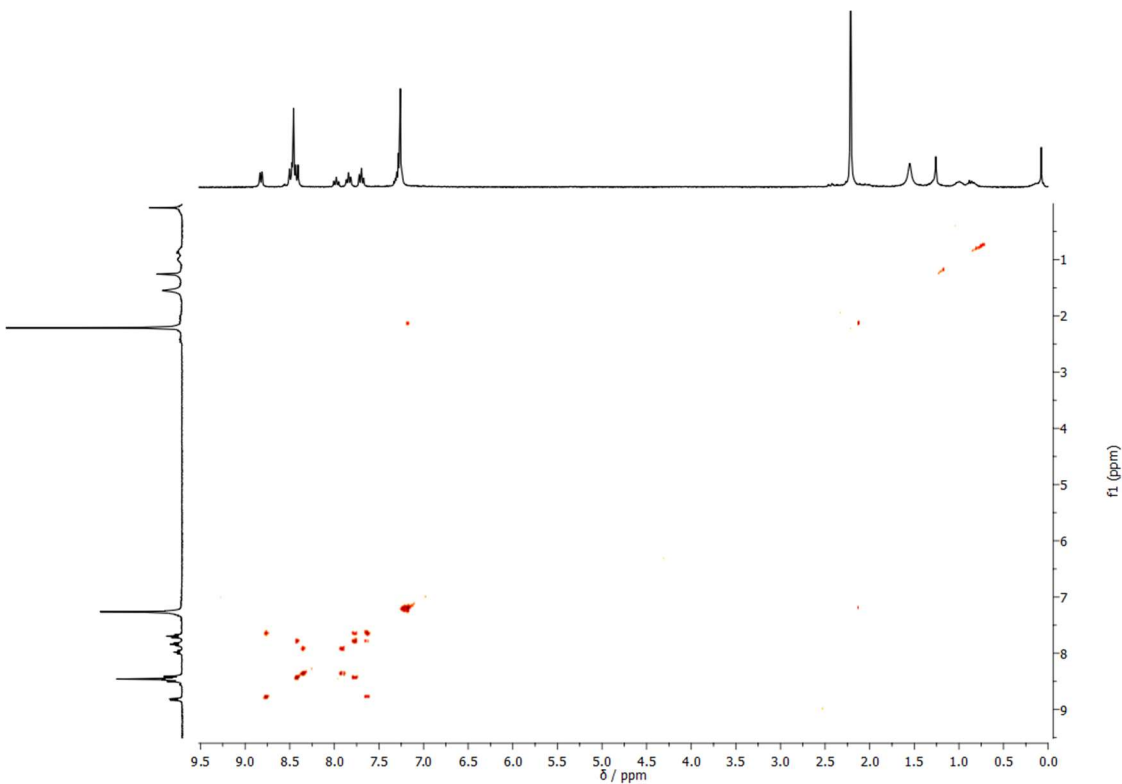


Figure A.42: 500 MHz ¹H-¹H COSY NMR of 2-38 in CDCl₃.

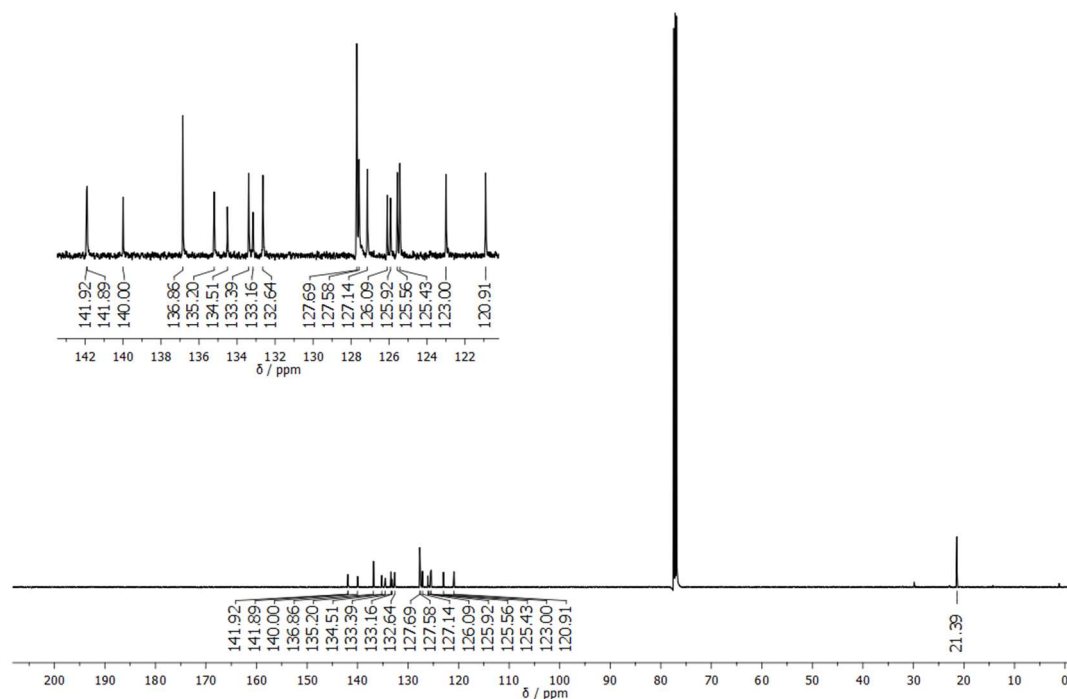


Figure A.43: 126 MHz ^{13}C -NMR of **2-38** in CDCl_3 .

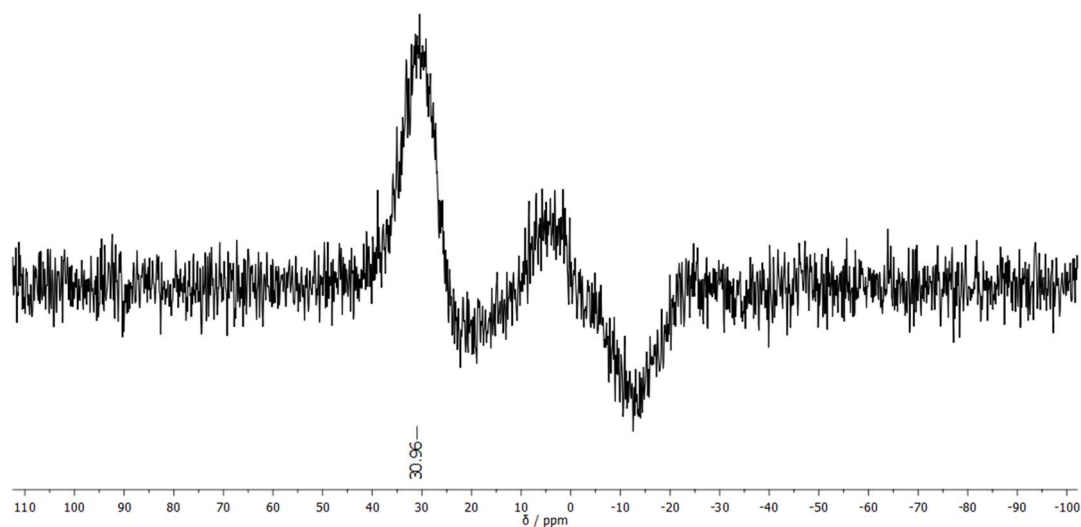


Figure A.44: 160 MHz ^{11}B -NMR of **2-38** in CDCl_3 (probe residual signal present from 10 to -10 ppm).

Appendix A

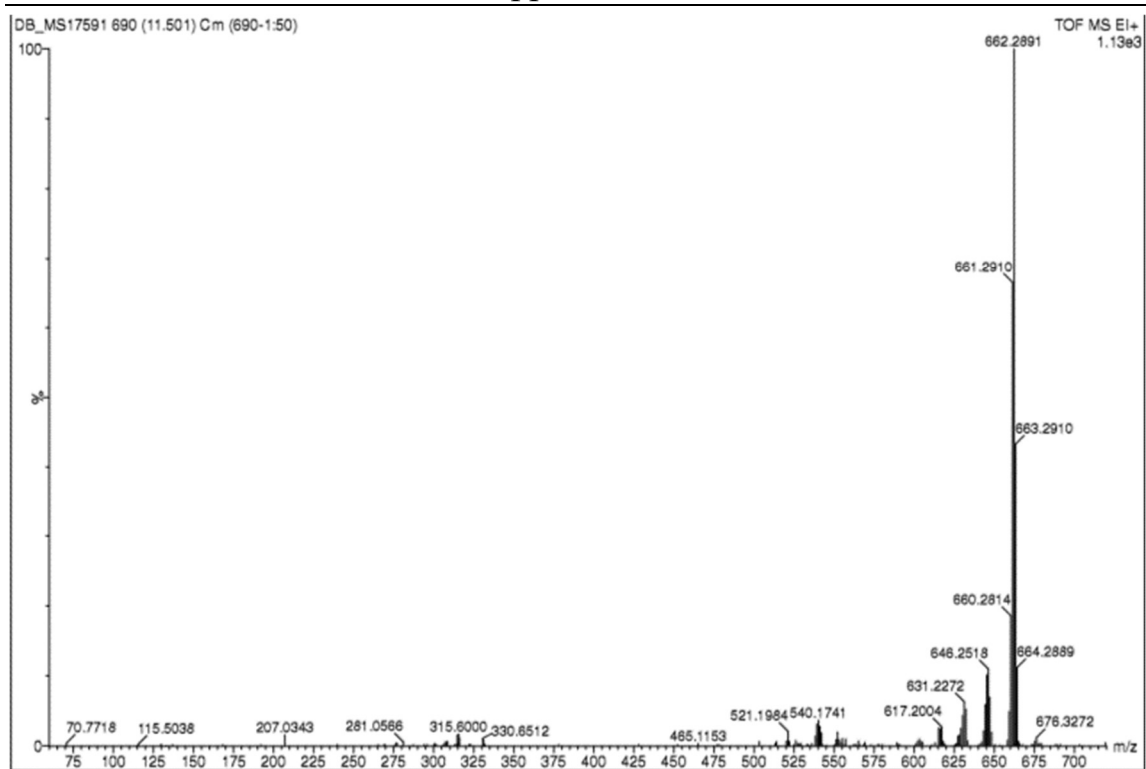
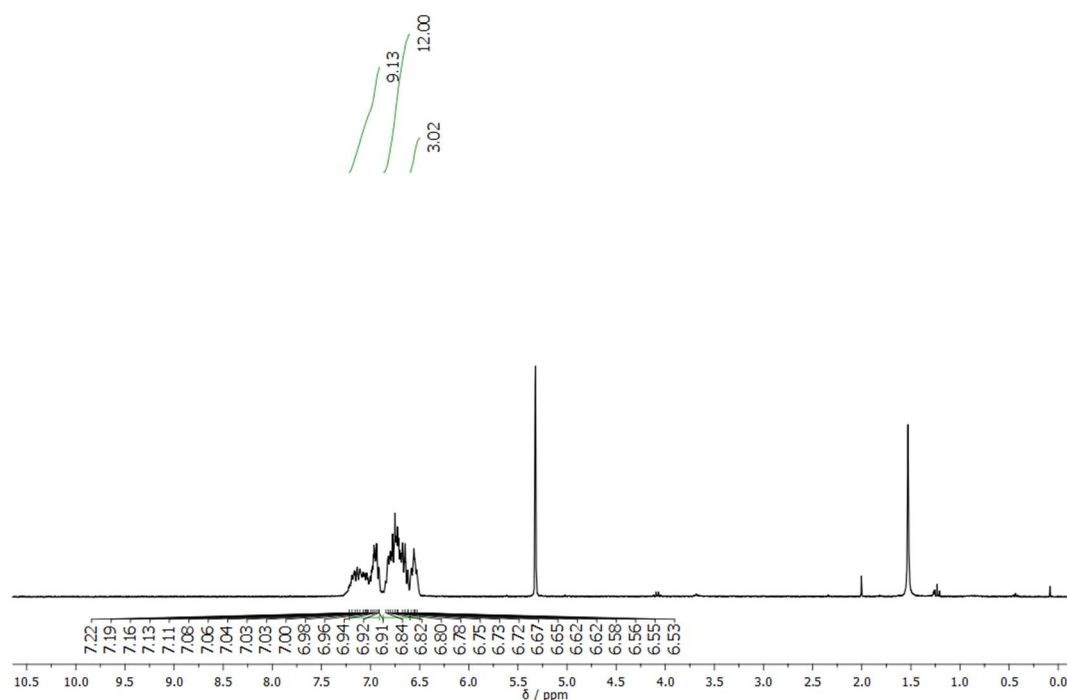
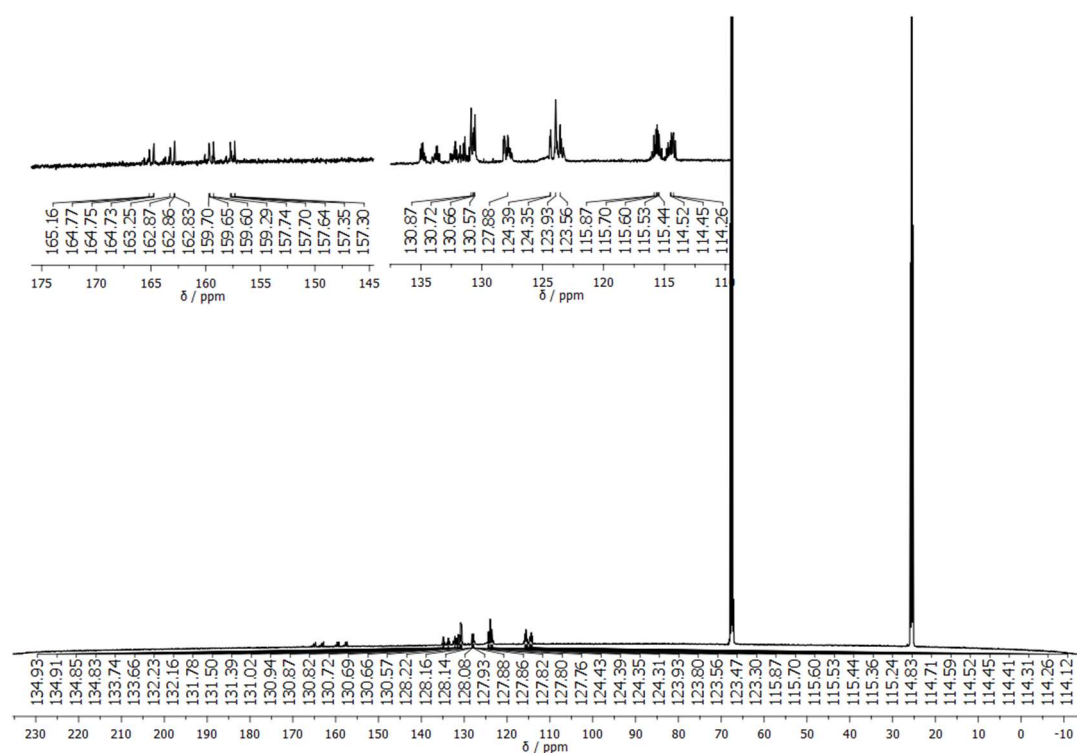


Figure A.45: EI⁺ HR-MS of 2-38.

12) Synthesis of B,B',B''-Tri[2-fluorophenyl]-N,N',N''-tri[2-fluorophenyl]borazine (2-40)**Figure A.46:** 300 MHz $^1\text{H-NMR}$ of **2-40** in CD_2Cl_2 .**Figure A.47:** 125 MHz $^{13}\text{C-NMR}$ of **2-40** in $\text{THF-}d_8$.

Appendix A

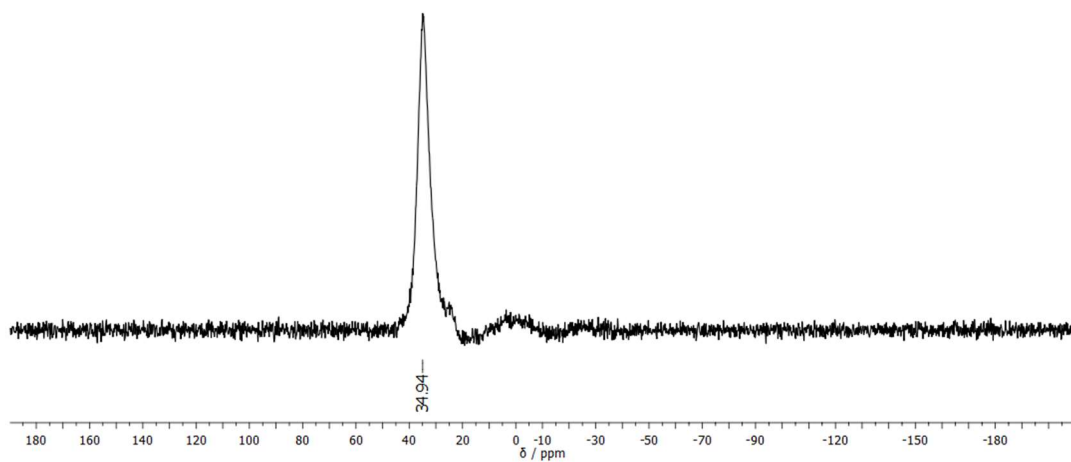


Figure A.48: 160 MHz ^{11}B -NMR of **2-40** in CD_2Cl_2 . (probe residual signal present from 10 to -10 ppm).

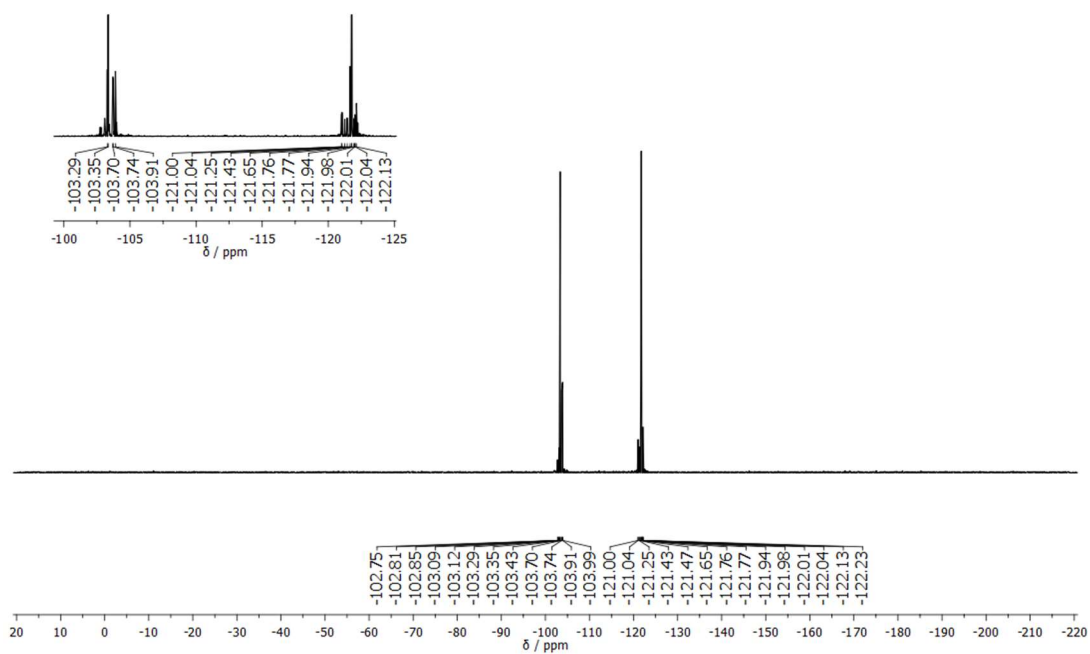


Figure A.49: 376 MHz ^{19}F -NMR of **2-40** in CD_2Cl_2 .

Appendix A

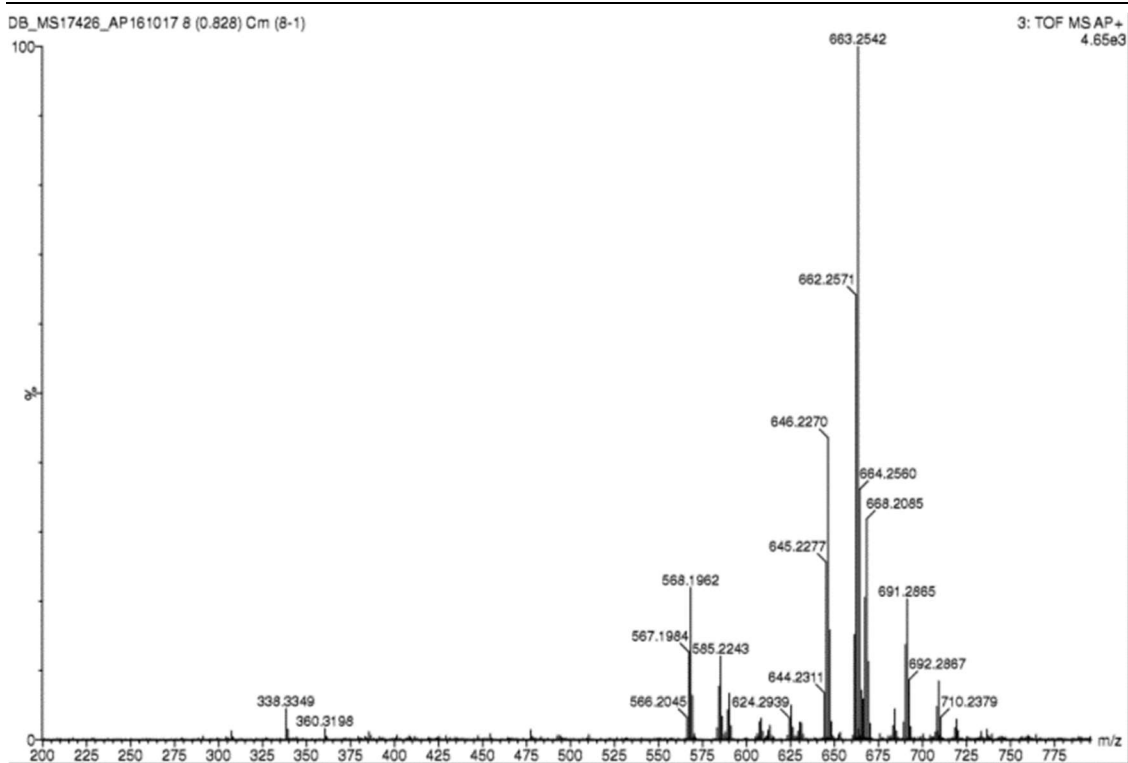
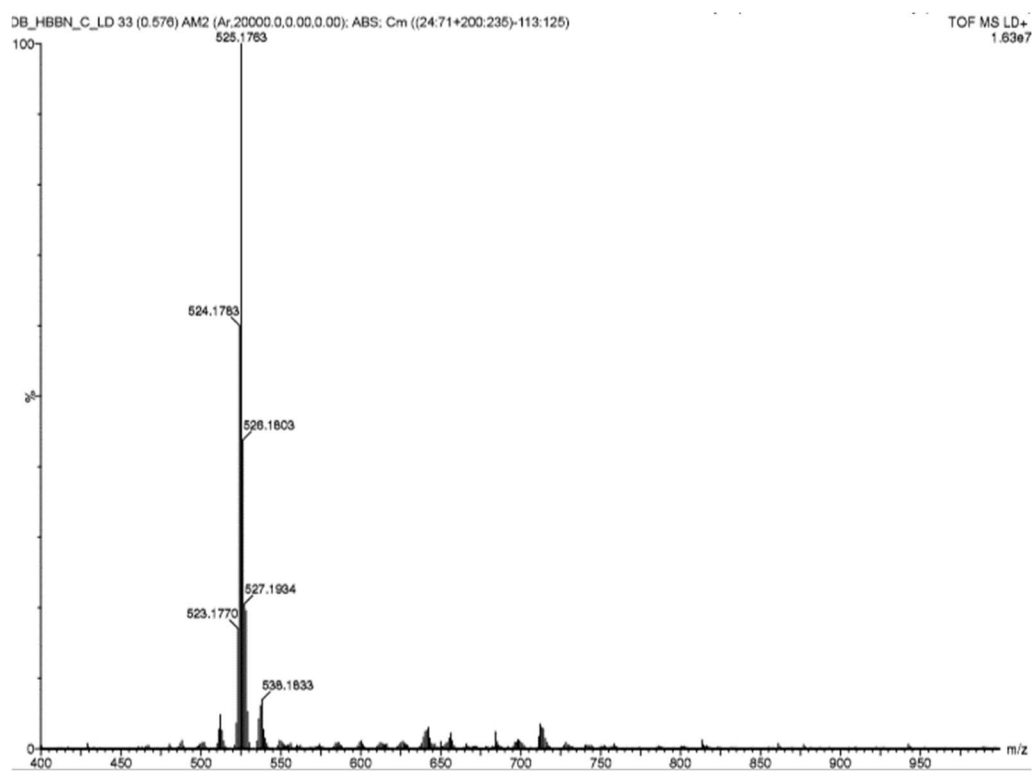
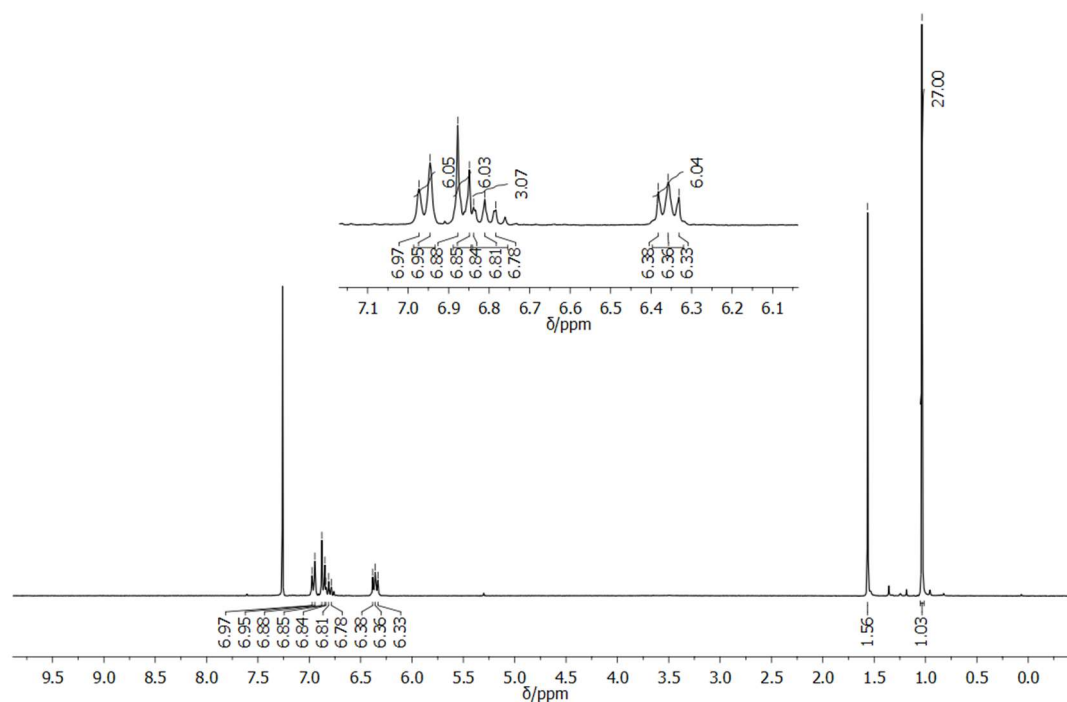
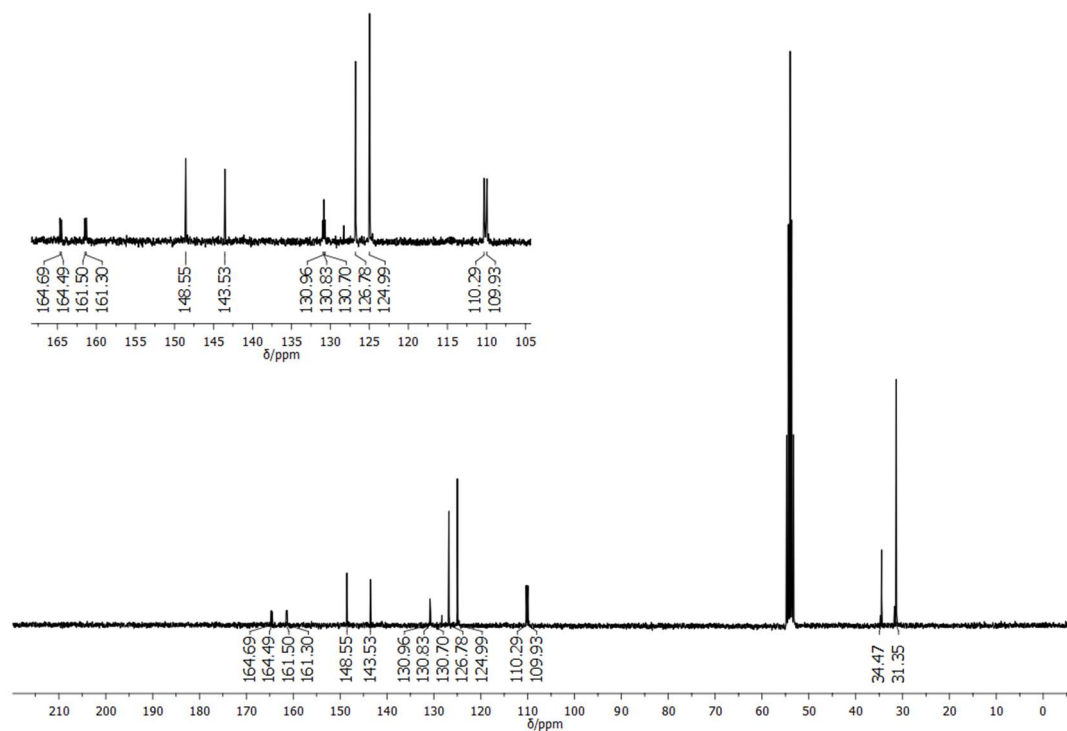


Figure A.50: AP⁺ HR-MS of 2-40.

13) 3a2,6b2,12b2-triaza-3b2,9b2,15b2-triborahexabenzo[bc,ef,hi,kl,no,qr]coronene (1-1)**Figure A.51: LD⁺ HR-MS of 1-1.**

14) B,B',B''-[2,6-(Difluoro)phenyl]-N,N',N''-tri[4-(tert-butyl) phenyl]-borazine (2-45)**Figure A.52:** 300 MHz $^1\text{H-NMR}$ of **2-45** in CDCl_3 .**Figure A.53:** 75 MHz $^{13}\text{C-NMR}$ of **2-45** in CD_2Cl_2 .

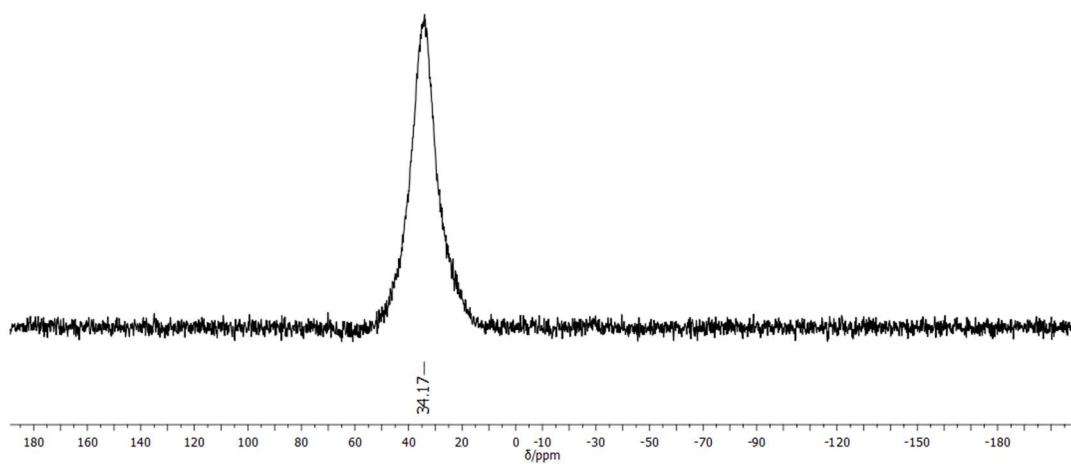


Figure A.54: 128 MHz ^{11}B -NMR of **2-45** in CDCl_3 .

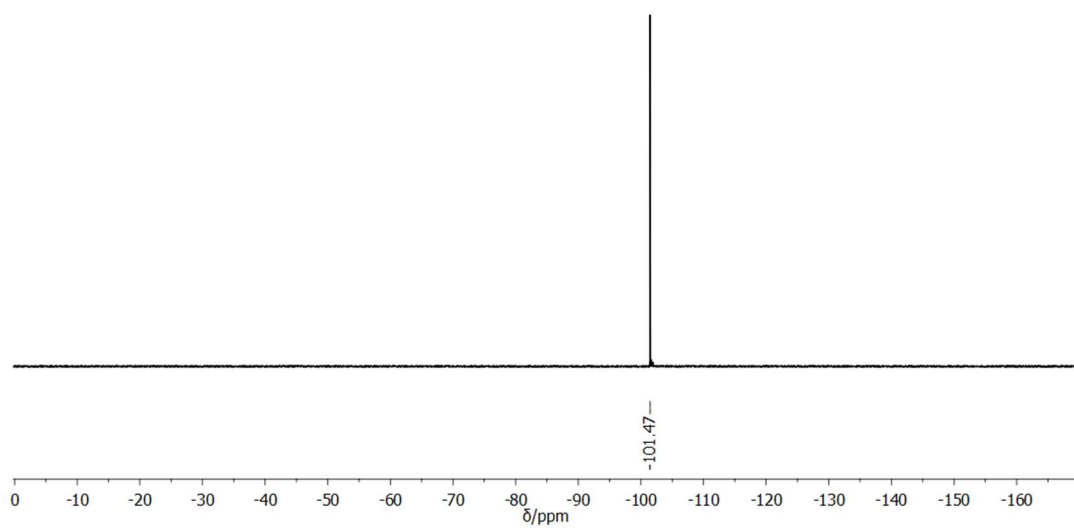


Figure A.55: 376 MHz ^{19}F -NMR of **2-45** in CDCl_3 .

Appendix A

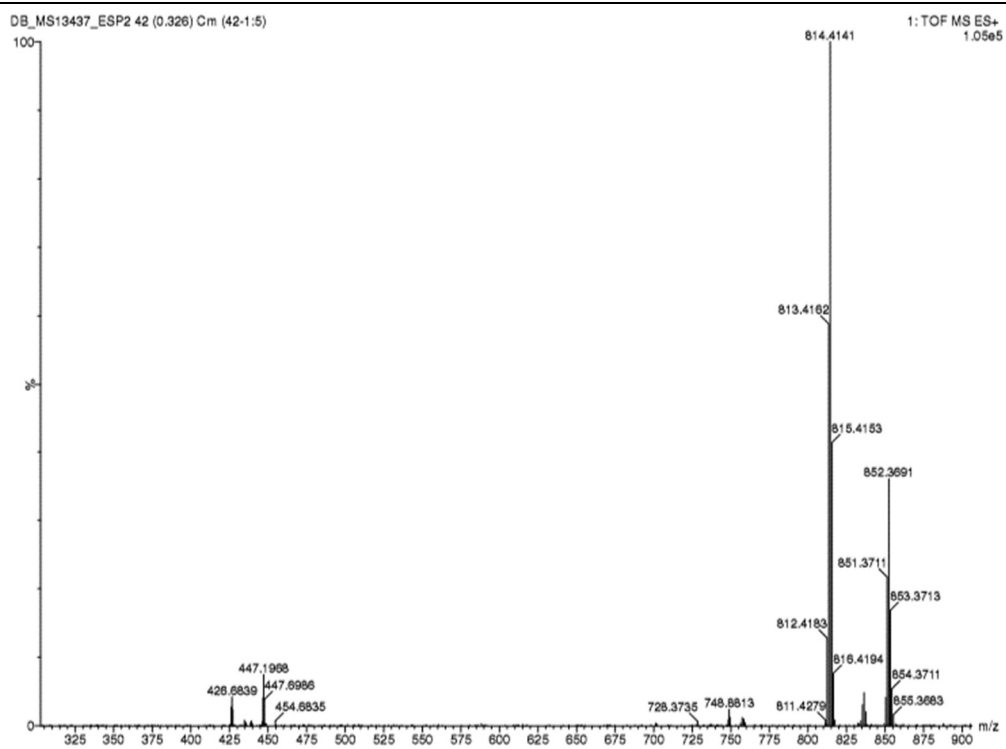


Figure A.56: ES⁺ HR-MS of 2-45.

Appendix A

15) B,B',B''-[2,6-(Difluoro)phenyl]-N,N',N''-tri[4-(dodecyl) phenyl]-borazine (2-48)

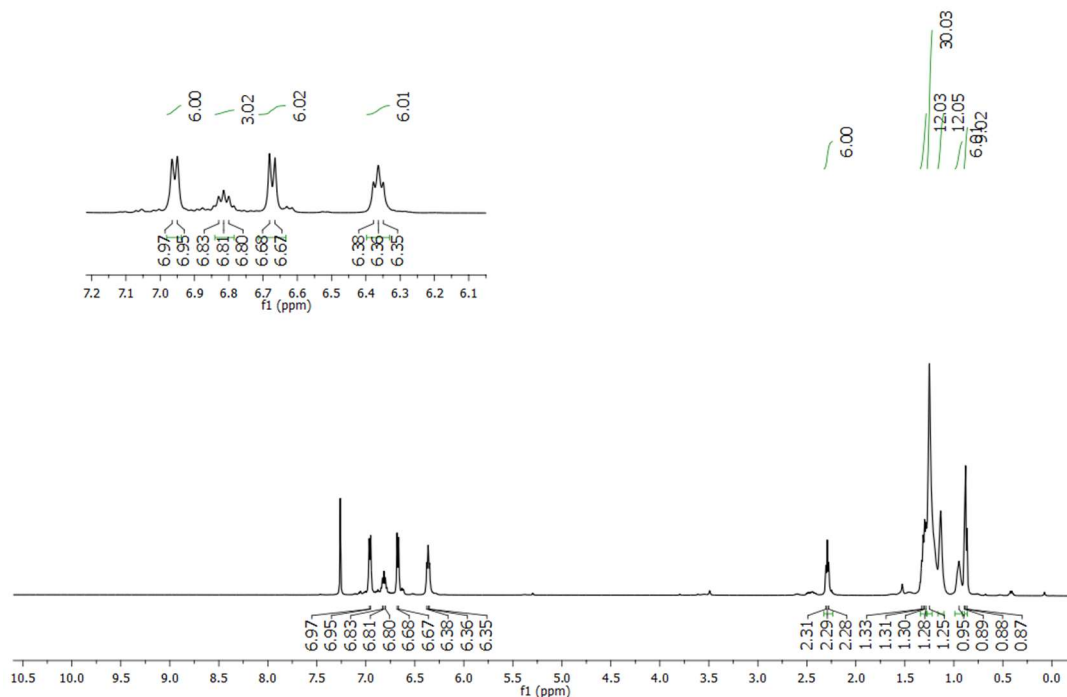


Figure A.57: 500 MHz ¹H-NMR of **2-48** in CDCl₃.

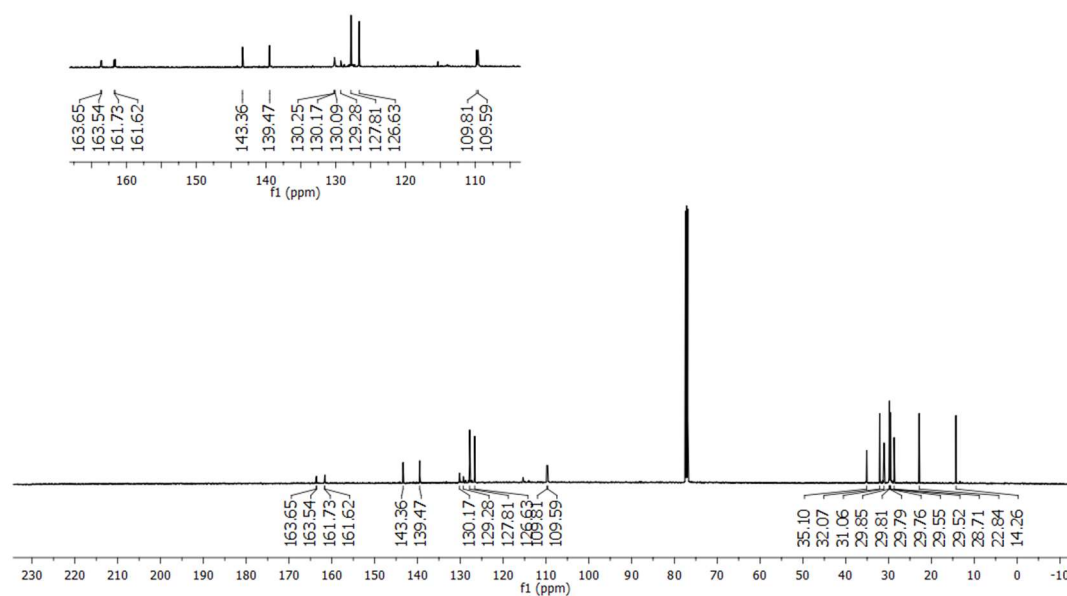


Figure A.58: 126 MHz ¹³C-NMR of **2-48** in CDCl₃.

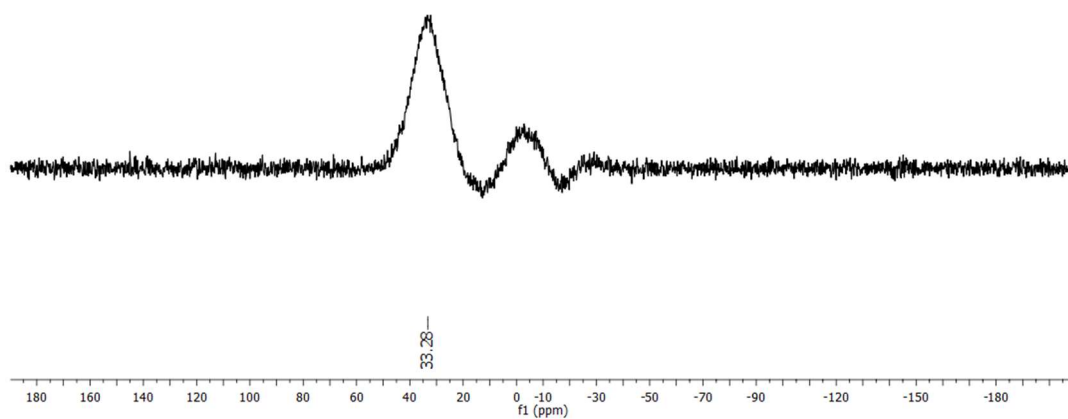


Figure A.59: 160 MHz ^{11}B -NMR of **2-48** in CDCl_3 . (probe residual signal present from 10 to -10 ppm).

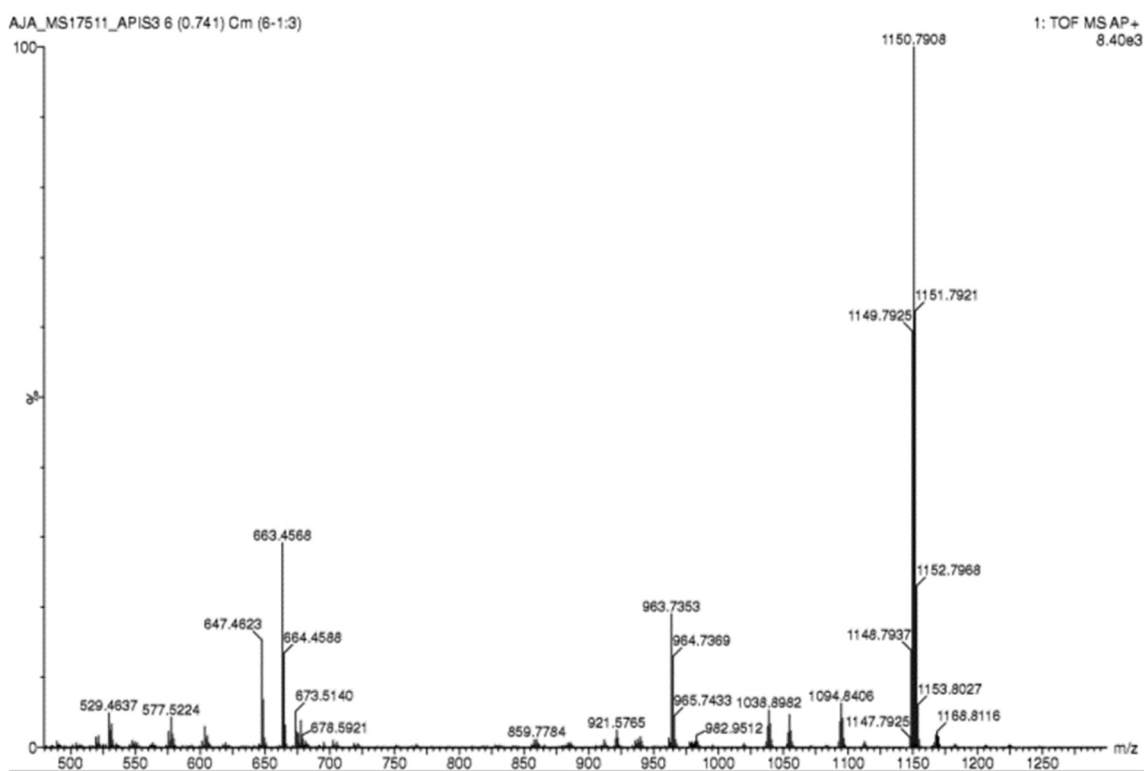


Figure A.60: ES⁺ HR-MS of **2-48**.

Appendix A

16) (4-Bromo-3,5-difluorophenoxy)triisopropylsilane (2-56)

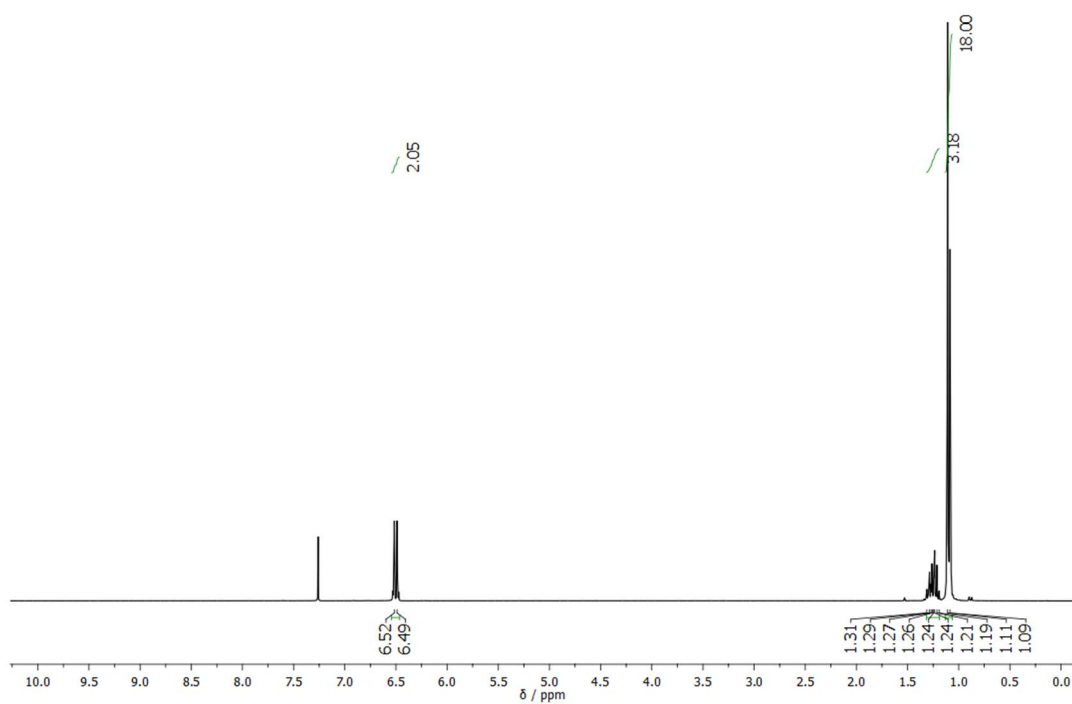


Figure A.61: 300 MHz ^1H -NMR of **2-56** in CDCl_3 .

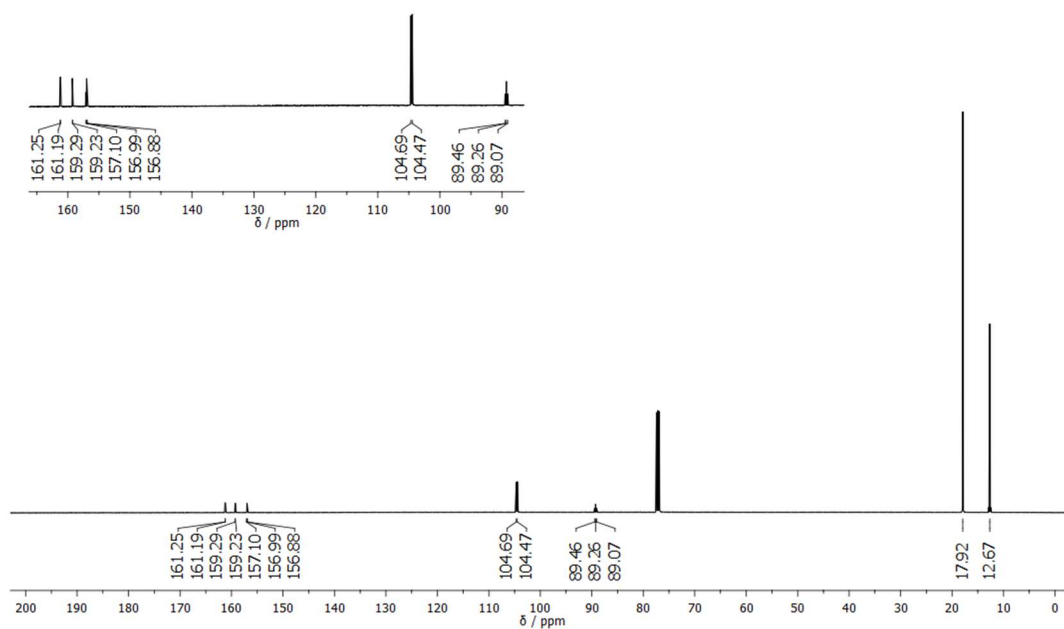


Figure A.62: 75 MHz ^{13}C -NMR of **2-56** in CDCl_3 .

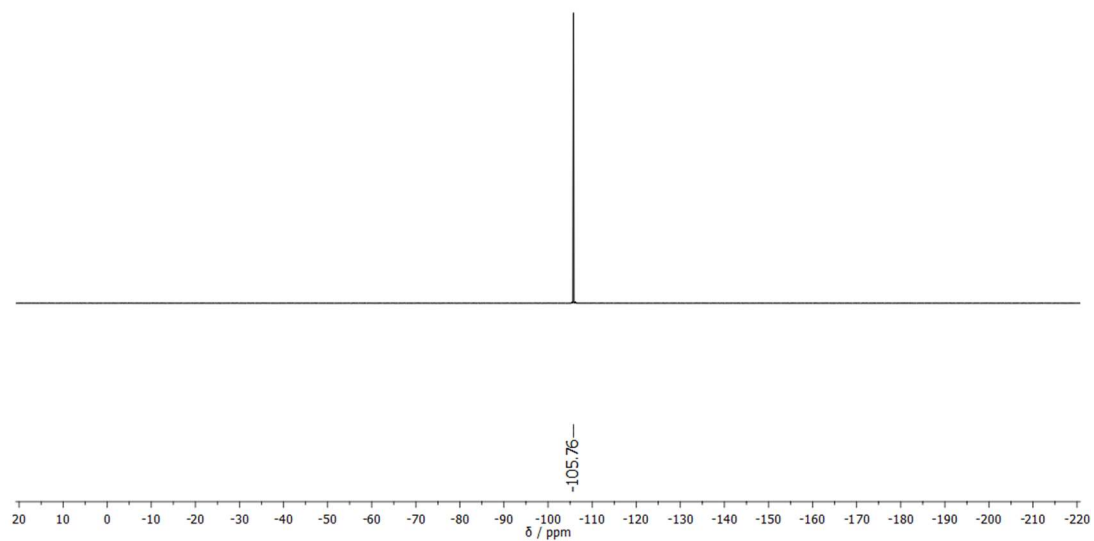


Figure A.63: 376 MHz ^{19}F -NMR of **2-56** in CDCl_3 .

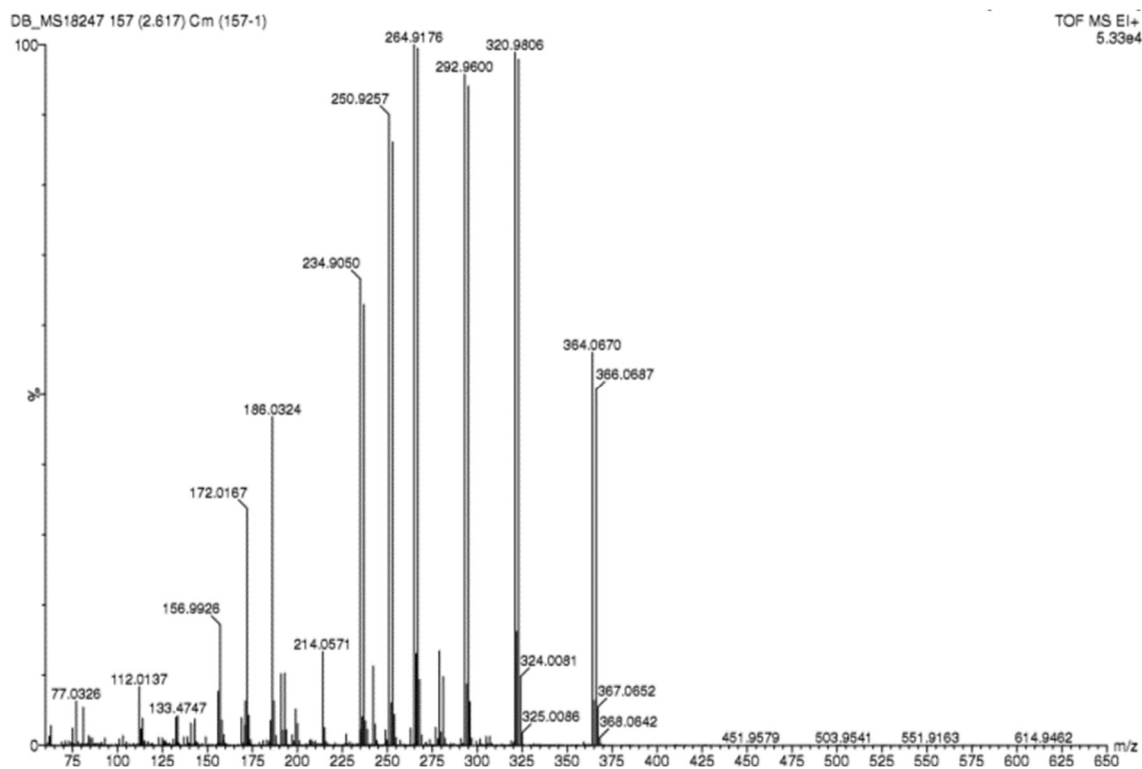


Figure A.64: EI⁺ HR-MS of **2-56**.

Appendix A

17) B,B',B''-[(3,5-Difluorophenoxy)triisopropylsilane]-N,N',N''-tri[4-(2,6-dimethylphenyl)phenyl]borazine (2-51)

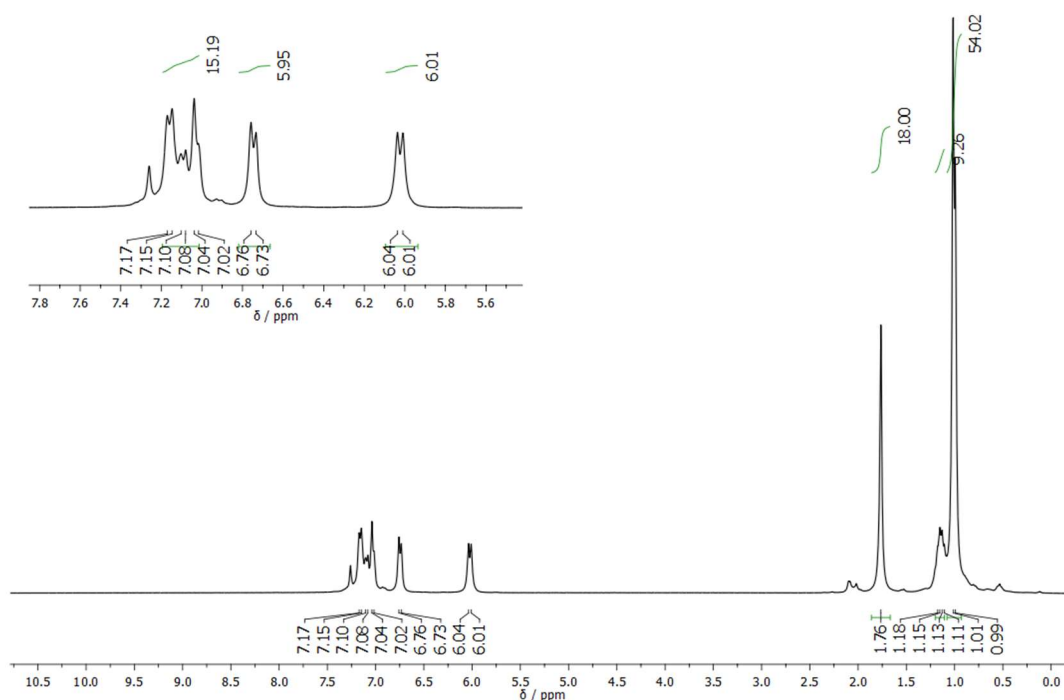


Figure A.65: 300 MHz ¹H-NMR of 2-51 in CDCl₃.

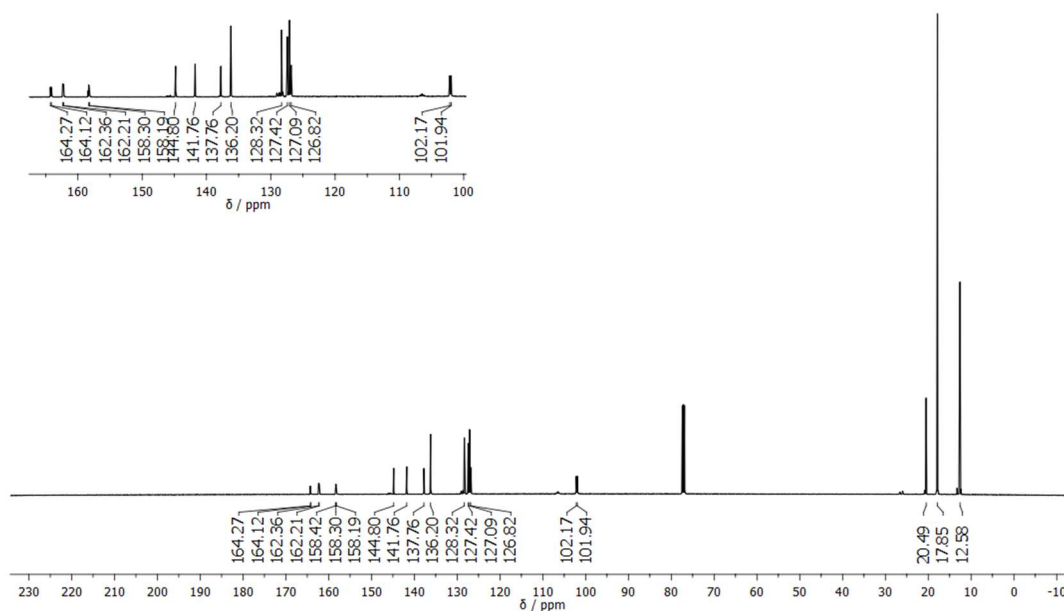


Figure A.66: 126 MHz ¹³C-NMR of 2-51 in CDCl₃.

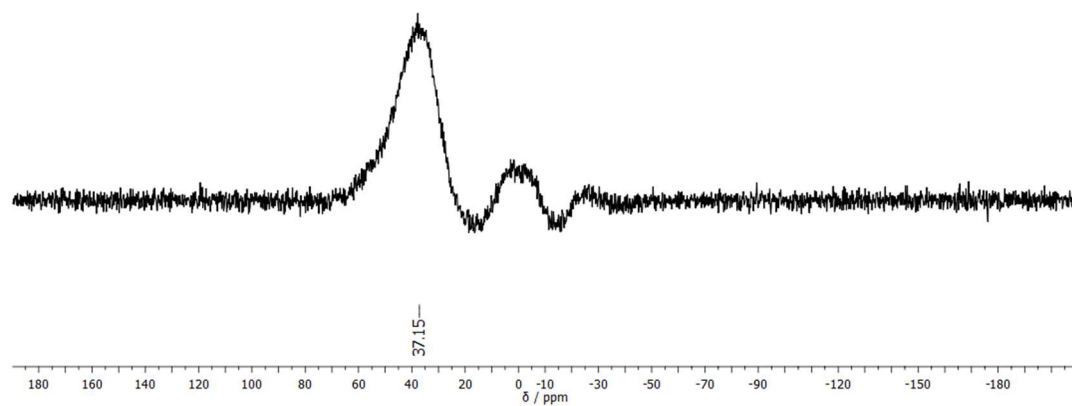


Figure A.67: 160 MHz ^{11}B -NMR of **2-51** in CDCl_3 (probe residual signal present from 10 to -10 ppm).

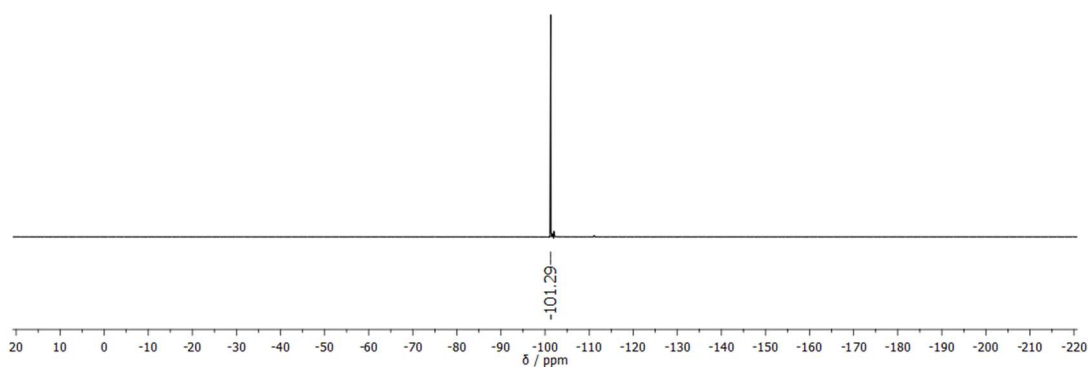


Figure A.68: 376 MHz ^{19}F -NMR of **2-51** in CDCl_3 .

Appendix A

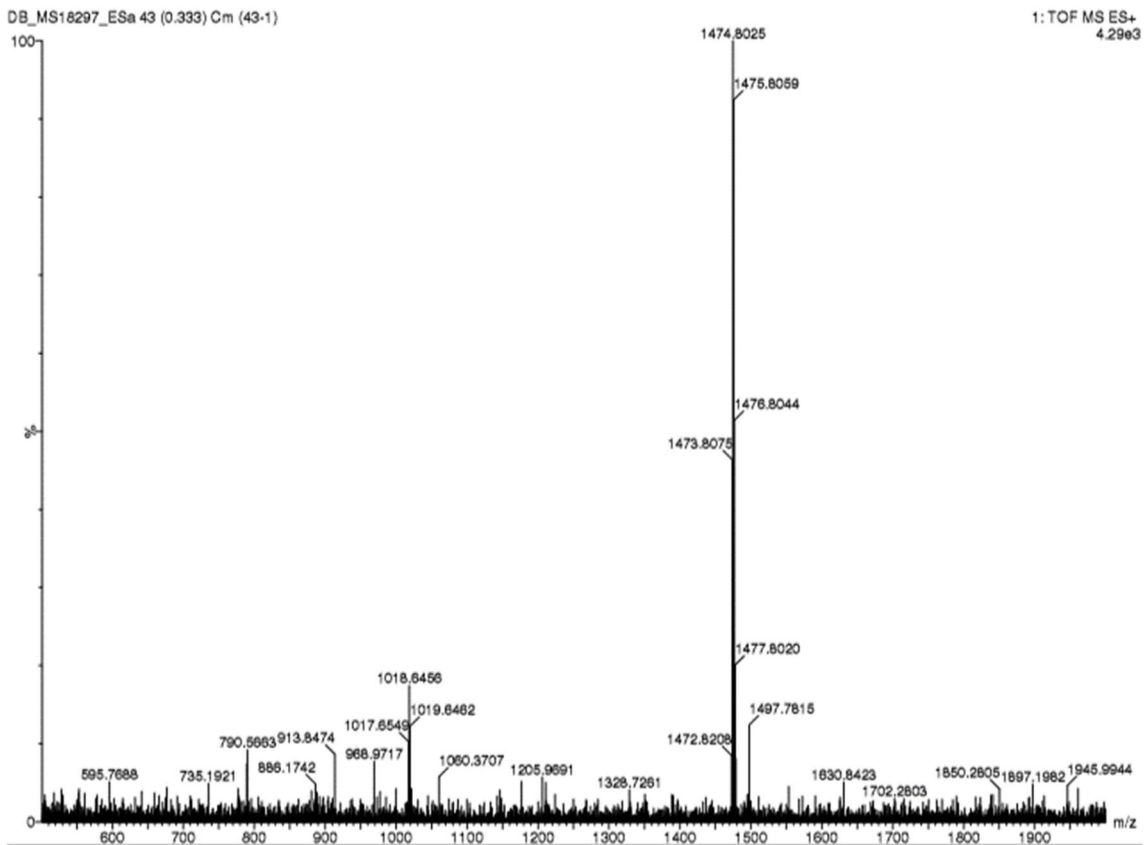


Figure A.69: ES⁺ HR-MS of 2-51.

CHAPTER 3

(For 3-2 intermediates only ^1H and ^{13}C -NMR reported, HR-MS can be found in corresponding papers)

18) 1,3,5-(4'-Hydroxyphenyl)-2,4,6-phenylbenzene (3-3)

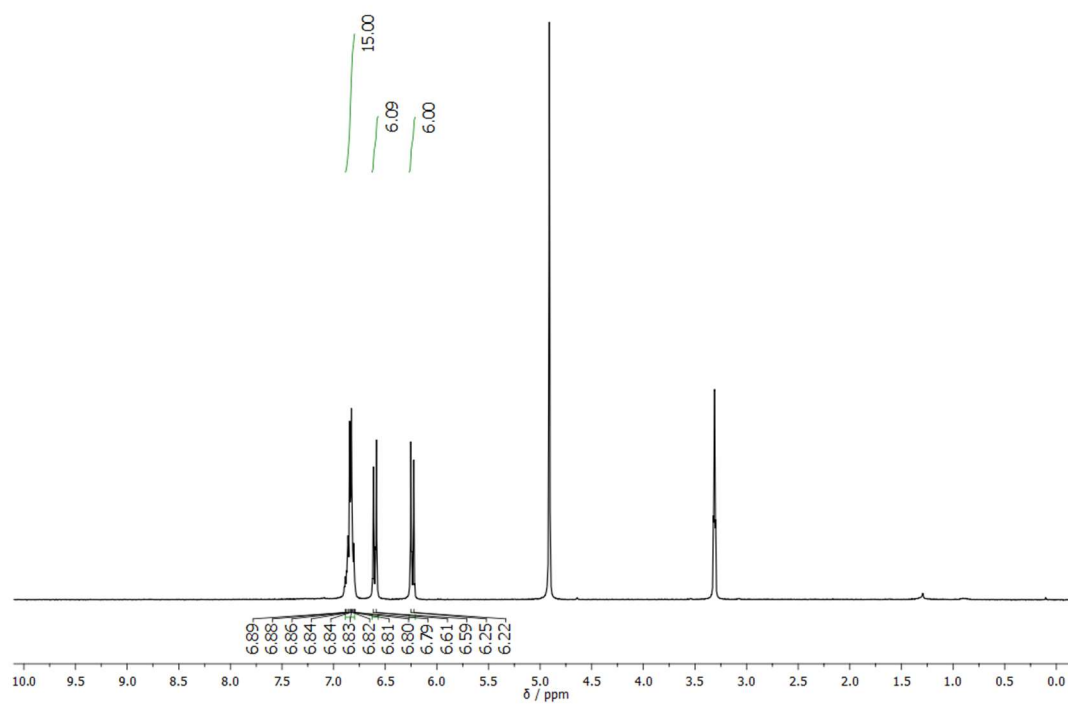


Figure A.70: 300 MHz ^1H -NMR of **3-3** in MeOD.

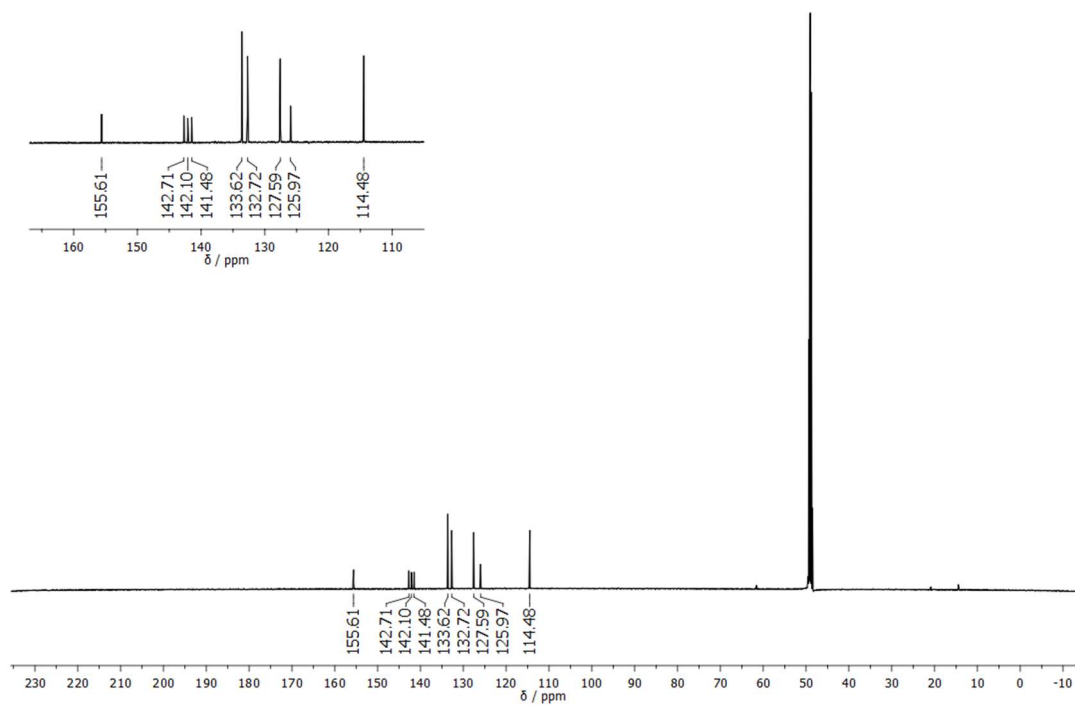


Figure A.71: 75 MHz ^1H -NMR of **3-3** in MeOD.

19) 1,3,5-(4'-Trifluoromethylsulfonylphenyl)-2,4,6-phenyl benzene (3-4)

Appendix A

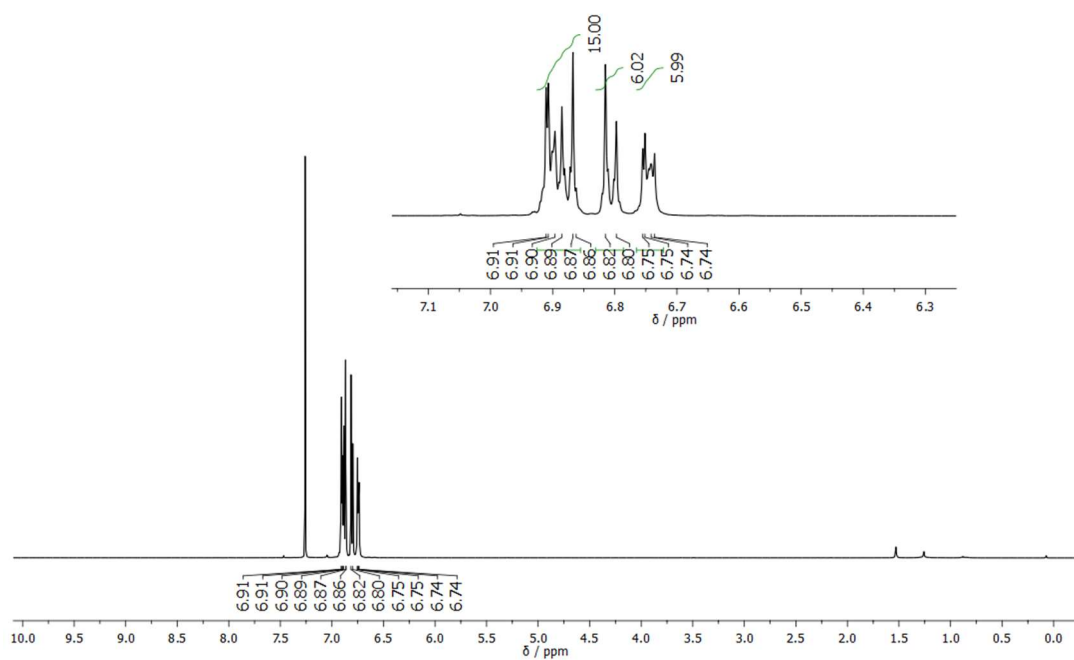


Figure A.72: 500 MHz $^1\text{H-NMR}$ of **3-4** in CDCl_3 .

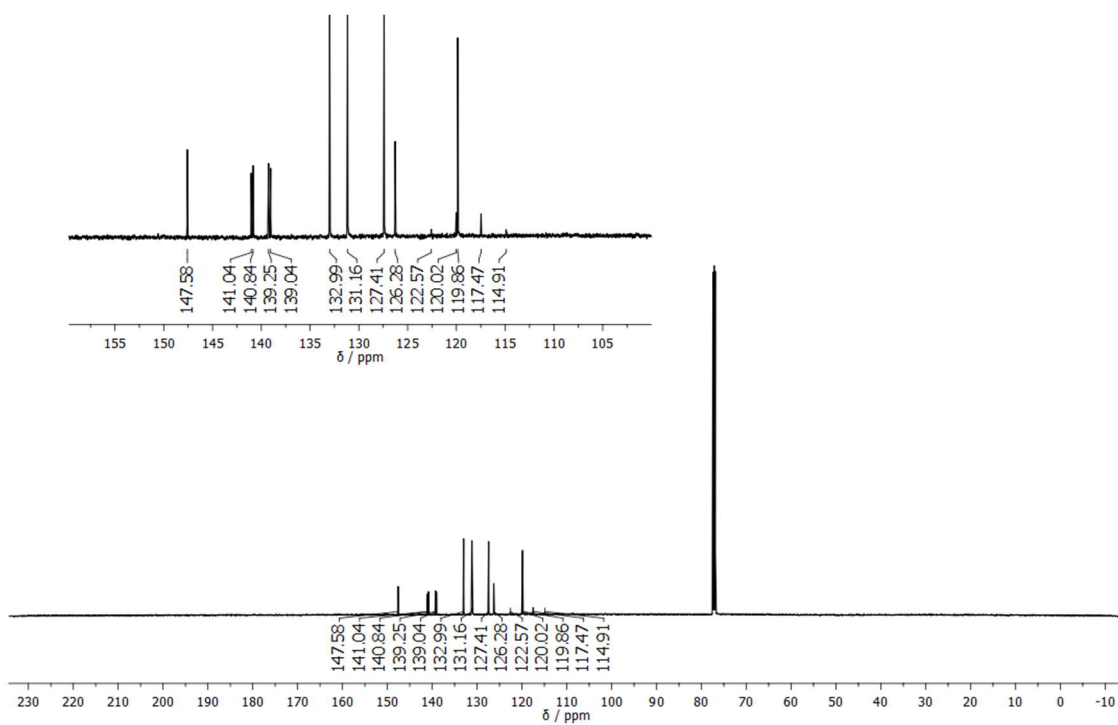
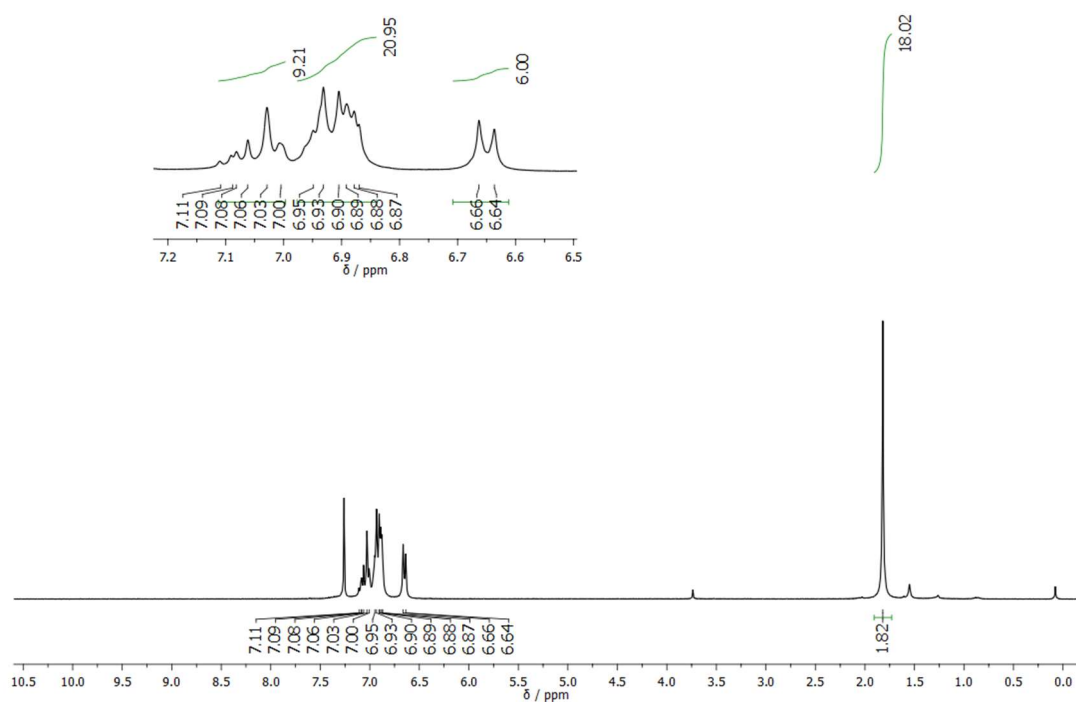
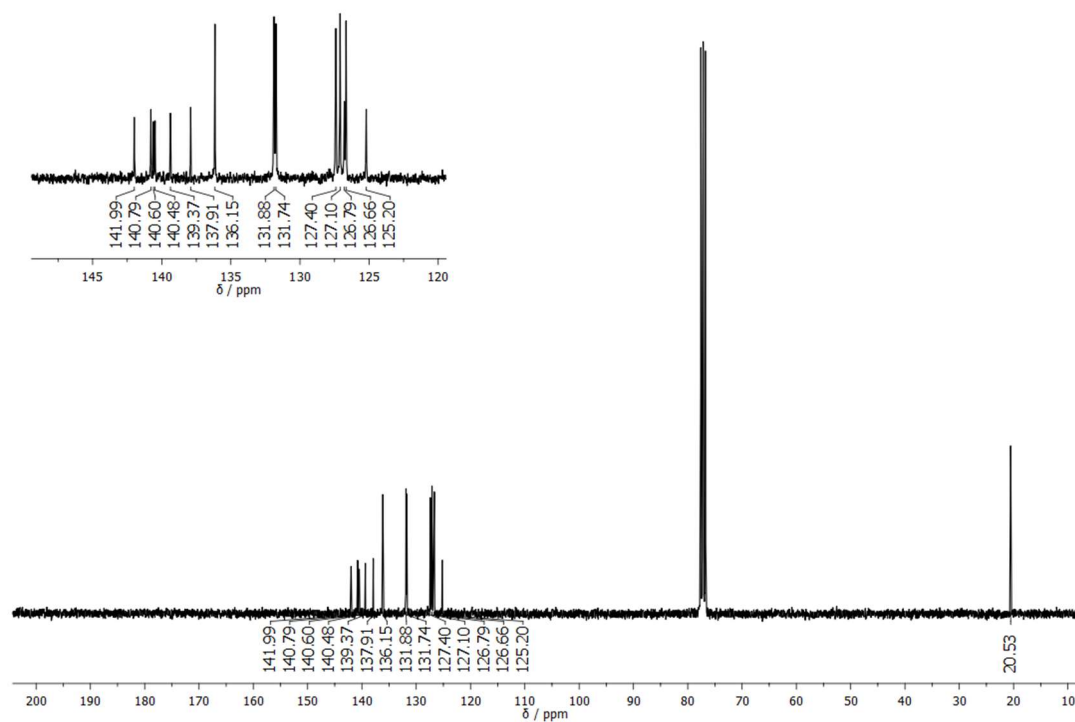


Figure A.73: 126 MHz $^{13}\text{C-NMR}$ of **3-4** in CDCl_3 .

20) 1,3,5-Tri(4-xylylphenyl)-2,4,6-triphenylbenzene (3-5)

Figure A.74: 300 MHz $^1\text{H-NMR}$ of 3-5 in CDCl_3 .Figure A.75: 75 MHz $^{13}\text{C-NMR}$ of 3-5 in CDCl_3 .

Appendix A

21) 2,8,14-Trixylyl-hexabenzocoronene (3-2)

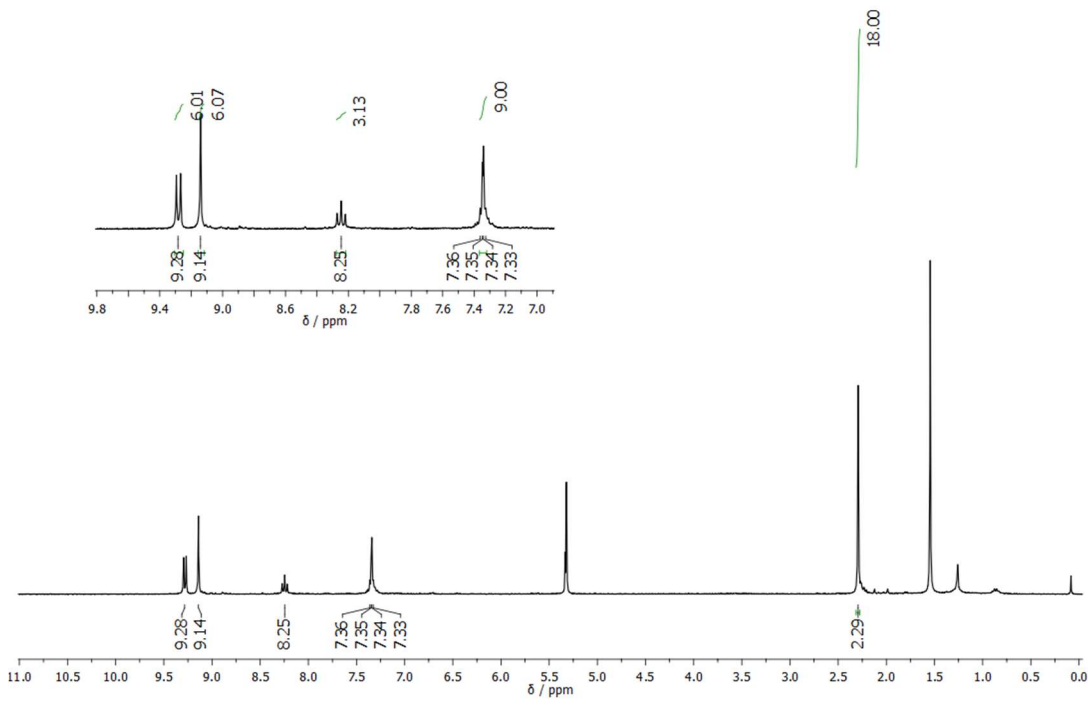


Figure A.76: 300 MHz ¹H-NMR of **3-2** in CD₂Cl₂.

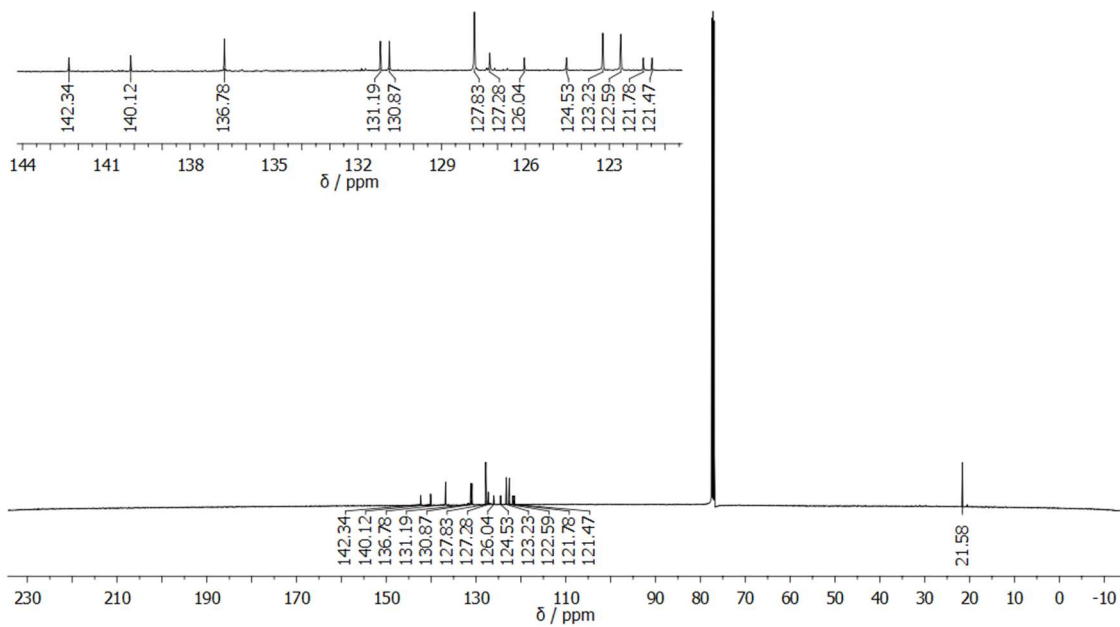


Figure A.77: 126 MHz ¹³C-NMR of **3-2** in CDCl₃.

Appendix A

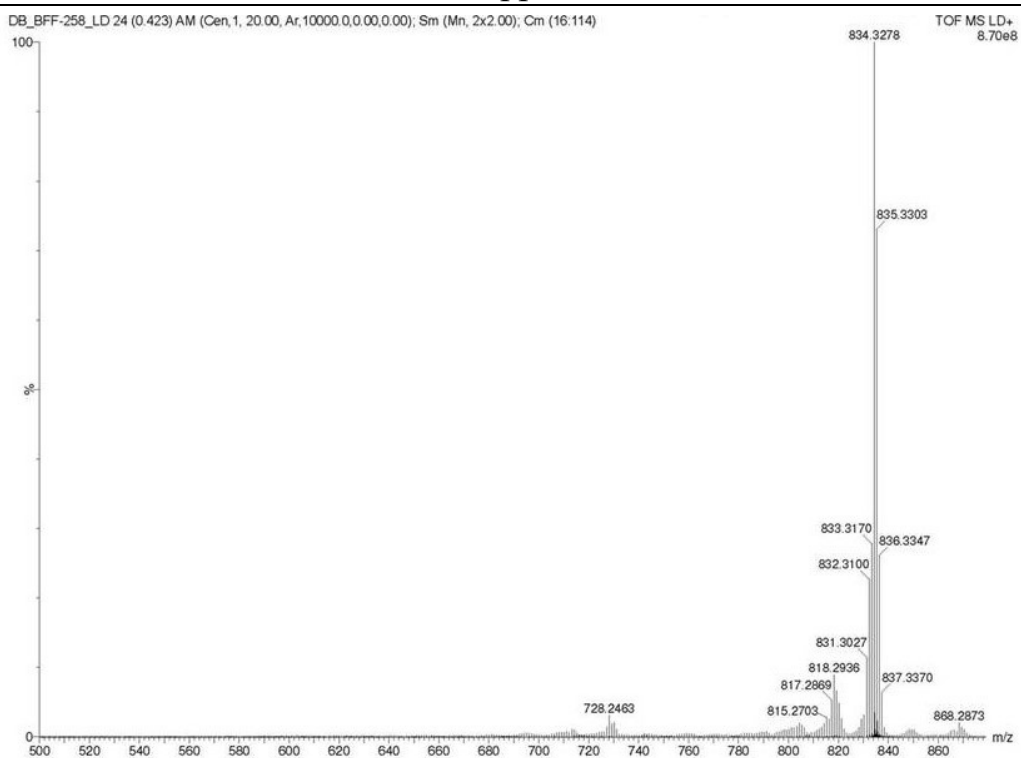


Figure A.78: LD⁺ HR-MS of **3-2**.

Appendix A

22) 5''-Phenyl-[1,1':2'',1'':3'',1''':2''',1''''-quinquephenyl]-3,3''''-diol (3-10)

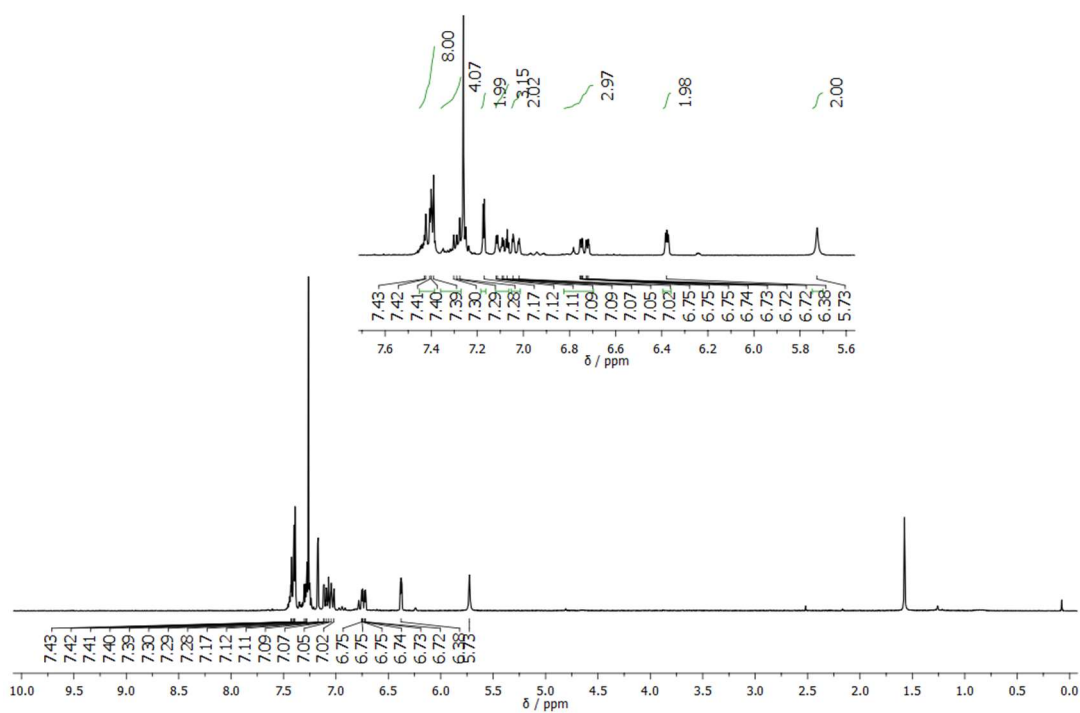


Figure A.79: 300 MHz $^1\text{H-NMR}$ of **3-10** in CDCl_3 .

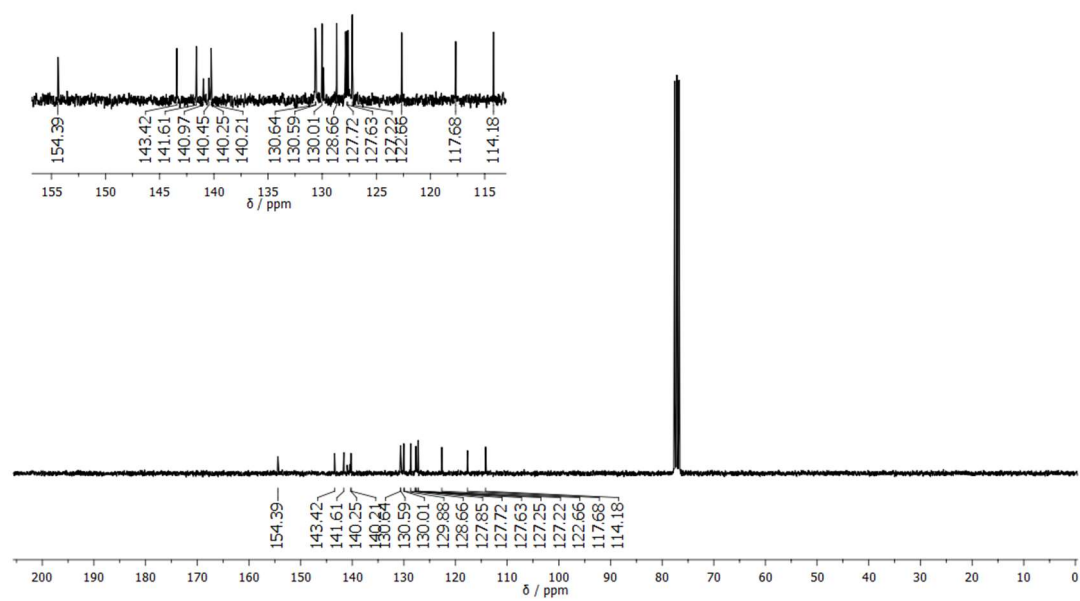


Figure A.80: 75 MHz $^{13}\text{C-NMR}$ of **3-10** in CDCl_3 .

Appendix A

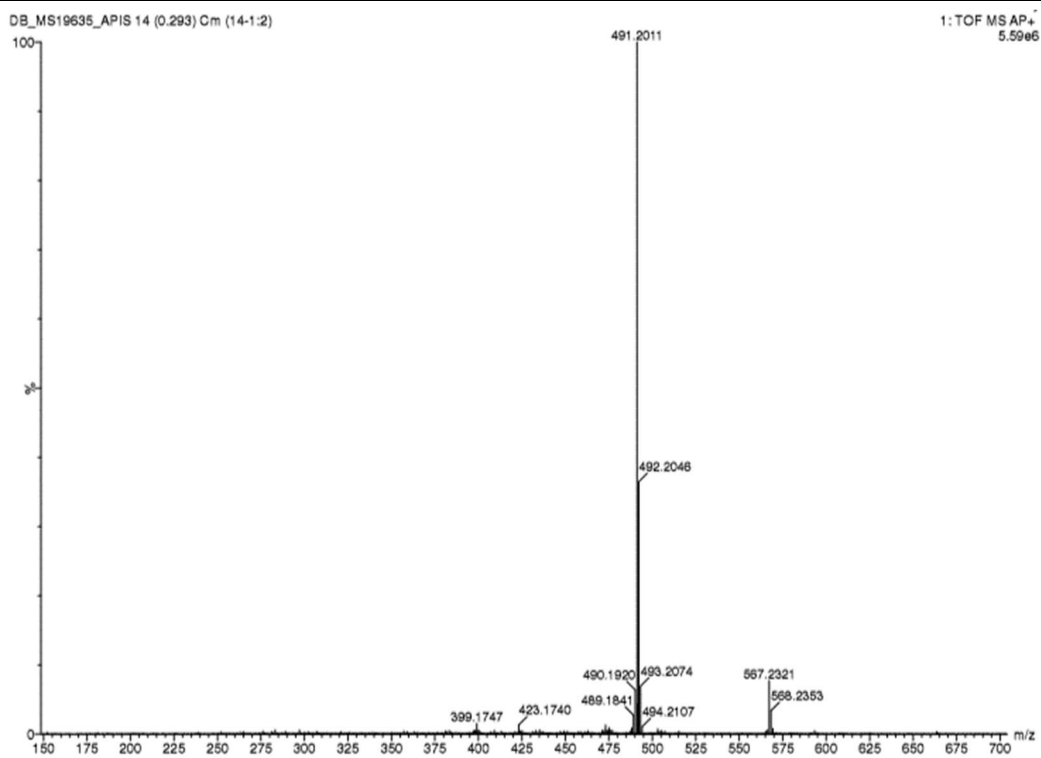


Figure A.81: AP⁺ HR-MS of **3-10**.

Appendix A

23) 5''-Phenyl-[1,1':2',1'':3'',1''':2''',1''''-quinquephenyl]-3,3''''-diyl bis(trifluoromethanesulfonate) (3-11)

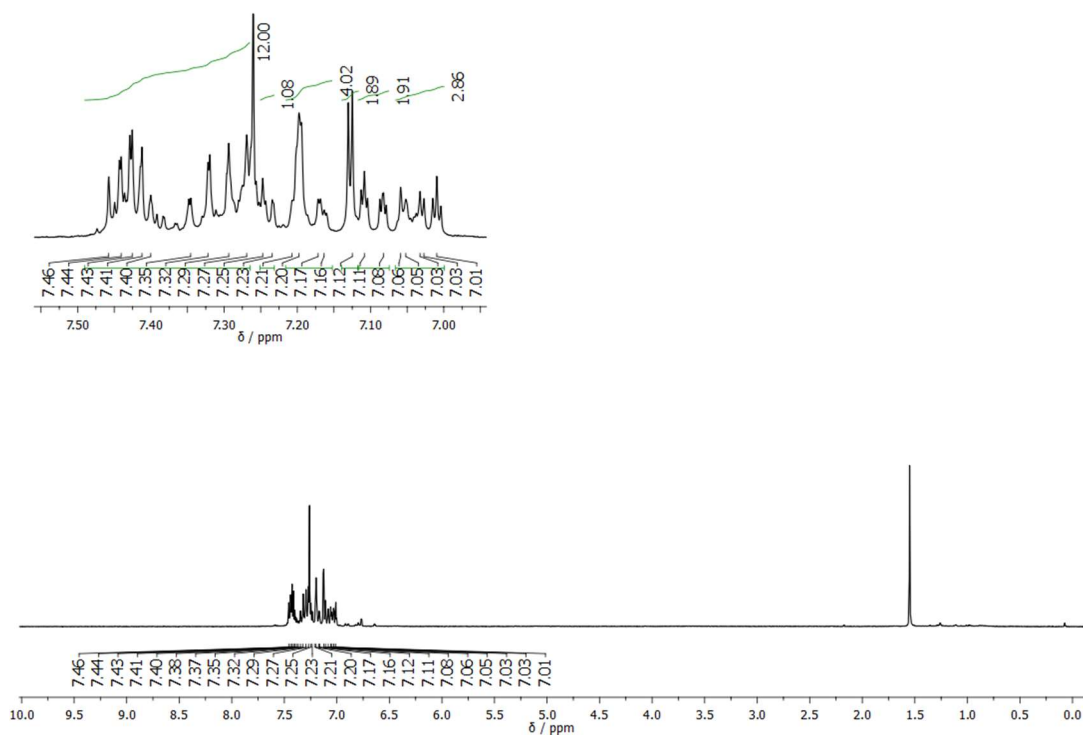


Figure A.82: 300 MHz $^1\text{H-NMR}$ of 3-11 in CDCl_3 .

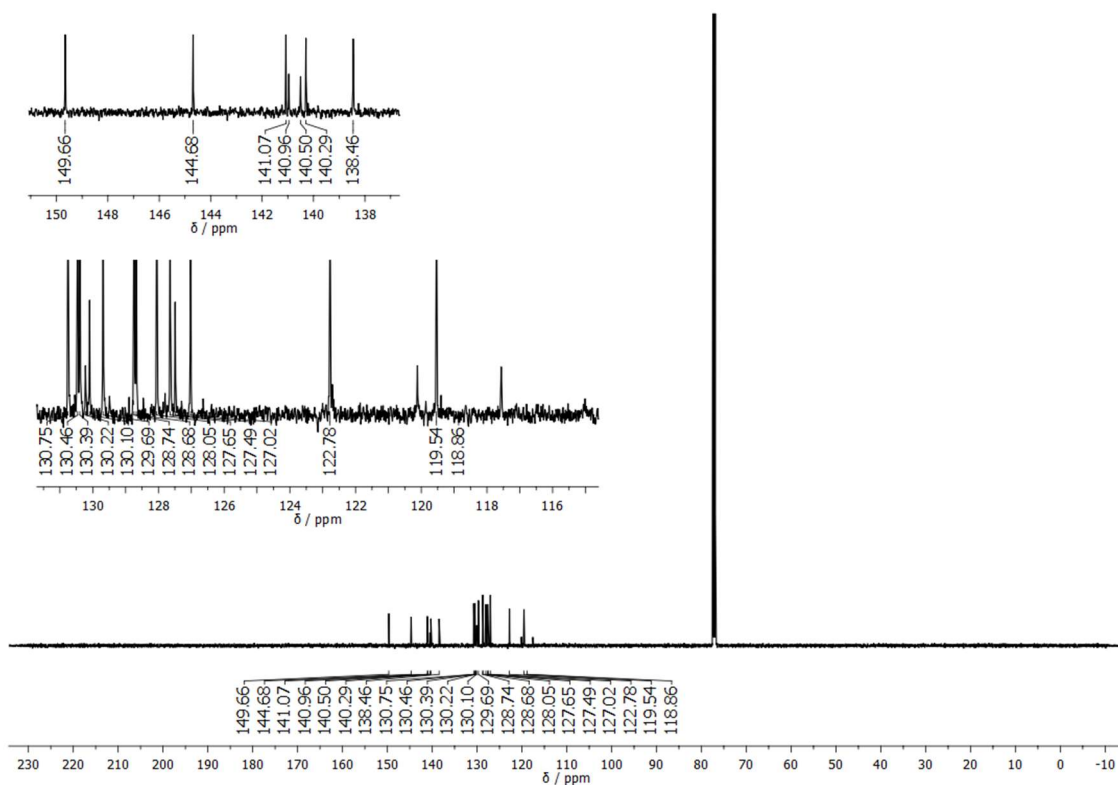


Figure A.83: 126 MHz $^{13}\text{C-NMR}$ of 3-11 in CDCl_3 .

Appendix A

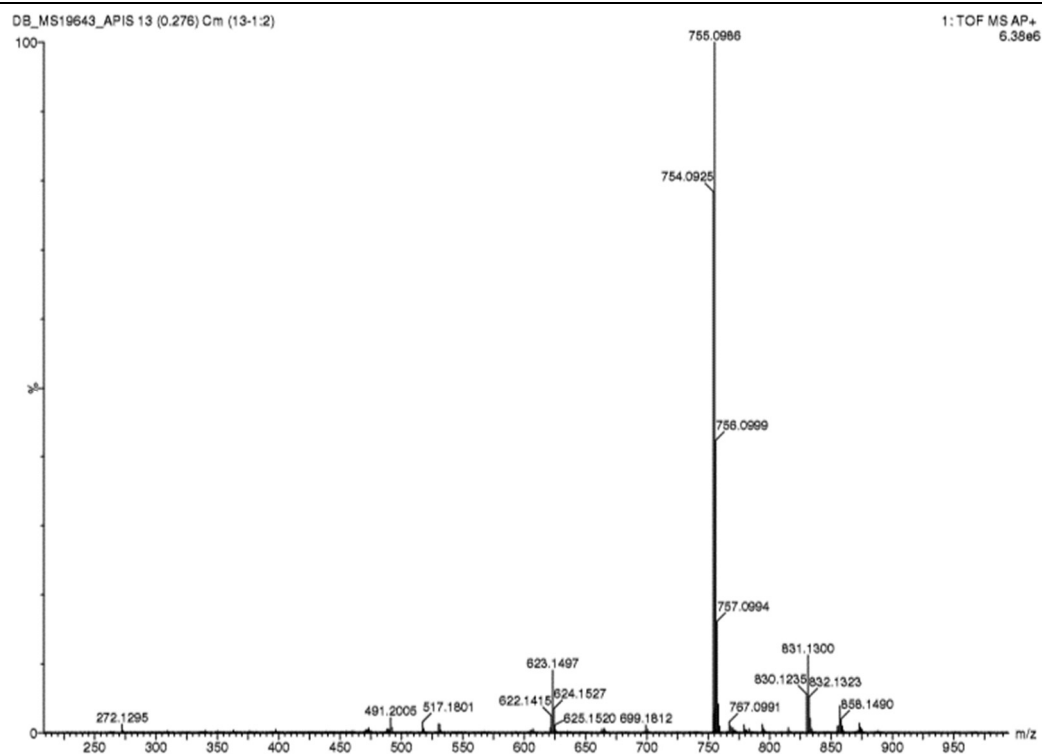


Figure A.84: AP⁺ HR-MS of 3-11.

Appendix A

24) 5''-Phenyl-[1,1':2'',1'':3'',1''':2''',1''''-quinquephenyl]-3,3''''-Xylen (3-12)

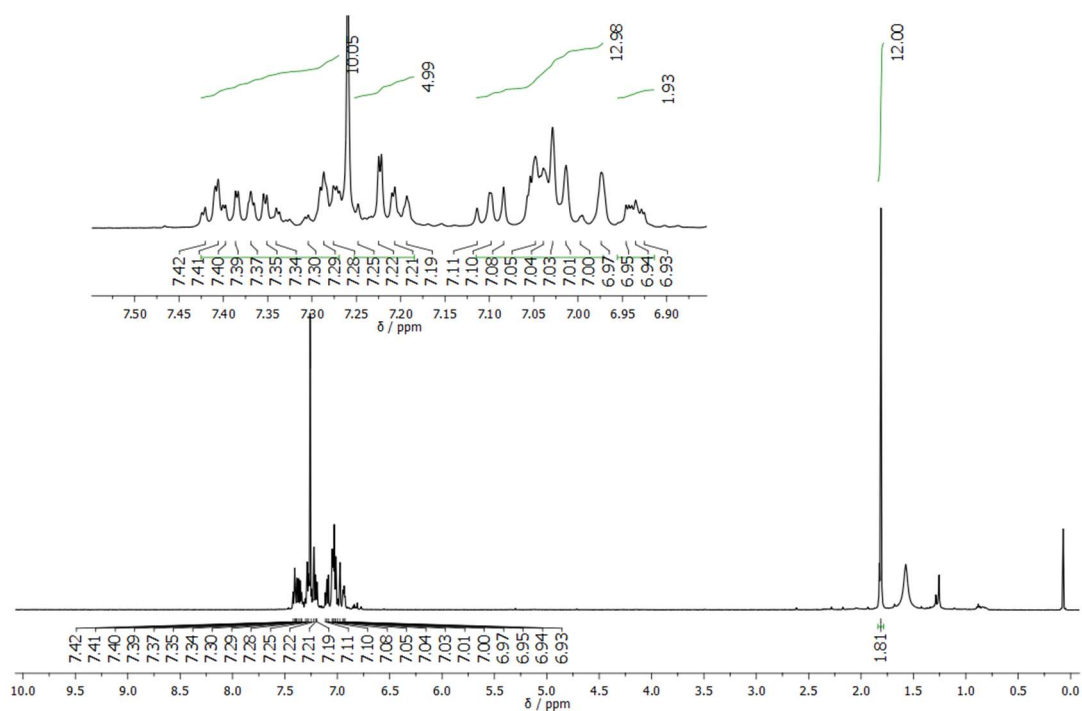


Figure A.85: 500 MHz $^1\text{H-NMR}$ of **3-12** in CDCl_3 .

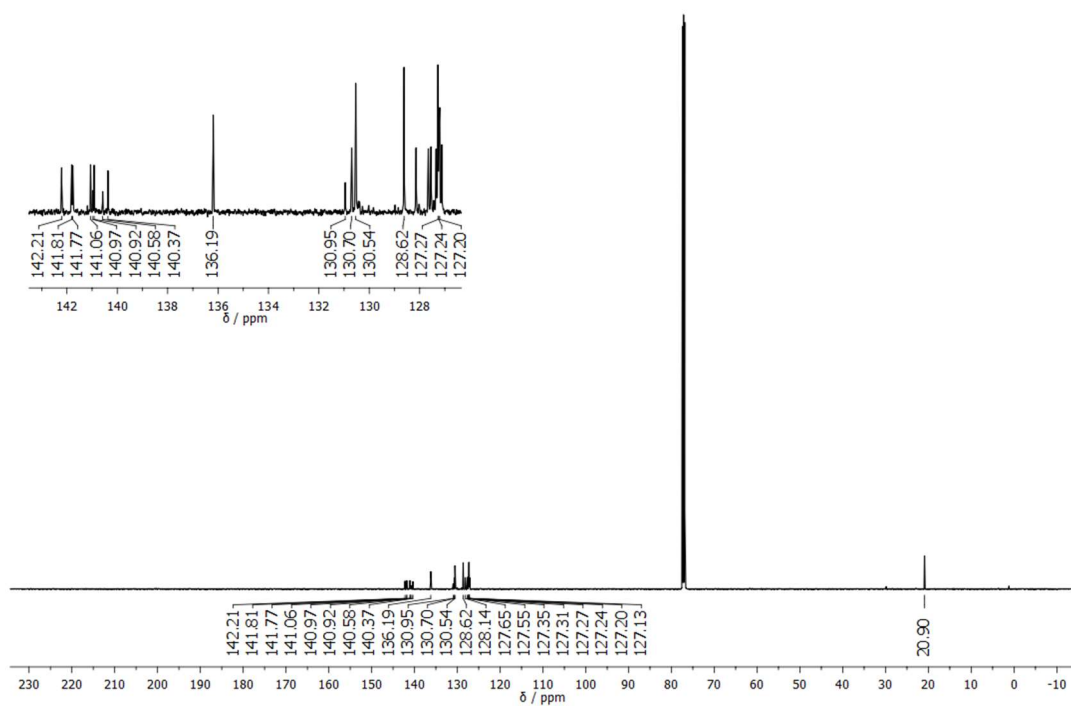


Figure A.86: 126 MHz $^{13}\text{C-NMR}$ of **3-12** in CDCl_3 .

Appendix A

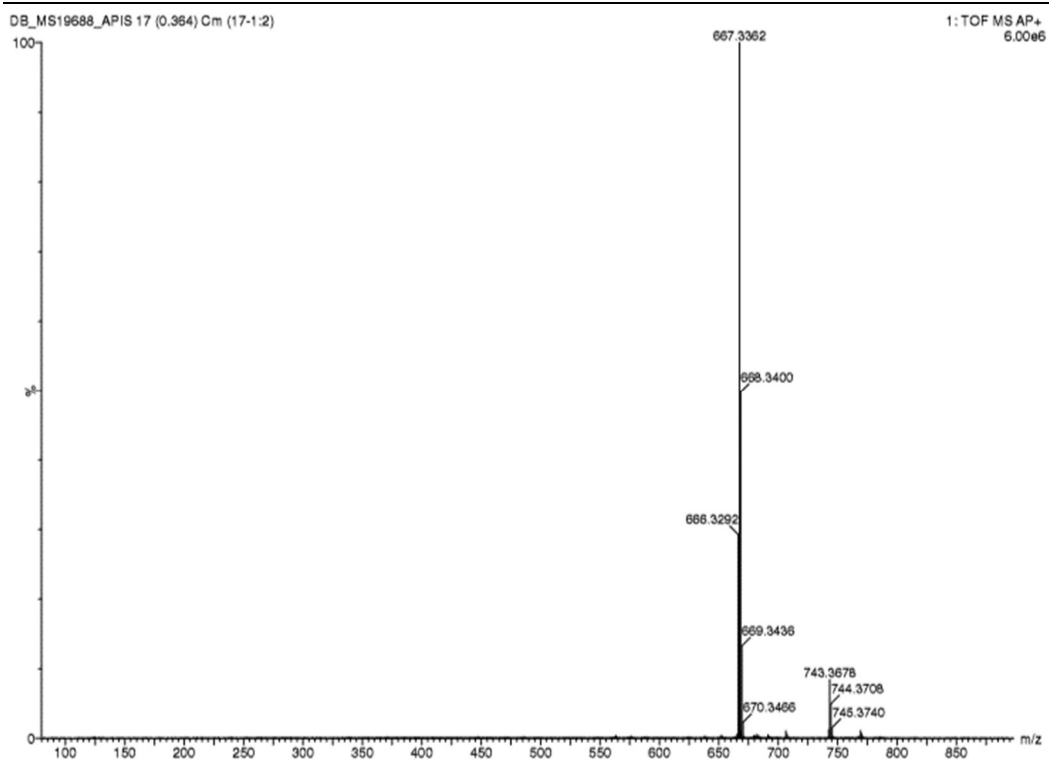


Figure A.87: AP⁺ HR-MS of **3-12**.

Appendix A

25) 6,12-Bis(2,6-dimethylphenyl)dibenzo[fg,ij]phenanthro[9,10,1,2,3-pqrst]pentaphene (3-13)

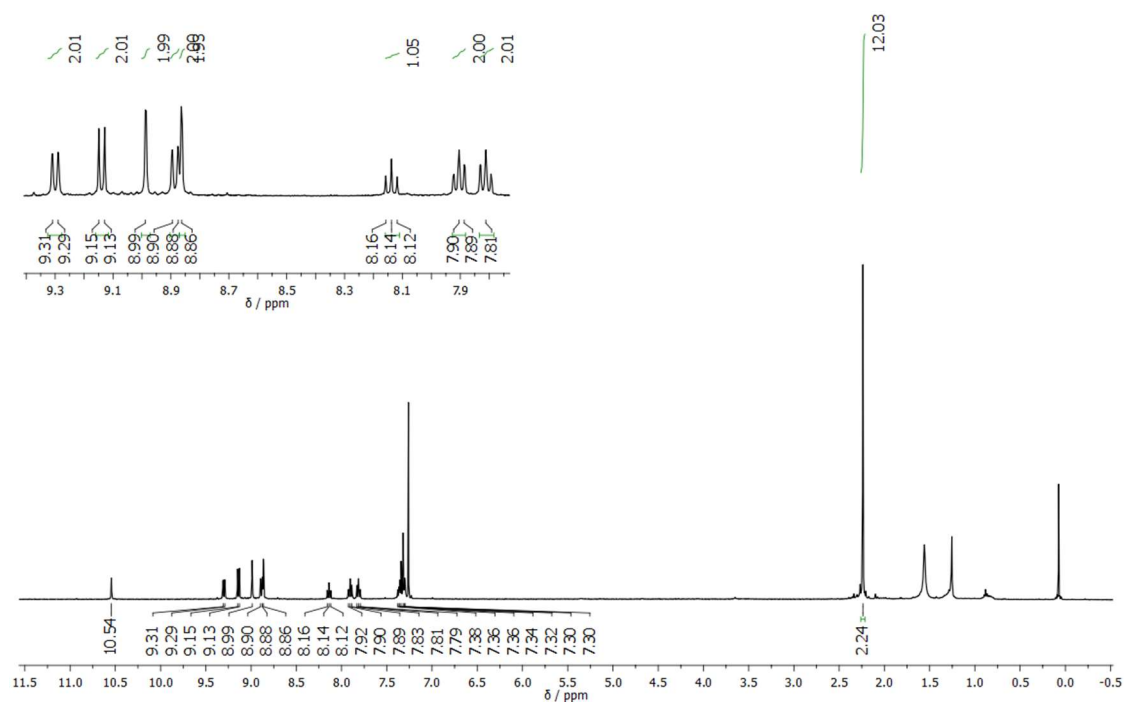


Figure A.88: 400 MHz $^1\text{H-NMR}$ of **3-13** in CDCl_3 .

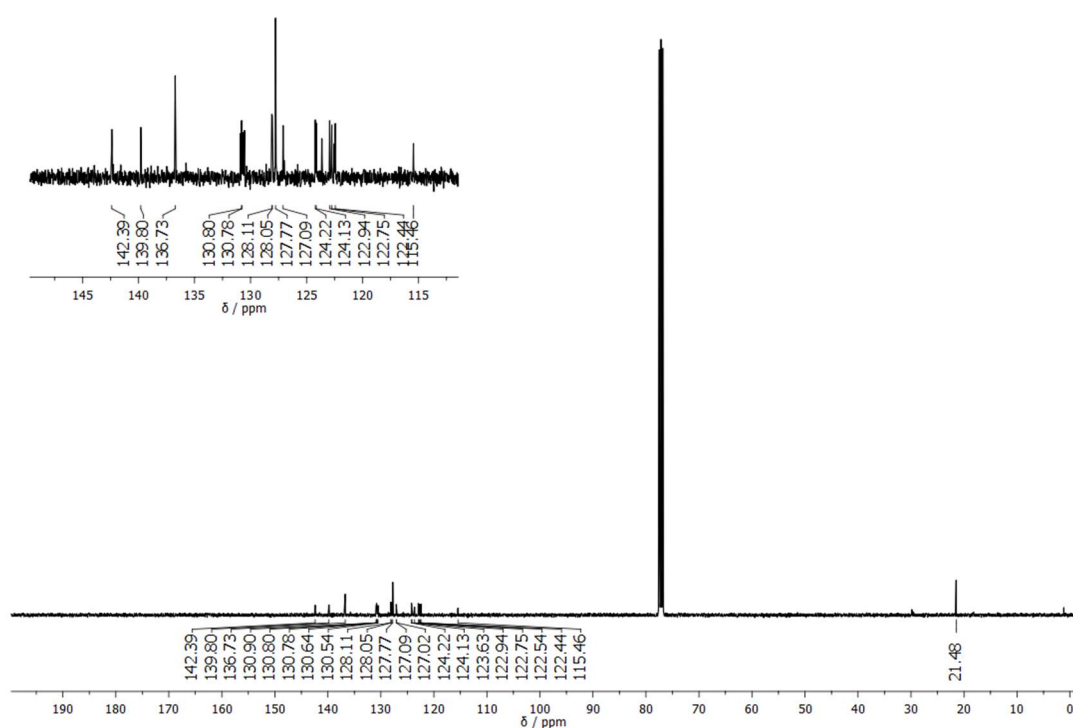


Figure A.89: 100 MHz $^{13}\text{C-NMR}$ of **3-13** in CDCl_3 .

Appendix A

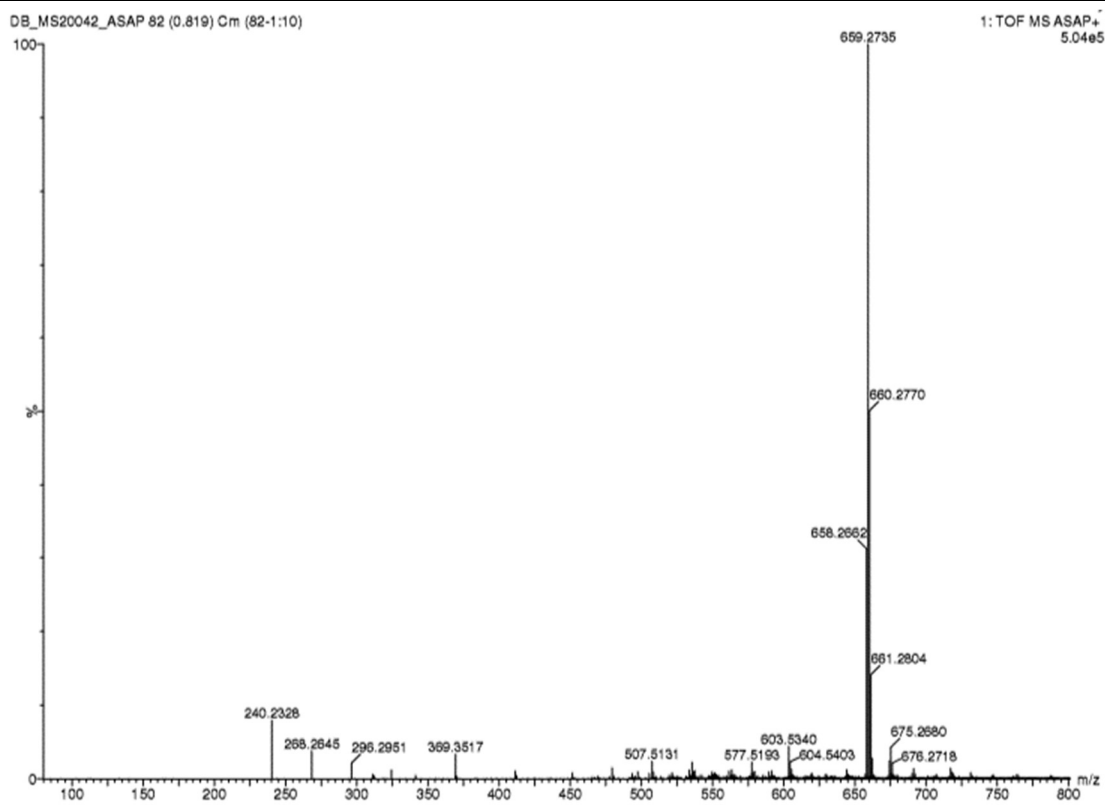


Figure A.90: ASAP⁺ HR-MS of 3-13.

Appendix A

26) 3'-Bromo-2,4,6-trimethyl-1,1'-biphenyl (3-19)

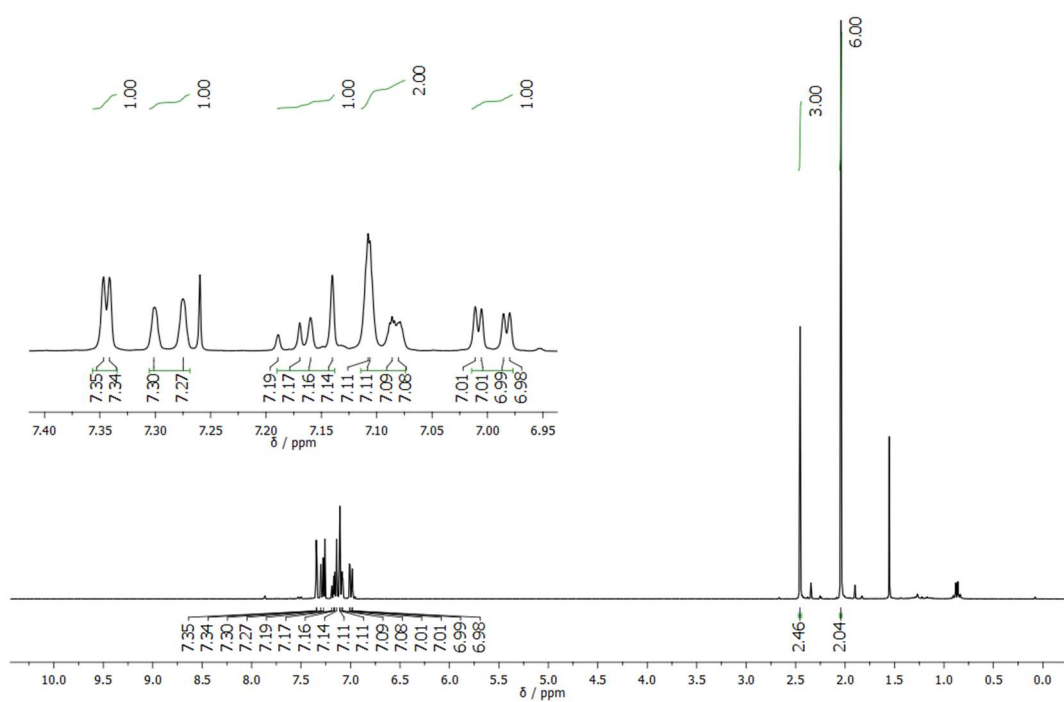


Figure A.91: 300 MHz ¹H-NMR of **3-19** in CDCl₃.

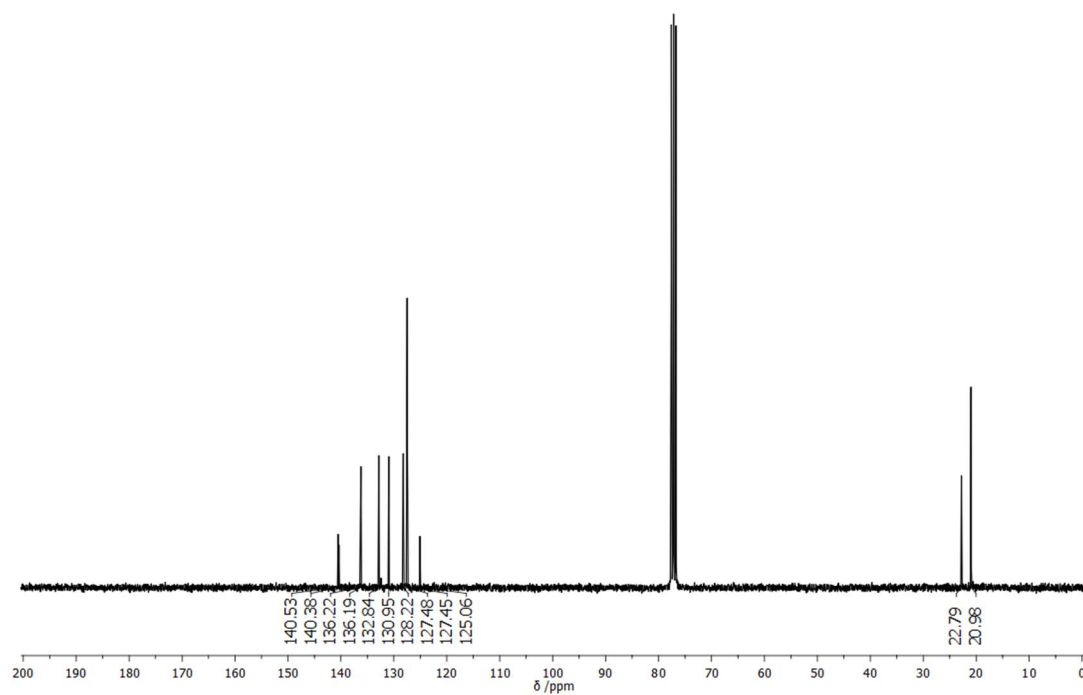
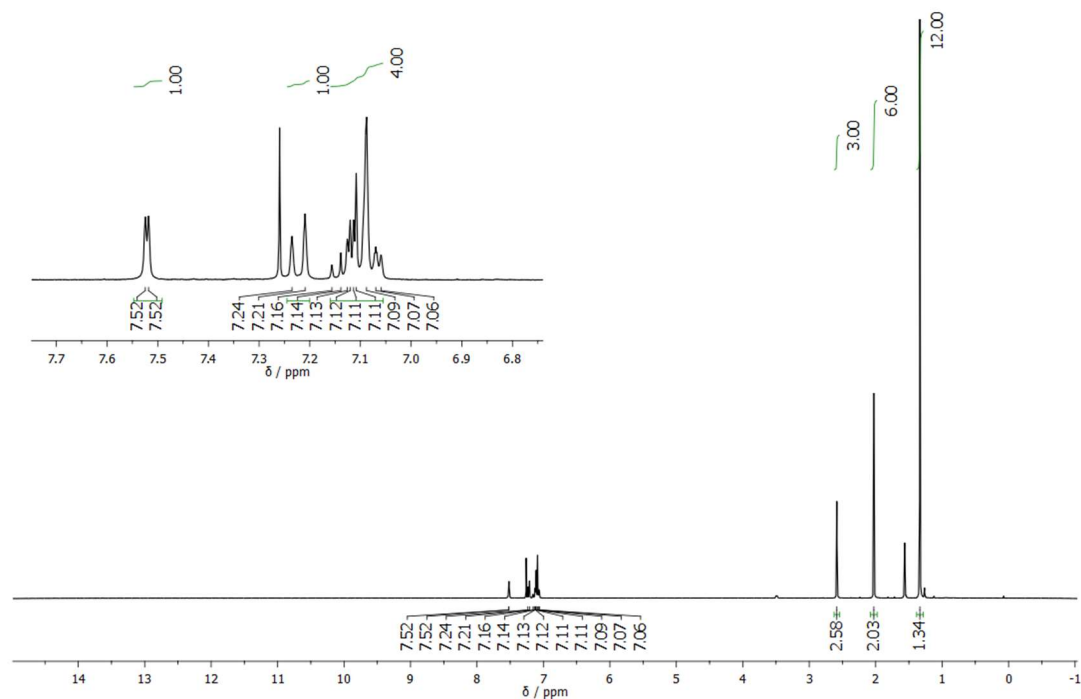
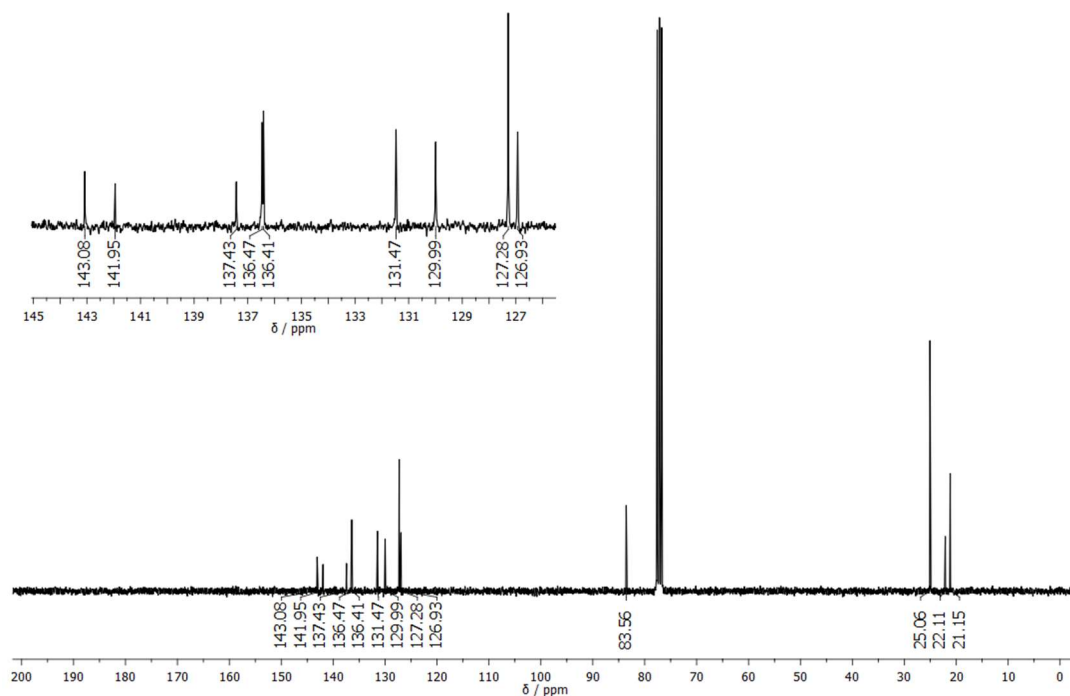


Figure A.92: 75 MHz ¹³C-NMR of **3-19** in CDCl₃.

27) 4,4,5,5-Tetramethyl-2-(2',4,6'-trimethyl-[1,1'-biphenyl]-3-yl)-1,3,2-dioxaborolane (3-20)**Figure A.93:** 300 MHz $^1\text{H-NMR}$ of 3-20 in CDCl_3 .**Figure A.94:** 75 MHz $^{13}\text{C-NMR}$ of 3-20 in CDCl_3 .

Appendix A

28) N,N-Diethyl-2'',6',6''-trimethyl-[1,1':3',1''-terphenyl]-2-carboxamide (3-22)

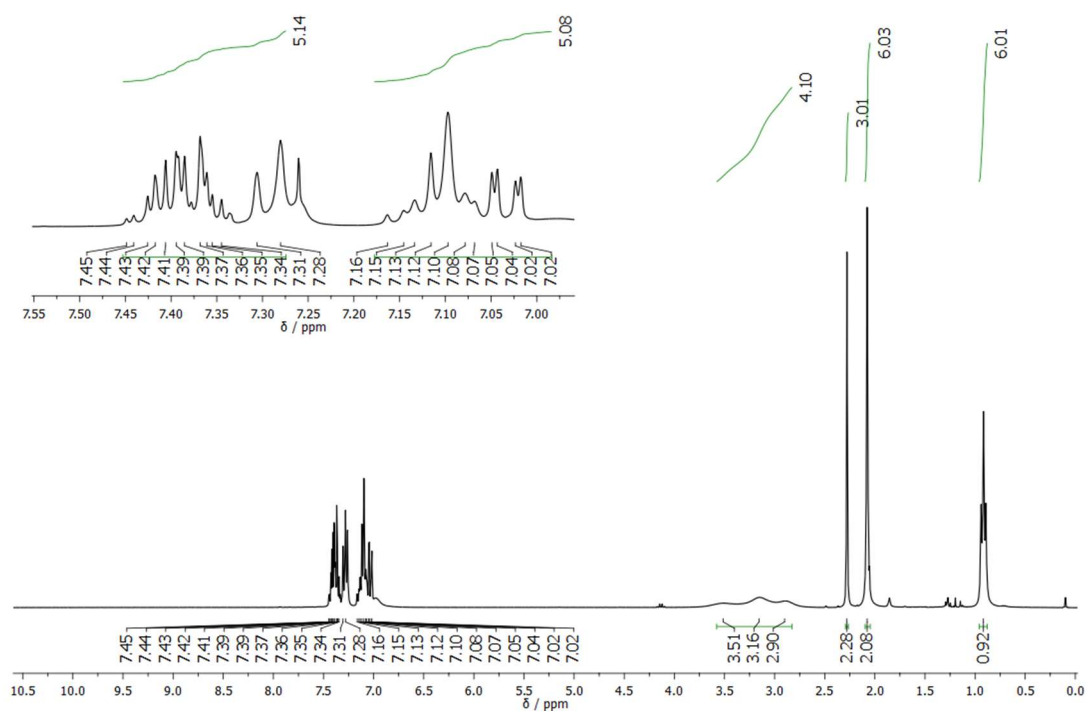


Figure A.95: 300 MHz ¹H-NMR of **3-22** in CDCl₃.

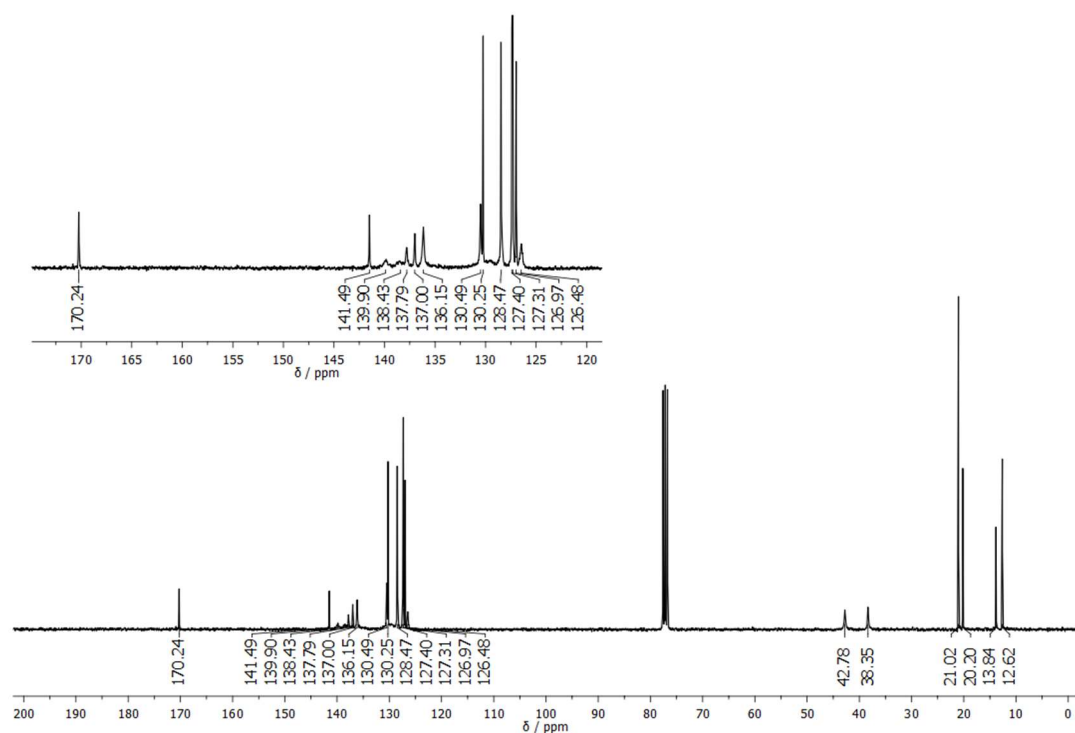
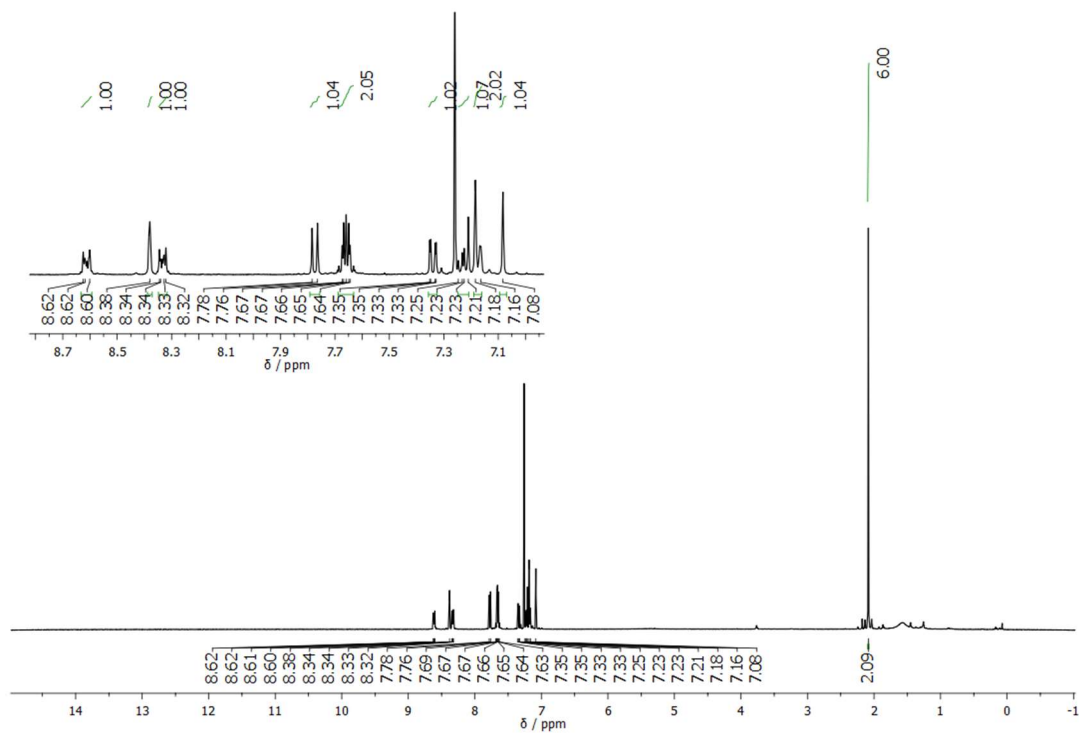
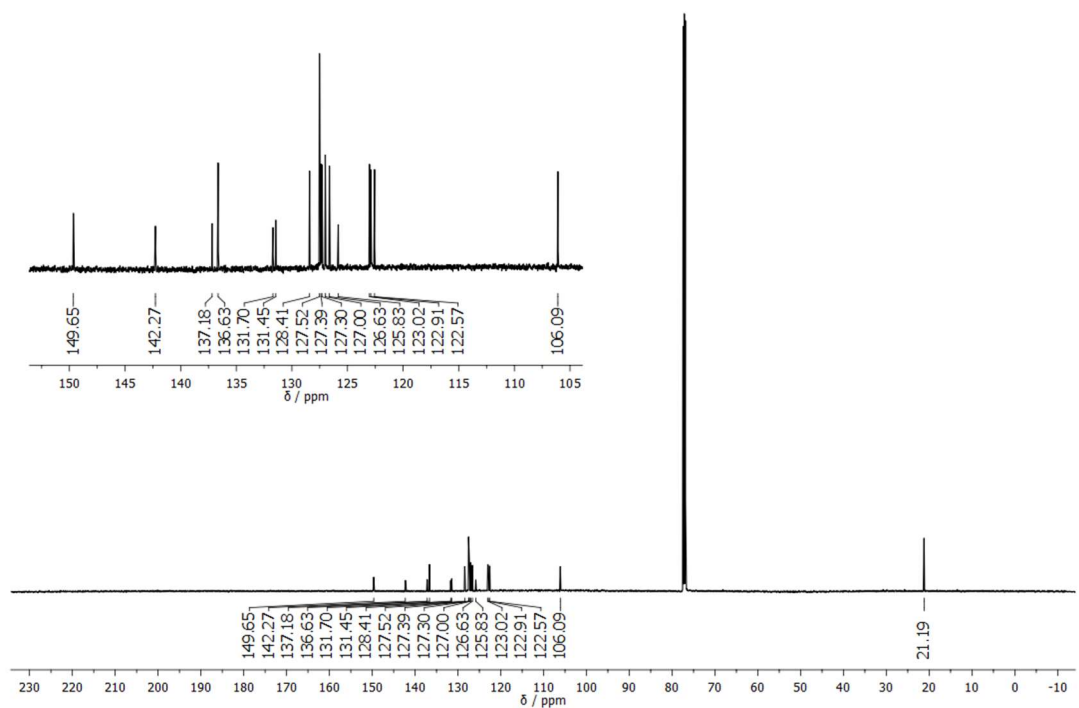


Figure A.96: 75 MHz ¹³C-NMR of **3-22** in CDCl₃.

29) 3-(2,6-Dimethylphenyl)phenanthren-9-ol (3-23)

Figure A.97: 400 MHz ^1H -NMR of **3-23** in CDCl_3 .Figure A.98: 126 MHz ^{13}C -NMR of **3-23** in CDCl_3 .

Appendix A

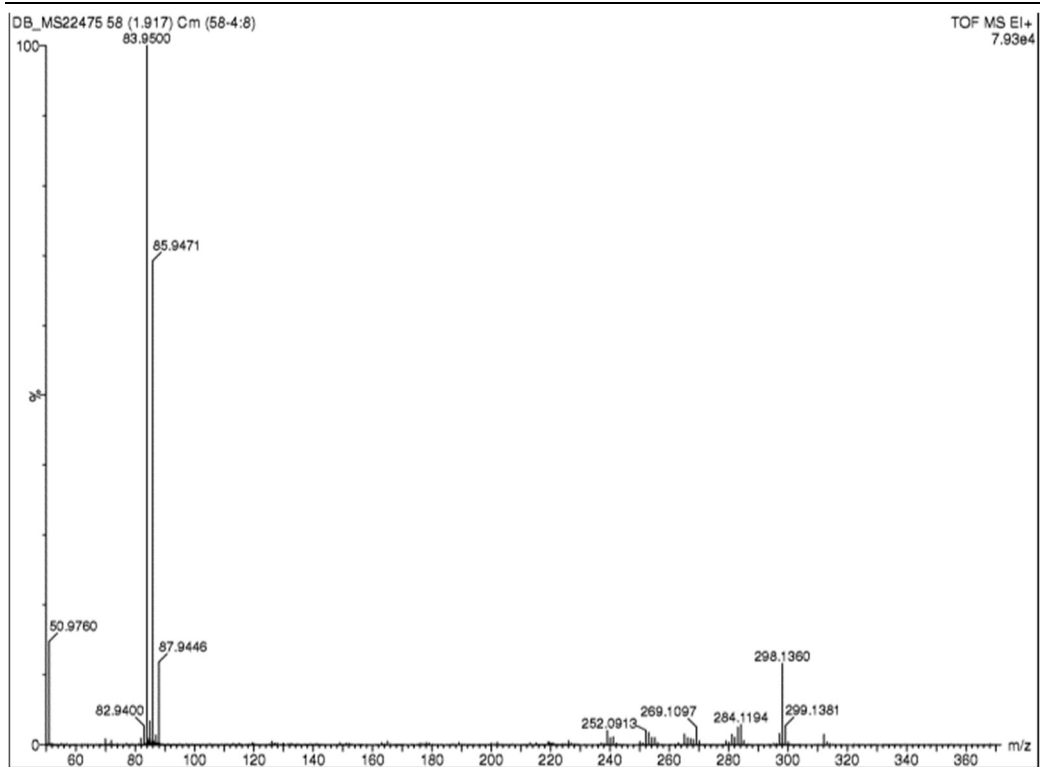
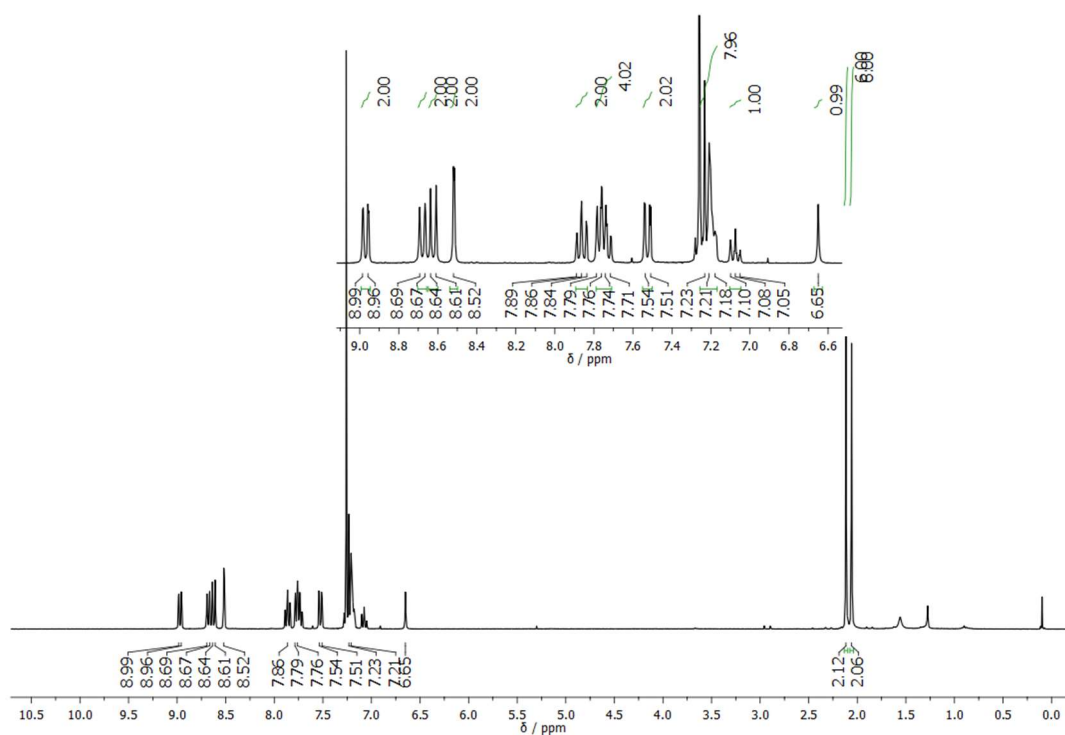
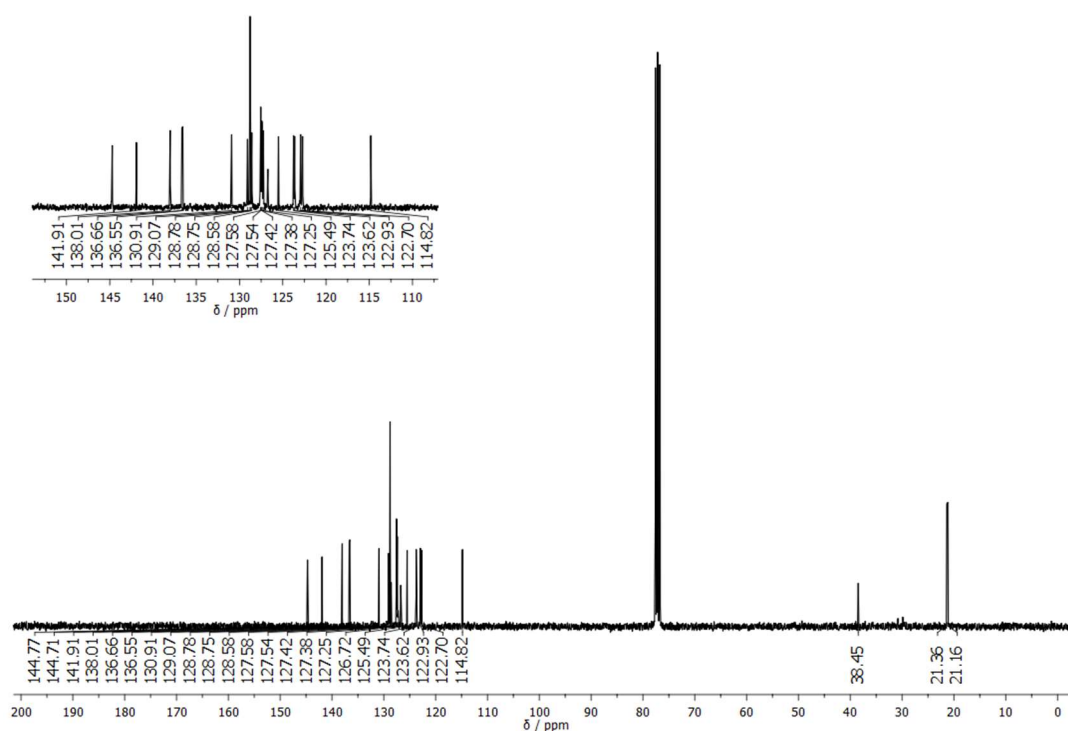


Figure A.99: EI⁺ HR-MS of 3-23.

30) 3,15-Bis(2,6-dimethylphenyl)-18-phenyl-18H-tetrabenzo[a,c,h,j]xanthenes (3-24)**Figure A.100:** 300 MHz $^1\text{H-NMR}$ of 3-24 in CDCl_3 .**Figure A.101:** 75 MHz $^{13}\text{C-NMR}$ of 3-24 in CDCl_3 .

Appendix A

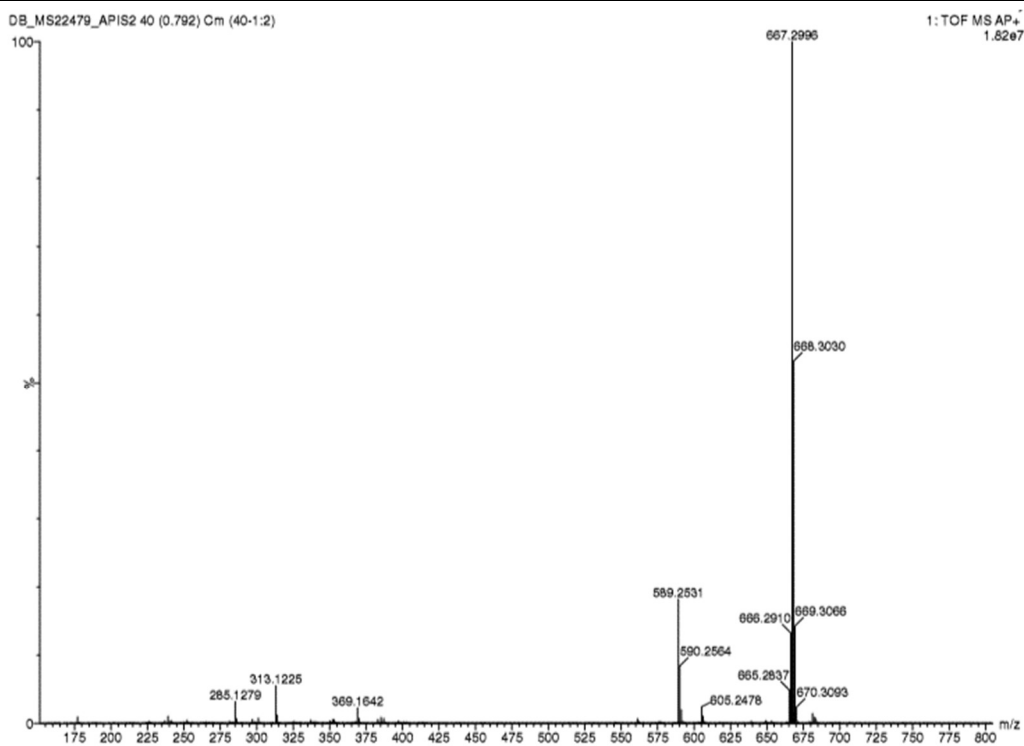
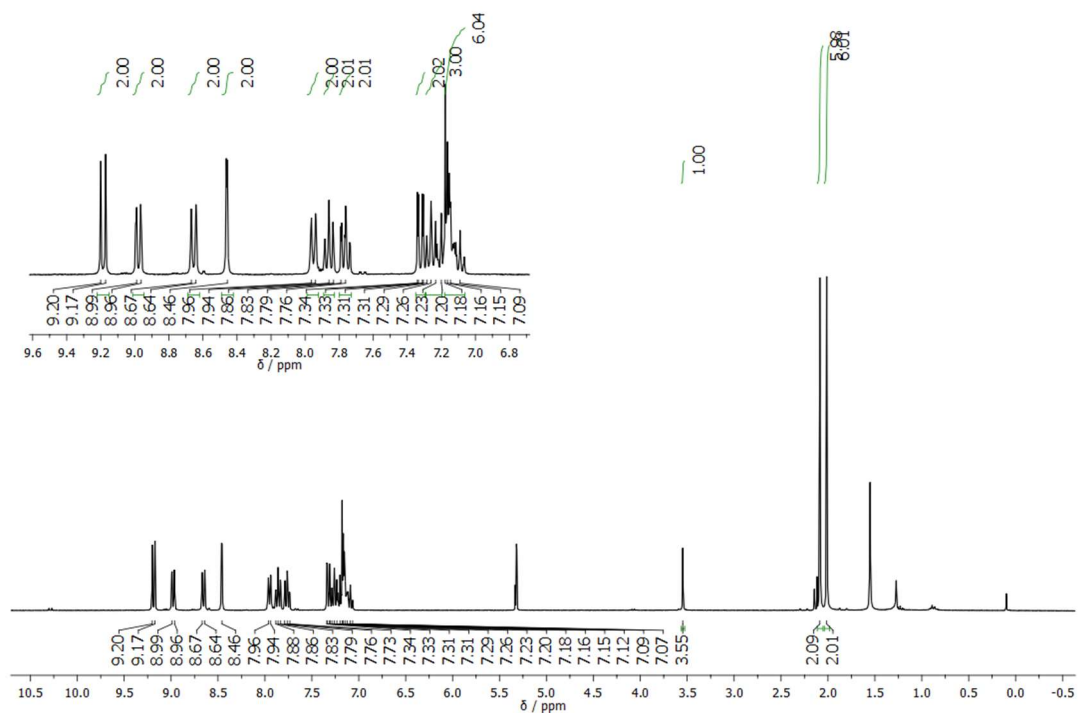
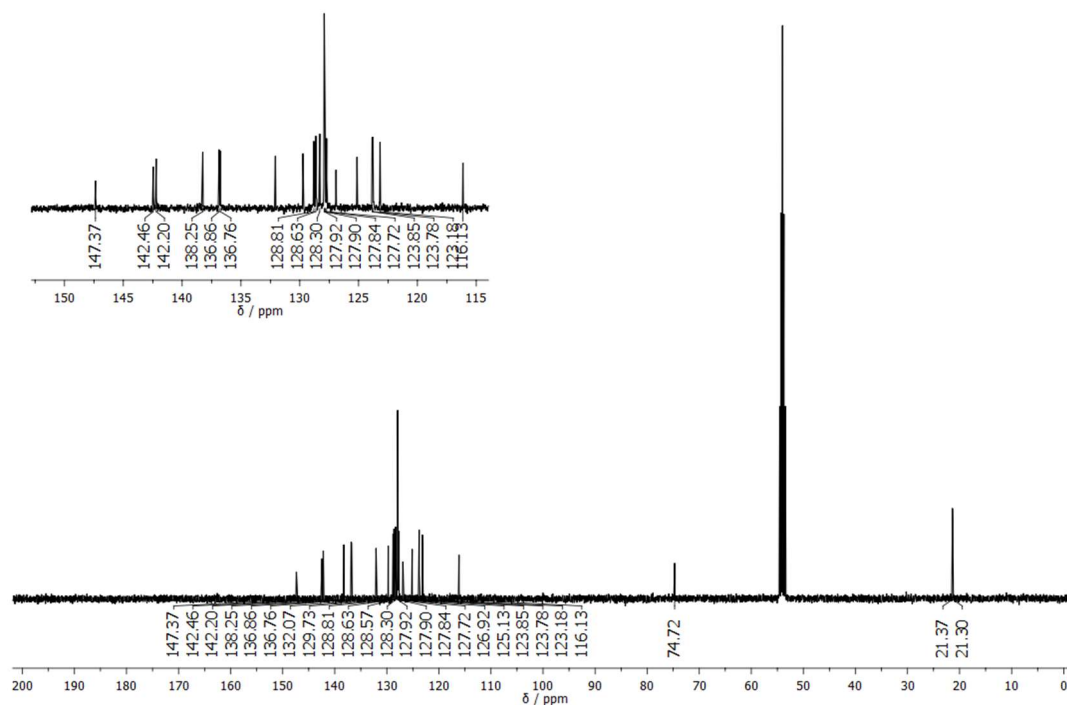


Figure A.102: AP⁺ HR-MS of 3-24.

31) 3,15-Bis(2,6-dimethylphenyl)-18-phenyl-18H-tetrabenzo[a,c,h,j]xanthen-18-ol (3-25)**Figure A.103:** 300 MHz $^1\text{H-NMR}$ of **3-25** in CD_2Cl_2 .**Figure A.104:** 100 MHz $^{13}\text{C-NMR}$ of **3-25** in CD_2Cl_2 .

Appendix A

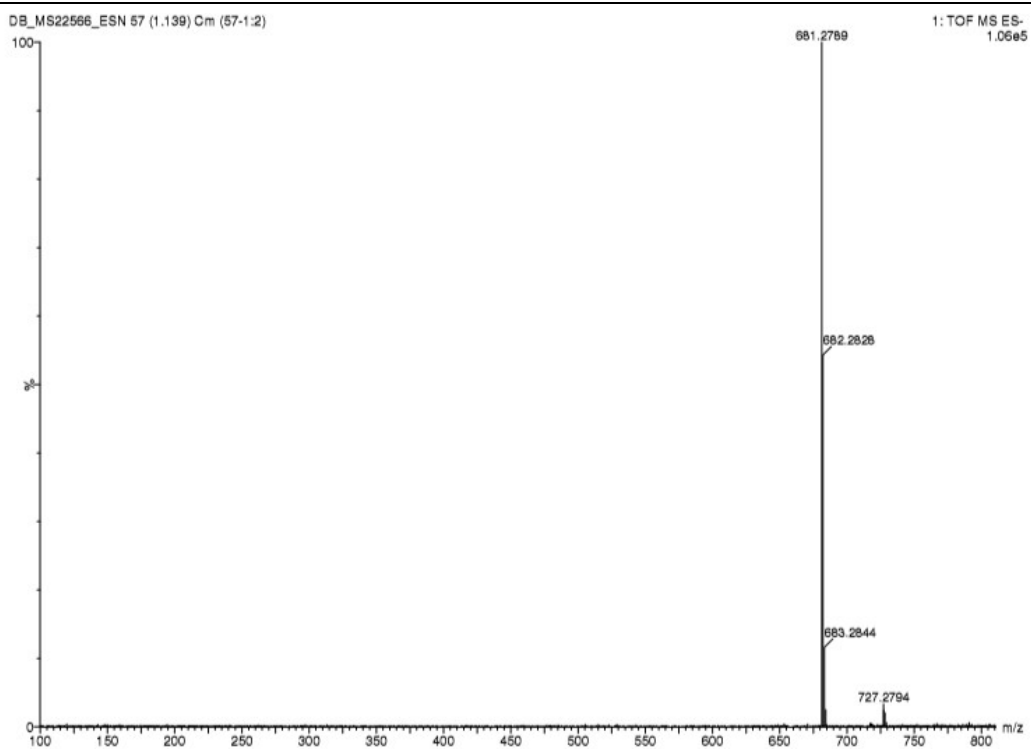
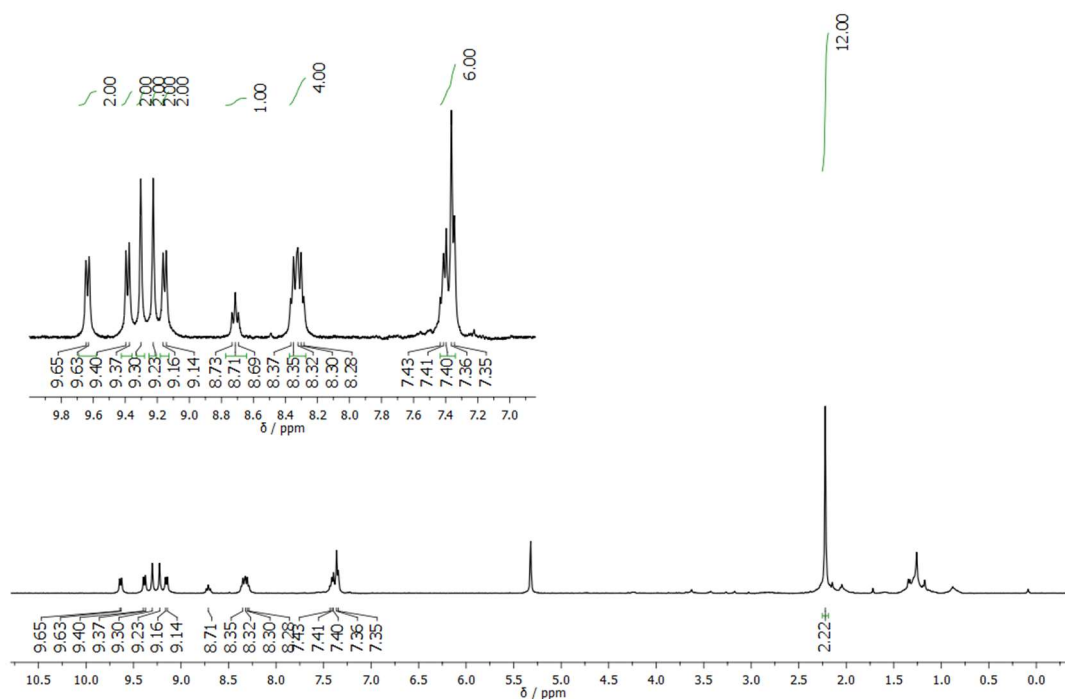
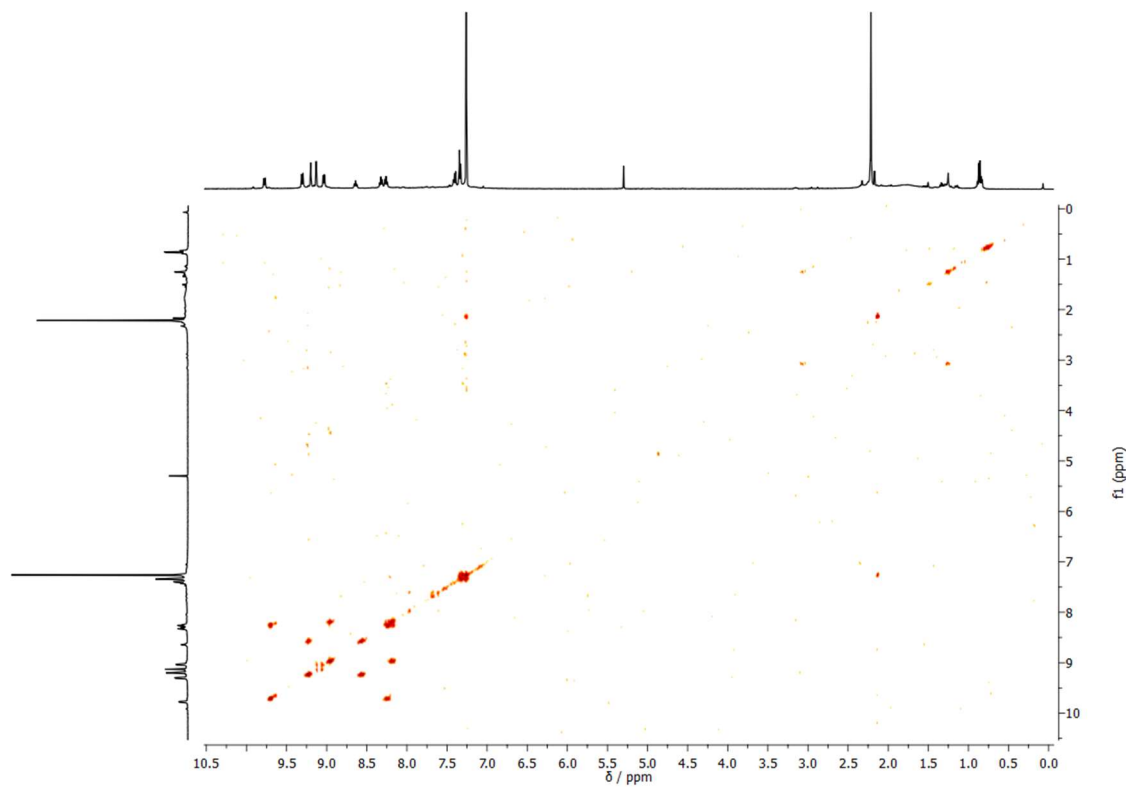


Figure A.105: ES- HR-MS of **3-25**.

32) 6,12-Bis(2,6-dimethylphenyl)dibenzo[*c,h*]benzo[5,6]tetraceno[1,12,11,10-*jklmna*]xanthen-18-ium tetrafluoro borate (3-27^{BF})**Figure A.106:** 400 MHz ¹H-NMR of **3-27^{BF}** in CD₂Cl₂.**Figure A.107:** 500 MHz ¹H-¹H COSY NMR of **3-27^{BF}** in CDCl₃.

Appendix A

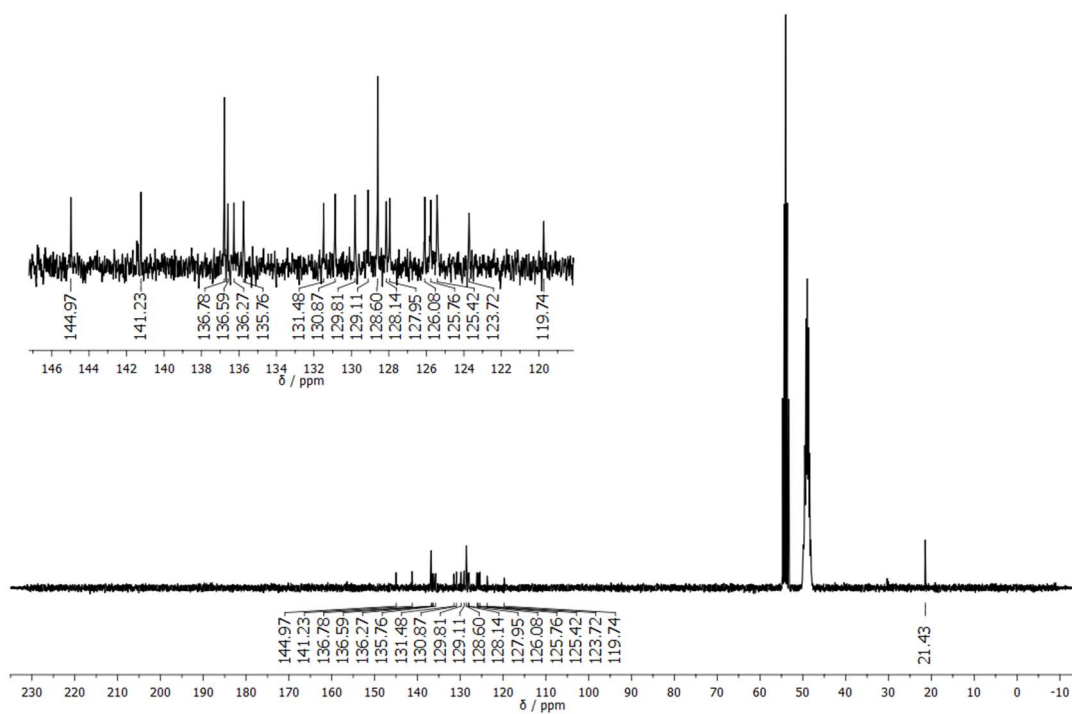


Figure A.108: 75 MHz ^{13}C -NMR of **3-27^{BF}** in $\text{CD}_2\text{Cl}_2/\text{MeOD}$ 1/1.

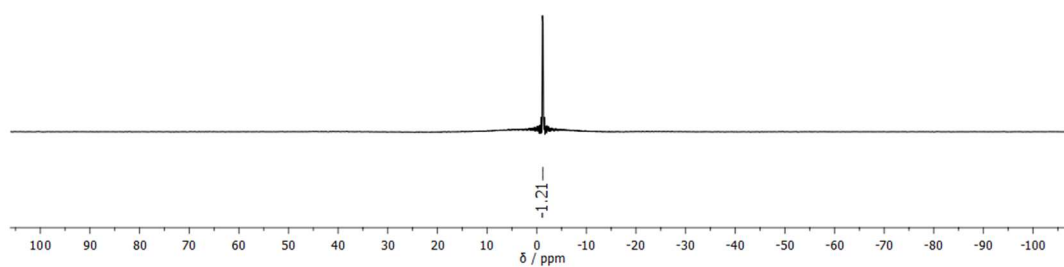


Figure A.109: 160 MHz ^{11}B -NMR of **3-27^{BF}** in CD_2Cl_2 .

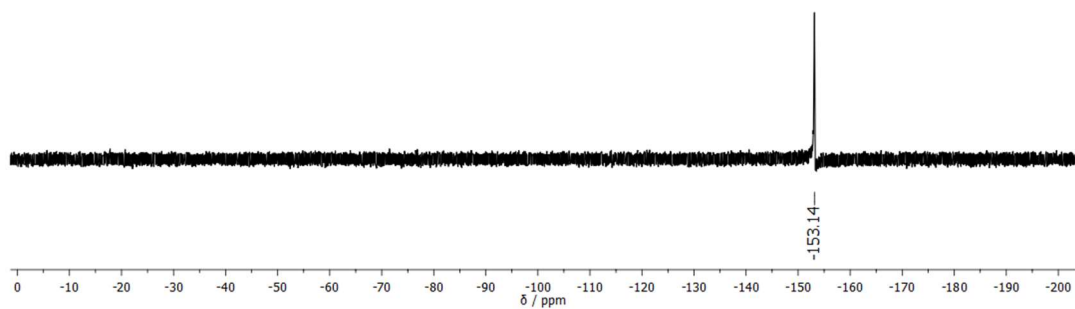


Figure A.110: 376 MHz ^{19}F -NMR of **3-27^{BF}** in CD_2Cl_2 .

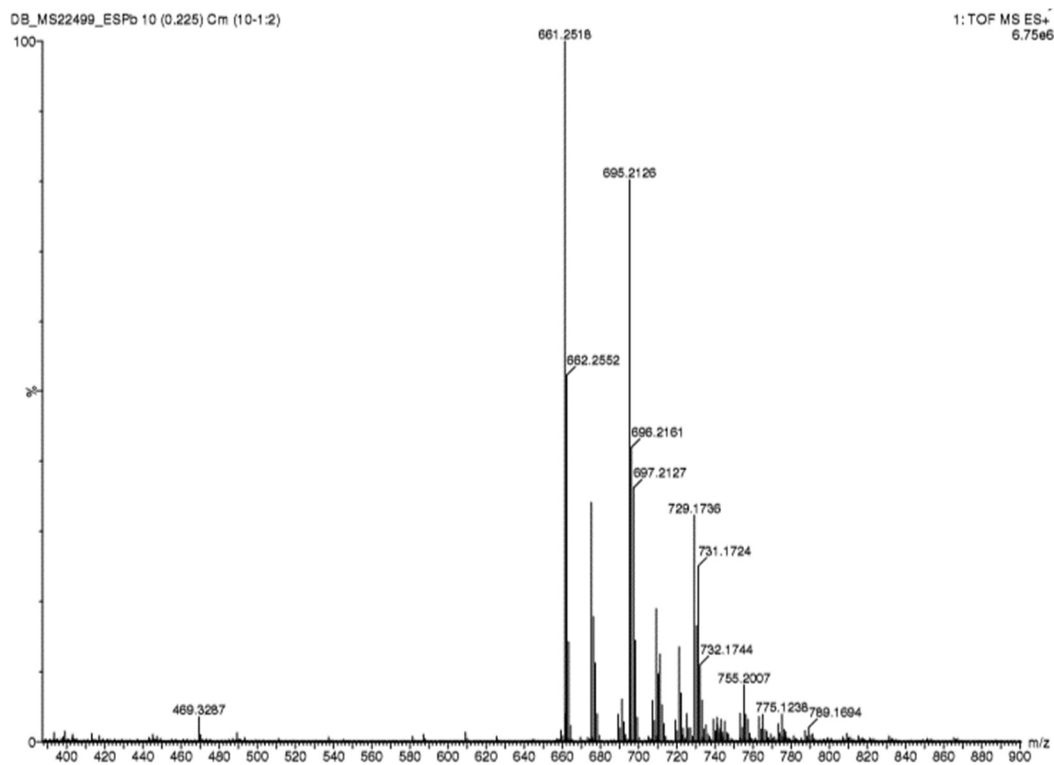
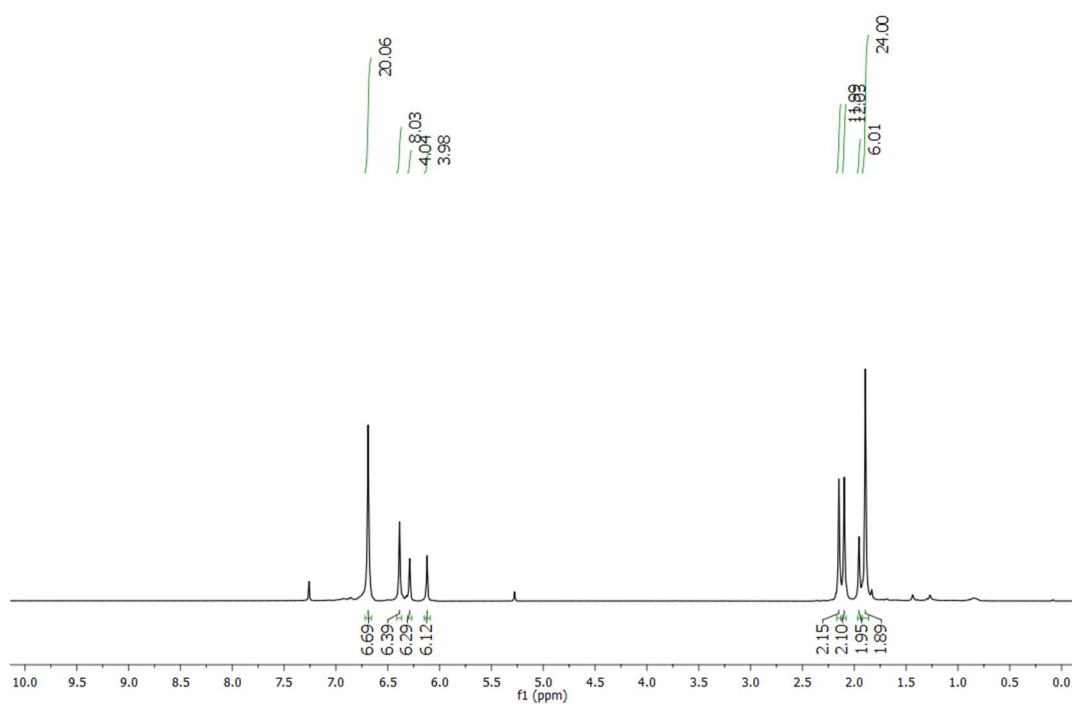
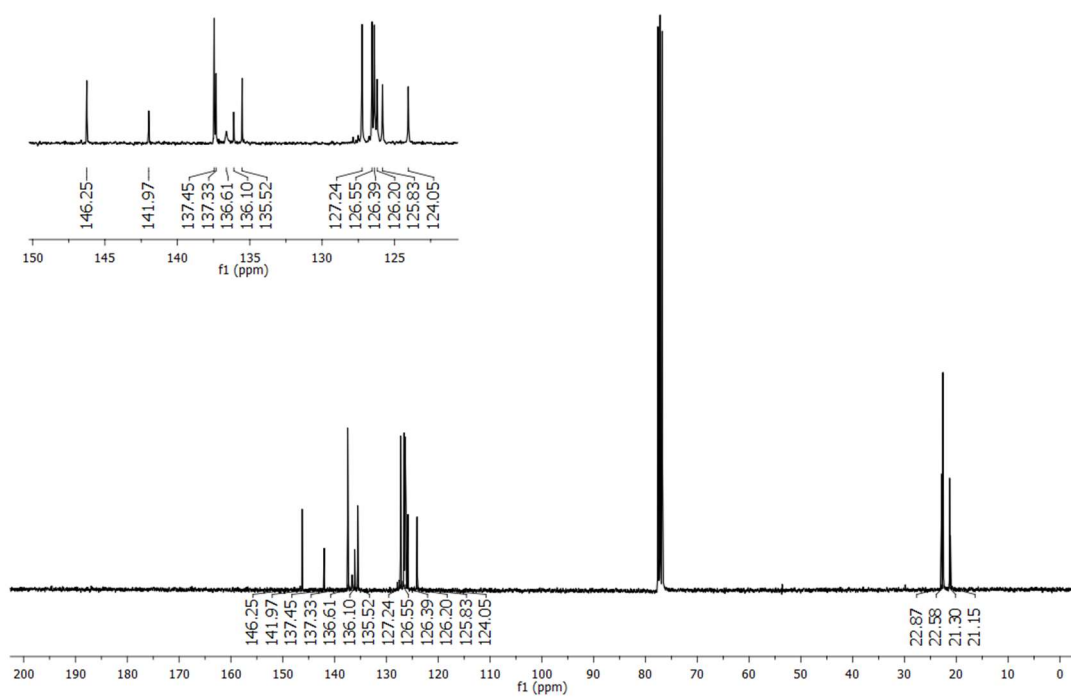


Figure A.111: ES⁺ HR-MS of **3-27^{BF}**.

Chapter 4

33) Characterization of 4-3

Figure A.112: 300 MHz ^1H -NMR of 4-3 in CDCl_3 .Figure A.113: 75 MHz ^{13}C -NMR of 4-3 in CDCl_3 .

Appendix A

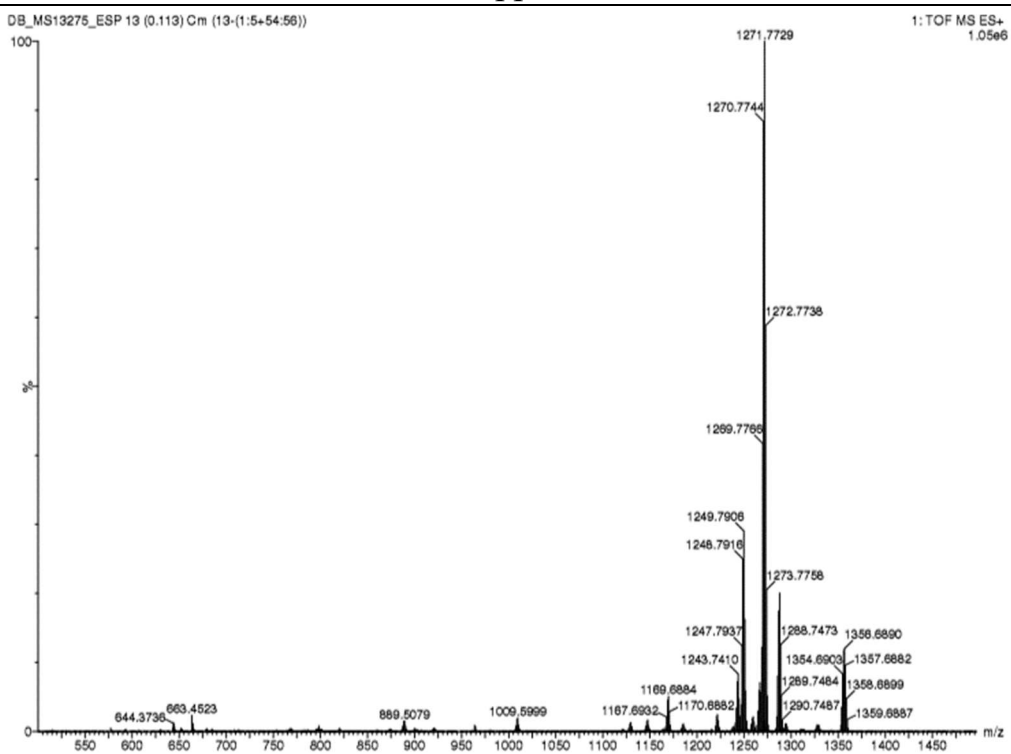
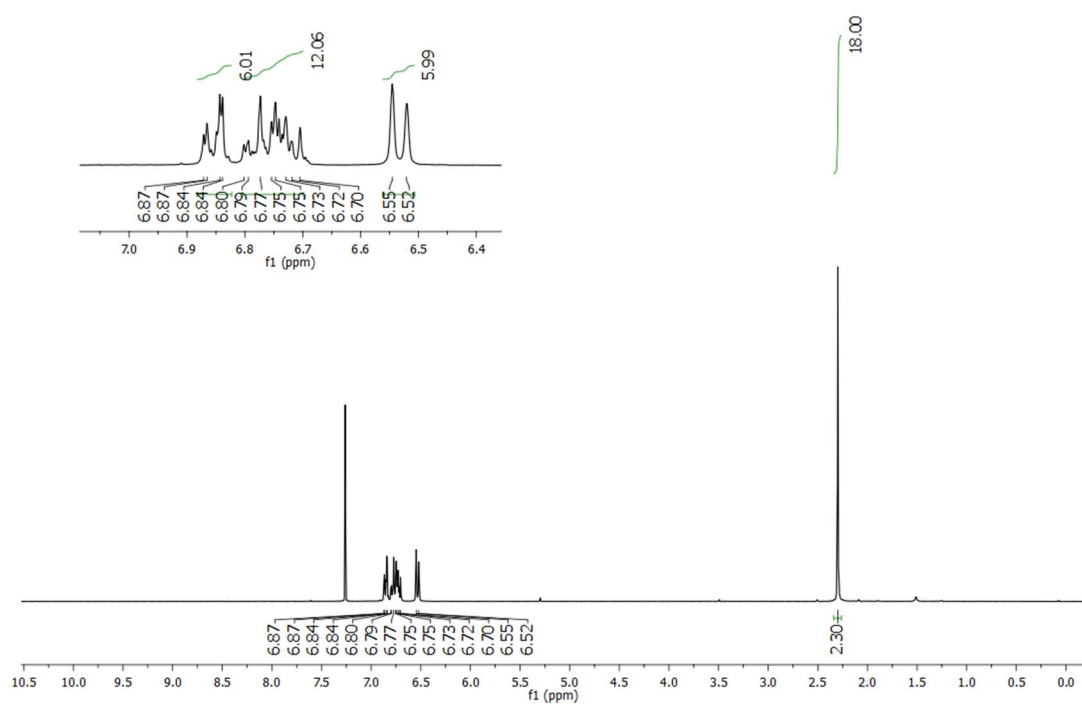
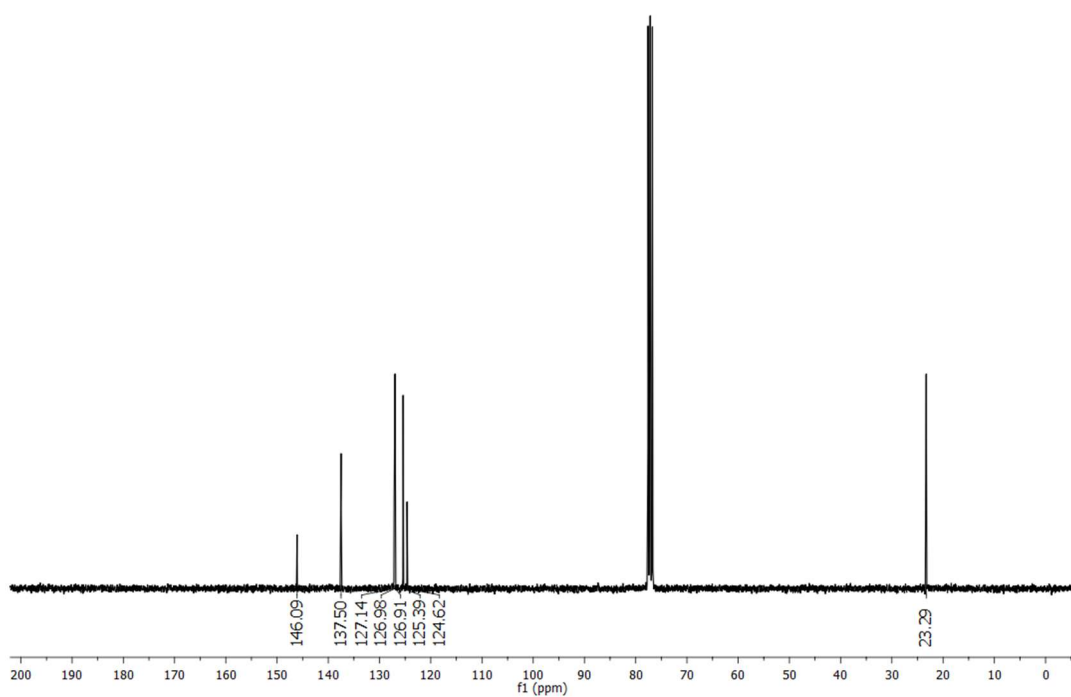


Figure A.114: ES⁺ HR-MS of 4-3.

34) Characterization of 4-8

Figure A.115: 300 MHz ^1H -NMR of 4-8 in CDCl_3 .Figure A.116: 75 MHz ^{13}C -NMR of 4-8 in CDCl_3 .

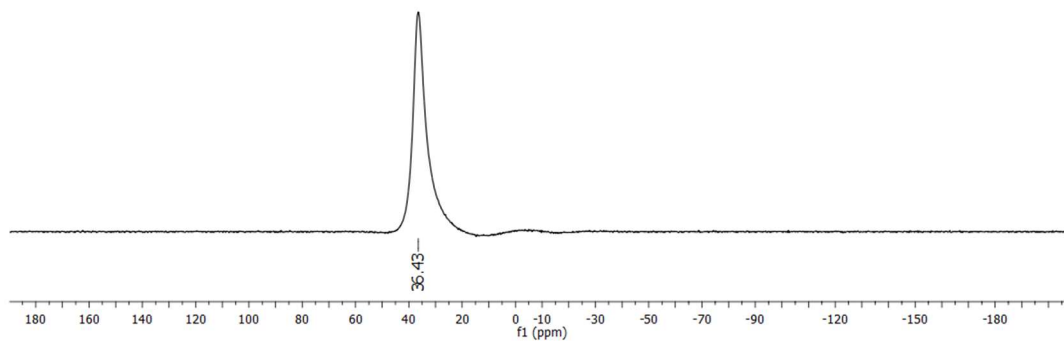


Figure A.117: 160 MHz ^{11}B -NMR of 4-8 in CDCl_3 .

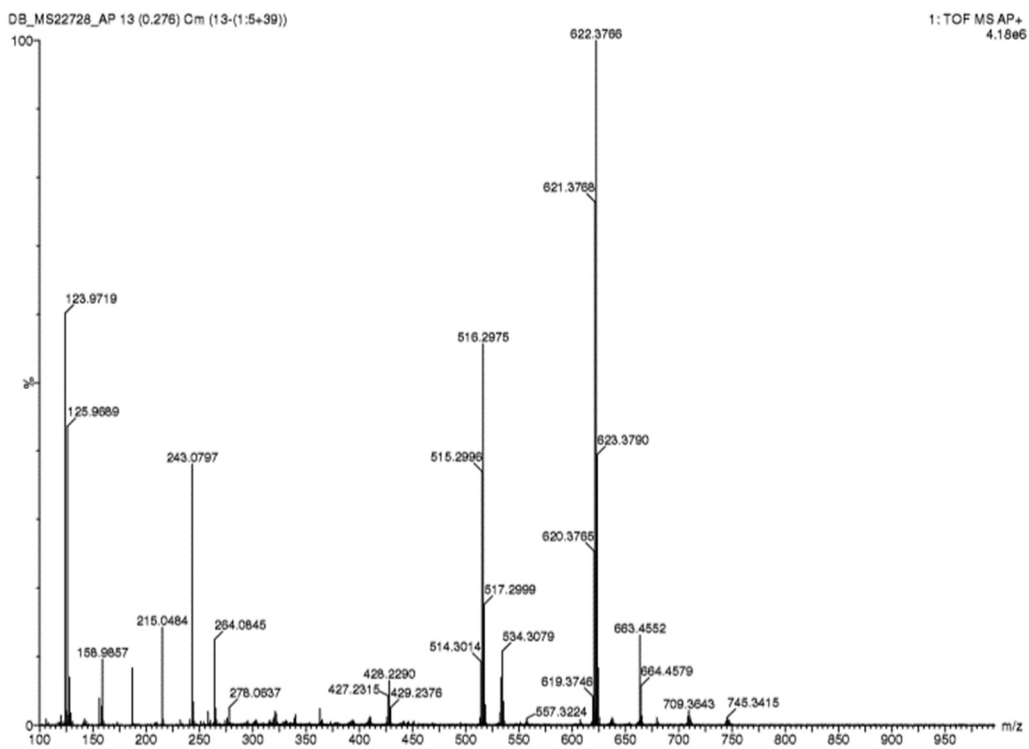
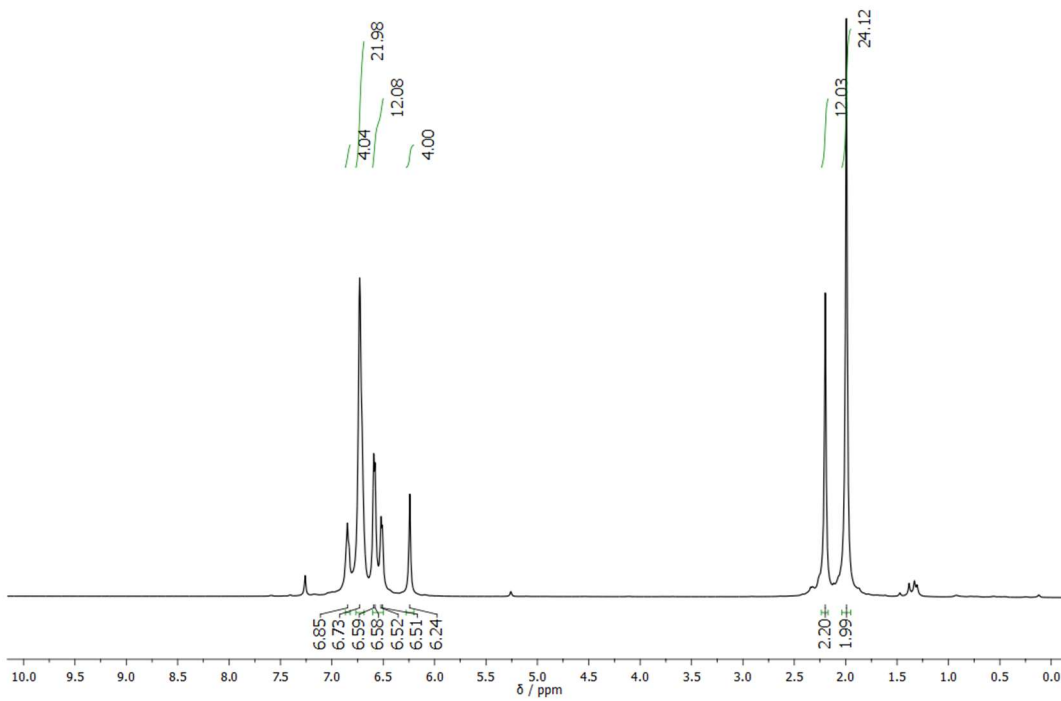
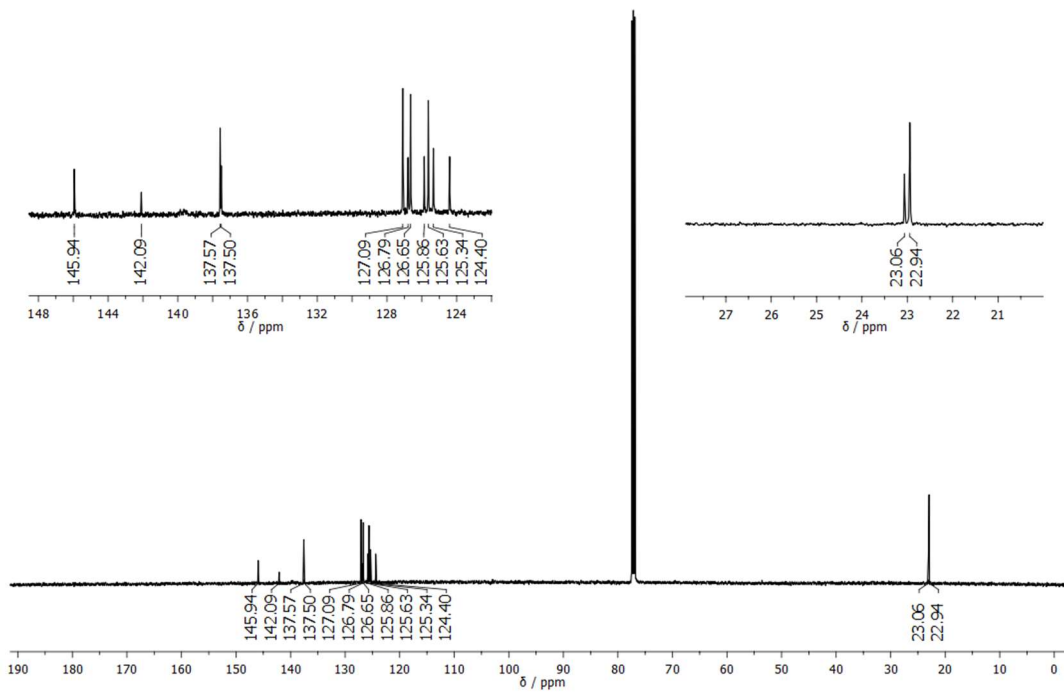


Figure A.118: AP⁺ HR-MS of 4-8.

35) Characterization of 4-9

Figure A.119: 500 MHz ^1H -NMR of 4-9 in CDCl_3 .Figure A.120: 126 MHz ^{13}C -NMR of 4-9 in CDCl_3 .

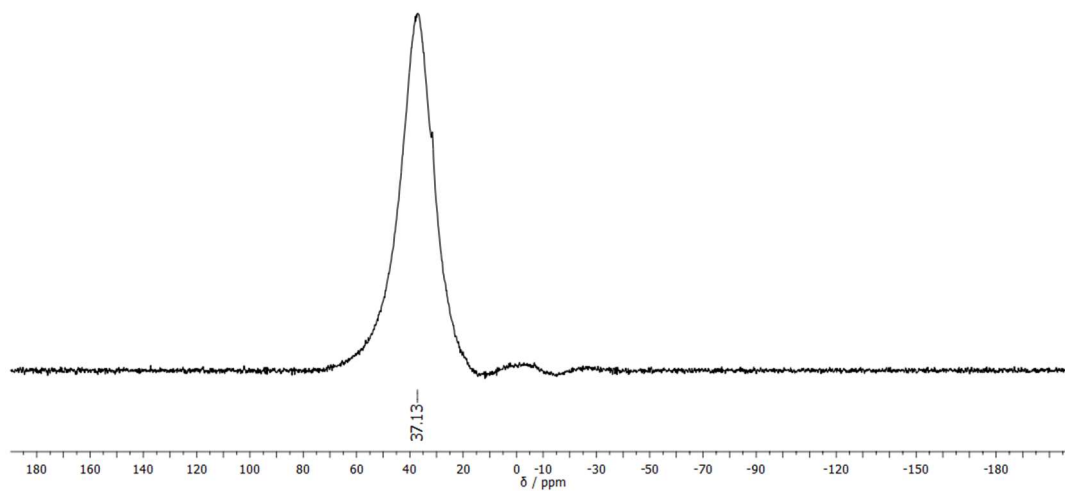


Figure A.121: 160 MHz ^{11}B -NMR of **4-9** in CDCl_3 .

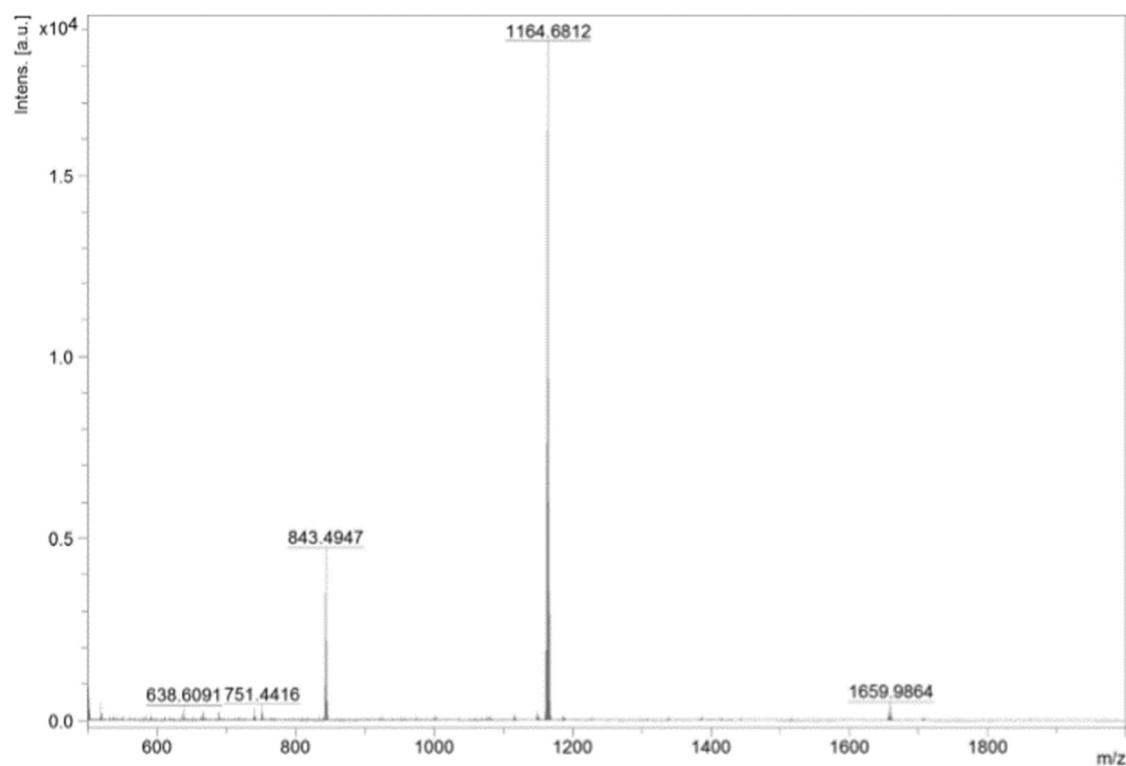
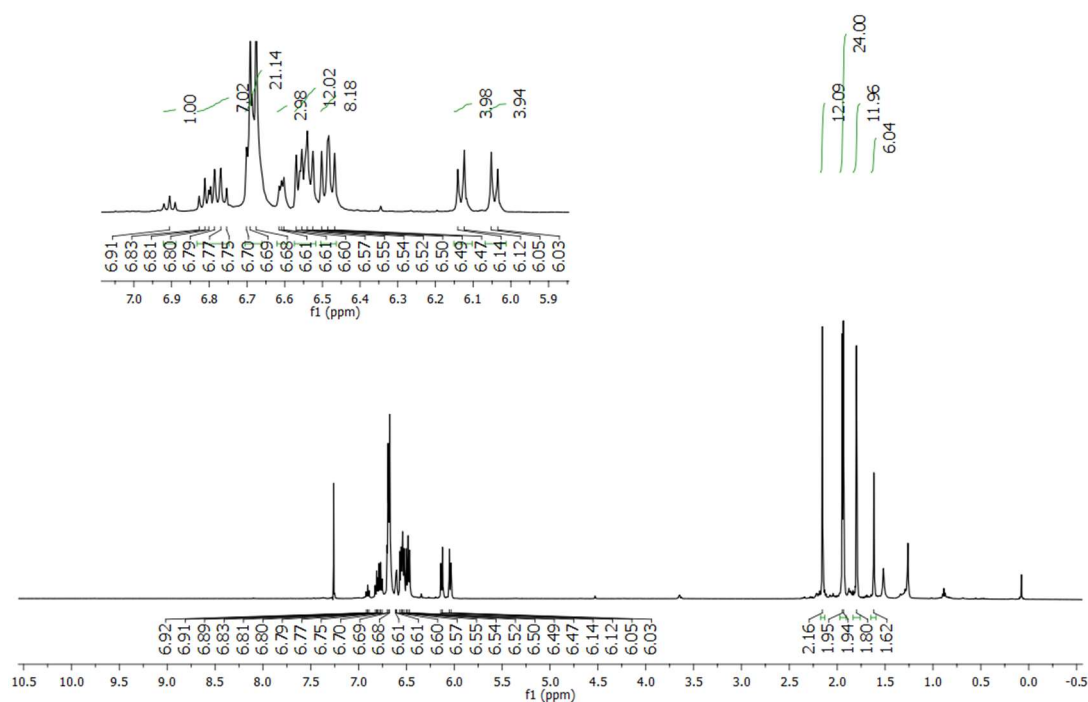
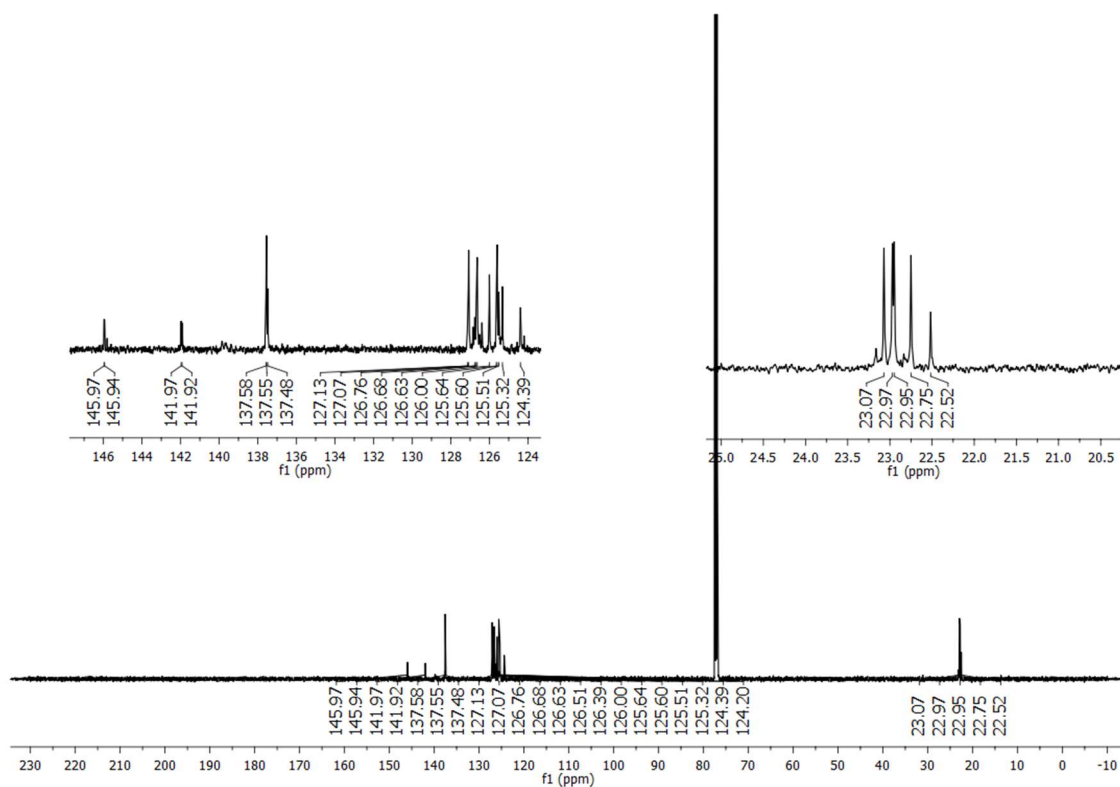


Figure A.122: MALDI+ HR-MS of **4-9**.

36) Characterization of 4-10

Figure A.123: 500 MHz ^1H -NMR of 4-10 in CDCl_3 .Figure A.124: 126 MHz ^{13}C -NMR of 4-10 in CDCl_3 .

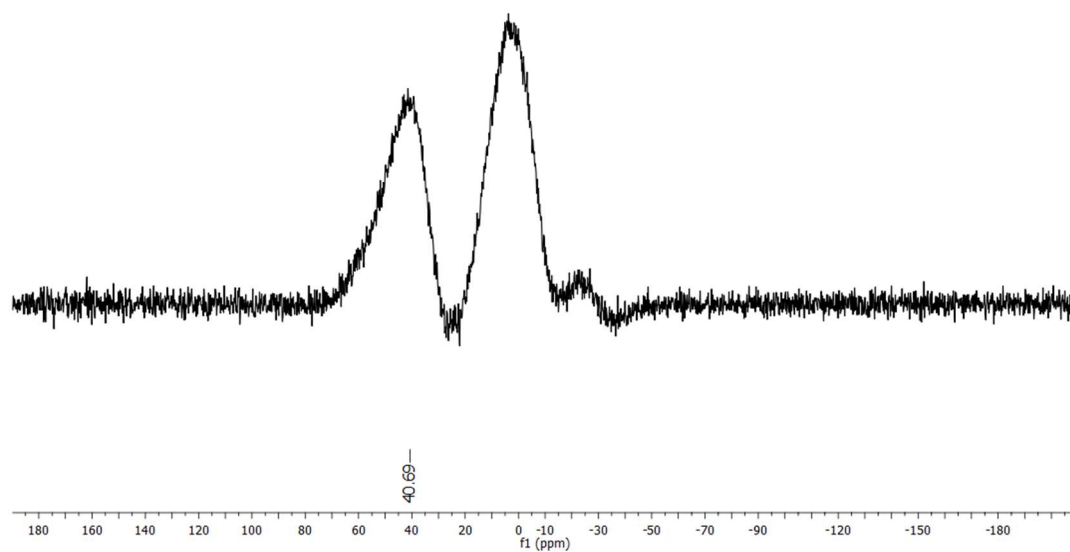


Figure A.125: 160 MHz ^{11}B -NMR of **4-10** in CDCl_3 (probe residual signal present from 10 to -10 ppm).

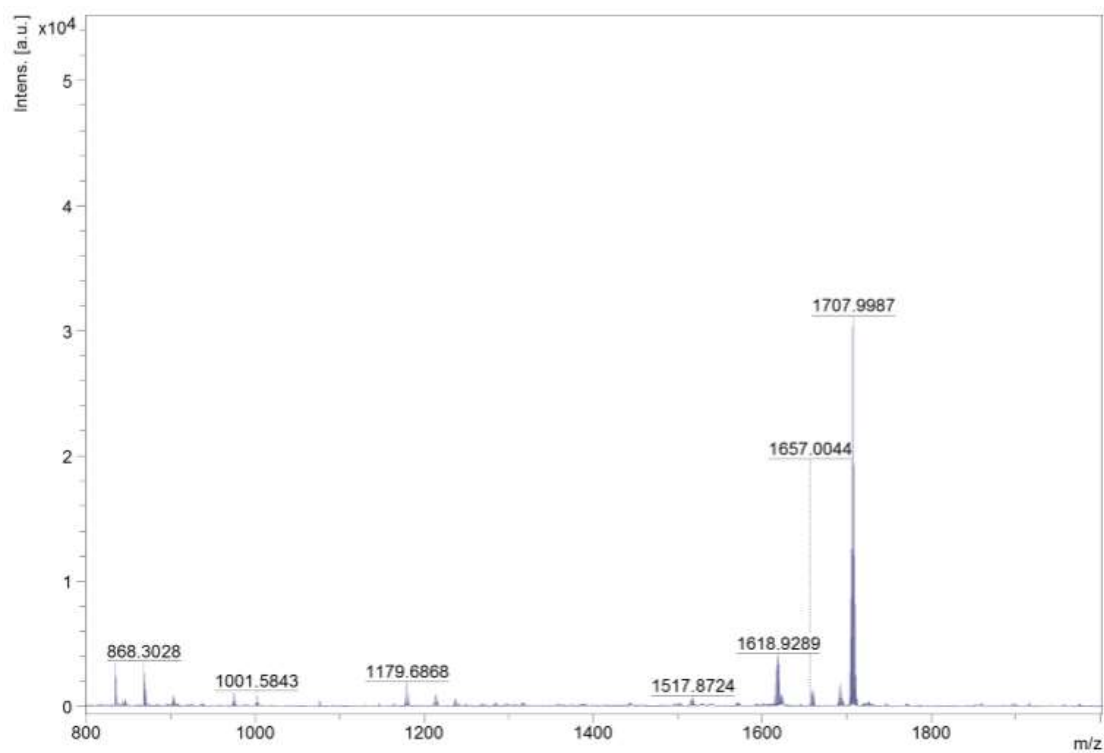
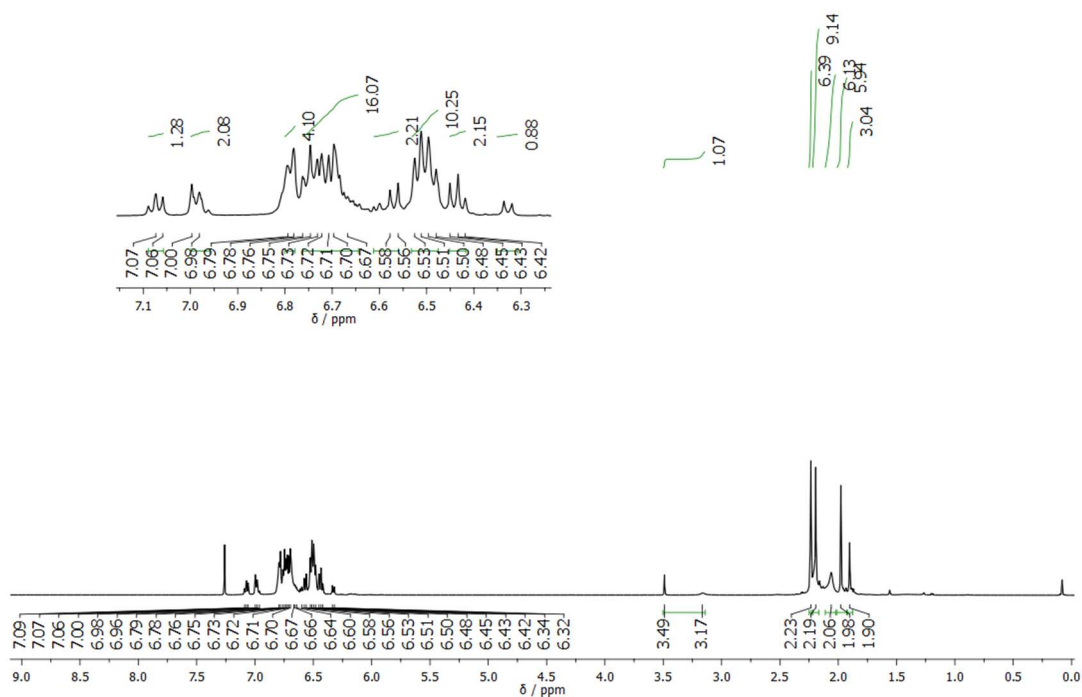
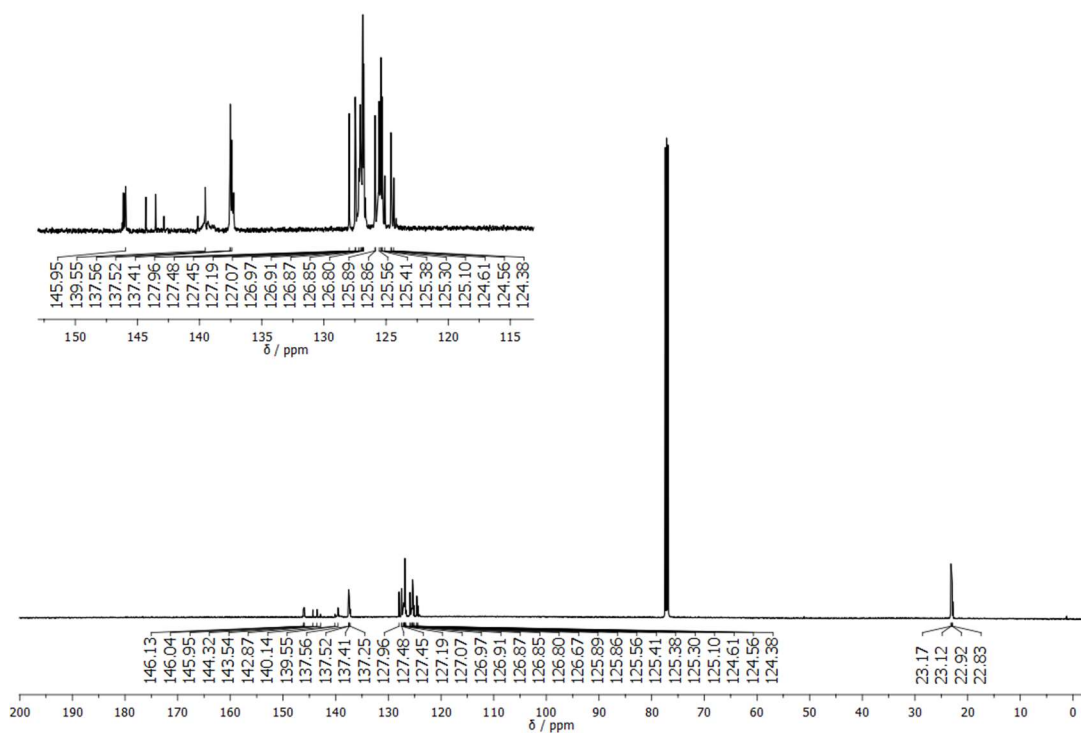


Figure A.126: MALDI $^+$ HR-MS of **4-10**.

37) Characterization of 4-11

Figure A.127: 500 MHz $^1\text{H-NMR}$ of 4-11 in CDCl_3 .Figure A.128: 126 MHz $^{13}\text{C-NMR}$ of 4-11 in CDCl_3 .

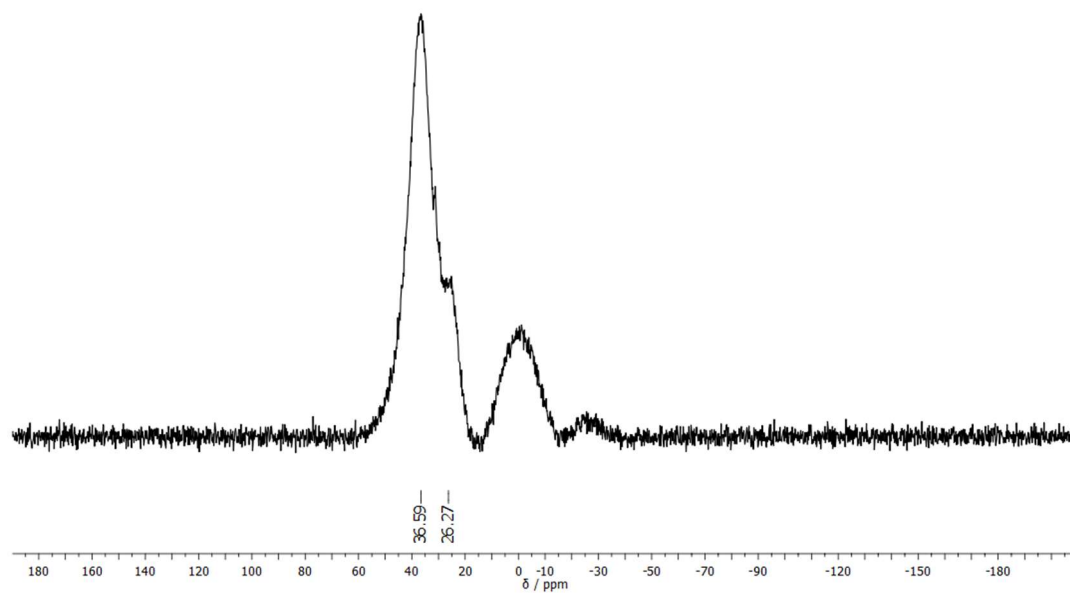


Figure A.129: 160 MHz ^{11}B -NMR of 4-11 in CDCl_3 (probe residual signal present from 10 to -10 ppm).

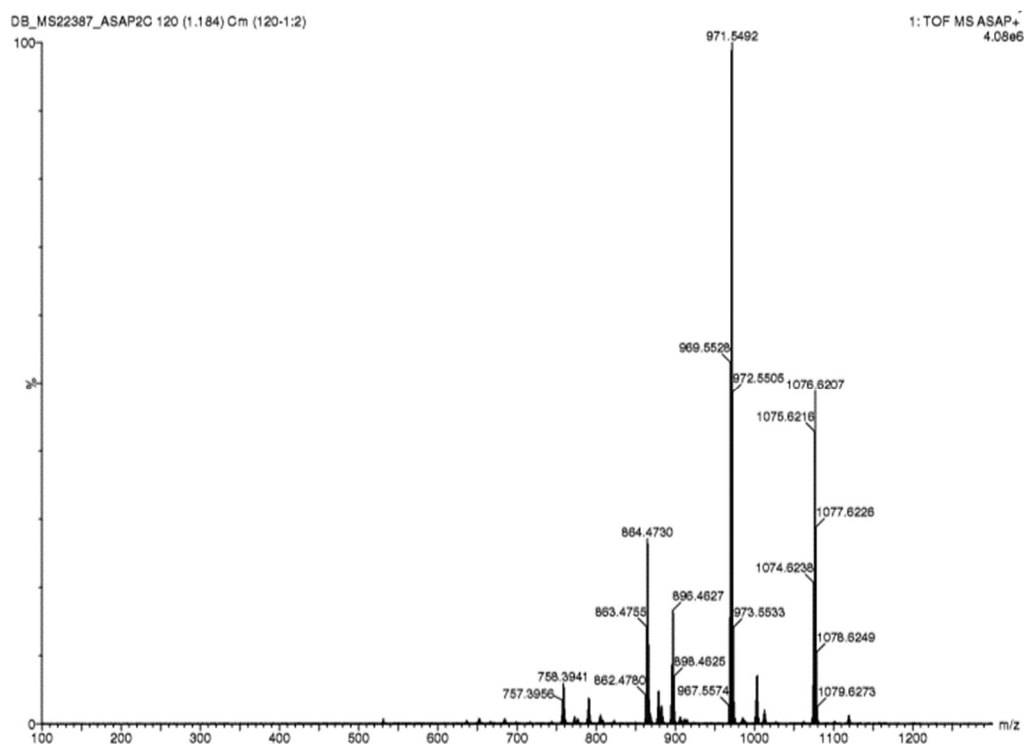
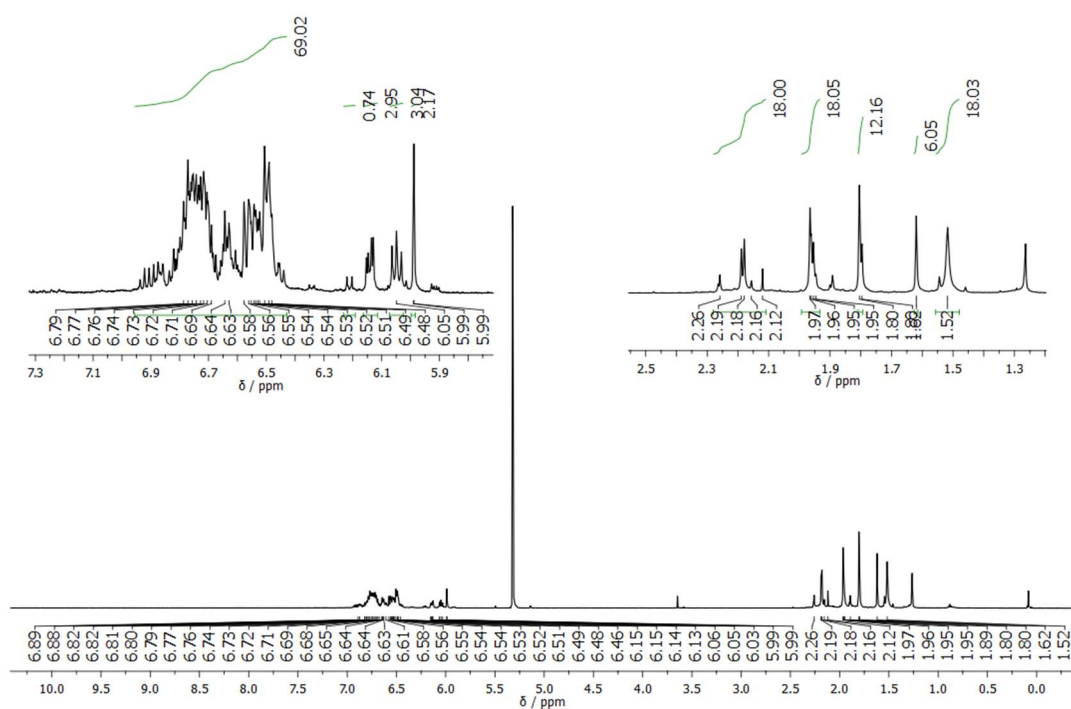
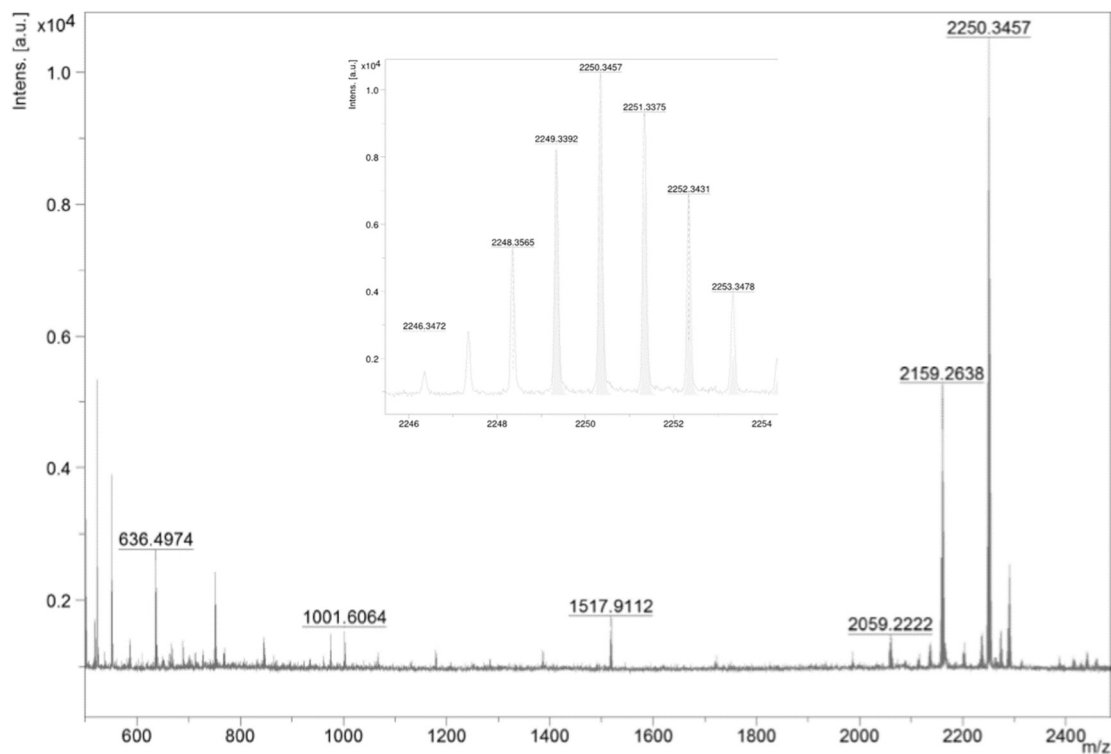


Figure A.130: ASAP⁺ HR-MS of 4-11.

38) Characterization of 4-12

Figure A.131: 500 MHz $^1\text{H-NMR}$ of **4-12** in CDCl_3 .Figure A.132: MALDI $^+$ HR-MS of **4-12**.

39) Characterization of 1,2-Di([1,1'-biphenyl]-3-yl)hydrazine (4-16)

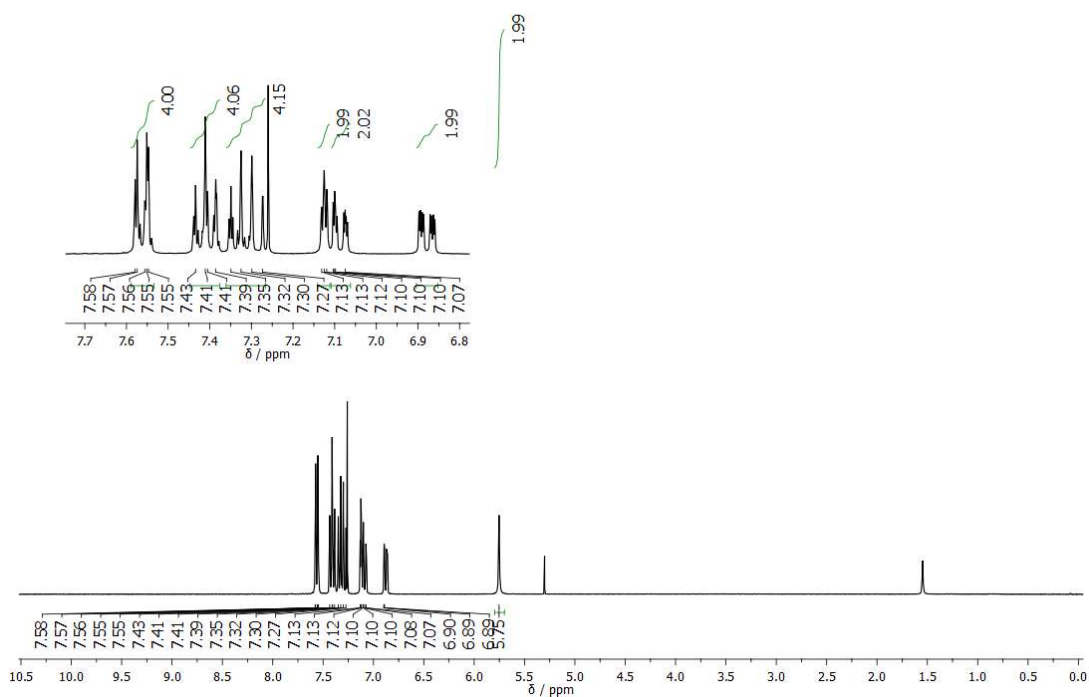


Figure A.133: 300 MHz $^1\text{H-NMR}$ of 4-16 in CDCl_3 (residual CH_2Cl_2 signal visible at 5.32 ppm).

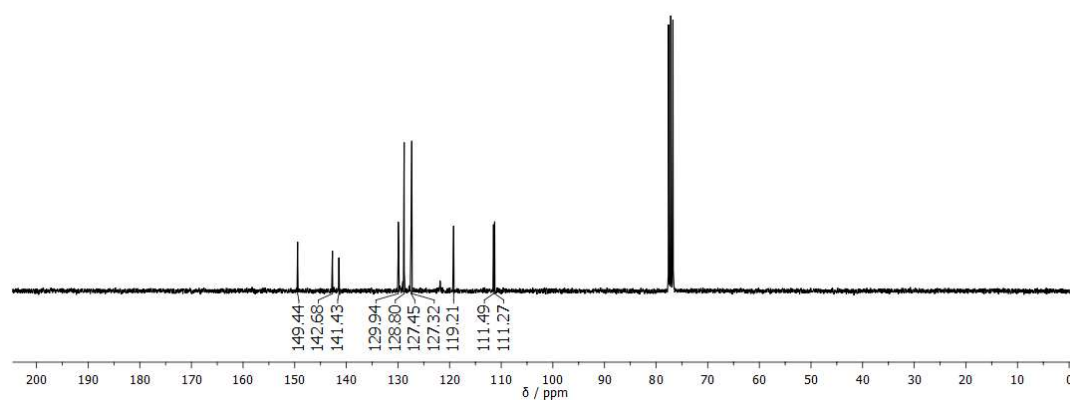


Figure A.134: 75 MHz $^{13}\text{C-NMR}$ of 4-16 in CDCl_3 .

Appendix A

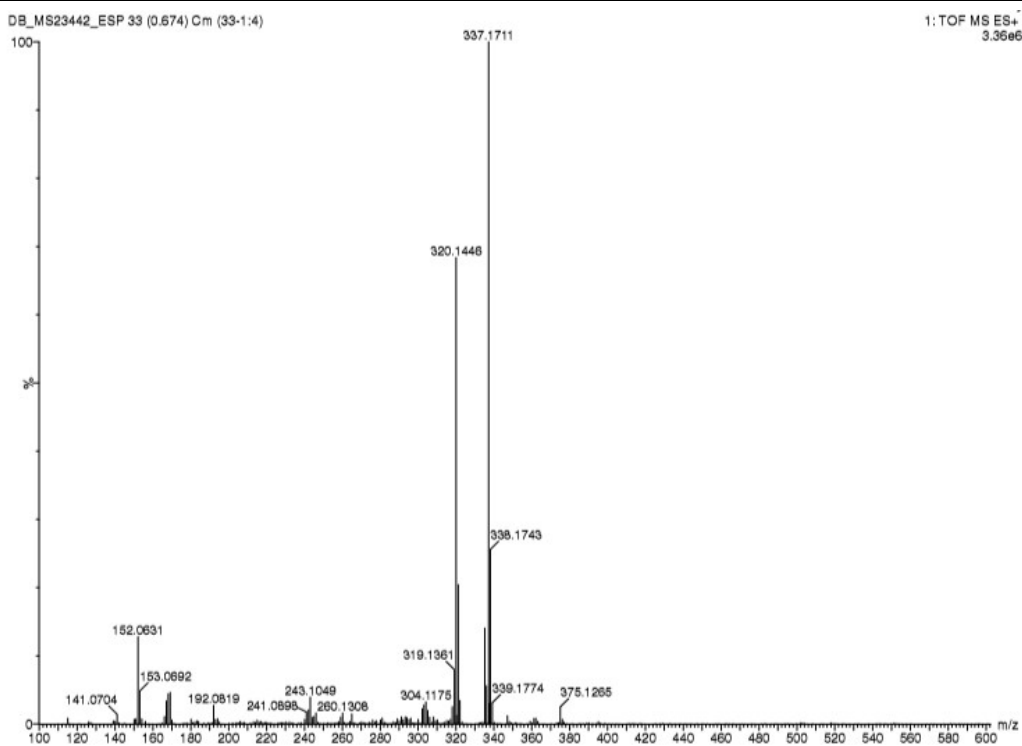
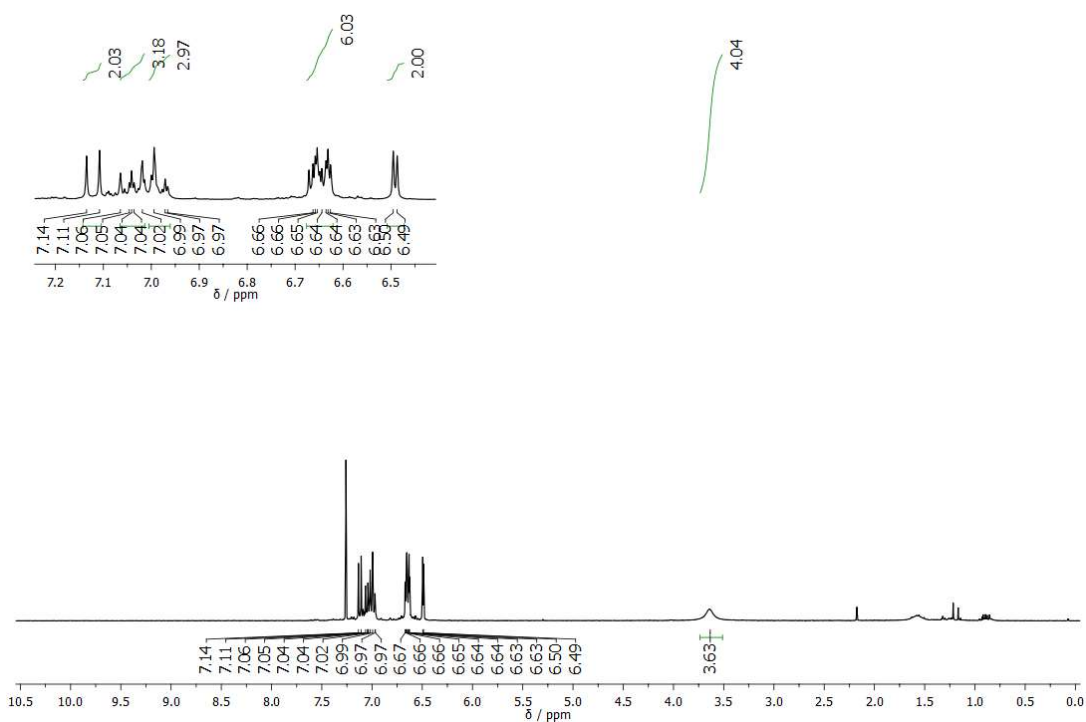
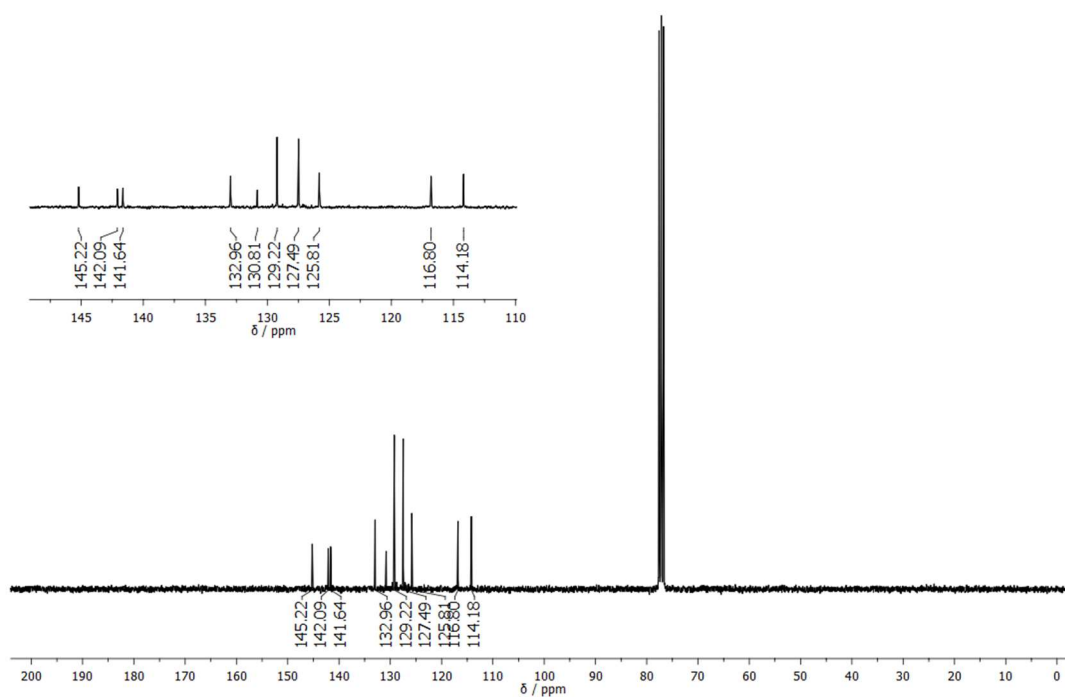


Figure A.135: ES⁺ HR-MS of 4-12.

40) Characterization of [1,1':2',1'':2'',1''':2''']-Quaterphenyl]-4'',5'-diamine (4-17)

Figure A.136: 300 MHz ¹H-NMR of 4-17 in CDCl₃.Figure A.137: 75 MHz ¹³C-NMR of 4-17 in CDCl₃.

Appendix A

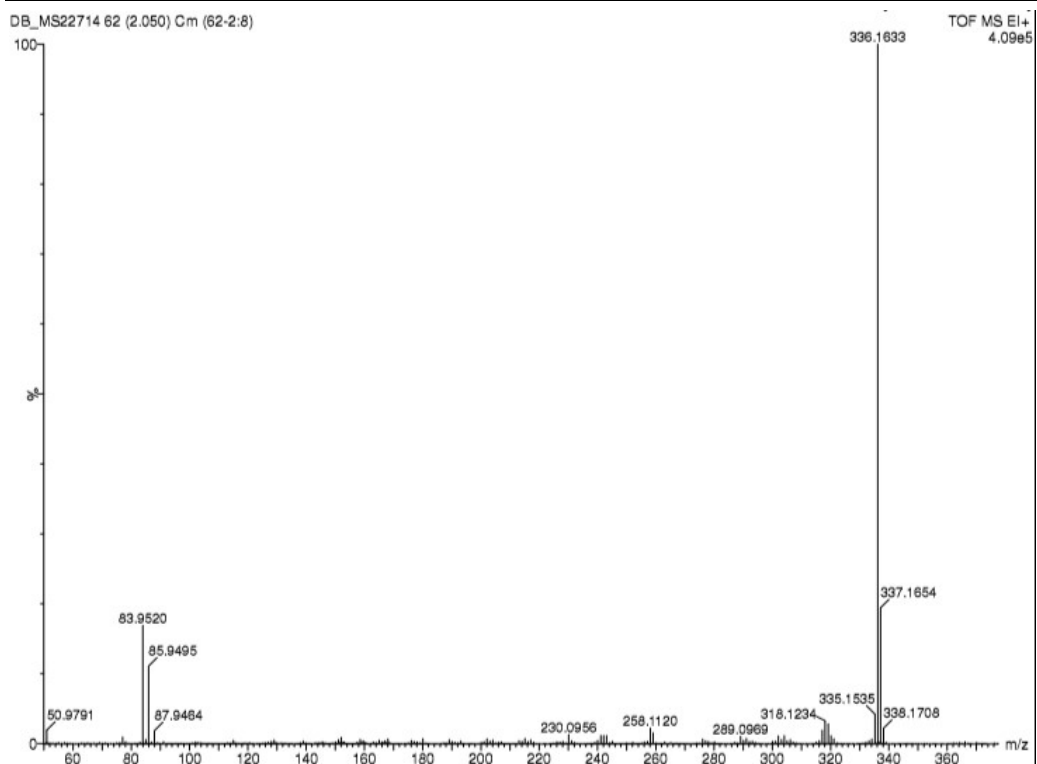
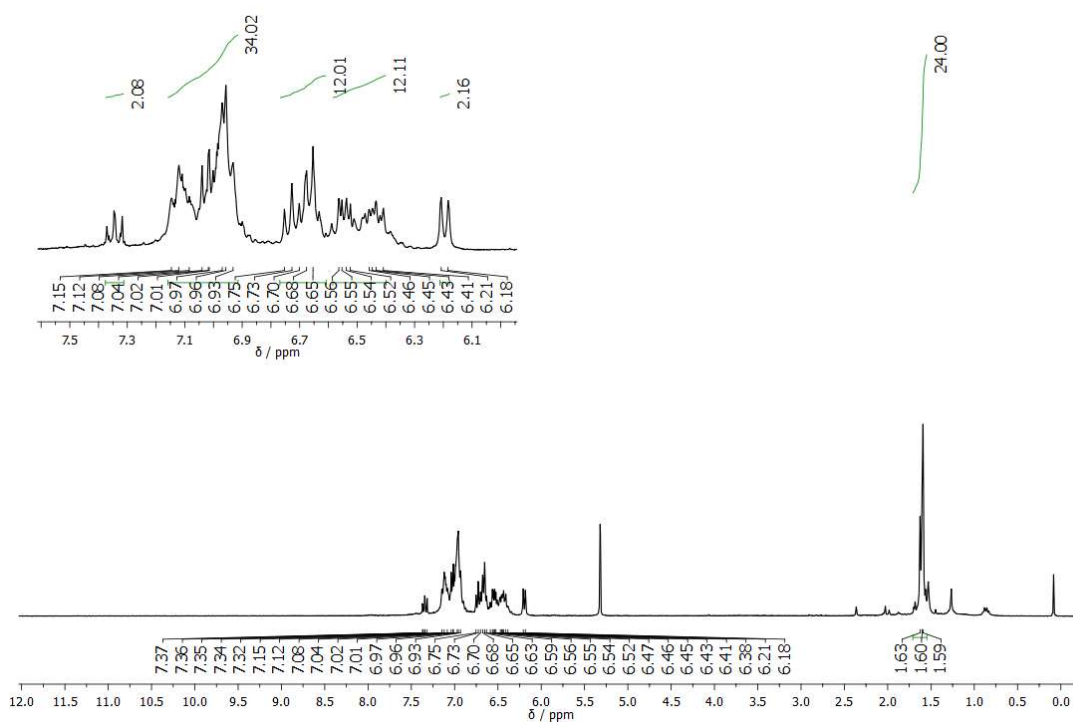
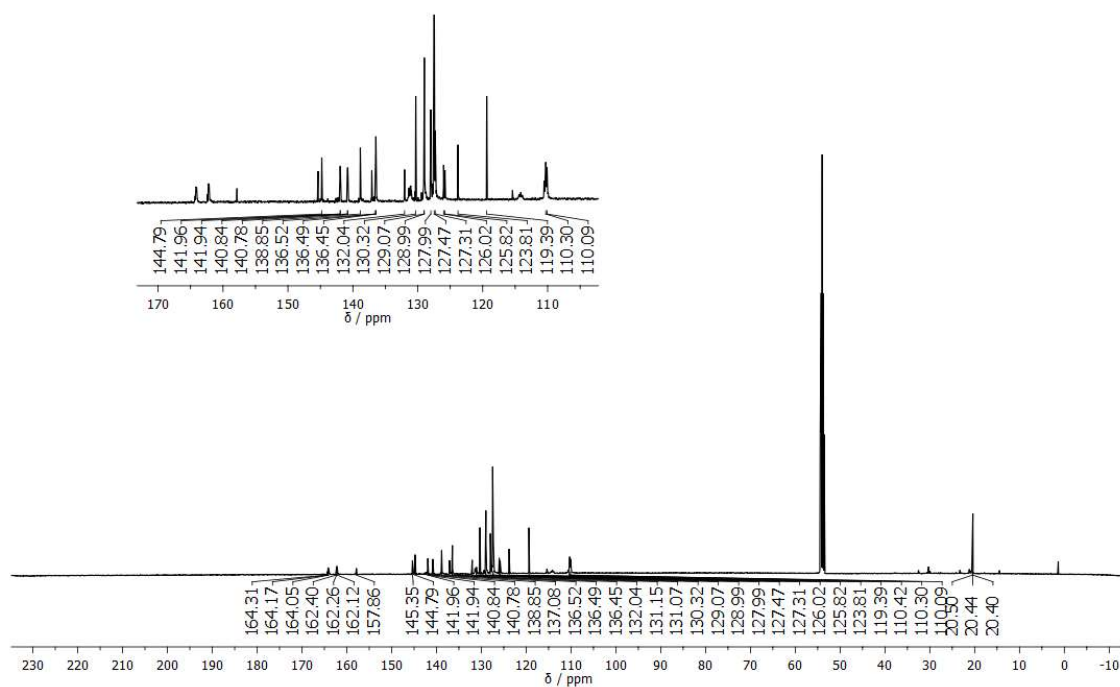


Figure A.138: EI⁺ HR-MS of 4-17.

41) Characterization of 4-19

Figure A.139: 300 MHz ^1H -NMR of 4-19 in CD_2Cl_2 .Figure A.140: 126 MHz ^{13}C -NMR of 4-19 in CD_2Cl_2 .

Appendix A

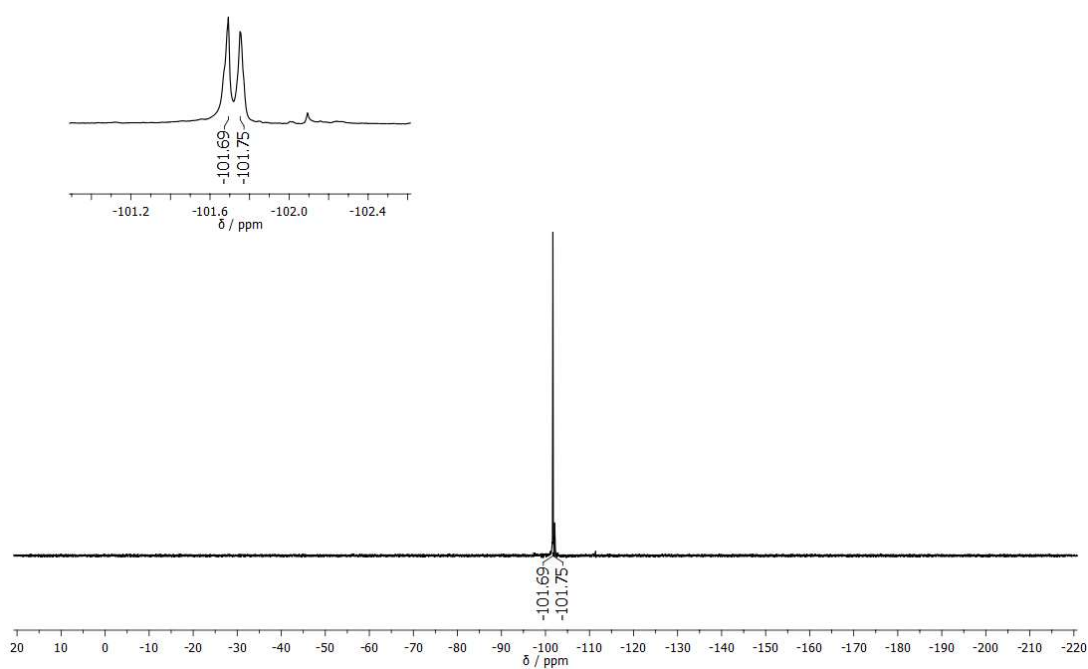


Figure A.141: 376 MHz ^{19}F -NMR of 4-19 in CD_2Cl_2 .

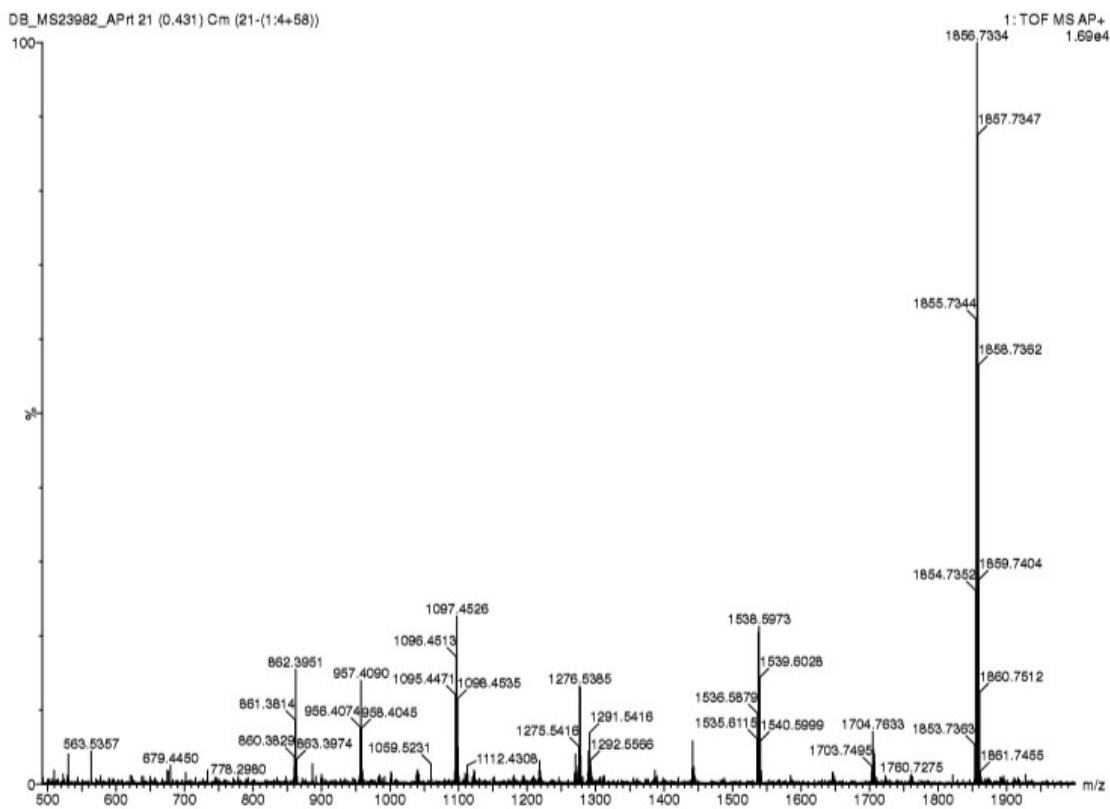
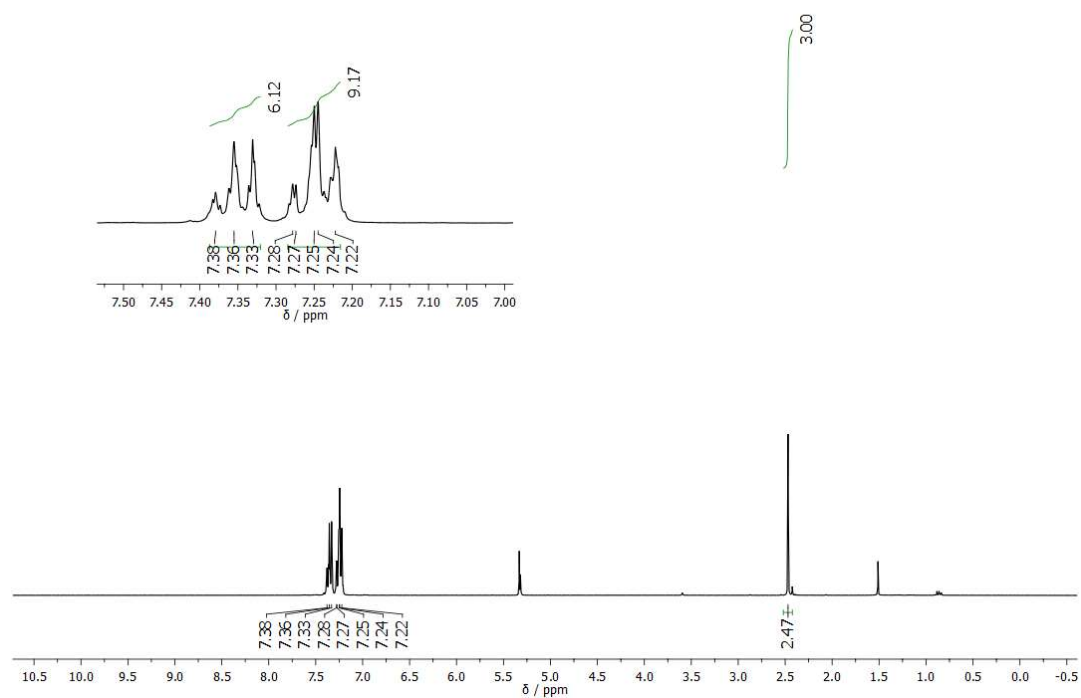
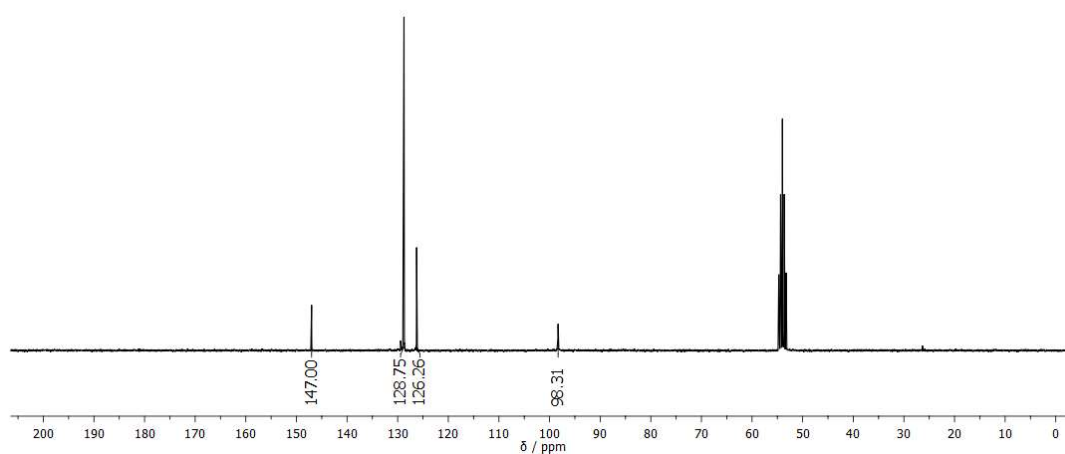


Figure A.142: AP⁺ HR-MS of 4-19.

Chapter 5

42) Characterization of B,B',B''-Triethynyl-N,N',N''-tri(phenyl)-borazine (5-2)

Figure A.143: 300 MHz ^1H -NMR of **5-2** in CD_2Cl_2 .Figure A.144: 75 MHz ^{13}C -NMR of **5-2** in CD_2Cl_2 .

Appendix A

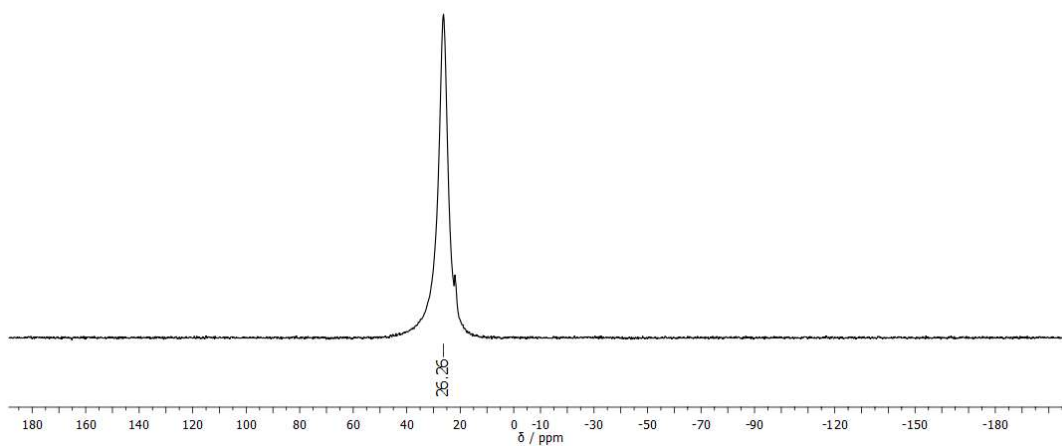


Figure A.145: 160 MHz ^{11}B -NMR of **5-2** in CDCl_3 .

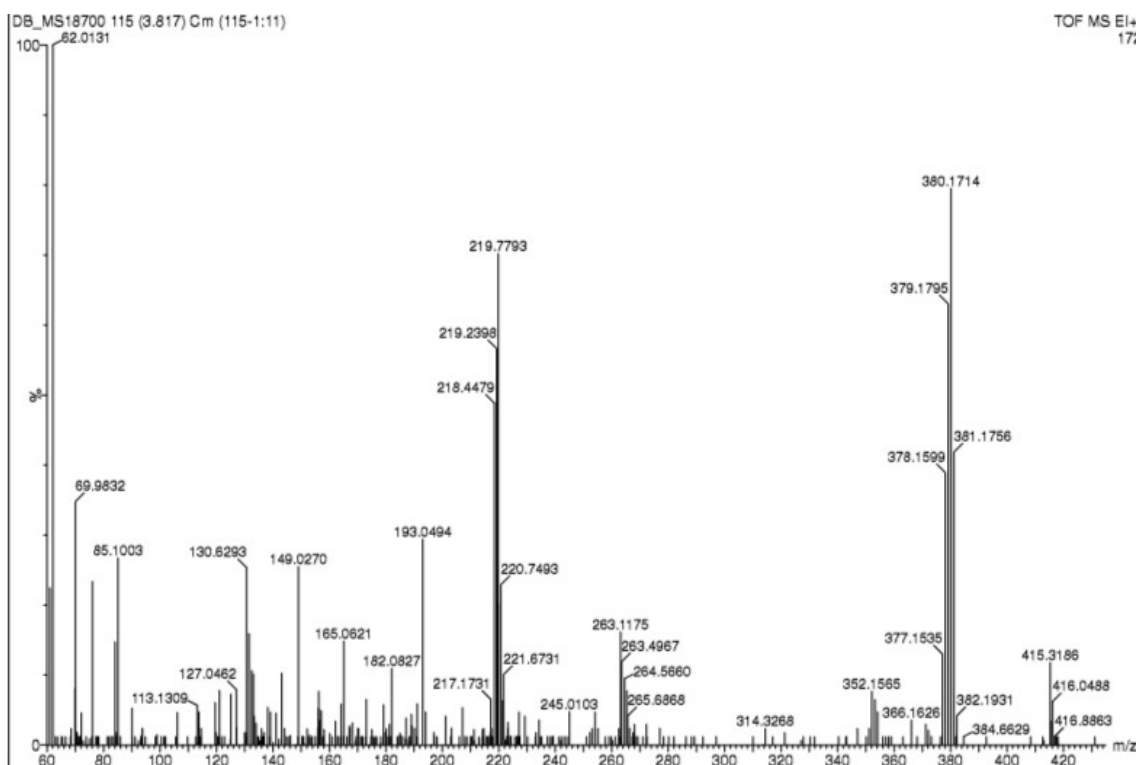
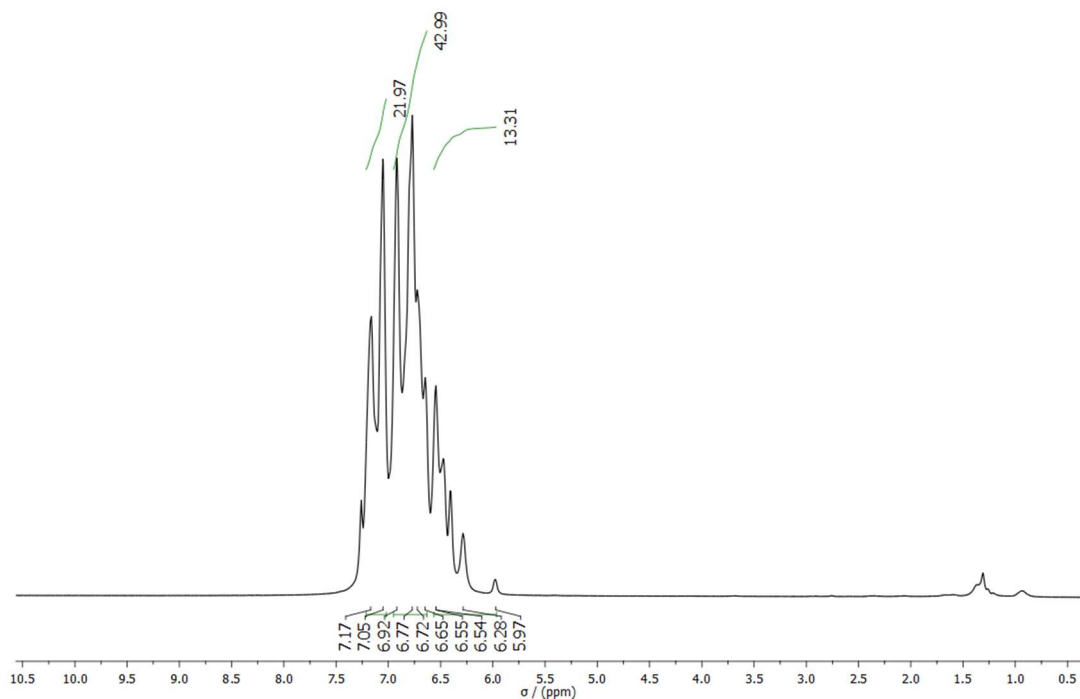
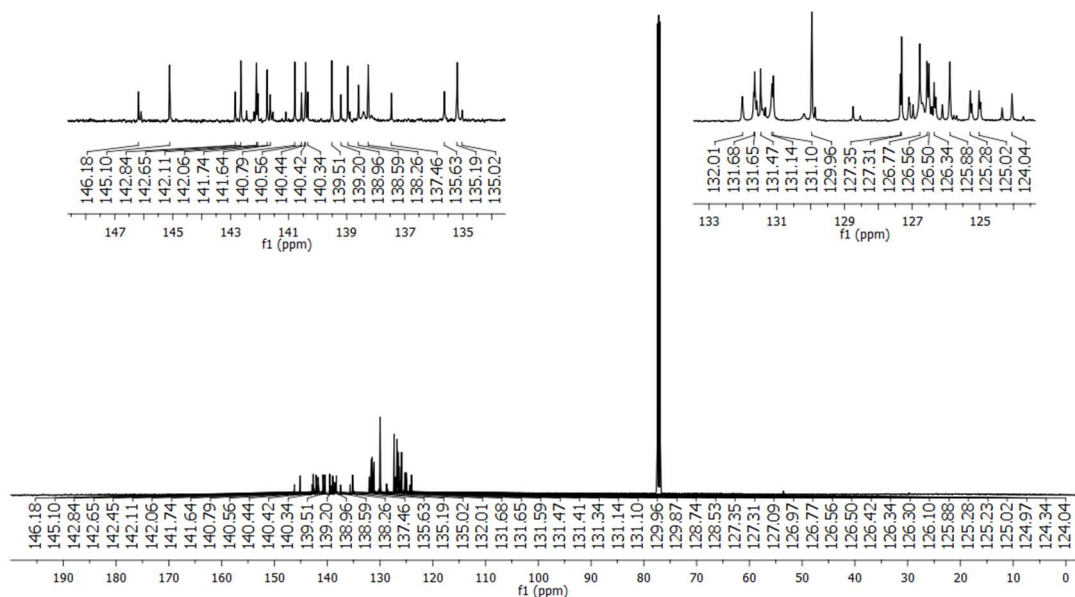


Figure A.146: EI⁺ HR-MS of **5-2**.

43) B,B',B''-Tri(3',4'-diphenyl-1,1':2',1''-terphenyl)-N,N',N''-tri(phenyl)-borazine (5-4)**Figure A.147:** 500 MHz $^1\text{H-NMR}$ of **5-4** in CDCl_3 .**Figure A.148:** 126 MHz $^{13}\text{C-NMR}$ of **5-4** in CDCl_3 .

Appendix A

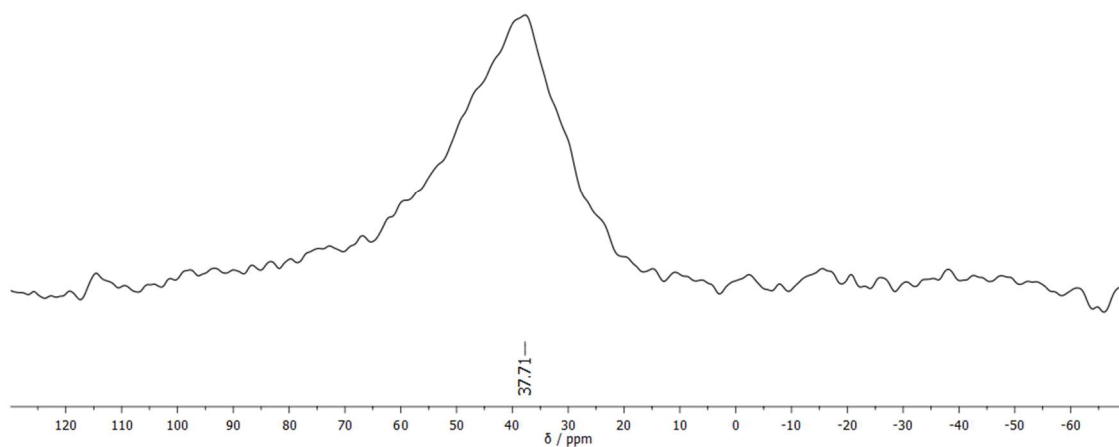


Figure A.149: 224 MHz ^{11}B -NMR of 5-4 in C_6D_6 .

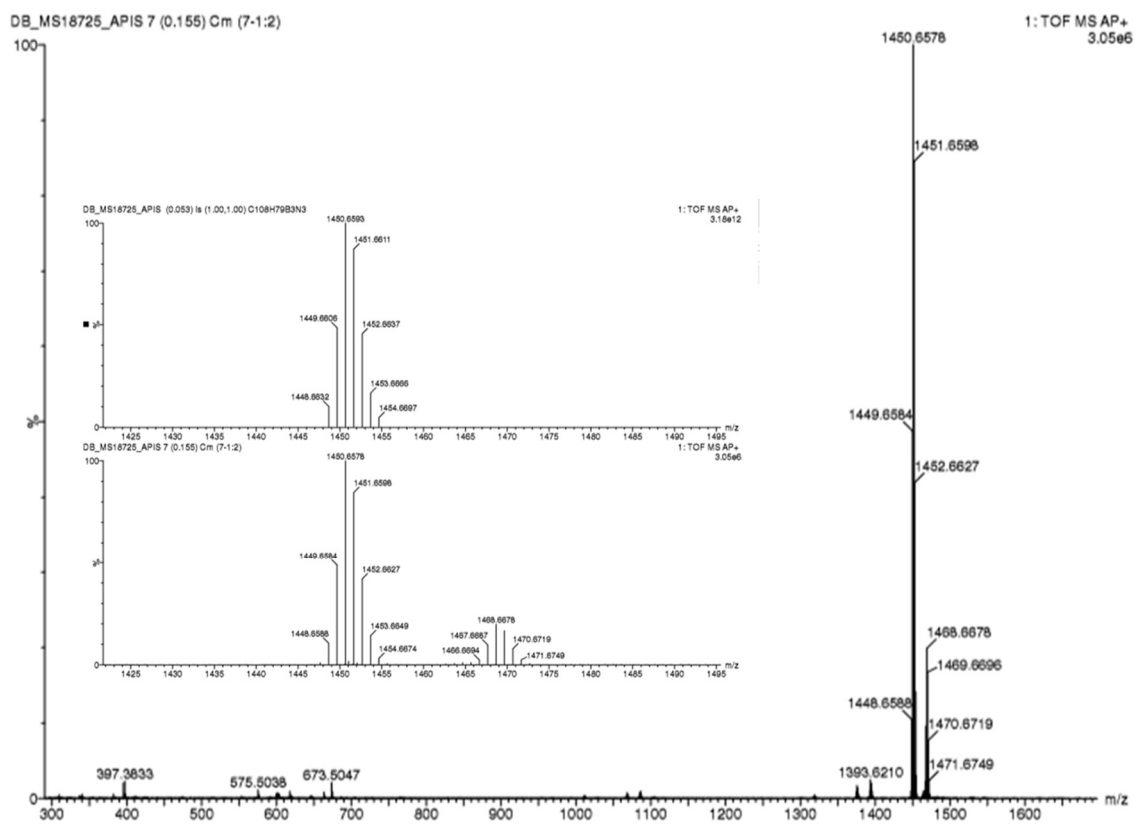


Figure A.150: AP⁺ HR-MS of 5-4.

Appendix A

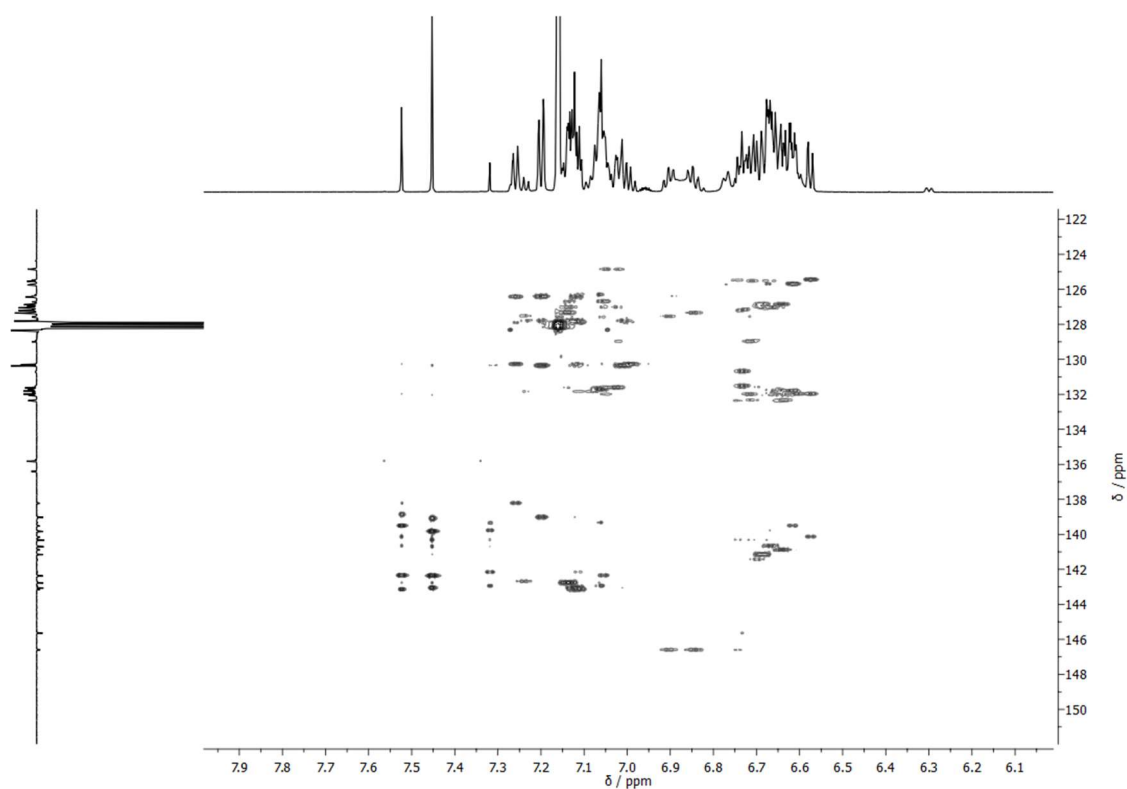


Figure A.153: ^1H - ^{13}C HMSC-NMR of **5-4** in C_6D_6 .

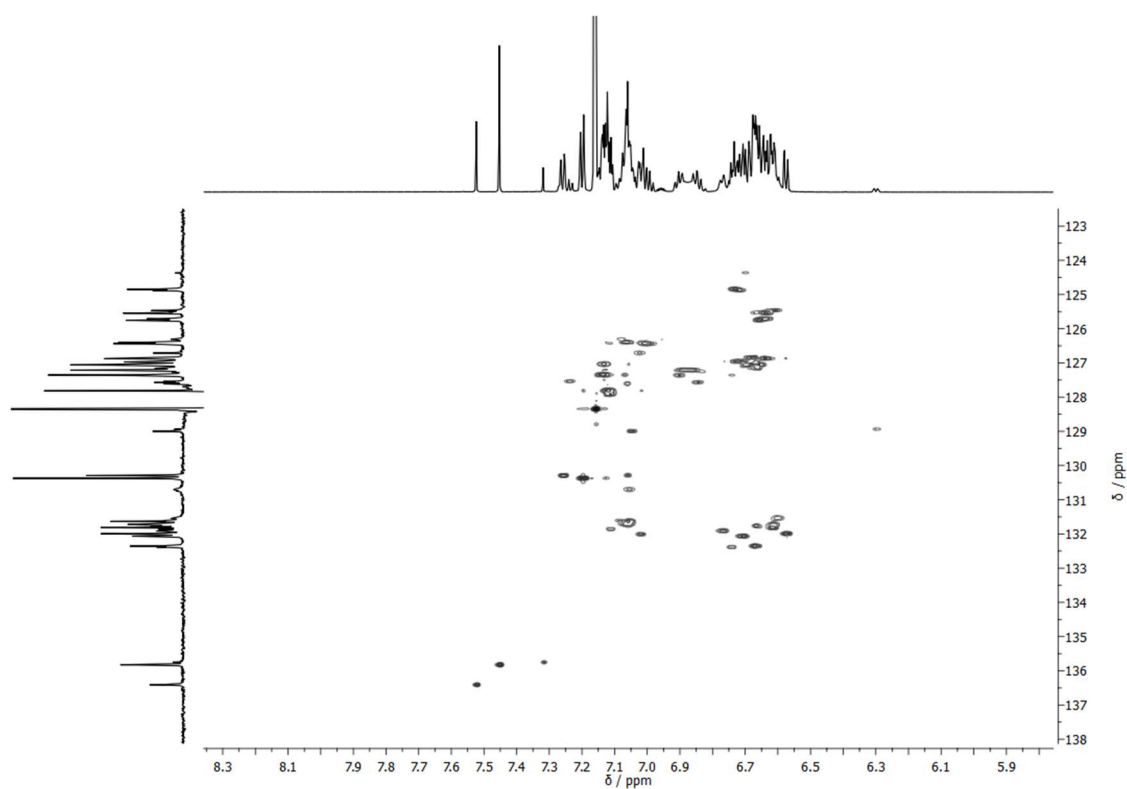
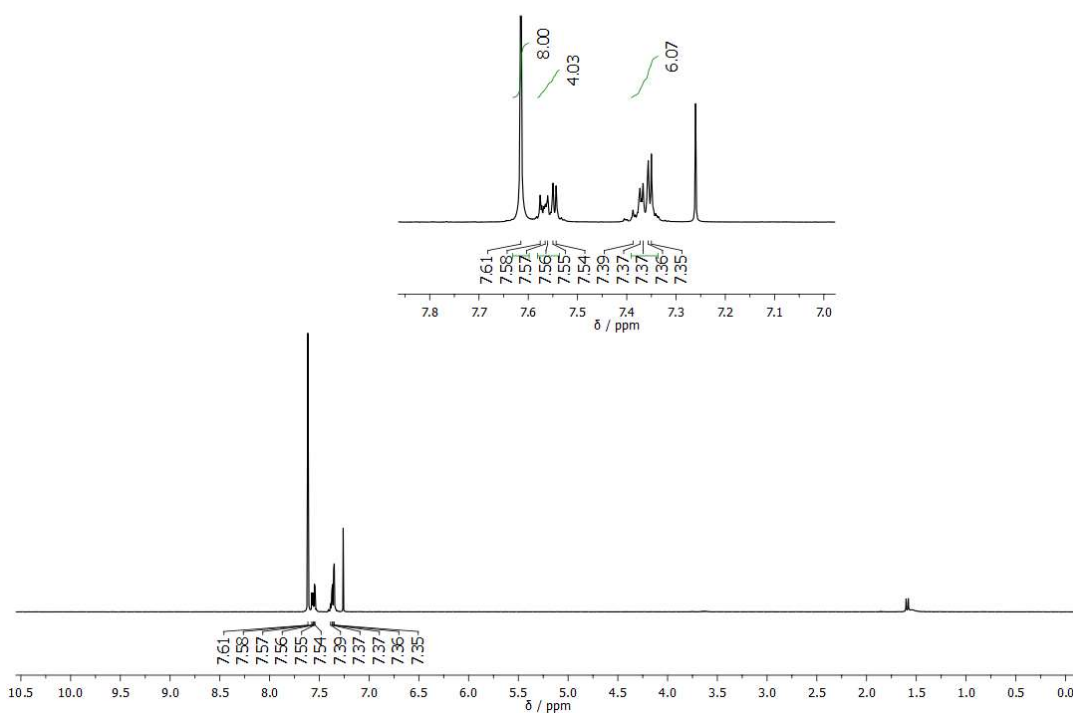
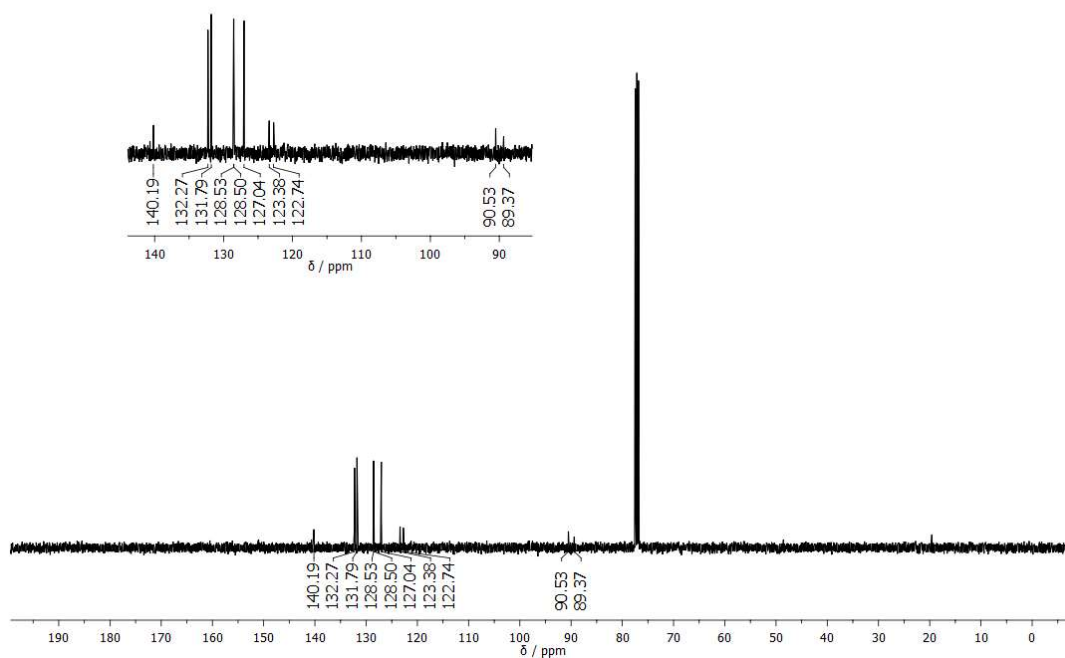


Figure A.154: ^1H - ^{13}C HQMC-NMR of **5-4** in C_6D_6 .

44) Characterization of 1,4-Bis(phenylethynyl)benzene (5-7)

Figure A.155: 300 MHz $^1\text{H-NMR}$ of 5-7 in CDCl_3 .Figure A.156: 100 MHz $^{13}\text{C-NMR}$ of 5-7 in CDCl_3 .

Appendix A

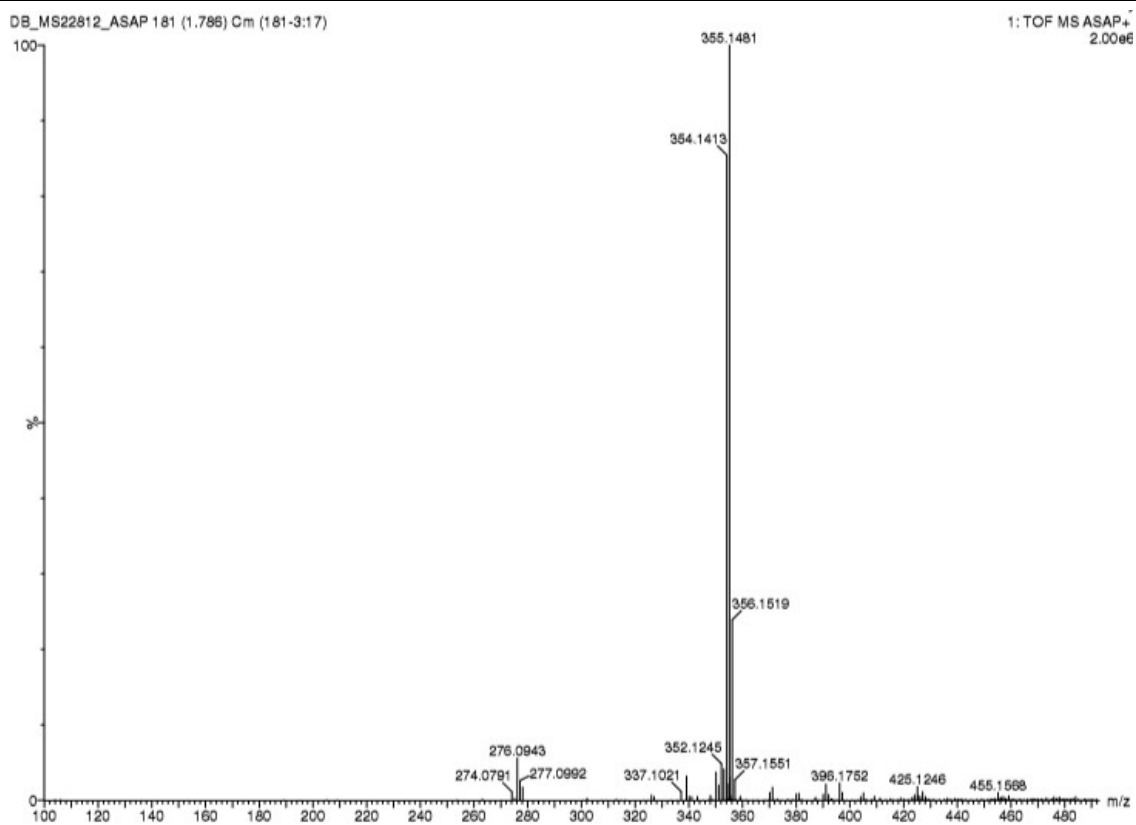
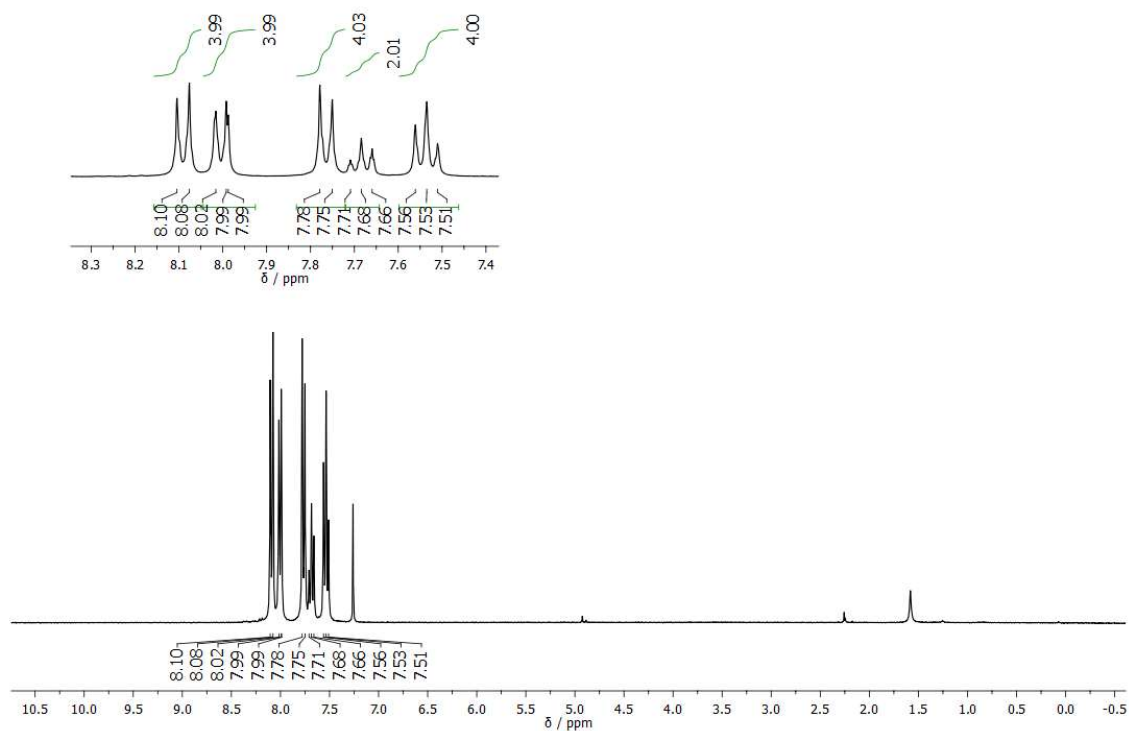
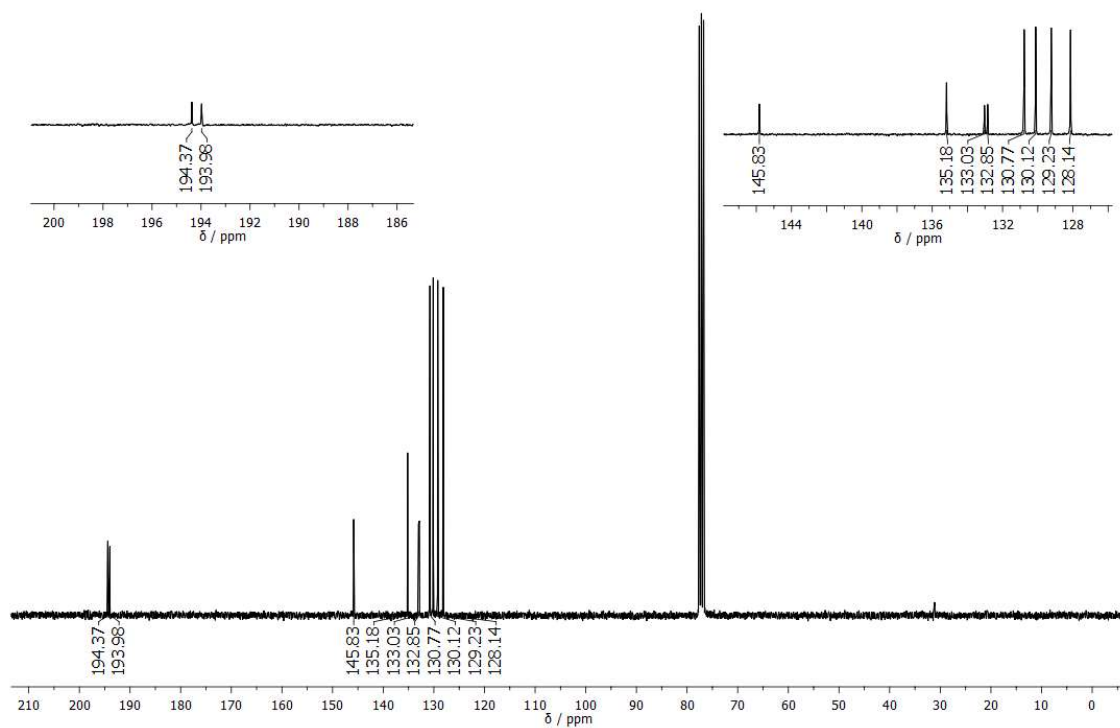


Figure A.157: ASAP⁺ HR-MS of 5-7.

45) Characterization of 2,2'-(1,4-Phenylene)bis(1-phenylethane-1,2-dione) (5-8)**Figure A.158:** 300 MHz $^1\text{H-NMR}$ of 5-8 in CDCl_3 .**Figure A.159:** 75 MHz $^1\text{H-NMR}$ of 5-8 in CDCl_3 .

Appendix A

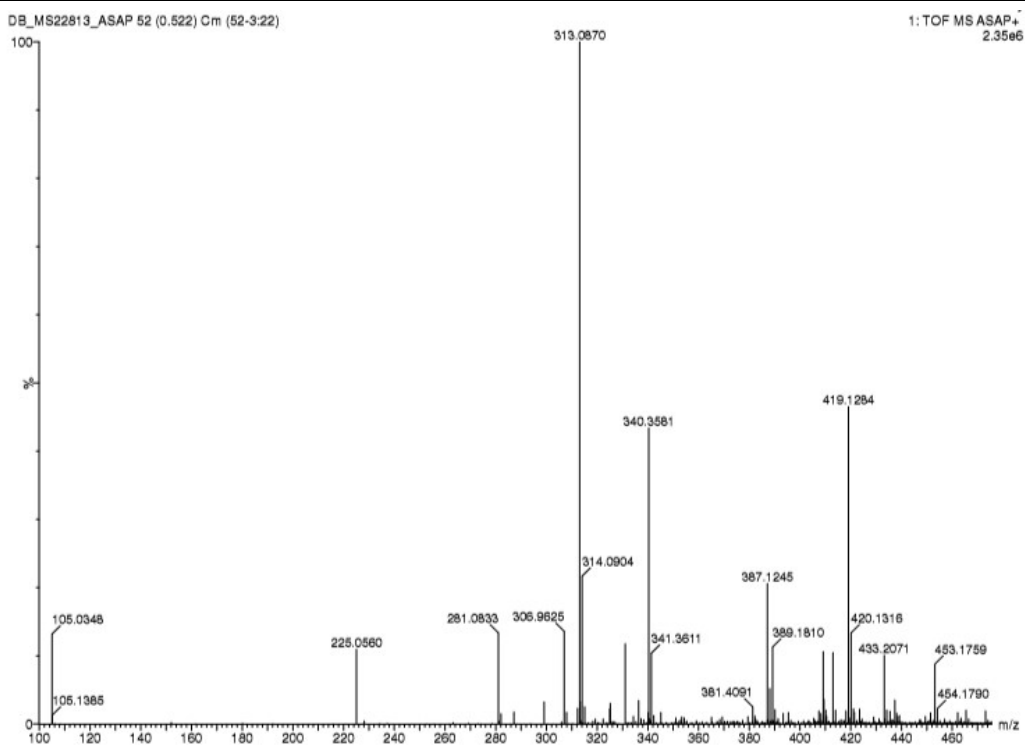


Figure A.160: ASAP⁺ HR-MS of 5-8.

Appendix A

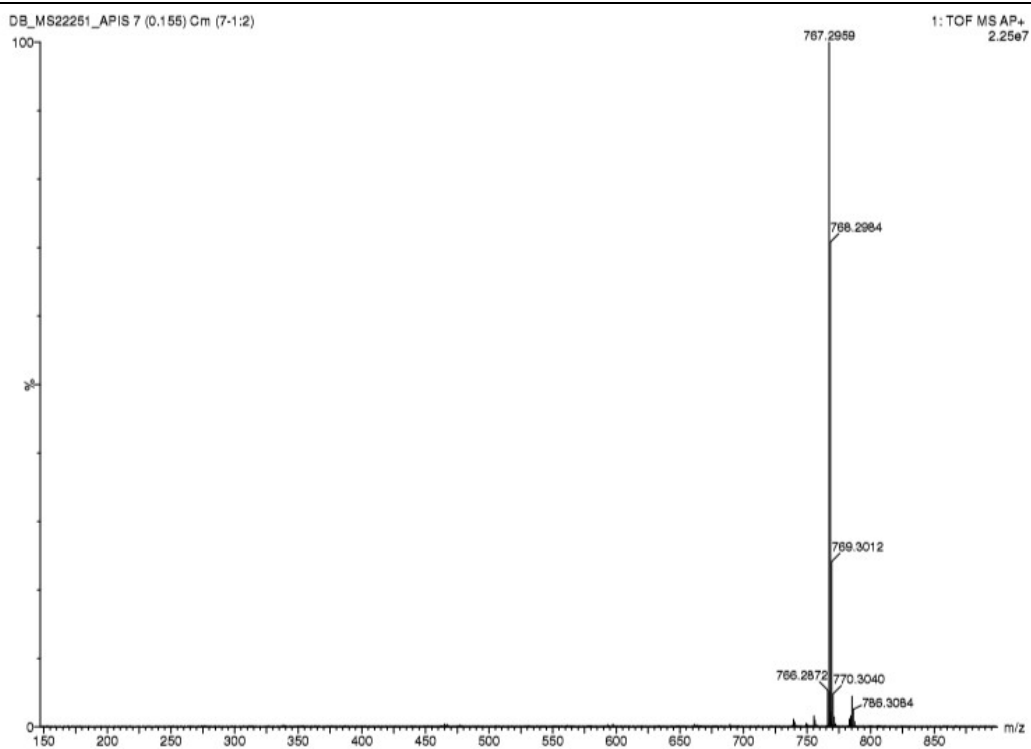


Figure A.163: AP⁺ HR-MS of 5-10.

